



Novus Scientia 2022

**19. Medzinárodná vedecká konferencia doktorandov strojnícckych fakúlt
technických univerzít a vysokých škôl**

Novus Scientia 2022

**Zborník príspevkov z XIX. Medzinárodnej vedeckej
konferencie doktorandov strojnícckych fakúlt technických univerzít a vysokých škôl**

20. 1. 2022

Strojnícka fakulta

Technická univerzita v Košiciach

Zameranie konferencie:

- Automatizácia, mechatronika a robotika
- Technologické a materiálové inžinierstvo
- Manažment, priemyselné a digitálne inžinierstvo
- Konštrukčné a procesné inžinierstvo
- Špeciálne inžinierske procesológie

Vedecký a organizačný výbor konferencie

Patronát konferencie

Dr.h.c. mult. prof. Ing. Jozef Živčák, PhD., MPH, Technická univerzita v Košiciach, Slovensko

Garant konferencie

prof. Ing. Ján Slota, PhD., Technická univerzita v Košiciach, Slovensko

Vedecký výbor konferencie

prof. Ing. Jozef Bocko, CSc., Technická univerzita v Košiciach, Slovensko

prof. Ing. Radovan Hudák, PhD., Technická univerzita v Košiciach, Slovensko

prof. Ing. Michal Kelemen, PhD., Technická univerzita v Košiciach, Slovensko

prof. Ing. Ervin Lumnitzer, PhD., Technická univerzita v Košiciach, Slovensko

prof. Ing. Emil Spišák, CSc., Technická univerzita v Košiciach, Slovensko

prof. Ing. Tomáš Brestovič, PhD., Technická univerzita v Košiciach, Slovensko

doc. Ing. Ján Kráľ, PhD., Technická univerzita v Košiciach, Slovensko

doc. Ing. Peter Frankovský, PhD., Technická univerzita v Košiciach, Slovensko

prof. Ing. Michal Hatala, PhD., Technická univerzita v Košiciach, Slovensko

prof. Ing. Eva Tillová, PhD., Žilinská univerzita v Žiline, Slovensko

prof. Ing. Stanislav Ďuriš, PhD., Slovenská technická univerzita v Bratislave, Slovensko

prof. Ing. Peter Šugár, CSc., Slovenská technická univerzita v Bratislave, Slovensko

prof. Ing. Ivan Křupka, Ph.D., Vysoké učení technické Brno, Česká republika

doc. Ing. Miroslav Mahdal, Ph.D., VŠB Technická univerzita Ostrava, Česká republika

prof. Ing. Tomáš Jirout, Ph.D., ČVUT Praha, Česká republika

doc. Ing. Petr Lepšík, Ph.D., Technická univerzita v Liberci, Česká republika

doc. Ing. Václav Vaněk, Ph.D., Západočeská univerzita v Plzni, Česká republika

dr hab. inż. Andrzej Burghardt, prof. PRz, Politechnika Rzeszowska, Poľsko

Dr inż. Tomasz Jachowicz, Politechnika Lubelska, Poľsko

Príspevky uvedené v zborníku z konferencie sú recenzované recenzentmi, členmi vedeckej rady konferencie. Za obsah, textovú a jazykovú úpravu, etiku citovania príspevku zodpovedajú autori.

OBSAH

<i>Autorský kolektív a názov príspevku</i>	<i>Strany</i>
Alžbeta Nováková, Miroslav Badida Analysis of sound absorption of recycled textiles from end-of-life vehicles	10-13
Tomáš Balint, Jozef Živčák, Radovan Hudák, Samuel Lancoš, Miroslav Kohan, Marek Schnitzer Production of biomedical filaments	14-19
Jozef Brindza, Michal Demko, Marek Vrabel', Peter Ižol Design and implementation of machining fixtures for small series production performed on CNC machines	20-25
Laura Džuňová, Ružena Králiková Analysis of the impact of lighting on humans using simulation tools in its evaluation	26-31
Ivan Grega Evaluation of cutting surface quality on the electrical steels Materials designed through microarchitecture	32-38
Maksym Grytsiv, Marek Sukop, Martin Kočan Indoor localization system for mobile robots based on ultrasonic signal	39-44
Ján Hašul', Janette Brezinová Possibilities of increasing the durability of molds and cores for die casting of aluminum alloys	45-50
Janette Brezinova, Henrich Sailer Quality evaluation of renovation layers in tribological conditions	51-57
Ľuboš Chromý, Viktória Rajtúková, Andrea Sinčák – Konečná, Radovan Hudák Methodology of sample preparation for testing the adhesiveness of metal-ceramic dental prostheses	58-64
Nikita Veligotskyi, Anna Guzanová, Albert Mareš Overview of software designed for modeling parts made of composite materials	65-71
Erik Janoško, Anna Guzanová Creation of a hybrid joint of aluminum alloy en aw-6082 t6 using flowdrill and adhesive bonding	72-77
Johnson Ugochukwu Ezenwankwo Shape Memory Behaviour of an Alloy using Comsol Multi-Physics	78-83
Elena Jurgovská, Ervin Lumnitzer Analysis of basic principles in objectification and evaluation of electromagnetic fields in the environment	84-89
Matúš Kačír, Róbert Grega Methodology for identification of the dual-mass flywheels properties	90-95
Jana Klímová, Zuzana Molčánová, Karel Saksl, Marek Schnitzer, Jozef Živčák, Radovan Hudák Scheme of methodology of magnesium powder preparation for 3D printing	96-100

Laura Lachvajderová, Jaroslava Kádárová Attitude of European and Slovak SMEs to digitalization during the COVID-19 pandemic	101-106
Maroš Palko, Miroslav Palko, Viktória Krajňáková, Ján Kráľ Mechanical drive system control optimizations for ultralight mobile devices	107-113
Martin Varga, Ivan Virgala, Michal Kelemen Mathematical model of a pneumatic bellows actuator	114-120
Matúš Lavčák, Marieta Šoltéssová, Michal Puškár Environmental impact of the automotive industry	121-127
Tomáš Merva, Ivan Virgala, Peter Girovský Soft Actor-Critic in robotic arm position control within ROS	128-133
Lukáš Mitrik, Marianna Trebuňová, Alena Findrik Balogová, Marek Schnitzer, Radovan Hudák, Jozef Živčák Methodology of degradation assessment of polymeric materials	134-139
Marek Mizerák, Peter Trebuňa, Ján Kopec Hardware support for localization technology	140-144
Wanda Miženková, Zuzana Molčanová, Beáta Ballóková, Karel Saksl Development and characterization of zinc alloys for orthopedic implants	145-151
Róbert Moro, Dagmar Draganovská Study of microgeometric characteristics after different preparation of metal surfaces focused on adhesive bonding	152-157
Dominik Novotný, Ján Kráľ Antimicrobial treatments for industrial equipment	158-164
Samuel Vílkovský, Janka Majerníková Evaluation of deep-drawability of selected types of steel sheets	165-173
František Kupec, Michal Fabian, Michal Puškár Development of elements optimizing car aerodynamics	174-181
Peter Palička, Róbert Huňady, Michal Fabian Determination of material properties of samples manufactured by additive technology using 3D digital image correlation	182-187
Branko Štefanovič, Lucia Bednarčíková, Jozef Živčák Thumb orthosis design using a CAD/CAM method	188-193
Denis Cmorej, Ľuboš Kaščák Numerical simulation of clinching of HCT600X+Z steel sheets	194-200
Pavol Tarbajovský, Michal Puškár Design of an internal combustion engine using RCCI technology	201-207
Štefan Ondočko, Jozef Svetlák, Tomáš Stejskal, Michal Šašala, Lukáš Hrivniak Application of inverse kinematics calculation of a robotic arm composed of URM modules for a defined path	208-213

Patrik Varga, Radovan Hudák, Marek Schnitzer Methodology of the personalized implants manufacturing process by additive technology	214-218
Kristián Pástor, Miroslav Badida Research of sound absorption of recycled rubber in compact and loose form	219-223
Peter Ján Sinčák, Ivan Virgala, Martin Varga, Michal Kelemen Kinematic analysis of redundant robot	224-229
Vladimír Rohal', Emil Spišák Evaluation of cutting surface quality on the electrical steels	230-235
Anna Yehorova, Ervin Lumnitzer, Veronika Gumanová Development of methods for drone noise assessment	236-241
Samuel Sivák, Silvia Maláková Influence of spur gear bodies shapes on the weight of the transmission mechanisms	242-247
Miroslava Badidová, Tibor Dzuro, Lydia Sobotová Research on acoustic conditions around the wastewater treatment plant	248-253
Filip Duda, Natália Jasminská, Tomáš Brestovič Construction design of a heat transfer intensifier for low-pressure vessel for storing hydrogen	254-259
Šimon Hudák, Marián Lázár Design of metal hydride tank with an internal heat intensifier	260-264
Ivan Mihálik, Tomáš Brestovič Time dependence of the decrease in the odorant concentration in the natural gas mixture	265-269
Lukáš Tóth, Tomáš Brestovič Processing of biogas from kitchen waste with a focus on hydrogen production	270-273
Gabriela Dancáková, Marek Schnitzer, Alena Findrik Balogová, Jozef Živčák, Radovan Hudák Software support and additive technologies for veterinary applications	274-279
Ivana Koláriková, Tatiana Kelemenová, Eduard Jakubkovič Verification of the properties of tilt angle sensors	280-289
Miroslav Palko, Maroš Palko, Viktória Krajňáková, Ján Král' Optimization of mechanical drive systems design for ultralight mobile devices	290-296
Bibiána Ondrejová, Lucia Bednarčíková, Monika Michalíková, Jaroslav Dulina, Jozef Živčák The effect of Neurac movement therapy on the treatment of scoliosis	297-302
Juliy Martyn Kulya, Miroslav Tomáš Verification of manufacturability and material selection for the shetmetal part using numerical simulation	303-308
Samuel Lancoš, Miroslav Kohan, Marek Schnitzer, Gabriela Dancáková, Tomáš Balint, Radovan Hudák Production of filaments and optimization of the 3D printing process for PLA/PHB material with an admixture of a ceramic component	309-314

[illegible]

Analysis of sound absorption of recycled textiles from end-of-life vehicles

Alžbeta Nováková ^{1*}, Miroslav Badida ²

¹ alzbeta.novakova@tuke.sk

² miroslav.badida@tuke.sk

* Correspondence: alzbeta.novakova@tuke.sk; Tel.: 055 602 2685

Abstract: The paper presents the acoustic properties of textile materials from vehicles after their lifetime. The sound absorption coefficient was determined for recycled textiles used in end-of-life vehicles using a Kundt tube. The properties of the material used for the research and the research method are briefly presented. The paper is focused on the comparison of compact and bulk material of the same fraction. For the selected parameter - coefficient of sound absorption, the material was tested for its potential application in sound insulation products.

Keywords: recycling; sound absorption coefficient; Kundt tube

1. Introduction

Reducing the negative effects of noise, especially from traffic, plays an important role in ensuring a more acoustically pleasant environment. An important aspect for noise reduction are materials that are used in structures with a sound insulation function. [1] The use of recycled textile residue materials from old vehicles to reduce noise has the advantage of low specific weight and low production costs. [2, 3] Knowledge of the acoustic properties of these materials is necessary for proper use in products such as noise barriers and barriers. [4]

This paper presents the results of scientific research focused on the analysis of acoustically suitable materials based on recycled textiles from end - of - life vehicles. The paper presents the results of pickling of a selected acoustic parameter (sound absorption coefficient - α), which were obtained using a Kundt tube.

2. Materials used for research

The automotive industry places demanding demands on the textile material used to make auto parts. Such a material has good thermal, anti-vibration and sound insulation properties. Compared to traditional materials, it shows better resistance to mold, moisture, high mechanical resistance and reduced flammability. These materials are unusable for further processing, as they are difficult to defibrate composite materials. To ensure physical and chemical properties, they are made of synthetic fibers. These textile parts consist of car mats, seat covers, interior acoustic and thermal insulation. [5, 6]

For the needs of the research, we cooperated with the company Krajné s.r.o., which provided material and suitable fractions for the research. The material is obtained as technological cuttings, cuttings and failures in the production of a new product from the primary material, finished pieces of carpets, upholstery, covers during the disassembly of the vehicle at the end of its life. Figure 1 shows the material and fraction obtained, which retain the original properties of the material and are also transferred to the properties of the new component. The homogenized material is formed into the board format by adding a binder based on a polyurethane prepolymer. [7]

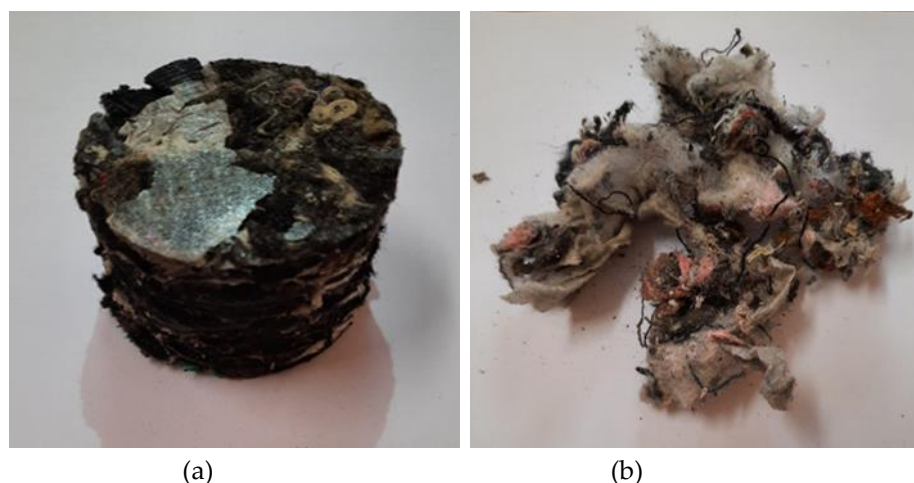


Figure 1. (a) Compact recycled textile material, (b) Cut recycled textile material

Table 1 lists selected properties of the experimental material. [8, 9]

Table 1. Properties of experimental material

Thermal conductivity value	$\lambda = 0,061$ [W/m.K]
Sound absorption class	A
Compressive stress at 10% compression	203 MPa
Tensile strength perpendicular to the plane of the board	322 MPa
Short-term absorption at partial immersion Wlp - procedure A	max. 20,0 [kg/m ²]
Long-term absorbency at partial immersion Wlp - procedure A	max. 25,0 [kg/m ²]
Compressibility	3,68 mm
Reaction to fire	Class E
Health safety	In accordance with the relevant provisions

3. Research method

One of the most widely used methods for determining sound absorption is the internationally standardized impedance tube method according to STN EN ISO 10534-2. It is based on measuring the transfer function between two microphone signals located inside the tube. In accordance with the measuring chain, a loudspeaker is located at the end of the tube.

The tube is fed in the 1/3 octave frequency band and a stationary plane wave is generated. The pressure measured by the microphones decomposes into incident and reflected components. Figure 2 shows the hardware device used to measure the sound absorption coefficient (α) for the frequency bands from 100 to 800 Hz and from 400 to 2500 Hz. The system includes a tube with an inner diameter of 60 mm (SW060-L) and a holder for the tested sample with an inner diameter of 60 mm (SW060-S). [10, 11]

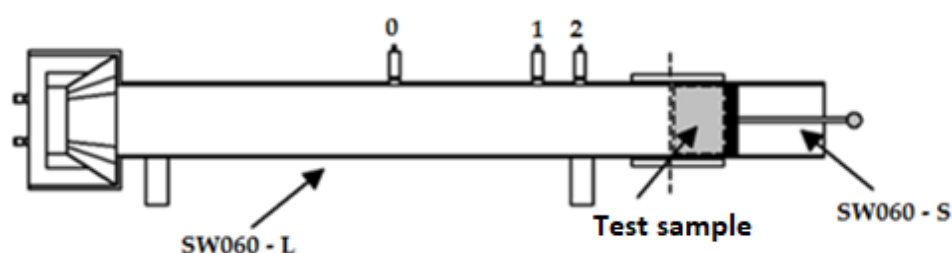


Figure 2. Sound absorption measuring system

4. Implementation of measurements and evaluation

This section presents the results obtained by experimental measurements. The sound absorption coefficient (α) is a dimensionless number ranging from 0 to 1. The closer the measured value is to 1 or equal to 1, the better the measured (higher) sound absorption will be. [12]

Measurements were performed for compact and bulk recycled textile material. First, a sample-free device was prepared to configure the microphones and calibrate them. Sound absorption is measured using two microphones in the selected position. After calibration, the sample is placed in a tube and the measurement is started. For each frequency, 5 measurements were made, from which the average was calculated and is shown in Table 2. The weight of the compact material measured was 37 g and the bulk material 8,4 g.

Table 2. Measured values of sound absorption

Frequency (Hz)	Compact material	Loose material
100	0,11	0,06
125	0,14	0,08
160	0,20	0,10
200	0,27	0,14
250	0,37	0,20
315	0,49	0,30
400	0,59	0,46
500	0,66	0,66
630	0,68	0,87
800	0,71	0,97
1000	0,75	0,91
1250	0,75	0,79
1600	0,80	0,69
2000	0,82	0,68
2500	0,82	0,75

Based on the measured sound absorption values (α) of the selected fractions, it was found that the best results were measured at frequencies from 630 Hz to 1 250 Hz for the bulk fraction. For compact materials, the best results were obtained from 800 Hz to 2 500 Hz. Worse results were found at low frequencies from 100 Hz to 200 Hz with loose textiles.

The frequency spectrum of traffic noise has its maximum in the range of 500 Hz to 1 500 Hz, while the highest noise is caused by the frequency of 1 000 Hz, so it can be stated that loose recycled textile material from end-of-life vehicles is suitable as a structural element for building noise barriers, as at given frequencies it performed better (0,91) than compact material (0,75). [12]

For better illustration, the measurement results are presented in Figure 3, where it is possible to see the change in sound absorption coefficient versus frequency for compact and bulk textile material from end-of-life vehicles.

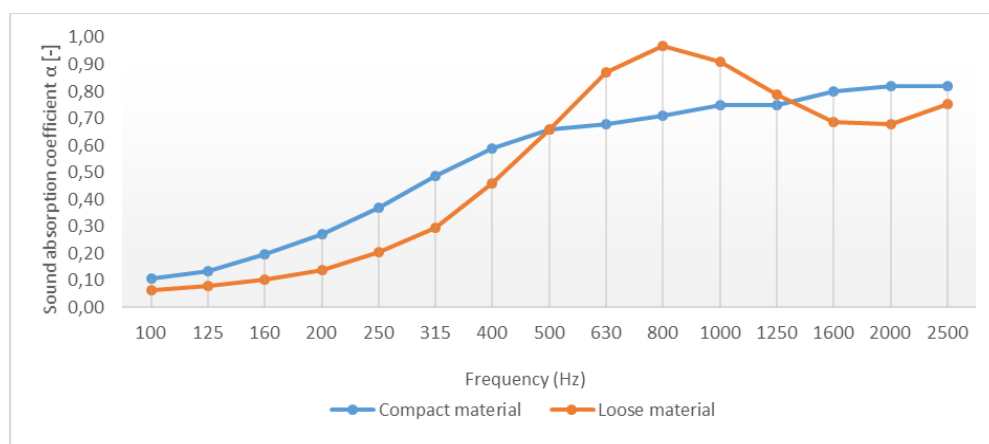


Figure 3. Sound absorption coefficient α - comparison of compact and loose material

5. Conclusions

The experiment was aimed at determining the sound absorption of recycled textiles from end-of-life vehicles. Two types of samples were tested - compact and loose textile material. Both samples showed good sound absorption at higher frequencies, a fact that recommends these materials for application in sound insulation products. However, these materials are not stand-alone and must be applied together with a support wall or frame which is made of, for example, plastic or aluminum.

Acknowledgments: The contribution was created on the basis of the solution of the project MŠVVaŠ SR KEGA no. 009 TUKE-4/2021 (50%) and the project MŠVVaŠ SR UNIVNET no. 021/0004/20 (50%).

References

1. Stanciu, M. D.; Curtu, I.; Cosereanu C.; Lica, D.; Nastac, S.: Research regarding acoustical properties of recycled composites. 8th International DAAAM Baltic Conference "INDUSTRIAL ENGINEERING " 19-21 April 2012, Tallinn, Estonia.
2. Youneung, L.; Changwhan, J.: Sound Absorption Properties Of Recycled Polyester Fibrous Assembly Absorbers, *Autex Research Journal*, Vol. 3, No2, June 2003.
3. Terci, O. M.; Curtu, I.; Cerbu, C.; Stanciu, M. D.: Mechanical Properties Of Composites Reinforced With Natural Fiber Fabrics, „Annals Of Daaam For 2011 & Proceedings Of The 22th International Daaam Symposium Intelligent Manufacturing & Automation”, 23-26 November 2011, ISSN 1726-9679, str. 607-608.
4. Badida, M. et al.: Development of technologies and techniques for waste recovery into sound and thermal insulation products, p 144 – 182. UNIVNET. Progressive technologies of waste recovery in the automotive industry, SPEKTRUM, Bratislava, 2021, ISBN: 978-80-553-3867-5
5. Eisenreich, J. et al.: Speed with silence - technologies and materials, Prokop Rail, Plzeň, 2015.
6. XINWU, X.; et al.: Sound Absorbing Properties of Perforated Composite Panels of Recycled Rubber, Fiberboard Sawdust and High Density Polyethylene. *Journal of Cleaner Production* Vol. 187 (2018), p. 215 – 221, ISSN 0959-6526.
7. Stred Technology. Available online: <http://www.stered.sk/>. (accessed 6. December 2021).
8. Properties of recycled textiles. Available online: <https://tepore.sk/portfolio-item/ekosen-ata/>. (accessed 7. December 2021).
9. ROSELY, C. V. M.; SILVA, R. H. A.; LINHARES, T. M.; ROCHA, C. M.: The Impedance Tube Construction and Acoustic Absorption Study Applied Materials Inside Vehicles. 41st International Congress and Exposition on Noise Control Engineering 2012. Vol. 2, No.1 (2012), pp. 872 – 888. ISBN: 978-1-62748-560-9.
10. STN EN ISO 10534-2: 1998. Acoustics—Determination of Sound Absorption Coefficient and Acoustic Impedance in Impedance Tubes—Part 2: Method of Transformation Function; International Organization for Standardization: Geneva, Switzerland, 1998.
11. STN EN ISO 10534-2: 1998. Acoustics—Determination of Sound Absorption Coefficient and Acoustic Impedance in Impedance Tubes—Part 2: Method of Transformation Function; International Organization for Standardization: Geneva, Switzerland, 1998.
12. Badida, M.; Lumnitzer, E.; Bartko, L.: Options for reducing traffic noise. ELFA, s.r.o., Košice, 2011, 274 p., ISBN 978-80-8086-181-0.



Production of biomedical filaments

Tomáš Balint¹, Jozef Živčák¹, Radovan Hudák¹, Samuel Lancoš¹, Miroslav Kohan¹, Marek Schnitzer¹

¹ jozef.zivcak@tuke.sk, radovan.hudak@tuke.sk, samuel.lancos@tuke.sk, miroslav.kohan@tuke.sk, marek.schnitzer@tuke.sk

Correspondent author: tomas.balint@tuke.sk

Abstract: In this study we try to produce biomedical polymers that have never been produced in such a proportion of materials. These fibers are intended for biomedical use in the future. All necessary parameters were recorded during production. Medically certified materials in the form of granules were used for production. The production took place on a filamentmaker Composer 450 from the company 3Devo, where 3 types of polymers PLA, PHB and thermoplastic starch were used. PLA is widely used in 3D applications because it is one of the most comfortable material that can be easily processed with FDM without the use of important vapor technologies. However, it is necessary to solve its solution thermal and high degradation rate during the stability of fiber production. A 25 percent amount of plasticizer in the first type of filament and a 30 percent amount of plasticizer in the second type of filament were added to the polymers.

Keywords: Additive technology FDM, filament, PLA, PHB

1. Introduction

Thermoplastic-based fibers used in additive technologies are produced using plastic extrusion machines called fiber extruders or filament mashers. These extrusion systems work with the logic of mixing raw plastic granules and other additives in a mechanical mixer and subsequently transporting the formed composite granules through a hopper to the nozzle side of the heater by means of a screw shaft. These sophisticated devices can be found in various companies engaged in mass production. At the Department of Biomedical Engineering and Measurement, we managed to produce filaments with optimal properties. These manufactured filaments are intended for use in the biomedical field in the future. In the production process, we made a number of attempts to optimize the parameters. We used equipment from the company 3Devo. When using the filament in additive technologies, it is essential that it meets the requirements necessary for quality 3D printing and subsequent application in a medical environment. In this study, we managed to optimize all the necessary parameters for successful 3D printing. The diameter of the produced filaments must be in the range from 1.65 mm to 1.85 mm. This is important so that the filament does not jam in the nozzle.

2. Filament production and printing using FDM technology

The production of medical filaments is a production process divided into several steps. The first step is to obtain the material in the form of granules, which are then dried in a dryer. After drying, it is possible to proceed to the production itself. After the production of the filament, storage under suitable temperature conditions is important to prevent moisture degradation. The filament produced in this way is suitable for 3D printing of objects using FDM technology. FDM additive technology is the process of applying molten material to a heated flat table surface in layers. The fibrous material enters the heated nozzle via a feeder (Figure 1). This additive production technology is becoming more widespread due to the advantages of the thermoplastic material used. Due to the simple principle and low need for equipment, the cost of 3D printing using the FDM method is lower than with other additive technologies.

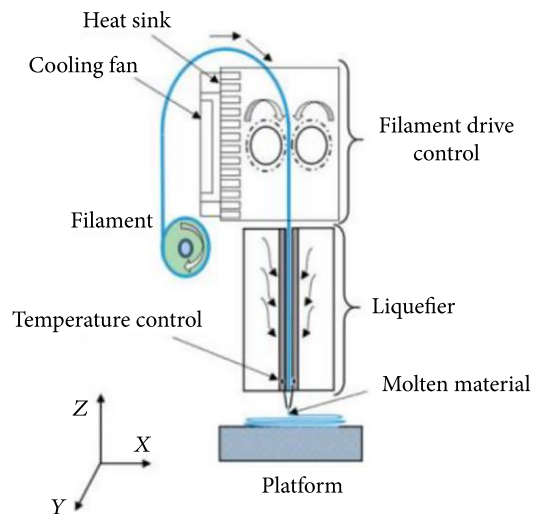


Figure.1. FDM 3D printing technology [5].

2.1. Preparation and drying of granulate in a dryer

To prevent the biodegradation process, the filament material was vacuumed in an opaque package. This material was supplied in the form of granules. Nevertheless, we dried the material in a dryer from 3devo (Figure 2). The drying temperature was set at 160 °C for 180 minutes.



Figure.2. Granulate drying.

2.2. Filament extrusion

The filaments were produced on a 3devo filament maker Composer 450 under ideal conditions in an air-conditioned room at 18 ° C (Figure 3).

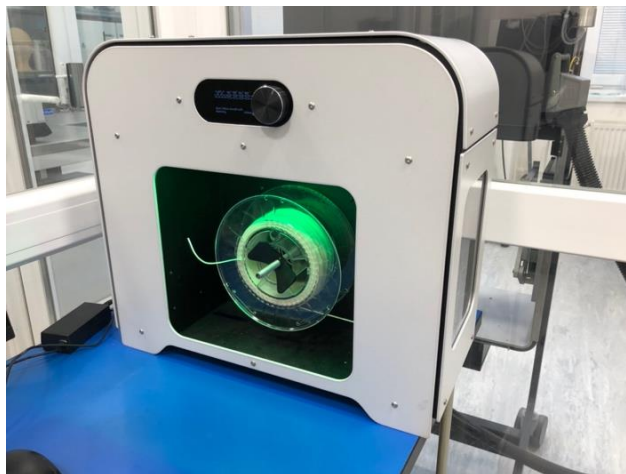


Figure.3. Filamentmaker Composer 450.

After cleaning the device, we poured the granulate into the hopper (Figure 4). In the production of the first medical filament with a 25% amount of plasticizer, we set the melting temperature to 170 ° C on 4th heater and to 171 ° C on other heaters. In the production of the second filament with a 30% amount of plasticizer, we set the temperature on first heater to 156 ° C, on second heater the temperature was 166 ° C, on third 155 ° C and on the last 4 heating element 150 ° C. We achieved these temperatures by combining knowledge about the melting temperature of PLA / PHB materials. After stabilizing the filament flow, we placed the extruded fiber in a sensor that measured the diameter of the filament. By monitoring and optimizing all production parameters, the filament was wound into a spool. The filament production parameters are summarized in Table 1 and Table 2. We managed to maintain the optimal filament diameter as can be seen in (Figure 5) and (Figure 6).



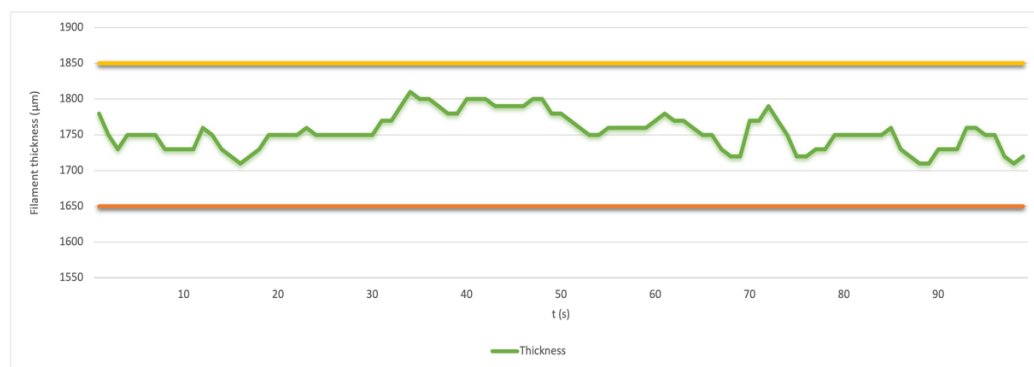
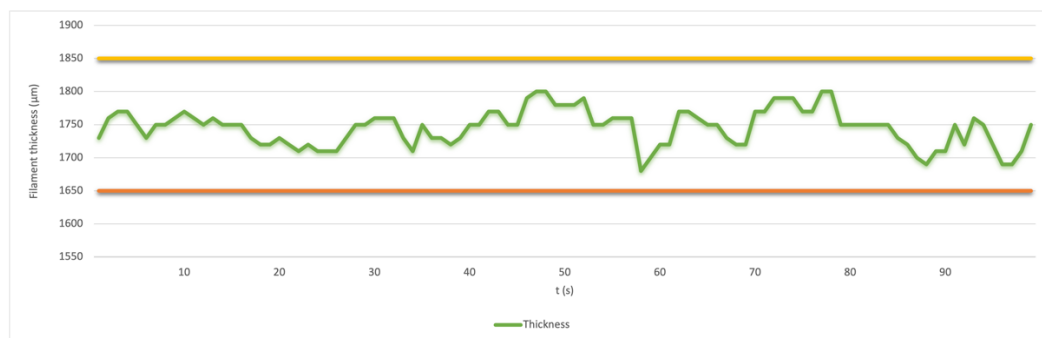
Figure.4. Granulate poured into a hopper.

Table 1. Production parameters of the first filament with 25% amount of plasticizer.

HEATING ELEMENT	4	3	2	1
REAL TEMPERATURE	170°C	170°C	172°C	171°C
SET TEMPERATURE	170°C	171°C	171°C	171°C
SET TEMPERATURE	2.0 RPM			
FAN PERFORMANCE	80%			

Table 2. Production parameters of the second filament with 30% amount of plasticizer.

HEATING ELEMENT	4	3	2	1
REAL TEMPERATURE	150°C	154°C	165°C	171°C
SET TEMPERATURE	150°C	155°C	166°C	156°C
SET TEMPERATURE	4.3 RPM			
FAN PERFORMANCE	100%			

**Figure.5.** Graph of the filament diameter with 25% of plasticizer per time (t).**Figure.6.** Graph of the filament diameter with 25% of plasticizer per time (t).

The diameters of both filaments were in the optimal range of 1.75 mm. The filament with 25% plasticizer weighed 410.13 g (Figure 7a) and the filament with 30% plasticizer weighed 556.82 g (Figure 7b).

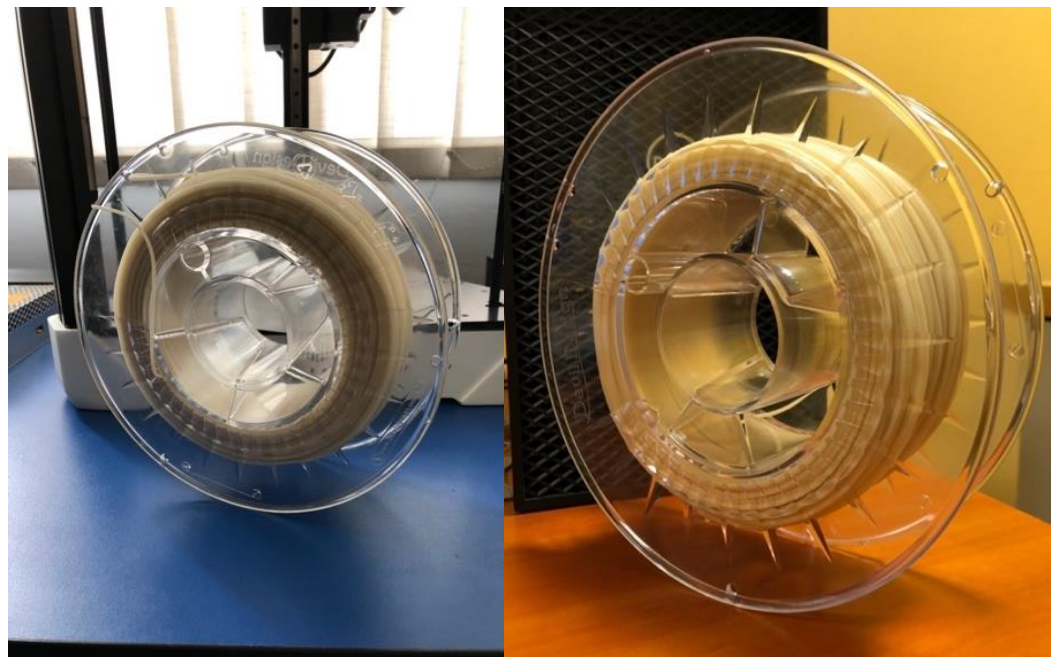


Figure 7a. Finished filament with 25% plasticizer, **Figure 7b.** Finished filament with 30% plasticizer.

3. Conclusion

The mentioned scientific study brings new knowledge in the field of materials engineering and is a theoretical output of the production of filaments that will be used in the field of medical applications. Both filaments were extruded from PLA / PHB / thermoplastic starch granules with the addition of 25% plasticizer in the first type of filament and with 30% addition of plasticizer in the second type of filament. The most important condition regarding the diameter of the filament was met and the individual filaments correspond to the stated tolerance and have a constant diameter of 1.75 mm along their entire length. With the help of the Composer 450 from 3devo, located in the Department of Biomedical Engineering and Measurement, results have been achieved that have significant benefits in the production, testing and use of medically certified materials. The future of research lies in destructive and non-destructive testing of extruded samples using FDM technology. We managed to describe additive technology in detail in the introductory chapter of this scientific article.

Acknowledgment: This scientific study was created thanks to support under the Operational Program Integrated Infrastructure for the project "Center for Medical Bioadditive Research and Production (CEMBAM), code ITMS2014 +: 313011V358, co-financed by the European Regional Development Fund", with the support of the project KEGA 040TUKE-4/2019 (Use of digitization methods to support the educational process in the field of aortic prosthetics) and with the support of the project VEGA 1/0179/19 Research, development and testing of a bioreactor for the cultivation of tissues and organs after bio-additive production. This publication was created thanks to support under the Operational Program Integrated Infrastructure for the project: Open Scientific Community for Modern Interdisciplinary Research in Medicine (OPENMED), code ITMS2014 +: 313011V455, co-financed by the European Regional Development Fund and thanks to support under the Operational Program Integrated infrastructure for the project: Center for Advanced Therapies of Chronic Inflammatory Diseases of the Musculoskeletal System (CPT ZOPA), code ITMS2014 +: 313011W410, co-financed by the European Regional Development Fund.

References

1. BALINT, T., ŽIVČÁK, J., HUDÁK, R., TÓTH, T., KOHAN, M., LANCOŠ, S. Destructive and non-destructive testing of samples from PLA and PETG materials. IOP Conference Series Materials Science and Engineering 1199(1):012045, doi: 10.1088/1757-899X/1199/1/012045.
2. ŽIVČÁK, J., NOVÁKOVÁ-MARCINČÍNOVÁ, E., NOVÁKOVÁ-MARCINČÍNOVÁ, L., BALINT, T., PUŠKÁR, M. Increasing Mechanical Properties of 3D Printed Samples by Direct Metal Laser Sintering Using Heat Treatment Process. J. Mar. Sci. Eng. (2021),9, 821, doi: 10.3390/jmse9080821.
3. MIRÓN, V., FERRÁNDIZ, F., JUÁREZ, D., MENGUEL, A.: Manufacturing and characterization of 3D printer filament using tailoring materials. Procedia manufacturing. 2017. Available on the internet: <https://www.sciencedirect.com/science/article/pii/S2351978917307886>.
4. BALINT, T., BALOGOVÁ, A., F., HUDÁK, R., ŽIVČÁK, J., SCHNITZER, M., FERANC, J.: Production, additive printing and mechanical testing of PLA/PHB material with different concentrations of TAC emollient. 19th World Symposium on Applied Machine Intelligence and Informatics (SAMI). 2021. Available on the internet: https://www.researchgate.net/publication/350301053_Production_additive_printing_and_mechanical_testing_of_PLAPHB_material_with_different_concentrations_of_TAC_emollient.
5. MIKULA, K., SKRZYPCZAK, D., IZYDORCZYK, G., WARCHOŁ, J., MOUSTAKAS, K., CHOJNACKA, K., WITEK-KROWIAK, A.: 3D printing filament as a second life of waste plastics - a review. Environmental Science and Pollution Research. 2020. Available on the internet: <https://link.springer.com/article/10.1007/s11356-020-10657-8>.
6. ÇANTI, E., AYDIN, M., YILDIRIM, F.: Production and Characterization of Composite Filaments for 3D Printing. Journal of Polytechnic. 2018. Available on the internet: https://www.researchgate.net/publication/322903568_Production_and_Characterization_of_Composite_Filaments_for_3D_Printing.



Design and implementation of fixtures for small series production realized on CNC machines

Jozef Brindza ^{1*}, Michal Demko ², Marek Vrabel' ³ and Peter Izol ⁴

¹ Prototyping and Innovation centre, Faculty of Mechanical Engineering, Technical University of Kosice, Slovak republic; jozef.brindza@tuke.sk

² Department of Technology, Materials and Computer Supported Production, Faculty of Mechanical Engineering, Technical University of Kosice, Slovak republic; michal.demko@tuke.sk

³ Prototyping and Innovation centre, Faculty of Mechanical Engineering, Technical University of Kosice, Slovak republic; marek.vrabel@tuke.sk

⁴ Department of Technology, Materials and Computer Supported Production, Faculty of Mechanical Engineering, Technical University of Kosice, Slovak republic; peter.izol@tuke.sk

* Correspondence: jozef.brindza@tuke.sk; Tel.: +421940 772 427

Abstract: The paper focuses on the design and production of fixtures for small series production on CNC machines. In the introduction is described issues of clamping at machining. The design and manufacturing of fixtures is time-consuming operation and increases total production costs. However, application of fixtures allows shorten clamping time and increase reliability of process. The main section of the paper contains part analysis, justification of the need for use fixtures and design of fixtures. It consists of design of fixture for milling machine and for lathe. Every subsection in detail describes individual components and method of clamping of workpiece. All design of fixtures were manufactured and surface treated. The results of the paper are custom fixtures, which were tested and applied on real machining production.

Keywords: design, fixtures, machining, CNC machines

1. Introduction

The modern engineering industry is characterized by multi-product production and a variable volume of production of products. The proportion of products with requirements to achieve high accuracy of dimensions, shapes, relative position of surfaces and quality of surfaces in accordance with their intended use is constantly increasing. Due to the expansion of the technological possibilities of modern machine tool, their high cost and the need to perform a large amount of work in the transition to machining other parts, all the possibilities of intensification of production processes are rapidly developing. In this context, great attention is paid to fixtures which make it possible to shorten the set-up and clamping times of semi-finished products and at the same time increase the reliability of the process by ensuring repeated accuracy and reliability of clamping. This helps to reduce production time, which has a positive effect on reducing production costs.

The urgency of shortening secondary times has become more pronounced with the advent of new technologies, especially various forms of high-speed machining. The reduction in main times as a result of the use of these technologies often causes main times to be shorter than secondary times. This fact also forces manufacturers to use fixtures as a means of reducing secondary times [5].

The fixtures are used in cases where the possibilities of standard clamping fixture, such as chucks or collets on lathes or clamping vices and clamps on milling machines, are not sufficient for the implementation of the technological step [3]. A complex of knowledge is needed for the design of fixtures, e. g. about geometric and dimensional

tolerances, production processes, technological possibilities of machines, tools, cutting conditions and cutting forces.

The basic task of fixtures for use in machine is the correct orientation and positioning of the part and its subsequent reliable clamping. The fixture must allow to access of tool to the manufactured elements or surfaces of the part. Resistance to the effects of the working environment is also a requirement, because machining processes are often implemented using process media. The design of the fixture must reliably absorb cutting forces so that deformations do not occur on the finished part. It is also a necessary condition to ensure the repeated functionality and accuracy of the fixture [2].

By default, the fixture contains three important components. The first is the positioning elements, which ensure the static balance of the semi-finished product and eliminate all degrees of freedom. The second component is the fastening elements, which press the semi-finished product onto the positioning elements and ensure the necessary rigidity and fixed position considering to the actuating cutting forces. The third component is additional support, helping to ensure rigidity and resilience to the actuating forces [1].

The process of designing the fixture for machine tools is divided into three stages. In the first stage, the planning of the fixture, the requirements related to the number of fixtures required, the type of fixture and the machining operations that the fixture are to handle are identified. In the second stage, the fixture is configured. The arrangement of the set of adjusting and fastening elements is determined so that the semi-finished product is correctly positioned and securely clamped. In the third stage, the design process itself is implemented, including the design of the components of the fixture and the fixture as a whole [1].

In the past, most fixtures have been designed for a specific operation on a single product. These are specialized fixtures without the possibility of use on other machines or for other products. The growing trend of increasing product variability and reducing series has forced the development of more flexible clamping systems based on modular elements. Their use streamlines the design and construction of fixtures. This advantage is further enhanced by the possibility of using electronic catalogues, allowing the necessary element of the product to be read directly by the CAD system [6].

The design and production of fixtures is time consuming and increases not only the time of the production cycle, but also the cost of production. The fact that the products are designed with narrow tolerances, standardly 30-50% of the tolerances on the manufactured part, also contributes to the increase in costs [1]. In addition, the components of the fixtures are made of quality (more expensive) materials to ensure long-term dimensional stability and prevent wear. The cost of fixture can represent 10-20% of the total cost of production. Therefore, ways are being sought to streamline the product design and production process. There are observable trends to create specialized systems called CAFD (Computer Aided Fixture Design), combining knowledge and design systems. The design of the fixture should be implemented in two steps - selection of the design of the fixture (if available in the database) and modification of the selected design in order to meet the specified requirements. If the appropriate initial solution is not in the database, it is necessary to implement a proposal for a new design of the fixture [4].

2. Description of the machined part

This work deals with the design of fixtures for clamping a part in small series production, which is shown in Figure 1. Because it is a small series production, accuracy, repeatability and in-process inspection must be observed during production. The part has most dimensions strictly symmetrically tolerated, i. e. ± 0.02 , ± 0.03 and ± 0.05 mm, remaining minor dimensions ± 0.1 – 0.2 mm. There are also geometric tolerances of shape and position, especially symmetry, coaxiality, cylindricity and position. These conditions must be considered in the design of the technological process, so that the part can be manufactured with all the conditions specified in the drawing documentation.

The part was produced by machining using the machine park of the Prototype and Innovation Center of the Faculty of Mechanical Engineering in Kosice. Based on the geometric shape of the part, the technological process of production was chosen, which consists of three clamps of the workpiece. The first and second clamping of the part was performed on a universal 5-axis milling machine DMG MORI DMU 60 eVo and the last clamping was performed on a CNC turning-milling centre DMG MORI ecoTurn 510.

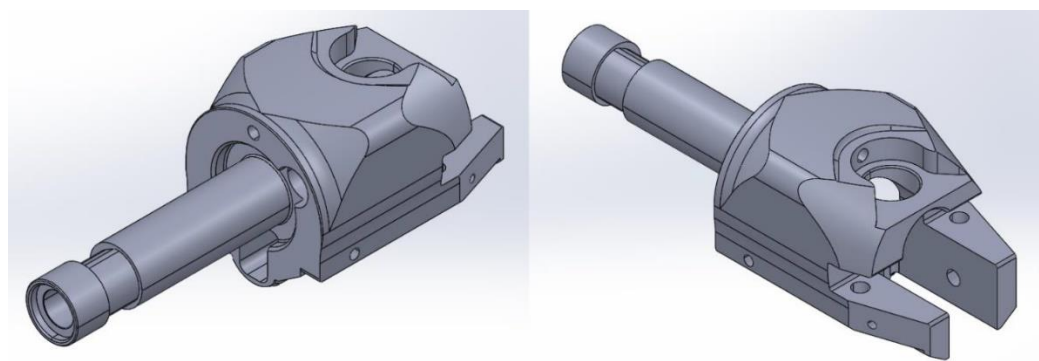


Figure 1. Production part

3. Design of fixtures

Due to the lack of the necessary suitable contact surfaces, it was necessary to design and manufacture fixture for the second and third clamping of the workpiece. During designing must be consider that the fixture should be relatively easy to manufacture and that the exact position of the workpiece in the fixture, repeatability and quick insertion and removal of the workpiece are ensured [7]. The design of the fixtures was performed in the CAD system SolidWorks 2019.

3.1. Design of the fixture for a milling machine

For machining the other side of the workpiece on a CNC 5-axis milling machine DMU 60 eVo, a fixture was designed, which consists of a fixed and a movable jaw for a mechanical vice, intended for the second clamping of the workpiece, shown in Figure 2.

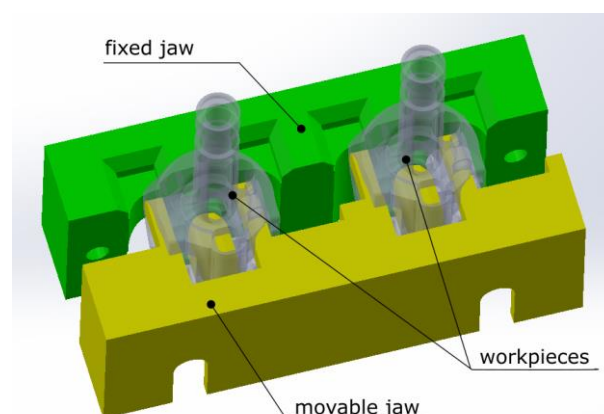


Figure 2. The first version of the fixture for clamping workpiece on milling machine

For a sufficient jaw length, the fixture was made to clamp two workpieces at the same time, thereby increasing productivity and machining efficiency. The manufactured fixture shown in Figure 3 was surface-nitrided after production.

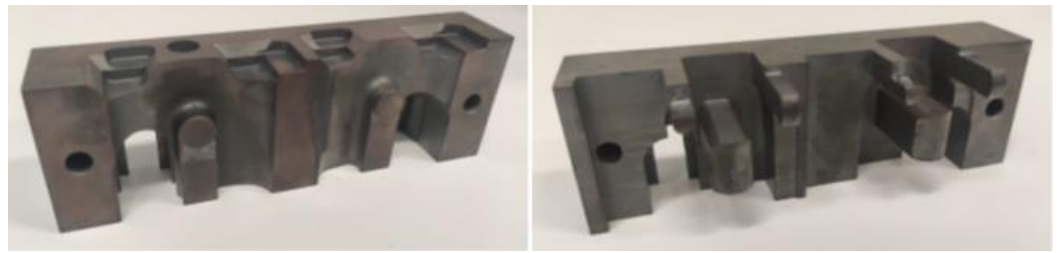


Figure 3. Manufactured the first version of the fixture for clamping workpiece

However, after the fixture has been manufactured, in checking the accuracy of the repeatability of the workpiece clamping in the fixture, deviations between the individual clamps were found. Even with the exact same clamping procedure, the required repeatability necessary to meet shape and position tolerances in small series production was not achieved. After performing all operations and measuring some dimensions with a 3D probe, the findings were confirmed. Also, after removing the workpiece, pressed marks remained on the contact surfaces, which was caused by insufficient rigidity of clamping the workpiece in the fixture. During roughing with a 20 mm diameter high-speed milling cutter, when the highest cutting forces occurred, there was probably a slight movement of the workpiece in the fixture.

Following these findings, it was necessary to design a new fixture to remedy the deficiencies. After the experience gained, the fixture must have more contact surfaces to remove all degrees of freedom, both displacement and rotation. The design of the new improved fixture is shown in Figure 4a. It is based on completely different contact surfaces than the first version. It consists of a movable and a fixed jaw, in which there are other movable components shown in Figure 4b.

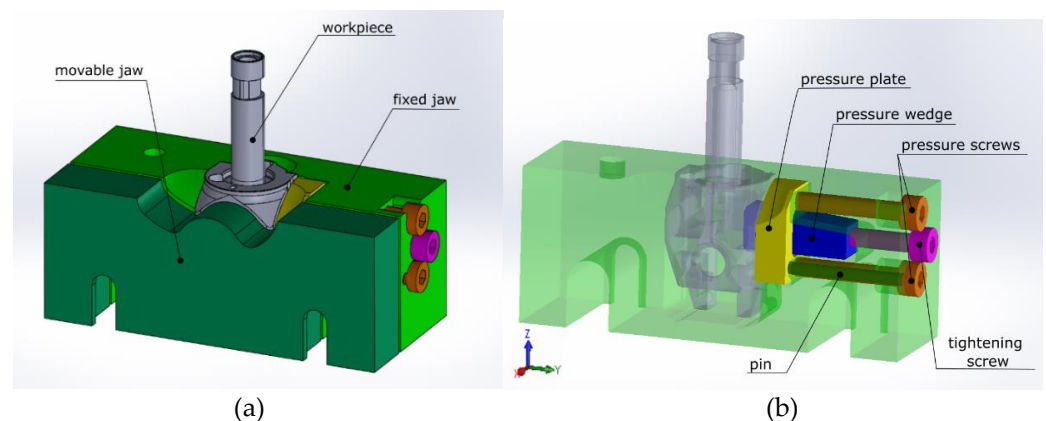


Figure 4. (a) The second version of the fixture for clamping workpiece on milling machine;
(b) Components of fixed fixture

By means of a pressure plate and two pressure screws, the tightening of which presses the plate against the workpiece and prevents the workpiece from moving in the Y axis. The pin secures position of the pressure plate. The position of the workpiece in the Z axis is ensured by tightening the middle tightening screw, which because of the shape of the pressure wedge, presses the workpiece onto the lower contact surfaces. Tightening the movable jaw ensures that the movement of the workpiece in the X axis is removed. The manufactured fixture shown in Figure 5 was tested by machining operations on the second workpiece clamping. After measuring the main dimensions, which were within the required tolerances, the surface was treated with nitriding, which significantly increased the wear resistance of the contact surfaces.

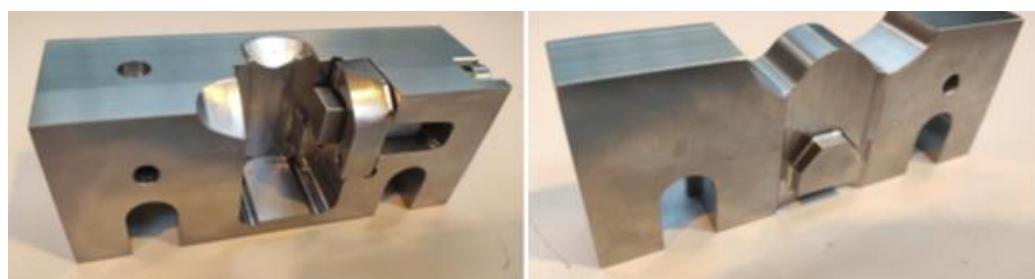


Figure 5. Manufactured the second version of the fixture for clamping workpiece

3.2 . Design of the fixture for a lathe

To make the last operation, i. e. axial groove on the CNC turning and milling centre ecoTurn 510, the fixture shown in Figure 6 is designed and manufactured.

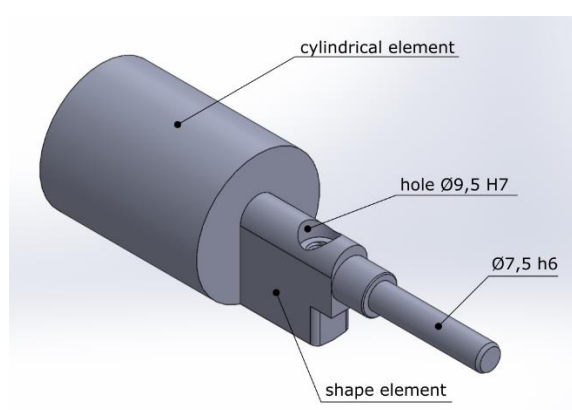


Figure 6. The fixture for clamping the workpiece on a lathe

The cylindrical part is used to clamp the fixture into turned soft jaws. With the accurate diameter $\text{Ø}7.5$ mm with tolerance h6, the centering of the workpiece in the fixture is ensured. The torque that is generated during turning is transmitted by the shaped part, which forms the negative of the workpiece part. The last element on the fixture is an accurate hole $\text{Ø}9.5$ mm with a tolerance of H7, followed by a metric thread M6. An accurate pin is inserted into this hole, which passes through a through hole (manufactured with a $\text{Ø}9.5$ mm H7 reamer), which is then tightened with an M6 Allen screw shown in the section in Figure 7. This secures the axial movement of the workpiece in the fixture during machining.

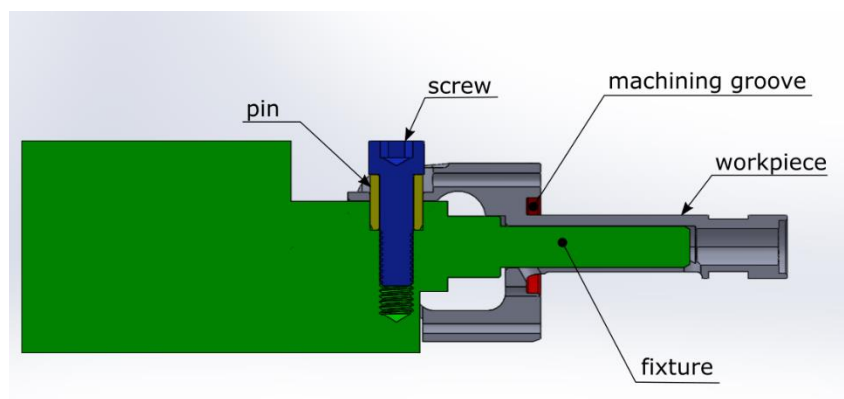


Figure 7. Assembly of clamping the workpiece on a lathe

The fixture was pre-prepared on a lathe and subsequently the shaped part was finished on a milling machine, therefore due to clamping in the vice, the cylindrical surface

is elongated and parallel surfaces were made at its end. The finished fixture after surface treatment is shown in Figure 8.



Figure 8. Manufactured fixture for clamping the workpiece on a lathe

4. Conclusion

At the first version of the fixture for the milling machine, significant problems with the accuracy and rigidity of the clamping occurred during machining, which led to the design and production of a new fixture concept, which eliminated the identified deficiencies. No deficiencies were found when testing the fixture on a lathe. The second version of the fixture for the milling machine and the fixture for the lathe were used in the real production of the specific part in small series production and thus their functionality and the repeatability of the clamping were tested. This was verified by keeping the geometric tolerances of the shape and position on the part in the required tolerance field during the whole series.

The required number of produced pieces was gradually handed over to the customer. The finished parts successfully passed the customer's incoming inspection and the measurement of the parts on a coordinate measuring machine. In the case of repeated production of the series in larger volumes, there is a possibility of further optimization of the technological process and thus also a change or design of new fixtures according to the needs of production.

Acknowledgment

The paper was created within the solution of the project VEGA 1/0457/21 Streamlining the machining of nickel superalloys by texturing cutting tools and using rigid process media.

References

1. Maniar, N. P. – Vakharia, D. P.: Design & Development of Fixture for CNC – Reviews, Practices & Future Directions. In: International Journal of Scientific & Engineering Research. Vol. 4 (2013), 11 p. ISSN 2229-5518.
2. Ivanov, V. – Zajac, J.: Flexible Fixtures for CNC Machining Centers in Multiproduct Manufacturing. In: Industrial Networks and Intelligent Systems. Vol. 4 (2018), 8 p. DOI: 10.4108/eai.10-1-2018.153552.
3. Maniar, N. P. – Vakharia, D. P.: Design & development of rotary fixture for CNC with computer aided mass balancing method as pre-mortem tool. In: Procedia Technology. Vol. 14 (2014), p. 397 – 404. DOI: 10.1016/j.protcy.2014.08.051.
4. Vukelic, D. – Zuperl, U. – Hodolic, J.: Complex system for fixture selection, modification and design. In: International Journal of Advanced Manufacturing Technology. Vol. 45 (2009), p. 731–748. DOI 10.1007/s00170-009-2014-y.
5. Radhakrishnan, P.: Computer Numerical Control Machines and Computer Aided Manufacture (2nd Edition) - 12.3 Fixtures for Machining Centres. New Academic Science. 2015. pp. 339-343. ISBN 978-1-78183-085-7
6. Nee, John G.: Fundamentals of Tool Design (6th Edition) - 11.1.2 Rigidity. Society of Manufacturing Engineers (SME). 2010. pp. 353-360. ISBN 978-087263-867-9
7. Rufe, Philip D.: Fundamentals of Manufacturing (3rd Edition) - 38.4.1.3 Modular Fixturing. Society of Manufacturing Engineers (SME). 2013. pp. 385-389. ISBN 978-0-87263-870-9



Analysis of the impact of lighting on humans using simulation tools in its evaluation

Laura Dzunova¹ a Ruzena Kralikova¹

¹ Technical University of Kosice, Faculty of Mechanical Engineering, Department of Environmental Engineering, Kosice; laura.dzunova@tuke.sk, ruzena.kralikova@tuke.sk

* Correspondence: laura.dzunova@tuke.sk

Abstract: In modern society, people spend most of their time in the interiors of buildings, whether at home, at work or at school, for example. Often, the natural light from the sunlight around us is replaced by artificial light sources. Light is an integral part of our lives and has a significant impact on our health, so the issue of appropriate lighting in buildings is very important. The paper focuses on the evaluation of interior lighting in one of the school classrooms using the classic method - measurement and a more modern method using simulation tools. The practical part of the paper is focused on measuring the lighting in the school classroom and then comparing the measured values with the values obtained using the simulation software DIALux EVO and at the same time using this software to propose improvements to lighting conditions in the classroom.

Keywords: lighting; health; lighting evaluation; simulation; lighting conditions; DIALux EVO

1. Introduction

Light sources can be divided into natural and artificial. Both natural and artificial light affect a person's biological clock and hormonal system and therefore affect their overall health. Unsuitable lighting conditions make it difficult to perceive the surroundings and can cause headaches, fatigue and other difficulties. Insufficient lighting in interiors, in addition to well-being and comfort, also affects a person's attention and performance [1, 2].

Lighting also has a significant impact on people's productivity and performance. Insufficient, poor lighting in the room can not only cause headaches and eye strain, but can also cause drowsiness and internal weakness. Conversely, high-intensity lighting, such as fluorescent and halogen lights, can also cause headaches. This type of lighting can also be harmful to the human eye because it makes it difficult to focus. Fluorescent lighting in particular has a number of negative effects on humans because it is known to cause eye strain and is also reported to trigger migraine headaches. Natural lighting reduces the frequency of headaches, reduces stress and drowsiness, and windows and views from the room are factors influencing people's satisfaction and comfort [3, 4]. In terms of artificial lighting, cooler blue light and bright lighting improve the ability to concentrate and stay alert. Blue light forms the predominant part of natural light and plays an important role in suppressing melatonin production, but we also encounter it in many light emitting diodes (lights, monitors, screens). Continuous suppression of melatonin production can lead to various health problems, so evening exposure to blue light should be minimized [5]. The light aspects that usually cause visual discomfort are insufficient or excessive lighting, shadows, haze, glare, and flicker. Working in poor lighting conditions triggers the release of the sleep hormone melatonin, which in turn reduces alertness and increases the likelihood of errors and accidents. Symptoms of eye strain vary from individual to individual, the most common being burning or itching of the eyes, headache, blurred vision, dry or watery eyes, and muscle tension [6, 7]. Lighting

should be designed to provide people with the right visual conditions to help them perform visual tasks efficiently, safely and comfortably.

2. Lighting evaluation

The evaluation of the lighting was carried out in the lighting laboratory located on the 1st floor of the Department of Environmental Engineering (Fig. 1). The dimensions of the classroom are 6.75 m x 5.9 m x 3.4 m (L x W x H). There are three windows in the classroom for daylight access. The source of artificial lighting is raster lamps Sylvania Octa Satinized Louvre 4x18W T8 (600x600) in the number of 6 pieces. The classroom walls are painted white and a large part of the classroom walls are covered with lighting samples.

A digital Luxesto Testo 545 camera was used to measure workplace lighting, including a measuring point memory, which allows you to quickly and reliably measure the intensity of lighting in workplaces and indoors.

The light intensity was measured on a horizontal plane at a height of 85 cm. The measured values of light intensity were read in a regular metric rectangular network of measuring points. These points shall be so arranged that the distance between them does not exceed the distance of the reflectors above the reference plane and that there are spaces between and below the lamps. The end points were spaced from the wall - the distance between the points. Screening by persons was excluded during the measurement, as well as screening of the head by room equipment or building components. Measurements of the illumination of the visual task site, the immediate vicinity of the visual task and the background were performed in the student's main visual zone. The measurement sites were selected so that the parts of the site with the lowest and highest luminosity were captured (Fig. 1). It was measured in the presence of a student, or was replaced by a meter so that the values measured corresponded to the lighting and shading during normal student performance. The number of measuring points and their distance were chosen depending on the area where the visual task is performed [8].

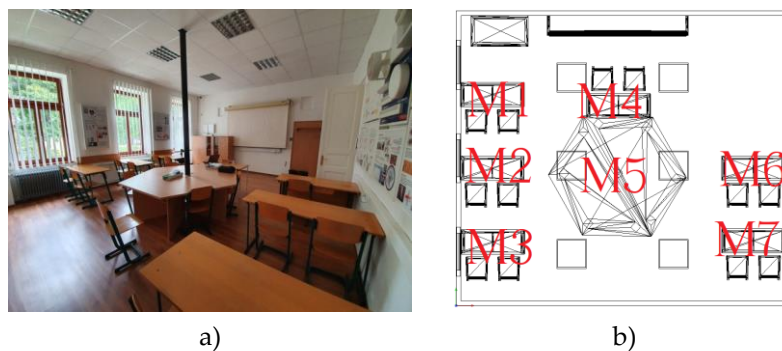


Figure 1 Light laboratory a) actual condition b) layout and measuring points

DIALux EVO software was used to calculate the lighting parameters and create a lighting laboratory model.

In this program, a digital version of the lighting laboratory was created (Fig. 2) using luminaires that reflect the real state of the lighting system in the classroom, i. 6 Sylvania Octa Satinized Louvre 4x18W T8 luminaires, with a luminous flux of 3475 lm and an output of 104 W. As the measurement results indicated insufficient lighting, especially at measuring points M6 and M7, a new lighting model was created using more powerful and at the same time less energy-intensive luminaires ESSYSTEM COSMO APEX 1060.LED, with a luminous flux of 6300 lm and an output of 41 W.



Figure 2 Light laboratory in DIALux EVO a) old model b) new model

The simulation was based on the above information about the space and its nature, we calculated the lighting under three conditions, without natural lighting, including natural lighting with a cloudy sky and also an average clear sky, which was also present during the actual measurement. The simulation results can be seen in the following figures. The following figures highlight the measuring planes for which the illuminance was calculated, the total illuminance was calculated, as well as the illuminance at the job sites, ie at the tables in the room and in their immediate vicinity. The figures show the floor plan of the measured room together with the calculated lighting values at individual points for the old lighting model and the new lighting model when considering the daylight in an average clear sky (Fig. 3) and also when excluding daylight (Fig. 4).

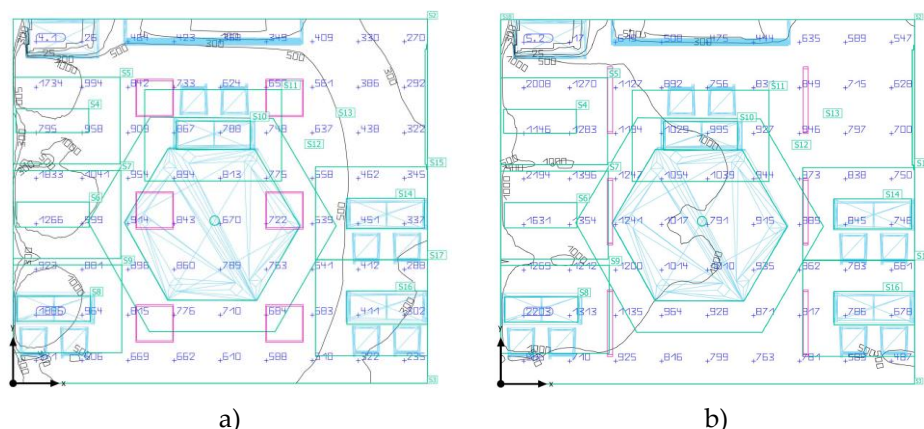


Figure 3 Calculated DIALux lighting values with daylight a) old model b) new model

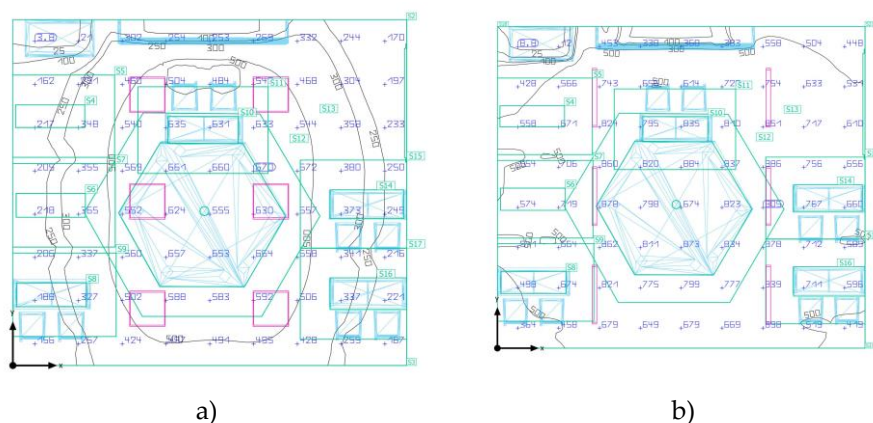


Figure 4 Calculated DIALux lighting values without daylight a) old model b) new model

The following figures show the floor plan of the measured room in which the levels of light intensity are differentiated by color (Fig. 5 - we take into account daylight from an average clear sky, Fig. 6 - daylight is neglected). We can see that the tables located by the windows, when counting with daylight, have the highest level of average light intensity and the lighting at the other end of the room has values borderline with the required i. min. 500lx. If we neglect the daylight factor (Fig. 6), which can happen in the afternoon in the winter months, we see that the tables around the perimeter of the room have an insufficient level of light intensity in the case of the old lighting model. Thus, we can see that if there was no combination of natural and artificial lighting in the room, the lighting requirements would be met only in the middle of the room and the tables by the walls would not meet the required value of the average lighting intensity. The combination of natural and artificial lighting is very important due to the benefits that natural lighting offers, so we can say that tables located near the windows are most suitable for students, but it is necessary to avoid glare from direct sunlight.

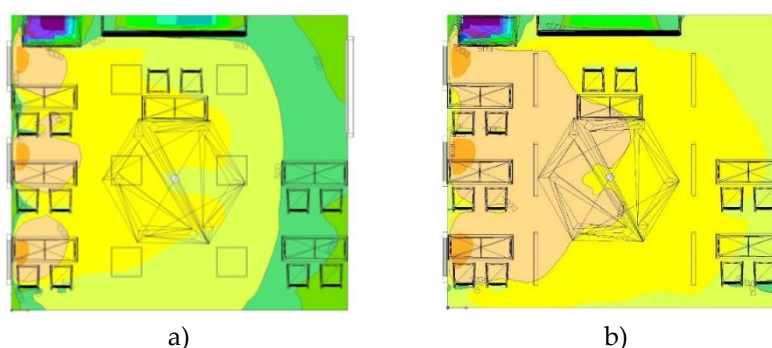


Figure 5 Light intensity - including daylight (average clear sky) a) old model b) new model

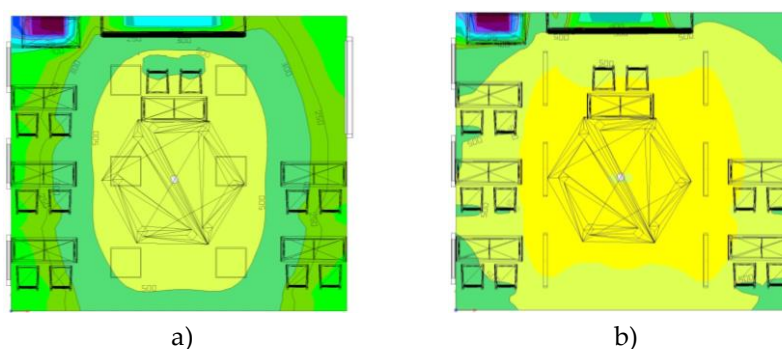


Figure 6 Light intensity - without daylight a) old model b) new model

The summary of the results shows that in the old model the requirements for the overall intensity of the room are not met, in the new model these requirements are met. Specifically, which places of work performance do not meet the requirements are shown in the following table (Table 1), where the measurement results and simulation results in the DIALux EVO program under an average clear sky are also compared.

Table 1 Comparison of results

	Measured $E_{m \pm U}$ [lx]	Dialux (old model)	Dialux (new model)
	$U=15\%$	E_m [lx]	E_m [lx]
Total lighting	$593 \pm 88,95$	678	938
M1	800 ± 120	891	1212
M1 - surroundings	$899 \pm 134,85$	1026	1337
M2	$1163 \pm 174,45$	1337	1694

M2 - surroundings	1098 ± 164,7	1051	1400
M3	1387 ± 197,55	1506	1838
M3 - surroundings	863 ± 121,95	981	1307
M4	712 ± 106,8	809	1002
M4 - surroundings	688 ± 103,2	804	987
M5	719 ± 107,85	809	1007
M5 - surroundings	679 ± 101,85	795	1040
M6	418 ± 63	384	791
M6 - surroundings	488 ± 73,2	447	831
M7	400 ± 60	349	727
M7 - surroundings	452 ± 67,8	389	740

Where:

E_m – average illuminance

U – measurement uncertainty determined by calculation (15%)

The DIALux program also allows you to easily and quickly calculate the energy consumption, LENI (Lighting Energy Numeric Indicator) and the financial costs associated with it. The LENI value represents the actual energy consumption of the lighting system in kWh per square meter and year. The values of energy consumption and costs based on our lighting design calculated by the DIALux evo program are given in Table 2.

Table 2 DIALux - energy consumption and energy costs

	Energy consumption [kWh/a]	LENI [kWh/a/m ²]	Estimated costs [€/a]
Old model	1100-1700	28-45	324-515
New model	430-680	11-18	128-203

3. Results

The aim of the paper was to compare 2 tools for lighting evaluation in the room, namely, first classical personal measurement using a measuring device (luxmeter) and secondly using computer software for lighting design, which in our case was DIALux lighting design software. EVO.

A comparison of the measurement and simulation results shows that the total illuminance, if neglected by the daylight factor, does not meet the lighting requirements. If we take into account the presence of daylight, the requirements for general lighting are met, but the measuring points that are furthest from the windows, i. M6 and M7 do not meet the requirements of light intensity (Tab. 1.) The results of measurement and simulation compared in Table 1 do not differ in almost all cases by more than the stated measurement uncertainty, the only exceptions are measuring points M4-surroundings and M5-surroundings where there was uncertainty. measurements slightly exceeded what could have been caused by inaccurate measurements. Regarding the final results and their comparison with the required value of the average light intensity (500 lx), the results of the manual measurement and the results of the DIALux program agree on the fulfillment resp. non-compliance with the required value at measuring points M6 and M7, which also applies to their immediate surroundings. In the new proposed lighting model, these shortcomings are eliminated and the required lighting value is met at all points of the job.

4. Conclusions

With the increasing time spent in building interiors, the topic of assessing lighting conditions is becoming more important, not only because of the impact of lighting on human health and comfort, but also from an economic and environmental point of view. As innovations are constantly taking place in the field of lighting systems, such as e.g. higher efficiency, lower environmental impact or automation of lighting systems is important evaluation and improvement of current lighting systems. Computer software for lighting design can be very useful in this regard.

The paper compares the results of lighting evaluation by measuring and using DIALux software. The measurement results and the results from DIALux agree on which of the measuring points meet the required values of the light intensity and which measuring points do not meet these requirements. The use of the software enabled a clearer processing of the results in numerical and graphical form. DIALux also automatically calculated the energy consumption and costs of a simulated lighting system. In the software, it is possible to easily and quickly compare different lighting system designs, either by changing the layout of the luminaires or by using new luminaires, which we can easily obtain by downloading from a freely available online library. By designing the new lighting, we have met the requirements for lighting throughout the room, as well as at all places of the job, even if the daylight factor is neglected, all while maintaining the layout and number of lamps. At the same time, we have achieved energy savings by using this computer software and changing the type of luminaires.

Acknowledgments: This contribution was created within the project KEGA 011TUKE-4/2021, which is being solved at the Technical University in Košice.

References

1. Boyce, P.R. Lighting research for interiors: The beginning of the end or the end of the beginning. *Light. Res. Technol.* 2004, 36, 283–293.
2. Gligor, V. Luminous Environment and Productivity at Workplaces. Thesis (Licentiate), Helsinki University of Technology, Espoo, Finland, 2004.
3. Kralikova, R.; Wessely, E. Lighting Quality, Productivity and Human Health. In Proceedings of the 27th DAAAM International Symposium on Intelligent Manufacturing and Automation, Mostar, Bosnia and Herzegovina, 26–29 October 2016; Volume 27, ISSN 1726-9679.
4. Schlangen, L.; Price, L. The Lighting Environment, Its Metrology, and Non-visual Responses. *Front. Neurol.* 2021, 12, 624861, doi:10.3389/fneur.2021.624861.
5. Figueiro, M.G.; Nagare, R.; Price, L. Non-visual effects of light: How to use light to promote circadian entrainment and elicit alertness. *Light. Res. Technol.* 2018, 50, 38–62, doi:10.1177/1477153517721598.
6. Baloch, R.M.; Maesano, C.N.; Christoffersen, J.; Mandin, C.; Csobod, E.; de Oliveira Fernandes, E.; Annesi-Maesano, I.; On Behalf of the SINPHONIE Consortium. Daylight and School Performance in European Schoolchildren. *Int. J. Environ. Res. Public Health* 2021, 18, 258, doi:10.3390/ijerph18010258.
7. Hastings MH, Reddy AB, Maywood ES: A clockwork web: circadian timing in brain and periphery, in health and disease: *Nature Rev Neuro*, 2003;4:649-661.
8. Vyhláška č. 206/2011 Z. z. a vyhláška č. 541/2007 Z. z. o podrobnostiach o požiadavkách na osvetlenie pri práci.
9. Dialux is the Software for Your Professional Lighting Design. Available online: <https://www.dialux.com/en-GB/dialux> (ac-cessed on 8 February 2021).



Materials designed through microarchitecture

Ivan Grega¹

¹ Department of Engineering, University of Cambridge, CB2 1PZ, UK, ig348@cam.ac.uk

Abstract: Material properties are typically coupled. For example, light materials are weak, while strong materials are heavy. We wish to design materials with unique combinations of mechanical properties which will overcome such constraints, for instance, materials with the density of water but the strength and toughness of steel. This is possible using cellular metamaterials through careful control of their microarchitecture. This article outlines the field of architected metamaterials, including their features, manufacturing methods, and possible applications.

Keywords: architected materials, metamaterials, micro-architected lattices

1. Introduction

Expansion of materials library. It is interesting to note that the evolution of human mankind has been closely tied with the discovery of new materials. Indeed, the naming of epochs (Stone Age, Bronze Age, Iron Age), reflects the state-of-the-art material which was available at the time. The materials library has been growing since prehistoric times, when only natural materials such as wood and stone were known, up to the present day, when many different alloys, composites, polymers, and semiconductors are widely used.

Materials have many different properties (mechanical: stiffness, strength, toughness; electrical: conductivity, permittivity, thermal: diffusivity; etc.). If we take a slice through the multidimensional property space, we can plot two properties on x - y axes for a range of materials. These plots are called *Ashby charts* after materials engineer Michael Ashby, a pioneer in the field of cellular materials who devised a systematic approach to materials selection. In Figure 1a, we plot strength versus density for a large number of material classes. Metals and ceramics are at top right, with densities approaching $10,000 \text{ kg m}^{-3}$ and failure strength σ_f up to 1 GPa. Foams are among the lightest materials with densities as low as 10 kg m^{-3} . Note that the axes of the chart are logarithmic – the ranges of densities and strengths span three and five orders of magnitude, respectively. There is a huge variety in the available materials library! Importantly, we observe that most materials are located along the main diagonal, which means that strong materials are typically heavy, while light materials are weak. This coupling of strength and density is an example of a constraint which we are trying to overcome by clever materials design.

Modern materials science has been using three main approaches to devise materials with enhanced properties. Firstly, manipulations through *chemistry* have enabled the creation of new metals through alloying (e.g. bronze, stainless steel), the doping of semiconductors (arsenic in germanium, boron in silicon), or the synthesis of hundreds of new polymers, which have replaced metals in many use cases. The second approach is to manipulate *microstructure*, as the distribution of phases and defects within material significantly

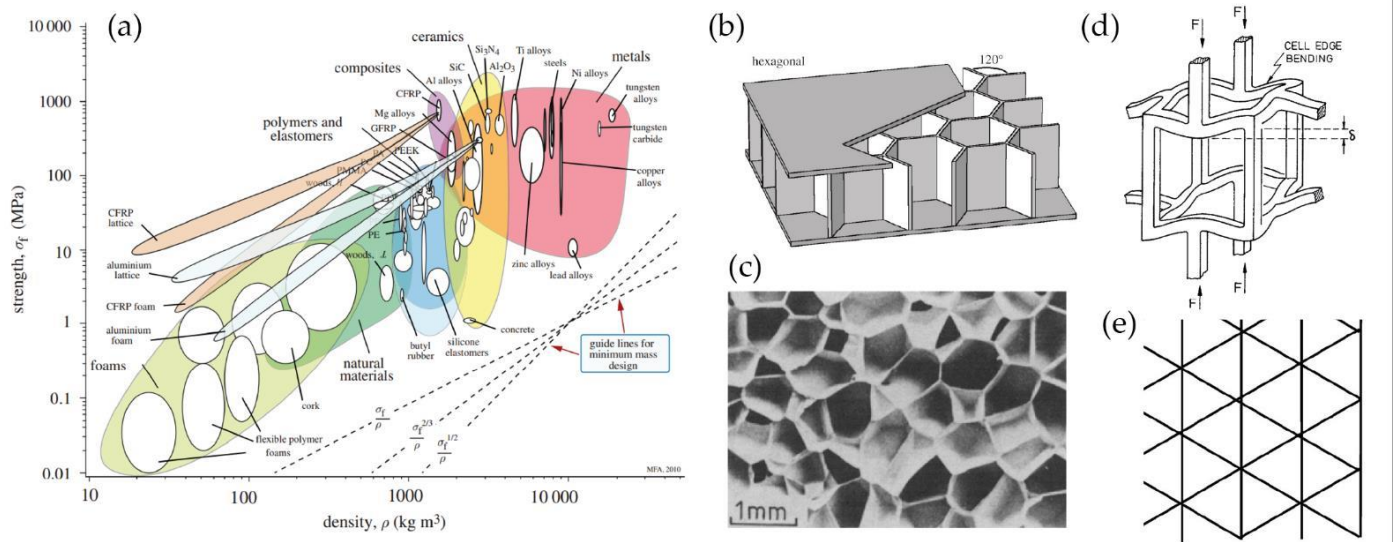


Figure 1. (a) So-called Ashby chart for a wide range of materials. In this specific property chart, strength (failure stress σ_f) is plotted against density ρ on logarithmic axes. Architected lattices and foams fill gaps in the property space, by offering high strength at low density. [24] (b) Hexagonal honeycomb used as sandwich panel core. [20] (c) Closed-celled foam. [25] (d) Bending-dominated open-celled foam. [27] (e) Stretching-dominated triangular lattice. [24]

are mostly composed of empty space, but have desirable properties for sandwich panels, insulation, or energy absorption. Composite materials (carbon fibre, glass fibre) are examples of combining ceramic fibres with polymer matrix in controlled orientations and proportions. The resulting material can achieve properties much better than the “rule of mixtures”. For example, glass fibre-reinforced epoxy has toughness higher than both glass and epoxy thanks to distributed cracking and is widely used in wind turbine blades. [1] *Evolutions in structural engineering.* The emergence of new materials has been followed by an evolution of methods in structural engineering. How structures are designed depends on the materials they use. Up until the end of the Middle Ages, most buildings were constructed from stone using mainly compression loading and considering thrust lines. With the arrival of the Industrial Revolution and mass production of steel, structural engineering shifted from stone and brick to steel frameworks. It turned out that the load-bearing capacity of a structure can be maximized when material is only used in the correct places. *Truss* frameworks make use of axial tension and compression of members and thus achieve a high efficiency in supporting a given load with minimum structural mass. (Fig. 2a)

Inspiration in nature. Let us now consider natural materials which have been around for millennia. Biological materials such as bone, wood, cork, and many others all have one feature in common – they have cellular microstructure. (Fig. 2e,f) Their porosity results not only in a reduced mass, but also gives rise to other features, such as crack arrest and increased fracture toughness. Consider, for example, hard biogenic materials nacre, dentin, and bone. They have both high strength and high fracture toughness, a combination of properties which are often exclusive. Other examples of features enabled in cellular materials include diffusion through pores and increased internal surface area available for chemical reactions or biological synthesis.

Lattice metamaterials. When we combine the nature-inspired microstructure (cellular solids) with the topological optimization of structural engineering (truss frameworks), we obtain lattice metamaterials. Periodic lattices have a well-defined geometry of struts and nodal connections. (Fig. 2) When the *unit cell* of the lattice is repeated many times, the dimensions of the resulting structure are much bigger than the dimensions of the individual members, and we call such structure *metamaterial*. In traditional materials, macroscopic properties are determined predominantly by chemistry (how atoms are bound together) and microstructure (how phases are distributed). In architected metamaterials,

it

is *topology* (how elements are connected) which governs the macroscopic properties. For instance, *bending-dominated* lattice with relative density $\bar{\rho} \sim 5\%$ is more than 10 times weaker than *stretching-dominated* lattice of the same relative density (see Fig. 1a,d,e). In addition, when the structural length-scale of the architected material is reduced to the macro- and nano-scale, interesting phenomena are observed. For example, a ceramic lattice composed of hollow alumina (Al_2O_3) struts, with walls only 20 nm thick, does not fail by brittle fracture (as the ceramic parent material would), but can fully recover after up to 50% compressive strain. [2] To take advantage of this *size effect*, we need manufacturing methods with micro- to nanoscale resolution.

2. Manufacturing of micro-architected materials

The materials we have been discussing often have complex geometry on the microscale level. As a result, they require manufacturing methods which can produce arbitrary shapes at a high precision. There are two main classes of manufacturing methods which are used for this task: additive manufacturing (AM) methods and self-assembly methods. Some specific techniques are briefly outlined below.

Additive manufacturing methods. A vast number of methods have been developed in the research setting. In the domain of *extrusion-based methods*, we mention *direct ink writing* (DIW), which can be used to make a variety of geometries on the microscale. [3, 4] DIW does not melt the material passing through the nozzle but uses materials with tailored shear thinning behaviour. These materials flow under shear inside the nozzle, but once deposited, they hold their shape. (Fig. 3a,b) A *light-based* counterpart of DIW is the *two-photon lithography* (2PL). [5] Light (laser) beam is focussed into a voxel in 3d space, which leads to the solidification of photosensitive polymer. The use of light allows for an unprecedented resolution on the nanometre scale, thus enabling the creation of precise 3d geometries. Both DIW and 2PL are inherently 0D processes – the structure is manufactured one *voxel* at a time. Projection micro-stereolithography (PμSL) is based on projecting the whole cross-section of the desired structure into the bath of photosensitive resin at once. [6]

By successive projections of consecutive cross-sections, the whole three-dimensional structure is built. In *three-dimensional interference lithography*, collimated light is shined onto a suitably designed photonic mask. Light passing through the mask produces interference pattern and photosensitive polymer solidifies in the areas of constructive interference. [7]

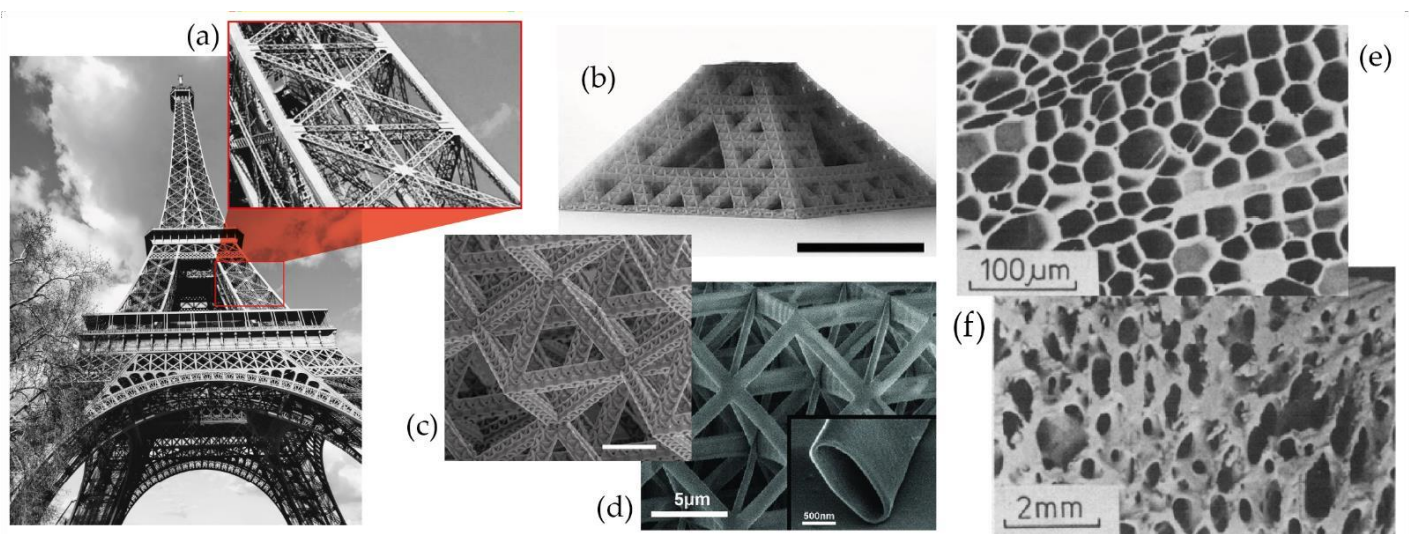


Figure 2. (a) Hierarchical trusses are widely used in structural engineering. Photo by the author. (b) Hierarchical alumina (Al_2O_3) octahedral lattice. Constituent beams are hollow with 20 nm walls. Scale bar 50 μm . [23] (c) Zoomed-in image of octahedral lattice. Scale bar 10 μm . [23] (d) Alumina octet-truss nanolattice showing zoomed-in view of hollow beams. [2] (e,f) Many natural materials have cellular structure. Balsa wood (e) and bone (f). [25]

A novel pseudo-3d method is *computer axial lithography* (CAL). (Fig. 3c,d) It is based on projecting images obtained via tomographic reconstruction algorithms into a rotating bath of photosensitive resin. [8] Additive manufacturing methods offer unprecedented flexibility in the range of attainable geometries, but this freedom comes at a price – because of their point-wise nature, most additive manufacturing methods are too slow, costly, and do not achieve the required throughput for production of macroscale quantities of metamaterials.

Self-assembly. An alternative which attempts to tackle these issues is self-assembly. The underlying idea of self-assembly is that particles or molecules can spontaneously assemble into hierarchical structures under suitable conditions. Polymerisation-induced phase separation based on spinodal decomposition has been used to produce shell-based architectures. [9, 10] It is possible to achieve tunable elastic anisotropy and extreme mechanical resilience. (Fig. 3e) In a different self-assembly method, spheres are made to assemble into close-packed crystals to create *opals*. Filling the gaps in these crystals with a second phase and subsequent removal of the precursor spheres leads to the formation of the *inverse opal*. [11, 12] (Fig. 3f,g) Overall, self-assembly methods achieve significant speed and throughput improvement over AM methods, but as a trade-off, they can only produce a very limited range of geometries.

3. Applications of architected materials

Thanks to their features spanning multiple length-scales, architected materials have numerous use cases. The properties of interest are not only mechanical, but also optical, electrical, acoustic, and others. A non-exhaustive selection of possible applications is outlined below.

Mechanical. Architected materials expand the available property space in the materials library. Depending on their topological design, relatively high stiffness, strength and toughness can be achieved at a very low weight. As a result, these metamaterials can be used as lightweight construction materials. Examples include sandwich panels, whereby the light cellular material creates separation between thin sheets which efficiently carry tension/compression. (Fig. 4a) The resulting sandwich panels have a high bending rigidity at a low weight, and for this reason, have been applied in the aviation industry. Moreover, architected metamaterials have desirable dynamic characteristics (e.g. wave propagation

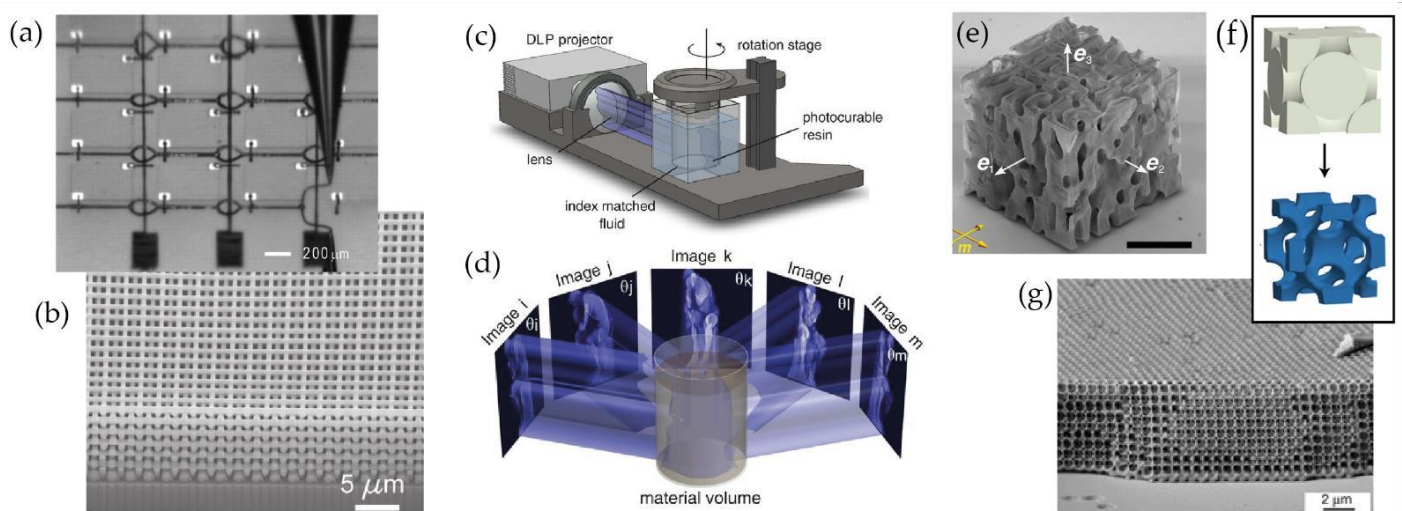


Figure 3. Manufacturing of architected materials. (a) Direct ink writing (DIW) of silver ink. [4] (b) Titania (TiO₂) lattice formed by DIW. [3] (c,d) Computer axial lithography (CAL) process. Tomographic reconstructions of model are projected into photosensitive resin. [8] (e) Self-assembled spinodal shell-like architecture. [10] (f) Process of inverse opal manufacture from opal template. [12] (g) SEM image of a large inverse opal crystal. [11]

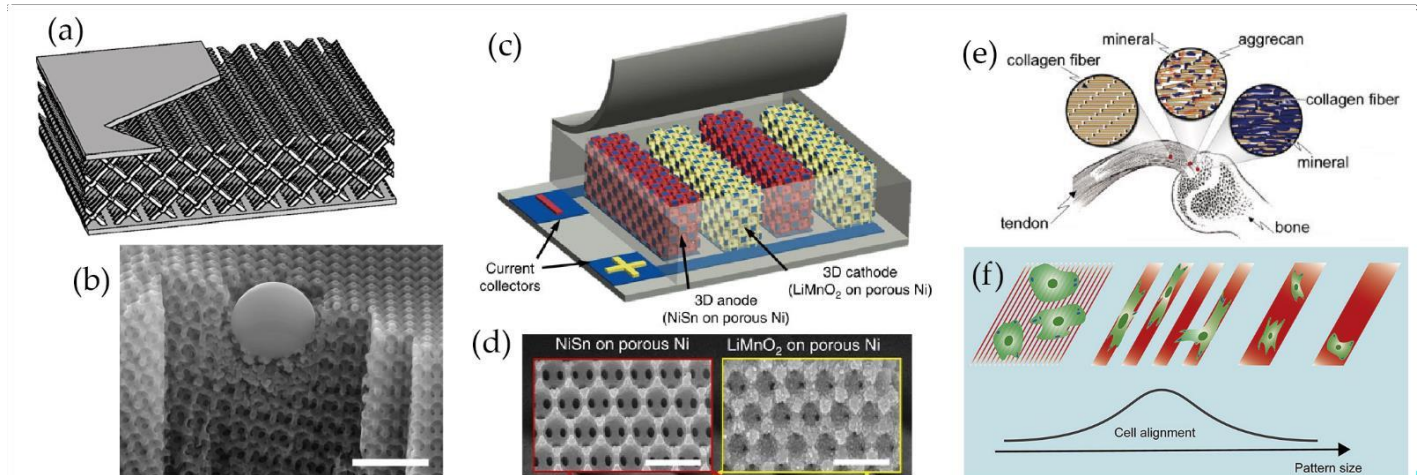


Figure 4. Applications of architected materials. (a) Lattice material used as the core in sandwich panel. [20] (b) Energy of projectile absorbed by nanoarchitected carbon lattice. Scale bar 10 μm . [21] (c) Nanoporous microbattery electrodes. [22] (d) SEM images of nanoarchitected electrodes from (d). Scale bars 1 μm . [22] (e) Functional grading of mineral and collagen in tendon-to-bone attachment. [19] (f) Cell alignment depends on surface morphology. [18]

and deformation under impacts). They are capable of efficient energy absorption (Fig. 4b) and can be used for blast protection, for example, to shield the underbody of military vehicles. Moreover, clever topological design can be used to achieve bistable behaviour. This enables the storage of elastic strain energy on top of plastic energy absorption. [13]

Electrical. There is an ever-growing push for using sustainable energy sources, but this relies to a large extent on the ability to store electrical energy. This is most often done in batteries or in capacitors. The power density of these devices depends on the rate at which they can be charged or discharged, which is governed by kinetics of electron and ion diffusion and by the formation of dendrites. Therefore, to increase the rates while avoiding dendrite formation due to high current density, surface area available to diffusion must be large. Architected metamaterials can have features manufactured on the microscale and in almost arbitrary shape. As a result, it is possible to make metamaterials with hierarchical surface features to act as battery electrodes with a relatively large surface area. (Fig. 4c,d) It has been demonstrated that 3D zinc architectures enable high-power discharge while suppressing dendrite formation. [14, 15]

Photonic and phononic crystals. Self-assembly of opals and inverse opals is a scalable process of manufacturing highly ordered crystals. When the diameter of precursor spheres is comparable to the photonic wavelengths ($\sim 400\text{ nm}$), the resulting crystal metamaterial interacts with incident light which gives rise to diffraction. Such metamaterials can be used in optical applications. When the spheres are orders of magnitude larger (millimetre range), the frequencies given by lattice spacing can be tuned for sound waves, and crystals with desirable phononic properties are created. [16, 17]

Biomechanics and biochemistry. The large freedom in geometry of the architected microstructures enables their use in biochemical applications. The shape can be precisely designed to include active sites for biological processes or chemical reactions. It has been shown that cell adhesion depends strongly on surface features of the substrate [18], therefore, micro-architected materials are promising for biomechanical use. The repair of joints, tendons and other biological tissues is an active area of innovation in medicine. As an example, the microarchitecture of implants can be tailored to match the microstructure of bone and thus act as bioscaffold for growth of surrounding tissue. [19]

4. Perspective

Improvements in design. We have emphasised that the key feature determining the macroscopic properties of architected materials is topology. Topology optimisation methods have been employed to search a large parameter space and come up with the geometry that has the required properties. A promising research avenue is to employ machine

learning algorithms for generative design of microstructures based on the desired mechanical response. If the algorithms can be scaled up, we will be able to design non-periodic lattices which could have desirable properties, for example, fracture resistance, where cracks originating on the surfaces could be blunted. A further improvement in the design of architected metamaterials will be to combine multiple materials within one micro-architecture, to achieve performance superior to any of the constituents – this is how natural materials such as nacre achieve their high strength and toughness.

Improvements in manufacture. Additive manufacturing methods are advancing at a rapid pace and architected materials can be made with almost arbitrary geometry. While there are still constraints to the selection of constituent material (for example, light-based methods require photosensitive materials), these challenges are being solved. An important area of focus is to increase the manufacturing throughput. Many methods are inherently 0D (voxel by voxel) and suffer from low speed. Volumetric methods and self-assembly processes are a promising way forward. Another area which needs to be addressed are manufacturing imperfections. While topology optimisation can predict microstructures with superior properties, once they are manufactured, we often find a discrepancy in real properties due to manufacturing defects. These defects arise under complex

circumstances which are hard to model such as nonuniform diffusion, thermal gradients and associated stresses. A promising way to tackle these challenges is to employ novel data-driven methods.

Acknowledgments: The author would like to thank his PhD supervisor Prof Vikram Deshpande for invaluable discussions in preparation of the manuscript.

Conflicts of Interest: The author declares no conflict of interest.

References

1. J. R. Greer and V. S. Deshpande, "Three-dimensional architected materials and structures: Design, fabrication, and mechanical behavior," *MRS Bulletin*, vol. 44, p. 750–757, 2019. doi: 10.1557/mrs.2019.232
2. L. R. Meza, S. Das and J. R. Greer, "Strong, lightweight, and recoverable three-dimensional ceramic nanolattices," *Science*, vol. 345, p. 1322–1326, 2014. doi: 10.1126/science.1255908
3. E. Duoss, M. Twardowski and J. Lewis, "Sol-Gel Inks for Direct-Write Assembly of Functional Oxides," *Advanced Materials*, vol. 19, p. 3485–3489, 2007. doi: 10.1002/adma.200701372
4. B. Y. Ahn, E. B. Duoss, M. J. Motala, X. Guo, S.-I. Park, Y. Xiong, J. Yoon, R. G. Nuzzo, J. A. Rogers and J. A. Lewis, "Omnidirectional Printing of Flexible, Stretchable, and Spanning Silver Microelectrodes," *Science*, vol. 323, p. 1590–1593, 2009. doi: 10.1126/science.1168375
5. S. Maruo, O. Nakamura and S. Kawata, "Three-dimensional microfabrication with two-photon-absorbed photopolymerization," *Optics Letters*, vol. 22, p. 132, 1997. doi: 10.1364/ol.22.000132
6. X. Zheng, J. Deotte, M. P. Alonso, G. R. Farquar, T. H. Weisgraber, S. Gemberling, H. Lee, N. Fang and C. M. Spadaccini, "Design and optimization of a light-emitting diode projection micro-stereolithography three-dimensional manufacturing system," *Review of Scientific Instruments*, vol. 83, p. 125001, 2012. doi: 10.1063/1.4769050
7. T. A. Schaedler, A. J. Jacobsen, A. Torrents, A. E. Sorensen, J. Lian, J. R. Greer, L. Valdevit and W. B. Carter, "Ultralight Metallic Microlattices," *Science*, vol. 334, p. 962–965, 2011. doi: 10.1126/science.1211649
8. B. E. Kelly, I. Bhattacharya, H. Heidari, M. Shusteff, C. M. Spadaccini and H. K. Taylor, "Volumetric additive manufacturing via tomographic reconstruction," *Science*, vol. 363, p. 1075–1079, 2019. doi: 10.1126/science.aau7114
9. A. Vidyasagar, S. Krödel and D. M. Kochmann, "Microstructural patterns with tunable mechanical anisotropy obtained by simulating anisotropic spinodal decomposition," *Proceedings of the Royal Society A: Mathematical, Physical and Engineering Sciences*, vol. 474, p. 20180535, 2018. doi: 10.1098/rspa.2018.0535
10. C. M. Portela, A. Vidyasagar, S. Krödel, T. Weissenbach, D. W. Yee, J. R. Greer and D. M. Kochmann, "Extreme mechanical resilience of self-assembled nanolabyrinthine materials," *Proceedings of the National Academy of Sciences*, vol. 117, p. 5686–5693, 2020. doi: 10.1073/pnas.1916817117
11. Y. A. Vlasov, X.-Z. Bo, J. C. Sturm and D. J. Norris, "On-chip natural assembly of silicon photonic bandgap crystals," *Nature*, vol. 414, p. 289–293, 2001. doi: 10.1038/35104529

12. J. H. Pikul, S. Ozerinç, B. Liu, R. Zhang, P. V. Braun, V. S. Deshpande and W. P. King, "High strength metallic wood from nanostructured nickel inverse opal materials," *Scientific Reports*, vol. 9, 2019. doi: 10.1038/s41598-018-36901-3
13. S. Shan, S. H. Kang, J. R. Raney, P. Wang, L. Fang, F. Candido, J. A. Lewis and K. Bertoldi, "Multistable Architected Materials for Trapping Elastic Strain Energy," *Advanced Materials*, vol. 27, p. 4296–4301, 2015. doi: 10.1002/adma.201501708
14. J. S. Ko, A. B. Geltmacher, B. J. Hopkins, D. R. Rolison, J. W. Long and J. F. Parker, "Robust 3D Zn Sponges Enable High-Power, Energy-Dense Alkaline Batteries," *ACS Applied Energy Materials*, vol. 2, p. 212–216, 2018. doi: 10.1021/acsaem.8b01946
15. J. H. Pikul and J. W. Long, "Architected materials for advanced electrochemical systems," *MRS Bulletin*, vol. 44, p. 789–795, 2019. doi: 10.1557/mrs.2019.229
16. E. Armstrong and C. O'Dwyer, "Artificial opal photonic crystals and inverse opal structures – fundamentals and applications from optics to energy storage," *Journal of Materials Chemistry C*, vol. 3, p. 6109–6143, 2015. doi: 10.1039/c5tc01083g
17. Z. Liu, X. Zhang, Y. Mao, Y. Y. Zhu, Z. Yang, C. T. Chan and P. Sheng, "Locally Resonant Sonic Materials," *Science*, vol. 289, p. 1734–1736, 2000. doi: 10.1126/science.289.5485.1734
18. A. B. C. Buskermolen, T. Ristori, D. Mostert, M. C. van Turnhout, S. S. Shishvan, S. Loerakker, N. A. Kurniawan, V. S. Deshpande and C. V. C. Bouten, "Cellular Contact Guidance Emerges from Gap Avoidance," *Cell Reports Physical Science*, vol. 1, p. 100055, 2020. doi: 10.1016/j.xcrp.2020.100055
19. S. Thomopoulos, G. M. Genin and L. M. Galatz, "The development and morphogenesis of the tendon-to-bone insertion - what development can teach us about healing," *Journal of Musculoskeletal and Neuronal Interactions*, vol. 10, pp. 35–45, 2010.
20. H. N. G. Wadley, "Multifunctional periodic cellular metals," *Philosophical Transactions of the Royal Society A: Mathematical, Physical and Engineering Sciences*, vol. 364, p. 31–68, 2005. doi: 10.1098/rsta.2005.1697
21. C. M. Portela, B. W. Edwards, D. Veyssset, Y. Sun, K. A. Nelson, D. M. Kochmann and J. R. Greer, "Supersonic impact resilience of nanoarchitected carbon," *Nature Materials*, vol. 20, p. 1491–1497, 2021. doi: 10.1038/s41563-021-01033-z
22. J. H. Pikul, H. G. Zhang, J. Cho, P. V. Braun and W. P. King, "High-power lithium ion microbatteries from interdigitated three-dimensional bicontinuous nanoporous electrodes," *Nature Communications*, vol. 4, 2013. doi: 10.1038/ncomms2747
23. L. R. Meza, A. J. Zelhofer, N. Clarke, A. J. Mateos, D. M. Kochmann and J. R. Greer, "Resilient 3D hierarchical architected metamaterials," *Proceedings of the National Academy of Sciences*, vol. 112, p. 11502–11507, 2015. doi: 10.1073/pnas.1509120112
24. N. A. Fleck, V. S. Deshpande and M. F. Ashby, "Micro-architected materials: past, present and future," *Proceedings of the Royal Society A: Mathematical, Physical and Engineering Sciences*, vol. 466, p. 2495–2516, 2010. doi: 10.1098/rspa.2010.0215
25. M. F. Ashby and R. F. M. Medalist, "The mechanical properties of cellular solids," *Metallurgical Transactions A*, vol. 14, p. 1755–1769, 1983. doi: 10.1007/bf02645546
26. W. Stöber, A. Fink and E. Bohn, "Controlled growth of monodisperse silica spheres in the micron size range," *Journal of Colloid and Interface Science*, vol. 26, p. 62–69, 1968. doi: 10.1016/0021-9797(68)90272-5
27. L. Gibson and M. F. Ashby, *Cellular solids : structure and properties*, Cambridge New York: Cambridge University Press, 1997. ISBN 978-1-139-87832-6

Indoor localization system for mobile robots based on ultrasonic signal.

Maksym Grytsiv ^{1*}, Marek Sukop ¹ Martin Kočan ¹

¹ Technical University of Kosice, Department of Manufacturing Engineering and Robotics

* Correspondence: maksym.grytsiv@tuke.sk; Tel.: +421 55 602 3156

Abstract: This article describes how we develop a location system for mobile robotics in the interior of buildings where GPS cannot be used. The article is divided into two main parts. The first describes algorithms developed in the Flowcode environment. These algorithms were used to test the basic function of such a localization system. The second part of the article lists the measurements currently performed on this system. Of course, additional measurements and tests are still needed.

Keywords: Mobile robot, Measurements, Ultrasonic, Localization

1. Introduction

Testing of the device operation as well as basic algorithms was performed using the Arduino UNO 328P platform [2]. The communication module for timing signals was used module nRF24L01, capable of transmitting signals on the carrier frequency 2.4MHz [4]. At the same time, these modules can be retuned to a different carrier frequency according to the selected channel. With a data throughput of up to 2Mb / s, 96 channels are available and with a data throughput of 1Mb / s, up to 127 channels are available [5]. Algorithms for testing were developed exclusively in the graphical programming and simulation environment Flowcode [3]. The arrangement of the basic elements in the system is shown in Fig.1 [12]

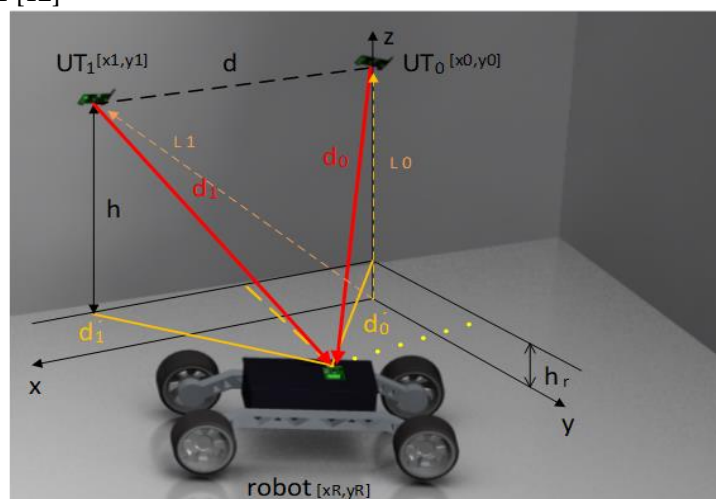


Fig. 1 indoor location system elements [12]

2. Generating signal transmitters and receivers

First one is Timing signal transmitter for system synchronization. This module sends a clock (synchronization) signal to all modules. The signal synchronizes the ultrasonic transmitter module with the receiver modules as well as the receiver modules with

respect to each other [1]. A simple algorithm in conjunction with Arduino Uno and nRF24L01 will ensure sufficiently accurate synchronization for our purposes. The block diagram of the test device is easy.

In the test application, a 100ms time loop was used to transmit the synchronization signal (Fig. 2). This means that the synchronization signal was transmitted 10 times per second and therefore the number of measurements is limited by this value.

The first ultrasound signal transmitter UT0 is activated and starts transmitting the ultrasound signal after the information 0b00001010 (10). The second transmitter UT1 is activated and transmits an ultrasonic signal after the information 0b11001100 (204). The ultrasonic signal receiver located on the robot can evaluate the time difference between the synchronization signal and the received ultrasonic signal. The time difference determines the distance between the transmitter and the receiver. After evaluating the distances d_0 and d_1 , it is not a problem to determine the position of the robot in space (x_R , y_R) since the coordinate z is given by the location of the receiver on the robot (Fig. 1).

$$x_R = d_0 \times \frac{d_0^2 + d_1^2 - d_2^2}{2 \times d \times d_0} \quad (1)$$

$$y_R = \sqrt{d_0^2 - x^2} \quad (2)$$

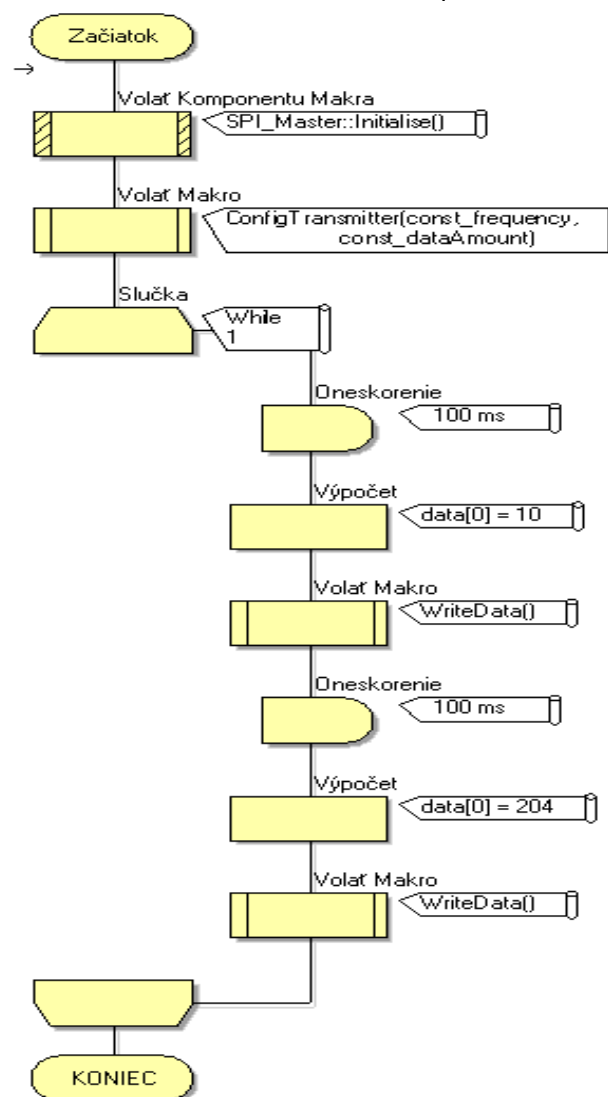


Fig. 2 Algorithm for synchronization module

The second will be Ultrasound Signal Transmitters UT0 and UT1. The tested transmitters were also implemented using the Arduino Uno platform. The nRF24L01 module receives the synchronization signal. The power section for transmitting the ultrasonic signal using the piezoelectric transducer UST-40T is converted using an H-bridge, which is primarily intended for controlling DC motors. Fig. 3 is a block diagram of an ultrasonic signal transmitter

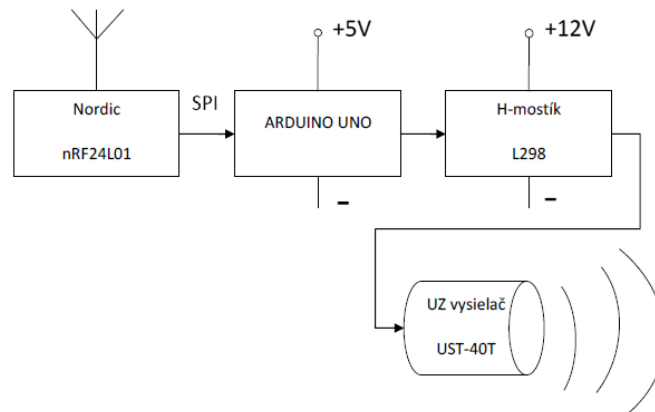


Fig. 3 block diagram of ultrasonic signal transmitters

Using the H-bridge, the SignalOutUS () macro creates a so-called a modified sine signal (Fig. 4), which is more suitable than just an ordinary AC rectangular signal fed to the piezoelectric ultrasonic signal transmitter UST-40T.

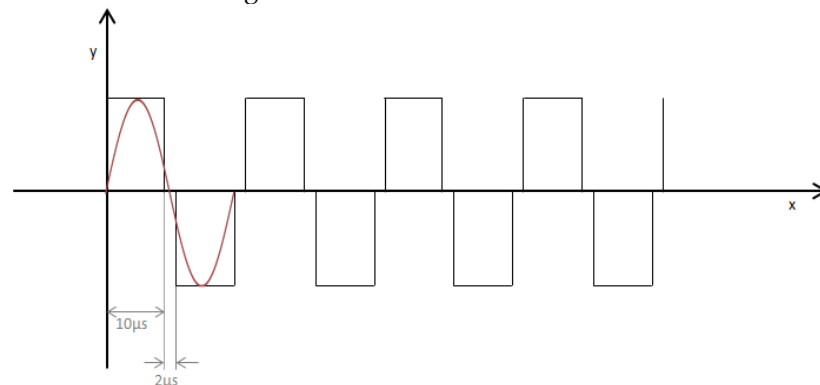


Fig. 4 Modified sine signal generated by the SignalOutUS () macro

The algorithm for the transmitters (Fig. 5) is the same except for the activation byte, which is equal to 0b00001010 (10) for UT0 and 0b11001100 (204) for UT1. The mentioned value is stored in the constant "const_numUStransmitter".

The SignalOutUS () macro in the main algorithm generates an ultrasonic wave with a duration of 40 periods, which is enough to be captured by an ultrasonic sensor on the robot. According to the performed measurements, the signal composed of approximately 20 periods is sufficient to elicit a response on the ultrasound receiver. Therefore, up to 40 sufficient periods are used, but at the same time such a signal still does not take long (= 1ms) to be repeated every 100ms. At the same time, 100ms is the time for which the signal in the space will attenuate and the echo of the signal will not be captured on the receiver. The SignalOutUS () macro is shown in Fig.6

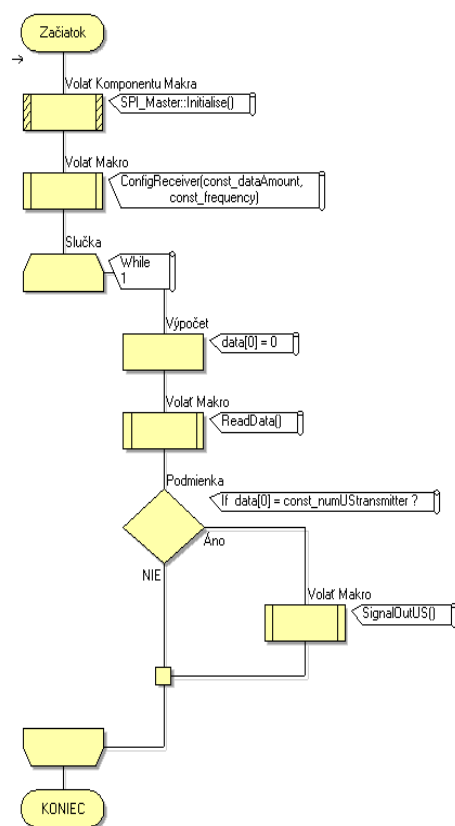


Fig. 5 Ultrasound signal transmitter algorithm

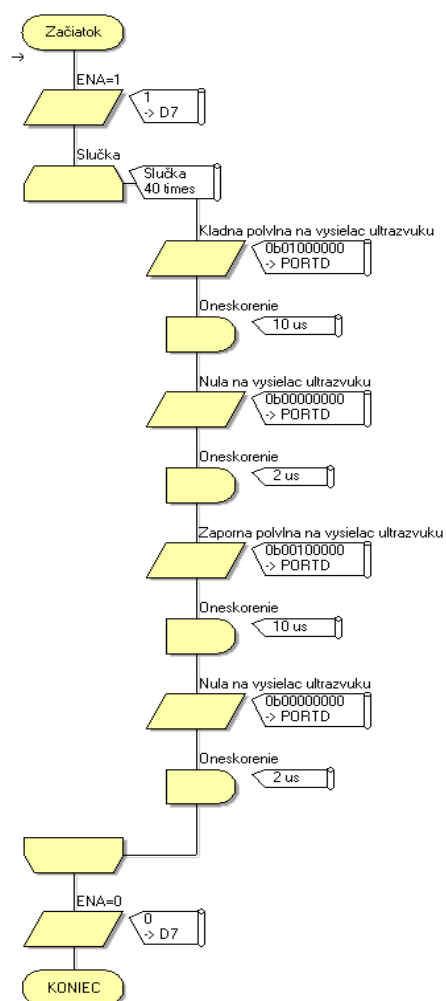


Fig. 6 Macro SignalOutUS ()

The third will be Ultrasound signal receiver. The task of this module is to receive an ultrasonic signal, evaluate the distances from the transmitters and finally use the above equations to calculate the position of the robot. The block diagram is shown in Fig.7.

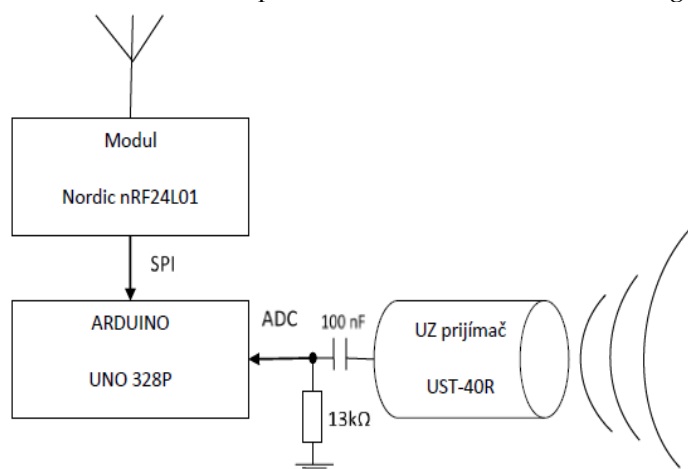


Fig. 7 block diagram of the ultrasonic sensor

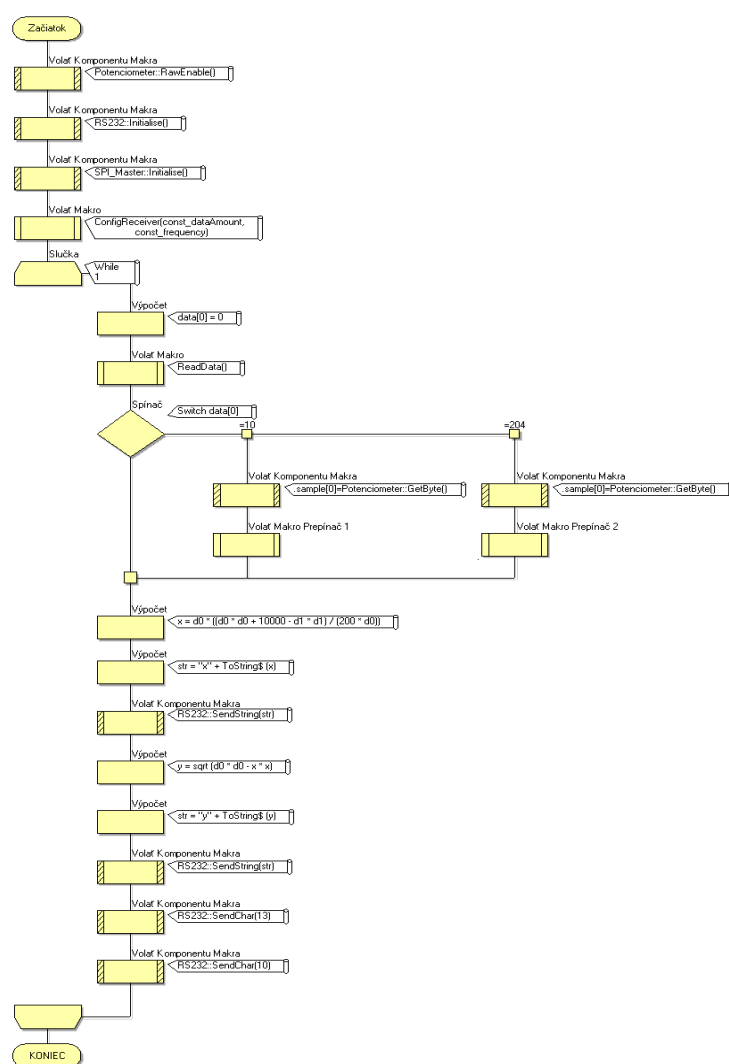
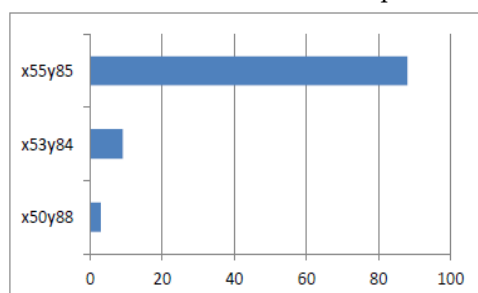


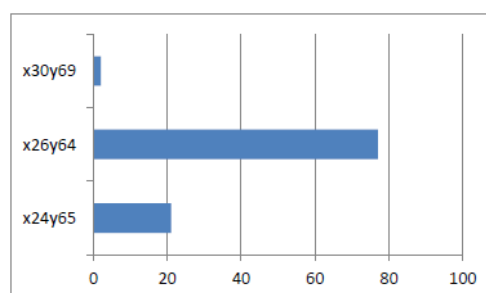
Fig. 8 Algorithm for ultrasonic signal receiver

3. Measurement Results

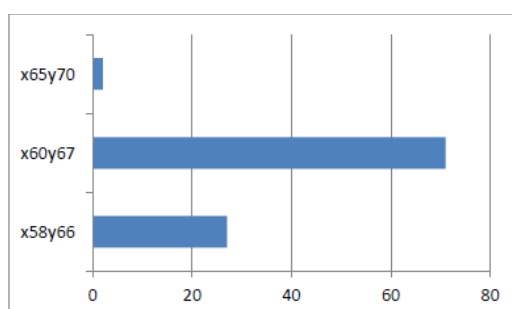
For the initial evaluation of the functionality of the proposed solution for evaluating the position of robots in the internal spaces of buildings, measurements were performed in three different positions of the ultrasonic signal receiver. 100 measurements were performed in each of these three positions. The distance between the transmitters d was 100cm. Positions in which the measurement was performed [55, 85], [25, 65], [60, 65]. The measurement results are shown in graphs 1, 2 and 3, which show the frequency of results for measurements at individual points.



Graph 1 measurement in point [55, 85] and frequency of results



Graph 2 measurement in point [26, 65] and frequency of results



Graph 3 measurement at point [60, 65] and frequency of results

4. Conclusions

The first results show that the design is viable, and it is probably possible to create a positioning device inside buildings with high accuracy at a very low cost. Of course, additional measurements are required. It is necessary to increase the range of the system at least 3-4 times, when using the matrix arrangement of transmitters in the ceiling will contain large spaces with the same accuracy. It is also necessary to work on increasing the stability of the system and eliminating external interference of the ultrasonic signal.

References

1. JURUŠ, Ondrej. Metódy určovania polohy a orientácie mobilných robotov vo vnútornom statickom prostredí. Košice, 2019. Dissertation work. Technical University of Košice. Thesis supervisor Doc. Ing. Marek Sukop PhD.
2. What is Arduino?. Arduino [online]. [cit. 2021-12-14]. <https://www.arduino.cc/>
3. Flowcode Dedicated Site. Matrixtsl [online]. [cit. 2021-12-14]. Dostupné z: <https://www.matrixtsl.com/flowcode/>
4. NRF24L01 and UNO R3 Tutorial. Forum arduino [online]. [cit. 2021-12-14]. Dostupné z: <https://forum.arduino.cc/t/nrf24l01-and-uno-r3-tutorial/135381>
5. Nordic semiconductor: nRF24 Series [online]. [cit. 2021-12-14]. Dostupné z: <https://www.nordicsemi.com/Products/nRF24-series>
6. Tancsák P.: Interný polohový systém pre mobilné roboty. Diplomová práca 2015, Strojnícka fakulta, Technická univerzita v Košiciach.
7. Mertan M.: Návrh univerzálneho interného pozičného systému pre servisnú robotiku. Diplomová práca 2015, Strojnícka fakulta, Technická univerzita v Košiciach.
8. MacArthur D.K.: Design and implementation of an ultrasonic position system for multiple vehicle control. University of Florida. 2003. http://cimar.mae.ufl.edu/CIMAR/pages/thesis/macarthur_d.pdf
9. Do-Eun Kim, et.al.: A Simple Ultrasonic GPS System for Indoor Mobile Robot System using Kalman Filtering. <http://robogames.net/symposium/2007/07-125-Kim-SungKyunKwanUniv-UltrasonicGPSIndoorMobileRobotSystem.pdf>
10. Saeed Shiry Ghidary, et.al.: A new Home Robot Positioning System (HRPS) using IR switched multi ultrasonic sensors. http://www.cs.cmu.edu/~motionplanning/papers/sbp_papers/integrated2/ghidary_ir_beacon.pdf
11. Soo-Yeong Yi, Byoung-Wook Choi: Autonomous Navigation of Indoor Mobile Robot Using Global Ultrasonic System. Seoul. Korea. <http://cdn.intechopen.com/pdfs-wm/145.pdf>
12. JURUŠ, Ondrej a Peter FERENČÍK. Ultrasonic Sensors used to Detect the Position of the Mobile Service Robot. In: Acta Mechanica Slovaca: VOLUME 25, No. 1. Kosice, 2021, 28 - 32. ISSN 1335-2393. Dostupné z: doi:10.21496/ams.2021.010
13. LI, Jian a Guangjie HAN. An Indoor Ultrasonic Positioning System Based on TOA for Internet of Things [online]. In: . [cit. 2021-12-14]. Dostupné z: <https://doi.org/10.1155/2016/4502867>
14. HAJDUK, Mikuláš a Marek SUKOP. Cognitive Multi-agent Systems. Kosice, 2019. ISBN: 978-3-319-93687-1
15. SUKOP, Marek a Ondrej JURUŠ. Algorithms of IPS for Mobile Robotics – Testing Application. Transfer inovácií. 2015, 32, 100-103.

Possibilities of increasing the durability of mold and cores for die casting of aluminum alloys

Ján Hašul¹, Janette Brezinová¹

¹ Technical University of Košice, Department of Technologies, Materials and Computer Supported Production, Mäsiarska 74, 040 01 Košice; e-mail: jan.hasul@tuke.sk; janette.brezinova@tuke.sk

Abstract: The paper presents the results of research aimed at increasing the life of molds and cores for high – pressure aluminum casting. The castings produce is intended for the automotive industry. Local impulse heating was applied to the surface of the base material of the Uddeholm Dievar molds. Three heating rates were used. After surface treatment, structural analysis was performed. PVD coating nAcRo3 was applied to the surface treated in this way. Coating deposition was performed by LARC technology. After laser treatment of the material surface and application of nAcRo3 coating, the surface microgeometry was evaluated according to ISO 25 178. The coated surface was then immersed in an Al-Si alloy melt at a temperature of $680 \pm 20^\circ\text{C}$ and remaining in the melt for 120- and 300-min. Experimental work has confirmed that the resistance of the mold surface has significantly increased. At present, the mold with a modified surface is included in the production and the four times exceeded its service life.

Keywords: die casting, aluminum, cores

1. Introduction

Aluminum is a widely used material in the automotive industry. The use of special aluminum alloys as materials to produce components and automotive parts allows the construction of lightweight components, which lead to an overall reduction in weight and thus to a reduction in fuel consumption. Aluminum alloys used for various body parts in the automotive industry are produced by gravity casting or high-pressure casting (HPDC). One of the main issues in the casting process is the durability of the molds and their components. In fact, in the high pressure die casting (HPDC), the molds are exposed to high temperatures of molted aluminum ($670^\circ\text{C} - 710^\circ\text{C}$), which flows into the mold at a high speed of $30 - 100\text{ m/s}$ and with an injection pressure of $50 - 80\text{ MPa}$. When casting aluminum alloys, the cyclic process leads to a thermocycle loading of the tool surface in the temperature range from $T = 90^\circ\text{C}$ during cooling to $T = 600^\circ\text{C}$. Therefore, the mold is exposed to erosion, corrosion, die soldering or matrix bonding due to frequent contact between the mold surface and the molten metal. Mold insert is an important part of molds commonly used in casting. The aim is to realize specific shapes in castings, such as cavities and undercuts [1-4]. Innovative hard coatings to protect surfaces against wear are of great interest to industry and research institutions in many areas, such as cutting, shaping, and casting tools, mechanical components in general and even biomedical prostheses. Coatings produces by physical vapor deposition (PVD) are recognized as one of the most interesting technologies for protection and surface treatment of products, given the existing potential for the synthesis of materials with unique mechanical, physical and chemical properties [1-4].

Uddeholm Dievar is a Cr-Mo-V tool steel designed to work at high temperatures, which offers very good resistance to heat control, rough cracking, hot wear, and plastic deformation. It is characterized [9]: excellent toughness and ductility, good weather resistance, excellent hardenability, good strength at high temperatures, dimensional stability during the heat treatment and coating deposition process. The chemical composition of the material is in Table 1:

Table 1 Chemical composition of the Uddeholm Dievar material [9]

Element	C	Si	Mn	Cr	Mo	V
(wt %)	0,38	0,2	0,5	5	2,3	0,6

The material excels with its excellent mechanical properties such as high tensile strength, yield strength, good hardness, and others [9]. Table 2 shows the values of mechanical properties of the material.

Table 2 Mechanical properties of the Uddeholm Dievar material [9]

Hardness [HRC]	Tensile strength [MPa]	Yield strength [MPa]	Ductility [%]
44	1480	1210	13

Areas of application of Uddeholm Dievar materials [9]: Forging, hot stamping of sheets, casting and hot forming, metal extrusion, die casting of aluminum and its alloys etc.

The main parameters of die casting were: cutting area was 225 mm², piston speed was 4 m/s, melt velocity in the cut was 100 m/s, filling of the mold cavity was 3 s, solidification of the casting in the mold was 2 s and the total contact time of the casting with the mold cavity, when the mold was closed and open was 14 s. Safety Lube 8715 release agent was used to treat the mold parts. As a basic test experiment, the aim of which was to obtain information on the structure and changes in the strength properties of the material was the direct exposure of ground and polished samples in the AlSi8Cu3 alloy melt for 15 and 300 minutes at a temperature of 680 ± 20 °C. The second test criterion was a comprehensive analysis of the materials of worn shaped parts of molds and cores. The wear analysis of the mold parts was focused on the identification of degradation mechanisms in those areas that were in contact with the molten metal and at the points of contact of the moving cores with the mold parts. The surface condition of the molded parts was examined by scanning electron microscopy and qualitative EDX microanalysis to obtain information on the morphology of the surface that was in contact with the aluminum melt, the surface morphology in the core and mold zones and the nature of cracks visually observed around the mold cavity ejectors. Samples for microstructure analysis were prepared in conductive dentacryl Polyfaste, ground on sandpaper grit 240, 400, 600 and 800, moistened with water, polished with diamond paste, grit 1/0 on satin moistened with kerosene, washed, and rinsed with benzyl alcohol. The samples were sonicated in methanol before observation. Samples were taken so that there was a zone of contact of the cores with the shaped part and a zone of contact of the aluminum melt and the shaped part on their surface. A solid-state laser operating in a continuous mode at 400 W with a beam diameter of 3 mm and a T₀₀ beam mode created three tracks on the surface with a beam speed of 20 mm/s, 30 mm/s, 40 mm/s, and 60 mm/s. The surface microgeometry of the PVD duplex coating deposited on the laser treated surface was evaluated according to ISO 25 178.

3. Results

In the test specimens with a ground and polished surface, after 15 minutes of exposure in the melt of the aluminum alloy, a hardened aluminum alloy remained on both

surfaces of the test specimens. An increased concentration of iron, chromium and manganese was detected in qualitative EDX microanalysis in a variable width aluminum alloy just at the test sample – AlSi8Cu3 alloy interface. The hardness of the insert material after 15 minutes of exposure in an AlSi8Cu3 melt at 680 ± 20 °C was 44 HRC (fig.2).



Fig. 2 Interface of insert material and AlSi8Cu3 after 15 minutes exposure in the melt at 680 ± 20 °C

After 300 minutes the exposure of the test specimens in the aluminum alloy melt was a non-compact peeling layer of solidified aluminum alloy on the ground and polished surfaces of the test specimens. The breach of integrity in the solidified aluminum alloy layer was mainly in the zone enriched with iron, chromium, and manganese. A portion of the enriched aluminum alloy layer was firmly anchored to the ground and polished surface of the test specimens. The hardness of the insert material after 300 minutes of exposure in an AlSi8Cu3 melt at 680 ± 20 °C was 21 HRC (fig.3).

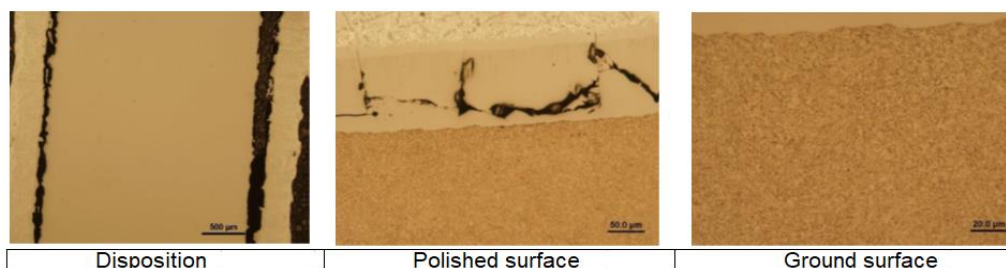


Fig. 3 Interface of insert material and AlSi8Cu3 after 300 minutes exposure in the melt at 680 ± 20 °C

On the surface to the shaped part of the movable half of the mold perpendicular to the parting plane, there were cracks in the vicinity of the ejector opening, which passed to the surface into the cavity for the solid core perpendicular to the parting plane. Mechanical wear of these parts occurred at the points of contact between the moving cores parallel to the parting plane and the shaped parts of the mold (fig.4).



Fig. 4 Contact area of the moving core and the shaped part of the mold - mechanical wear

Changes in the microstructure and defects typical of thermal fatigue wear not observed by light microscopy in the zones of contact of the aluminum melt with the mold part. There was a compact layer 1 µm to 5 µm thick on the surface of the shaped parts,

which were in contact with the aluminum alloy melt and in the die casting process. On the surface of the shaped parts, due to repeated impacts of the moving core on the surface of the shaped parts of the mold, it caused intense plastic deformation associated with the separation of the plastically deformed parts of the surface of the shaped part. Surface damage occurred around contact between the moving core and the mold parts. The surface of the insert was repeatedly treated with a release agent during the casting process (fig.5). At the laser beam speeds were determined the heating depths as showing in fig.6.



Fig. 5 Area of repeated contact - impact of the movable core parallel to the parting plane with the surface of the mold part – inserts

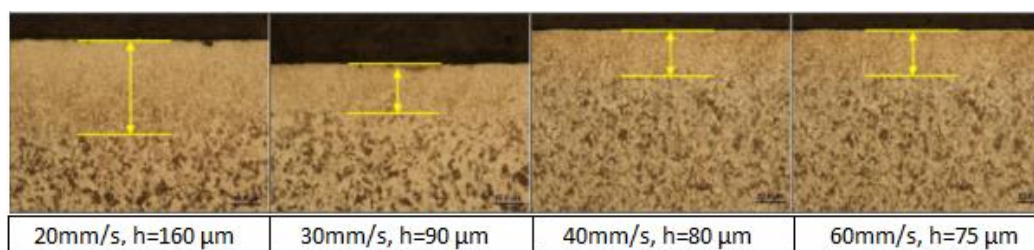


Fig. 6 Surface hardening by laser

A martensitic – carbide fine grained structure formed below the surface, which passed into the sorbitic microstructure through a not fully austenitized zone. The aim was to determine the parameters of the laser heat treatment so that the surface did not melt. The surface microgeometry parameters (tab.3) of the PVD duplex nACRo³ coating evaluated according to ISO 25 178 were not significantly affected by the surface pretreatment by laser heat treatment and grinding with respect to the ground surfaces.

Table 3: Surface parameters according to ISO 25 178 nACRo³

PVD coating duplex nACRo ³			PVD coating duplex nACRo ³ on a laser treated surface		
Sq	1,04329	µm	Sq	0,378681	µm
Ssk	0,115223		Ssk	0,248894	
Sku	3,06638		Sku	10,4354	
Sp	4,47994	µm	Sp	24,0865	µm
Sv	4,81328	µm	Sv	7,5516	µm
Sz	9,29322	µm	Sz	31,6381	µm
Sa	0,824397	µm	Sa	0,29495	µm

5. Conclusions

The high pressure die casting of aluminum alloys is one of the widely used production methods, as it is a technology, that can simultaneously meet the requirements for precision and productivity in the production of cars and various mechanical parts. Die casting molds are exposed to various thermal and mechanical loads. Thermal cracking, erosion and die soldering are usually the most important phenomena that shorten the life of die casting molds. There are several ways to modify die casting related to life predictions and failure modes, along with designs, heat treatments and surface engineering techniques in the form of hard nanostructured coating to extend mold life. In ground and polished samples after 15 minutes in the melting of Al alloy, a solidified Al alloy was detected on the surface. EDX analysis revealed higher concentrations of Fe, Cr and Mn with a hardness of 44 HRC a temperature of 680 ± 20 °C. After 300 minutes of exposure of the samples in Al alloy melt, a non-pact peeling layer of solidified Al alloy occurred, mainly in the zone, where higher concentrations of Fe, Cr and Mn were found with hardness of 21 HRC. Cracks formed perpendicular to the parting plane of the mold around the ejector opening. Mechanical wear of the moving cores and mold parts has occurred. Using light microscopy in the area of contact of the Al alloy with the mold part, no changes in the microstructure typical of the thermal fatigue of the mold were found. Plastic deformation has occurred on the surface of the shaped parts due to repeated impacts of the core and mold. Laser heating depths from 75 μm to 160 μm at 4 different laser speeds were determined. A hard martensitic-carbide fine grained structure was formed, respectively sorbitic structure. The microgeometry parameters of the nACRo3 coated surface were not significantly affected by laser surface treatment. The mold with a modified surface is included in the production and the four times exceeded its service life.

Acknowledgments: The contribution (paper) is the result of the project implementation „Innovative approaches of the restoration of functional surfaces by laser weld overlaying (APVV-20-0303), supported by the Slovak Research and Development agency; the Scientific Grant Agency „Application of progressive technologies in restoration of functional surfaces of products “(1/0497/20).

References

1. Lukaszkowicz, K. et.al.: Characteristics of CrAlSiN + DLC coating deposited by lateral rotating cathode arc PVD and PACVD process, *Applied Surface Science*, 2014, Vol. 312, p. 126-133
2. Fiorentini, F. et.al.: Study of two alternative cooling systems of a mold insert used in die casting process of light alloy components, *Procedia Structural Integrity*, 2019, Vol. 24, p. 569-582
3. Settineri, L. et.al.: Evaluation of wear resistance AlSiTiN and AlSiCrN nanocomposite coatings for cutting tools, *Manufacturing Technology*, 2008, Vol. 57, p.575-578
4. Paiva, M.J. et.al.: Tribological and Wear Performance of Nanocomposite PVD Hard Coatings Deposited on Aluminum Die Casting Tool, *Materials*, 2018, Vol. 11, p. 358...
5. Mattox, D.M.: *Handbook of physical vapor deposition (PVD) processing*, 2nd-ed. Amsterdam, Elsevier 2010, ISBN 978-0-81-552037-5
6. Kolaklieva, L. et.al.: Mechanical and structural properties of nanocomposite CrAlSiN-AlSiN coating with periodically modulated composition, *Coatings*, 2020, 10(1), 41
7. Jakubčzyová D, Ballóková B.: The analyses of nanocomposite thin coatings using specimens prepared by focused ion beam milling, *Material Science Forum*, 2017, Vol.891, p.579-585
8. Fernandez, I.A.: Behavior of PVD coatings in the turning of austenitic stainless steel, *Procedia Engineering*, 2013, Vol. 63, p.133-141
9. Sjöström J., Bergström J: Thermal fatigue testing of chromium martensitic hot-work tool steel after different austenitizing treatments. *Journal of Materials Processing Technology*, 2004, Vol. 153., p.1089-1096



Evaluation of the quality of renovation layers in tribological conditions

Janette Brezinova¹, Henrich Sailer^{1*}

¹ Technical university in Kosice, Faculty of mechanical engineering, Department of Technology, Materials and Computer Aided Manufacturing, Slovakia, janette.brezinova@tuke.sk

¹ Technical university in Kosice, Faculty of mechanical engineering, Department of Technology, Materials and Computer Aided Manufacturing, Slovakia, henrich.sailer@tuke.sk

* Correspondence: henrich.sailer@tuke.sk;

Abstract: *Molds designed for high-pressure casting of aluminum are exposed to very intense thermal, mechanical but also chemical stress during their operation. This stress leads to a synergistic effect of a combination of high-temperature corrosion processes in molten metals, under real conditions associated with mechanical wear. High-temperature corrosion in the environment of liquid metals occurs in the foundry industry, when casting molten metal most often into steel molds. Repair of worn parts of molds by welding, which can be performed even after their irreversible surface degradation, is a very efficient, cost-effective and environmentally acceptable form of their maintenance, while the chemical and physical properties are welded layers if they exceed the properties of the original material.*

Keywords: *Die casting, damage surface, casting dies, molten Aluminium, cladding, High-temperature corrosion, Laser, MIG Puls*

1. Introduction

High Pressure Die Casting (HDPC) is a technological process widely used for casting complex aluminum castings, mainly associated with the automotive industry. In this process, molten metal with a temperature of 670-710 °C is forced into the cavities of the molds at filling speeds of 30-100m/s, under pressures ranging from 40-80 MPa [1]. This loading, in combination with the corrosive properties of liquid aluminum, leads to aluminization or oxidation of the old surface, which results in thermal fatigue of the surfaces followed by cracking, soldering and erosive wear. The service life of die matrices made of steel alloys is approximately 100,000 cycles and can be increased either by heat treatment, thin coating or welding [2-4]. At present, the issue of surface treatment of various materials is becoming more and more important. It offers savings in strategic materials and at the same time enables the production of components with specific surface and volume properties. Because resources are limited by conventional technologies, it is becoming increasingly difficult to meet more advanced customer needs [5-6]. There are many methods for substrate treatment, but coatings developed, for example, by electrostatic, chemical, physical deposition techniques, have lower bond strengths or very low reproducibility than surfacing. Refurbishing worn parts of machines is a very efficient and environmentally friendly form of their maintenance. This option can reduce the environmental impact over the whole lifecycle of the component by up to 63.8% [7].

Laser cladding

Laser welding is a technology used to create coating layers with improved properties, or to recover defects in worn parts of the surface and base layers of components. Due to the high energy density and relatively small heat affected area, this method is suitable for processing a wide range of materials. It is mainly used in the automotive, aerospace,

medical, nuclear and oil industries. In the aero space industry, the welding of layers to aluminum alloys has an increasing potential to improve their surface properties [8-10].

This technology uses highly concentrated waves of light, concentrated at a certain point. In the area affected by the laser beam, atomic bonds disintegrate, causing it to heat up. The three most common types of lasers used in laser welding equipment are gas, semiconductor and fiber. The laser beam is guided into the welding device by one or more optical fibers concentrated at one point. With each fiber added, the intensity of the laser beam also increases [11-14]. Before the laser beam leaves the welding device, a combination of collimator and focusing lenses is often used to direct this radiation to a very small area. An important part of the laser welding equipment is also the nozzle supplying the protective atmosphere gas, most often CO₂. this gas prevents contact between the weld pool and the atmosphere. Another possibility is laser welding without a protective atmosphere, for example when welding plastics. Vacuum welding is possible but difficult to use, due to the high demands on the construction of the welding equipment[13].

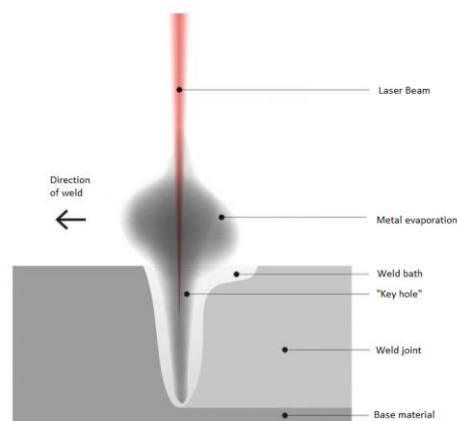


Figure 1. Schematic representation of laser beam welding [13]

MIG / MAG welding (GMAW)

The principle of the MIG / MAG method is to burn an electric arc between the continuously fed melting electrode and the material to be welded. The welding wire is wound on a spool, from which it is fed to the welding gun via a system of drive rollers. The electrical voltage is applied to the electrode via a contact nozzle, which is usually connected to the positive pole of the source, while the workpiece is connected to the negative pole. The shielding gas is supplied by a gas nozzle surrounding the contact nozzle. At an increased load of 300 - 500 A, the welding gun is usually water-cooled [15-17].

The additional material in the form of wire is divided into 2 basic groups. The first is a solid wire designed for welding with inert and active gases in diameters of 0.6 - 2.4 mm. Such wires are coated with a thin layer of copper, especially for larger diameters, due to the increased power supply. The second group are core wires, which consist of a metal outer sheath enclosing a flux, or a metal powder located in the core of the electrode. such electrodes are mainly used for welding thicker sheets, for rounded and butt welds, or for welding with robots in a horizontal position [18]. The use of these wires increases the resistance of welds to cracking, provide deeper penetration into the welded material, increase the range of applicability of the welding equipment. The disadvantages are the higher cost, the finishing operations of the weld surfaces and the increased production of harmful fumes [19-20].

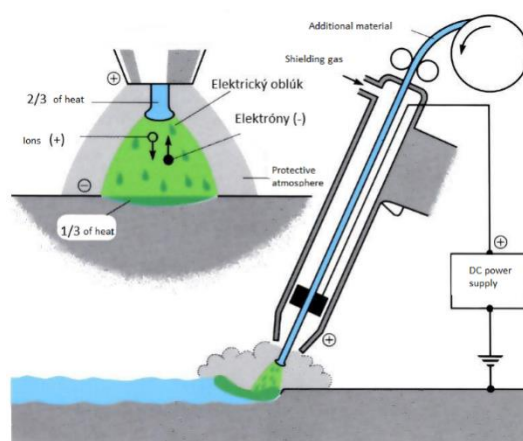


Figure 2. Schematic representation of the MIG / MAG method [18]

2. Materials and Methods

Two different technologies were used for the production of the samples below, while the aim of the work was to determine the impact of individual technologies not only the quality but also the chemical composition of the welds and the minimization of the heat-affected area. Each of the technologies listed below has a different heat input, which is reflected not only in the quality of the weld but also in the degree of mixing of the base material with the weld metal.

Two disk laser welding samples (sample 01), MIG Pulse (sample 03), were applied to the additive material. Sample welds marked 01, 03 were applied on a substrate of nickel - chromium - molybdenum - vanadium steel 1.2714, DIN - 56NiCrMoV7. Uddeholm Deivar 1.2344, DIN - X40CrMoV51 1.2 mm diameter welding wire was used as an additional material. Pin on disk tests and hardness curves were performed on the samples.

The welds were applied to samples of two base materials. On base material made of nickel - chrome - molybdenum vanadium steel 1.2714, DIN - 56NiCrMoV7, with hardness 44 HRC Tab. 1.

Table 1. Chemical composition of the base material

Element	C	Mn	Si	P	S	Cr	Fe	Ni	Mo	V	W
Wt. [%]	0.397	0.72	0.238	0.004	0.002	0.969	95.76	1.253	0.438	0.089	0.12

Uddeholm Deivar 1.2344 welding wire, DIN-X40CrMoV51 with a diameter of 1.2 mm and a hardness of 51 HRC was used as an additional material for the formation of welding layers [36].

Table 2. Chemical composition of the additive material [36]

Element	C	Cr	Si	Mo	Mn	V
Wt. [%]	0.35	5.00	0.20	2.30	0.50	0.60

Table 3. Parameters of welding

Welding technology	Disc laser welding		MIG Pulse Welding:
Welding equipment	The TruDisk 4002 solid-state disk laser with BEO D70 focusing	Welding equipment	Fronius TPS600i welding power source
Focal length	200 mm	Welding current	196 A

Laser power	1.8 kW	Welding voltage	23.8 V
Optical fiber diameter	400 μm	Wire feed speed	6.5 m. min ⁻¹
Welding speed	10 mm. s ⁻¹	Welding speed	8 mm. s ⁻¹
Focusing	- +6 mm	Arc length correction	3
Wire feed speed	70 cm. min ⁻¹	Pulse/dynamics correction	0.0
Shielding gas flow rate	Ar 30 l. min ⁻¹	Shielding gas flow rate	Ar 30 l. min ⁻¹
		Pre heating of base material	base material was preheated to 300 ° C before welding
			5 mm
		Distance burner - sheet metal surface	19 mm

3. Results

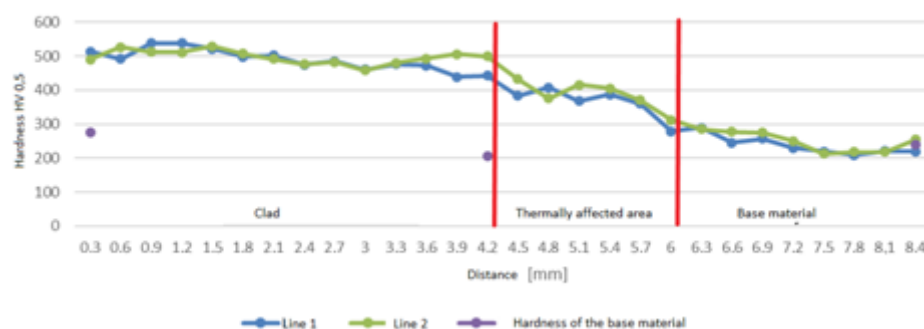


Figure 3. Graph shows the individual values of the hardness of the welds measured in two lines and the value of the hardness of the base material on the sample 01, created by disk laser welding

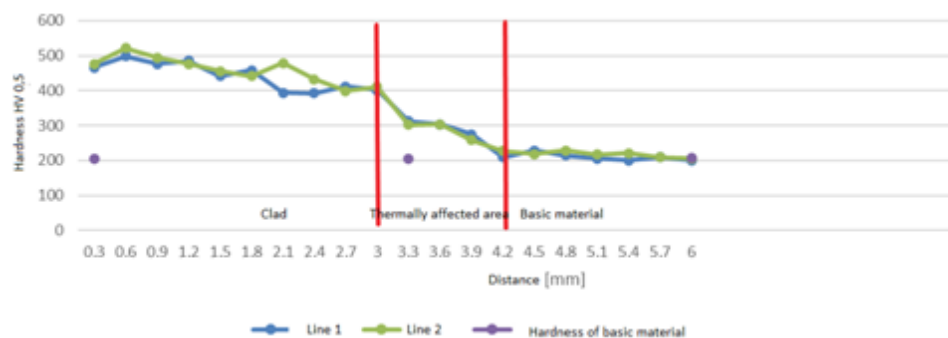


Figure 4. Graph shows the individual hardness values measured in two lines and the hardness value of the base material on sample 03, created by MIG Pulse technology

Since one step was 0.3 mm when measuring hardness, the thicknesses of the welds ranged from 2.8 to 4.7 mm. The weld 01 had an average hardness value in the range of 450-500 HV0.5. In sample 03, see. Figure 4, 20 measurements were made, the average value of the hardness of the weld metal being in the range of 400-500 HV0.5. From the fact that the hardness of all samples is in the range of 500 HV0.5, it is clear that the mixing of the base material and the weld metal has been eliminated, therefore in neither method it is necessary to apply another layer during welding. At weld 03 (MIG Pulse), the width of the heat affected zone was around 1.2 mm. the wider heat affected area was recorded by disk laser welding on a sample marked 01, the width of which was around 1.8 mm.

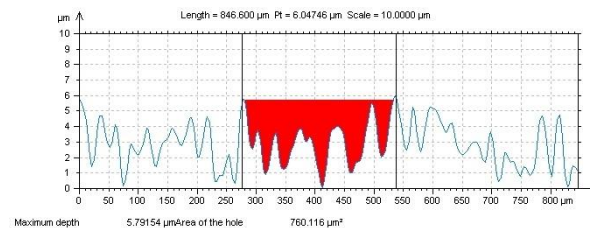


Figure 5. Scheme of the tribo wear track on sample 01 produced by the Pin-on-Disc test

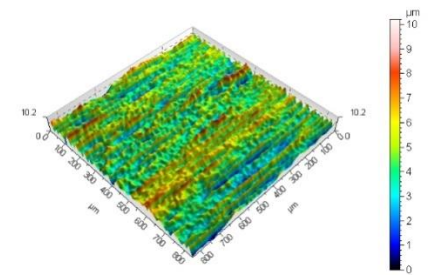


Figure 6. 3D picture of the tribo wear track on sample 01 produced by the Pin-on-Disc test

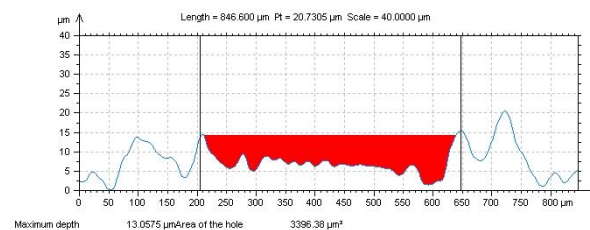


Figure 7. Scheme of the tribo wear track on sample 03 produced by the Pin-on-Disc test

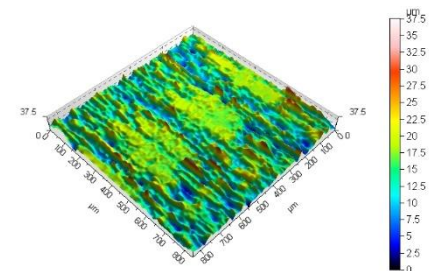


Figure 8. 3D picture of the tribo wear track on sample 03 produced by the Pin-on-Disc test

The comparison of the surface of the sample 01 coating (see Figure 6) with that of sample 03 surface (see Figure 8) indicated that the wear track of the latter was by far shallower and smoother and the shift of the coating material from the centre to the sides of the wear track was less pronounced.

5. Conclusions

The presented article is focused on the analysis of the quality of two types of welds intended for the renovation of molds in high-pressure aluminum casting. Two different welding and disk laser welding technologies and MIG Pulse welding were used to produce the test specimens. Uddeholm Dievar 1.2344 welding wire was used as an additional material in all samples due to the fact that this material is used in the renewal and renovation of functional parts of molds, for die-casting of aluminum. In the theoretical part, the problems and mechanisms of wear of die matrices for high-pressure aluminum casting are characterized, together with an overview of welding technologies used in the formation of welding layers in various industries. The experimental part was focused on determining the quality of the above welds. The quality of the welds was assessed on the

basis of the heat-affected zone, which was determined from the course of the graphs, when measuring the hardness. Tribological parameters of the welds were investigated using the Pin-on-disc test. From the measurement of the hardness of individual samples, it is possible to deduce that the narrowest heat-affected area had a weld marked 03, created by the Mig Pulse method. The widest heat affected area was recorded on a sample labeled 01, created by a disk laser. Based on the Pin-on-disc test, it is possible to use that sample 03 is much smoother and the shift of the coating material from the center to the wear sides was less pronounced. Based on the implemented experimental work, it is possible to recommend these technologies in practice in order to renovate the molds. Better results were obtained with a sample of weld 3 marked Mig Pulse.

Acknowledgments:

This work was supported by scientific grant agency of the Ministry of Education of the Slovak Republic VEGA No. 1/0154/19 "Research of the combined technologies of joining dissimilar materials for automotive industry" and KEGA 001STU- 4/2019.

References

1. Changrong Chen et al.: Energy based approach to thermal fatigue life of tool steels for die casting dies. In: International Journal of Fatigue Volume 92, Part 1, November 2016, Pages 166-178.
2. J. Lin et al.: Design methodology for optimized die coatings: The case for aluminum pressure die-casting In: Surface and Coatings Technology 201 (2006) pp. 2930–2941.
3. K. Domkin, J.H. Hattel, J. Thorborg, Modeling of high temperature- and diffusion-controlled die soldering in aluminum high pressure die casting, J. Mater. Process. Technol. 209 (8) (2009) 4051–4061.
4. Sundqvist M., Hogmark S.: Effects of liquid aluminium on hot-work tool steel Tribol. Int. 26 (1993) in International Journal of Fatigue p. 129.
5. H. Zhu, J. Guo, J. Jia, Experimental study and theoretical analysis on die soldering in aluminum die casting, J. Mater. Process. Technol. 123 (2) (2002) 229–235.
6. Z.W. Chen, M.Z. Jahedi, Die erosion and its effect on soldering formation in high pressure die casting of aluminium alloys, Mater. Des. 20 (6) (1999) 303–309.
7. K. Venkatesan, R. Shivpuri, Experimental and numerical investigation of the effect of process parameters on the erosive wear of die casting dies, J. Mater. Eng. Perform. 4 (2) (1995) 166–174. R. Markežič et al. Engineering Failure Analysis 95 (2019) 171–180179.
8. A Mohammed, M.B. Marshall, R. Lewis, Development of a method for assessing erosive wear damage on dies used in aluminium casting, Wear 332–333 (2015)1215–1224.
9. LF. Hou, Y.H. Wei, Y.G. Li, B.S. Liu, H.Y. Du, C.L. Guo, Erosion process analysis of die-casting inserts for magnesium alloy components, Eng. Fail. Anal. 33 (2013)457–564.

10. D.W.C. Baker, K.H. Jolliffe, D. Pearson, The resistance of materials to impact erosion damage, *Philos. Trans. R. Soc. A Math. Phys. Eng. Sci.* 260 (1110) (1966) 193–203.
11. A. Persson, S. Hogmark, J. Bergström, Temperature profiles and conditions for thermal fatigue cracking in brass die casting dies, *J. Mater. Process. Technol.* 152(2) (2004) 228–236.
12. C. Rosbrook, Analysis of Thermal Fatigue and Heat Checking in Die-Casting Dies: A Finite Element Approach, PhD thesis Ohio State University, 1992.
13. F. Medjedoub, G. Dour, S. Le Roux, P. Lamesle, M. Salem, P. Hairy, F. Rézaï-Aria, Experimental conditions and environment effects on thermal fatigue damage accumulation and life of die-casting steel X38CrMoV5 (AISI H11), *Int. J. Microstruct. Mater. Propert.* 3 (2–3) (2008).
14. P. Hansson, “Modern prehardened tool steels in die-casting applications,” *Materials and Manufacturing Processes*, vol. 24, no. 7-8, pp. 824–827, 2009.
15. Uddeholm, “Dievar,” 2014, (18.10.2021) internet: <http://www.uddeholm.com>
16. D. Klobčar, J. Tušek, B. Taljat, Thermal fatigue of materials for die-casting tooling, *Mater. Sci. Eng. A* 472 (1) (2008) 198–207.
17. D. Schwam, J. F. Wallace, and S. Birceanu, “Die Materials for Critical Applications and Increased Production Rates,” Case Western Reserve University, 2002.
18. Methodical measurement and evaluation of adhesive cohesive behavior of thin film - substrate systems, 2005, (19.10.2021) internet: <https://www.opi.zcu.cz/adheze.html>
19. J. Tkáčová, E. Zdravecká, E. Evin, M. Tomáš, D. Jakuběczyová: *Koroze a ochrana materiálu* 63(4) 159-166 (2019).
20. D. Klobčar, et al.: Thermo fatigue cracking of die casting dies. In: *Engineering Failure Analysis* Volume 20, March 2012, pp. 43-53.



Methodology of sample preparation for testing the adhesiveness of metal-ceramic dental prostheses

Luboš Chromý¹, Viktória Rajtúková¹, Andrea Sinčák – Konečná² and Radovan Hudák¹

¹ Technical University of Košice, Faculty of Mechanical Engineering, Department of Biomedical Engineering and Measurement,

Letná 9, Košice, 040 01; lubos.chromy@tuke.sk, viktorija.rajtukova@tuke.sk, radovan.hudak@tuke.sk

² Pavol Josef Šafárik University in Košice, Faculty of Medicine, Košice, 040 01; andrea.konecna@upjs.sk

* Correspondence address: lubos.chromy@tuke.sk; Tel.: +421556022651

Abstract: The present study aims to determine the methodology of sample preparation for testing the adhesion of metal-ceramic dental prostheses. The first part describes the design of the shape of samples for CAD software and their subsequent production using 3D printing and CNC milling. Subsequently, the procedure of applying the ceramic component to the prepared metal-based samples is described in detail. In the next part, the study focuses on the standardization of sample testing and the determination of indentation testing methodology.

Key words: ceramic; adhesivity; CoCr sample, Ti sample, zirconium

1. Introduction

Over the last five decades, the development of biological materials has advanced significantly and visibly improved the durability and quality of dental prostheses. Each biomaterial has its specific chemical, physical, mechanical and biological properties, which are important especially for the behaviour and the resulting effect of the implant.

The forces that act on the teeth vary depending on what type of food is chewed. The force applied to one tooth is also different to the total force between all the contacting teeth during chewing. The maximum bite force ranges from 500 N to 700 N. [1]. These high forces are thought to be a decisive factor in the friction of the tooth surfaces and the abrasiveness of the tooth surface [2].

The chewing of an individual is influenced by various factors that manifest themselves throughout life. Such basic factors include the following: age (low, high), food status (mushy, hard), pathology (bruxism).

Bruxism often results in physical damage to the enamel or altered chewing muscle function. Since muscles are the main generators of chewing force, a change in their function may be reflected in the value of the maximum bite force (MBF). According to a study [1], patients who regularly train their masticatory muscles can develop more bite force over the time.

Several studies describe the various factors and influences that can cause an increase in the value of the maximum bite force. Such examined factors include the sex of the individual, where the anatomical differences of the individuals as well as the average of the muscle fiber thickness and the incidence of bruxism in the given individuals were examined. [2-8]

The role of dental materials used in dental prosthetics is to supplement defect of hard tissue in the oral cavity with removable and fixed dental prostheses. They are part of the human body and participate in one of the most important activities of food processing - chewing.

In the oral cavity, dental materials are constantly exposed to body fluids and the strength of the masticatory muscles. These forces act on the teeth, producing various reactions leading to deformation, which can impair durability over the time.

Prosthetic materials that are used in dental must meet strict criteria such as mechanical properties, biocompatibility, wear resistance, high corrosion resistance, osseointegration, non-toxicity and long fatigue life. [9] [10].

Based on these findings, the present study is focused on the elaboration of a sample preparation methodology, which will be used to the test adhesivity of metal-ceramic dental materials.

2. Material and methods

The present study aims to develop a methodology for the preparation of samples intended for testing adhesivity of materials used to produce metal-ceramic dental prostheses.

2.1 Methodology of sample production

The methodology of production specimens includes proposition of adequate shapes and dimensions, material selection, production of three-dimensional objects in the shape of boards using a 3D printer (Mlab Cusing R (GE Additive, USA) and CNC milling machine Ceramill Motion 2 (Amann Girrbach, Germany), their grinding, cleaning and manual application ceramics and related configuration of suitable kiln parameters and additional cleaning of samples.

2.1.1. Design of samples

The test specimen was modelled in SolidWorks 2018 3D CAD software (SolidWorks Corporation, USA). Based on ASTM C1624 (Standard Test Method for Adhesive Strength and Mechanical Damage of Ceramic Coatings Using Quantitative Single Point Scratch Testing), which explains in detail the scratch test principles along with limitations, applicability to various coatings, terminology, methodology, sample and equipment requirements, calibration, test procedure or even specific calculations, a rectangular shape of the test sample was selected. The frontal plane in which the model was selected was selected in the software. Subsequently, a "Central Rectangular" was selected from the toolbar and modelled with a page size of 20 mm x 20 mm. The "Add by extrusion" function was used to select a body thickness of 3 mm. The resulting model was exported to .stl format, which can be imported into software for 3D printing and CNC milling. [11].

2.1.2. Production of samples

Three types of test materials were chosen to produce samples. The first material is cobalt-chromium powder Starbond Easy CoCr Powder (Scheftner Dental, Germany). The second group is Rematitan CL (Dentaurum, Germany) formed by TiAl and Vanadium. The last group is ceramics with zirconium base Ceramill Zolid HT + white. 5 pieces of test samples are produced from each group of materials.

The Mlab Cusing R 3D printer was used to prepare test samples from the CoCr and Ti bases. This 3D printer works using the SLM (Selective laser melting) method. The produced samples were prepared for further processing.

The last group is different, it does not have a metal base, but a ceramic one, the production of which is different. Five samples of zircon material with the required shape with dimensions of 20x20x3 mm were made on a 5-axis Ceramill Motion 2 milling machine. The advantage of this material is the fact that it is not necessary to apply surface ceramics as in the case of metal bases. The advantage of using zirconium is the combination of its high mechanical properties (flexural strength is around 1100 MPa +/- 150 MPa) and aesthetic properties (high translucency and transparency).

2.1.3. Ceramic application to test specimens

The first step before applying the ceramic was to sand the sample to ensure a homogeneous surface. The samples were cleaned with distilled steam and dried with compressed air. In the first step, a layer of Ceram Bond powder mixed with the liquid was applied to the CoCr and Ti sample with a brush to form a homogeneous mass. The application of this layer is important in order to create a mechanical and chemical bond between the metal base and the ceramic. These samples were placed in a kiln and the desired program given by the manufacturer was selected. The whole firing process took place in a vacuum and was divided into four basic phases:

- 1. 550°C, holding temperature (evaporation H₂O),
- 2. 600°- 980°C, temperature rise 55°C/min,
- 3. 980°C, burning,
- 4. gradual cooling.



Figure 1. Samples after firing the first layer of Ceram Bond [own processing]

It took about 15 minutes to burn the first layer. After firing, each sample had to be steam cleaned and dried. Subsequently, it was possible to apply the second layer - opaque. The opaque is a cover layer for covering the metal to prevent the metal part from shining through the ceramic part. The powdered opaque was mixed with distilled water to the desired consistency and a thin uniform layer was again applied with a brush. After application, the structure was placed in the furnace and the firing process with individual phases was repeated.

The third applied layer was already ceramics. The ceramic powder specially designed for the CoCr substrate was mixed with the modelling fluid. The light pink slurry was then brushed onto the metal samples from centre to edge. Again, 4 phases of firing followed.

After the samples had cooled, it was again necessary to steam clean the surface and then dry it so that the last layer of ceramic could be applied. The process was repeated. When applying the ceramic, it was necessary to consider the contraction of the ceramic, which after firing reaches a value of up to 10% compared to the unfired mass. The firing lasted approximately 27 minutes. Figure 2 shows the final visualization of the samples prepared for testing by mechanical tests.



Figure 2. CoCr samples after last firing [own processing]

The procedure for Ti samples was the same as for CoCr samples, but a different type of ceramic (GC Initial, USA) was used, which is used to work with titanium.

Ceramics were not applied to the group of zircon samples, because zircon is a ceramic, therefore it has excellent mechanical and aesthetic properties, which are like ceramics applied to a metal substrate.

2.2. Standardization of sample testing

Several standards are set to ensure relevant results of biotribology studies. Standards such as ISO, ASTM, and others regulate and define a specific biotribological wear test to mimic various real-time conditions. ISO standards define the solution of procedures, methods of measurement, calibration and validation. This defines in detail the test parameters such as applied load, ambient temperature, movement speed, number of cycles, sample sizes and shapes and others. Table.7 shows information about ISO standards.

Tab 1. ISO standards for nano-indentation [12]

Name of the standard	Title	Year of publication	Subject
ISO 14577-1	Hardness and material penetration test (part 1)	2002 (modified in 2015)	Describes the test method
ISO 14577-2	Hardness and material penetration test (part 2)	2002 (modified in 2015)	Describes the procedures for verification and calibration of testing machines
ISO 14577-3	Hardness and material penetration test (part 3)	2002 modified in 2015)	Describes the calibration of reference blocks
ISO 14577-4	Hardness and material penetration test (part 4)	2007 (modified in 2016)	Describes the penetration of coatings and thin films

Nano-indentation is a universal technique that is widely used to characterize the mechanical response of materials. This is a technique in which scratches are smaller than 200nm (based on ISO 14577-1). Thin coatings have a thickness of the order of a few microns, so the conventional embossing method is not suitable for obtaining mechanical and tribological properties. It requires destruction and large dimensions of materials, which is economically unprofitable [12].

An optimal combination of metal and ceramic is required for a long-term clinical result. Separation of the ceramic from the metal is unacceptable to the patient and requires a redesign. The rate of reconstruction of metal-ceramic crowns is about 5-8% [13] [14]. Based on the specification of the American Dental Association 38 (2000) and the ISO 9793: 2012 standard, the strength of metal-ceramic dental prostheses is set at a minimum of 25 MPa. The mechanism of bonding of metal and ceramic is the result of chemical bonding, mechanical bonding, compressive and Van der Waals forces. Chemical bonding is the

most important bonding mechanism that occurs when firing ceramics. The most important factors influencing the quality of the chemical bond include temperature [$^{\circ}\text{C}$], time [min], number of burns [n] and atmospheric pressure [kPa] [15-22]. Studies have shown that a slight change in the number and firing temperature of opaque layers will increase the strength of metal-ceramic dental prostheses. [23] To support the bonding of the layers, McLean recommends firing the opaque layer at a temperature 20°C higher than the production temperature for firing ceramics [24] [25].

2.3. Indentation testing methodology

„Pin on disc“

The tribological properties of the applied layers can be measured at the IPR SAS in Košice. The CSM THT high temperature tribometer in a "pin on disc" configuration will be used for the measurement. Mechanical properties such as Young's modulus and hardness will be investigated. Tribological pathways will be examined with a Neox Plu optical microscope (Sensofar, Spain).

All three types of materials (CoCr, Ti and Zr) will be tested. There will be two samples from each material. One sample from each type of material will be tested with a friction force of 5 N, the other with a friction force of 10 N. A zirconia pin with a diameter of 5 mm is used as the friction body. Measurements will be performed in air, at a temperature of 37°C . Humidity will be 90%, which corresponds to a humid environment in the oral cavity. All layers will be analyzed at a constant rotation speed of 180 mm / s, which corresponds to 100 revolutions per minute with a wheel diameter of 35 mm. The length of the test track will be 200 m.

Scratch test

The Bruker UMT 3 universal tribometer is used to measure mechanical properties such as adhesion, delamination and hardness. As it has a wider load range than the CSM THT high temperature tribometer, tests up to 1000 N can be performed. The effect of the applied load on coefficient of friction and wear of the layer.

Again, three types of materials (CoCr, Ti and Zr) covered with a ceramic layer will be tested. Samples are polished before testing. The polished surfaces of the samples will be arbitrarily divided into three fields resp. areas (left part of the sample, middle part and right part of the sample) (Figure 3) in order to avoid scratching on already existing scratches and to allow more tests to be performed on one sample.

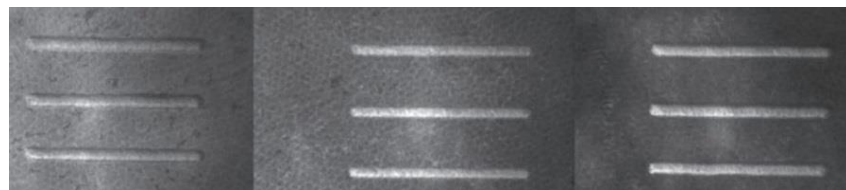


Figure 3. Breakdown of samples shown under a microscope

Nine different loads of 30 N, 50 N, 60 N, 80 N, 100 N, 120 N, 150 N, 180 N and 200 N with a constant loading force are selected. Thus, three samples from each type of material will be examined. A Vickers diamond indenter with a four-walled pyramid tip with an apex angle of 136° is selected for the study. The device is configured to perform a reciprocating motion at a speed of 10 mm / s. It will be tested under lubricated conditions with an ambient temperature of 37°C . The effect of the applied load on the coefficient of friction and wear of the layers will be investigated. For this purpose, all layers will be analyzed under nine different loads.

3. Discussion

As part of the theoretical research, the horizon of ceramic coatings has broadened and hardness test strategies have been identified. The purpose of the present study was to investigate the wear resistance of dental ceramic samples. The basic material of these coatings was metals and zirconium. The microstructure of the applied ceramic layers was formed by hard anchored particles. The particle properties determine the overall properties of the coating. A study of the wear mechanisms of the applied metal-ceramic layers has shown that, depending on the method of wear and the properties of the particles of applied ceramic, wear occurs preferentially in some structural samples. Therefore, attention was focused on determining the individual properties of the samples using nano-indentor tests, which allow to determine their basic mechanical properties - hardness and modulus of elasticity. Their mutual E/H ratio characterizes the elastic-plastic properties of the evaluated materials. Knowledge of these basic mechanical characteristics not only makes it possible to directly predict their resistance to wear and brittle failure, but is also necessary to determine other material constants, such as resistance to crack propagation evaluated by the method of measuring indentation fracture toughness.

4. Conclusion

The present study focuses on the design of a sample production methodology for testing the adhesiveness of metal-ceramic dental prostheses and on determining the most suitable methods for testing the samples themselves.

For the purposes of this study, three types of materials were selected, namely titanium, cobalt-chromium and zirconium. Metal samples were made on a Mlab Cusing R 3D printer (Concept Laser Inc., USA), zirconia were milled on a 5-axis Ceramill Motion 2 milling machine (Amann Girrbach, Germany). Layers of ceramics were applied to the metal substrates, which were applied by hand with a brush in the form of several layers so that the final thickness was in the range of 1 mm - 1.5 mm. The samples were fired in kilns at high temperatures under vacuum. Subsequently, a methodology of mechanical tests using "pin-on-disk" and "scratch test" methods was developed.

Acknowledgments This research was supported by project KEGA 040TUKE-4/2019 Use of digitization technologies for educational process support in the field of prosthetics and orthotics. This publication is the result of the project implementation Center for Advanced Therapies of Chronic Inflammatory Diseases of the Locomotion, ITMS2014+: 313011W410 supported by the Operational Programme Integrated Infrastructure funded by the European Regional Development Fund. This publication is the result of the project implementation Open scientific community for modern interdisciplinary research in medicine (Acronym: OPENMED), ITMS2014+: 313011V455 supported by the Operational Programme Integrated Infrastructure funded by the European Regional Development Fund.

Conflicts of Interest: The authors declare no conflict of interest

References

1. Available from the Internet <<https://pocketdentistry.com/10-force-factors-related-to-patient-conditions-a-determinant-for-implant-number-and-size/>>
2. XU, W.L. – BRONLUND, J.E. – POTGIETER, J. et al.: Review of the human masticatory system and masticatory robotics. *Mechanism and Machine Theory*. 43 (2008) p. 1353-1375.
3. HELKIMO, E. - INGERVALL, B.: Bite force and functional state of the masticatory system in young men, *Swed. Dent. J.* 2 (1978) 167-175.
4. TODIĆ, J.T. - MITIĆ, A. - LAZIĆ, D. et al.: Effects of bruxism on the maximum bite force, *Vojnosanit Pregl* 2017; 74(2): 138-144
5. GIBBS, CH. - MAHAN, PE. - MAUDERLI, A. et al.: Limits of human bite strength. *J Prosthet Dent* 1986; 56(2): 226-9.
6. PEREIRA-CENCI, T. - PEREIRA, L.J. - CENCI, MS.: Maximal bite force and its association with temporomandibular disorders. *Braz Dent J* 2007; 18(1): 65-8.
7. BONAKDARCHIAN, M. - ASKARI, N. - ASKARI, M.: Effect of face form on maximal molar bite force with natural dentition. *Arch Oral Biol* 2009; 54(3): 201-4.
8. COSME, DC. - BALDISSEROTTO, SM. - CANABARROSD, A. et al.: Bruxism and voluntary maximal bite force in young dentate adults. *Int J Prosthodont* 2005; 18(4): 328-32.

9. HUSSEIN, A. M. – MOHAMMED, A. S. - AL-AQEELI, N.: Wear Characteristics of Metallic Biomaterials: A Review. *Materials* 2015, 8, 2749-2768. ISSN 1996-1944.
10. BRANEMARK, P.I.: Osseointegration and its experimental background. *J. Pros. Dent.* 1983, 50, 399–410.
11. DR. NICHOLAS - X. RANDALL, Scratch Test [online] [cit.2021-12-14]. Dostupné z: <https://www.qualitymag.com/articles/89229-scratch-test>
12. 51]. ABDULAZIZ S.- i HUSSAIN A.: Finite element modeling of nano-indentation technique to characterize thin film coatings. *Diel* 31, Vydanie 1, Január 2019, strana 61-69
13. POWERS JM- WATAHA JC. *Dental Materials: Properties and Manipulation*. 9 th edn. St. Louis, Missouri: Elsevier; 2008
14. HATRICK CD - EAKLE WS - BIRD WF. *Dental Materials: clinical applications for dental assistants and dental hygienists*. 2 nd edn. St. Louis, Missouri: Elsevier; 2011:100-26.
15. CHEUNG KC - DARVELL BW.: Sintering of dental porcelain: effect of time and temperature on appearance and porosity. *Dental materials* 2002; 18: 163-73.
16. GUPTA KL - NEERAJ N.: Evaluation of the bond strength of porcelain to nonprecious metal copings under different firing atmospheres. *Indian Journal of Dental Sciences* 2011; 2(3): 1-4
17. RAYYAN MM.: Effect of multiple firing cycles on the shear bond strength and failure mode between veneering ceramic and zirconia cores. *Egyptian Dental Journal* 2014; 60(3): 3325-33.
18. SAYED NM.: Shear bond strength and failure mode between veneering ceramic and metal cores after multiple firing cycles. *Egyptian Dental Journal* 2015; 61: 659-66.
19. VASCONCELLOS LG - BUSO L - LOMBARDO GH - SOUZA RO - NOGUEIRA JR L - BOTTINO MA et al.: Opaque layer firing temperature and aging effect on the flexural strength of ceramic fused to cobalt-chromium alloy. *Journal of prosthodontics* 2010; 19: 471-477.
20. MONIKA S - YASHPCAL S - ARVIND T - SAUMYENDRA VS - BIKRAMJIT B - SURESH C.: Effect of firing temperatures on interface of porcelain fused to metal restorations: An in vitro study. *Indian J Stomatol* 2011; 2(4): 222-26.
21. ALI RT - ISMAIL K - SERDAR P - MERAL AM - MEHMET D.: The effect of repeated porcelain firings on corrosion resistance of different dental alloys. *J Adv Prosthodont* 2013; 5: 44-50.
22. TUNCDEMIR AR - KARAHAN I - POLAT S - MALKOC MA - DALKIZ M.: The effect of repeated porcelain firings on corrosion resistance of different dental alloys. *J Adv Prosthodont* 2013; 5: 44-50.
23. VASCONCELLOS LG - BUSO L - LOMBARDO GH - SOUZA RO - NOGUEIRA JR L - BOTTINO MA - et al.: Opaque layer firing temperature and aging effect on the flexural strength of ceramic fused to cobalt-chromium alloy. *Journal of prosthodontics* 2010; 19: 471-477.
24. OLIVIERI KAN - NEISSER MP - BOTTINO MA - MIRANDA ME.: Bond characteristics of porcelain fused to cast and milled titanium. *Braz J Oral sci* 2005; 4(15): 923-8.
25. GIANNARACHIS C - MARMANDIU C - VASILESCU VG - VASILESCU E - PATRASCU I.: Studies on the importance of metal-ceramic bond in merging ceramic mass on metal component. *Fascicula* 2013; 17(2): 5-12.



Overview of software designed for modelling parts made of composite materials

Nikita Veligotskyi ^{1,*}, Anna Guzanová ¹ and Albert Mareš ²

¹ Technical University of Košice, Faculty of Mechanical Engineering, Department of Technologies, Materials and Computer Aided Production, Slovakia; anna.guzanova@tuke.sk

² Technical University of Košice, Faculty of Mechanical Engineering, Department of Automotive Production, Slovakia; albert.mares@tuke.sk

* Correspondence: nikita.veligotskyi@tuke.sk;

Abstract: The paper deals with the description of selected software applications suitable for creating models of parts from composite materials. The article contains an overview of composite materials and a more detailed description of selected software in which a part made of composite material can be modelled.

Keywords: Reinforced composite materials, CATIA V5, SolidWorks, Helius Composite, Autodesk Fusion 360, Comsol Multiphysics, ANSYS Composite PrepPost, ANSYS Composite Cure Simulation, MSC NASTRAN.

1. Introduction

The field of production technologies is constantly being improved and developed. Development and innovation lead many manufacturers to implement new materials in vehicle construction. Composite materials also belong to such materials.

As the production of these materials is economically and time consuming, the constant production of test specimens and their testing and finding the best solution would be economically and time consuming. To help manufacturers, special applications have been created in which it is possible to model a specific part, define its material, test its response to different types of stress and find optimal solutions. It is also possible to combine parts into an assembly and monitor its behavior in different conditions. The aim of the paper is to give an overview of composite materials and describe the main functions of selected software, which are most often used to model parts made from these materials.

2. Reinforced composite materials

Composite materials for cars are increasingly competing with commonly used metals. They are gradually replacing not only steel, but also aluminum alloys, which until recently were considered the best in all respects. At present, it is possible to produce most automotive parts from composite materials. A comparison of selected properties of composites in comparison with steel and aluminum is shown in Figure 1 [1].

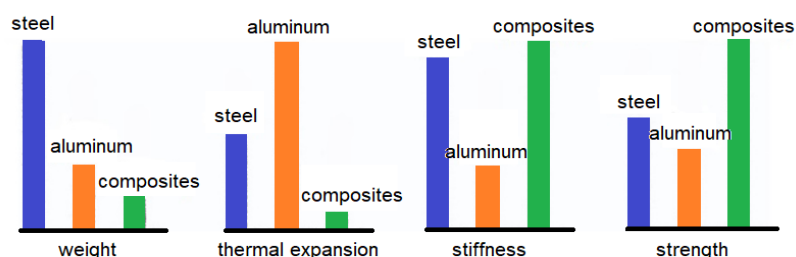


Figure 1. Comparison of selected properties of composite materials with steel and aluminum [2].

Composite materials are created by combining two or more components into a common system, in which each component retains its specific properties. When looking at composites from a microscopic point of view, each phase has its own interface. The composites contain at least two phases: one phase is continuous - matrix, the other is discontinuous - reinforcing phase. Most preferably, the reinforcing phase is microscopic, because the thinner the fibre or particle, the better the resulting properties of the composite [2].

The properties of composite materials depend on the composition of the phases, their combination, and the intensity of bonding between them. The reinforcing phase can be in the form of fibres, ropes, threads, tapes, or multilayer fabrics. According to the type of reinforcement, composite materials are divided into fiberglass, carbon, boron and organic [2].

Composite matrices can be made from metals and their alloys, as well as polymers, ceramics, carbon and other materials. The price of a composite depends on its resulting mechanical properties.

Types of composite materials:

1. Metal matrix composites: They consist of a metal matrix (most often Al, Mg, Ni and their alloys), reinforced with high-strength fibres (fibre-reinforced composites) or finely dispersed refractory particles that do not dissolve in the base metal (dispersion-reinforced composites). The metal matrix connects the reinforcing phase (fibres, particles) into one unit [2].

2. Composites with non-metallic matrix: Non-metallic matrices are made of polymeric, carbon or ceramic materials. The most common polymer matrices are epoxy, phenol-formaldehyde and polyamide matrices [2].

3. Description of selected software applications suitable for modelling parts made of composite materials

At present, special modelling software are used before any body part or interior part of a vehicle is created from composite material. In these software, engineers have the ability to model the shape of the required part, define the material and perform some analyses. Because composite materials have their own specifics that need to be taken into account when creating models, it is not possible to use any CAD system for their modelling. The following is an overview of some selected software that supports modelling of composite parts.

3.1. CATIA V5

CATIA V5 is designed to model and describe a product at all stages of its life cycle. In this system, complex 3D modelling functions are implemented, combined with a description of all model creation processes, Figure 2.

CATIA V5 modules can be grouped according to various criteria, such as the area of application of this program. Today, there are seven: mechanical engineering, systems synthesis of industrial products, product design development, engineering analysis, systems and communications design, design management and data exchange, and machine tool programming [3].

The CATIA V5 concept has three platform levels: P1, P2 and P3. The first platform is basic and is a solution for small companies. P2 contains modules that allow you to manage the digital model of the product and perform its collective development. P3 contains various specialized modules that provide the highest functionality and system performance.

CATIA V5 is delivered to customers in the form of precisely defined configurations, i.e. groups of modules designed to solve a certain range of tasks. If necessary, it is possible to extend the functionality of configurations by integrating the appropriate software components into them [3].

Advantages of the program:

1. It allows to model complicated planar parts and to add material, e.g. Composite material.

2. CATIA V5 is not just a CAD system, but also a PLM (Product Lifecycle Management) system, so once a modeled part, it can be used for the entire life cycle.
3. CATIA is intended to be used for Architectural, Design, Electrical, and Mechanical streams.

Disadvantages of the program:

1. Expensive software
2. Difficult to operate for beginners

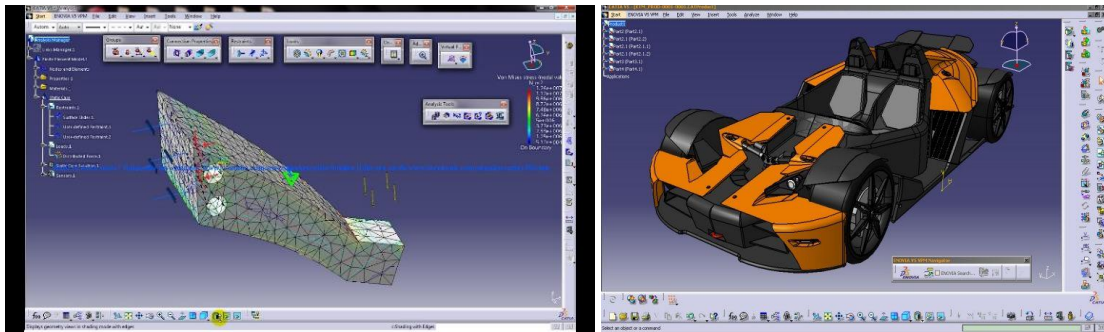


Figure 2. Examples of modelling in Catia V5 [4].

3.2. SolidWorks

The following features are available in SolidWorks:

- Volumetric modelling with the development of products that have the properties of completely real physical objects. It is almost ideal for product visualization.
- Surface modelling, using curves or splines. The result is products with smooth curves.
- Wire modelling [5].

The 3D modelling process is performed using sketches. On the existing base plane, the base shape is created using basic geometric elements and then drawn into space by operations such as rotating, extruding, drawing a sketch along a section or path. The object can also be rounded, mirrored, create the necessary thin-walled elements and perform other operations, Figure 3 [5].

Advantages of the program:

1. SolidWorks is more user-friendly compared to CATIA V5.
2. SolidWorks is rich in Advanced Surfacing features that can create mid surfaces, planar surfaces, extend, freeform-radiated surface, Min Radius Analysis, Surface Fill, Swept, Symmetry Check Analysis, Trim, Undercut Analysis, and much more, but it's not as extensive as CATIA V5
3. Suitable for mechanics and machinery-related solid modeling projects
4. Offers a demo or trial version

Disadvantages of the program:

1. Does not support the whole PLM (Product Lifecycle Management) product
2. Runs only on Windows

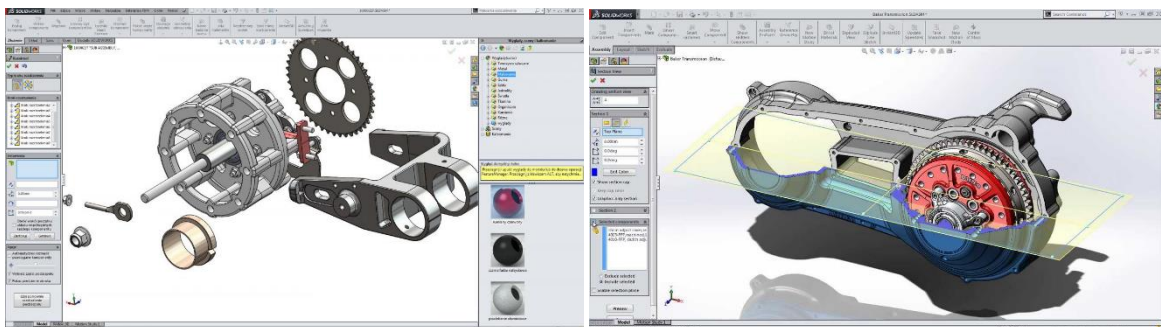


Figure 3. Examples of modeling in SolidWorks [6].

3.3. Heliuss Composite

Autodesk Heliuss Composite is the next generation of the popular Simulation Composite Design and CompositePro software for designing and analysing fibre-reinforced composite materials, laminates, and other structures. Heliuss Composite provides access to a variety of composite analysis tools based on classical laminate theory (CLT) and micromechanics [7].

Heliuss Composite provides fast and accurate solutions for bending, vibration and deformation of laminate boards, sandwich panels, laminate pipes and beams. In addition, it calculates a wide range of laminate response data, such as laminate matrix stiffness and flexibility, equivalent technical properties, stresses and curvature of the laminate inter-layer, layer stress, layer deformation, laminate strength, progressive laminate failure reactions, failure extent, etc.

Heliuss Composite comes with an extensive database of predefined composite materials that can be used to create laminates, fibres, matrices and core materials that can be used to create new composites, composite laminates and sandwich panels, and new composite materials can be added to the materials database, as well as basic materials and laminates, Figure 4 [7].

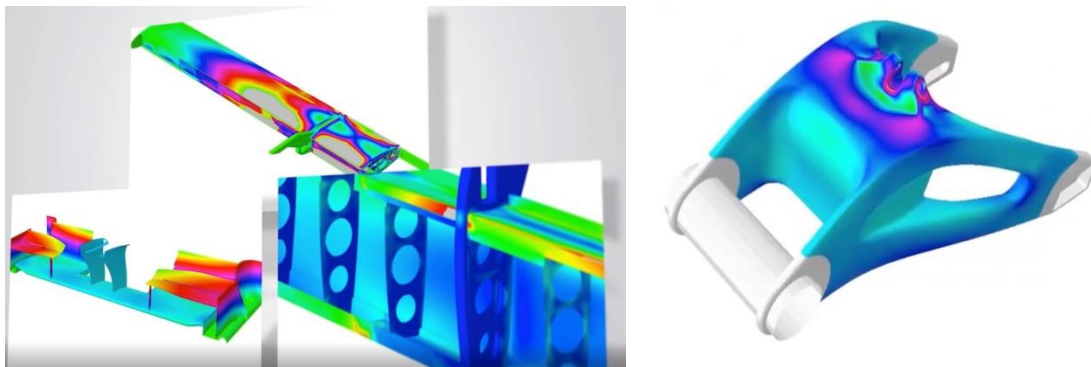


Figure 4. Examples of modeling in Heliuss Composite [8].

3.4. Autodesk Fusion 360

The Fusion 360 software product includes a wide range of user options, Figure 5. Of these, special attention deserves:

- Spline modeling. T-spline technology allows you to create objects by entering an exact curvature.
- Volumetric modeling.
- Network models.
- Parametric modeling. Any change in parameters leads to a subsequent transformation of all related elements [9].

The following technologies are also implemented in the Fusion 360 program:

- Thermal and thermo-mechanical stress analysis;
- Static voltages and natural frequencies;
- Nonlinear stresses;
- Simulation of impact load;
- Shape optimization;
- Analysis of fasteners [9].

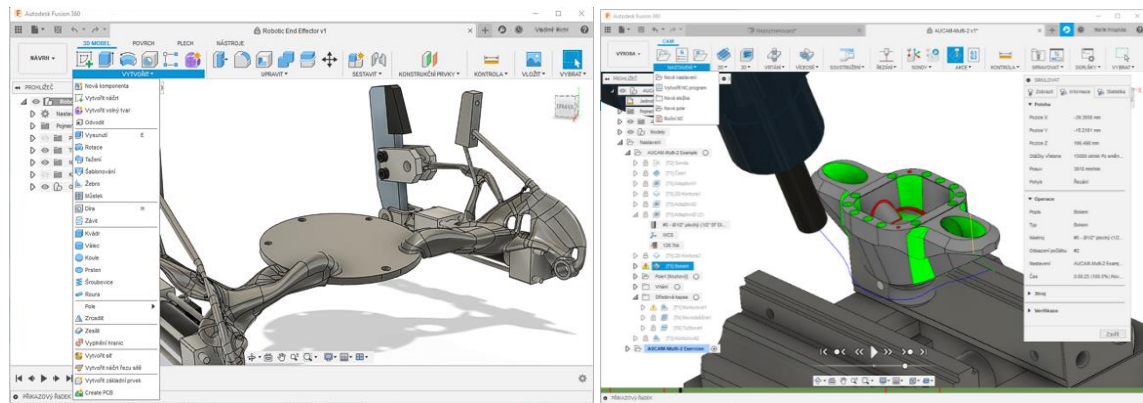


Figure 5. Examples of modeling in Autodesk Fusion 360 [10].

3.5. Comsol Multiphysics

COMSOL Multiphysics is an integrated modelling platform that includes all steps from creating geometry, defining material properties and describing physical phenomena, to customizing the solution and subsequent processing to achieve accurate and reliable results, Figure 6.

Modelling in COMSOL Multiphysics allows you to assess electromagnetism, structural mechanics, acoustics, fluid dynamics, heat transfer and chemical reactions in one software environment, as well as any other physical phenomenon that can be described by systems of partial differential equations. All these physical phenomena can be combined into one model [11].

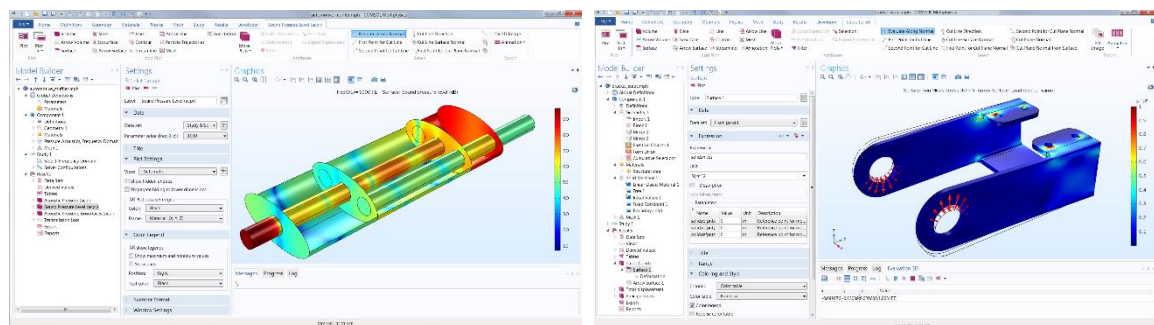


Figure 6. Examples of modeling in Comsol Multiphysics [11].

3.6. ANSYS Composite PrepPost and ANSYS Composite Cure Simulation

ANSYS Composite PrepPost is a specialized tool that allows you to easily and conveniently model complex composite structures. This significantly speeds up the calculation process while maintaining high accuracy of results. ANSYS Composite PrepPost includes all the features needed to design laminate composite products. It allows to determine stresses and strains and verify them on the basis of selected fracture criteria for composite materials, Figure 7 [12].

In the process of creating composite materials, the parts change their original shape and acquire a new one according to the state of stress and tension, which affects the further operation of the product. The curing simulation in **ANSYS Composite Cure Simulation (ACCS)** also allows you to take into account the effect of part deformation and adjust the workflow [12].

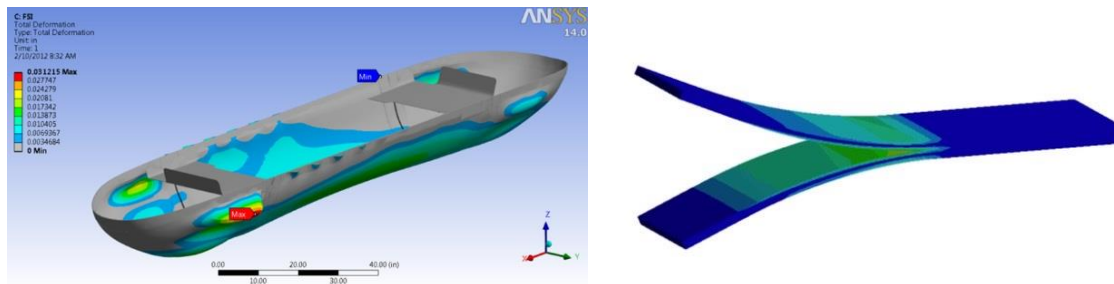


Figure 7. Examples of modeling in ANSYS Composite PrepPost [12].

3.7. MSC NASTRAN

MSC Nastran provides a complete set of calculations, including stress state calculations, safety factors, natural frequencies and vibration modes, stability analysis, steady-state and transient dynamic process studies, heat transfer troubleshooting, acoustic phenomena, nonlinear static and dynamic transitions, complex contact interaction analysis, calculation of critical frequencies and vibrations of rotating parts, analysis of frequency characteristics under the action of random load and pulsed broadband impact. It is possible to model almost all types of materials, including composite and hyperelastic. MSC Nastran includes a tool for automatic optimization of parameters, shape and topology of structures. The tool allows the use of MSC Nastran for automatic identification of computer simulation model and design of experiments, Figure 8 [13].

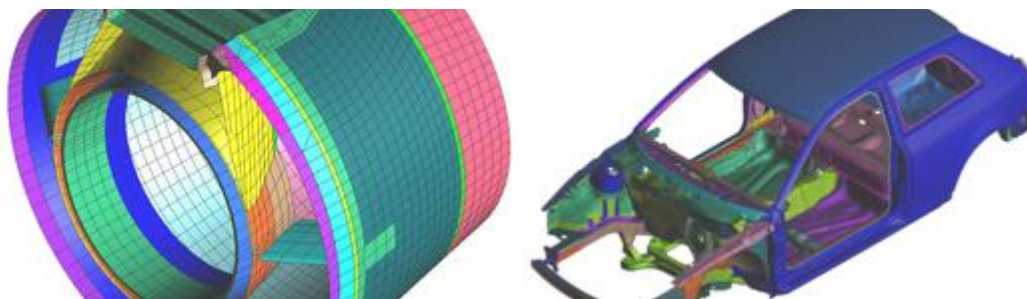


Figure 8. Examples of modelling in MSC NASTRAN [13].

5. Conclusions

The paper presents the types of composite materials used and a description of the main functions of the software that are most often used to create parts made from these materials. In these programs, engineers can create a model of the required part, define its material, determine its dimensions and perform analyses. This is necessary to identify the various problems or errors of the prototype in the modelling phase, to calculate the required amount of material, etc. These software make it possible to reduce the time required to develop prototypes, reduce the number of tests required during the modelling phase and reduce the necessary costs for the development of composite parts.

Acknowledgments: The contribution was created within solution of the project VEGA 1/0154/19: Research of the combined technologies of joining dissimilar materials for automotive industry.

References

1. Kompozitnye materialy dla avtomobilstroenia. Available online: <http://www.hccomposite.com/sectors/132/> (05.10.2021)
2. Klassifikacia kompozicionnyh materialov i ich rol v sovremennom mashinostroenii. Available online: <https://docplayer.ru/70865955-Klassifikaciya-kompozicionnyh-materialov-i-ih-rol-v-sovremennom-mashinostroenii.html> (05.10.2021)
3. Programma Catia. Available online: <http://www.axispanel.ru/working-party/programs/catia.php> (07.10.2021)

4. CAD POINT KUMBAKONAM. Available online: <http://cadpointkumbakonam.blogspot.com/2018/04/learn-hybrid-modeling-using-catia-v5-r20.html> (07.10.2021)
5. Podrobnýj obzor programy SolidWorks. Available online: <https://junior3d.ru/article/solidworks.html> (12.10.2021)
6. COM-X: SOLIDWORKS. Available online: <https://www.com-x.com.hk/software/solidworks> (12.10.2021)
7. Helius Composite – Introduction. Available online: <https://knowledge.autodesk.com/support/helius-composite/learn-explore/caas/CloudHelp/cloudhelp/2017/ENU/ACMPDS/files/GUID-DBBB35EC-ED08-4867-9EC4-F6C859556426-hm.html> (19.10.2021)
8. Helius Composite. Available online: <https://www.autodesk.co.uk/products/helius-composite/subscribe?plc=AC-MPDS&term=1-YEAR&support=ADVANCED&quantity=1> (19.10.2021)
9. Autodesk Fusion 360: osobnosti i sfery primeneniya. Available online: <http://we-it.net/index.php/zhelezo/ostalnye-ustrojstva/344-autodesk-fusion-360-osobnosti-i-sfera-primeneniya> (23.10.2021)
10. FUSION 360 Proč začít vyrábět s Fusionem? Available online: <https://cam.cadstudio.cz/fusion/benefit-cam/> (23.10.2021)
11. Analizirujte, prognozirujte povedenie i optimizirujte inženernye rascetnye projekty s pomosiu programy COMSOL Multiphysics. Available online: <https://www.comsol.ru/comsol-multiphysics#geometry-cad> (02.11.2021)
12. ANSYS Composite PrepPost. Available online: <https://cadfem.com.ua/software/mekhanika-deformirovanija-tverdogo-tela-mekhanika-razrushenijateploobmen-ustalostnaja-dolgovechnost/ansys-composite-preppost/> (05.11.2021)
13. MSC Nastran Rascet i optimizacia konstrukcij. Available online: <http://www.mssoftware.ru/products/msc-nastran> (08.11.2021)



CREATION OF A HYBRID JOINT OF ALUMINUM ALLOY EN AW-6082 T6 USING FLOWDRILL AND ADHESIVE BONDING

Erik Janoško ¹, Anna GUZANOVÁ ¹

¹ Technical University of Košice, Faculty of Mechanical Engineering, Department of Technologies, Materials and Computer Aided Production, Slovakia ; erik.janosko@tuke.sk; anna.guzanova@tuke.sk

* Correspondence: erik.janosko@tuke.sk

Abstract: The paper deals with the creation of a single lap joint and a hybrid single lap joint with adhesive bonding created by flowdrill technology. Al alloy EN AW-6082 T6 was chosen as the material for forming the joints. The load-bearing capacity of the joints was tested in shear under tensile stress according to the standard STN EN ISO 12996. The shape of the bushing was found to be satisfactory and without defects. Hybrid joints made by flowdrill technology using an adhesive have a higher load-bearing capacity than joints made using flowdrill technology alone.

Keywords: flowdrill; hybrid joints; adhesive bonding; EN AW-6082 T6

1. Introduction

Nowadays, in numerous industrial applications, the fixing of thin sheet metal with the thin walled section and pipe-shaped profiles fitting are widely used. Moreover, due to the development of modern design in the automobile industry, the requirement of lightweight structures is high to increase the efficiency of automotive vehicles. [1].

The thermal drilling process is described as sleeve or bush forming in a single processing step by using rotating thermal drill tool without removal of the chip [2]. This process uses the frictional heat produced by a rotating tool to form a bush. This frictional heat, which is happened by friction or rubbing between the tool and sheet metal and leads to forming a hole by extrusion of sheet metal. It is clean, easy and unconventional sheet metal hole drilling method. The process is also named as friction drilling, flow drilling, thermo-mechanical drilling, friction stir drilling, flow drilling, thermal friction drilling and form drilling. The purpose of this unconventional hole production method is to increase screwing length in thin-walled sheet metals through the formation of the bush, to assembly thin sheet metals.

In the thermal drilling process, the possibility of producing reliable strong bolted fastenings by bush shape formation which is about 3-times thicker than the original sheet metal, because the metal at drilling zone is deformed without any metal loss. As per the working principle of process, the volume of material displaced is the same as the volume of material deformed by bushing can be calculated as follows where D_i and D_o represent inner diameter and outer diameter of bush, W_t is the workpiece thickness and BH denotes bushing height in mm.

$$B_H = \frac{D_i^2}{[D_0^2 - D_i^2]} * W_t$$

2. Materials and Methods

2.1 Material

Aluminium alloy 6082 is a medium strength alloy with remarkable corrosion resistance. T6 implies that the alloy is heat treated and artificially aged. It has the highest strength of the 6xxx series. Aluminium alloy 6082-T6 shows excellent performance in machining operations. This grade substitutes to the conventional 6061 alloy in many structural applications in which improved mechanical properties are required. It is widely used in transport and structural applications in which high stress resistance is essential. It can be found in the exterior of the planes fuselages and it is a real alternative to conventional mild steel in automotive body panels and structures [3]. Mechanical properties are listed in table 1. The chemical composition of the material (% of weight) is reported in table 2.

Table 1. Mechanical properties and some specific conditions of material

	EN AW-6082 T6
Re [MPa]	290
Rm [MPa]	340
A ₈₀ [%]	14
Thickness [mm]	1
condition	solution treated, artificially aged


Table 2. Chemical composition of material

EN AW-6082 T6	1.0%Si, 0.4% Fe, 0.06% Cu, 0.44% Mn, 0.02% Cr, 0.08% Zn, 0.03% Ti, Al-balance
---------------	--

2.2 Flowdrilling process

According to the thickness of the joined materials and the thickness of the overall joint, the Flowdrill Long thermal drilling tool with a diameter of 5.3 mm was chosen. The tool did not have a collar cut part. Process parameters are given in table3.

Table 2. Flowdrill tool and parameters

	
Cutting speed of the tool	113 m·min ⁻¹
Revolutions per minute	7200 min ⁻¹
Tool penetration speed	200 mm·min ⁻¹

The tool penetrated 0.1mm (figure 1) below the level of the upper material. The tool remained in this position for 0.8 s. The process was performed on a DMC 635V ecoline machine.

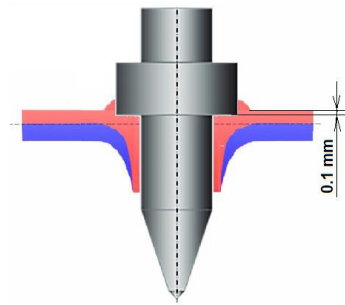


Figure 1. Tool penetration in process

2.3 Shape and dimensions of test samples

The samples were prepared according to the standard STN EN ISO 12996 [4]. The main parameter was the tool diameter. The resulting sample dimensions are shown in the figure2. The hole is always created in the middle of the overlapped area.

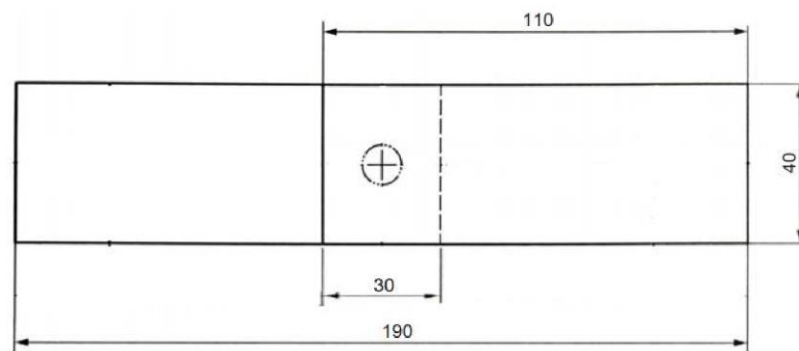


Figure 2. Dimensions of the sample and joint assembly

Adhesive RB 5197 (Henkel) was used to bond the samples.

2.4 Adhesive joining

The adhesive used is based on rubber. The adhesive is suitable for combination joints with resistance welding. The thickness of the adhesive was 0.2 mm. The tensile strength of the adhesive is 12 MPa, the shear strength at 20 °C is > 15MPa.

Pretreatment of bonded materials before adhesive joining was as follows:

1. degreasing
2. immersion in an organosilane solution to improve adhesion.

Procedure for creating hybrid joints:

1. application of adhesive
2. joining two samples with defined overlap
3. flowdrill process
4. curing adhesive (175 °C, 25 min) in the oven.

2.5 Testing of assemblies

The load-bearing capacity was tested in shear under tensile load. The joints were tested on a TIRA test 2300 universal tearing machine. The loading speed was 10 mm·min⁻¹.

1. Load-displacement dependence was recorded during the load. From the obtained dependences we determined the following mechanical characteristics of the joints, recommended by the standard STN EN ISO 12996:

- F_{max} - tensile shear force, maximum force recorded during the test.
- sF_{max} - displacement at tensile shear force F_{max} .
- $0.3F_{max}$ - tensile shear force on the descending part of the curve corresponding to 30% of F_{max} .
- $s0.3F_{max}$ - displacement at $0.3F_{max}$.

3. Results and discussion

According to [5-7], the quality of the joints is dependent on the shape and integrity of the bushing. It is desirable to create a continual bushing, without petals. A broken bushing is undesirable. The figure 3 shows the created joint in two positions.



Figure 3. Flowdrill sample

The figure 4 and 5 show metallographic cross-section through joint created by flowdrill technique and flowdrill and adhesive bonding hybrid joint.

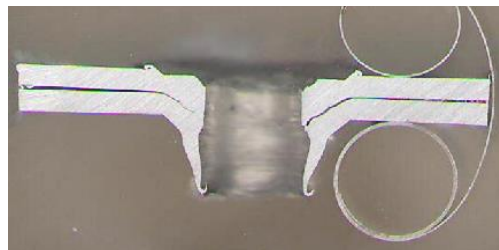


Figure 4. Flowdrill cross-section

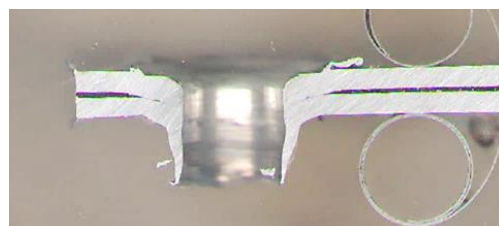


Figure 5. Flowdrill + adhesive bonding cross-section

Metallographic study proved compact bushing without petals.

Figure 6 and table 4 shows the load-displacement curves for flowdrill and flowdrill + adhesive bonding assemblies.

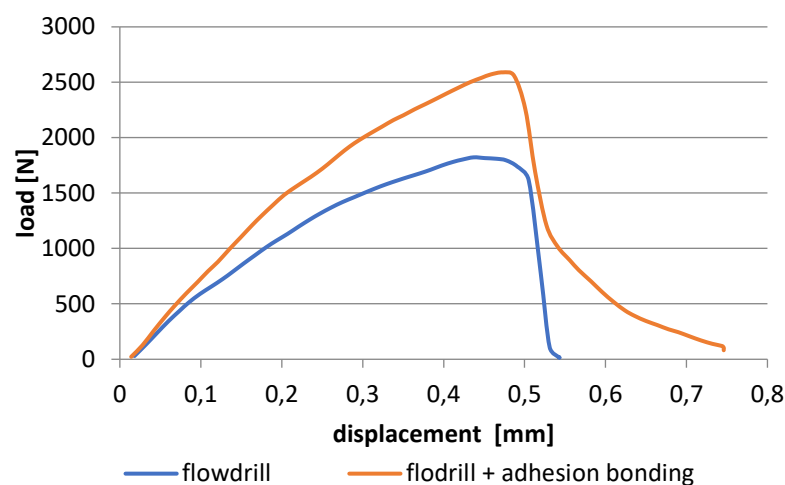


Figure 6. Measured experimental curves

The hybrid joint has approximately 45% higher F_{max} . The more important parameter $0.3F_{max}$ indicates that the hybrid joint is 60% more loaded. The difference between sF_{max} and $s0.3F_{max}$ for flowdrill and flowdrill + adhesive bonding is minimal, but higher for hybrid joint, indicating higher absorption of load energy.

Table 5. Flowdrill parameters

	flowdrill	flowdrill + adhesive bonding
F_{max} [N]	1769±438	2786±233
sF_{max} [mm]	0.43±0.10	0.48±0.02
$0.3F_{max}$ [N]	531±131	836±70
$s0.3F_{max}$ [mm]	0.53±0.11	0.57±0.06

4. Conclusions

From the point of view of energy absorption under load, it is advantageous that the above-mentioned characteristics (F_{max} , $0.3F_{max}$) are as high as possible. The values of the displacement sF_{max} and $s0.3F_{max}$ are particularly important. The higher these values, the more energy the joint absorbs before failure, which is positive in terms of crash safety.

The experimental results obtained in this article can be summarized as follows:

- Aluminum alloy 6082-T6 is possible to join together by creation a joint using flowdrill technology.
- At the selected experimental parameters, the bush shape is continual, without cracks, defects.
- The hybrid joint, made by flowdrill and adhesive bonding proved higher load-bearing capacity compared to simple flowdrill joint.

Acknowledgement

The contribution was created within solution of the project VEGA 1/0154/19: Research of the combined technologies of joining dissimilar materials for automotive industry.

References

1. L.M. Alves, E.J. Dias, P.A.F. Martins, Joining sheet panels to thin-walled tubular profiles by tube end forming, *J. Clean. Prod.* 19 (2011) 712-719. DOI: 10.1016/j.jclepro.2010.12.014 Author 1, A.; Author 2, B. Title of the chapter. In *Book Title*, 2nd ed.; Editor 1, A., Editor 2, B., Eds.; Publisher: Publisher Location, Country, 2007; Volume 3, pp. 154–196.
2. E. Solmaz, K. Çavdar, Experimental Determination of Screw Efficiency, TMMOB Chamber of Mechanical Engineers Konya Branch II. Machine Design and Manufacturing Technologies Congress, Konya, Turkey, 2003. Author 1, A.B.; Author 2, C. Title of Unpublished Work. *Abbreviated Journal Name* stage of publication (under review; accepted; in press).
3. M. Rodriguez-Millán, A. Vaz-Romero, A. Rusinek, J. Rodriguez-Martinez, A. Arias Experimental study on the perforation process of 5754-H111 and 6082-T6 aluminium plates subjected to normal impact by conical, hemispherical and blunt projectiles *Exp. Mech.*, 54 (2014), pp. 729-742 <https://doi.org/10.1007/s11340-013-9829-z>
4. STN EN ISO 12996: Mechanical joining — Destructive testing of joints — Specimen dimensions and test procedure for tensile shear testing of single joints, SÚTN, 2014.
5. F. Aslan, L. Langlois, T. Balan, Experimental analysis of the flowdrill screwdriving process, *International Journal of Advanced Manufacturing Technology*. 104, 5-8 (2019), 2377 – 2388. <https://doi.org/10.1007/s00170-019-04097-z>
6. P. Krasauskas. Experimental and statistical investigation of thermomechanical friction drilling process, *Mechanika*, 17 (2011), pp. 681-686 <http://dx.doi.org/10.5755/j01.mech.17.6.1014Jop>
7. S.F. Miller, R. Li, H. Wang, A.J. Shih, Experimental and numerical analysis of the friction drilling process. *J. Manuf. Sci. Eng.* 128 (2006), 802 – 810. <https://doi.org/10.1115/1.2193554>



Shape Memory Behaviour of an Alloy using Parametric Sweep in Comsol Multi-Physics

Johnson Ugochukwu Ezenwankwo

johnson.ezenwankwo@tul.cz

Abstract

The Finite Element Analysis of a Shape Memory Alloy is performed using COMSOL-Multiphysics 5.4. Three different studies were conducted; for the first study, a parametric sweep function in Comsol was run for two temperatures (328K, 348K) which are above the austenite finish temperature – an axial load of 920MPa was applied. A second parametric sweep was performed on axial displacement while the temperature remained constant at 320K for an axial strain of 0.068. Relaxation was initiated until the load is only 35%, the load is then ramped up to 85% before a full relaxation to zero. Finally, at a constant temperature below the austenite start temperature (280K), a third parametric sweep is conducted. After the first cycle, the temperature is increased by 20K to achieve the reverse transformation to austenite.

Keywords: Austenite, Martensite, Relaxation, Axial Load, Phase Fraction, Multiphysics

Introduction

Smart materials are known generally to modify their properties (shape) upon the application of external stimuli such as stress, temperature, electric and magnetic fields etc. Shape memory alloys have found wide applications in many areas of science and technology including medicine (stents to clear blockages in blood vessels, catheters, embolization to manage aneurysm), aviation (trailing edge of flaps in aircrafts) [1]. Pseudo-elasticity entails SMA's ability to exhibit reversible hysteretic stress versus strain behaviour to produce large inelastic strains. The development of large strains gives rise to its useful application in biomedical engineering as stents [2]. Shape Memory Effect is the characteristic behaviour exhibited by all shape memory materials. SMAs possess two phases controlled by temperature. The two phases are martensite and austenite. At lower temperature, the system exhibits two martensitic structures, twinned and deformed (detwinned) and then at higher temperatures it is austenite. Four transformation temperatures exist, namely, austenitic start (A_s), austenitic finish (A_f), martensitic start (M_s) and the martensitic finish temperature (M_f). The former are called the reverse transformation whereas the latter forward transformation. The governing equations were described in details by R. C. Smith and Heintze O. (2005) [3, 4]. The influence of latent heat of transformation and thermo-mechanical coupling was evaluated on the performance of an SMA and one other study analyzed the effect stretching-bending loadings on a chosen SMA as it affects the thermomechanical behaviour [5, 6]. An experiment on micro-actuation via joule heating was

performed using silicon bimorph of two coupled SMA materials to highlight the challenges of actuator performance [7]. Indirect heating can be achieved by infusing electrical conductive elements into the system and by joule heating, raise the temperature [8]. To successfully determine important SMA parameters, [8] try to match experimental results with a dual technique of density optimization, and fixed parameters and a second method actually totally incorporates these parameters into the said density relation.

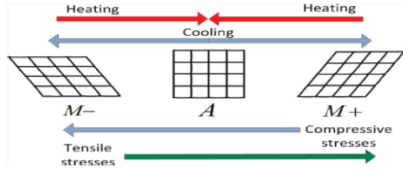


Plate 1: Uniaxial SMA Phase Transformation
(John H. C. et. al. 2012)

SMA's Governing Equations

Although the computational efficiency of empirical models tend to be markedly higher compared to physical models; it requires more complexity to be able to account for inherent hysteretic behaviour. Also the rate dependence on phase fractions $[x_A, x_{M_+}, x_{M_-}; x(0 \leq x \leq 1)]$ is not readily captured.

Each of the phase fractions $x_\alpha (\alpha = A, +, -)$ dynamics and evolution is governed by the rate laws given below:

$$\dot{x}_{M_+}(t) = x_A(t)p_{A \rightarrow M_+}(T, \sigma) - x_{M_+}(t)p_{M_+ \rightarrow A}(T, \sigma) = -x_+p^{+A} + x_Ap^{A+} \quad (1)$$

$$\dot{x}_{M_-}(t) = x_A(t)p_{A \rightarrow M_-}(T, \sigma) - x_{M_-}(t)p_{M_- \rightarrow A}(T, \sigma) = -x_-p^{-A} + x_Ap^{A-} \quad (2)$$

where $p^{\alpha\beta}$ are transition probabilities; such that p^{-A} , for instance, will represent a transition from the phases M_- to A . This has a direct relation with the Gibbs free energy and Helmholtz energy; two which play a key role in determining the minimum energies required to overcome the barrier responsible for change of phase at the atomic level; the main reason for two values for Young's Modulus. The non-linear stress-strain relationship is thus given by the following relation describing the total stress:

$$\sigma(t) = \frac{E_M[\varepsilon - (x_+ - x_-)\varepsilon_T]}{x_+ + x_- + \frac{E_M}{E_A}x_A} \quad (3)$$

This can also be expressed in terms of the total recoverable strain, ε_T , as

$$\sigma(t) = \frac{\varepsilon(t) - \varepsilon_T[x_{M_+}(t) - x_{M_-}(t)]}{\frac{1 - x_{M_+}(t) - x_{M_-}(t)}{E_A} + \frac{x_{M_-}(t) + x_{M_+}(t)}{E_M}} = \frac{\varepsilon(t) - \varepsilon_T[x_{M_+}(t) - x_{M_-}(t)]}{\frac{x_A(t)}{E_A} + \frac{x_{M_-}(t) + x_{M_+}(t)}{E_M}} \quad (4)$$

where $\sigma(t)$ is the stress in the SMA specimen, $\varepsilon(t)$ is its strain, E_A and E_M are the values the Young's Modulus or the austenite and martensite phases respectively.

Finally, the thermodynamic behaviour of the system is described by the relation

$$\rho c_p \dot{T} = -\alpha A_s [T - T_0] - (h_{M+} - h_A) \dot{x}_{M+}(t) - (h_{M-} - h_A) \dot{x}_{M-}(t) + j(t) \quad (5)$$

where ρ is the density of the SMA wire, c_p is the heat capacity, α is the convective heat transfer coefficient, T_0 is the ambient air temperature, A_s is the area-volume ratio of the SMA specimen, the terms $h_{M\pm} - h_A$ are called the latent heat of the transformations and $j(t)$ is the joule heating

Execution in COMSOL MULTIPHYSICS

A system of ordinary differential equation (ODEs) is employed in COMSOL to solve the set of equations when the elements of the governing matrices are correctly specified. This is readily available in COMSOL's partial differential equations (PDE). The general form is given as

$$e_a \cdot \frac{\partial^2 u}{\partial t^2} + d_a \cdot \frac{\partial u}{\partial t} + \Delta \Gamma = f \quad (6)$$

where e_a is considered the mass matrix, d_a is the damping matrix, Γ is the flux matrix while f is the source term. The model from COMSOL (6) is used to solve for both phase fractions (1) and (2) and the constitutive relation (3) and (4). The different terms in terms in (6) are input with the coefficient of their matrices to give the following:

$$e_a = 0; d_a = \begin{bmatrix} 0 & 0 & 0 & 0 \\ 0 & 1 & 0 & 0 \\ 0 & 0 & 1 & 0 \\ 0 & h_{M+} - h_A & h_{M-} - h_A & \rho_{SMA} \cdot C_p \end{bmatrix}; \Gamma = \begin{bmatrix} \sigma(x) \\ 0 \\ 0 \\ 0 \end{bmatrix}, \text{ and}$$

$$F = \begin{bmatrix} 0 \\ -x_+ p^{+A}(\sigma, T) + (1 - x_+ - x_-) p^{A+}(\sigma, T) \\ -x_- p^{-A}(\sigma, T) + (1 - x_+ - x_-) p^{A-}(\sigma, T) \\ -\alpha \frac{A_{SMA}}{V_{SMA}} [(T(t) - T_0) + j(t)] \end{bmatrix}$$

The state variables in (7) is given as

$$u = \begin{bmatrix} u_x(t) & x_{M+}(t) & x_{M-}(t) & T(t) \end{bmatrix}^T \text{ or } \begin{bmatrix} u_x(t) \\ x_{M+}(t) \\ x_{M-}(t) \\ T(t) \end{bmatrix}$$

Boundary Conditions

Two different boundary conditions are incorporated into the system;

the Dirichlet boundary condition; controls displacement in isothermal condition

$$(\text{at } x = 0); r_1 = hu + b = 0 : u(0, t) = 0 \Rightarrow r_1 = u \text{ and} \quad (7)$$

the Neumann boundary condition; controls the Force at the free end under adiabatic condition

$$(\text{at } x = L); -n \cdot \Gamma = g_1 : A(L)\sigma(L, t) = F(t) \Rightarrow g_1 = F(t) \quad (8)$$

No restriction exists on all values of phase fractions at both ends so that for x_α , it is implemented as

$$r_\alpha = 0$$

Lagoudas SMA Model is employed to analyse the material. Material property was obtained from literature as $E_A = 56.76$ GPa, $E_M = 46.38$ GPa, Poisson ratio = 0.33, $C_p = 500$ J/(kg.K) and the density is given as 6500 kg/m³, Clausius-Clapeyron coefficient (slope of the limit curves for Austenite and martensie) is given as 7.4 MPa/K and the maximum transformation strain, $\epsilon_T = 0.063$ and $M_s = 317.8$ K, $M_f = 300.9$ K, $A_s = 330$ K and $A_f = 345$ K [11, 12].

Results and Discussion

The result is obtained from Comsol Post-processing. The plots of stress, strain, volume fraction and time in the relevant direction are briefly highlighted.

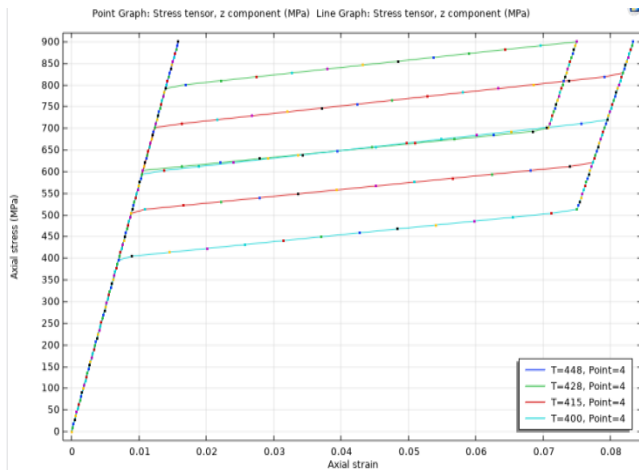


Fig 2: Axial Strain vs. Axial Stress

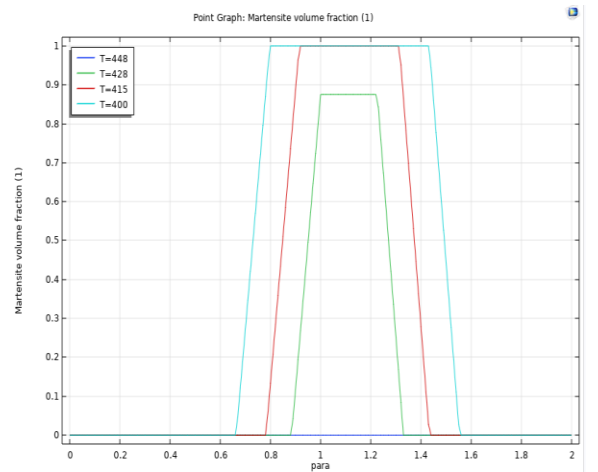


Fig. 3: Martensitic Volume Fraction Vs Auxiliary Range

Fig. 2 shows the stress-strain relation of the SMA for 4 chosen temperatures (448K, 428K, 415K and 400K). During loading, the behaviour remained linear up until about 380MPa, then the austenite-martensite transformation sets in.

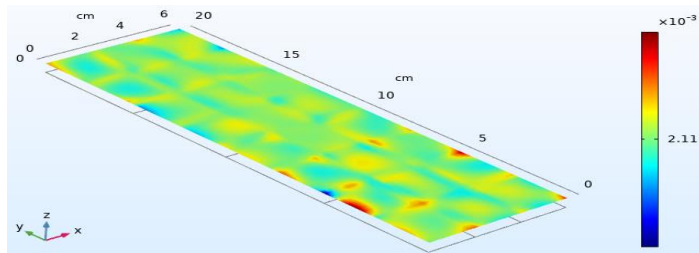


Fig 4: 2-D Surface Plot of Parametric Sweep at 400K

The relaxation behaviour is also seen to happen at a lower stress as the unloading progresses. The axial stress-strain curve for a prescribed temperature of 340 K (between the austenite start and finish temperatures) depicts that the forward and reverse transformations occur at lower levels of stress. It is also seen that, the reverse transformation is incomplete at the time when the load is totally discontinued. This can be seen in Fig 5 where the forward transformation occurs sooner, that is, at lower stress level. The initial phase is austenite; martensitic volume fraction is 0 and then it transforms to martensite where this value is equal to 1. The backward transformation starts later, and it is not complete at the end of the sweep as can be seen from the plot.

Conclusion

Finite Element Simulation of tests apart from the one-directional uniaxial tensile test has proven to provide more detailed information on shape memory behaviour and superelasticity considering various conditions which is vital for various applications in science and technology. However, results have shown that FEA is a powerful tool that can be used to examine and create a better in-depth understanding of the behaviour of SMAs under different loading, unloading mechanical and thermal conditions.

Acknowledgement:

This publication was written at the Technical University of Liberec as part of the project "Research of advanced materials, and application of machine learning in the area of control and modeling of mechanical systems" nr. SGS-2022-5072 with the support of the Specific University Research Grant, as provided by the Ministry of Education, Youth and Sports of the Czech Republic in the year 2022.

References

- [1] Hartl D., Lagoudas D., Mabe J., Calkins F., and Mooney J. *Use of Ni60Ti (Notinol) Shape Memory Alloy for Active Jet Engine Chevron Application – Experimentally Validate Numerical Analysis, Smart Materials and Structures*. (2009) 19(1).
- [2] Migliavacca F., Petrini L., Colombo M., Auricchio F., Pietrabissa R. *Mechanical Behaviour of Coronary Stents Investigated Through the Finite Element Method*. Journal of Biomechanics, (2002) 35, pp. 803–811.
- [3] Jordan E. M. and Ralph C. S. (2005). *A Homogenized Free Energy Model for Hysteresis in Thin-film Shape Memory Alloys*. *Thin Solid Films*, 489(12): 266 - 290.
- [4] Heintze O. and Seelecke S. *A Free Energy Model for the Inner Loop Behaviour of Pseudoelastic Shape Memory Alloys*. In: Proceedings of materials research society symposium, (2005) vol. 881, pp. cc 1.6.1–12. Cambridge University Press.
- [5] Majid T. and Darren J. H. *Influence of the Latent Heat of Transformation and Thermo-mechanical Coupling on the Performance of Shape Memory Alloy Actuators*. Proceedings of the ASME (2012) Conference on Smart Materials, Adaptive Structures and Intelligent Systems. DOI: 10.1115/SMASIS2012-8188.
- [6] Auricchio F. and Sacco E. (2001) *Thermo-mechanical Modelling of a Superelastic Shape-Memory Wire Under Cyclic Stretching-Bending Loadings*. International Journal of Solids and Structures, (2012) 38(1), pp. 6123–6145.
- [7] Gowthan A., Zixiong L., Sabrina C., Prasanth V., Eckhard Q., Manfred K. *Temperature Homogenization of Co-Integrated Shape Memory-Silicon Bimorph Actuators*. Proceedings of the 1st International Electronic Conference on Actuators Technology. (IeCAT, 2020).
- [8] Hu J. (2014) *Shape Memory Polymers: Fundamentals, Advances and Applications*. Smithers Rapra Technology Ltd. City: (2020) Shawbury, United Kingdom.
- [9] John H. C., Ralph C. S., Kyle M. P., Jennifer C. H. and Gregory D. B. *Data-driven Techniques to Estimate Parameters in the Homogenized Energy Model for Shape Memory Alloys*. Journal of Intelligent Material Systems and Structures. (2012) 23(17) 1897–1920.
- [10] Gregory Buckner *Design Optimization of a Shape Memory Alloy-Actuated Robotic Catheter*. Journal of Intelligent Material Systems and Structures, (2012) DOI: 10.1177/1045389X12436738. 23(5) 545–562.
- [11] Brian A. D. *Investigation of the Thermo-mechanical Response of Shape Memory Alloy Hybrid Composite Beams* North Carolina State University, North Carolina, (2005) NASA/CR-2005-213929.
- [12] Travis L. T. *Thermo-mechanical Response of Shape Memory Alloy Hybrid Composites*, NASA Center for Aerospace Information (CASI), 7121 Standard Drive, Hanover, MD (2001) 21076-1320, (301) 621-0390.



Analysis of basic principles in objectification and evaluation of electromagnetic fields generated by mobile base stations

Elena Jurgovská ^{1*}, Ervin Lumnitzer¹

¹ Technical University of Košice, Faculty of Mechanical Engineering, Department of Environmental Engineering

* Correspondence: elena.jurgovska@tuke.sk

Abstract: The paper deals with methodological and organizational measures for assessing the impact of electromagnetic fields generated by mobile operator base stations on humans. It offers the classification of the most common sources of electromagnetic fields in the living, working and living environment. Attention is also paid to the effect of the electromagnetic field on the human body. It describes the performed experiment, which was focused on a detailed analysis of the state in the field of electromagnetic fields in a specific locality. In the experiment, measurements of the intensity of electromagnetic fields in the interior and exterior were made. The result of the measurements is also cumulative values, which give us a closer indication of the differences between the internal and external measurements. This experiment forms the basis for the developed methodology for the assessment of electromagnetic fields in the environment, which aims to increase the efficiency of the assessment process.

Keywords: electromagnetic fields, base station, measurement in practice.

1. Introduction

In today's modern society, radio communications and wireless technologies are an integral part of everyday life. Simple communication, such as a mobile phone call, relies on radio and wireless technology. The accompanying phenomenon of all radio communication systems is the electromagnetic fields (EMF) in the radio frequency part of the electromagnetic spectrum, which have a negative effect on the environment. In recent years, wireless technology has advanced significantly, especially in the area of data transmission, which is becoming dominant. High-speed 3G and 4G data have changed the availability of mobile phones and wireless services. With the advent of 5G, the 5th generation of mobile networks, public interest in the use of mobile services has increased. These low energy radio devices transmit and receive signals from a network of fixed low energy base stations. Each base station provides coverage for a given area. Depending on the number of calls handled and the amount of data transmitted, base stations can range from several hundred meters in large cities to several kilometers in rural areas.

Exposure to electromagnetic fields generated by mobile operator base stations is subject to current legislation. From the point of view of the safety of the population, mobile operators must ensure hygienic measurements in the event of any change in technology at base stations. However, it is important to analyze the impact of these changes on the electromagnetic fields to which the population is exposed.

2. Sources and effects of electromagnetic fields

Nowadays exposure to electric and magnetic fields is an integral part of daily human functioning. Their operation is based on many sources used, including electrical equipment, broadcast transmissions and communication equipment. Most sources of electromagnetic fields present in homes or work environments generate extremely low levels of

exposure and it is unlikely that the most common activities would lead to exposures that exceed the action and exposure limit values set by current legislation.

In terms of protecting the health of citizens and employees from the effects of EMF in the work and environment, the sources of electromagnetic fields are divided into:

- static electric and magnetic fields with a frequency lower than 1Hz,
- electric and magnetic fields with very low frequency from 1Hz to 60Hz,
- low frequency EMF with frequency from 60 Hz to 10kHz,
- high frequency EMF with frequency from 10kHz to 300GHz.

Electromagnetic fields can be divided into natural and artificial. The natural sources of the electromagnetic field include the Earth's geomagnetic field, but also cosmic radiation. In addition to the natural sources of the electromagnetic field, mankind has created a number of artificial sources, e.g., X-rays, mobile applications, radio and television broadcasting, data transmission, radar technology and many other applications. Various types of high-frequency radio waves are used to transmit information - whether via television antennas, radio stations or mobile phone base stations. [1] [2]

According to current knowledge, the interaction of EMF with the human body produces thermal and non-thermal effects. Thermal effects cause tissues to warm at high field densities. Non-thermal effects change the electrical properties of the cells and affect the colloidal composition of the cell contents. With long-term action, the effects can be manifested in impaired memory, headaches, exhaustion, and weakness, as well as fatigue and sleep disorders. Energy absorption is related to thermal effects. This absorption can cause an increase in temperature in certain areas of the body. The increase in temperature cannot be detected until six minutes after exposure. The most commonly reported heat effects are damage to the inner ear, clouding of the lens of the eye, and corneal damage. [1] [2]

3. Analysis of approaches in the assessment of EMF generated by base stations of mobile operators

The study by Martin et al. describes the impact of EMP on the health problems of the inhabitants of selected cities in France. The measurements used in the study were performed in living spaces with a maximum distance of 250 m from the base stations. Based on these measurements and completed questionnaires, they assessed that the study contributes to a body of evidence that does not suggest any adverse effect of RFM exposure from mobile operator base stations on the development of self-reported non-specific or insomnia-like symptoms in the general population. [3]

Authors Mladen Koprivica et al. in their publication Statistical analysis of electromagnetic radiation measurements near a GSM / UMTS base station installed on buildings in Serbia performed measurements whose results showed that the maximum recorded exposure to electromagnetic field exceeded reference levels exposure of the International Commission on Non-Ionizing Radiation Protection to 2.5% of cities and Serbian national reference levels to 15.6% of cities. It should be emphasized that values exceeding the reference levels were observed only in the outdoor environment, while in the indoor environment the total intensity of the electromagnetic field did not exceed the defined reference levels. [4]

4. EMF exposure measurement in the selected location

We performed an experiment to assess changes in the intensity of electromagnetic fields generated by base stations of mobile operators in a selected location. We selected this area due to a change in the base station location. To assess the effect of electromagnetic fields, they performed measurements in the interior of the office building where the new MBTS mobile base station was located, and measurements in the exterior around it. As there were changes in the location of the base station in the area, we wanted to analyze what effect this change will have on the differences in EMF intensity around the building, but also in its interior. The measurements were performed in two modes of operation,

namely the operation of the base station designated V5, which is at a distance of 120 m from the building, and subsequently after its exchange for the mobile base station MBTS. The mobile base station is located in close proximity to the administrative building. Figure 1 shows the location of the measuring points in the administrative building, the measuring points in the exterior and the MBTS.



Figure 1. Location of measuring points in outdoor and indoor environment

Five measuring points marked M11 - M15 were selected in the two-storey administrative building. The M11 measuring point is located on the ground floor, oriented towards the MBTS and with a direct view of the MBTS through the window opening. Measuring points M12 - M15 were chosen on the second floor in the four corners of the building. In the exterior, four measurements of the location around the building were selected.

We performed measurements using a measuring instrument Narda SRM - 3006, which consists of a spectrum analyzer and a probe for measuring the electrical component of the field. We had the measuring device placed on a tripod at a height of 1.5 m above ground level. The measurement time is set at 6 minutes. The resulting graphs show the frequency spectrum over the entire duration of the measurement. The measuring chain is able to operate in the frequency band from 420 MHz to 6 GHz. During the measurement, the dynamic measurement range of 10 V/m, RBW - 5MHz, the minimum display frequency F_{\min} - 700 MHz and the maximum display frequency F_{\max} - 3.5 MHz were set on the device.

4.1. Experiment evaluation

When evaluating the measured data obtained by the experiment, we performed an analysis of the frequency spectrum, analysis of the output data and evaluation of the results of the experiment. Data from individual measurements are arranged according to significance. The measurement output is also frequency spectrum graphs and cumulative EMP intensity values for all measuring points.

When processing the results, we set the interface of individual graphs to the frequency range F_{\min} 750 MHz and F_{\max} 3400 MHz. On the graph we can see significant peak values - peaks, which occur during the activity at a certain frequency according to the intensity of EMP. The resulting tables list the 10 most important peaks with the highest radiation intensity for a particular base station.

The M12 measuring point is located in the administrative building on the second floor and is oriented towards the V5 and MBTS. In the exterior, compared to the M12, we have a measuring point M4. In figure 2 is a view of the measuring point M12 in the building.

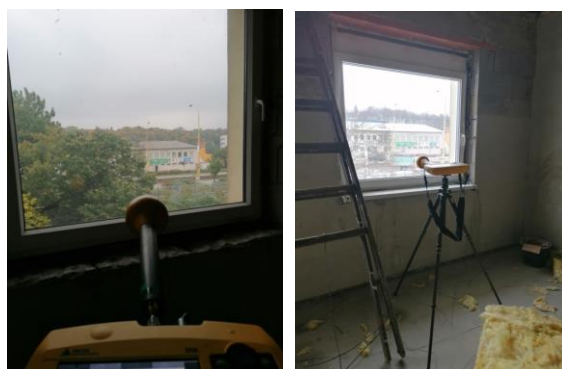


Figure 2. View of measuring point M12

The evaluation was performed at each measuring point. Table 1 shows selected results from the M12 indoor and outdoor M4 measurement sites that were located in the immediate vicinity of the MBTS base station.

Table 1. Results of measurements at measuring point M12 interior (orange) and M4 exterior (green)

Index	ZS V5		MBTS		ZS V5		MBTS	
	Frequency [MHz]	Act [mV/m]	Frequency [MHz]	Act [mV/m]	Frequency [MHz]	Act [mV/m]	Frequency [MHz]	Act [mV/m]
1	934	259	935	114,7	938	340,3	954	576
2	2639	220,5	1866	95,25	2119	321,4	1867	339,6
3	952	75,66	956	92,41	1861	283,9	798	320,4
4	2109	61,34	951	87,4	955	270,3	2137	184,4
5	2624	56	799	78,18	2639	141,9	2133	166,4
6	2117	49,37	796	62,56	1839	126,1	937	162,8
7	799	47,6	814	59,14	799	111,3	2646	135,3
8	789	34,74	1822	37,3	789	100,7	808	108,4
9	1804	27,1	2113	26,2	1804	77,87	1839	103
10	814	21,17	708	26,02	2135	61,05	1809	100,2

The following changes occurred during measurements in the interior and exterior and when the location of the base station was changed (see Table 1):

- Frequency 2100 Hz - during operation of remote ZS V5 the intensity value is 61.34 mV/m in the interior and the intensity value is 321.4 mV/m in the exterior (marked in yellow)
- Frequency 2100 Hz - in MBTS operation the intensity value is 26.2 mV/m indoors and the intensity value 166.4 mV/m outdoors

Figures 3 and 4 show the frequency spectrum of the EMF at measuring points M12 and M4 during the operation of the base station V5. Figures 5 and 6 show the frequency spectrum at the same measuring points, but with the functionality of the MBTS source. In both cases, we can clearly see that the intensity of the electromagnetic field is significantly lower in the interior than in the exterior. The reason for these differences is the building structures and the good damping effects of the materials.

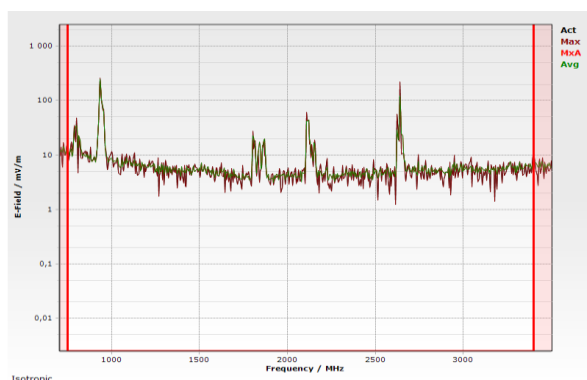


Figure 3. Frequency spectrum in M12 - V5 source switched on

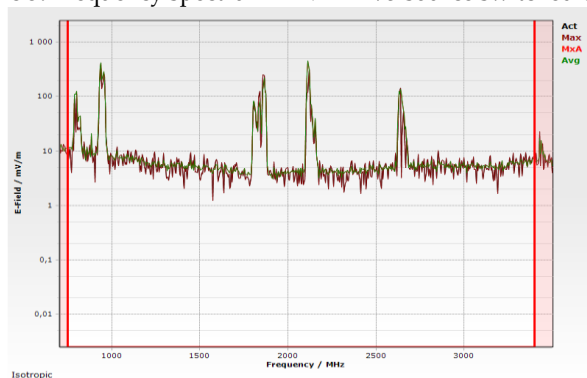


Figure 4. Frequency spectrum in M4 - V5 source switched on

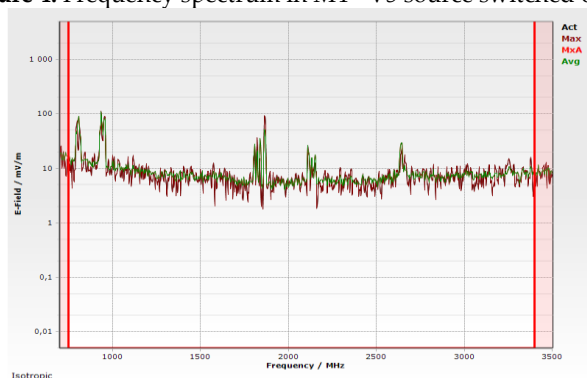


Figure 5. Frequency spectrum in M12 - MBTS source

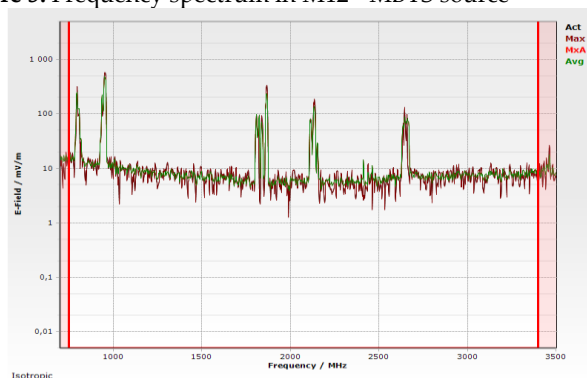




Figure 6. Frequency spectrum in M4 - MBTS source

From the evaluation of the measurement results, the changes in the intensity of the electromagnetic field for individual measuring points are evident when the location of the base station and the location of the measuring points change. These changes in all measuring points can be seen even with cumulative values. Table 2 shows the cumulative values for the individual measuring points in the different operating modes and their locations.

Table 2. Cumulative values of measuring points indoors and adjacent outdoors

Measuring point	M11	M12	M13	M14	M15	M4	M1	M2	M8
ZS V5 [mV/m]	326,1	321,0	357,9	150,1	256,6	632,0	778,0	252,3	486,0
MBTS [mV/m]	294,8	300,6	200,4	211,4	336,8	1043	756,6	397,5	270,2

The legend:

 - measuring points in the interior  - measuring points in the exterior

The cumulative values from the individual measuring points in the interior point to the differences that occurred when changing the location of the base station, which, however, are not significant at the individual measuring points. Table 2 shows, for comparison, the cumulative values of the electromagnetic field strength from measuring points M11-M15, which were located indoors, and the cumulative values of measuring points located outdoors near the building. Based on these values, we can conclude that the measurements performed indoors achieve significantly lower values of EMF intensity than outdoors, all values are well below the EMF action values set in the applicable legislation.

5. Conclusion

In the last few decades, the intensity of the electromagnetic field in the environment has increased more than a million times. This makes it clear that the sources of electromagnetic fields and their effects on humans must be addressed. The impact of EMF on the health of the population and, in particular, the relation of action values to clearly identified health disorders are not yet clearly demonstrated across the whole range of studies carried out on a global scale. In the contribution we described an experiment in which we carried out measurements of EMP intensity in the interior and exterior. Based on the cumulative values from the individual measurement points, it can be concluded that the measurements carried out in the interior achieve significantly lower EMF intensities than in the exterior, all values far below the EMF action values laid down in the legislation in force. This experiment is the starting point of a more extensive research, which the authors focus on, and which aims to objectively assess the impact of technical interventions in the construction of base stations on changes in the electromagnetic field around the base station.

Acknowledgments: This contribution was created within the project KEGA 011TUKE-4/2021 Implementation of current scientific research, technical and methodological solutions in the field of environmental engineering into the educational process at universities.

Conflicts of Interest: The authors do not declare any conflict of interest.

References

1. Salvatore, J. R.: Electromagnetic Fields. Encyclopedia of Toxicology, 2014. 316-319s. ISBN 978-0-12-386454-3.
2. Lumnitzer, Ervin et al.: Elektromagnetické polia v životnom a pracovnom prostredí. Košice: TU, 2014. 96s. ISBN 978-80-553-1910-0
3. Sylvie, Martin et al.: Health disturbances and exposure to radiofrequency electromagnetic fields from mobile-phone base stations in French urban areas. In: Environmental Research, vol 193, February 2021, 110583. Online: <https://www.sciencedirect.com/science/article/pii/S0013935120314808>
4. Koprivica, Mladen et al.: Statistical analysis of electromagnetic radiation measurements in the vicinity of GSM/UMTS base station installed on buildings in Serbia. In: Radiat Prot Dosimetry; 168(4):489-502. Online: <https://pubmed.ncbi.nlm.nih.gov/26231558/>
5. Lumnitzer, Ervin et al.: Posudzovanie zdrojov elektromagnetických polí po ich zriaďovaní a rekonštrukcii. Fyzikálne faktory prostredia. Roč. 5, č. 2 2015. 61-66s. ISSN 1338-3922



Methodology for identification of the dual-mass flywheels properties

Matúš Kačír¹, Róbert Grega²

¹ Technická univerzita v Košiciach, Strojnícka fakulta, Katedra konštrukčného a dopravného inžinierstva, matus.kacir@tuke.sk

² Technická univerzita v Košiciach, Strojnícka fakulta, Katedra konštrukčného a dopravného inžinierstva, robert.grega@tuke.sk

Abstract: The history of automotive manufacturing has brought and is currently bringing many innovations and improvements in all spheres of the automotive industry. Stricter emission standards and increased driving comfort lead to optimizations and changes in all parts of the car. The desired results are achieved by reducing the overall weight of the automobile, reducing aerodynamic drag, increasing power while maintaining engine capacity, and many other modifications to all vehicle components. Some adjustments, e.g., reduction of aerodynamic noise, led to overall noise reduction of the vehicle in the interior, while other sounds disrupting driving comfort came to the fore.

One of the important parts of the car that ensures a quieter and more comfortable ride is a two-mass flywheel called DMF. Developments and changes in the design of the dual-mass flywheel have led to a reduction in torsional vibrations and vibrations that are transmitted from the engine to the input shaft of the transmission. By researching and obtaining parameters of the dynamic properties, torsional stiffness and damping of the oscillations emanating from the engine, it is possible to further innovate the functional elements of the dual-mass flywheel and thus improve the ride comfort of passengers.

To determine the properties and required parameters, a device for measuring properties by simulating torsional oscillations is used in laboratory conditions.

Keywords: load characteristics; dual mass flywheel; simulation of torsional oscillations

1. Introduction

The rise of the road transport and emission standards tightening are forcing manufacturers and designers of internal combustion engines to adjust the design and components of the engine to reach the required targets. These adjustments include, for example: downsizing, downspeeding, cylinder deactivation. In the future, high-performance, highly boosted units with a smaller number of cylinders will emerge, which will introduce even greater torsional vibrations into the drivetrain compared to today's engines. As a result, reducing torsional vibrations is becoming a crucial task for developers and designers. Most damping systems, currently available, reach their limits, especially given the tightening requirements for the elimination of torsional units in the future. Figure 1 shows a comparison of vibrations between traditional internal combustion engines with a conventional clutch and newly developed low-emission internal combustion engines with DMF [1,2].

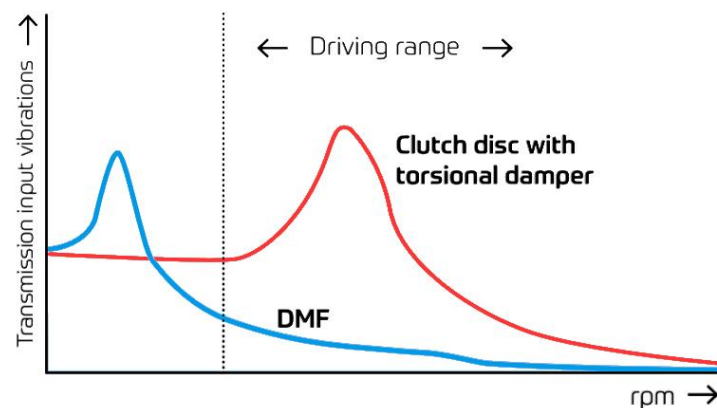


Figure 1. Comparison of SMF and DMF [3].

The aim of the article is to point out the importance of testing DMF and developing new types of DMF that will meet the requirements of current and future combustion engines.

DMF construction development trends

The primary property of DMF is almost complete isolation of torsional vibrations. Figure 4. shows the values of torsional vibrations at idle. In SMF, unfiltered vibrations are transmitted to the transmission, which causes the edges of the gear teeth to collide. The dual mass flywheel serves as a damper that filters out the torsional vibrations caused by the engine. This prevents wear of the components in the gearbox and reduces excessive noise. [4]

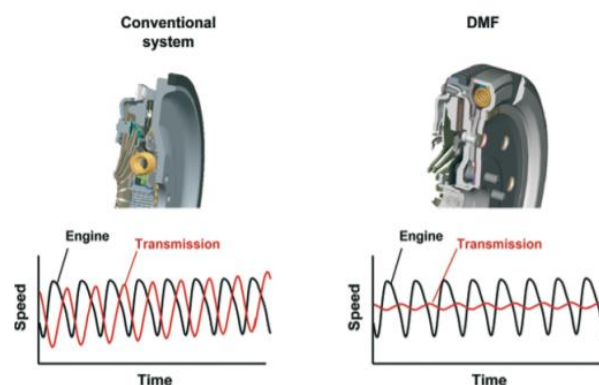


Figure 2 Torsional vibration difference with SMF and DMF [4].

1.1 Coil springs DMF

The design beginnings of the two-mass flywheels consisted of a structure with a pair of coil springs. As internal combustion engines evolve and DMF requirements increase, it is necessary to improve and design new DMF types. The current leaders in the DMF market are Valeo, LuK, ZF and SACHS. The Valeo DMF (Fig. 6) resonant region falls below the engine idle speed. As a result, there is no increased gear noise in the normal vehicle speed range. This increases the comfort of the vehicle's passengers. [5]

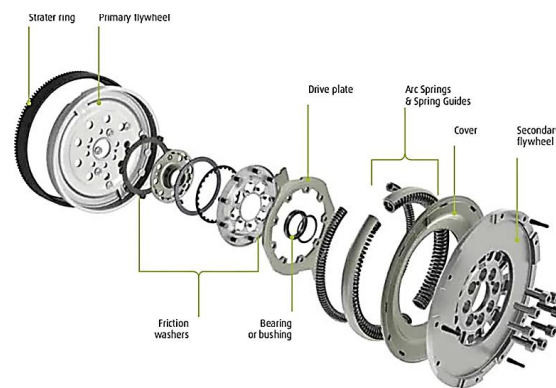


Figure 3 DMF valeo construction [5]

The primary flywheel is bolted directly to the crankshaft and includes damping springs. The secondary flywheel is equipped with a classic clutch cover and a fixed disc with lower inertia, which improves the gear shifting. Between the flywheels are two long curved springs that absorb the vibrations of the engine. The main advantage is the greater angular damping, up to 60° , which allows the filtration of torsional vibrations. If a spring with the same stiffness is replaced by two springs with different stiffness, a change in the load characteristic is achieved, what improves the ability of the engine to start. Figure 7 shows the load characteristics of DMF with one-stage curved spring (on the left) and two-stage curved spring (on the right) [5].

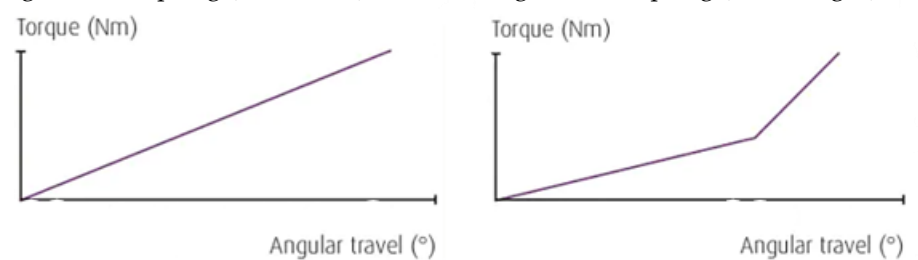


Figure 4. Load characteristics with one and two springs.

The German company ZF is the most innovative in products such as SMF and DMF. ZF produces about 60 different types of DMF (Figure 8) for different car models [3].



Figure 5. ZF DMF [3].

All ZF DMFs have multistage torsional characteristics. This is achieved by combining different amount of compression springs with different stiffnesses. The soft starting stage ensures excellent engine starting and starting behaviour. The following harder stages provide effective separation of torsional vibrations and sufficient protection against overload at normal driving speeds. Figure 9 compares torsional stiffnesses between DMF with two spring stiffnesses (blue curve) and three spring stiffnesses (red curve) [3].

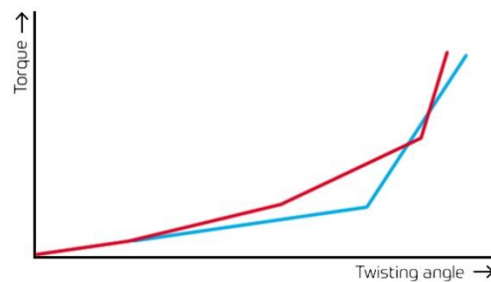


Figure 6. Comparison of DMF with two and three springs of different stiffness [3].

1.2 DMF with flat spiral spring

An alternative solution is usage of DMF which damping system composes of coil springs, that replace the classic arcuate coil springs (Figure 10). The device can be used for both manual transmissions and hybrid automatic transmissions. Its characteristic feature is the elastic behaviour, that is defined almost exclusively by the stiffness of the coil springs, while being marginally influenced by the torque and the rotational speed. In addition, the system does not require any lubrication, so no sealing is required [6].



Figure 7. Flat spiral spring DMF [6].

Real condition tests were performed with DMF design where the arc spring was removed and a coil spring was designed and tested using a torsional stiffness tester, fem analysis. Upon completion of the tests, it was found, that the use of such coil springs is not suitable for DFM due to its short life. Under real conditions, the maximum DMF service life was 25,000 km. The load characteristic results are shown in Figure 11 [6].

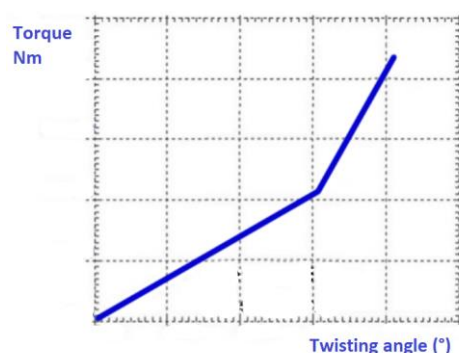


Figure 8. Flat spiral spring DMF load characteristics [6].

2. DMF property identification device

It is clear from the above examples that the load characteristics are among the most important properties to be identified in DMF. From detected load characteristic, we can determine the torsional stiffness of the tested flywheel. The design and construction of new torsional vibration damping devices requires suitable laboratory conditions for their testing and for obtaining detailed information in the form of data that can be analysed. The staff of the Technical University of Košice has built a device with kinematic excitation of torsional oscillations (Figure 12, 13) for testing and identification of the properties of flexible couplings. The aim of the device is to test DMF and develop a two-mass flywheel where the elastic member will not be compression springs but gaseous medium [7].

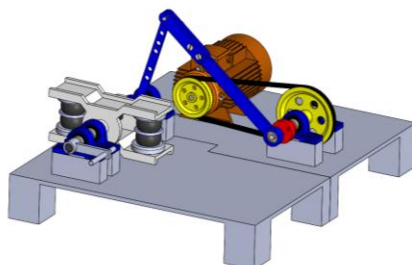


Figure 9. DMF property identification device.

The test equipment allows the simulation of different operating modes, which are characterized by different load frequencies, amplitudes, and biases. The main part of the test equipment, which allows to simulate operating conditions, is a transducer that changes the rotational movement to oscillating - in this case, it is a four-joint mechanism [7].

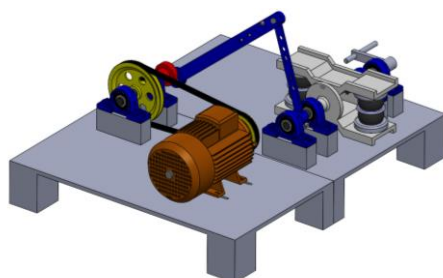


Figure 10. DMF property identification device.

The device is designed for measurement with a free load on the output. In this method, it is necessary to measure the dependence of the excitation frequency ω and the excitation amplitude of the coupling rotation ϕ_A . ϕ_{\max} is determined from the measured values. ϕ_{\max} is obtained when the system resonates, which is clear from the theoretical analyses and practical measurements. Since the amplitude of the mass rotation at the input side with the given mass moment is determined by the geometry of the four-joint drive mechanism and is therefore known, then the damping coefficient b of the coupling is calculated after determining the moment of inertia at output I_Z and oscillation frequency at output ω_2 according to formula (1) which is suitable for couplings with linear and nonlinear characteristics [7].

$$b = \frac{\phi_A}{\phi_{\max}} \cdot I_Z \cdot \omega_2 \quad (1)$$

3. Conclusions

The constant pressure to reduce emissions and the associated resulting vibrations and torsional vibrations is a problem for today's automotive designers. The development and design of new, often unconventional, design solutions bring opportunities that move the research of more than just two-mass flywheels forward. For this reason, it is necessary to determine the characteristics of current equipment and to design innovations or new equipment whose parameters will meet current and future requirements. Given the possibilities of testing DFM parameters, the vision is to design DFM structures in the future with subsequent identification of their properties and determination of the most suitable DMF structure.

Acknowledgments This paper was developed within the projects implementation KEGA 029TUKE-4/2021 "Implementation of modern educational approaches in the design of transmission mechanisms, VEGA 1/0528/20 "Solution of new elements for mechanical system tuning".

Conflicts of Interest: "The authors declare no conflict of interest."

References

1. Róbert Grega; Peter Baran. Comparison of dynamic properties of dual mass flywheel. 2015
2. Jurgen Kroll; Ad Kooy; Roland Seebacher. Torsionsschwingungsdämpfung für zukünftige Motoren; 2010
3. ZF Friedrichshafen AG. Clutch Systems. 2017
4. Balashov, D., Burkovski, L., Ferderer, F., Fidlin, A., Kremer M., Pennec, B., Simulation Bei Drehschwingungsdämpfern. 2006
5. VALEO. Transmission Systems Dual-Mass Flywheel DMF valeoscope product focus. 2016
6. Daniela Maffiodo, Raffaella Sesana, Dino Paolucci, Sabrina Bertaggia. Finite life fatigue design of spiral springs of dual-mass flywheels: Analytical estimation and experimental results. 2018 DOI: 10.1177/1687814018778474
7. Grega R.: Monitoring vibrácií mechanických sústav a testovanie pružných spojok, Technická univerzita v Košiciach, Univerzitná knižnica Technickej univerzity v Košiciach, 2019



Scheme of methodology of magnesium powder preparation for 3D printing

Jana Klímová^{1*}, Zuzana Molčanová², Karel Saksl², Marianna Trebuňová¹, Marek Schnitzer¹, Jozef Živčák¹, Radovan Hudák¹

¹ Technical University of Košice, Faculty of Mechanical Engineering; jana.klimova@tuke.sk, marianna.tre-
bunova@tuke.sk, marek.schnitzer@tuke.sk, jozef.zivcak@tuke.sk, radovan.hudak@tuke.sk

² Slovak Academic of Science, Institute of materials research; molcanova@saske.sk, saksl@saske.sk

* Correspondence: jana.klimova@tuke.sk

Abstract: Magnesium alloys are very attractive as biodegradable implant materials. This work deals with the preparation of a methodology for the production of magnesium powder with the aim of an amorphous structure for additive production. The powder is prepared on the basis of magnesium, calcium and zinc with the possible addition of yttrium to increase mechanical properties. The powder production itself consists of a suitable ratio of elements, chamber pressures and melting temperature. Based on the obtained data, it has not yet been possible to determine a suitable combination of individual parts in order to achieve a positive result. Achieving the required results is also hampered by the lack of professional literature in the field. The work explains the methodology of magnesium powder preparation.

Keywords: magnesium alloys, biodegradation, additive manufacturing

1. Introduction

Magnesium (Mg) as a metal with low weight, mechanical properties similar to bone tissue, importance in biological processes of the human body and degradation in the living organism is suitable for the production of biocompatible, biodegradable and osteoconductive implants in orthopedic or cardiovascular applications. In contrast to the titanium alloys used so far, the application of magnesium alloys is much more suitable.

2. Usage of magnesium

Biodegradable implants are the focus of the industry and have faced increasing interest in recent years. The main reason for the development of biodegradable implants is precisely their degradability in the physiological environment (the words "degradability" and "corrosion" have similar meanings but are used in the context of in vivo or in vitro). The advantage provided by this class of material is that the clinical function of the permanent implant is achievable and if successfully completed, the implant will disintegrate if it is no longer needed. Another of the main advantages of biodegradable implants is the elimination of the subsequent operation to remove the implant after sufficient tissue healing as with permanent implants. Thus, it means reducing or eliminating lifelong problems caused by permanent implants such as prolonged endothelial dysfunction, permanent physical irritation, and chronic local inflammatory reactions. Nevertheless, polymeric materials have a dominant position in current medical applications, but magnesium, iron and zinc based alloys have been introduced as more advantageous biodegradable materials for load-bearing and loaded implants due to their first-class combination of strength and toughness over polymers. [1]

3. Methodology of powder preparation

The surface energy of magnesium powder is high due to the small particle size. As a result, Mg powder oxidizes easily and is difficult to deposit in layers. Therefore, alloying is usually used to reduce the sensitivity to oxidation. Some common non-toxic alloying elements include calcium, zinc and manganese. These elements affect the obtained grain structure, strength and heat resistance of magnesium. [2]

The prepared alloys contain magnesium, calcium and zinc. Yttrium 2%, 4%, 6% was gradually added at the expense of magnesium to increase the mechanical properties.

At present, the amorphous structure of the alloy $\text{Mg}_{66}\text{Zn}_{30}\text{Ca}_4$, $\text{Mg}_{64}\text{Zn}_{30}\text{Ca}_4\text{Y}_2$, $\text{Mg}_{62}\text{Zn}_{30}\text{Ca}_4\text{Y}_4$, $\text{Mg}_{60}\text{Zn}_{30}\text{Ca}_4\text{Y}_6$ is being prepared at the Institute of Materials Research of the Slovak Academy of Sciences.

First, the proportions of the elements to the weight of 5g are weighed. Initially, only $\text{Mg}_{66}\text{Zn}_{30}\text{Ca}_4$ was used but the samples were very fragile. Therefore, yttrium was added to increase the mechanical properties. The firing process was also modified, because before that only the melting point of all the elements present was reached and fired, but now it remains at a temperature of about 12-15 min. Initially, the elements are weighed, pressed and placed in a graphite tube. It is operated at the Melt Spinner SC plant (Edmund Bühler GmbH, Germany) where a high vacuum is gradually generated by means of an argon overpressure.

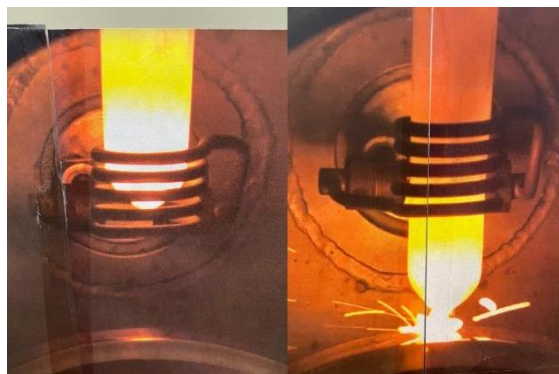


Figure 1. Melt Spinner; left-heating the tube, right-firing the contents of the tube under argon pressure

Initially, a pre-vacuum is created using a rotary pump and a second time it is pulled with a $5 \cdot 10^{-2}$ millibar high vacuum turbomolecular pump. When the chamber is ready, the insert is lowered to be in a coil where it is gradually heated up to 600 degrees Celsius to homogenize the entire contents of the graphite tube (Figure 1). At a temperature of 600 degrees, it is held for about 15 minutes. The insert is then fired under argon pressure as the tube is lowered. The copper mold into which it is cast is cooled by water. It is cast at a temperature of 730-740 degrees.



Figure 2. Cast samples $\text{Mg}_{66}\text{Zn}_{30}\text{Ca}_4$

The goal is to create a solid rod with an amorphous structure (Figure 2). Samples were monitored with a ZEISS METROTOM 1500 non-destructive industrial tomograph (Carl Zeiss, Germany) (Figure 3). The Carl Zeiss meter enables non-destructive non-contact measurement of components in their entire volume by applying X-rays. Using computed tomography (CT), we get a comprehensive view of the part from any side and in any section. The point cloud representing the volume of the part is obtained from the number of X-rays taken to measure the part as it rotates about the vertical axis. In the process of generating a point cloud, the images are analyzed and in the resolution given by the high accuracy of the system, each point is assigned exact coordinates in space and its intensity, which corresponds to the density of the part material. [3]

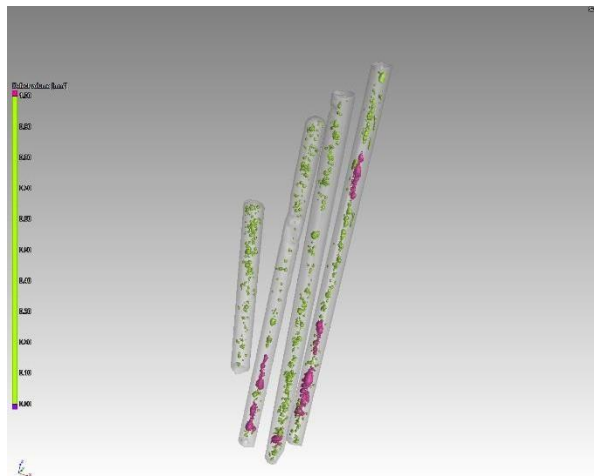


Figure 3. CT scan ($\text{Mg}_{66}\text{Zn}_{30}\text{Ca}_4$); green color is defects smaller than 1mm^3 , pink color - defects larger than 1mm^3

From figure 3, it is possible to state a high presence of defects along the entire length of the cast bar. Mechanical testing on such samples would not be relevant as the result would be affected by input defects. The samples that were formed had a high porosity, so exhausts were made in the copper mold so that the bubbles could be released during the casting process.

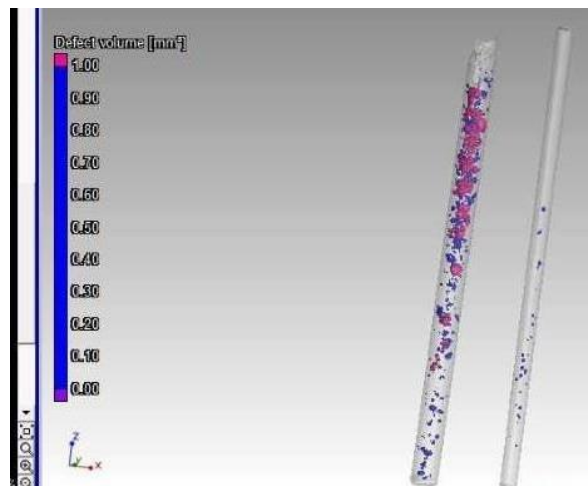


Figure 4. CT scan ($\text{Mg}_{66}\text{Zn}_{30}\text{Ca}_4$) after casting with exhausts with lower porosity

For 5 mm diameter the porosity is 7.63%, for 3 mm 0.345%, the porosity of the sample was reduced (Figure 4).

4. Further testing

The produced samples will then be subjected to several tests. Among the first will be a mechanical pressure test. The samples for the pressure test will be adjusted to a size ratio of 1: 2, with a diameter of 3mm and a length of 6mm. The pressure test will take place on a Tiratest 2300 (Tira GmbH, Germany), which will monitor the maximum rupture force, of which the ultimate strength and the assumed yield strength. The goal is to get the strength limit R_m higher than 550 MPa, because according to Wang and the team (Figure 5), they reached strength strengths of up to 600 MPa with similar alloys. [4.5]

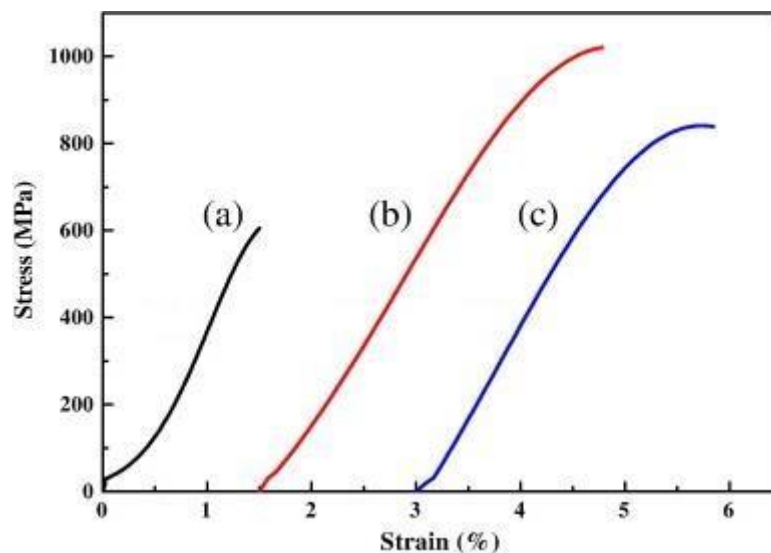


Figure 5. Deformation stress curves between alloy bars (a) $\text{Mg}_{68}\text{Zn}_{28}\text{Ca}_4\text{Y}_1$, (b) $\text{Mg}_{68}\text{Zn}_{27}\text{Ca}_4\text{Y}_1$ and (c) $\text{Mg}_{68}\text{Zn}_{25}\text{Ca}_4\text{Y}_3$ with a diameter of 1.5 mm when compressed at room temperature. [4]

At the same time, the samples will be subjected to biodegradation. Half of the tested samples will be surface treated with chitosan, which should slow down the degradation. The other half will be uncoated, all samples will be soaked in Hank's solution (Hank's solution is an example of an artificial solution that is standardly used for corrosion testing in laboratory conditions) for 45 days, when weighed every 15 days, taken by industrial

tomograph so that the course of degradation is clear and at the same time the pH is equalized to 7.4 before re-immersion. The samples in the tubes will be at a stable temperature of 36 ° C to simulate body temperature and will be placed on a shaker that will simulate the movement of body fluids. [6]

5. Conclusions

Magnesium as a newly discovered material for implantation provides a very promising future in the field of regenerative medicine. However, the complexity of its processing slows down the development in additive production. This article deals with the preparation of magnesium alloys, with a view to the future possibility of implantation, so that they are suitable for processing by additive technology.

Acknowledgments: This work was supported by the Agency for the Support of Research and Development on the basis of Contract No. APVV-17-0278. This work was supported by the Agency for the Support of Research and Development on the basis of Contract No. APVV-20-0068. This work was created with the support of project KEGA 023TUKE-4/2020, 01/2020 - 12/2022 laboratory equipment and diagnostic instruments for measuring physical and technical quantities. This publication was created thanks to support under the Operational Program Integrated Infrastructure for the project: Center for Advanced Therapies of Chronic Inflammatory Diseases of the Musculoskeletal System (CPT ZOPA), code ITMS2014 +: 313011W410, co-financed by the European Regional Development Fund.

Conflicts of Interest: The authors declare no conflict of interest.

References

1. Carlo Di M, Griffiths H, Goktekin O, et al. Drug-Eluting Bioabsorbable Magnesium Stent. *Journal of Interventional Cardiology* [online]. 2004, 17(6), 391-395 [cit. 2021-12-24]. ISSN 0896-4327.
2. Liu Ch, Zhang M, Chen Ch. Effect of laser processing parameters on porosity, microstructure and mechanical properties of porous Mg-Ca alloys produced by laser additive manufacturing. *Materials Science and Engineering* [online]. 2017, 703, 359-371 [cit. 2021-12-20]. doi: 10.1016/j.msea.2017.07.031. ISSN 09215093
3. Portál strojárskaj metrológie. Web TUKE [online]. Košice, 2010 [cit. 2021-12-20]. Available via: <http://web.tuke.sk/smetrologia/l8.html>
4. Wang J F, Wei Y Y, Guo S F, Huang S, Zhou X E, Pan F S. The Y-doped MgZnCa alloys with ultrahigh specific strength and good corrosion resistance in simulated body fluid. *Materials Letters* [online]. 2012, 81, 112-114 [cit. 2021-12-18]. ISSN 0167577X. doi:10.1016/j.matlet.2012.04.130
5. Beck B, Marcus R. Impact of Physical Activity on Age-Related Bone Loss. *The Aging Skeleton* [online]. 1999, 467-478 [cit. 2021-12-18]. ISBN 9780120986552. doi:10.1016/B978-012098655-2/50041-7
6. Bernáthová I, Halama M, Fujda M, Staško I. Korózne vlastnosti biomateriálov nti, cpti a ti6al4v v podmienkach simulovanej telesnej tekutiny. *Chemické listy* [online]. 2011(105), 558-560 [cit. 2021-12-24]. Available via: http://www.chemicke-listy.cz/docs/full/2011_16_s552-s560.pdf



Attitude of European SMEs to digitalization and digital transformation during the COVID-19 pandemic

Laura Lachvajderová* and Jaroslava Kádárová

Department of Industrial and Digital Engineering, Institute of Industrial Engineering, Management and Environmental Engineering, Technical University of Košice, Park Komenského 9, 040 01 Košice, Slovakia; laura.lachvajderova@tuke.sk; jaroslava.kadarova@tuke.sk

* Correspondence: laura.lachvajderova@tuke.sk; Tel.: + 421 55 602 2724

Abstract: The digitization of industry has become a global trend of the 21st century. The Covid-19 pandemic has significantly accelerated the implementation of Industry 4.0 in practice, mainly due to benefits in various areas. The aim of this study is to characterize the attitude of small and medium-sized enterprises (SMEs) in Europe towards digital transformation (DT) and to find common or different views in their perceptions. To this end, this article aims to define the consequences and the very attitude of companies to the impact of a pandemic on their DT. Finally, this article focuses on the reflection of the two global trends that prevail in 2021, namely the pandemic from a social point of view and digitization from a technological point of view. This study analyzes the literature and the European DigitaliseSME survey, which was developed as a case study. The article also deals with methods of comparison and summarization.

Keywords: digitalization, digital transformation, SMEs, COVID-19, analysis

1. Introduction

According to [1], digitization became the dominant technological trend in 2021. The current pandemic situation has rapidly accelerated the digitization of public sectors (authorities, government), private companies and especially people's lives [2]. The Covid-19 pandemic has significantly widened technological development and management gaps, affected customer behavior, exposed knowledge gaps and, finally, reduced the funding needed for future development [3]. According to [4], the timeliness of digitization has reinforced the need for smart strategic solutions that allow SMEs to respond flexibly to individual changes. Unforeseen situations such as the Covid-19 pandemic and an environment that is changing dynamically call for the definition of new forms of competitive advantage for SMEs. Unfortunately, factors that guarantee business success, such as performance, production volume, high or low quality, price, and time, are no longer enough. Through the transformation of processes that digitalization guarantees, modern businesses are investing and reaping various benefits. The use, construction, development, stabilization and implementation of communication and information technologies have a positive impact on business management and support for the sustainability of business development in all areas (economic, social, environmental) [4]. Digitization in Industry 4.0 is a complex process of change caused by the intensive use of communication and information technologies. Digitization serves as a tool to streamline business activity through process and business transformations based on modern technology and innovation [5].

We rank the data, innovations, needs and expectations of customers among the driving forces of digitization. The corporate governance strategy, which aims to support digital development, is an accelerator of successful and sustainable business [5]. Strategies that lead to digitization are a way to achieve the goals set in the Industry 4.0 concept,

which guarantees the satisfaction not only of current requirements and preferences of customers but also of future ones. For individual strategies (marketing, financial, HR, digital, research, etc.) to work effectively, it is necessary to harmonize them uniformly and collectively. The four-year needs model, consisting of the steps of creating awareness, implementing the strategy, continuously improving processes, and finally adapting to practice, meets the needs of SMEs [6].

The main threat of digitization is the lack of support for digital projects due to limited funding during a pandemic situation. The aim of this study is to correctly identify different and common views on the digitization of European SMEs in the period 2018-2020. we also assessed the global state of SMEs in the wake of the Covid-19 pandemic.

2. Materials and Methods

The Scopus and Web of Science scientific databases were used to search for professional resources. Attention was focused on the concept of the digitalization of SMEs. The criteria for the selection of literature were:

- time relevance - articles were to be published between 2018 and 2021,
- professional relevance - content focus on digitization and digital transformation of SMEs in the concept of Industry 4.0, which can be considered as its synonym.

The main goal of this study is to identify the approach of SMEs in the field of digitization and DT and to define different and common elements of the problem. The study also aims to define the global level, attitude, and state of the impact of the Covid-19 pandemic on the digitization of SMEs. We used the DigitaliseSME survey to analyze the European Union. This project supports digitization to increase the ability of SMEs to go abroad and innovate their processes. It is funded by the European Union and the primary goal is also to support DT mid-cap companies in Europe. Digital experts, also known as "Digital Enablers", have teamed up with companies to help these companies innovate. This initiative has simplified and enabled SMEs to work with Digital Enablers in such a way that these experts have supported the company abroad, resp. in another European country where digitization was needed. For a period of two weeks, the Digital Enabler took an interest in running the business, visiting the offices, helping to initiate and set up the project to lead to the digitalization of the business. The results of the DigitaliseSME project, under the auspices of the European Parliament, provide a basis for developing a wider EU-wide agenda [7].

The DigitaliseSME survey provides data from 2018 to 2020 across Europe. The survey contained three questions that respondents answered. The questions focused on the feasibility of solutions in practice and areas for improvement using DT and satisfaction with digitized processes. As with every survey, the DigitaliseSME survey suffers from certain shortcomings. The primary limitations of this survey were the smaller sample size, the involvement of companies from different sectors and the limited number of issues. However, despite these limitations, the authors still find the survey sufficiently interesting and relevant. In Table 1 below, it is possible to see more detailed objectives of the project phases themselves and their timing.

Table 1. Ciele a časové rozpätie jednotlivých fáz projektu DigitaliseSME, Zdroj: [7]

June – September 2018	September 2018 – February 2019	March 2019 - January 2020
Design phase	Pilot phase	Execution phase

Aimed at setting criteria and requirements for participation in the program that corresponds to SMEs and digital devices.	It consists of five months, which allowed to test the way of connecting companies and Digital Enablers in the way that is most advantageous for both parties.	Based on the findings from the pilot phase, Digital Enablers and companies merged on a larger basis.
---	---	--

3. Results

The DigitaliseSME survey appears to be of great benefit to both Digital Enablers and companies, resulting in helping companies connect with digital professionals across Europe, which can be a steppingstone to overcome the so-called digitization gap. Regarding the participation of companies in this project, 68 SME managers took part in the DigitaliseSME European research activity out of 9 industries. Figure 1 shows the percentage of European SMEs by sector.

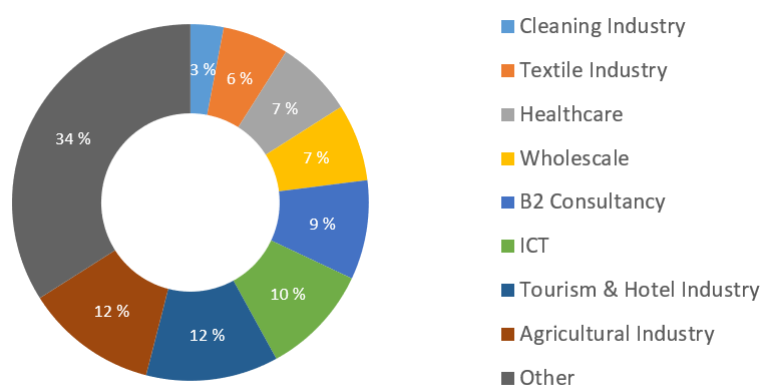


Figure 1. SMEs by industry (DigitaliseSME), Source: Own research based on [7]

SMEs, which focus on traditional sectors such as agriculture and construction, digitize at only 2%. The DigitaliseSME survey revealed large regional disparities between 2018 and 2020, which have a major impact on the adoption of Industry 4.0 concepts [7]. The results of our analysis based on the DigitaliseSME survey, which lists the digital needs of SMEs in the EU, are shown in Figure 1.

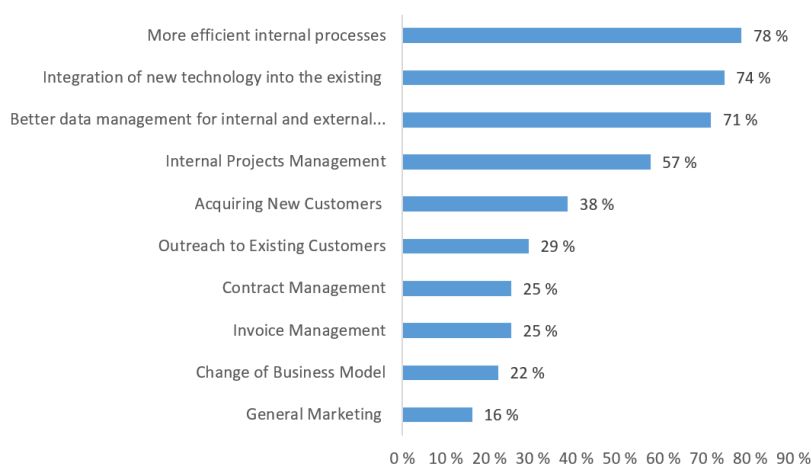


Figure 2. Digital needs identified during the DigitaliseSME survey, Source: Own research based on [7]

The analysis of the DigitaliseSME survey found that as many as 97% of respondents were satisfied with the new form of process digitization and 55% said that DT had helped them implement effective and workable solutions to their problems [7]. In the case of smaller companies, the deficit of funds for investing in new digital technologies dominates. If they invest less, they feel great uncertainty about the return on that investment. In addition, small businesses lack sufficient awareness of the effective ways to optimize the processes that digitization provides [7]. Other research activities, similar to DigitaliseSME, will be carried out between 2021 and 2027 with the help of the Digital Europe program.

4. Discussion

The best way to understand DT is to see real statistics and facts that will help us understand how DT makes a business more efficient, how DT helps to connect businesses with customers and, of course, how it allows revenue growth [8]. Globally, according to data from [8], the average budget set aside for DT in 2018 among 1,200 midsize and large U.S. companies was \$ 14 million, according to the survey. However, global spending on DT in 2022 is expected to reach \$ 1.78 trillion [8]. Regular analyzes of the state of digitization in major global corporations are performed by companies providing consulting, tax, auditing, financial and many other services. These are companies such as IDG Capital, McKinsey, Tech Pro Research, Research and Markets, IDC, PwC, Deloitte, Prophet, Harvard Business Review, Futurum, Fujitsu, Forrester, Digital Adaption, Adobe, Vision Critical.

According to most consulting and research companies, DT is an even more important topic after the pandemic. It is expected that companies are likely to invest more in new technologies such as IoT, AI and AR / VR in the coming years. DT's comprehensive list of statistics and surveys for business leaders and researchers comes from trusted sources at these companies. These surveys can help businesses or management better assess and assess digitization needs, take action, and stay ahead of the competition. According to the company AI Multiple, which represents the so-called technology industry analysts, the digital market in 2025 together with CAGR (compound annual growth rate) will grow by 23% compared to 2019. In the near future, experts predict that by the end of 2023 there will be an increase in adoption in SMEs by 18%. Statistics from 2020, despite the Covid-19 pandemic, confirm that investment in DT has increased by 10% [8]. According to advisers from PwC (Pricewaterhouse-Coopers), because of the pandemic, up to 52% of SMEs plan to reduce their investment costs in the future, while only 9% will reduce digitization costs. According to a study by IDC (International Data Corporation) and Research and Markets, the technologies that will be preferred by 2025 are the Internet of Things and artificial intelligence [8]. The results of a survey by the Boston company IDG Capital claim that 89% of companies have adapted to the original form of digital strategy. Businesses are constantly striving to improve this digital strategy and adapt it to market conditions. The computer company Tech Pro Research claims that 70% of companies have already implemented a digital strategy or are working on its future use and development. Deloitte, full name Deloitte Touche Tohmatsu Limited, has found that up to 87% of businesses perceive a large impact of digitization on their business. On the other hand, only 44% of respondents said they were ready for DT. According to the Harvard Business Review, only 23% of businesses worldwide do not need digitization. DT is the driving force of competitiveness, as evidenced by the growth of the DT market by up to 51%. Following the Covid-19 pandemic, business managers aim to accelerate DT (37%) and promote teleworking (37%) [8]. Experts from the American company McKinsey are of the opinion that if the company belongs to the group of SMEs with less than 100 employees, it has up to three times better chance of being more successful in DT than large companies. However, the reluctance of employees to change or they are afraid to give up the stereotypical way of working often seems to be a problem [8]. Companies will benefit most from DT by recognizing the challenges and avoiding the pitfalls of finding the right set of skills, resisting change, sticking

to regulations that have the negative effect of slowing down the initiative or having difficulty measuring ROI. McKinsey, Forrester, Adobe and Vision Critical argue that companies that have a digital director and regularly adopt innovative technologies have a fully integrated digital strategy, manage DT twice as efficiently as the competition, and are based on experience [8]. According to [9], it is recommended that digitization be perceived by companies as a competitive advantage, to involve all their stakeholders in the process, not to confuse optimization and transformation of processes and to have a long-term vision with the main focus on the customer.

Digitization and digital transformation in companies are no longer debatable today because they are becoming a necessity, the so-called industry standard that must be met in every sector, not only because of competition but also mainly for the survival of companies in the market [10]. The Covid-19 pandemic disrupted numerous industries and forced businesses (regardless of size) to quickly rethink their business, from operations to products to services and business models.

5. Conclusions

Initially, this study aimed to identify the European level of SME approach to digitalization and digital transformation. The analysis of the DigitaliseSME project and later the analysis of case studies of foreign companies that have been providing market consulting services and monitoring SMEs in the market for many years helped us in this. The primary objective of this scientific study was to analyze the DigitaliseSME survey, supported by the European Parliament, over a period of three years (2018-2020). We presented the primary goals of DigitaliseSME, its sample of respondents and the results themselves. After analyzing the results of the DigitaliseSME survey at the European level and case studies of foreign consulting companies, the following essential elements emerged:

- medium and large enterprises are at the forefront of digitization,
- enterprises in Europe prefer digital transformation only to increase profits, social or environmental factors are not mentioned in the survey,
- significant financial deficit for small businesses to digitize,
- preferred area for technology implementation is internal processes,
- although awareness of the issue is increasing, it is still not of sufficient quality and optimal.

The biggest trend difference reported in the DigitaliseSME survey is the integration of new and old technologies. Enterprises in the EU, compared to Slovakia, for example, are generally better prepared for change, and Slovakia is unfortunately on the tail of European SMEs. Experts, enterprises, and the rest of the world see the Covid-19 pandemic as the driving force behind the acceleration and growth of digitization. Experts believe that it is very important to constantly raise the awareness of employees and managers in the field of digitization and to modify thinking at the national level. Even in this case, the approach of small and medium-sized enterprises in the field of digital transformation can improve even in times of pandemic.

Acknowledgments: This article was created with the support of projects: KEGA 009TUKE-4/2020 "Transfer of digitalization to education in the study program Business Management and Economics" and VEGA 1/0340/21 "The impact of the pandemic and the subsequent economic crisis on the development of digitalization of companies and society in Slovakia."

Conflicts of Interest: The authors declare no conflict of interest.

References

1. Rast, Ch. The top 10 tech trends of 2021. **2021**. Available online: <https://home.kpmg/xx/en/blogs/home/posts/2021/01/the-top-10-tech-trends-of-2021.html>.
2. Bai, Ch., Quayson, M., Sarkis, J. COVID-19 pandemic digitization lessons for sustainable development of micro and small-enterprises, *Sustainable Production and Consumption*, **2021**, Volume 27, pp. 1989-2001, ISSN 2352-5509. <https://doi.org/10.1016/j.spc.2021.04.035>.

3. Cone, L. et al. Pandemic Acceleration: Covid-19 and the emergency digitalization of European education. *European Educational Research Journal*, **2021**. <https://doi.org/10.1177%2F14749041211041793>
4. van de Wetering, R., Kurnia, S., Kotusev, S. The Role of Enterprise Architecture for Digital Transformations. *Sustainability* **2021**, Volume 13, 2237. <https://doi.org/10.3390/su13042237>
5. Faraj, S., Renno, W., Bhardwaj, A. Unto the breach: What the COVID-19 pandemic exposes about digitalization. *Information and Organization*, **2021**, Volume 31, Issue 1, 100337, ISSN 1471-7727. <https://doi.org/10.1016/j.infoandorg.2021.100337>.
6. Sehlin, D., Truedsson, M. and Cronemyr, P. A conceptual cooperative model designed for processes, digitalisation and innovation. *International Journal of Quality and Service Sciences*, **2019**, Volume 11, No. 4, pp. 504-522. <https://doi.org/10.1108/IJQSS-02-2019-0028>
7. DigitaliseSME. **2020**. Enabling the Digital Transformation of European SMEs. Available online: <https://digitalisesme.eu/wp-content/uploads/2020/02/DigitaliseSME-Final-Brochure-Enabling-the-Digital-Transformation-of-European-SMEs.pdf>
8. AI Multiple. **2021**. 85+ Digital Transformation Stats from reputable sources. Available online: <https://research.aimultiple.com/digital-transformation-stats/>
9. Bika, N. **2020**. 26 Recent Digital Transformation Statistics. Available online: <https://acquire.io/blog/digital-transformation-statistics/>
10. Lachvajderová, L., Kádárová, J. Digitalizácia v priemyselných podnikoch. *Novus Scientia*, **2021**, Volume 18. Technická univerzita v Košiciach, pp. 166-171, ISBN 978-80-553-3798-2.



Mechanical drive system control optimizations for ultralight mobile devices

Maroš Palko¹, Miroslav Palko¹ Viktória Krajňáková^{2*} and Ján Král¹

¹ Ing. Maroš Palko 1; maros.palko@tuke.sk

¹ Ing. Miroslav Palko 2; miroslav.palko@tuke.sk

² Ing. Viktória Krajňáková, PhD.; viktoria.krajnakova@tuke.sk

¹ doc. Ing. Ján Král, PhD. 2; kral@tuke.sk

* Correspondence: viktoria.krajnakova@tuke.sk; Tel.: +421 55 602 2733

Abstract: Current trends in the automotive industry are leading to increased performance and reduced pollutants in exhaust gases, while reducing fuel consumption. Related to this is the tremendous development in the control of internal combustion engines using electronic control systems in recent years. By removing the mechanical parts of ignition control such as the vacuum- and centrifugal-controlled distributor, ignition timing is refined and by replacing vacuum-controlled carburetors with injection in combination with a lambda probe and a three-way catalytic converter, manufacturers are now meeting the demands of the customer, but above all the ever-tightening emission standards. The control unit is required to have high flexi-mobility and speed to intervene in the controlled processes. It has to meet conflicting requirements such as controlling exhaust emissions, reducing fuel consumption and providing the required torque at minimum cost for sensors and actuators. For this reason, it is necessary to know the operation of the internal combustion engine and the possibilities of its control. [1] This thesis deals with the history of internal combustion engines and their control, the history of ignition systems and the control of combustion mixture formation. It briefly describes the distribution of internal combustion engines and the current state of internal combustion engines and their control. It also touches on the distribution of ignition systems. The thesis is treated as an overview to assist in the construction or modification of an internal combustion engine adapted for the Shell-eco marathon competition.

Keywords: automotive; internal commerce; internal combustion engine; propulsion system

1. Introduction

This thesis deals with the history of internal combustion engines and their control, the history of ignition systems and the control of combustion mixture formation. It briefly describes the distribution of internal combustion engines and the present state of internal combustion engines and their control. It also touches on the distribution of ignition systems. The thesis is treated as an overview to assist in the construction or modification of an internal combustion engine adapted for the Shell-eco marathon competition. The Faculty of Mechanical Engineering of the Technical University of Košice has been participating in the Shell-eco marathon competition for several years. Until 2010, 3 internal combustion engines were manufactured at the faculty. Since 2010, however, the development has focused on the modification of the combustion engine.

2. Division of internal combustion engines

- depending on where the combustion occurs at

- internal combustion engines (most current internal combustion engines)
- external combustion engines, for which a distinction can be made as to

whether the energy enters the working space

- working gas supply (e.g. gas turbine)
- by heat transfer through the heater of the working substance (e.g. Stirling engine)

- according to the working cycle on

- continuous duty engines (e.g. combustion turbine)
- intermittent duty cycle motors
- two-stroke
- four- stroke [2]

- according to the basic working principle on:

- reciprocating internal combustion engines
- straight reciprocating piston engines (most current internal combustion engines)
- reciprocating engines (Wankel engine)
- turbine engines (turbines)
- reactive engines (jet , or rocket) [3]

- reciprocating internal combustion engines are divided into:

- spark ignition - combustion is triggered by energy from an external source - the spark plug spark
- diesel - where combustion causes heating of the compressed mixture above the ignition temperature
- engines with combined ignition
- glow engines [4]

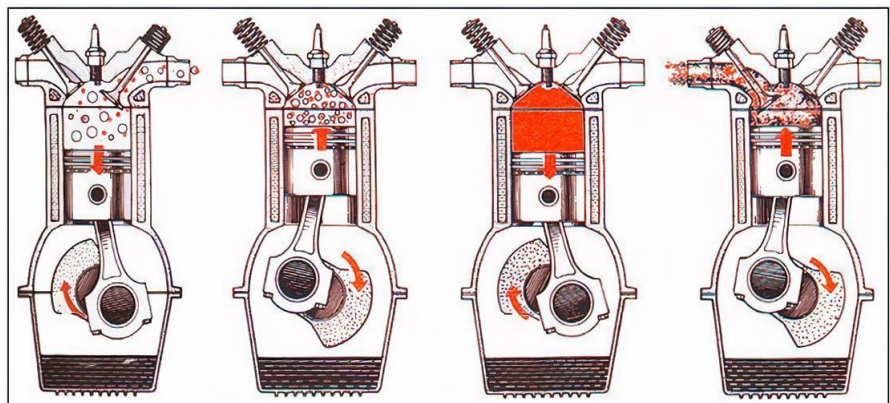


Fig. 1 – Four-stroke engine duty cycle- soaking, compression, combustion and expansion, exhaust [5]

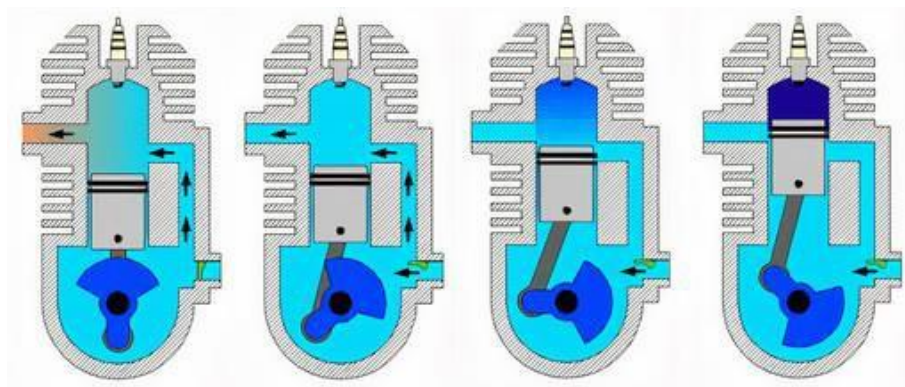


Fig. 2 – Two-stroke engine duty cycle [5]

Control unit

A typical control unit contains the standard microcomputer hardware and at least one additional piece of hardware, the so-called time synchronization unit (TPU). The role of the TPU is to synchronize the control signals with the repeating four-cycle cycle of the internal combustion engine [3]. The programming of the control algorithms is implemented by means of development environments. In [6], the basic task of the control unit is to modify the signal from the sensors for easier processing, most often by an A/D converter, then process the acquired data and amplify the output signal back to the power level required by the actuator. [7]

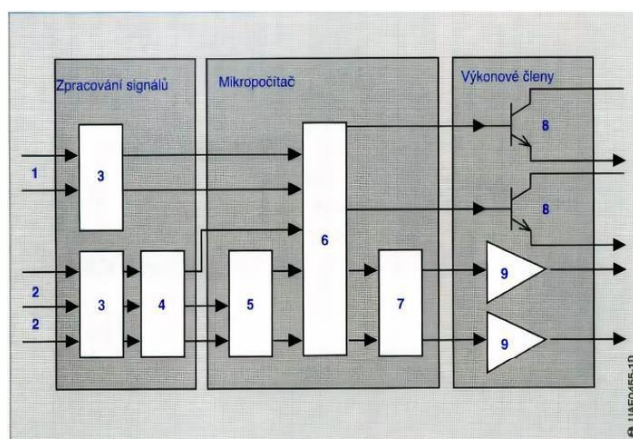


Fig. 3 – Signal processing in the control unit [8]

1. digital input signals
2. analog input signals
3. protection circuits
4. amplifier, filter
5. A/D converter
6. digital signal processing
7. A/D converter
8. power switches
9. power amplifier

The electronic sensor signals fed to the control unit may take different forms, for example analogue, digital or pulse signals.

Analog input signals are signals that are supplied by the sensors as different voltage values, at a specific interval. [9] They are physical quantities that can be passed to the control unit as analog measured values, such as intake air mass, intake manifold pressure, turbocharger charge pressure, atmospheric pressure, accumulator voltage, coolant temperature, intake air temperature, and fuel temperature. These analogue measured values must be converted into digital values by the analogue-to-digital converter (A/D converter) in the microprocessor (controller) of the control unit. [10]

Digital input signals are periodic "rectangular" signals. They occur in only two states, namely "high" and "low" or "on" or "off". Signals of this type are emitted, for example, by Hall sensors such as camshaft position or speed sensors. These signals can be processed directly by the microprocessor of the control unit without the use of a converter.

Pulse input signals are sent by inductive speed sensors or reference marks. They are pre-processed in the control unit's own circuitry and converted into digital signals. Any interfering impulses (infiltration of extraneous signals) are suppressed. [11]

Petrol engines with indirect injection

Whereas there used to be injection devices that operated mechanically and performed electronically controlled functions after the fact, such as a system that injected continuously (continuously, permanently), today's injection devices are entirely electronically controlled and inject fuel (intermittently). [12] For intermittent indirect injection, the following three types of injection valve devices are distinguished: simultaneous injection, semi-sequential (or group injection), sequential injection. [13]

Division of ignition systems

Ignition systems are divided according to several criteria:

1. According to the electrical component used, which accumulates the electrical energy needed for the discharge:

- Induction ignition: the magnetic field of the coil is used to store the electrical energy
- Capacitive ignition: the electrical energy is stored in a capacitor [14]

2. By power source:

- Battery ignition: energy is obtained classically from the battery
- Magnetic ignition: the necessary energy is generated directly by the engine through its mechanical work
- Piezoelectric ignition: mechanical pressure on the piezoelectric crystals generates the necessary energy. [15]

3. According to the type of switch and timer used:

- Contact operated ignition
- Transistor contact ignition
- Transistor contactless ignition
 - with inductive sensor
 - with Hall sensor
 - with opto-electric sensor [16]

Classic ignition

Conventional ignition is defined as battery (accumulator) ignition otherwise known as conventional ignition. It is an inductive ignition, which means that the ignition coil serves to both store and transform the supplied electrical energy. [17] This fact that the interspace of the ignition coil is used to accumulate the applied voltage is the main and distinguishing feature of induction ignition. [18] In spite of the long term development, the principle of battery ignition is still the same as the one Bosch came up with over 100 years ago in Germany. Of course, the elements used have changed over time, and nowadays the classic all-contact ignition is practically not used. [19] As the development went forward all the contact parts that were stressed mechanically but also el-electrically were gradually changed and replaced by non-contact sensors and the whole system in the case of electronic ignition started to be controlled by a control unit. The battery ignition delivers excess energy mainly at low speeds and the energy delivered decreases as the speed increases, which is due to the design of this type of ignition. When the ignition system is switched on, current starts flowing from the battery to the ignition coil at terminal 15. [20] If the interrupter is connected (or its contacts), an electric current flows through the primary winding of the coil, which causes a magnetic field in the coil. When this magnetic field is created, due to self-induction, a voltage is induced in the primary winding of the coil in the opposite direction to the applied voltage. This self-induced voltage hinders the otherwise rapid emergence of a magnetic field of the same direction as that of the applied current. This retardation (delayed generation of a magnetic field in the same direction as the injected current) is precisely the cause of the drop in ignition voltage at high speed, which also has a significant negative effect on the quality of the ignition spark itself. [21] This phenomenon is a major problem especially in the case of multi-cylinder engines, because the more cylinders, the less time it takes to ignite a particular cylinder. The ignition coil has to be completely discharged and the system has to recharge overall, which takes some time. The minimum ignition time is somewhere around 0.3 ms, if this time is not maintained there is a risk of misfire. [22] The limiting factor for this type of ignition is the time it takes for the entire system to prepare for a new cycle. Therefore, at high engine speeds and in multi-cylinder engines, there may be problems with ignition of the mixture, due to the lack of time for the system to recharge and completely discharge the coil [23].

3. Results

As a result of this work, we provide a brief overview of mechanical drive systems. This overview can be used to build or modify an internal combustion engine for the Shell-eco marathon competition. The Shell Eco-marathon is an international competition

aimed at developing the most fuel efficient vehicle possible. The Faculty of Mechanical Engineering of the Technical University of Košice has been participating in this competition for 25 years, during which time it has developed 8 vehicles. Not only low fuel consumption but also high safety are important for the vehicles. In addition to the low aerodynamic drag of the vehicle, the low weight of the vehicle is important to achieve low fuel consumption. This is achieved by the use of ultra-light and strong materials in all vehicle components. The latest generation vehicle (2018) uses a self-supporting body, which increases the stiffness requirements at the front and rear. [24]

The competition is divided into two main categories- Urban concept and Prototype. Both categories are further divided according to the type of propulsion, whether it is an internal combustion engine, an electric motor or a hydrogen engine. Our faculty is working on the Prototype category and the internal combustion engine development. Since the beginning of the participation of the Faculty of Mechanical Engineering of the Technical University of Košice in these competitions, the focus has been on the development and construction of its own body and, last but not least, on the development and production of its own internal combustion engines that would achieve the best possible result in the competition. By 2010, the faculty had produced 3 functional combustion engines with which the faculty participated in Shell-eco marathon events. Since 2010, faculty development has focused on modifying and improving the commercially produced Honda GX35 internal combustion engine. [25] In 2019, the Faculty of Mechanical Engineering of the Technical University of Košice, with the modified Honda GX35 engine, set a new Slovak record for this competition, which is 825km travelled on 1l of fuel. At the same time, the Faculty of Mechanical Engineering became the best team among the teams that were dedicated to the modification of the Honda GX35 engine. [26]

References

1. SLOBODA, Aurel – BUGÁR, Tibor – SLOBODA, Oskar, KRÁL, Ján – KONEČNÝ, Branislav: 25 rokov experimentálnych vozidiel : Technická univerzita v Košiciach, Strojnícka fakulta, 2019, 141 s. ISBN 978-80-553-3328-1
2. SHELL ECO MARATHON 2020 OFFICIAL RULES [online]. : [cit. 10.05.2020]. Dostupné na internete: <<https://www.makethefuture.shell/en-gb/shell-eco-marathon/global-rules>>
3. GASOLINE [online]. : [cit. 17.05.2020]. Dostupné na internete: <<https://www.britannica.com/technology/gasoline-fuel>>
4. DIESEL FUEL [online]. : [cit. 17.05.2020]. Dostupné na internete: <<https://www.britannica.com/technology/diesel-fuel>>
5. ETHYL ALCOHOL [online]. : [cit. 17.05.2020]. Dostupné na internete: <<https://www.britannica.com/science/ethyl-alcohol>>
6. SHELL GTL FUEL [online]. : [cit. 17.05.2020]. Dostupné na internete: <<https://www.shell.com/business-customers/commercial-fuels/shell-gtl-fuel.html>>
7. SLOBODA, Aurel – BUGÁR, Tibor, - TOMKOVÁ, Marianna – SLOBODA ml., Aurel – PILA, Ján – TKÁČ, Zdenko: Konštrukcia automobilov I. : Technická univerzita v Košiciach, Strojnícka fakulta, 2006, 402 s. ISBN 80 -8073 – 718 - 5
8. TAJOMNÝ SVET ŠTVORTAKTOV [online]. : [cit. 28.05.2020]. Dostupné na internete: <<http://www.countrycross.sk/clanky/894-tajomny-svet-stvortaktov>>
9. WANKEL ROTARY ENGINE [online]. : [cit. 28.05.2020]. Dostupné na internete: <<http://www.citroenet.org.uk/miscellaneous/wankel/wankel2.html>>
10. MOTORY- JENOM PEKNY FOTKY [online]. : [cit. 02.06.2020]. Dostupné na internete: <<http://m-power.blog.auto.cz/2007-01/motory-jenom-pekny-fotky/>>
11. STRANKY PRE FANÚŠIKOV SUBARU [online]. : [cit. 02.06.2020]. Dostupné na internete: <<http://www.subaru-als.estranky.cz/>>
12. FERENC, Bohumil: Spalovací motory : Karburátory a vstříkování paliva. Praha: Computer Press, 2004, 388 s. ISBN 80-251-0207-10
13. SÚBOR: T CYCLE SEILIGER.PNG [online]. : [cit. 05.06.2020]. Dostupné na internete: <http://sk.wikipedia.org/wiki/S%C3%BABor:T_cycle_Seiliger.png>
14. RAUSCHER, Jaroslav: Spalovací motory. Brno: studijní podklady, 2005, 235 s.
15. GRT GAZ ET LA JOLIVERIE, PARTENAIRES DE LA MOBILITÉ GAZ [online]. : [cit. 06.06.2020]. Dostupné na internete: <<http://www.grtgaz.com/fileadmin/medias/communiques/2015/fr/CP-GRTgaz-Joliveriemicrojoule-19032015.pdf>>

16. REMMI TEAM INFO [online]. : [cit. 06.06.2020]. Dostupné na internete: <<http://remmi-team.com/>>
17. THE TEAM [online]. : [cit. 06.06.2020]. Dostupné na internete: <http://higtech.se/?page_id=28>
18. THE CARS [online]. : [cit. 06.06.2020]. Dostupné na internete: <http://higtech.se/?page_id=456>
19. ČINNOST ŠTVORTAKTNÉHO ZÁŽIHOVÉHO MOTORA [online]. : [cit. 07.06.2020]. Dostupné na internete: <<http://www.aaautoskola.sk/p1204.html>>
20. VLK, František. Vozidlové spalovací motory. Brno: Prof.Ing.František Vlk, DrSc, 2003, 578 s. ISBN 80-238-8756-4.
21. SÚBOR: T CYCLE ATKINSONMILLER.PNG [online]. : [cit. 10.06.2020]. Dostupné na internete: <https://sk.wikipedia.org/wiki/Motor_s_Atkinsonov%C3%BDm_cyklom#/media/S%C3%BAbor:T_cycle_AtkinsonMiller.png>
22. MOTEJL, Vladimír. Vstřikovací zařízení vznětových motorů. České Budějovice : Kopp, 2001. 181 s. ISBN 80-7232-142-0.
23. VARIABLE COMPRESSION- SAAB SVC [online]. : [cit. 10.06.2020]. Dostupné na internete: <http://www.autozine.org/technical_school/engine/Compression.html#SVC>
24. LASER IGNITED COMBUSTION ENGINE – AN EXPERIMENTAL STUDY [online]. : [cit. 11.06.2020]. Dostupné na internete: <https://www.researchgate.net/publication/313649424_Laser_ignited_internal_combustion_engine_-_An_experimental_study>
25. HEYWOOD, John. Internal Combustion Engine Fundamentals. Jaguar books, 1988, 829 s. ISBN: 978-0070286375
26. EFFECTS OF THE STROKE / BORE RATIO ON THE PERFORMANCE PARAMETERS OF A DUAL-SPARK-IGNITION (DSI) ENGINE [online]. [cit. 11.06.2020]. Dostupné na internete: <https://www.researchgate.net/publication/231273616_Effects_of_the_StrokeBore_Ratio_on_the_Performance_Parameter_s_of_a_Dual-Spark-Ignition_DSI_Engine>



Mathematical model of a pneumatic bellows actuator

Martin VARGA¹, Ivan VIRGALA² and Michal KELEMEN³

¹ Technical university of Košice, Faculty of Mechanical Engineering, Department of Mechatronics, Slovakia; martin.varga.2@tuke.sk

² Technical university of Košice, Faculty of Mechanical Engineering, Department of Mechatronics, Slovakia; ivan.virgala@tuke.sk

³ Technical university of Košice, Faculty of Mechanical Engineering, Department of Mechatronics, Slovakia; michal.kelemen@tuke.sk

Abstract: Currently, a significant proportion of actuators are used in the manufacturing industry is pneumatic in nature. Pneumatic bellows are a special category of pneumatic actuators. These actuators have many advantages not only over actuators that also use compressed air, but also over hydraulic and electric actuators. Due to precise positioning of bellows actuators being a complex task, they are mainly used as discrete two-position actuators. This article deals with the issue of creating a mathematical model of a pneumatic bellows in order to be able to reliably position it, which would open the possibility of its application in tasks previously occupied by other types of actuators. The resulting mathematical model is then used to build a simulation model. Finally, the outputs of the simulation model is compared to experimental data. The model will be built for the Dunlop 2¾ bellows.

Keywords: *pneumatics, actuator, bellows*

1. Introduction

Compressed air is one of the basic forms of energy media that are widely used in manufacturing industry. Pneumatic actuators operate on the principle of different pressures acting on the walls of a pressure vessel, this difference causing deformation of the actuator or displacement of the actuator wall.

These actuators are generally inexpensive, robust, compact, and offer high forces and speeds. On the other hand, they are unsuitable for precise positioning due to air compressibility and general nonlinear behaviour.

Pneumatic actuators can be divided into two basic groups, namely piston actuators and deformation actuators. Examples of deformation actuators are McKibben muscles and pneumatic bellows. Pneumatic bellows consist of a flexible closed bellows body with an opening for the supply of compressed air. When the compressed air is introduced into the bellows, the bellows starts to deform in a predictable way. Unlike pneumatic muscles, they are easier to manufacture [1].

Compared to piston actuators, they are more compact and resistant to improper mounting and radial forces, but are mathematically more complex to describe, difficult to position and have a nonlinear behavior [2].

2. Deriving the mathematical model of a pneumatic bellows

The pneumatic bellows is a linear pneumatic actuator. From a pneumatic point of view, it is a pneumatic spring with a continuously adjustable equilibrium position and stiffness. The equilibrium position of the pneumatic bellows and its stiffness depends on the stiffness of the pneumatic bellows material and on the internal pressure. The bellows can be viewed as a spring, mass and damper system (Fig. 2).

As the pressure in the pneumatic bellows increases, its equilibrium position changes. At this point, the bellows behaves like a compressed / stretched spring. The direction of the force exerted by the spring is in the direction from the current position to the equilibrium position (Fig. 1).

The pneumatic bellows is made of rubber. This bellows, without the application of pressure, has its own stiffness with its own equilibrium position and acts as a separate spring.

The equilibrium position of the pneumatic bellows under pressure is at the point where the sum of the gravitational forces acting on the bellows, the pneumatic forces from the manometric pressure inside the bellows and the forces from the stiffness of the bellows itself are zero. This state is described by Equation 1 [3].

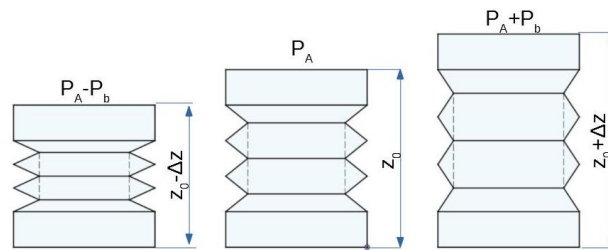


Fig. 1 Sketch of a pneumatic bellows

z_0 — equilibrium height at zero manometric pressure; Δz — deviation of the bellows height from the equilibrium position

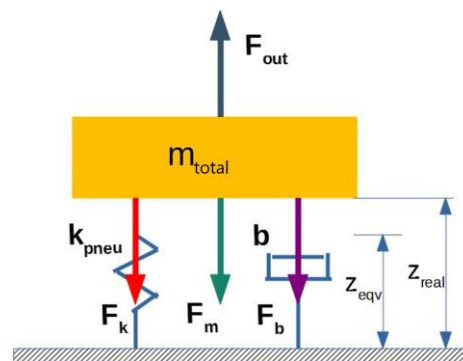


Fig. 2 Pneumatic bellows force analysis [4]

$$0 = F_m + F_b + F_k - F_{OUT} \quad (1)$$

F_m — force from gravitational and inertial effects; F_b — damping force; F_k — force from the stiffness of the spring; F_{OUT} — external loading force

$$F_g = m_{total} \cdot g \quad (2)$$

$$F_a = m_{total} \cdot a_z \quad (3)$$

$$F_m = F_g + F_a \quad (4)$$

g – gravitational acceleration; a_z – acceleration of the pneumatic bellows in the direction of the bellows axis; m_{total} – the total weight of the mass that the pneumatic bellows must lift, F_g – gravity from the mass that the pneumatic bellows must lift

$$m_{total} = m_{bellows/2} + m_{mass} \quad (5)$$

m_{mass} – the mass of the superstructure and other objects which the bellows must lift;
 $m_{bellows/2}$ – weight of the bellows divided by two

Force from spring stiffness F_k is equal to the pneumatic stiffness of the bellows F_{kpneu} , which is dependent on the stiffness of the bellows material $F_{krubber}$, as is shown in equation (6). The dependence of F_{kpneu} from $F_{krubber}$ result from F_{kpneu} being dependent on the equilibrium height z_{eqv} , which is dependent on the stiffness force of the material $F_{krubber}$, as is shown in equation (7). The equilibrium length of the pneumatic bellows was measured experimentally and is visualised in figure 3.

$$F_k = F_{kpneu}(F_{krubber}) \quad (6)$$

F_{kpneu} – pneumatic stiffness of the bellows; $F_{krubber}$ – force from the stiffness of the bellows material

$$F_{kpneu} = k_{pneu} \cdot (z_{eqv}(F_{krubber}) - z_{real}) \quad (7)$$

z_{eqv} – equilibrium height of the bellows; z_{real} – real length of the bellows; k_{pneu} – pneumatic stiffness of the pneumatic spring

To calculate the force from the pneumatic stiffness of the bellows, it is necessary to have the stiffness of the pneumatic spring. In the following part, the relation for the calculation of this quantity will be derived.

$$P_0 = P_A + P_B \quad (8)$$

$$F_B = P_B \cdot A = (P_0 - P_A) \cdot A \quad (9)$$

$$k_{pneu} = \frac{dF}{dz} = \frac{d(P_B \cdot A)}{dz} = P_B \cdot \frac{dA}{dz} + A \cdot \frac{dP_0}{dz} \quad (10)$$

When the pressure in the bellows changes and then subsequently the volume of air in the bellows changes, it is a polytropic event, so we can write:

$$P_0 \cdot V^2 = \text{constant} \quad (11)$$

Derivating equation (11) we get:

$$\frac{d(P_0 \cdot V^2)}{dz} = P_0 \cdot V^{n-1} \cdot \frac{dV}{dz} + V \cdot n \frac{dP_0}{dz} = 0 \quad (12)$$

After rearrangement:

$$\frac{dP_0}{dz} = \frac{P_0 \cdot n \cdot A}{V} \quad (13)$$

Inserting equation (13) into (10) and rearrangement we receive :

$$k_{pneu} = \frac{P_0 \cdot n \cdot A^2}{V} + P_B \cdot \frac{dA}{dz} \quad (14)$$

P_0 – absolute pressure inside the bellows; P_A – atmospheric pressure; P_B – manometric pressure at the inlet in to the bellows; n – polytropic constant; A – active surface of the bellows; V – volume of air inside the bellows; z – bellows length

$$F_b = b \cdot v_z \quad (15)$$

b – damping constant; v_z – speed of bellows extension

3. Identification of missing parameters

To create a bellows computational model, it is necessary to identify all relevant parameters. The measured parameters will be for the Dunlop 2 ¾ pneumatic bellows.

To create a model of pneumatic stiffness of a pneumatic spring, we need the active surface on which the pressure acts, the total air volume in the bellows, the polytropic constant describing this process and the equilibrium height of the cylinder at certain inlet pressures. The polytropic constant for this event is $n = 1$.

The active surface of the cylinder is obtained from the calculation by measuring the active radius of the cylinder. The active radius of the cylinder is $R_{act} = 0.0359$ m. It follows that the effective surface of the pneumatic bellows is $A = 0.004$ m². The active surface does not change as the bellows deforms. The volume of air in the bellows changes as the bellows deforms.

For the correct creation of the bellows model, it is necessary to determine the volume of air in the bellows, which is represented by equation (16). Due to the more complex geometry of the bellows, especially in its deformed state, a simplified model of the bellows was adopted. The grooves of the bellows are replaced by rings with a forming cross-section in the shape of an isosceles triangle. The volume is represented by equation (17). A more precise method of determining the volume is described in [5].

$$V = V_{cyl} + n_{nvr} \cdot V_{ring} + 2 \cdot V_{plug} + V_{hose} \quad (16)$$

$$V_{ring} = z_{base} \cdot \pi \cdot (R_{max} - R_{min}) \cdot \left[\frac{(R_{max} - R_{min})}{3} + R_{min} \right] \quad (17)$$

$$V_{plug} = z_{plug} \cdot \pi \cdot R_{plug}^2 \quad (18)$$

$$V_{hose} = L_{length} \cdot \pi \cdot R_{hose}^2 \quad (19)$$

$$z_{bellows} = z_{0bellows} + \Delta z \quad (20)$$

$$z_{base} = (z - z_{re} \cdot n_{nvr}) / n_{nvr} \quad (21)$$

$$V_{cyl} = z_{plug} \cdot \pi \cdot R_{min}^2 \quad (22)$$

$z_{bellows}$ – equilibrium height of the bellows at non-zero manometric pressure; $z_{0bellows}$ – equilibrium height of the bellows at zero manometric pressure; Δz – deviation from equilibrium height; z_{re} – height of one reinforcement hoop; n_{nvr} – number of bellows toroid parts; z_{base} – height of the bellows base; R_{min} – radius of the inner cylindrical part of the bellows; R_{max} – radius of the outer cylindrical part of the bellows; R_{plug} – radius of the inner plug cavity;

R_{hose} – inner radius of the hose; L_{length} – hose length; V_{cyl} – volume of the cylindrical part of the bellows; V_{ring} – volume of one toroid part; V_{plug} – volume of air in the plug; V_{hose} – volume of air in the hose between the bellows and the pressure regulator; V – total amount of air influencing the stroke of the bellows

An important parameter for the correct definition of the behavior of a pneumatic bellows is the equilibrium length of the bellows. This parameter was identified by measuring the height of the unloaded cylinder oriented so that the direction of extension is collinear and opposite to the direction of gravitational forces. The overall change of the equilibrium position of the extension was later linearly interpolated via the measured points (Fig. 3).

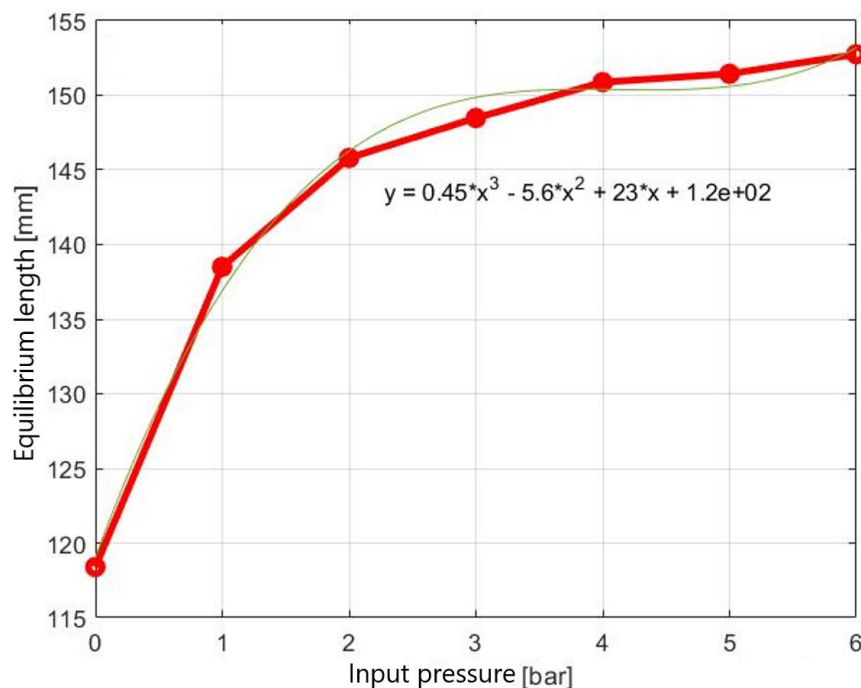


Fig. 3 Dependence of the equilibrium position of the bellows on the input manometric pressure

It can be seen from the measured values that the value of the equilibrium height increases nonlinearly with increasing inlet pressure. Since the measured dependence within the measured range can be interpolated by a continuous function and no unpredictable bellows behavior was observed during the experiment, it is possible to create a simple model of the pneumatic bellows equilibrium height using the measured data.

4. Comparison between the outputs of the simulation model and the experiment

The pneumatic bellows simulation model was created in the Matlab / Simulink program. A comparison between the simulation model and the real behavior of the pneumatic bellows was performed for inlet internal manometric pressures of 1, 2, 3, 4, 5 and 6 bar. For each of these pressures, weights weighing 1, 2, 3, 4, 5, 6, 7 kg were gradually hung on the suspended bellows, and then the total length of the bellows was measured. The initial elongation value of 118.39 mm at a pressure of 0 bar is different from the nominal bellows size of 115 mm, due to the fact that

the bellows in this experiment was suspended and thus subjected to its own weight. A comparison of the simulation and experiment results is shown in Fig. 4 to Fig. 6.

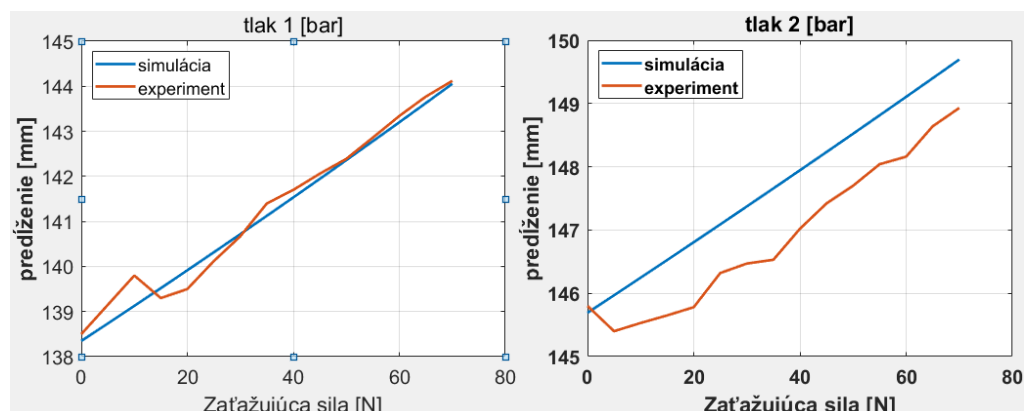


Fig. 1 Experiment vs. simulation at pressure 1 bar (left) and 2 bar (right)

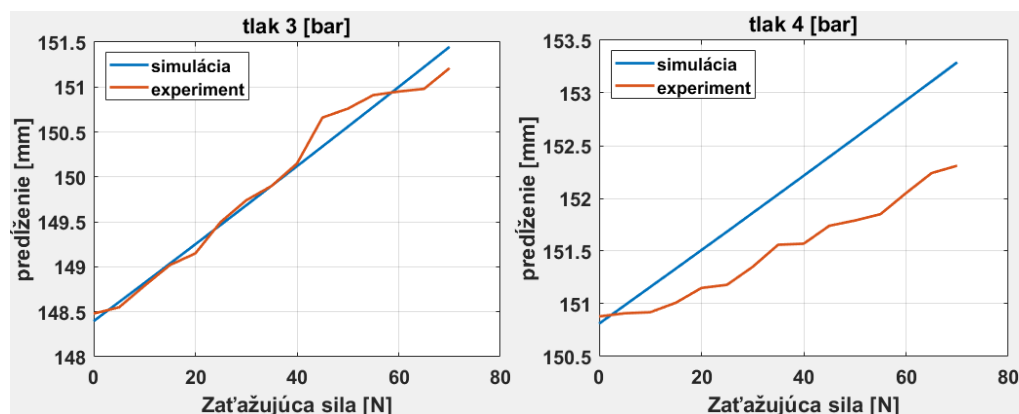


Fig. 5 Experiment vs. simulation at pressure 3 bar (left) and 4 bar (right)

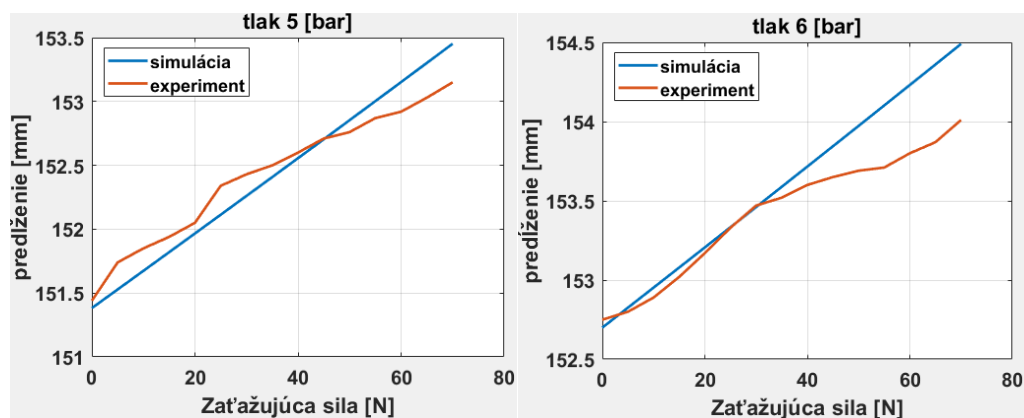


Fig. 6 Experiment vs. simulation at pressure 5 bar (left) and 6 bar (right)

Conclusion

The attached graphs (Fig. 4 to Fig. 6) show that the given model of pneumatic bellows gives satisfactory results for steady state. The maximum deviation of the simulation from the measurements does not exceed 1.2 mm for all pressures, except for the inlet manometric pressure of 0 bar. At this pressure, the deviation at loads above 30 N exceeds 1 mm. From these values, it can be concluded that an error occurred during this measurement, or the behavior of the bellows at a pressure of 0 bar is influenced by influences that are negligible at other pressures. It can be assumed that the deviations between the simulation and the measurement come from errors made during the measurement or from phenomena that the relatively simple bellows model does not capture.

Acknowledgment

The authors would like to thank Slovak grant agency- project VEGA 1/0389/18, KEGA 030TUK-4/2020 a VEGA 1/0201/21.

References

1. Andrikopoulos, G.; Nikolopoulos, G.; Mamesis S. (2011). A Survey on Pneumatic Muscle Actuators Modeling 2011 IEEE International Symposium on Industrial Electronics, 2011, pp. 1263-1269, doi: 10.1109/ISIE.2011.5984340
2. Sudani, D.; Deng, M.; Wakimoto, S. (2018). Modelling and Operator-Based Nonlinear Control for a Miniature Pneumatic Bending Rubber Actuator Considering Bellows Actuators, 2018, 7(2), 26; <https://doi.org/10.3390/act7020026>
3. Zeng, X.; Zhang, L.; Yu, Y.; Shi, M.; Zhou, J. (2016). The Stiffness and Damping Characteristics of a Dual-Chamber Air Spring Device Applied to Motion Suppression of Marine Structures; Appl. Sci. 2016, 6, 74;doi:10.3390/app6030074
4. Zhou, Q. ; Yuan, P.; Tudor, T.; et. al. (2019). Method for Determining Accurate Initial Air Pressure Range of Air Suspension Airbag Based on Vehicle Ride Comfort IOP Conf. Series: Materials Science and Engineering 538 (2019) 012068, IOP Publishing, doi:10.1088/1757-899X/538/1/012068
5. Melo, F.; Pereira, A.; Morais, A. 2018. The Simulation of an Automotive Air Spring Suspension Using a Pseudo-Dynamic Procedure Appl. Sci. 2018, 8, 1049; doi:10.3390/app8071049

Environmental impact of the automotive industry

Matúš Lavčák ^{1*}, Marieta Šoltésová ² and Michal Puškár ³,

¹ Faculty of Mechanical Engineering, TU Košice, Letná 9, 040 01 Košice, Slovak Republic; matus.lavcak@tuke.sk

² Faculty of Mining, Ecology, Process Control and Geotechnology, TU Košice, Park Komenského 19, 040 01 Košice, Slovakia; marieta.soltesova@tuke.sk

³ Faculty of Mechanical Engineering, TU Košice, Letná 9, 040 01 Košice, Slovak Republic; michal.puskar@tuke.sk

* Correspondence matus.lavcak@tuke.sk; Tel.: 0944 344 186;

Abstract: Due to the unfavorable climate situation, which results mainly from excessive emissions, world organizations and powers are trying to ensure such changes that will eliminate or at least reduce emissions in all industries. The European Parliament is also taking major steps, creating legislative steps that will reduce emissions by 60% by 2030 compared to 1990. These steps, or restrictions, will affect all industries, including the automotive industry, which is the most comprehensive producer. pollution worldwide at all. The solution could be research into alternative fuels as well as the implementation of new knowledge in engine design.

Keywords: HCCI engine, automotive industry, pollution, emissions

1. Introduction

The automotive industry is the largest producer of pollution in Europe as well as worldwide. This pollution results from the actual production of vehicles and their parts, but of course also with the subsequent maintenance and recycling of used vehicles or their partial vehicles. The ever-increasing number of vehicles in the world, despite increasingly stringent rules, is failing in the world's emissions. Thus, it is still true that the effects of the effects of factors in industry are increasing much faster than the environment can deal with them on its own. In view of this, the European Union is adopting stricter laws and rules to prevent a growing trend in emissions. From 2025, the European Union plans to bring in force new standards, starting with EURO 7, which will still limit the production of motor vehicle emissions in the near future.

Table 1 Overview of permitted emissions of vehicles with internal combustion engines

	Gasoline [$g * km^{-1}$]	Diesel [$g * km^{-1}$]
EURO 6	60	80
EURO 7	30	30

Table 1, as we can see, provides an overview of the emission limit values applicable to the still-regulated EURO 6 standard, as well as the maximum emission values for the EURO 7 standard, which is still in the planning stage and therefore cannot be changed at all. tightening of planned emission ceilings. By developing new production processes in industry, but by developing new ways of driving vehicles, it is possible to reduce world emissions.

2. Types of pollution caused by the automotive industry

The automotive industry as a whole affects every sector of the environment. Whether it is a direct or indirect impact, the fact remains that negative interventions cause negative changes affecting the environment.

We can therefore divide these environmental sectors into five subgroups of pollution that more or less affect the fauna and flora occurring in a given area:

- air pollution
- water pollution
- soil contamination
- sound pollution
- light pollution

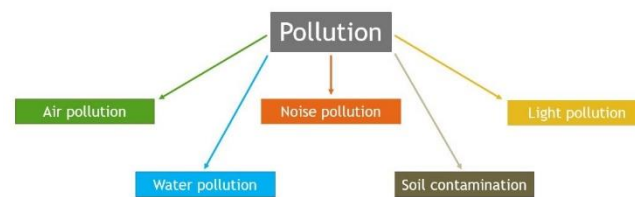


Figure 1. Distribution of pollution from the automotive industry

2.1. Air pollution

We can describe air pollution, or rather, as the presence of substances in the atmosphere, which results in the devastation of living organisms, the climate and the environment as such. We call these substances emissions and they affect the environment either directly or indirectly.

→ **Direct method:**

Inhalation of these toxic emissions by respiration causes serious diseases of the respiratory system, and thus the organisms that directly inhale these toxic substances are the most affected. These substances then settle in the respiratory system.

→ **Indirect method:**

Substances that are unnatural to the environment accumulate in the atmosphere, where they interact with air humidity, but also interact with each other. These chemical processes then produce toxic compounds that deplete the ozone layer, creating ozone holes. Areas that are not protected by the ozone layer are then directly exposed to ultra-violet radiation, which is detrimental to the environment. By limiting the production of emissions, it is gradually possible to renew the layer of the zone in the atmosphere.

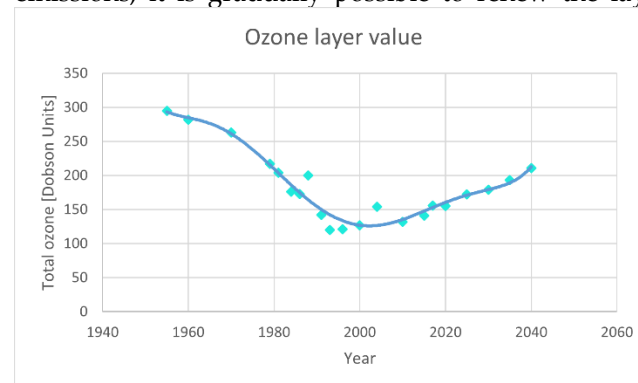


Figure 2 The value of the level of ozone in the atmosphere [11]

Figure 2 is a graph presenting the value of ozone levels in the atmosphere and predicting its growth in the future.

Part of the emissions and their derivatives remain in the atmosphere and deplete the ozone layer. However, some of the emissions react with the humidity and in the form of precipitation, these emissions fall to the ground like acid rain. Figure 3 describes the process of acid rain formation.

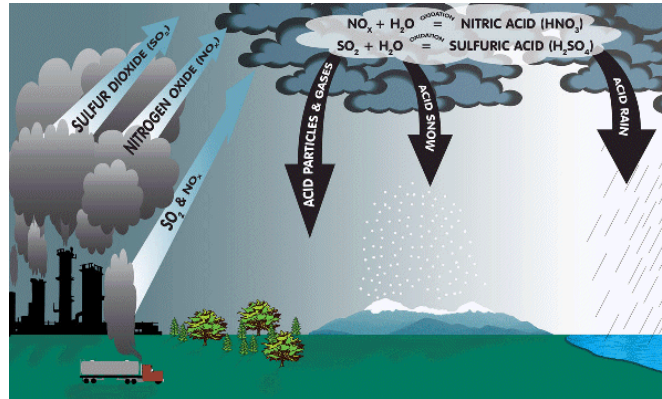


Figure 3 Formation of acid rains [12]

2.2. Water pollution

The automotive industry also has a large impact on water purity. In the manufacture of vehicles and their parts, and in the operation of the vehicles themselves, partial parts of their manufacture enter the water and water bodies. During the operation of cars, various unwanted parts and emissions are released from them, which are carried into water bodies by air flow and rain. Subsequently, they evaporate into the atmosphere, where they enter the soil and crops in the form of rain.

2.3. Soil contamination

Soil pollution or contamination is caused by the direct action of the automotive industry but by indirect action.

→ Direct method:

During the operation and maintenance of the vehicle, toxic substances or parts of the vehicle are released from it, which settle near the roads and enter the soil or remain freely on the surface of the water. In this way, they enter the digestive tract of animals, where they cause health complications.

→ Indirect method:

The indirect way of polluting the soil is that the soil absorbs water and air in which toxic emissions are dispersed. These then fall to the ground in the form of acid rain and are absorbed by the soil.

2.4. Noise pollution

Sound pollution is defined as the long-term effects of unnatural sound on the environment and living organisms. Despite its perceived innocuousness, the automotive industry and the cars themselves are a significant creator of this type of pollution. In humans, long-term exposure to this type of pollution can cause irreversible complications, starting with hearing disorders but also much more serious diseases and disorders of the cardiovascular and nervous systems.

Similarly, there are living organisms for which such pollution is not natural. Many animals use echolocation for spatial orientation and navigation, which is disrupted by excessive sound.

2.5. Light pollution

Light pollution is defined by the presence of man-made light in the night environment. Light pollution is therefore only observable at night. Light pollution is most similar

to sound pollution. As with long-term exposure to excessive sound, long-term exposure to light can cause health complications by disrupting the natural biorhythm of living organisms and humans. Just as sound pollution causes health complications, especially insomnia, which is associated with diseases of the heart and vascular system, but also other serious mental and mental illnesses. Light pollution has a similar effect on living organisms. Behavioral abnormalities and other health complications, but nocturnal dysfunction, have been observed in living organisms.

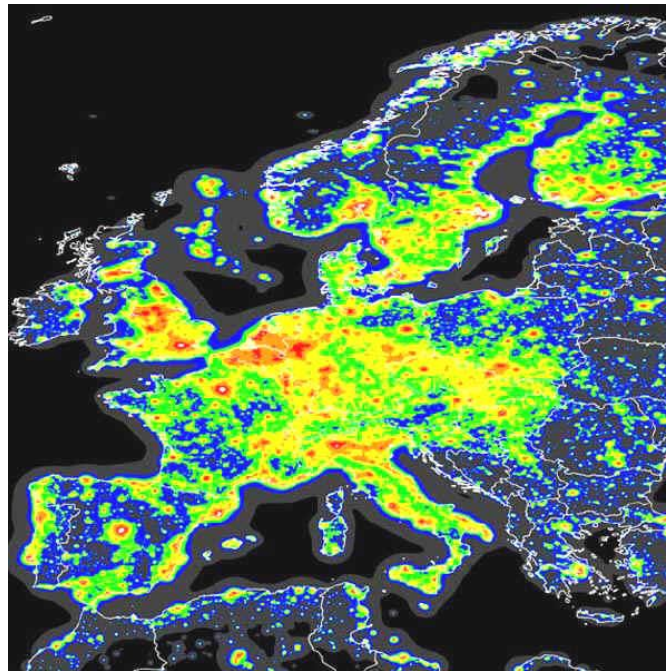


Figure 4 Map of a light pollution of Europe [13]

Figure 6 shows a map of light pollution in Europe. It is clear that metropolitan areas and densely populated areas are more affected by this type of pollution than less populated areas.

3. Solution design

As the situation of increasing environmental pollution caused by the automotive industry continues to worsen, companies developing and producing vehicles are working to address this issue. As mentioned in the introduction to this article, nature has the capacity to cope to some extent with the negative impact of the car industry. As this capacity is limited, efforts must be made to mitigate the impact of the automotive industry, to create rules and restrictions aimed at neutralizing the environmental impact of this segment of the industry.

Another possibility is the search for such design solutions and alternative fuels, or types of drives, which would achieve such a reduction in emissions.

Currently, the development in the automotive industry is largely focused on the electrification of vehicles, ie the replacement of the drive formed by a conventional internal combustion engine with an electric drive, or a combination of combustion and electric drive. Despite the best efforts of developers and also of the European Parliament to sell such vehicles, their share of the road is only 18%. Figure 7 shows the percentage of electric cars sold and the assumption of representation in the future.

Replacing internal combustion vehicles with electric cars is a step forward in reducing emissions, but the fact that 80% of world electricity production still comes from fossil fuels needs to be considered. The percentage distribution of electricity producers is shown

in Figure 8. Thus, the electric car as such does not produce emissions, but the production of electricity still represents a significant producer of greenhouse gas emissions.

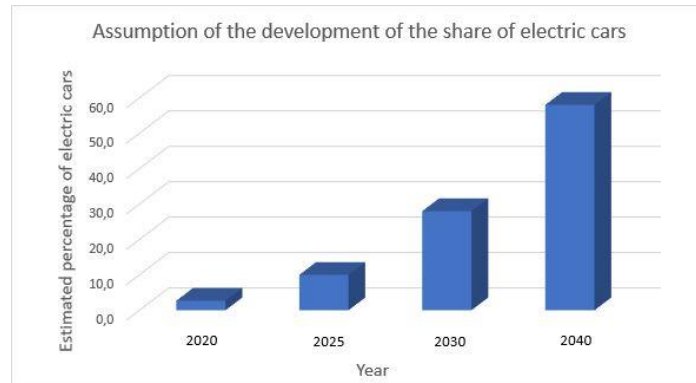


Figure 5 Assumption of the development of the share electric car [14]

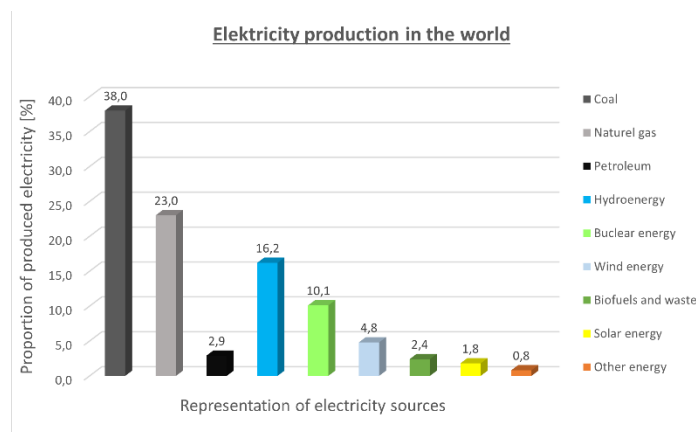


Figure 6 Percentual representation of electricity sources [15]

Another possibility is the research of hydrogen technologies and further development of HCCI and RCCI engines, which offer high performance with low consumption and low emissions. Of course, the positive features of these types of engines are also conditioned by significant shortcomings, and it is therefore necessary to carry out further extensive research.

3.1. Implementation of the solution

Based on the available information from vehicle manufacturers and energy producers, a table was compiled comparing the emissions of electric cars, petrol vehicles, SPCCIs and HCCIs. the values of produced emissions are summarized in Table 2. Due to their generally significantly higher CO₂ emissions, diesel engines have been omitted from the table.

The CO₂ / km emission values were determined using the data of the emission producers and the performance parameters from the vehicle manufacturer according to the relationship:

$$Vc = \frac{D}{Bc}; (1)$$

where Vc = vehicle consumption

D = distance

Bc = battery capacity

The formula was then fitted to the formula for calculating the amount of emissions, and the formula was derived by further modification:

$$Ae = Vc * Se = Vc * \frac{D}{Bc}; (2)$$

where Ae = Amount of emissions
Se = Specific emissions.

By substituting it into the formula, it is therefore possible to determine the value of the emissions produced in the production of the energy needed to charge the vehicle for a 1 km long journey.

The data required for installation were obtained from the energy producer's website and from the catalog sheets of the vehicle type.

$$Ae = 106,7g * kwh^{-1} * \frac{58 kWh}{390 km} = 15,87 g * km^{-1}$$

Table 2 Overview of produced emissions of vehicles with internal combustion engines

Vehicle engine type	Power [kw]	CO ₂ emissions [g * km ⁻¹]
Petrol engine	132	127
Electro engine	132	15,87
HCCI engine	132	52
SPCCI engine	132	96

It is therefore possible to conclude from the table that electric cars are the best choice when it comes to emissions. Nevertheless, the fact remains that the production and subsequent disposal of used batteries places a significant burden on the environment and creates irreversible changes. Therefore, it is ideal to research HCCI and SPCCI technology.

4. Conclusion

The findings show that further research and development in the field of less environmentally demanding vehicles is succeeding in slowing down the growing trend of emissions, which is slowly alleviating the beginning of the global climate crisis. Partial or complete replacement of internal combustion vehicles with electric cars can still help to improve the climate issue. However, other promising options in the field of alternative fuels should not be forgotten. Also, innovative design solutions and research and implementation of new technologies can help gradually reduce emissions.

Acknowledgments: This work was supported by the Slovak Research and Development Agency under the Contract no. APVV-19-0328. The article was written in the framework of Grant Projects: VEGA 1/0318/21 "Research and development of innovations for more efficient utilization of renewable energy sources and for reduction of the carbon footprint of vehicles" and KEGA 006TUKE-4/2020 "Implementation of Knowledge from Research Focused on Reduction of Motor Vehicle Emissions into the Educational Process."

Conflicts of Interest: The authors declare no conflict of interest.

References

1. HOU, J.; QIAO, X.; WANG, Z.; LIU, W.; HUANG Z.: Characterization of knocking combustion in HCCI DME engine using wavelet packet transform. *Appl Energy* 2010, 87: 1239–1246; Volume 3, pp. 154–196.
2. JUANG L.-H.: Finite element modelling for a piezoelectric ultrasonic system, *Measurement* 2010, 43 (10): 1387–1397.
3. PUŠKÁR, M.; BIGOŠ, P.: Output Performance Increase of Two-stroke Combustion Engine with Detonation Combustion Optimization, *Strojárstvo* 2010: Vol. 52, no. 5 (2010), p. 577–587, ISSN 0562-1887

4. PUŠKÁR, M.; BIGOŠ, P.; PUŠKÁROVÁ, P.: Accurate measurements of output characteristics and detonations of motorbike high-speed racing engine and their optimization at actual atmospheric conditions and combusted mixture composition, *Measurement* 2012, Vol. 45, no. 5 (2012), p. 1067–1076, ISSN 0263-2241
5. TOMAN, R., POLÓNI, M., CHRÍBIK, A.; Preliminary study on combustion and overall parameters of syngas fuel mixtures for spark ignition combustion engine. In *Acta Polytechnica*. Vol. 57, no. 1 (2017),
6. CHRÍBIK, A., POLÓNI, M., LACH, J., RAGAN, B. The effect of adding hydrogen on the performance and the cyclic variability of a spark ignition engine powered by natural gas. In *Acta Polytechnica*. Vol. 54, No. 1 (2014), s. 10-14. ISSN 1210-2709.
7. Nedeliaková, E., Babin, M., Barta, D., 2011. Rationalization of static transport [Racionalizácia statickej dopravy], *Transport and the environment* (Vol. 2), proceedings of the 9th SoNorA University Think Tank Conference (Bologna). 19th of October 2011, s. 15-33, ISSN 1868-8411.
8. Czech P. Diagnosis of Industrial Gearboxes Condition By Vibration and Time-Frequency, Scale-Frequency, Frequency-Frequency Analysis. *METALURGIJA*. Volume: 51, Issue: 4, 2012, Pages: 521-524.
9. D.E. Newby, P.M. Mannucci, G.S. Tell, et al.; Expert position paper on air pollution and cardiovascular disease,, *Eur Heart J*, 36 (2015), pp. 83-93
10. Steven, A.;; A Low-pollution engine solution. *Scientific American* 2001, Vol. 284, No.6: 90–95.
11. Simon Chabrillat, Simon Chabrillat Belgian Institute for Space Aeronomy: Report on 2014 Antarctic ozone hole studies [online], Belgicko, 9.3. 2015, https://www.researchgate.net/publication/285581201_Report_on_2014_Antarctic_ozone_hole_studies, DOI:10.13140/RG.2.1.4397.1922
12. Nand Lai, Chhatrapati Shahu Ji Maharaj University: Effect of Simulated Acid Rain on Sunflower Plant [online], Kanpur, India: LAP LAMBERT Academic Publishing GmbH & Co. KG: 9/2016. https://www.researchgate.net/publication/309703789_Effect_of_Simulated_Acid_Rain_on_Sunflower_Plant, ISBN: 978-3659955013
13. P. Cinzano, Department of astronomy, University of Padov, Italy, F. Falchi, Institute of science, technology, Thiene, Italy, C. D. Elvidge, Office of the Director, NOAA National Geophysical Data Center, USA: The first World Atlas of the artificial night sky brightness [online]. Italy, 27.7. 2001. <http://www.inquinamentoluminoso.it/worldatlas/pages/>
14. Eco Auto team: Electric car sales in the EU. [online]. Detva, Slovakia: 13.3. 2018. <https://www.ecoauto.sk/post/predaj-elektroaut-v-eu>.
15. Wikimedia Commons, the free media repository: Renewable energy source: [online]. 2018. https://sk.wikipedia.org/wiki/Obnovite%C4%BEn%C3%BD_zdroj_energie



Soft Actor-Critic in robotic arm position control within ROS

Tomáš Merva^{1,*}, Ivan Virgala¹ and Peter Girovský²

¹ Department of industrial automation and mechatronics, Technical university of Košice, Slovakia

² Department of electrical engineering and mechatronics, Technical university of Košice, Slovakia

* Correspondence: tomas.merva@tuke.sk;

Abstract: Limited applications of robots in the real world are caused by the stochasticity and randomness of environments, which makes it very difficult to hard-code a robot's movement. The aim of this paper is to implement reinforcement learning algorithms within robotics in order to create a reliable policy that would be robust against the dynamics of environments. The approach uses the Soft Actor-Critic algorithm extended with the Hindsight Experience Replay algorithm, which can deal with the problem of sparse rewards, to function as a motion planner for a robotic arm. The combination of the algorithms is tested on a custom open-source robotic environment created with the ROS platform. The results show that the combination of SAC and HER solves a robotic task that cannot be solved by SAC itself.

Keywords: actor-critic policy, reinforcement learning, robotics, ROS

1. Introduction

Nowadays, robots are an integral part of society, although the vast majority of robotic applications consist of simple repetitive tasks in structured deterministic factory environments. In the case of implementing robots to complex tasks, such as DARPA Robotics Challenge 2015 [1], the challenge is designing a robotic control pipeline for autonomous operation. At every stage of the pipeline, some kind of mistake can be made, which results in accumulating the error as it goes through other stages and the robot will not do anything useful. As a consequence, the whole decision process has to be slowed down in order to avoid that assumptions within each stage are not violated too much. [2]

On the other hand, reinforcement learning policies offer a different approach on how to design hard-to-engineer behaviours. The main idea behind reinforcement learning is that it enables an agent, in our case a robot, to autonomously discover an optimal behaviour through trial-and-error interactions with its environment. Instead of providing a detailed solution to a problem by a supervisor, the agent learns through feedback in terms of a numerical value, reward, that measures the one-step performance of the agent. The agent aims to maximize this reward over time. [3] In recent years the reinforcement learning has been famously used to overcome world champions in strategy games such as Go [4] and Dota [5]. However, using reinforcement learning within robotics is substantially more challenging than well-studied discrete benchmark problems. Tasks in robotics are mostly represented with high-dimensional, continuous states and actions. The observation of the true state is most of the time incomplete and consists of a lot of noise. As a consequence, a robot is not able to know exactly in which state it is. Another issue is that many completely different states seem similar, which results in robot's unreasonable actions. Besides the aforementioned problems, there are many other challenges such as sparse rewards, model errors, sample inefficiency, or an appropriate learning method. [3]

The recent progress in the field of the model-free deep RL algorithms for continuous state and action space is the off-policy algorithm Soft Actor-Critic (SAC) [6], which presents sample-efficiency and stability at the same time. This algorithm has successfully solved robotic tasks such as rotating a valve or stacking Lego blocks. [7][8]. One of the

challenges of robotic tasks is using sparse rewards as an agent's feedback since it is much easier to use than designing a complex dense reward function. Therefore, in order to create a more robust algorithm, we decided to test the SAC algorithm extended with the Hindsight Experience Replay (HER) algorithm [9], which is capable to solve the problem with sparse rewards. The contribution of this paper is twofold:

- 1) We extended the model-free off-policy SAC algorithm with HER to solve the MuJoCo benchmark robotic environments [10] with sparse rewards.
- 2) We have created the open-source environment using the ROS framework that can be used as a platform for future research.

2. Preliminaries

2.1. Notation

In reinforcement learning the agent and environment, comprising everything outside of the agent, interact at discrete time steps $t = 0, 1, 2, \dots$. At each time step t , the agent gets some representation of state s_t , which belongs to the state space S , and according to the state the agent selects an action a_t , which belongs to the actions space A . As a consequence of its action, the agent receives a numerical reward r_{t+1} , which is computed and finds itself in a new state s_{t+1} . [11] The process of this interaction is shown in Fig. 1.

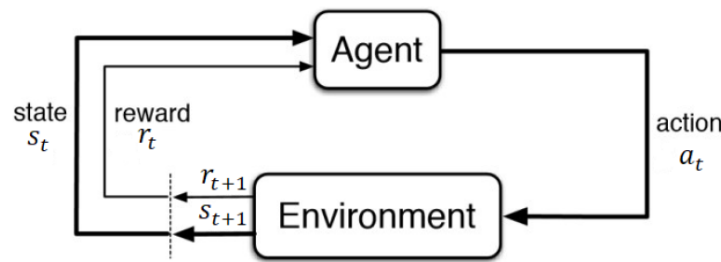


Figure 1. Scheme of RL agent-environment interaction [11]

The core of a reinforcement learning agent that defines the agent's way of behaving at a given time is called a policy denoted as π . A policy π is essentially a map from a state to an action. A reinforcement learning algorithm is used for teaching a policy in a way that it guides changes of the policy's parameters in order to maximize a reward:

$$\pi^* = \operatorname{argmax}_{\pi} J(\pi) = \operatorname{argmax}_{\pi} \sum_{t=0} E[r(s_t|a_t)] \quad (1)$$

where $J(\pi)$ represents the expected sum of the rewards. In this paper, we deal with stochastic policies, especially diagonal Gaussian policies, that outputs a probability distribution over actions [12].

2.2. Soft Actor-Critic

The SAC algorithm is a state-of-the-art off-policy algorithm for the continuous control domain based on maximum entropy reinforcement learning. Maximum entropy RL leverages the entropy from the information theory. The entropy says how unpredictable the probability distribution p is or how random a random variable is. The easiest example of what entropy represents is tossing a coin. There is a 50/50 chance of either outcome, so it has high entropy. If the coin is biased so that it always comes up the head, then entropy is low. Maximum entropy RL extends the standard goal of an agent (Eq. 1) with the expected entropy of the policy as follows: [6][12]

$$J(\pi) = \sum_{t=0} E[r(s_t, a_t) + \alpha \cdot H(\pi(\cdot | s_t))], \quad (2)$$

where the parameter α is called the temperature parameter, which determines the stochasticity of the optimal policy. The higher coefficient α supports more exploration of

the environment, whereas in the limit $\alpha \rightarrow 0$ the standard maximum expected return objective is recovered. In order to ensure that the sum of expected returns and entropies is finite, it is common practice to use a discount factor γ . Consequently, the 2nd equation is modified as follows: [6][12]

$$J(\pi) = E \sum_{t=0}^{\infty} \gamma^t [r(s_t, a_t) + \alpha \cdot H(\pi(\cdot | s_t))] \quad (3)$$

This form of the objective function has three main advantages. The first benefit is that the policy is forced to explore widely and unpromising areas are ignored. The second advantage is related to the first one. As the result of improved exploration, the learning speed is improved over methods using the standard objective. The last but not least advantage is that in cases where multiple actions seem to be equally promising, the probability mass of those actions would be equal. [6][12]

2.3. Hindsight Experience Replay

The state space of robotic environments is hard to explore because of its large size. As a consequence, an agent receives the reward $r_t = -1$ almost every timestep, which results that a standard RL algorithm is bound to fail. Despite the problems with sparse rewards, using dense rewards is much more inconvenient due to the need to design the right reward function that is capable of reflecting the task precisely but is also carefully shaped in order to guide the policy optimization. Therefore we decided to use the HER algorithm that can easily solve this issue. The simple idea of HER is that an agent can learn from his mistakes. Even though the agent would not accomplish the desired goal, we can pretend that the achieved state is the desired goal state and therefore the agent can obtain a positive learning signal. Repeating this process will result in successfully accomplishing arbitrary goals as well as the desired goals. The next advantage of HER is that it enables an agent to be flexible in terms of accomplishing different goals in the same environment. In order to want to learn only one specific goal, it is still recommended to learn multiple goals since HER learns faster using multiple goals. [9][10]

3. Implementation

The combination of SAC and HER has been tested using the ROS Melodic framework and KUKA Agilus KR 6 R900 CR. We first introduce the concept of motion control and the custom environment thereafter.

3.1. Basic motion control architecture

To ensure that the position of each joint is correct during the whole trajectory execution, the *ros_control* package and *MoveIt* are used. The *ros_control* package provides real-time robot controllers that take an actual and desired state of a joint and control the output sent to an actuator utilizing a generic control loop feedback mechanism. The *ros_control* package also provides the high-level controller called *Joint Trajectory Controller*. *MoveIt* generates a trajectory, which is a set of waypoints consisting of positions for joints. Consequently, the role of *Joint Trajectory Controller* is to ensure that these waypoints are executed at specific time instants.

With regard to the paper, the agent determines the $[X, Y, Z]$ coordinates of an end-effector together with its constant orientation described by the quaternion $[x, y, z, w]$ and inputs them to the *TRACK-IK* solver thereafter. The solver computes a set of position waypoints in order to achieve the desired $[X, Y, Z, x, y, z, w]$ coordinates and consequently, these waypoints are passed to *Joint Trajectory Controller*. This architecture has been employed because of the reason that it allows to change the trajectory smoothly during its execution without any impact on the quality of the robot's movement.

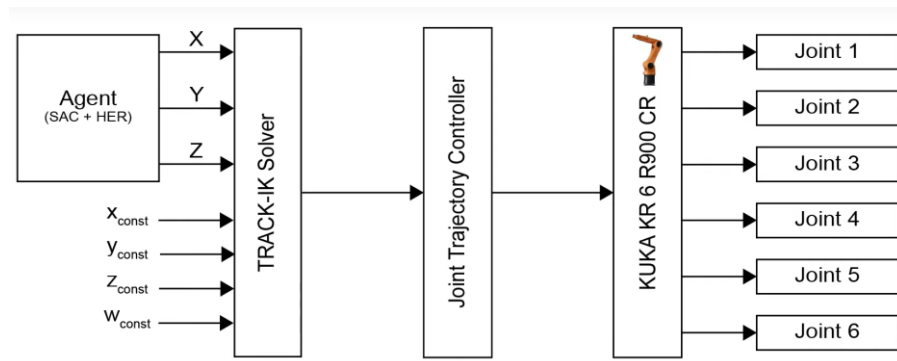


Figure 3. Motion control architecture

3.2. KUKA Push task

For the purpose of testing the SAC + HER combination, the “KUKA Push” task has been created, which involves training the KUKA robot to push a block towards the goal position, which is randomly chosen within the predefined robot workspace.

3.2.1. Reward function

As it was already mentioned in the previous chapters, using dense rewards is not convenient due to difficulties in designing a suitable reward function. As a result, the KUKA Reach environment use the following reward function:

$$R(g_{ach}, g_{des}) = \begin{cases} 0 & \text{if } |g_{ach} - g_{des}| < \varepsilon \\ -1 & \text{otherwise} \end{cases} \quad (4)$$

where g_{ach} denotes the achieved goal, g_{des} is the desired goal and ε represents tolerance. The desired goal is a goal position g_{des} of a block and the achieved goal g_{ach} is an actual position of the block. The tolerance ε is set to 1 cm. The goal position of the block and the initial block position are randomly chosen on the table surface within the robot workspace.

3.2.2. States

The state space within this task is 26-dimensional. The properties of the state represent the following features:

- 1) The pose of the end-effector with respect to the world frame
 - given in 3 positional elements $[X, Y, Z]$
 - given in 4 rotational elements $[x, y, z, w]$ (a quaternion)
- 2) The pose of the block relative to the world frame
 - given in 3 positional elements $[X, Y, Z]$
 - given in 4 rotational elements $[x, y, z, w]$
- 3) The position of the block relative to the end-effector
 - given in 3 positional elements $[X, Y, Z]$
- 4) The linear velocity of the block
 - given in 3 linear velocity elements $[vx, vy, vz]$
- 5) The angular velocity of the block
 - given in 3 angular velocity elements $[wx, wy, wz]$
- 6) The linear velocity of the end-effector
 - given in 3 linear velocity elements $[vx, vy, vz]$

The pose of the end-effector is obtained using *MoveIt* and its linear velocities are computed using the actual and previous position of the end-effector. The object’s pose and velocities are defined by the custom plugin that was created in the Gazebo simulator to publish the properties of the object. The publishing rate is 1000 Hz, whereas the sampling time needed for computing velocities is 40 ms (the sampling rate is 25 Hz). This sampling time is defined by the size of the timestep within RL interactions.

3.2.3. Actions

The policy outputs three continuous actions representing $[X,Y,Z]$ position coordinates. Each action value is from bounded interval $(-1,0;1,0)$. After choosing actions, these action values are converted thereafter into the valid values of the robot workspace.

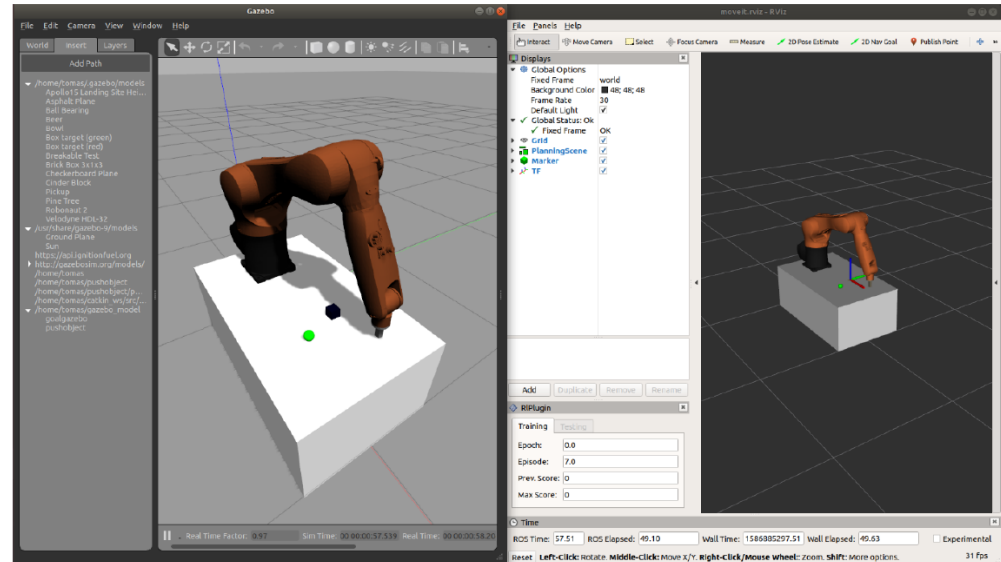


Figure 4. KUKA Push environment

4. Results

The experimental analysis has two objectives. The first aim is to train the robust policy that is capable of solving the KUKA Push task, whereas the second goal is to train it in the shortest time possible. On a system with the 8 core Intel i7-9700K CPU and NVIDIA RTX 2080 Super GPU, training our policy take approximately 7 epochs (approx. 116 minutes or 3 500 episodes). However, to test the stability of the policy we let the training process last for 30 epochs (approx. 8 hours or 15 000 episodes). The learned policy is capable of solving the task with a 100% success rate and it is robust to external forces that can change the object's pose.



Figure 5. Learning performance of SAC+HER in KUKA Push environment

The training process brought many complications. The first issue concerned the shape of the gripper. The cylindrical gripper caused that the object was thrown away from the robot workspace each time the gripper hit some edge of the object. This is the result of using the Gazebo simulator that lacks support regarding the applying contacts between objects. Changing the original cylindrical gripper with the cuboid gripper representing a finger has resolved this issue.

Choosing the right features, which represent the input to the policy, was also problematic and it is necessary to realize what exactly the agent needs to know in order to solve a task. Regarding our work, the velocities of the object and the gripper were crucial conditions for accomplishing the task. The final main problem was to define the robot workspace and initial positions of the object and a goal position. The agent could not learn if the space of initial positions was too large.

5. Conclusions

The aim of this paper was to verify the Soft Actor-Critic and Hindsight Experience Replay algorithms in the custom-created environment within ROS. The simulation results of the KUKA Push task prove that the combination of SAC+HER has state-of-the-art performance within robotic environments. The next logical step should be verifying the agents in the real world. Besides that, the future work could have two options. The first option would be to use this combination for solving more difficult robotic environments using ROS, such as handling compliant food objects or trying to achieve even better performance by using LSTM neural networks. The other option would be to work on new types of algorithms and test them on the environments that have been created within the thesis. The algorithm that seems to be particularly interesting is the Monte Carlo Tree Search algorithm for continuous action and state space. Regarding this paper, we hope that the created open-source environments could enable the ROS community to test different RL algorithms or motivate its members to create other environments.

References

1. DARPA Robotics Challenge. Available online: <https://www.darpa.mil/program/darpa-robotics-challenge> (accessed on 19.11.2021)
2. Levine, S. Deep Robotic Learning. Lecture of RL Seminar, Carnegie Mellon University, 2017
3. Kober, J., Bagnell, J.A., Peters, J. Reinforcement learning in robotics: A survey. 11, s.l.: The International Journal of Robotics Research, 2013, Vol. 32.
4. Silver, D., et al. Mastering the game of Go with deep neural networks and tree search. *Nature*, 2016, 529, 484–489
5. Berner, Ch., et al. Dota 2 with Large Scale Deep Reinforcement Learning. arXiv preprint, 2019. arXiv:1912.06680
6. Haarnoja, T., et al. Soft Actor-Critic: Off-Policy Maximum Entropy Deep Reinforcement Learning with a Stochastic Actor. arXiv preprint, 2018. arXiv:1801.01290.
7. Henderson, P., et al. Deep Reinforcement Learning that Matters. New Orleans: The Thirty-Second AAAI Conference on Artificial Intelligence, 2018.
8. Haarnoja, T., et al. Soft Actor-Critic Algorithms and Applications. arXiv preprint, 2018, arXiv:1812.05905
9. Andrychowicz, M., et al. Hindsight Experience Replay. arXiv preprint, 2017, arXiv:1707.01495
10. Plappert, M., et al. Ingredients for Robotics Research. OpenAI. Available online: <https://openai.com/blog/ingredients-for-robotics-research/> (accessed on 19.11.2021)
11. Sutton, R., Barto, A. G., Reinforcement Learning: An Introduction. The MIT Press, 1998. ISBN 0-262-19398-1.
12. Achiam, J., Abbeel, P., OpenAI Spinning Up., Available online: <https://spinningup.openai.com/en/latest/index.html>. (accessed on 19.11.2021)



Methodology of degradation assessment of polymeric materials

Lukáš Mitřík ^{1*}, Marianna Trebuňová ¹, Alena Findrik Balogová ¹, Marek Schnitzer ¹, Radovan Hudák ¹, Jozef Živčák ¹

¹ Technical University of Košice, Faculty of Mechanical Engineering, Department of Biomedical engineering and Measurement; lukas.mitrik@tuke.sk; marianna.trebunova@tuke.sk; alena.findrik.balogova@tuke.sk; jozef.zivcak@tuke.sk

* Correspondence author: lukas.mitrik@tuke.sk

Abstract: The presented study deals with the definition of biomaterials and the degree of biocompatibility, which is important in the interaction of the organism with a foreign entity. Furthermore, the process of biodegradation of materials to which any material implanted in a living organism is subjected is developed. Since one of the conditions for the introduction of new biomaterials into clinical practice is a series of in vivo and in vitro testing, the authors collective focused on the in vitro method, where a methodology for assessing the biodegradation of polymeric materials was proposed. The choice of polymeric materials was not random, but purposeful due to the increasing use in implantology because of their excellent mechanical properties, easy availability, and cheap manufacturability.

Key words: biodegradation, testing methodology, polymer materials

1. Introduction

An integral part of modern medicine is an intensive connection with the field of implantology. Since ancient times, people have tried to replace damaged tissues or missing parts of the human body with available natural materials such as wood or animal skin. However, over time, synthetic materials began to come to the fore, which were characterized by better mechanical properties, increased functionality, and the ability to better withstand degradation processes. Subsequently, the interest of scientists in the field of regenerative medicine, cell biology, tissue engineering, biomedical engineering, etc., focused on the development of bioresorbable materials, which would support the growth of new living cells and thus initiate increased regeneration of the human body to the point where the damaged tissue or segment in the living organism was completely replaced. As a result of the biodegradation taking place in the human body, the material would decompose into bioabsorbable particles upon termination of its function, thus achieving a state where reoperation of the damaged part would no longer be necessary due to implant failure and thus increase patient comfort itself. However, in order to achieve such bold goals, it is necessary to know to a sufficient extent how biodegradation affects the mechanical-physical-chemical properties of given materials over time. These results can be achieved by a series of tests using the in vitro method, which is also the subject of the research of the present work [1].

2. Biomaterials and their interaction with the human body

According to the author Kulinets, biomaterial can be defined as material that comes into contact with a living organism in order to perform the desired function. Because biomaterials can be created from a wide range of solids, liquids, and gels, the definition itself has changed over the years to demonstrate the current state.

At present, biomaterials can be divided into three basic groups:

- Synthetic materials (metals, polymers, ceramics, composites)

- Natural materials (plant origin, animal origin)
- Polysynthetic or hybrid materials

Because medicine uses biomaterials to treat, augment, or replace organs and tissues, it is essential that the material meets clinical, manufacturing, and economic requirements. In order to achieve the desired result, chemical, physical, biological, and mechanical requirements are considered in the selection of a suitable material. The material must not undergo spontaneous degradation during implantation, must not cause allergic and inflammatory reactions, nor must it be non-radioactive, non-carcinogenic and non-toxic [1]. All of these requirements determine the degree of biocompatibility of the material, which is crucial because, when a tissue is injured, an immediate healing reaction occurs in the body by flooding the damaged area with blood. The soluble fibrinogen contained in the blood converts to fibrin and forms a blood clot that promotes platelet adhesion. Subsequently, monocytes aggregate, which differentiate into macrophages, which absorb foreign microbes and cells, thus cleaning up the site of injury. The blood clot is transformed into vascularized granulation tissue by fibroblasts and endothelial cells, which is gradually replaced by the extracellular matrix (ECM). The degree of ECM remodeling depends on the extent and location of the injury, where the result is either a total regeneration of the tissue structure or the formation of different types of scar tissue. When any material is implanted in an organism, a process called a foreign body reaction occurs in the human body (Figure 1). Immediately after implantation, non-specific adsorption of proteins occurs on the surface of the implant. The paradox is that this phenomenon never occurs during natural physiological wound healing. Due to the excessive adsorption of individual cells, inflammatory processes are triggered at the implantation site, resulting in the formation of multinucleated cells surrounding the implant. The final stage is the complete isolation of the implant by avascular, collagen tissue [2].

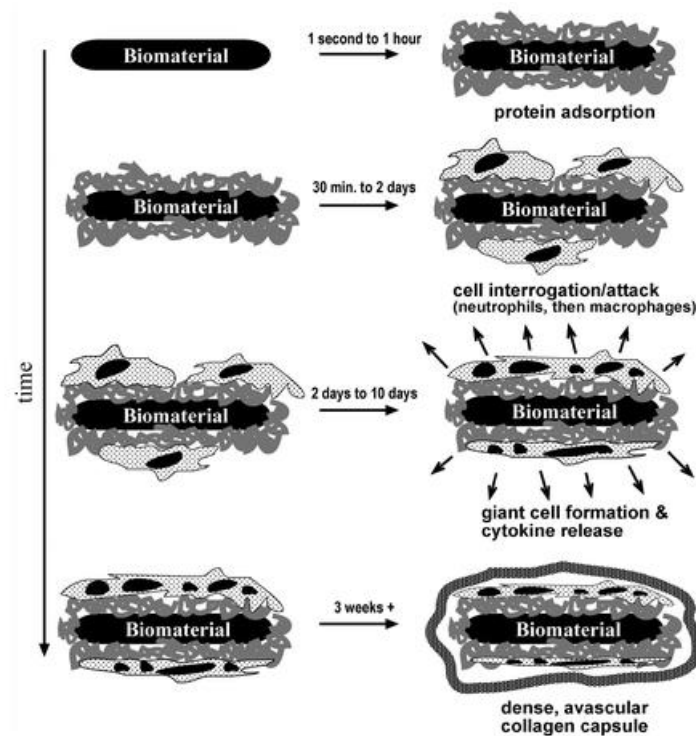


Figure 1. The organism reaction to a foreign entity [2]

3. Degradation of materials and their testing in vivo and in vitro

Degradation can be defined as an irreversible process in which the structure of a given material changes permanently over a period of time. In the case of components implanted in living tissue, this term is called biodegradation. In the process of biodegradation, organic and inorganic substances are decomposed into simpler and more easily degradable compounds with the help of living organisms [3]. Experts in the field of surgery, therapeutic medicine and biomedical engineering are increasingly looking at the process of biodegradation as a targeted phenomenon, which brings with it a wide range of usability. Examples are biomaterials that are implanted in the human body for the gradual release of drugs, in the case of tissue engineering these are porous structures on which living cells are deposited. Such a scaffold provides the body with a suitable environment for the damaged tissue to regenerate to such an extent that the porous structure is no longer needed. Controlled biodegradation by the immune response results in gradual degradation of the scaffold without intoxication of the body [4-6].

3.1 Possibilities of biodegradation

When implementing any material into clinical practice, the material must be subjected to a series of tests, which are performed using two methods, *in vivo* and *in vitro*.

The *in vivo* method is based on the principle of monitoring changes in the implanted material that take place directly in the living organism, for example animal models, in the case of clinical studies humans [7].

The *in vitro* method is performed under laboratory conditions in which the environment of the living organism is simulated in the presence or absence of cellular structures, while the interaction of the material with the solution is monitored. It should be added that in order to obtain the most relevant results, it is necessary to subject the investigated material to both test methods [8].

4. Design of the methodology for biodegradation of polymeric materials *in vitro*

In the presented work, we focused on the evaluation of polymeric materials *in vitro* due to the fact that they are widely used in the field of implantology because they are easily manufactured in various forms and their composition is similar to those found in living organisms.

The design of the *in vitro* methodology was preceded by research of scientific publications in the field of biodegradation of polymeric materials, which is listed in Table 1.

Table 1. Overview of scientific biodegradation studies

Material	Degradation solution	Time of degradation	Authors collective
PCL	PBS solution + lipase	28 days	Neumann et al., 2019 [9]
PHB/HA	Suspended growth medium	30 days	Senatov et al., 2017 [10]
PLA	SBF solution	8 months	Guo et al., 2017 [11]
PLA/PCL	PBS solution	4 weeks	Navarro-Baena et al., 2016 [12]
PLA/BG	PBS solution	6 months	Vergnol et al., 2015 [13]
PLA/PEG	SBF solution	8 weeks	Barbeck et al., 2017 [14]
PLA/BG	SBF solution	600 days	Blaker et al., 2011 [15]
PCL	PBS solution + NaOH	6 weeks	Lam et al., 2008 [16]
PLA/PHB	PBS solution	12 months	Freier et al., 2002 [17]

The first step in evaluating polymeric materials *in vitro* is to select the material to be tested and determine a suitable biodegradation method.

Accelerated in vitro biodegradation, in which the test material is exposed to more demanding conditions, which can be induced by accelerating the flow in a mechanical mixer, by increasing the ambient temperature as well as by changing the pH. The advantage of this method is the delivery of results in a short period of time, which ultimately leads to a reduction in the cost of the testing itself. The disadvantage is the need to verify the relevance of the results by standard non-accelerated testing [18].

Natural biodegradation simulates real processes that take place in the body after implantation of the material. Both of these methods are included in the European standard ISO 10993-13, which specifies values such as pH, ambient temperature, duration of the experiment, etc. [19].

The second step is to select a biodegradation medium that depends on the selected material and its solubility. The difference between the individual solutions lies in their composition, speed of action and in the properties themselves. The following media are used for biodegradation experiments.

The saline solution, which contains 9 grams of NaCl dissolved in 1 liter of water, reaches an almost identical osmolality value with the blood plasma, which has a value of 287 mOsm/kg. For this reason, it is widely used in molecular biology, cell biology and medicine, where it is infused in dehydration or serves as a solvent for various drugs [6].

Phosphate-buffered saline (PBS) can be defined as an aqueous salt solution containing compounds such as potassium dihydrogen phosphate, sodium hydrogen phosphate, sodium chloride or potassium chloride. Due to the correct salt concentrations and stable pH, it is one of the most widely used solutions in the field of biodegradation [13].

Simulated body fluid (SBF), while maintaining physiological temperature and constant pH, is able to reach the osmolality value of blood plasma, similar to physiological solution. It is used to evaluate the bioactivity of the material because it contains a large amount of calcium and phosphate ions, which cause spontaneous growth of bone cells on the surface of the biomaterial. [15]

Hank's solution (HS) consists of inorganic salts that are rich in bicarbonate ions supplemented with glucose. It is used in cell culture media because it maintains a physiological pH of 7-7.4, which is necessary for proper cell growth [6].

The third step is the preparation of test samples. In the case of polymeric materials, based on a review of the scientific literature, it is appropriate to use additive technology, i.e., 3D printing, to produce samples. Based on the prepared samples, the duration of the experiment, the ambient temperature and the required pH values are determined. As it is necessary to ensure constant conditions throughout the biodegradation assessment, regular monitoring of these conditions is necessary to achieve relevant results.

The fourth step is to insert the test samples into the individual solutions. Prior to self-storage, samples must be weighed, and this process repeated at each condition check.

The fifth step is to evaluate the results obtained. Biodegradation can be assessed based on changes in the weight of individual samples. From these data, the absorption of the samples and the weight loss of the samples can then be calculated. The absorption analysis of the samples provides important information regarding the hydrophilic nature of the test material and the weight loss analysis can define the rate of degradation of the samples in each solution. By analyzing pH changes, it is possible to determine which solution showed the most stable pH values during biodegradation. Industrial tomography analysis provides more detailed information regarding changes in sample volume, surface area, and radius compared to a non-degraded sample. The analysis of mechanical stress will make it possible to determine the influence of biodegradation on the mechanical properties of the monitored materials.

5. Conclusion

The presented work dealt with the methodology for the evaluation of biodegradation of polymeric materials using the in vitro method. The design was preceded by an overview of scientific publications listed in Table 1, in which the authors monitored the effect

of biodegradation solutions on individual polymeric materials. The aim of this study was to summarize the available information and create a clear background material that will be used for further research and subsequent publications.

Acknowledgments: This work was created with the support of projects KEGA 023TUKE-4/2020, 01/2020 - 12/2022 Increasing the synergy of methods of teaching biophysics using laboratory equipment and diagnostic devices aimed at measuring physical and technical quantities; Center for Medical Bioadditive Research and Production (CEMBAM), ITMS2014 +: 313011V358, 01/2020 - 06/2023; Center for Advanced Therapies of Chronic Inflammatory Diseases of the Musculoskeletal System (CPT ZOPA) ITMS2014 +: 313011W410, 05/2020 - 06/2023; Open Scientific Community for Modern Interdisciplinary Research in Medicine (OPENMED), ITMS2014 +: 313011V455, 11/2019 - 06/2023.

Conflict of interest: Authors declare no conflict of interest

References

1. Kulinets, I. Biomaterials and their applications in medicine. *Regulatory Affairs for Biomaterials and Medical Devices*, Amato, S. F., Ezzell, R. M. Jr; Woodhead Publishing, 2015, 1–10., doi:10.1533/9780857099204.1
2. Rantner, B.D.; Bryant, S.J. Biomaterials: Where We Have Been and Where We Are Going. *Annual Review of Biomedical Engineering* **2004**, Volume 6, 41 – 75., doi: 10.1146/annurev.bioeng.6.040803.140027
3. Tahri, N., Bahafid, W., Sayel, H., & El Ghachtouli, N. (2013). Biodegradation: Involved Microorganisms and Genetically Engineered Microorganisms. *Biodegradation. Biodegradation: Life of Science*, Chamy, R.; IntechOpen, 2013, 289-320., doi:10.5772/56194
4. Gu, J.-D. Microbiological deterioration and degradation of synthetic polymeric materials: recent research advances. *International Biodeterioration & Biodegradation* **2003**, Volume 52(2), 69–91., doi:10.1016/s0964-8305(02)00177-4
5. Amini, A. R., Wallace, J. S., Nukavarapu, S. P. Short-Term and Long-Term Effects of Orthopedic Biodegradable Implants. *Journal of Long-Term Effects of Medical Implants* **2011**, Volume 21(2), 93–122., doi:10.1615/jlongtermeffmedimplants.v21.i2.10
6. Deroiné, M., César, G., Le Duigou, A., Davies, P., Bruzard, S. Natural Degradation and Biodegradation of Poly(3-Hydroxybutyrate-co-3-Hydroxyvalerate) in Liquid and Solid Marine Environments. *Journal of Polymers and the Environment* **2015**, Volume 23(4), 493–505., doi:10.1007/s10924-015-0736-5
7. Weiler, A., Hoffmann, R. F. G., Stähelin, A. C., Helling, H.-J., Südkamp, N. P. Biodegradable Implants in Sports Medicine: The Biological Base. *Arthroscopy: The Journal of Arthroscopic and Related Surgery* **2000**, Volume 16(3), 305–321., doi:10.1016/s0749-8063(00)90055-0
8. Zhuang, H., Zheng, J. P., Gao, H., De Yao, K. In vitro biodegradation and biocompatibility of gelatin/montmorillonite-chitosan intercalated nanocomposite. *Journal of Materials Science: Materials in Medicine* **2007**, Volume 18(5), 951–957., doi:10.1007/s10856-006-0093-y
9. Umann, R., Neunzehn, J., Hinueber, C., Flath, T., Schulze, F.P., Wiesmann, H.-P. 3D-printed poly-ε-caprolactone-CaCO₃-biocomposite-scaffolds for hard tissue regeneration. *Express Polymer Letters* **2019**, Volume 13(1), 2-17., doi:10.3144/express-polymlett.2019.2
10. Senatov, F., Anisimova, N., Kiselevskiy, M., Kopylov, A., Tcherdyntsev, V., Maksimkin, A. (2017). Polyhydroxybutyrate/Hydroxyapatite Highly Porous Scaffold for Small Bone Defects Replacement in the Nonload-bearing Parts. *Journal of Bionic Engineering* **2017**, Volume 14(4), 648–658., doi:10.1016/s1672-6529(16)60431-6
11. Guo, Z., Yang, C., Zhou, Z., Chen, S., Li, F. Characterization of biodegradable poly(lactic acid) porous scaffolds prepared using selective enzymatic degradation for tissue engineering. *RSC Advances* **2017**, Volume 7(54), 34063–34070., doi:10.1039/c7ra03574h
12. Navarro-Baena, I., Sessini, V., Dominici, F., Torre, L., Kenny, J. M., Peponi, L. Design of biodegradable blends based on PLA and PCL: From morphological, thermal and mechanical studies to shape memory behavior. *Polymer Degradation and Stability* **2016**, Volume 132, 97–108., doi: 10.1016/j.polyimdegradstab.2016.03.037
13. Vergnol, G., Ginsac, N., Rivory, P., Meille, S., Chenal, J.-M., Balvay, S., Chevalier, J., Hartmann, D. J. In vitro and in vivo evaluation of a polylactic acid-bioactive glass composite for bone fixation devices. *Journal of Biomedical Materials Research Part B: Applied Biomaterials* **2015**, Volume 104(1), 180–191., doi:10.1002/jbm.b.33364
14. Barbeck, M., Serra, T., Booms, P., Stojanovic, S., Najman, S., Engel, E., Sader, R., Kirkpatrick, Ch.J., Navarro, M., Ghanaati, S. Analysis of the in vitro degradation and the in vivo tissue response to bi-layered 3D-printed scaffolds combining PLA and biphasic PLA/bioglass components – Guidance of the inflammatory response as basis for osteochondral regeneration. *Bioactive Materials* **2017**, Volume 2(4), 208–223., doi: 10.1016/j.bioactmat.2017.06.001
15. Blaker, J. J., Nazhat, S. N., Maquet, V., Boccacini, A. R. Long-term in vitro degradation of PDLA/Bioglass® bone scaffolds in acellular simulated body fluid. *Acta Biomaterialia* **2011**, Volume 7(2), 829–840., doi: 10.1016/j.actbio.2010.09.013

16. Lam, C. X. F., Savalani, M. M., Teoh, S.-H., Hutmacher, D. W. Dynamics of in vitro polymer degradation of polycaprolactone-based scaffolds: accelerated versus simulated physiological conditions. *Biomedical Materials* **2008**, Volume 3(3), doi:10.1088/1748-6041/3/3/034108
17. Freier, T., Kunze, C., Nischan, C., Kramer, S., Sternberg, K., Saß, M., Hopt, U.T., Schmitz, K.-P. In vitro and in vivo degradation studies for development of a biodegradable patch based on poly(3-hydroxybutyrate). *Biomaterials* **2002**, Volume 23(13), 2649–2657., doi:10.1016/s0142-9612(01)00405-7
18. Pan, R., Crispin, T. A hierarchical modeling approach to accelerated degradation testing data analysis: A case study. *Quality and Reliability Engineering International* **2011**, Volume 27(2), 229–237., doi:10.1002/qre.1100
19. Das, D., Zhang, Z., Winkler, T., Mour, M., Günter, C.I., Morlock, M.M., Machens, H.-G., Schilling, A.F. Bioresorption and degradation of biomaterials. *Advances in Biochemical Engineering/Biotechnology* **2012**, Volume 126, 317–333., doi: 10.1007/10_2011_119

Hardware support for localization technology

Marek Mizerák ^{1*}, Peter Trebuňa ² and Ján Kopec ²

¹ Marek Mizerák1; marek.mizerak@tuke.sk

² Peter Trebuňa2; peter.trebuna@tuke.sk

³ Ján Kopec3; jan.kopec@tuke.sk

* Correspondence: marek.mizerak@tuke.sk, Tel.: + 421 55 602 3232

Abstract: This paper deals with the issue of localization systems in the field of its hardware parts. Currently, this technology is on the rise, thanks to the idea of Industry 4.0. It is the fourth industrial revolution that lays the foundations of the Smart Factory, making the exponential "Internet of Things" function an integral part of this whole. Thanks to localization systems, we can create a digital twin of the production plant and thus create conditions for possible optimizations of not only material but also production flows. The main idea of this article can be considered a description of the hardware part of this technology, where its basic parameters and parts will be described. The hardware will be divided into anchors and tags that form the basis of this technology and bring very remarkable results today.

Keywords: RTLS, system, UWB, technology, hardware

1. Introduction

RTLS stands for Real Time Localization System. As the name suggests, this is a real-time location. In this case, the basic component is the position just mentioned. If we want something, we must know what position and position it is in. If we want to point to something, we need to know the right position. A manufacturing enterprise can implement processes to ensure that certain items are in a predetermined location and thus increase sales.

On the other hand, the company can also ensure the implementation of processes that allow the employee to find materials or tools in a significantly lower time using localization technology. This case also focuses on security. Under this idea it is possible to understand the possible finding of an injured person in large manufacturing companies and thus increased the percentage of survival abroad of the worker.

2. RTLS system

RTLS allows us to monitor the location inside buildings, halls or other enclosed spaces. It can be said that it is actually GPS that works in enclosed spaces, in defined zones that are covered by radio frequencies.

There are two types of RTLS:

- Precision-Based RTLS
- Proximity-Based RTLS

Precision-Based RTLS is implemented via either UWB (ultra-wide band) or Wi-Fi based technologies. Precision-Based RTLS allows you to track things in a perfectly accurate position, which can be used for inventory management. The disadvantage is the high initial cost and requires a large infrastructure to be able to measure with high accuracy. Depending on the technology used, the price of receivers and transmitters may also increase.

Proximity-Based RTLS can accurately determine a location of up to approximately 12m², making it ideal for use when we do not need an exact location. For example, if we know the employee is in room 302, we can easily find him there. These systems are cheaper, do not need such a large infrastructure as Precision-Based and also have relatively cheaper receivers and transmitters.

3. RTLS system by SEWIO Networks

Sewio networks is a manufacturer of RTLS systems for indoor monitoring, which drive business results in warehouses, logistics, the entertainment industry as well as animal husbandry. It provides customers and partners with a precise, reliable, fully scalable and customer-oriented Internet of Things (IoT) solution for internal tracking that enables process visibility, increases production efficiency, simplifies the inventory process and results in an overall better view of production managers. Last but not least, this technology provides an incomparable increase in the safety of not only workers but also production technology and technology.



Figure 1. Logo of SEWIO Networks

This technology works on the principle of UWB technology. This technology is used at the Department of Industrial and Digital Engineering with a valid license for both the hardware and software part of this localization technology.

To determine the position of the object, Sewio RTLS uses several hardware devices that collect UWB signals and transmit them to the server, where the position is determined by a localization mechanism. RTLS technology consists of three main parts: tags, transmitters and software support in the form of RTLS Studio. Transmitters, resp. the anchors are placed in spaces in tactically pre-selected places, preferably in the corners of rooms or walls. Moving tags transmit a relatively short UWB signal at constant intervals, which is received by the anchors.

The anchors send time records from UWB signals via Ethernet or WiFi to the RTLS server, which is then connected to the software part by the already mentioned RTLS Studio. This software then determines the exact location and stores the collected data in a database. The location data is then available through the API. RTLS Studio also allows you to visualize real-time monitoring and analyze stored data.

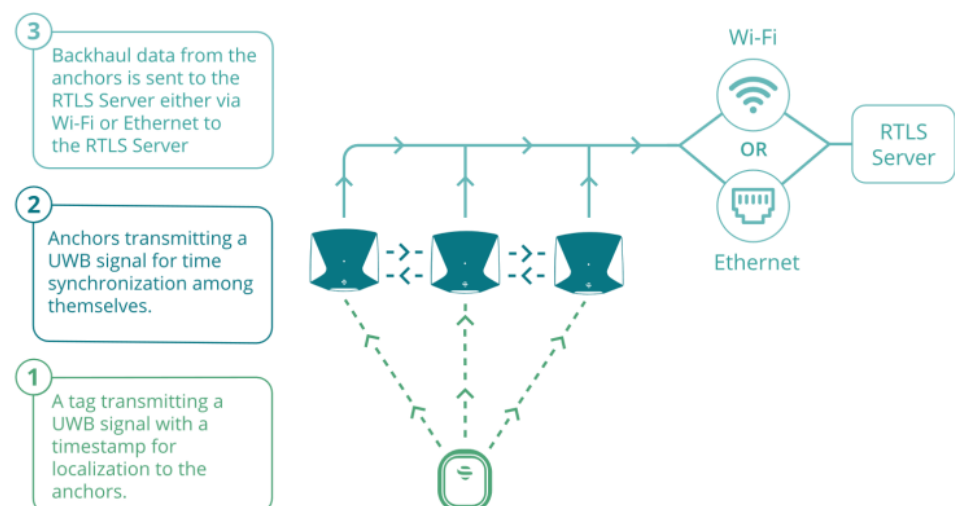


Figure 2. Scheme of operation of UWB RTLS technology

The main advantages of Sewio RTLS localization technology are a high level of system control, high accuracy and easy scalability.



Figure 3. Logo of SEWIO hardware products

4. Basic hardware components

4.1 Anchors

These are static devices that receive UWB signals from tags. The set of transmitters forms the localization infrastructure of the building. RTLS is fully scalable, which allows endless expansion of the covered area by adding additional anchors to the network. The anchor provides great reach and strong consistent coverage. Its uniform radiation model minimizes the possibility of "blind spots" in the placement area. The anchor is ready for use in industry because it uses an active PoE injector with a DC 48V output and a robust housing to meet safety standards. Robust synchronization ensures proven reliability in harsh environmental conditions.

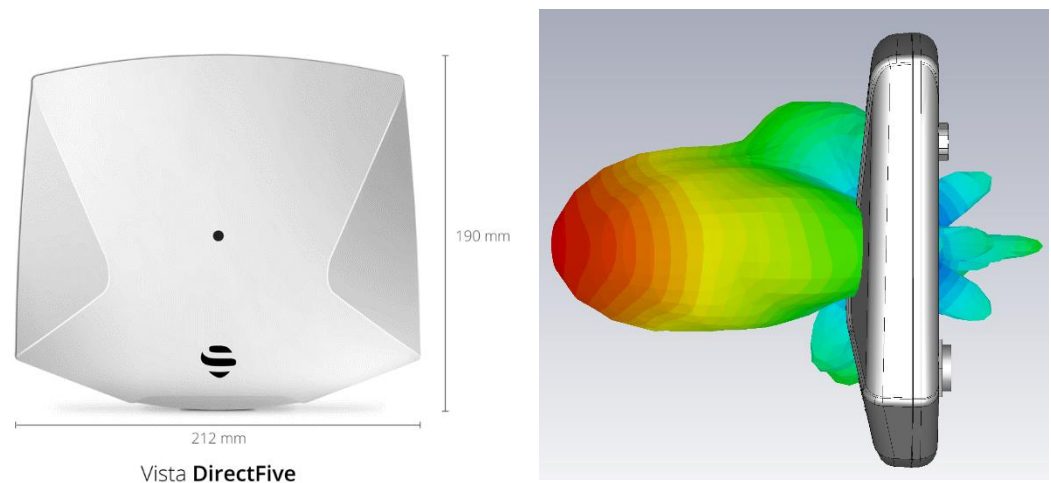


Figure 4. SEWIO anchor Vista DirectFive with Radiation Pattern

Features:

- http configuration and control interface,
- remote configuration using RTLS Manager,
- High number of configuration parameters,
- positioning accuracy up to 30 cm,
- locators from <10 to <1000,
- system from 1 cell consisting of 4 antennas to several cells,
- refresh rate from 100ms to 60s.

Table 1. Technical Parameters - Vista DirectFive

Size	212 x 190 x 36
Weight	390 g
Power Supply	PoE 802.3af or DC 48V (Passive PoE)
Power Requirements	2.5W
Operating Conditions	-20 - 60 °C 20 – 85% humidity
Enclosure	IP65 RJ45 Feed-thru lock connector shall be properly mounted to provide IP65 rating.
Warm-up Time	Immediate
Environment	Industrial Warehouse Manufacturing Retail Sports Tracking Livestock
Placement	Indoor
UWB Antenna	Directional CH5
WiFi 2.4 GHz (optional)	Omnidirectional Antenna
UWB Radiated Power CH5 6.5 GHz	-41.3 dBm/Hz
Approvals	RED/CE FCC

4.2 Tags

In a real-time location system, (RTLS) tags are small electronic devices that are attached to objects that need to be tracked. The tags send out blinks that are received by anchors and forwarded to the location server for calculating the tags' position. RTLS Tags are used for asset tracking, vehicle tracking, material flow analysis and employee location tracking for safety reasons.

As each vertical and use case bring in different tag requirements, Sewio developed three different tags to allow customers to choose the right tag to meet both their needs and budget. The design of the system also enables Sewio partners to further customize the tags.

For midsize organizations to enterprises that are struggling to increase their efficiency, Sewio RTLS tags provide a real-time tracking and identification solution. Unlike traditional indoor tracking technologies, only Sewio provides high accuracy together with a long tag battery life, enabling the tracking of thousands of tags within one area. Sewio offers three types of tags:

- Leonardo Personal: People/employee tracking and identification,
- Leonardo Asset: Object tracking and identification – coin battery powered,
- Leonardo Vehicle: Object tracking and identification with an external power supply.



Figure 5. SEWIO type of tags

5. Conclusions

Today, localization technologies are becoming an integral "collaborator" for executives and managers, who ultimately help them with a general overview of the operation of a manufacturing company. In such cases, it is possible to build on other optimization options, both material and production flows.

Localization systems should always be designed to cover the area with the lowest possible number of receivers (anchors), which keeps the cost of the project itself low. In real cases, the layout of production halls is complex and involves a huge number of corridors and narrow alleys, which requires many receivers and cabling to them, so the cost of the installation itself increases. Thanks to 1D motion tracking using directional antennas, it is possible to achieve the required accuracy with fewer receivers and cabling. 1D is thus a revolutionary step for the indoor localization market, as it significantly reduces project costs and project payback times.

Acknowledgments:

This article was supported by projects VEGA 1/0438/20 Interaction of digital technologies to support software and hardware communication of an advanced production system platform, KEGA 001TUKE-4/2020 Modernization of industrial engineering teaching to develop the skills of the existing training program in a specialized laboratory, APVV- 17-0258 Digital engineering elements application in innovation and optimization of production flows, APVV-19-0418 Intelligent solutions to enhance business innovation capability in the process of transforming them into smart businesses.

References

1. Digitálny podnik. [cit. 25/02/2016]. Available on the Internet: <http://www.priemyselneinzinierstvo.sk/?page_id=1534>. Country, 2007; Volume 3, pp. 154–196.
2. Sewio Networks. Technology comparison. General information Dostupné na internete - <https://www.sewio.net/uwb-technology/rtls-technology-comparison/>
3. Sewio Networks. Uwb. General information Dostupné na internete - <https://www.sewio.net/real-time-location-system-rtls-on-uwb/>
4. EDL, M. - KUDRNA, J.: Metody průmyslového inženýrství. 1. vyd. Plzeň : Smart Motion, s.r.o., 2013, ISBN: 978-80-87539-40-8
5. MALIK, M.: RTLS for Dummies, Eiley Publishing, Hoboken, JJ,, 2009.
6. RIZOS, C., Demplster, B. Indoor positioning techniques based on wireless lan. 2007.
7. SILANICAY M., Lokalizačný systém na sledovanie mobilných objektov – nová stratégia rozvoja podnikov. [online] Dostupné na internete: <https://opac.crzp.sk/?fn=docviewChild0003B032>
8. TREBUŇA, P.: Plánovanie merania v priemyselnom inžinierstve, In: Strojárstvo : strojárstvo extra. Č. 1-2 (2010), s. 74/8-75/9. - ISSN 1335-2938.



Development and characterization of zinc alloys for orthopedic implants

Wanda Miženková^{1,2}, Zuzana Molčanová² Beáta Ballóková² and Karel Saks^{2,*}

¹ Technical University of Košice, Faculty of Mechanical Engineering, Department of Biomedical Engineering and Measurement;

wanda.mizenkova@tuke.sk

² Slovak Academy of Science, Institute of Material Research; molcanova@saske.sk, bballokova@saske.sk,

ksaksl@saske.sk, wmizenkova@saske.sk

*Correspondence: wanda.mizenkova@tuke.sk Tel.: +421949 118 041, Letná 9, Košice

Abstract: In this study, completely new metal alloys were investigated materially and technologically, which are made of bioabsorbable elements Zn, Ca, Mg, that are found in the human body, and to which the body has a natural biocompatibility. In order to improve the mechanical and chemical properties, these alloys were micro-alloyed with Mn. The use of these materials is directed to the field of medicine - for the preparation of intracorporeal implants using several manufacturing technologies, including additive manufacturing with targeted biodegradation in the patient's body. The microhardness of alloys was increased by the method of rapid casting into a cooled mold. With the addition of Mn, the microhardness increased on average by 30% for pre-alloys and by 40% for rapid cooling alloys. The microhardness was increased by an average of 25% by rapid cooling. The highest microhardness value of 130.6 ± 6.0 was measured for the Zn-0.4Mg-0.4Ca-0.8Mn alloy.

Keywords: biocompatibility, zinc alloys, biodegradation

1. Introduction

Conventional non-degradable biomaterials, such as stainless steel (SS), cobalt-chromium (Co-Cr) alloys or titanium (Ti) and its alloys are generally used as permanent or temporary implants. These metallic biomaterials have been extensively used for diverse biomedical applications, including joint replacements, fracture fixation, cardiovascular stents, and remodeling of bone, because of their high mechanical strength and corrosion resistance. [1] However, these materials contain various alloying elements such as aluminum (Al), vanadium (V), chromium (Cr) and nickel (Ni), which adversely affect their biocompatibility for tissue engineering applications. Moreover, the mismatch between the elastic modulus of natural bone (3-30 GPa) and those of these metallic implant materials (190-200 GPa for SS, 210-240 GPa for Co-Cr alloys, and 90-110 GPa for Ti alloys) leads to stress shielding of the surrounding bone that causes bone resorption and subsequent implant loosening. Such implant failures often require additional complex revision surgeries to remove or replace them. For new types of materials containing exclusively all the elements that occur in the human body (biodegradable / bioresorbable, (BM)), the problem of revision surgery is eliminated. BMs can provide the necessary support to host tissues undergoing a regeneration process and they degrade naturally in the physiological environment and dissolve entirely after sufficient tissue healing, while

their by-products can be metabolized by the body as they are usually non-toxic. Even its products of degradation Zn, Ca, Mg ions help in the healing and regeneration of the surrounding damaged soft tissue. [2,3,4] In our research, we consider the development of alloys combining elements: zinc, magnesium, calcium with the addition of micro-alloy manganese, lithium and silver. All the main elements are represented in the human body. The recommended daily allowance for an adult person is 1000 mg Ca [5], 420 mg Mg [6], 10 mg Zn [7] and 2.3 mg Mn [8]. The dominant (matrix) element of our alloys is zinc, which has an important function in bone metabolism. Zinc supplementation stimulates osteoblast bone formation, meanwhile inhibiting osteoclast differentiation, and results in increased bone strength. Recent research also confirms that bioresorbable zinc alloys show significantly better mechanical properties in orthopedic implants, compared to bioresorbable polymers and magnesium alloys with a maximum strength of 350 MPa. [5] Zn exhibits a lower corrosion rate than Mg, because its electrode potential is from -2.37 V to -0.76 V. Mg-based alloys generally degrade rapidly in the body, 2-3 months following implantation and their rapid degradation is associated with evolution of excessive hydrogen gas (H₂) at the interface between surrounding tissue and the implant. However, Zn-based alloys exhibit intermediate degradation rates and their degradation products are fully bioresorbable without evolving excessive H₂ gas. [9,10,11] A summary of some physical and mechanical properties of existing non-biodegradable and biodegradable metallic biomaterials, along with features of natural bone tissues, is given in Table 1. It can be seen that pure Zn shows the lowest ultimate tensile strength σ_{UTS} , tensile yield strength σ_{TYS} and elongation ϵ among all metallic biomaterials. Therefore, the development of zinc alloys with higher σ_{UTS} , σ_{TYS} , and ϵ is one of the main challenges to its suitability as a candidate material for biomedical applications. The mechanical properties of Zn alloys can be enhanced by tailoring their microstructures via alloying and thermodeformation treatment. [1]

Table 1 Comparison of physical and mechanical properties of bone tissues along with existing non-biodegradable and biodegradable metallic materials. [1]

Tissue/Material	ρ (g/cm ³)	σ_{UTS} (MPa)	σ_{TYS} (MPa)	E (GPa)	ϵ (%)
Cortical bone	1.8–2.0	35–283	105–114	5–23	1.07–2.1
Trabecular bone	1.0–1.4	1.5–38	1–12	0.01–1.6	2.20–8.5
316L stainless steel	8.0	450–650	200–300	190	30–40
Co–Cr alloy (ASTM F90)	9.2	860	310	210	20
Ti–6Al–4V (Annealed)	4.4	895–1025	825–869	110–114	6–10
Pure Mg	1.7–2.0	90–190	65–100	41–45	2–10
Pure Fe (99.8%)	7.8	180–210	120–150	211.4	40
Pure Zn (As cast and hot-rolled)	7.14	18–140	10–110	1.2–2.1	0.3–36

2. Development of alloys with required mechanical properties

There were prepared and characterized completely new, unpublished ternary alloys of the Zn-Mg-Ca type, alloyed by a small addition of Mn. From the point of view of mechanical properties, we consider the biggest challenge to increase the plasticity of these alloys above 15% while maintaining the strength > 450 MPa with corrosion resistance.

A very important process influencing the properties of the final products from these alloys is the method of their production. Conventional techniques for the production and processing of alloys, such as the casting of alloys and their thermomechanical processing into final products, have been chosen.

Preparing Zn-0.4Mg-0.4Ca-xMn, (x=0, 0.2, 0.4, 0.6, 0.8, 1.1wt%) - elements Mg, Ca, Mn, stabilize the solid solution and increase the toughness and strength of the alloy. The

alloys will be prepared in the shape of rollers \varnothing 20 mm, length 50 mm, by gravity casting into graphite molds, each weighing about 100 g.

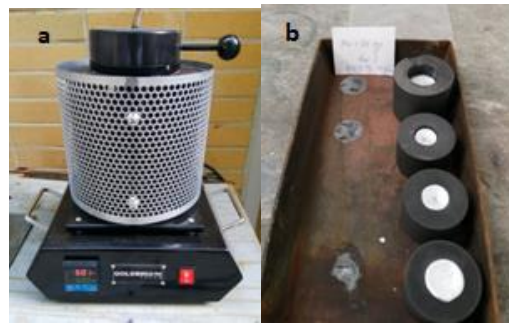


Figure 1 a. melting furnace –Goldbrunn therm, b. cast \varnothing 20 mm and length 50 mm inside the graphite mold

In order to obtain higher strengths, the states of the analyzed alloys will be prepared by processing the castings, which will allow the refinement of the grain of the solid solution. It is method of rapid cooling of the melt in cooled Cu form in the Melt spinner SC device.

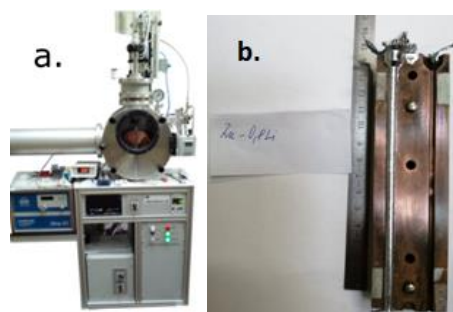


Figure 2 a. equipment - Melt spinner SC, version with the possibility of low pressure die casting of the melt into a cooled Cu mold, b. cast \varnothing 5 mm and length 130 mm inside a copper mold

2.1. Characterization of the prepared samples

The phase composition and structure of the individual states of the analyzed alloys were evaluated by the X-ray diffraction analysis on a Philips X Pert Pro diffractometer. Alloys were measured in the range 2θ 10-140°. The step size was 0.03° and the endurance on the step was 25s. Analysis of the chemical composition of the alloys was performed using SEM (scanning electron microscope) Jeol JSM 700F supplemented by elemental EDX analysis (Energy-Dispersive X-ray analysis) locally at selected points as well as over the area.

With regard to the future use of alloys in applications for intracorporeal bioresorbable implants, specific weight (density) measurements were performed for the analyzed alloy states on the Kern ABT 120-4M analytical scales and microhardness measurements on the Wilsom-Wolper Tukon 1102 microhardness tester with a Wickers indenter using a load of 0.1 kg- HV_{0.1}.

3. Results

3.1 EDX analysis

Table 2 contains information of the real chemical element composition of the produced alloys, which were confirmed by EDX chemical semi-quantitative analysis of the elements present. The actual chemical composition varies from the required to 2wt% for pre-alloys and by 0.1wt% for alloys after rapid cooling.

Table 2 Chemical elemental composition of manufactured alloys

Sample	EDX [wt%] Pre-alloy	EDX [wt%] After rapid cooling
Zn	Zn	Zn
Zn-0,4Mg-0,4Ca	Zn-0,24Mg-0,37Ca	Zn-0,37Mg0,4Ca
Zn-0,4Mg-0,4Ca-0,2Mn	Zn-0,53Mg-0,37Ca-0,2Mn	Zn-0,32Mg0,29Ca-0,24Mn
Zn-0,4Mg-0,4Ca-0,4Mn	Zn-0,45Mg-0,42Ca-0,38Mn	Zn-0,35Mg0,41Ca-0,4Mn
Zn-0,4Mg-0,4Ca-0,6Mn	Zn-0,6Mg-0,48Ca-0,56Mn	Zn-0,42Mg-0,44Ca-0,6Mn
Zn-0,4Mg-0,4Ca-0,8Mn	Zn-0,55Mg-0,43Ca-0,85Mn	Zn-0,36Mg-0,43Ca-0,8Mn
Zn-0,4Mg-0,4Ca-1,1Mn	Zn-0,44Mg-0,38Ca-1,15Mn	Zn-0,30Mg-0,36Ca-1,1Mn

3.2 X-ray diffraction analysis

Using the Ritveld refinement method of the XRD records, the sizes of the lattice parameters a , c for the castings, which were casted under the Ar atmosphere with low pressure by rapid cooling were determined. At the same time, it was determined that these alloys form a supersaturated solid solution. It is clear from Fig. 3 that the lattice parameter c decreases while the parameter a increases. The result is substitution hardening, where Zn is replaced at certain positions in lattice by Mn. These alloys crystallize in a hexagonal lattice with a space group $P 6_3 / m m c$.

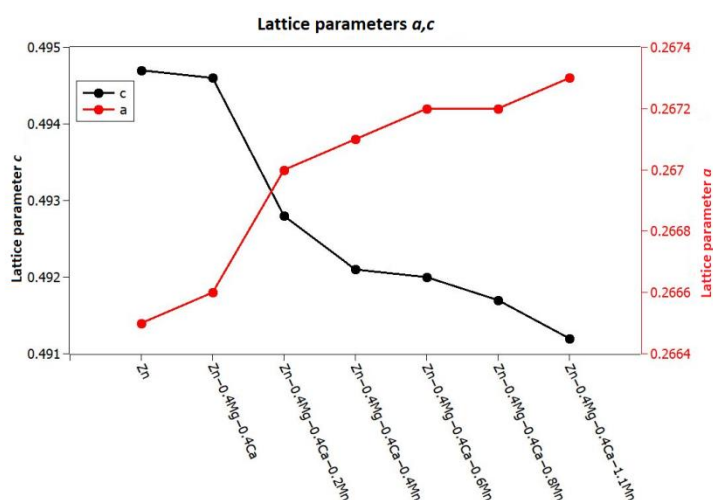


Figure 3 Lattice parameters a , c pure Zn and ternary Zn-based alloys

3.3 Specific weight (density)

The Archimedes method determined the specific weight of the pre-alloys and samples after rapid cooling while comparing the measured data. It can be seen from Fig. 4 that the specific weight increased by rapid cooling of the melt, since a porous structure was present in the pre-alloys prepared by gravity casting. The Mg and Ca elements they lighten Zn and with the addition of Mn the specific gravity increases slightly.

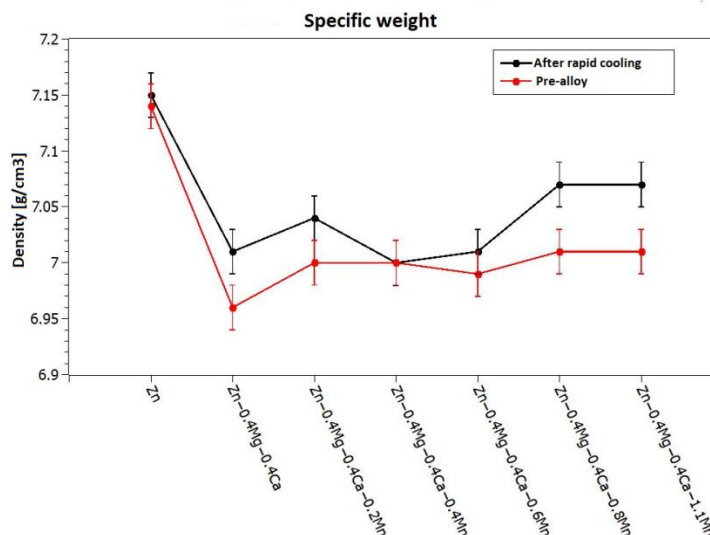


Figure 4 Specific weight of Zn pre-alloys and Zn alloys after rapid cooling

3.4 Microhardness HV_{0.1}

HV_{0.1} microhardness measurements with a 10s endurance were performed on a Wilson-Wolper Tukon 1102. The hardness of the castings, which were processed by low pressure die casting into a cooled mold, increased. This process resulted in grain refinement followed by curing. It is also clear that by adding Mn to Zn alloys we obtain better mechanical properties. The highest microhardness value of 130.6 ± 6.0 was measured for the Zn-0.4Mg-0.4Ca-0.8Mn alloy. With the addition of Mn, the hardness increased on average by 30% for pre-alloys and by 40% for rapid cooling alloys. The hardness was increased by an average of 25% by rapid low pressure die casting and thus grain refinement.

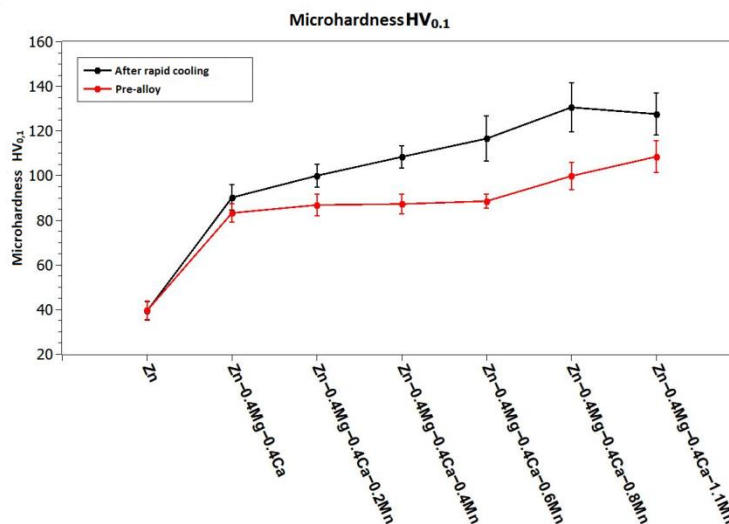


Figure 5 Microhardness HV_{0,1} Zn pre-alloys and Zn alloys after rapid cooling

4. Conclusions

Through the synthesis of information obtained from various types of experiments, new types of metal alloys were introduced, as well as the technology of their processing in the production of the most advanced intracorporeal implants with targeted dissolution in the patient's body. A clear benefit of this research is the design of materials that meet the complex requirements for intracorporeal implants that are used in traumatic injuries. The mechanical properties of the alloys were increased by the method of rapid casting into a cooled mold. To achieve even higher mechanical properties, it is appropriate to use other processes, such as homogenization annealing followed by thermomechanical consolidation. The next step in this research is the design of an additive technology for processing these ternary powder alloys into the shape of an implant. Additive manufacturing of implants from bioresorbable alloys and tailored to the patient will be a significant shift towards orthopedics, with the least invasive effect on the patient.

Acknowledgements

The article was created with the support of projects: Development of new bioresorbable alloys for intracellular implants APVV-20-0068, Development of new biodegradable metal alloys intended for medical applications VEGA2 / 0013/19. Research, development and testing of bioreactor for tissue and organ cultivation after bioadditive production VEGA 1/0179/1.

The achieved results were created within the solution of the project no. 2018/14432: 1-26C0, which is supported by the Ministry of Education, Science, Research and Sports of the Slovak Republic within the provided incentives for research and development from the state budget in accordance with Act No. 185/2009 Coll. on incentives for research and development.

References

- [1] H. Kabir, et al. Recent research and progress of biodegradable zinc alloys and composites for biomedical application: Biomechanical and biocorrosion perspectives. *Bioactive Materials* 6 (2021) 836–879
- [2] A. Tahmasebifar, S.M. Kayhan, Z. Evis, A. Tezcaner, H. Çinici, M. Koç, Mechanical, electrochemical and biocompatibility evaluation of AZ91D magnesium alloy as a biomaterial, *J. Alloys Compd.* 687 (2016) 906–919.
- [3] M. Saini, Y. Singh, P. Arora, V. Arora, K. Jain, Implant biomaterials: a comprehensive review, *World J. Clin. Cases* 3 (2015) 52–57.
- [4] N. Manam, W. Harun, D.N.A. Shri, S.A.C. Ghani, T. Kurniawan, M. Ismail, M. Ibrahim, Study of corrosion in biocompatible metals for implants: a review, *J. Alloys Compd.* 701 (2017) 698.
- [5] Food and Nutrition Board IoM: Dietary reference intakes for calcium, phosphorus, magnesium, vitamin D, and fluoride, Washington, DC: National Academies Press, 1997, pp. 190–249.
- [6] J. Vormann: Magnesium: nutrition and metabolism, *Mol. Aspects. Med.* 24, 2003; pp. 27–37.
- [7] Food and Nutrition Board IoM: Dietary reference intakes for vitamin A, vitamin K, arsenic, boron, chromium, copper, iodine, iron, manganese, molybdenum, nickel, silicon, vanadium, and zinc, Washington, DC: National Academies Press, 2001, pp. 442–501.
- [8] <https://ods.od.nih.gov/factsheets/Manganese-HealthProfessional/>.

-
- [9] H. Yang et al., Alloying design of biodegradable zinc as promising bone implants for load-bearing applications. *Nature communications*. (2020) 1- 14.
- [10] P.K. Bowen, J. Drelich, J. Goldman, Zinc exhibits ideal physiological corrosion behavior for bioabsorbable stents, *Adv. Mater.* 25 (2013) 2577–2582.
- [11] G. Levy, J. Goldman, E. Aghion, The prospects of zinc as a structural material for biodegradable implants-a review paper, *Metals* 7 (2017) 402.



Study of microgeometric characteristics after different preparation of metal surfaces focused on adhesive bonding

Róbert Moro ^{1*} and Dagmar Draganovská ¹

¹ Technical University of Košice, Faculty of Mechanical Engineering, Institute of Technological and Materials Engineering, Department of Technology, Materials and Computer Aided Production, Mäsiarska 74, 040 01, Košice; robert.moro@tuke.sk, dagmar.draganovska@tuke.sk

* Correspondence: robert.moro@tuke.sk; Tel.: +421-55-602-3586

Abstract: The production process of the components itself significantly affects the obtained surface roughness. For this reason, it is necessary to constantly monitor the surface changes that occur during the production process. One of the most important surface properties is the ability to achieve the highest possible level of adhesion after applying a layer of paint or adhesive. To guarantee this property, it is important to select the correct pre-treatment. A paper deals on chemical surface pre-treatment, the so-called conversion coatings. The paper focuses on the evaluation of morphological surface changes after the application of various selected types of chemical pretreatments, based on roughness parameters. The measured values were subjected to statistical analysis.

Keywords: roughness; surface; chemical pretreatment

1. Introduction

The resulting properties of the metal components are determined by the condition of the surface. Surface imperfections often affect the properties of a material, whether physical or technological. In practical cases, the actual metal surface is mediated by external conditions and therefore it is necessary to study the properties and subsequent changes of the material on the surface layer. The surfaces of the components reflect their production processes, which significantly affect the obtained surface roughness and therefore it is necessary to monitor these changes of surface in terms of roughness. [1,2,3]

Another important property of the surface is the ability to achieve the highest possible degree of adhesion with respect to the subsequently applied coating or the best possible bond of substrate and adhesive in the technology of adhering materials by gluing. The technology of bonding materials has been known for a long time and is still widely used for its undeniable advantages, which it provides over technologies using additional adhesive element. It is important to implement proper surface pretreatment, which greatly contributes to achieving high adhesion of bonded surfaces. [4,5,6]

The pretreatment can be done by using chemical surface pretreatment, the so-called conversion coatings. The formation of conversion coatings consists in the reaction of the metal surface with the surrounding environment in which the metal is present during the surface pretreatment. Conversion coatings are characterized by high electrical resistance, which affects the corrosion protection of metal surfaces. [7] Conversion coatings have high level of adhesion to the base material and insolubility in water and solvents. Coatings or adhesives, which are then applied into the conversion coatings, show excellent anchorage to the surface thus pretreated. [8,9,10]

The paper is focused on the evaluation of surface changes after the application of various types of chemical pretreatments using individual roughness parameters. The results were then subjected to statistical evaluation.

2. Material and methodic of experimental work

The basic material is galvanized microalloyed steel with the designation HX340LAD + Z (W. Nr. 1.0933) - (hereinafter only Zn).

It is characterized by a fine structure and increased cold formability and therefore finds application in dynamically stressed vehicle parts.

Methods of chemical pretreatment of basic material

The base material was pretreated by the following methods of chemical surface pretreatment:

1. *Without surface treatment* - the sheet was preserved by electrostatic oiling with an oil weight of 0.5 - 2.5 g.m⁻²

2. *Surface treated with chip-free zirconate passivation* (hereinafter referred to as BP) - does not contain chromium ions or other substances harmful to the environment, it can be used as a conversion layer before coating or gluing. The procedure for passivation with chromium-free zirconate was as follows: degreasing, washing, passivation of zirconate (RT, 3 min.), Rinsing, rinsing in demineralized water, drying.

3. *Surface with a layer of iron phosphate* (hereinafter referred to as PHFe) - creates a compact coating of ferric phosphate on steel with an average coating weight of 0.5g.m⁻². The phosphating procedure was as follows: degreasing, rinsing, phosphating (60 ° C, 3 minutes), rinsing, rinsing in demineralized water, drying.

4. *Surface with a layer of zinc phosphate* (hereinafter referred to as PHZn) - serves as corrosion protection or as a base layer under coatings to improve their adhesion. The phosphating process was as follows: degreasing, rinsing, activation at RT - 3 min. - bath stirring, phosphating at 60 ° C - 5 min., Rinsing, rinsing in demineralized water, drying.

5. *Surface treated with organosilane* (hereinafter referred to as Adhez.) - an agent that increases the adhesion of organic coatings and adhesives. The procedure for the application of the organosilane was as follows: degreasing, rinsing, immersion in an aqueous solution of the organosilane preparation (RT, 10 min.), Drying.

Roughness evaluation methodology and its statistical evaluation

The evaluation of the surface roughness of individual samples was carried out in accordance with the international standard STN EN ISO 4287, according to which the roughness parameters were assessed: Ra - mean arithmetic deviation of the profile, Rz - largest profile height, RSm - mean width of profile elements.

The measured values of the parameters of the individual samples were subsequently subjected to statistical evaluation using statistical characteristics and the Kruskal - Wallis normality test, which specifies a nonparametric parallel to the single - phase analysis of variance (Anova). Anova is used when comparing the assessed mean values of more than two independent files in the event that the conditions for the use of parametric analysis of variance (file normality test) are not met.

The contact roughness tester - SurfTest - SJ 301, Mitutoyo, Japan was used to measure the specified roughness parameters. This profilometer can be characterized this as a tactile device, works on the principle of evaluating the sample by contact scanning the microgeometry of the surface using a probe with a diamond tip with a radius of 5 µm.

3. Results and discussion

Parameter Ra

The individual statistical characteristics for the parameter Ra are shown in the graphical representation. From the measured values it can be stated that the highest average value was recorded for the sample Zn. On the contrary, the lowest value was recorded for the Zn - BP sample. When determining the extreme differences for the parameter Ra, any

presence of outliers was refuted. The values of the parameter Ra do not come from numerical selection with a normal distribution and based on this fact non-parametric tests were used.

The measured values and their differences between the samples to which different chemical pretreatments were applied are visible on the graphic representation, Figure 1.

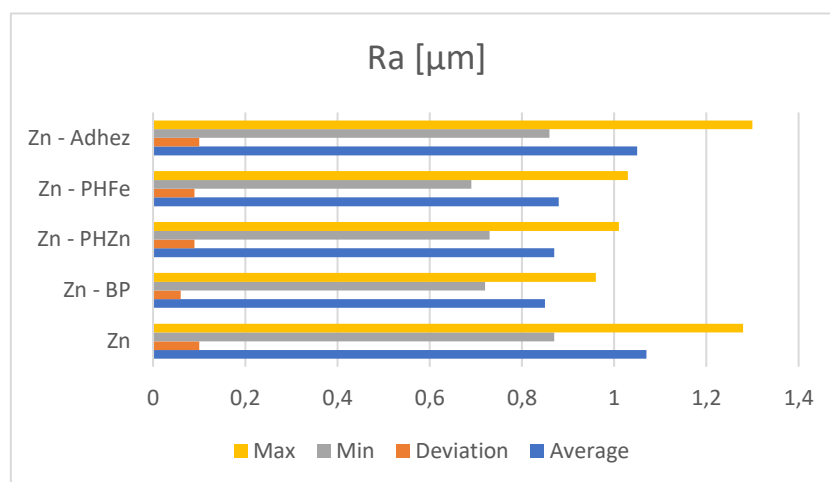
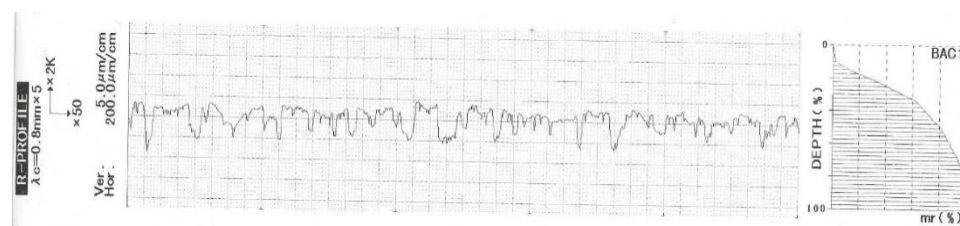


Figure 1. The statistical quantities and measured values for the parameter Ra

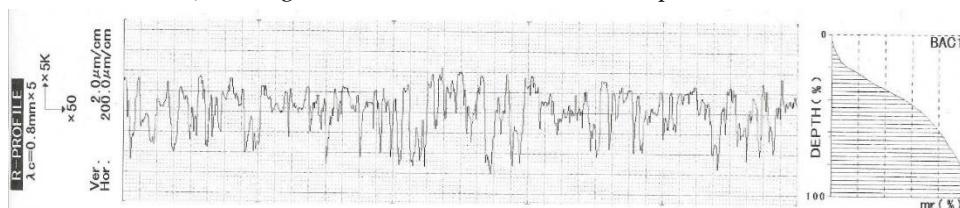
Subsequently, statistical significance was verified by ANOVA. Hypotheses were formulated: H0: the type of chemical treatment does not affect the value of the parameter Ra, H1: the type of chemical treatment affects the value of the parameter Ra.

The resulting value was for $p = 0.0000$, which is less than the significance level $\alpha = 0.05$, so we reject the null hypothesis about the equality of the parameter Ra between the groups at the significance level $\alpha = 0.05$. This means that between the samples Zn to Zn - Adhez. are statistically significant differences and we can state that chemical pretreatment has an effect on the surface roughness parameter Ra.

Profilograms and Firest - Abbot curves for individual surface pretreatments, Figure 2, document the difference of surfaces after the application of the monitored types of surface pretreatments on the Zn material.



a) Profilogram + Firest - Abbot curve for sample Zn



b) Profilogram + Firest - Abbot curve for sample Zn - BP

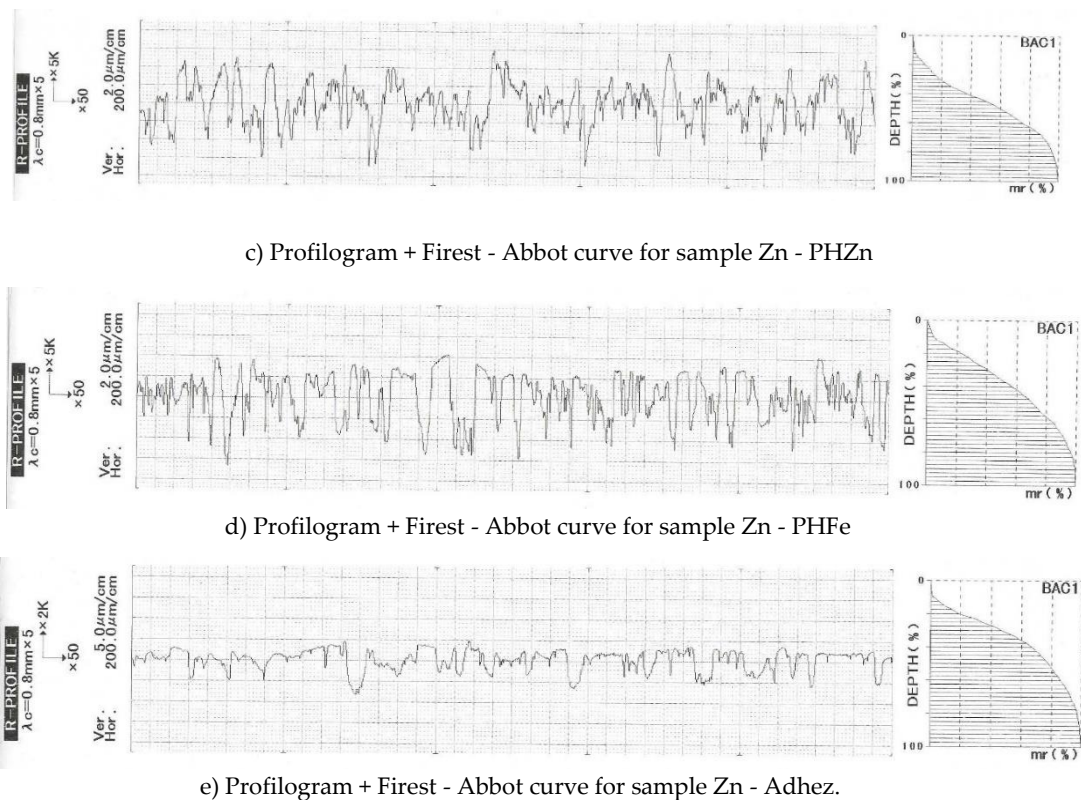


Figure 2. Profilograms and Firest - Abbot curves for evaluated samples

From the mentioned profilograms it is possible to state differences in the morphology of pretreated surfaces of Zn material. The most obvious change in surface morphology is after zinc phosphating. The number of protrusions is clearly higher, which corresponds to the fine phosphate crystals that have formed on the surface as a result of the chemical reactions of iron and phosphates dissolved in the phosphating solution. The surfaces after passivation and application of organosilane only copy the original surface of the Zn material. The surface after iron phosphating is amorphous in nature and also copies the original surface of the sheet.

Parameter Rz

The statistical characteristics for the parameter Rz are contained in Figure 3. From the values that were measured, it can be stated that the highest average value of Rz was recorded in the sample Zn - Adhez. and the lowest for the Zn - PHFe sample.

Even for this parameter, the measured values do not come from numerical selection with a normal distribution and non-parametric tests were used.

Verification was performed by Kruskal - Wallis test based on the resulting p value of samples H (4, N = 150) = 49.55876, p = 0.0000. The test confirmed that $p < \alpha$, so at the level of significance $\alpha = 0.05$, the null hypothesis of equality of mean values is rejected.

Thus, the chemical pretreatment also had an effect on the surface roughness parameter Rz.

A graphical representation of the values of the parameter Rz, where the difference of the measured values manifested itself, is documented in Figure 3.

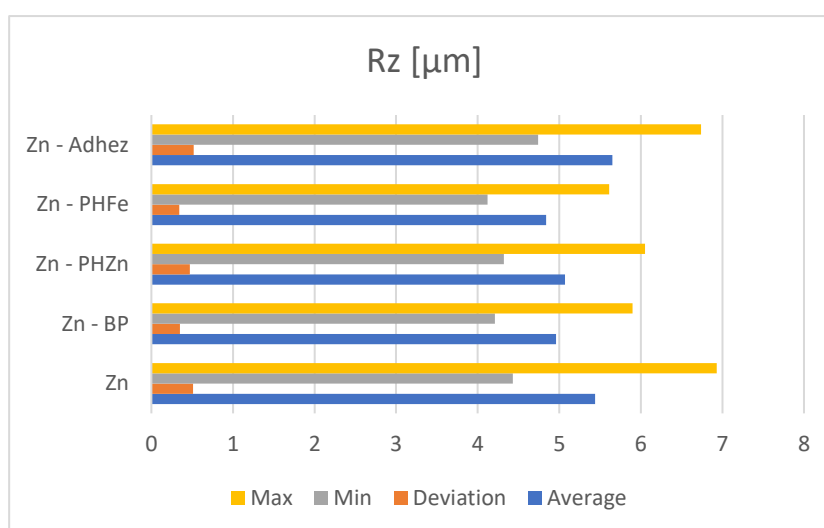


Figure 3. The statistical quantities and measured values for the parameter Rz

Parameter RSm

Statistical characteristics for the RSm parameter are shown in Figure 4. The highest average RSm value was recorded for the sample Zn - Adhez. and the lowest average value for Zn - PHFe.

Also for this parameter the measured values do not come from numerical selection with normal distribution and non-parametric tests were used. The difference of the measured values between Zn samples to which different chemical pretreatments were applied are visible in Figure 4.

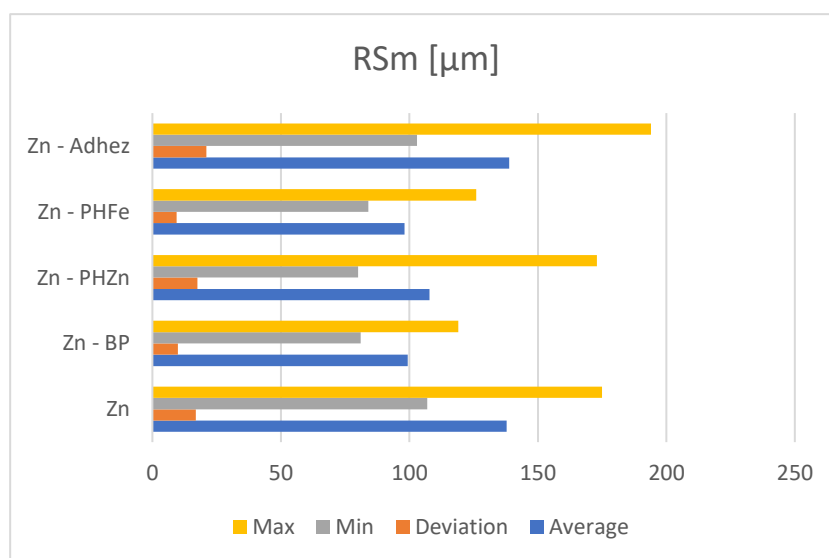


Figure 4. The statistical quantities and measured values for the parameter RSm

Subsequent experimental measurements of roughness parameters clearly show that the value of the parameter Ra does not change significantly for individual surface pretreatments - from 0.85 to 1.07 μm . Based on analyzes, the Rz parameter can be specified as relatively stable - from 4.84 to 5.65 μm . The differences between the individual surface treatments were more pronounced for the RSm parameter from 98.10 to 138.87 μm . Surface differences were also seen in the courses of profilograms and Firest - Abbot curves.

In the case of the use of such surfaces for adhesive bonding technology, it is possible to expect an increase in the contact area between the adhesive and the surface-treated material.

4. Conclusions

Based on the results obtained during the experimental work, can be stated that all applied types of chemical pretreatments have a major impact on the achieved values of the examined surface roughness parameters in the assessed microalloyed steel marked HX340LAD + Z. This phenomenon is presented by measured which are depicted in Firest - Abbot curves are also supported by the performed statistical analysis.

The applied chemical surface pretreatment contributes to the increase of the contact area, which is extremely important for achieving good adhesion and subsequently applied coatings or for increasing the overall strength of the adhesively bonded joint. Good results are also achieved by experimentally verified surface treatment with organosilane, which is simple (rinse-free) and technologically undemanding (does not require heating of process fluids, takes place at room temperature).

Acknowledgments: This contribution was prepared with the support of projects VEGA 1/0154/19 and VEGA 1/0497/20.

Conflicts of Interest: The authors declare no conflict of interest. The funders had no role in the design of the study; in the collection, analyses, or interpretation of data; in the writing of the manuscript, or in the decision to publish the results.

References

1. Guzanová, A.; Brezinová, J.; Draganovská, D.; Jaš, F. A study of the effect of surface pre-treatment on the adhesion of coatings. *J. Adhes. Sci. Technol.* **2014**, *28*, 1-18.
2. Whitehouse, D.J. Surface metrology. *Meas. Sci. Technol.* **1997**, *8*, 955-972.
3. Jane Jiang, X.; Whitehouse, D. J. Technological shifts in surface metrology. *CIRP Annals - Manufacturing Technology* **2012**, *61*, 815-836.
4. Draganovská, D.; Ižariková, G.; Brezinová, J.; Guzanová, A. The Study of Parameters of Surface Roughness by the Correlation Analysis. *Mater. Sci. Forum* **2015**, *818*, 15-18.
5. Draganovská, D.; Tomáš, M.; Ižol, P. Evaluation of micro-geometry changes on surfaces after chemical pretreatment. *Arch. Mech. Technol. Automation.* **2014**, *34*, 17-24.
6. Whitehouse, D. J. Functional Fractal Analysis of Surfaces. *Nanotechnology and Precision Engineering* **2009**, *7*, 19-28.
7. Wiklund, D.; Wihlborg, A.; Rosén, B.-G. Evaluation of Surface Topography Parameters for Friction Prediction in Stamping. *Wear* **2004**, *257*, 1296-1300.
8. Whitehouse J. D. Surface and Their Measurement, *Taylor a Francis Books, Inc.* **2002**, 192-220
9. Brezinová, J. et. Al. Korózia materiálov a špeciálne technológie povrchových úprav. *Technická univerzita v Košiciach - Elfa Košice* **2020**, 147-169
10. Draganovská D. et. al. General Regression Model for Predicting Surface Topography after Abrasive Blasting, *Metals. Basel*, **2018**, 8(11), 938



Antimicrobial treatments for industrial equipment

Jan Kral ¹, Dominik Novotný ²

Technical university of Kosice, Faculty of Mechanical Engineering, Department of Manufacturing Technologies and Robotics, Slovakia

Corresponding author: jan.kral2@tuke.sk

dominik.novotny@tuke.sk

Abstract:

This article deals with antimicrobial treatments applicable to industrial equipment that can effectively eliminate the presence of bacteria, fungi and viruses, including Covid-19. Usability in various industries where this type of treatment is suitable. The article introduces the various ways in which we can prevent the multiplication of bacteria, fungi, fungi, algae or viruses. Antimicrobial treatments are improving not only in healthcare but also in industrial sectors.

The development in this area occurred not only in the application of antimicrobial treatment to textiles or medical devices, but also directly to industrial equipment using coatings, foils. This industry is developing directly in industrial equipment such as fans, nanotechnology filters, polymers.

Keywords: antimicrobial equipment, clean room, Covid-19, optimization, virus

Introduction

Products containing antimicrobial ingredients help keep our homes, schools, offices and other public places clean and hygienic every day. By helping to prevent the growth of unwanted microbes, antimicrobial chemicals can help people from the disease.

Antimicrobial use protects industrial processes, water treatment systems, food processing equipment, medical technology and others. For example, cooling towers that regulate heating, ventilation and air conditioning in residential, office or medical facilities or large industrial buildings. These areas are particularly susceptible to microbial growth.

Antimicrobial surfaces are designed to either inhibit the ability of microorganisms to grow or damage them by physical processes. These surfaces are especially important for healthcare. Designing effective antimicrobial surfaces requires a deep understanding of the initial mechanisms of microbial adhesion to the surface. Molecular dynamics simulation and time-lapse imaging are commonly used to investigate these mechanisms.

By optimizing the equipment, we can use antimicrobial treatments to eliminate the risk of SARS-CoV-2 virus infection, which causes Covid-19 and spreads through contaminated surfaces, by inhalation and persistence in a contaminated environment.

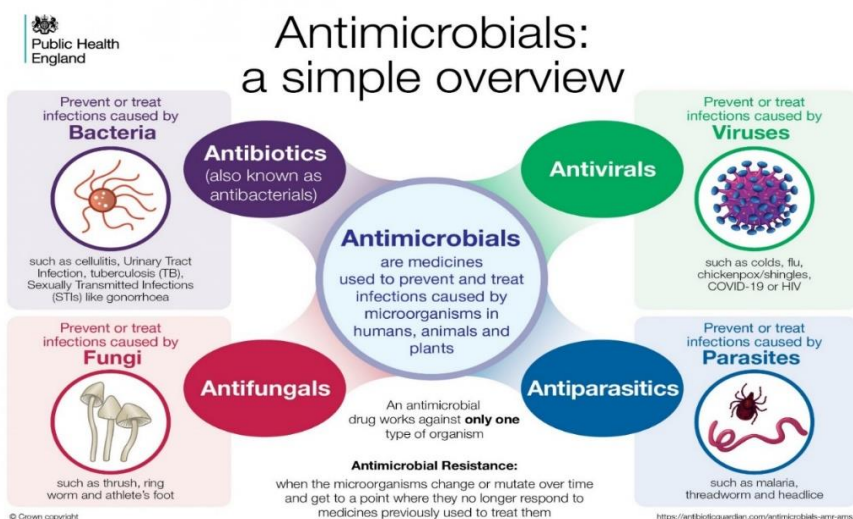
1. Antimicrobial technology

Antimicrobial technology describes the collective knowledge, expertise and methods of using ingredients to create products that are permanently protected against bacteria, fungi and viruses [1]. We call antimicrobials compounds that could reduce, eliminate the presence of microbes such as bacteria or viruses [2].



What is antimicrobial [3]

Antimicrobials are compounds that have the ability to reduce, eliminate the presence of microbes such as bacteria or viruses. [2]



Antimicrobials a simple overview [4]

Types of antimicrobial substances

The main antimicrobials include:

- Silver compounds (Ag) - antimicrobial effect destroys the cell membrane of microbes,

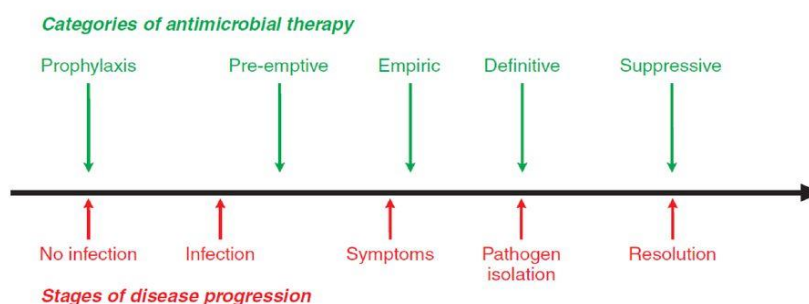
- Copper oxide (CuO) - copper oxide nanoparticles are highly effective against certain types of bacteria,
- Zinc oxide (ZnO) - in combination with iron oxide shows sufficient antimicrobial activity,
- Titanium dioxide (TiO₂) - shows antimicrobial activity by self-cleaning ability and potential of toxic decomposition, titanium nanofibers are prepared by electrostatic spinning,
- Magnesium oxide (MgO) - stops the growth of microbes, especially intestinal bacteria,
- Nitric oxide (NO-) nanoparticles - has a significant antimicrobial effect with a focus on MRSA (methicillin-resistant *Staphylococcus aureus*). [5]

TYPES OF ANTIMICROBIAL TREATMENT

- Antimicrobial coating,
- Antimicrobial foil,
- Antimicrobial textiles,
- Antimicrobial filters,
- Germicidal emitters. [6]

A useful way to organize the types and goals of antimicrobial treatment is to consider where treatment will begin over the course of the disease progression. Therapy can be prophylactic, preventative, empirical, definitive, or suppressive. [7]

Types and goals of antimicrobial therapy



Antimicrobial therapy-disease progression timeline. [7]

Methods of final antimicrobial treatment

Antimicrobial agents can be applied to textile substrates by suction, curing, coating, spraying and foaming. [8]

Various methods to improve the durability of the surface treatment include:

- Insolubilisation of active substances in / on fiber,
- Fiber treatment with resin, condensate or crosslinking agents,
- Microencapsulation of antimicrobial agents with a fiber matrix,

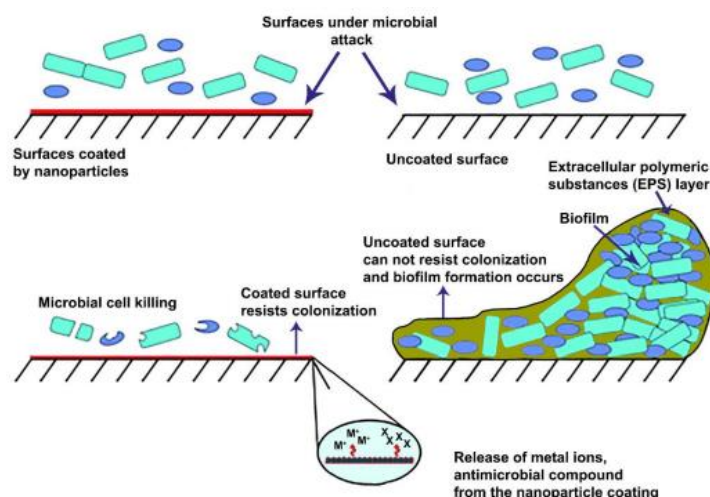
- Fiber surface coating,
- Chemical modification of the fiber by forming a covalent bond,
- Use of graft polymers, homopolymers or fiber copolymerization. [9,10]

Application of antimicrobials in various sectors:

- Paints and coatings,
- Plastics,
- Consumer products,
- Food and beverage processing,
- Medical and healthcare,
- Restaurants and restaurants and other. [11, 12]

2. APPLICATION OF ANTIBACTERIAL NANOTECHNOLOGY IN INDUSTRIAL CONDITIONS

The primary role of surface coatings in industrial applications was to provide corrosion protection and mechanical resistance. Recently, with advances in nanoscience, polymer / nanocomposite coatings have been developed and used for several purposes, including biomedical applications such as antibacterial surfaces.

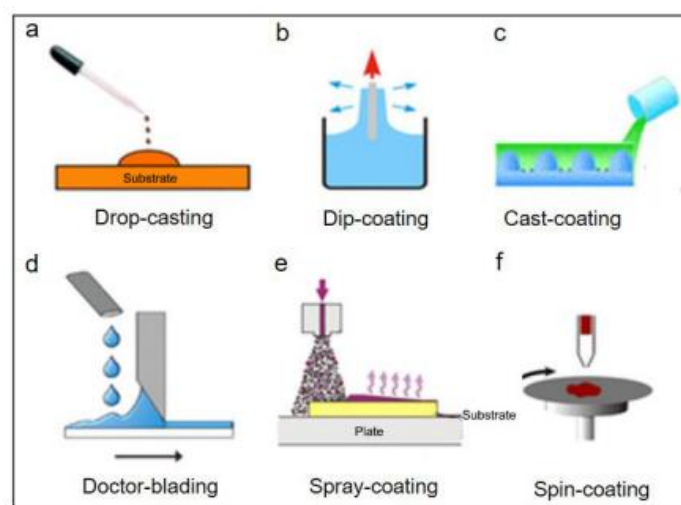


The difference between unprotected and protected surface by antimicrobial treatment. [13]

Types of methods for applying antimicrobial nanotechnological coatings:

- Easy solution application,
- Immersion coating,
- Cast paint,
- Application with an abrasive trowel,
- Spray,
- Rotation method.

In a simple solution application, the solution is added dropwise and applied to a substrate and allowed to evaporate. The immersion technique involves immersion in a polymer melt or solution followed by drawing and subsequent drying. A cast coating where a polymer solution is applied to the non-stick surface of a mold of the desired shape and then the solvent is evaporated. Abrasive application is one of the commonly used methods for forming thin layers over large areas. Drying occurs when the thin layer is subsequently applied to the surface. The spraying method is also a fast method that is mainly used for three-dimensional solid objects. The rotary method is applied by dripping a drop into the center of the surface and at a selected speed the coating spreads over the surface and forms a high quality and fine film. [13]



Schematic representation of common coating techniques [13]

The current SARS-CoV-2 pandemic, which causes Covid-19, has shown great potential for antimicrobial treatment. The effectiveness of antimicrobial technologies in combating pandemics is highly effective and its use is broad in industry. With the development of antimicrobials, controlling the spread of viruses, bacteria and fungi, including Covid-19, will be easier and more effective. The antimicrobial device will be designed for the elimination of the Covid-19 virus, but also for the classic elimination of viruses, bacteria, fungi and algae. The aim of the antimicrobial device will be to achieve the highest possible sterility in the areas where it will be applied, thus achieving the "Clean Room" effect. The development of such devices will make the fight against pandemics, viruses, bacteria or fungi highly effective, where, in addition, it will ensure a minimum of dust in the environment, in which it automatically adjusts its performance according to the contamination of the area.

CONCLUSION

The purpose of the article is to include general knowledge about antimicrobial treatment and to briefly describe the importance of anti-microbial treatment, their applicability in various industries and to point out their effectiveness. Antimicrobial treatments have many advantages, and these technologies are constantly advancing, whether in the form

of coatings, foils, the creation of antimicrobial fabrics, filters, germicidal radiators. Antimicrobial materials are suitable in our industrial facilities for the elimination of Covid-19 virus in the air, which achieves the effect of "Clean Room". With the gradual development of antimicrobial devices, we can see increasing opportunities in industry, healthcare, food and application is expected in more and more industries. Antimicrobial treatments and devices are becoming more and more popular, and their future is very favorable.

ACKNOWLEDGMENT

The article was created with the support of the project:

ITMS2014+ 313011AVF5 Center for the Development of Textile Intelligence and Antimicrobial Technologies.

References

- [1] Bharadishettar, N.; Bhat K, U.; Bhat Panemangalore, D. Coating Technologies for Copper Based Antimicrobial Active Surfaces: A Perspective Review. *Metals* 2021, 11, 711. <https://doi.org/10.3390/met11050711>, [cit. 20.12.2021]. Online (world wide web): [Metals | Free Full-Text | Coating Technologies for Copper Based Antimicrobial Active Surfaces: A Perspective Review \(mdpi.com\)](#)
- [2] Antimicrobial coating of devices for prevention of infection: Principles and protection The International Journal of Artificial Organs / Vol. 30 / no. 9, 2007 / pp. 820-827, [cit. 20.12.2021]. Online (world wide web): [Antimicrobial coating of devices for prevention of infection: principles and protection - PubMed \(nih.gov\)](#)
- [3] [online]. Dostupné z: <https://www.microban.com/antimicrobial-solutions/overview/defining-antimicrobial-technology>
- [4] [online]. Dostupné z: <https://antibioticguardian.com/antimicrobials-amr-ams/>
- [5] Erkoc, P.; Ulucan-Karnak, F. Nanotechnology-Based Antimicrobial and Antiviral Surface Coating Strategies. *Prosthesis* 2021, 3, 25–52. <https://doi.org/10.3390/prosthesis3010005>, [cit. 25.12.2021]. Online (world wide web): [Prosthesis | Free Full-Text | Nanotechnology-Based Antimicrobial and Antiviral Surface Coating Strategies \(mdpi.com\)](#)
- [6] W. Han, Z. Wu, Y. Li, Y. Wang, Graphene family nanomaterials (GFNs)—promising materials for antimicrobial coating and film: a review, *Chemical Engineering Journal* (2018), doi: <https://doi.org/10.1016/j.cej.2018.10.106>, [cit. 25.12.2021]. Online (world wide web): [Graphene family nanomaterials \(GFNs\)—promising materials for antimicrobial coating and film: A review - ScienceDirect](#)
- [7] *Polymers* 2011, 3, 340-366; doi:10.3390/polym3010340, [cit. 26.12.2021]. Online (world wide web): [Polymers | An Open Access Journal from MDPI](#)
- [8] Anton Nikiforov et al 2016 *J. Phys. D: Appl. Phys.* 49 204002, [cit. 26.12.2021]. Online (world wide web): [Non-thermal plasma technology for the development of antimicrobial surfaces: a review - IOPscience](#)
- [9] Pinho, A.C.; Piedade, A.P. Polymeric Coatings with Antimicrobial Activity: A Short Review. *Polymers* 2020, 12, 2469. <https://doi.org/10.3390/polym12112469>, [cit. 26.12.2021]. Online (world wide web): [Polymers | Free Full-Text | Polymeric Coatings with Antimicrobial Activity: A Short Review \(mdpi.com\)](#)
- [10] Muhammad Jawwad Saif, Khalid Mahmood Zia, Fazal-ur Rehman, Mirza Nadeem Ahmad, Shumaila Kiran & Tahsin Gulzar (2014): An eco-friendly, permanent, and non-leaching antimicrobial coating on cotton fabrics, *The Journal of The Textile Institute*, DOI: 10.1080/00405000.2014.952137, [cit. 28.12.2021]. Online (world wide web): [Polymers | Free Full-Text | Polymeric Coatings with Antimicrobial Activity: A Short Review \(mdpi.com\)](#)
- [11] Swaminathan, Meenakshisundaram & Sharma, Naresh. (2017). Antimicrobial Activity of Engineered Nanoparticles used as Coating agents, [cit. 02.01.2022]. Online (world wide web): [\(PDF\) Antimicrobial Activity of Engineered Nanoparticles used as Coating agents \(researchgate.net\)](#)
- [12] A.C.F. Tornero et al. *Progress in Organic Coatings* 121 (2018) 130–141, [cit. 04.01.2022]. Online (world wide web): [\(PDF\) Antimicrobial Activity of Engineered Nanoparticles used as Coating agents \(researchgate.net\)](#)

-
- [13] Erkoc, P.; Ulucan-Karnak, F. Nanotechnology-Based Antimicrobial and Antiviral Surface Coating Strategies. *Prosthesis* 2021, 3, 25–52. <https://doi.org/10.3390/prosthesis3010005>, [cit. 28.12.2021]. Online (world wide web): [Prosthesis | Free Full-Text | Nanotechnology-Based Antimicrobial and Antiviral Surface Coating Strategies \(mdpi.com\)](#)



Evaluation of deep-drawability of selected types of steel sheets

Samuel Vilkovský¹, Janka Majerníková¹

¹ Technical University of Košice, Department of Technology, Materials and Computer Aided Production;
samuel.vilkovsky@tuke.sk, janka.majernikova@tuke.sk

Abstract: High-strength steels have suitable mechanical properties to meet all the requirements of the end consumer, strict environmental standards while being economically suitable for the manufacturer. The main use of these materials is in the automotive industry, where reducing the weight of cars and increasing passenger safety is required. This article deals with the evaluation of deep-drawability of two types of steel sheets - steel with transformation-induced plasticity TRIP RAK40/70 and deep-drawing steel DC06. The mechanical properties of the examined materials were evaluated by a uniaxial tensile test. With the use of cup test we evaluated the mean ear height and mean ear height expressed as a percentage on cylindrical cups with diameters of 69.15 mm without and with the use of lubricant.

Key words: TRIP steels, deep-drawing steels, limit drawing ratio, anisotropy, mean ear height

1 Introduction

The development of materials for the automotive industry is currently facing several conflicting requirements, such as the search for weight reduction, sufficient rigidity or high strength for the safety of passengers. [1]

In addition to these requirements, today's cars must meet standards that push for air protection and fuel efficiency, which is associated with the weight of the vehicle. All this under strictly economic constraints. For these reasons, the choice of material when designing a car structure is a key decision for designers. [2,4,5]

In research and development, the greatest attention is currently focused on progressive high-strength steels (AHSS) and ultra-high-strength steels, which are mainly formed by a group of martensitic steels. The AHSS group includes transformer-induced plasticity steels (TRIP steels) and two-phase steels (DP steels). All these groups of steels show a suitable combination of mechanical properties, together with environmental, safety and economic standards. [6,6]

In this paper, we will evaluate the deep-drawability of high-strength steels compared to deep-drawing steels based on the limit drawing ratio and the average normal anisotropy ratio, which was proposed by The International Deep Drawing Research Group (IDDRG).

2 Experimental materials

Two grades of steel sheets were used in the experimental research - deep-drawing steel DC06BZE75/75PHOL (marked M1) and steel with transformation-induced plasticity TRIP RAK40/70Z100MBO (marked M2). The evaluated steel sheets were electrolytically galvanized on both sides - material M1 with the amount of zinc 75 g/m², for material M2 it represents the amount of zinc 100g/m². The chemical composition of the materials is given in Tab. 1. [7]

Tab. 1. Chemical composition of materials

	C	Mn	P	S	Ti	Si	Al	Cr	Cu	Ni
M1	0,02	0,25	0,02	0,02	0,3					
M2	0,205	1,683	0,018	0,003	0,009	0,2	1,73	0,055	0,028	0,018

The values of mechanical properties of the examined sheets obtained by uniaxial tensile test according to STN EN ISO 6892-1 are given in Tab. 2

Tab. 2 Mechanical properties of materials

	Thickness (mm)	R _p 0,2 (MPa)	R _m (MPa)	A ₈₀ (%)
M1	0,75	140	278	51,7
M2	0,75	443	766	26,3

3 Deep-drawability evaluation

According to STN 42 0127, cold-rolled steel sheets are divided into quality groups listed in Tab. 3. [8]

Tab. 3 Evaluation of sheet metal quality according to the mechanical properties

R _{p0,2} [MPa]	A ₈₀ [%]	r _m	Limit drawing ratio	IDDRG
<180	> 40	≥ 1,65	≤ 0,45	EDDQ-S
180 ÷ 200	38 ÷ 40	1,50 ÷ 1,65	0,45 ÷ 0,48	EDDQ
200 ÷ 240	36 ÷ 40	1,30 ÷ 1,50	0,48 ÷ 0,50	DDQ
> 240	28 ÷ 36	0,90 ÷ 1,3	0,50 ÷ 0,55	DQ

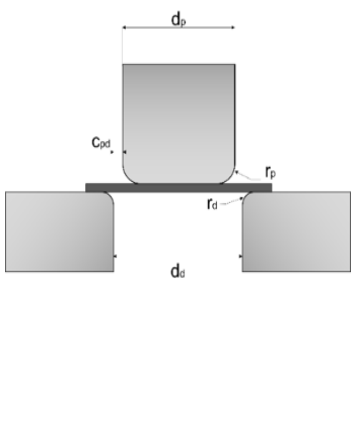
Tests for the evaluation of the deep-drawability of experimental materials were performed on a hydraulic tearing machine ZD 40 with a tool (Fig. 1) with exchangeable functional parts for testing the drawability of thin sheets. The tests were performed in order to determine limit drawing ratio and mean ear height.



Figure 1 Tool for deep-drawability evaluation

The parameters of the deep-drawing tool are given in Tab. 4.

Tab. 4 Deep-drawing tool parameters

	Parameters	Dimensions [mm]
	Die diameter - d_d	71.25
	Punch diameter - p_p	69.15
	Clearance between punch and die - c_{pd}	1.05
	Punch radius - r_p	6
	Die radius - r_d	6

Cup test for an inner diameter of 69.15 mm without the use of lubricant

The limit drawing ratio LDR is defined as the ratio of the cup diameter to the initial diameter of the blank. The method for determining the limit drawing ratio is based on the fact that the dependence of the force F_t on the blank diameter is linear. The point at which the regression line intersects the line of maximum force (force required to tear off the bottom F_{max}) determines the limit diameter D_0 on the x-axis. In order to construct the regression line, measurements of the force F_t were performed for each of blank diameters of the materials M1 and M2.

In this test, flat-bottomed cylindrical extracts with a diameter of 69.15 mm were drawn from circular blanks with diameters of 119, 123, 128, 133, 138 and 144 mm. From every blank three cups were made.

The measured values of the forces when drawing cups from the material M1 are shown in Fig. 2. The limit blank diameter determined mathematically for material M1 is $D_{0max} = 157.84$ mm. The limit drawing ratio in the first draw of the examined sheet has a value of $LDR = 0.437$.

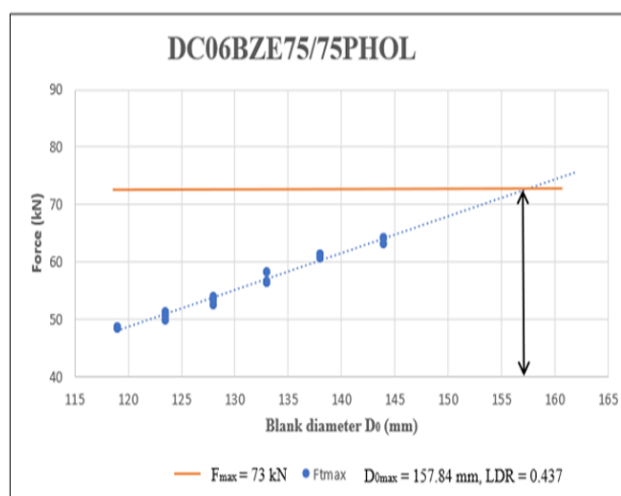


Figure 2 Forces for cups of inner diameter 69.15 mm for M1 without the use of lubricant

The measured maximum forces for the individual blank diameters and the bottom breaking force for the samples of experimental material M2 are shown in Fig. 3. The limit blank diameter determined mathematically $D_{0max} = 143.94$ mm. The limit drawing ratio in the first draw of the examined sheet has a value of $LDR = 0.479$.

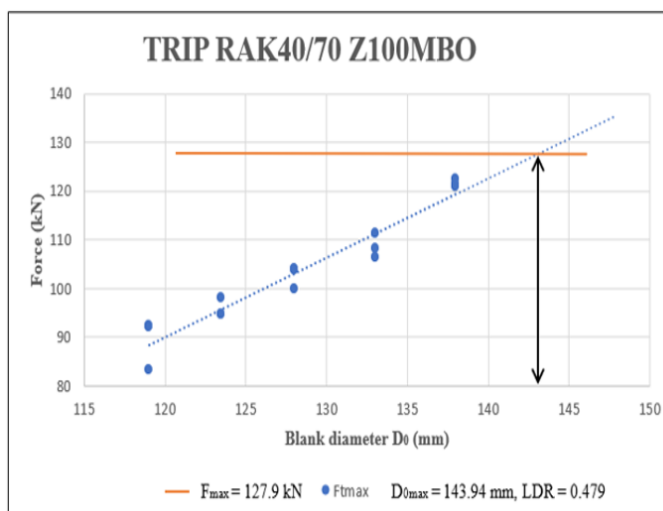


Figure 3 Forces for cups of inner diameter 69.15 mm for M2 without the use of lubricant

Cup test for an inner diameter of 69.15 mm with the use of lubricant

In this experiment, as a lubricant was used plastic foil to reduce friction between the die and the materials. The measured maximum forces for the individual blank diameters and bottom breaking forces for blanks of experimental material M1 are shown in Fig. 4. The limit blank diameter determined mathematically represents $D_{0max} = 162.91$ mm. The limit drawing ratio in the first draw of the examined sheet has a value of $LDR = 0.423$.

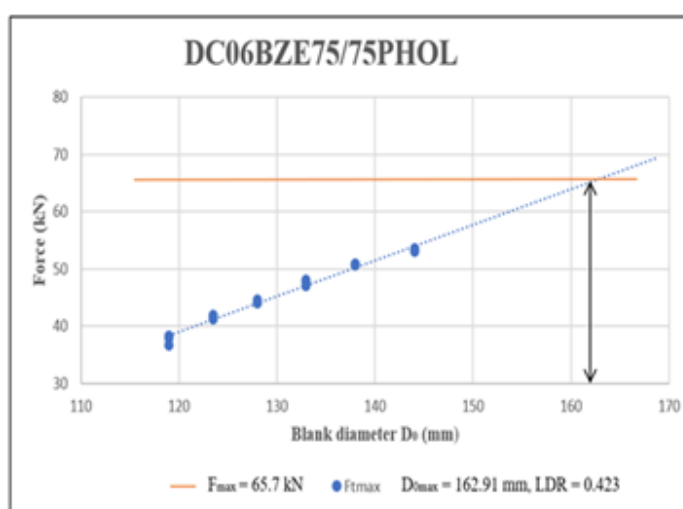


Figure 4 Forces for cups of inner diameter 69.15 mm for M1 with the use of lubricant

The measured maximum forces for the individual blank diameters and bottom breaking forces for samples of experimental material M2 are shown in Fig. 5. The limit blank diameter determined mathematically represents $D_{0max} = 154.28$ mm. The limit drawing ratio in the first draw of the examined sheet has a value of $LDR = 0.447$.

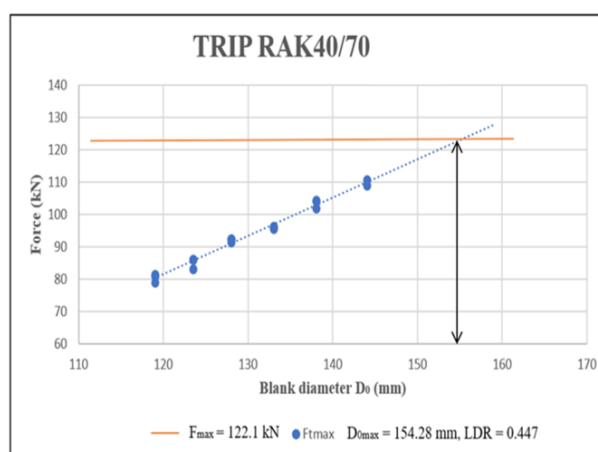


Figure 5 Forces for cups of inner diameter 69.15 mm for M1 with the use of lubricant

According to the scale of qualitative evaluation given in Tab. 3., Tab. 5 shows the classification of the examined sheets for the inner diameter of 69.15 mm.

Tab. 4 Material classification to quality scale according to LDR

Material	LDR (without lubricant)	Category	LDR (with lubricant)	Category
M1	0.437	EDDQ-S	0.423	EDDQ-S
M2	0.479	EDDQ	0.447	EDDQ-S

With the use of a lubricant, the values of the limit drawing ratio of both examined materials were improved and the blanks from the M2 material also changed the category from EDDQ to EDDQ-S.

4 Earing evaluation

Evaluation of the normal anisotropy ratio was performed according to the standard STN 42 0401. Blanks from materials M1 and M2 were evaluated in the directions 0°, 45° and 90° with respect to the rolling direction. The resulting values of planar anisotropy parameter Δr are given in Tab. 6 for M1 and for the material M2 in Tab. 7. Three samples were evaluated for each direction.

Tab. 6 Anisotropic properties for M1 material

Direction [°]	$r_{avg.}$	r_m	Δr
0°	1.604	1.732	0.268
45°	1.598		
90°	2.127		

Normal anisotropy ratio has reached the maximum value in the 90° direction and the minimum value in the direction of 45° for M1 with respect to the rolling direction of the sheet.

Tab. 7 Anisotropy properties for M2 material

Direction [°]	$r_{avg.}$	r_m	Δr
0°	0.686		

45°	0.870	0.816	- 0.108
90°	0.838		

Normal anisotropy ratio has reached the maximum value in the 45° direction and the minimum value in the direction of 0° for M1 with respect to the rolling direction of the sheet

According to the evaluation scale of sheet quality based on the value normal anisotropy ratio given in Tab. 3 qualitative evaluation of the examined sheets is given in Tab. 8.

Tab. 8 Qualitative evaluation of the materials according to the normal anisotropy ratio

Material	Des.	r_m	Quality category
DC 06BZE75/75PHOL	M1	1.732	EDDQ-S
TRIP RAK40/70 Z100MBO	M2	0.816	DQ

According to the value of Δr , it is possible to determine the susceptibility of the sheet to form earing during deep drawing. Ears are formed in sheet directions in which the value of the normal anisotropy ratio r is maximum. If:

- $\Delta r > 0$ – ears will form in 0° and 90° to the rolling direction
- $\Delta r = 0$ – ears will not form
- $\Delta r < 0$ – ears will form in 45° direction to the rolling direction

Earing of the cups was evaluated by the ear height expressed as a percentage and by mean ear height. The values of mean ear height were calculated from the relation (1).

$$\Delta H = \frac{1}{2} (H_0 - 2 \cdot H_{45} + H_{90}) \quad (1)$$

where: H_0 , H_{45} , H_{90} – cup height in the direction of 0°, 45° and 90°, with respect to the rolling direction

The values of the ear height expressed as a percentage were calculated from the relation (2) :

$$\Delta Z = \frac{H_{max} - H_{min}}{H_{min}} \cdot 100 [\%] \quad (2)$$

Earing test

In this test, flat-bottomed cylindrical extracts were drawn from blanks of materials M1 and M2 with diameters of 119, 123, 128, 133, 138, and 144 mm in a drawing tool, the parameters of which are given in Tab. 4.

The height was measured in eight places around the circumference of the cup. In the direction of 0° twice, in the direction of 45° four times and in the direction of 90° twice. The average values of the ears heights were calculated from the values for the individual directions. From these height averages, average values were figured for cups drawn from the same diameter of the blank. We calculated the mean ear height ΔH according to (1) and the ear height expressed as percentage Z according to (2).

Tab. 9 contains the measured values for deep-drawn cups without the use of lubricant.

Tab. 9 Measured values for M1

	Blank diameter [mm]	H ₀ [mm]	H ₄₅ [mm]	H ₉₀ [mm]	ΔH [mm]	Z [%]
DC06-Y (M1)	119	37.3	36.5	37.36	0.805	2.29
	123	41.8	40.83	41.63	0.887	2.38
	128	46.19	45	45.88	1.053	3.69
	133	51.39	50.8	52.33	1.104	3.1
	138	55.08	54.1	55.19	1.149	3.04
	144	61.75	60.7	61.6	1.159	3.80
RAK40/70 (M2)	119	34.75	34.6	33.74	-0.311	2.99
	123	38.77	38.29	37.17	-0.312	4.31
	128	42.93	42.3	40.98	-0.317	4.76
	133	46.41	46,8	46.34	-0.435	1.01
	138	51.83	52,9	52.71	-0.625	2.05
	144	58.1	59.5	59.14	-0.856	2.37

The DC06 deep-drawn steel cups show ears in the 0° and 90° directions with respect to the rolling direction, which is in agreement with the calculated value of the degree of planar anisotropy $\Delta r = 0.268$.

Tab. 10 shows the values of the ΔH and Z with the use of lubricant.

Tab. 10 Measured values for M2

	Blank diameter [mm]	H ₀ [mm]	H ₄₅ [mm]	H ₉₀ [mm]	ΔH [mm]	Z [%]
DC06-Y (M1)	119	35.78	34.8	35.45	0.815	2.81
	123	39.85	38.76	39.12	0.824	2.91
	128	44.02	42.6	43.16	0.981	3.32
	133	48.87	47.6	48.39	1.024	2.65
	138	54.58	52.8	53.65	1.3	3.34
	144	60.71	58.7	59.81	1.525	3.36
RAK40/70 (M2)	119	34.54	34.74	33.91	-0.52	2.45
	123	38.13	38.33	37.51	-0.61	2.19
	128	41.89	42.29	41.22	-0.74	2.59
	133	46.58	46.91	45.34	-0.95	3.47
	138	51.69	52.12	50.70	-0.93	2.80
	144	58.13	58.23	56.45	-0.94	3.15

The TRIP steel cups show ears in the directions of 45 ° with respect to the rolling direction depending on the blank diameter $\Delta r = -0.108$. This finding is in accordance with the negative sign of planar anisotropy Δr .

Dependence of the mean ear height ΔH on the blank diameter for drawing $\varnothing 69.15$ mm cylindrical cup - without lubricant and with lubricant is shown in Fig.6.

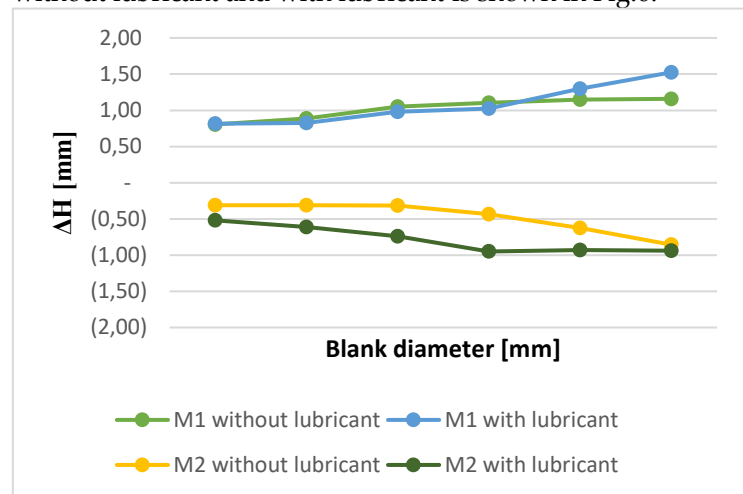


Figure 6 Dependence of mean ear height ΔH on the blank diameter without and with lubrication

5 Conclusion

In this paper, deep-drawability of two types of steel sheets - deep drawing steel DC06 (M1) and steel with transformation-induced plasticity TRIP RAK40/70 (M2) were evaluated on the basis of a qualitative evaluation scale designed by The International Deep Drawing Research Group (IDDRG).

The results of the cup test show that both examined materials have a lower limit drawing ratio with the use of a lubricant. At the same time, use of the lubricant changed the quality category of M2 material from EDDQ to EDDQ-S. Based on the qualitative evaluation of the examined materials according to the normal anisotropy ratio we classified the material M1 in the category EDDQ-S and the material M2 in the category DQ.

The results of the earing test show that the mean ear height ΔH of the deep-drawing steel DC06 acquires positive values and the TRIP steel RAK40/70 acquires negative values for the cups drawn with or without the use of lubricant. The TRIP steel cups show ears in the directions of 45° with respect to the rolling direction. This finding is in accordance with the negative sign of planar anisotropy $\Delta r = -0.108$.

As the diameter of the blank increases, the value of the mean ear height expressed as a percentage ΔZ of the DC06 steel cups increases during deep-drawing with or without the use of lubricant. The value of the mean ear height expressed as a percentage ΔZ of cups made of TRIP steel RAK40/70 increases with diameters of 119 - 128 mm and decreases with diameters of 133 - 144 mm when drawing with or without the use of lubricant. We consider the increase of the mean ear height ΔH and the mean ear height as a percentage ΔZ with increasing diameter as an adverse effect.

Acknowledgements:

The authors are grateful to APVV-17-0381 and VEGA 1/0384/20.

Conflicts of Interest: Declare conflicts of interest or state "The authors declare no conflict of interest." Authors must identify and declare any personal circumstances or interest that may be perceived as inappropriately influencing the representation or interpretation of reported research results. Any role of the funders in the design of the study; in the collection, analyses or interpretation of data; in the writing of the manuscript, or in the decision to publish the results must be declared

in this section. If there is no role, please state "The funders had no role in the design of the study; in the collection, analyses, or interpretation of data; in the writing of the manuscript, or in the decision to publish the results".

References

1. KUZIAK, R. - KAWALLA, R. – WAENGLERA S.: Advanced high strength steels for automotive industry. In: Archives of Civil and Mechanical Engineering. Vol.8 (2008), p. 103-117. ISSN 1644-9665.
2. SUTAR, V. - DHARANKAR, C.S - THIRUPATHI RAJU, B.: High Strength Steel for Automotive Applications. In: International Research Journal of Engineering and Technology (IRJET). Vol. 3, Issue 5, (2016), p. 966-968. ISSN 2395 -0056
3. SPIŠÁK, E. - MAJERNÍKOVÁ, J.: A Study of Thickness Change of Spherical Cup Made from TRIP Steel after Hydraulic Bulge Test. In: Key Engineering Materials. Vol. 635 (2015), p. 157-160. - ISBN 978-3-03835-344-7 - ISSN 1662-9795.
4. BRUSCHI, S. et al.: Testing and modelling of material behaviour and formability in sheet metal forming. CIRP Ann. (2014), Vol. 63, Issue 2., p. 727–749, doi.org/10.1016/j.cirp.2014.05.005.
5. RAMAZANI, A. et al.: Analysis of DP600 Steel during the Cross-Die Test Computational Materials Science, 64 (2012), pp. 101-105, doi:10.1016/j.commatsci.2012.01.031
6. SPIŠÁK, E. - MAJERNÍKOVÁ, J.: Analysis of variance of mechanical properties of sheets as the input parameters for simulation of processes. In: Acta Metallurgica Slovaca. Vol. 18, I. 2-3 (2013), p. 109-116. - ISSN 1335-1532
7. HUDÁK, J. – TOMÁŠ, M.: Hodnotenie procesovej tvárnosti ocelí pre automobilový priemysel. In: Transfer inovácií. (2009), p. 104-108. ISSN: 1337-709
8. POLLÁK, L.- HUDÁK, J.- POLLÁKOVÁ, G.- HANDŽÁK, M.: Štúdium procesov plastického pretvorenia pri hlbokom ťahaní. Grantový vedecký projekt č. 1/334/94, Košice 1994-5



Development of element optimizing car aerodynamics

František Kupec ^{1,*}, Michal Fabian ² and Michal Puškár ³

^{1,2} Technical University of Kosice, Faculty of Mechanical Engineering, Department of Automotive Manufacturing, Slovakia; frantisek.kupec@tuke.sk, michal.fabian@tuke.sk

³ Technical university of Kosice, Faculty of Mechanical Engineering, Department of Machine Design Engineering and Transport Engineering, Slovakia; michal.puskar@tuke.sk

* Correspondence: frantisek.kupec@tuke.sk; Tel.: +421 55 602 3530

Abstract: The current trend in the automotive industry in Europe is to reduce harmful emissions from the operation of individual road transport while increasing the efficiency of propulsion, regardless of the energy source. This paper describes the design of a passenger car body optimization solution in an aerodynamic context to increase drive efficiency. The method by which the research is performed is a virtual engineering procedure using CFD simulation. The results describe the complexity of passenger car aerodynamics and point to further steps that may be the subject of further research.

Keywords: car aerodynamics, emissions, aerodynamic optimization, CFD simulation

1. Introduction

One of the greenhouse gases that contributes to global warming is carbon dioxide, which is produced by burning fossil fuels. Individual car transport, which still burns fossil fuels to a high degree, has a significant share in the production of these emissions. In 2019, the concentration of carbon dioxide in the atmosphere was the highest in the last two million years. For this reason, important regulations and goals are approached, which aim to increase energy efficiency. The European Union's continued pressure to reduce emissions motivates carmakers to innovate to reduce input energy requirements and increase the efficiency of energy conversion.

One of the biggest resistances that cars overcome when moving is air resistance. At 100 km / h, air resistance represents 75 to 80% of the total running resistance. [1] Therefore, great emphasis is placed on reducing the air drag coefficient.

Aerodynamic optimization of the vehicle is one of the directions that reduces the consumption of input energy and prolongs the range of the car. From the point of view of a single car, these are small savings, but from the point of view of mass production, we can speak of a significant reduction in emissions from the burning of fossil fuels.

The trend towards aerodynamic optimization is increasingly visible on vehicle bodies. Their geometry adapts to the ideal aerodynamic shape while maintaining the requirements of the vehicle concept. Research teams of automotive development centers, as well as teams of scientists, are engaged in the research of optimization solutions.

Kumar et al. [2] performed a comprehensive analysis of the vehicle with aerodynamic optimization of the shape of the rear bumper with the air duct at angles from 0 ° to 13 °. Huminic, A. et al. [3] dealt with the rear diffuser of the vehicle and additional shapes that may affect the flow. The structure of the flow in front of and around the rearview mirror of passenger cars was investigated by Kim, J. et al. [4]. Wang J. [5] et al. investigated passive control of the air flow by means of a blown rear-view mirror of the car. Cheng S.Y. et al. [6] verified the effect of a change in the geometry A and C of the vehicle body pillar on overall airflow.

2. Significant parameters of vehicle aerodynamics

Aerodynamics is a science that studies the movement of gases, in this case air, and its interactions with solid objects, in this case with the automobile. [7] Several forces and moments acting on the car while driving are monitored in the assessment and optimization of the vehicle's aerodynamics. These resist not only the direction of travel of the vehicles but also cause the car body to tilt and tilt. These are diverse forces and moments - for simplicity, plotted in relation to a coordinate system starting at the center of the vehicle (Figure 1).

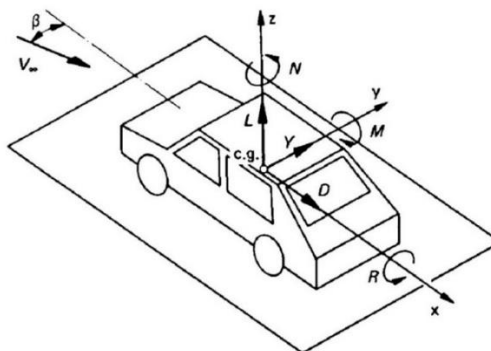


Figure 1. Graphic interpretation of aerodynamic forces and moments acting on the car [1]

The most significant of the components indicated in Figure 1 is the force acting directly against the movement of the vehicle F_d [N]. As Table 1 shows, the dimensionless air resistance coefficient c_d [-], the vehicle speed in v [$km \cdot h^{-1}$], the density of the flowing medium ρ and the content of the front surface of the vehicle A [m^2] are included in the calculation. At the same time, the aerodynamic drag increases with the square of the speed of the moving car.

The discussed force F_d has the greatest effect on reducing the energy consumption of the vehicle and thus increasing the efficiency of its drive. The other forces and moments listed in Tables 1 and 2 affect the other driving characteristics of the car and the behavior under non-standard conditions, such as strong crosswinds, will therefore not be discussed here.

Table 1. Aerodynamic forces acting on the car while driving [1].

Force specification	Relation
Aerodynamic drag	$F_D = \frac{1}{2} \cdot C_D \cdot \rho \cdot v^2 \cdot A$
Buoyancy lift	$F_L = \frac{1}{2} \cdot C_L \cdot \rho \cdot v^2 \cdot A$
Side force	$F_Y = \frac{1}{2} \cdot C_Y \cdot \rho \cdot v^2 \cdot A$

Table 2. Aerodynamic moments acting on the car while driving [1].

Moment specification	Relation
Moment of yawing	$M_M = \frac{1}{2} \cdot C_M \cdot \rho \cdot v^2 \cdot A \cdot l$
Moment of roll	$M_R = \frac{1}{2} \cdot C_R \cdot \rho \cdot v^2 \cdot A \cdot l$
Moment of pitching	$M_N = \frac{1}{2} \cdot C_N \cdot \rho \cdot v^2 \cdot A \cdot l$

When designing vehicles, their front surface is influenced by the requirements for body design and vehicle concept. As a result, efforts to reduce the air resistance force F_d

focus on reducing the air resistance coefficient c_d . This depends mainly on the shape of the body, but also on individual zones and parts such as the chassis, discs, tires, or rear-view mirrors. Looking at Figure 2, this is one example where it can be shown that two cars can have the same value of air resistance coefficient and at the same time a fundamentally different physical shape. This is due to the different front surface depending on the arrangement of the vehicle body surfaces and at the same time the optimization of individual details. The current values of air resistance c_d of cars range from 0.23 to 0.35 [8].



Figure 2. Comparison of two cars with the same air coefficient and different body shape. From above Opel GT MY 1968 $c_d = 0,41$, $A = 1,51 \text{ m}^2$, from below VW Scirocco MY 1974 $c_d = 0,41$, $A = 1,73 \text{ m}^2$ [1].

3. Elements and nodes optimizing vehicle aerodynamics

In the automotive industry, the geometry and development of special elements that can bring further optimization measures are constantly being researched. The partial contribution of the resistance reduction measures is very small in terms of numbers, the contribution of several such measures in total contributes to the reduction of the vehicle air resistance. Figure 3 illustrates several nodes whose geometric adjustment helps to reduce the coefficient of air resistance.

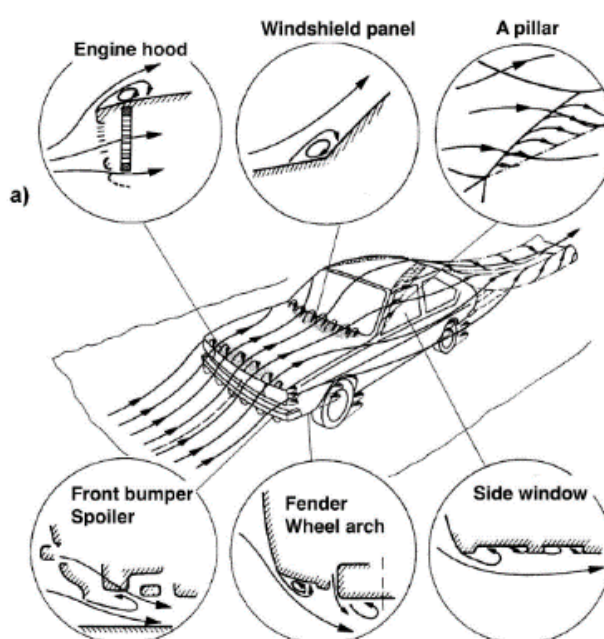


Figure 3. Selection of optimization nodes for individual parts of the vehicle body [1].

Due to the small numbers in the aerodynamic optimization, the conversion of the coefficient into points is used in practice for simplification, whereby it holds:

$$0,001 = 1 \text{ point} \quad (1)$$

and the individual optimization nodes and elements contribute to the reduction of the resistance c_d usually by 2 to 10 points [8]. The numerical contributions of individual nodes can be explained on specific examples, they are discussed in subchapters 3.1 to 3.3.

3.1. Aerodynamic measure – air curtain

The rotating wheels of the car increase the coefficient of air resistance of the car. The reduction of the coefficient and the reduction of the wheel interference is achieved by using the air curtain element visualized by the CFD simulation in Figure 4. The screen reduces the vortices and brings the reflected air flow back to the body. The functionality of the screen is achieved by choosing a suitable geometry, i.e. the size, location and angle of the inlet, the length of the inner duct and the air outlet system. The air curtain is structurally designed as a plastic channel, which is part of the front bumper and fender of the vehicle. The estimated benefits of this element are 2 to 3 points depending on the overall geometry of the car.

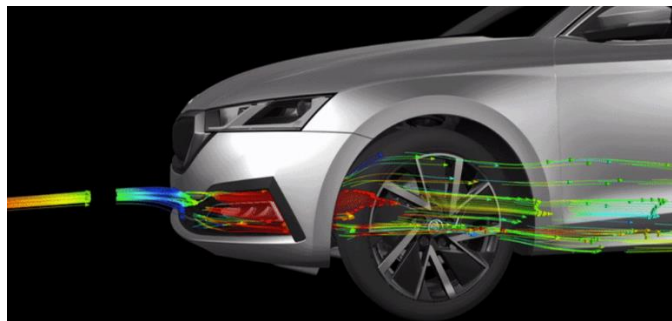


Figure 4. Air curtain as one of the optimization elements [9].

3.2 Aerodynamic measure – blown roof spoiler

The rear vacuum behind the vehicle should be balanced and as small as possible. This is aided by active or passive control by means of a roof spoiler on the fifth door of the vehicle body. The innovative spoiler shown in Figure 5 with the slit positively affects the shape of the flood behind the vehicle.

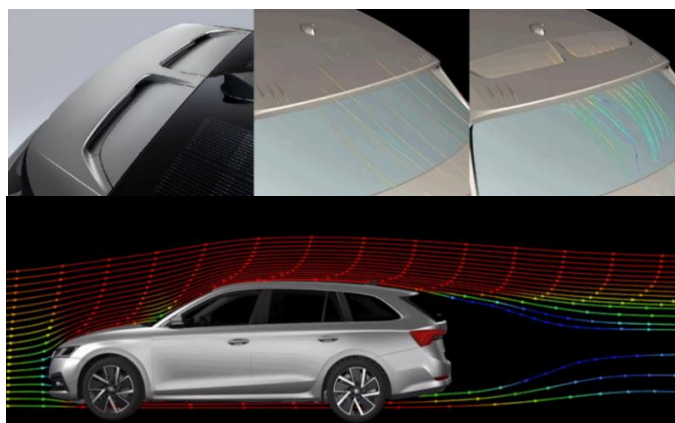


Figure 5. Top from the top roof spoiler of the fifth body of the Hyundai Ioniq 5 MY 2021 vehicle. From below, visualization of the rear vacuum behind the Škoda Octavia SW MY 2019. [9, 10].

The roof spoiler is often a key component in optimizing vehicle aerodynamics. It reduces the force F_L , i.e. the lift of the vehicle, improves driving stability by minimizing eddy current and reduces flooding behind the vehicle. The estimated benefit of this solution is 3 to 5 points, depending on the geometry of the vehicle.

3.3 Aerodynamic measure – blown C-pillar

In addition to the roof spoiler, slotted passive air control can also be used in other parts of the body. An example of use is the air duct formed in the C-pillar of the Kia Niro 2022 in Figure 6. As with the spoiler, the slit directs the air behind the vehicle with a positive impact on the rear vacuum with a suitable geometric setting.



Figure 6. Production version of the integrated air duct in the vehicle's C-pillar Kia Niro MY 2022 [11].

4. Design of the optimization element

The subject of the article is a description of the proposed optimization of the node in the area A of the vehicle pillar. This is where the side effect occurs. The flow in the area of the windscreen is schematically shown in Figure 7 and comprises three parts where the interruption occurs:

- In the area between the front hood and the windshield;
- Above the windshield;
- On the A-pillars of the body.

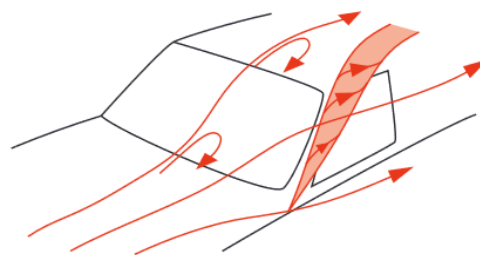


Figure 7. The main directions of air flow in the area of the car windshield are shown [5].

In the case of the first two disturbing areas, noises or transverse vortices may be generated. However, they do not have a significant effect on the overall air resistance. Even in the case of the area above the windscreen, the edge is perfectly rounded in the current concepts of automobiles and there are no separation areas which would influence the flow break-off and increase the air resistance coefficient.

However, in the case of vehicle A-pillars, undesired longitudinal vortex occurs, its visualization is shown by the black circles in Figure 8. In this area, the air flows at high speed around the column, there is a vacuum in the vortex cores and thus also the contribution of the coefficient of aerodynamic drag of the air. Vortices arising on the A-pillars

of the vehicle also result in noises present on the side windows of the car, very close to the hearing of the passengers. [1]

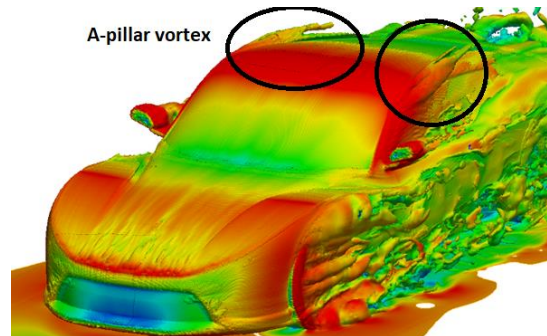


Figure 8. The phenomenon of the emerging A-column vortex shown by CFD post-processing is shown. [12].

These optimizations can eliminate the undesirable phenomena of the emerging vortex:

- Increasing the angle between the bonnet and the windscreen;
- Conical shape of the upper part of the car cabin;
- Significant rounding of A-pillars. [1]

However, as these optimization solutions often undermine the conceptual intent of lower-class passenger cars - adverse effects on viewing conditions, interior width and passenger headroom, other optimization options have been tested..

For verifying the solution, a Škoda Kodiaq vehicle was selected from the D-SUV category. The air resistance of the vehicle before optimization is 0.3171 (2.0 TDI 4x4 140 kW) [13]. And the column vortex created on the Škoda Kodiaq can contribute to an increase in the air resistance coefficient of approximately 2 to 3 points.

Plastic spoilers above the A-pillar of the body were designed. The inspiration was the concept of the fuel-efficient Renault Eolab from 2014. An air duct was created between the spoiler and the pillar. The distribution of the flowing air in the area of the vehicle windscreen above the body and at the sides of the body is assumed to eliminate the formation of the A-pillar vortex. Due to the fact that each vehicle geometry is unique for aerodynamics and no optimization element is universal, an increase in the vehicle's air resistance coefficient is expected first. The aim is to verify the effect of this spoiler on the geometry of the D-SUV and to find the most appropriate direction of the solution.

In the first phase, five variants of spoiler shapes were verified, which were added as an additional component to the original body. Their shapes can be seen in Figure 9 (b to f) proposed in A-class surfaces in ICEM Surf software.



(a)



(b)



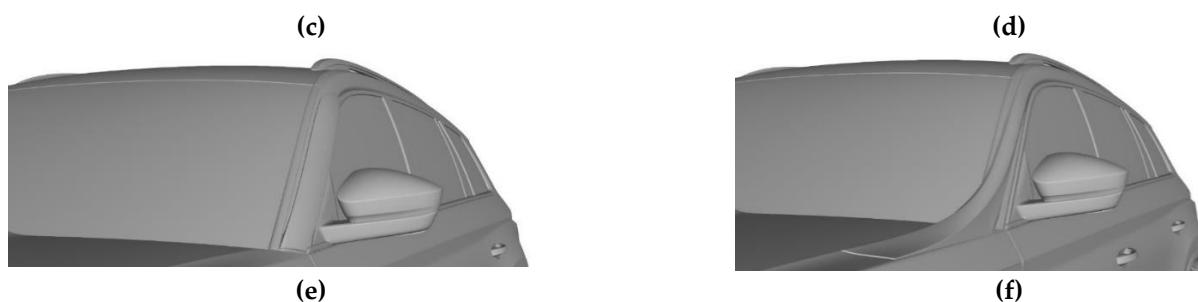


Figure 9. The original condition of the original A-pillar shape of the Škoda Kodiaq MY 2017 (a) and the five proposed A-pillar spoiler shapes (b, c, d, e, f).

CFD simulations of the developed spoiler variants above the A-pillars were made using of OpenFOAM software tools and the methodology of the CCX computational solver.

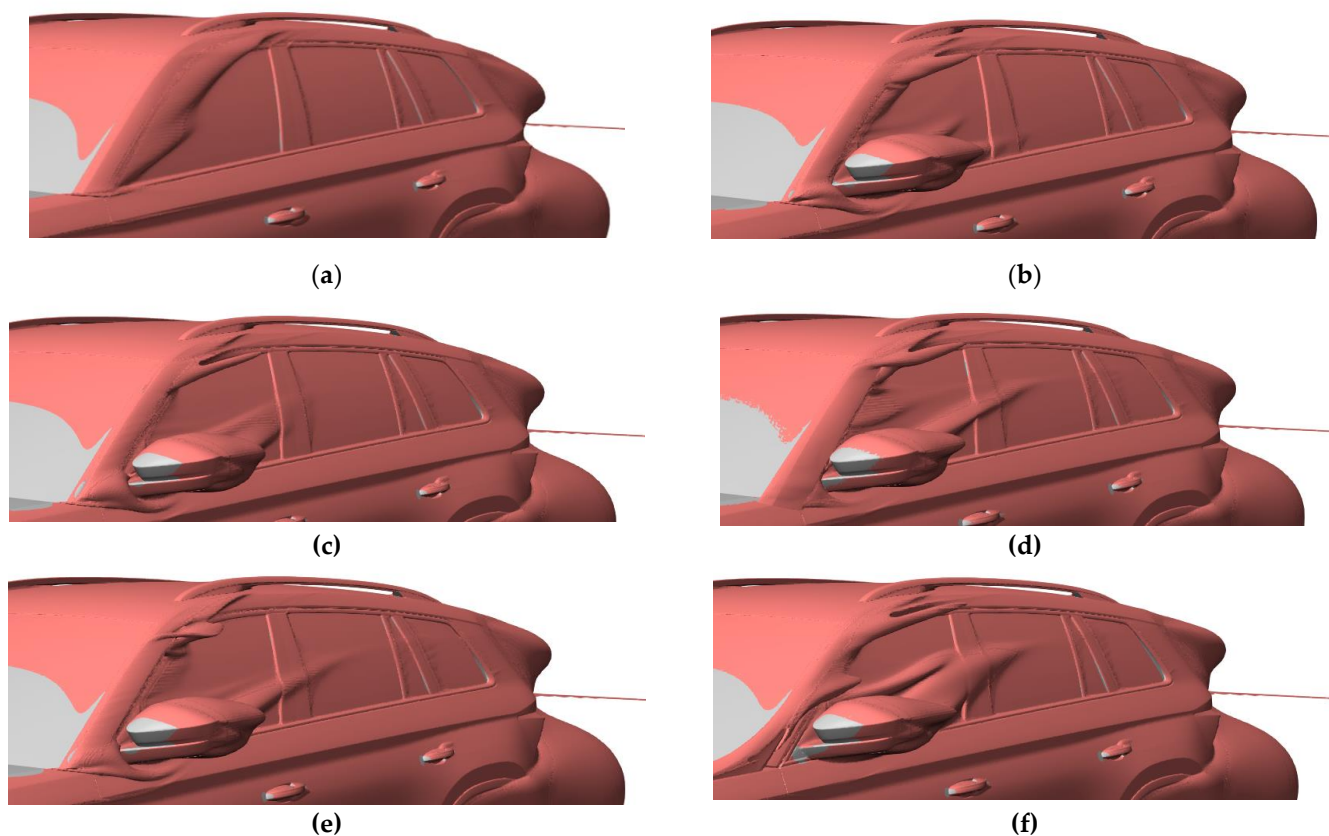


Figure 10. Post-processing images - generated visualizations of vortices using ISO surfaces. Variant a - original, variant b, c, d, e, f - investigated.

The results of CFD simulations are shown using images with ISO (isoparametric) surfaces, which identify the emerging aerodynamic vortices. In each variant of Figure 10 (b to f), an attempt can be made to eliminate the A-column vortex. In the case of variants b, c, d, the vortex was divided into partial, smaller ones. Variants d, f have a significant negative effect because they amplify the formation and size of the resulting vortex, while increasing the negative impact of the rearview mirror. Variant e seems to be the most suitable in the displayed ISO areas. The air resistance coefficient was expected to increase by 2 to 9 points.

Table 3. Numerical influence of individual spoilers on the total coefficient of air resistance of the vehicle.

Variant	Basic a	b	c	d	e	f
c_d	0,3171	0,3223	0,3218	0,3231	0,3236	0,3268
Δc_d	-	+0,0052	+0,0047	+0,006	+0,0065	+0,0097

Based on the results from Table 3, it can be concluded that the appropriate direction of the optimal path is variant b.

5. Discussion

The proposed solutions were designed so as not to violate the basic geometry of the Škoda Kodiaq vehicle. Neither design changes nor changes in the shape of the original components were considered. The achieved results of five different spoiler variants above the A-pillars point to the need for further processing - modification of the geometry and design changes to reduce the coefficient of air resistance of the vehicle.

The subject of further research may be the verification of the integrated spoiler and the air duct in the original geometry of the vehicle, where the initial front surface is preserved and thus the net influence of the duct on the flow around the body can be verified.

6. Conclusions

The article verified the impact of the design of the vehicle aerodynamics optimization solution on the existing body geometry of the Škoda Kodiaq MY 2017. The achieved results pointed to the need for a more comprehensive elaboration of the study and the incorporation of further research proposals. The research was carried out in cooperation with the Škoda Auto Development Center, Mladá Boleslav.

Acknowledgments: The work was accomplished under the grant project VEGA 2/0080/19 "Prediction of weldability and formability for laser welded tailored blanks made of combined high strength steels with CAE support" and VEGA 1/0318/21 "Research and development of innovations for more efficient use of renewable energy sources and reducing the carbon footprint of vehicles".

References

1. H. Schuetz CH.: Aerodynamics of Road Vehicles, Fifth Edition, Hardcover, 1312 s., ISBN-10:0768079772, SAE International, 2015
2. Kumar, B.R. et al.: Aerodynamic design optimization of automobile car using computational fluid dynamics approach, Australian Journal of Mechanical Engineering, 2019
3. Huminic, A., & Huminic, G.: Aerodynamics of curved underbody diffusers using CFD, Journal of Wind Engineering and Industrial Aerodynamics, 205 s., 2020.
4. Kim, J.-H., & Han, Y. O.: Experimental investigation of wake structure around an external rear view mirror of a passenger car, Journal of Wind Engineering and Industrial Aerodynamics, vol. 99 (12), s. 1197–1206, 2020.
5. Oettle, N & Sims-Williams, D.; Automotive aeroacoustics: An overview. Proceedings of the Institution of Mechanical Engineers, Part D: Journal of Automobile Engineering. 231.,2017.
6. Cheng, S.Y. et. al.: Aerodynamic stability of road vehicles in dynamic pitching motion, Journal of Wind Engineering and Industrial Aerodynamics, vol. 122, p. 146-156, ISSN 0147-6105, 2013.
7. Aerodynamika [online], [cit. 10.12.2021], Wikipedia. Available online: <<http://sk.wikipedia.org/wiki/Aerodynamika>>
8. Heisler H.: Advanced vehicle technology, Second Edition, Society of Automotive Engineers, Inc., Warrendale, ISBN 0 7680 1071 3. 2002.
9. Skoda Octavia, SKODA Storyboard [online], [cit. 10.12.2021]. Available online: <<https://www.skoda-storyboard.com/cs/skoda-svet/cs/inovace-a-technologie/perfektne-aerodynamicka-skoda-octavia/>>
10. Hyundai Motor Group; [online], [cit. 10.12.2021]. Available online: <<https://news.hyundaimotorgroup.com/Article/The-Exquisite-Combination-The-aerodynamic-design-of-IONIQ-5>>
11. Reyes A.; 2023 Kia Niro debuts with quirky styling and sustainable construction [online], [cit. 11.12.2021]. Available online: <<https://www.slashgear.com/2023-kia-nero-debuts-with-quirky-styling-and-sustainable-construction-29700595/>>
12. Automotive Example and Applications; [online], [cit. 12.12.2021]; Available online: <<https://engys.com/applications/automotive/>>.
13. Skoda Kodiaq; [internal material Škoda Auto]



Determination of material properties of the samples manufactured by additive technology using 3D digital image correlation

Peter Palička ^{1,*}, Róbert Huňady ¹ and Michal Fabian ²

¹ Department of Applied Mechanics and Mechanical Engineering, Faculty of Mechanical Engineering, Technical University of Košice, Letná 9/B, 042 00 Košice, Slovakia; peter.palicka@tuke.sk; robert.hunady@tuke.sk;

² Department of Automotive Production, Faculty of Mechanical Engineering, Technical University of Košice, Mäsiarska 74, 040 01 Košice, Slovakia; michal.fabian@tuke.sk

* Correspondence: peter.palicka@tuke.sk

Abstract: Currently, additive technologies are a very attractive area for researchers. In practice, they are used more and more often due to their good mechanical properties, which brings researchers around the world many ideas and research opportunities. Plastics and composites have become an integral part of various industries such as automotive production, aircraft production and many more. The advantage of additive technologies is the creation of complicated shapes and the creation of complicated and necessary internal structures to ensure resistance to mechanical loading. The aim of this work is to determine the Young's modulus and the Poisson's ratio of plastic samples printed on a 3D printer. Tensile tests were performed on the tensile machine, and the deformation was measured using 3D digital image correlation.

Keywords: tensile test; 3D DIC; additive technology; plastic samples; polymer.

1. Introduction

The additive technology of manufacturing of various parts has many advantages over the still used methods of plastic injection, mold casting, etc. The main advantage is the creation of complicated shapes without creating an often very expensive form. Another advantage is the creation of the internal structure of the part, which provides better mechanical resistance to loading. Researchers around the world are studying the various properties of these products. Studies have shown the role of the internal pattern on the mechanical properties leading to the production of the part in a specific pattern to material savings and cost reduction [1]. Reviews and researches are being created regarding the methodology of testing 3D printed samples and the use of ASTM and ISO standards to determine the mechanical properties in tensile, compression, bending tests as well as impact and fatigue tests [2]. The results are compared, e.g. tensile and bending tests and the impact on the results due to different techniques for the production of plastic samples. A study [3] was conducted, comparing the mechanical properties of laminates with continuous carbon fiber reinforcement printed using a commercially-available 3D printer with carbon fiber fabric-resin composites produced using manual layup techniques. The aim of this paper is to experimentally determine the Young's modulus of elasticity and the Poisson's ratio of material called Z-ULTRAT. To determine these material constants, a tensile test was performed while deformations were measured using 3D digital image correlation (3D DIC).

2. Materials and Methods

The tested samples (see Figure 1) made of Z-ULTRAT material were made by 3D printer Zortrax M200 with the nozzle diameter of 0.4 mm. The layer thickness was 0.19 mm and the infill density was 100%. There was used cross hatch patter +/- 45°. Tensile tests were performed according to the ČSN ISO 527-4 standard [5].

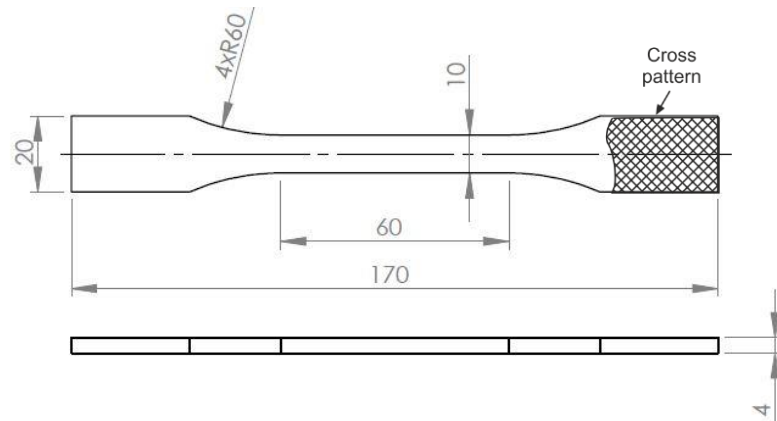


Figure 1. Sample dimensions.

The digital image correlation (DIC) method is an optical method to measure strain and displacements, using the digital image registration technique [6]. It is an experimental contactless method using low-speed or high-speed cameras to measure deformations and strains of the samples under various loads including tensile tests or compression tests. When measuring is proceeded using one camera it is the planar image correlation (2D DIC). The camera must be aimed perpendicular to the surface of the measured object. If two cameras are used and positioned stereoscopically it is the spatial image correlation (3D DIC). A stochastic black and white pattern must be created on the surface of measured object. The used pattern must be dull in nature, because different reflections can cause data loss when correlating images [7]. Before the actual measurement take place, it is necessary to calibrate the cameras. The principle of the method is correlation of the images taken during loading of the tested sample or the measured object. Based on the set parameters, the system creates an evaluation grid and determines image facets at each point of the grid. Each facet contains a unique random pattern. During the correlation itself, the system evaluates the position of the facets and compares it with the reference one. In this way, the system can draw strain fields and displacement fields in post-processing. Istra 4D software by Dantec Dynamics is used to evaluate the measurements [4].

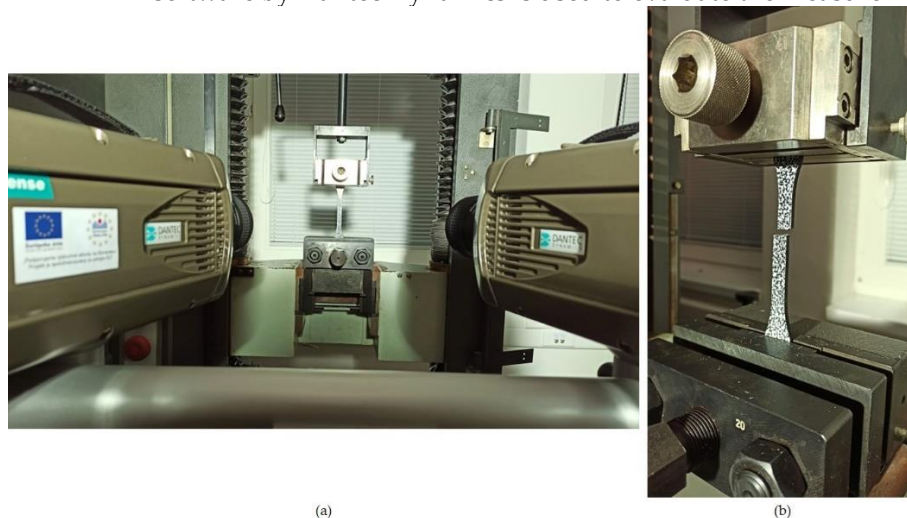


Figure 2. (a) Measuring workplace; (b) Ruptured sample.

The Dantec Dynamics Q-450 high-speed camera system was used to measure the deformation during the tensile tests. The main system features are:

- Camera sensor CMOS resolution: 1.2 Mpx.
- Dynamic range: 3140 fps at full sensor resolution. At a reduced resolution up to 50,000 fps.
- Measuring range: $\text{mm}^2 - \text{m}^2$.
- Measurement sensitivity:
 - Displacements: $1 \mu\text{m}$,
 - Strains: 10^{-4} strain

The tensile force was measured with force gauge ranging from 0 kN to 4 kN. The force data were measured in Volts using a AD converter connected to PC. In postprocessing, the voltage values were multiplied by the conversion coefficient. The processing of the measurement results was based on the basic relationships of the mechanics of the flexible body. The force values at each time step of the measurement were divided by the initial cross-sectional area of the sample, thus obtaining the stress values at each time point from the beginning of the loading to the rupture of the sample. The sampling frequency of the cameras was set to 50 frames per second. Stress and strain values in axial and transversal direction were used to plot the stress-strain diagram and to calculate the material constants. The Young's modulus and Poisson's ratio were determined in the linear area. The measurement was performed for two loading speeds (6 and 84 mm/min).

3. Results

3.1. Evaluation

The measurements were evaluated in Istra 4D software. An area was created on the sample in which the measurements were evaluated and the correlation itself took place. Figure 3a shown the sample before the loading. The strain field of the loaded sample before the rupture is shown in Figure 3b.

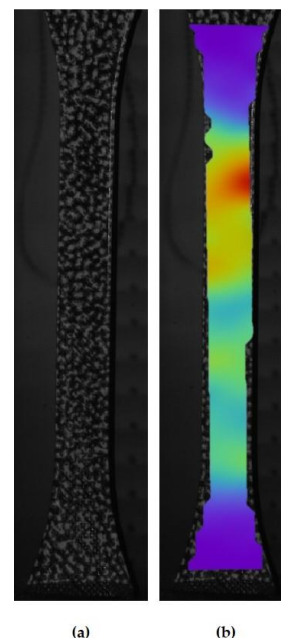


Figure 3. (a) Image of the sample at the beginning of the measurement; (b) Strain field of the sample before the rupture.

Strains were evaluated using a line gauges (virtual line sensors) and calculated according to measured displacements on these sensors in transverse and axial direction using the relation (1):

$$\varepsilon = \frac{\Delta l}{l_0}, \quad (1)$$

where, ε is strain, Δl is relative elongation and l_0 is reference length of the gauge.

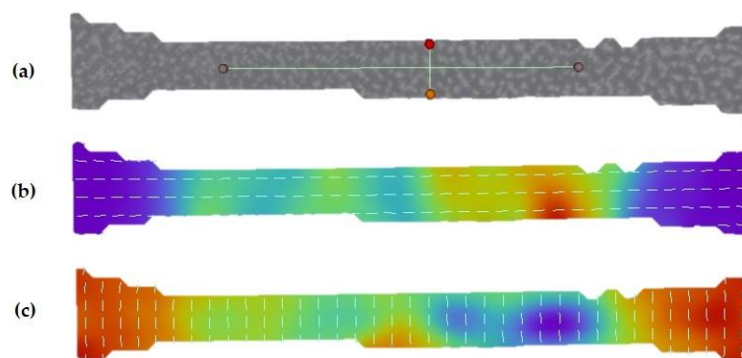


Figure 4. (a) Virtual line gauges; (b) Principal strain in y-direction (axial strain); (c) Principal strain in x-direction (transverse strain).

3.2. Evaluation results

The dependence between stress and strain can be seen in Figure 5. From the linear area from 10 - 30 MPa, the Young's modulus of elasticity was evaluated by linear regression (see Figure 6).

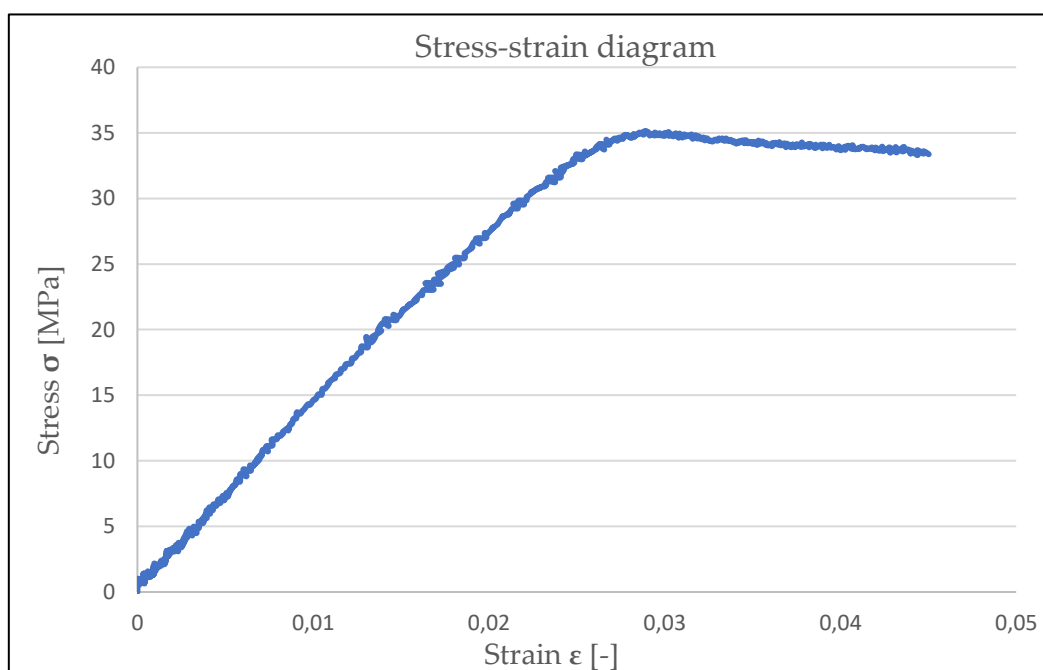


Figure 5. Stress-strain diagram.

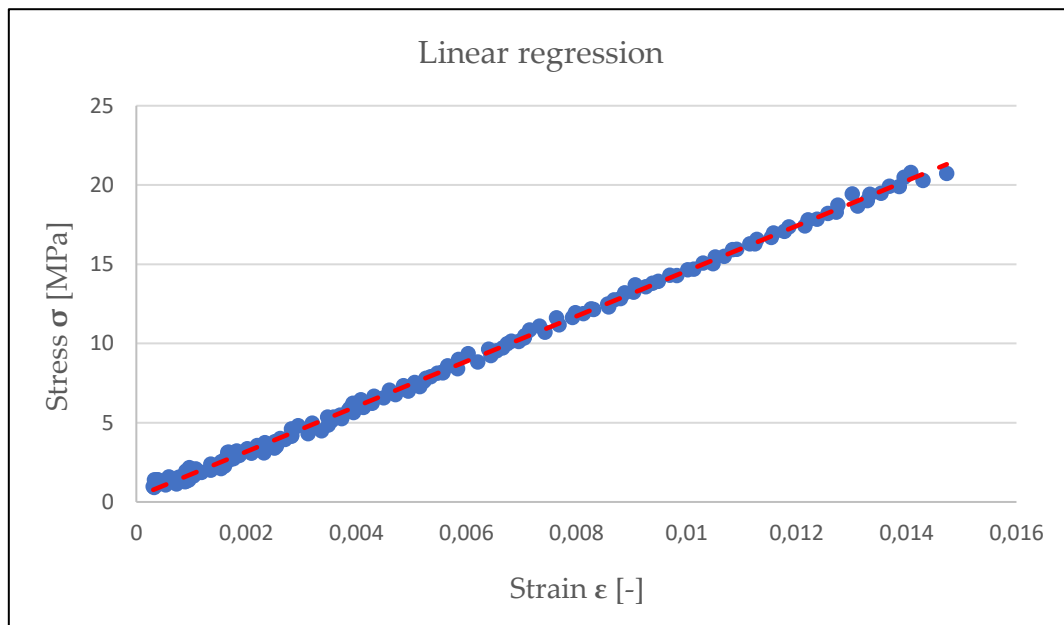


Figure 6. Linear regression of the linear area of stress-strain diagram.

The Poisson's ratio μ was evaluated from the same linear area as ratio of transverse strain ϵ_x to axial strain ϵ_y as follows:

$$\mu = \frac{\epsilon_x}{\epsilon_y} . \quad (2)$$

In Figure 7 is shown Poisson's ratio during the tensile test in the linear area.

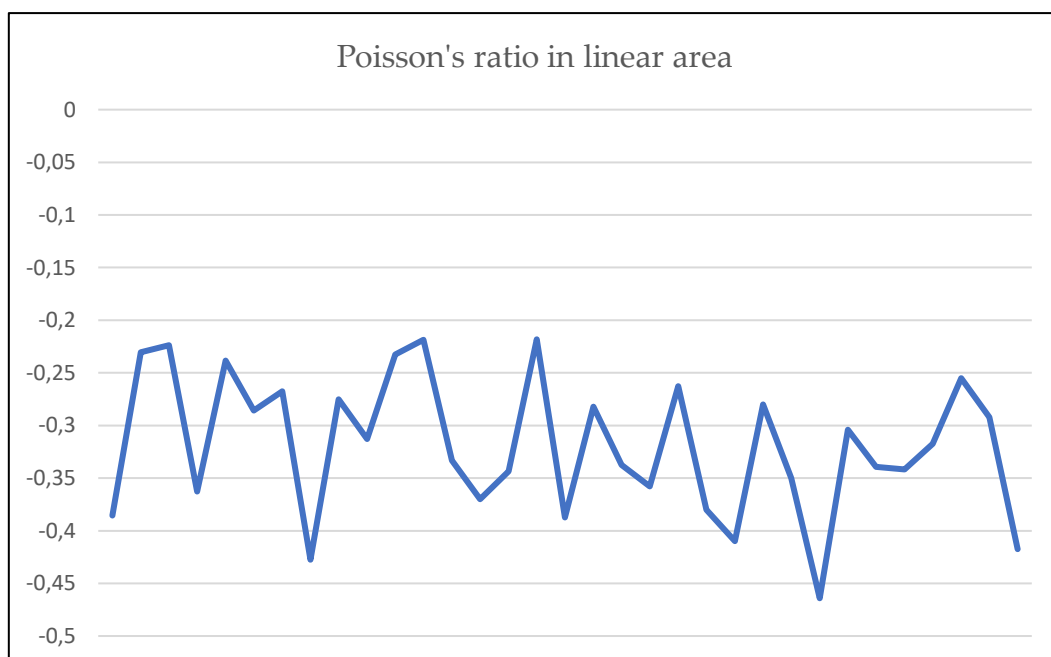


Figure 7. Poisson's ratio in the linear area.

The resultant Young's modulus and Poisson's ratio for both load rates are listed in Table 1 and Table 2.

Table 1. Results of samples loaded at 6 mm/min.

Sample	Young's Modulus [MPa]	Poisson's ratio [-]
VZ_01	1270	0.31
VZ_02	1198	0.3
VZ_03	1132	0.3
Average	1200	0.3

Table 2. Results of samples loaded at 84 mm/min.

Sample	Young's Modulus [MPa]	Poisson's ratio [-]
VZ_01	1269	0.3
VZ_02	1355	0.36
VZ_03	1345	0.36
Average	1323	0.34

4. Discussion

This paper describes the measurement of Young's modulus and Poisson's ratio of the plastic samples manufactured by additive technology using 3D printer. The samples had 100% infill and were tested at two loading speeds 6 and 84 mm/min. The force needed to rupture the samples was in average 1200 N at 6 mm/min loading speed, and 1300 N at 84 mm/min. Material constants are shown in Table 1 and Table 2. The authors will perform measurements on the samples made by the same approach with different internal structure and percentage infill density. Material properties will be determined by conventional methods described in this article. Modal analysis on the plastic plates will also be performed and material properties will be determined by a non-destructive method. The methodology of this approach needs to be described what will be the goal of the research. The measurement results will be used to create a material model in Abaqus CAE software.

Acknowledgments: This work was supported by the Slovak Research and Development Agency under the grant project VEGA No. 1/0500/20 and VEGA No. 1/0355/18.

Conflicts of Interest: The authors declare no conflict of interest.

References

1. Sourabh Tandon, Ruchin Kacker, K.G. Sudhakar, Experimental investigation on tensile properties of the polymer and composite specimens printed in a Triangular pattern, *Journal of Manufacturing Processes*, Volume 68, Part A, 2021, Pages 706-715, ISSN 1526-6125, <https://doi.org/10.1016/j.jmapro.2021.05.074>.
2. John Ryan C. Dizon, Alejandro H. Espera, Qiyi Chen, Rigoberto C. Advincula, Mechanical characterization of 3D-printed polymers, *Additive Manufacturing*, Volume 20, 2018, Pages 44-67, ISSN 2214-8604, <https://doi.org/10.1016/j.addma.2017.12.002>.
3. Andrew Y. Chen, Sebastian Baehr, Austin Turner, Zilan Zhang, Grace X. Gu, Carbon-fiber reinforced polymer composites: A comparison of manufacturing methods on mechanical properties, *International Journal of Lightweight Materials and Manufacture*, Volume 4, Issue 4, 2021, Pages 468-479, ISSN 2588-8404, <https://doi.org/10.1016/j.ijlmm.2021.04.001>.
4. M. Hagara, R. Huňady, F. Trebuňa, Stress Analysis Performed in the Near Surrounding of Small Hole by a Digital Image Correlation Method, In: *Acta Mechanica Slovaca* 18 (3-4), 2014, p. 74-81.
5. ČSN ISO 57-4: Plastics - Determination of tensile properties - Part 4: Test conditions for isotropic and orthotropic fibre-reinforced plastic composites (in Czech), 1998.
6. F. Trebuňa, R. Huňady, P. Frankovský, Metóda digitálnej obrazovej korelácie, *Strojárstvo*, 2011, Online: <https://www.engineering.sk/clanky2/stroje-a-technologie/434-metoda-digitalnej-obrazovej-korelacie>.
7. F. Trebuňa et al, *Optické metódy v mechanike*, TUKE, Košice, 2017, ISBN 978-80-553-3168-3.

Thumb orthosis design using a CAD/CAM method.

Branko Štefanovič^{1,*}, Lucia Bednarcíková¹ and Jozef Živčák¹

¹ Technical university of Košice, Letná 9, 04200, Košice, Slovakia; branko.stefanovic@tuke.sk, lucia.bednarcikova@tuke.sk, jozef.zivcak@tuke.sk

* Correspondence: branko.stefanovic@tuke.sk

Abstract: The aim of this work is a comprehensive methodology of thumb orthosis design using modern technologies. The methodology consists in taking the patient's positive using 3D scanning, CAD design of a 3D model of the current orthotic device and its preparation for additive production. The Artec Eva handheld 3D scanner was used to obtain the 3D positive of the hand, for which an individual thumb orthosis was designed in the freely downloadable CAD software Autodesk Meshmixer. Finally, in the PrusaSlicer software, the orthosis model was positioned on the virtual working platform of the 3D printer and the printing parameters were set.

Keywords: thumb orthosis, upper limb, hand 3D scanning, CAD software, additive manufacturing, FFF

1. Introduction

An orthosis, or orthotic device, is a device applied to the body that replaces lost musculoskeletal function or helps restore lost or damaged function, stabilize, or immobilize a body part, correct position, prevent deformation, protect against injury, or assist in movement. The modern approach to creating orthotic devices begins with the digitization of the human body and its parts to obtain input data from the patient's body for the needs of 3D modeling of orthotic devices in CAD (Computer Aided Design) software and subsequent additive manufacturing (AM). [1-20]

The aim of this article is to design a comprehensive methodology for the design of the thumb orthosis using modern approaches and technologies.

2. Materials and methods

When creating individual prosthetic and orthotic devices, in the first step it is necessary to obtain the shape of the positive or somatometric data of the subject (lengths, circuits, etc.). The traditional way of taking measurements with hand gauges and gaining the positive of a body segment by plastering will be replaced by an innovative method of 3D scanning. Using 3D scanning technology, we obtain an exact copy of a body segment in the form of a 3D model (scale 1: 1), which is then used to design individual devices. The aim is to present the design methodology, so the information about the scanned subject is not relevant.

An Artec Eva handheld 3D scanner (Artec 3D, Luxembourg, Luxembourg) is used to obtain positives. The resolution of the device is suitable for use in prosthetics and orthotics and the operation of this device is simple and intuitive. The subject is recorded in real time in Artec Studio 13 Professional software (Artec 3D, Luxembourg, Luxembourg). The ideal distance from the scanner to the subject to obtain a quality scan is approximately 40 cm. The scan frequency is adjustable (1 to 16 fps). Because the data will be used to design prosthetic devices, it is ideal to scan at the lowest possible frequency (minimum 3 fps) to avoid accidental errors during scanning and to reduce the amount of data obtained. Autodesk Meshmixer software (Autodesk, Inc., San Rafael, CA, USA) will be used to post-process 3D scan models and create digital prosthesis and orthosis models. It is a freely

available modeling software in which it is possible to create and edit 3D objects and contains functions suitable for the design of prosthetic and orthotic devices.

2.1. Arm and forearm 3D scanning

The arm and forearm of the subject are scanned, with the entire upper limb abducted with 30 ° rotation in the shoulder joint and 100 ° flexion in the elbow joint, the thumb in opposition to the fingers and wrists at an extension of 10 ° to 20 °, with the elbow resting on the table for better support. During scanning, it is important that the axis of the scanning beam falls vertically to the scanned surface. The scanner must be moved 360 ° around the forearm, and when scanning the arm, both the dorsal and palmar sides need to be emphasized to capture the thumb area in detail. However, it is not necessary for the fingers to be scanned in detail, as their models will not be used (Figure 1).

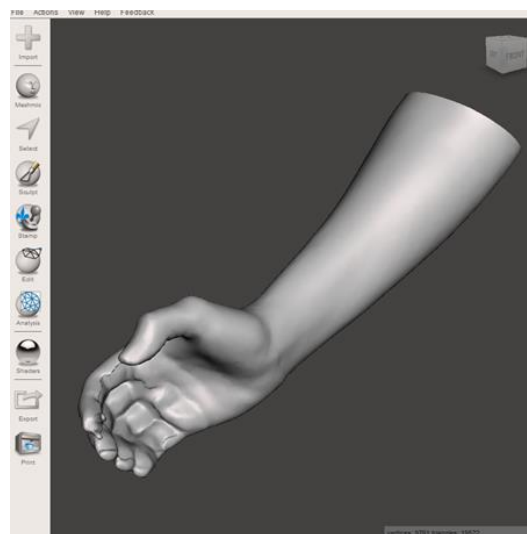


Figure 1. 3D model of the hand and forearm scan.

2.2. Editing a 3D scan model in Meshmixer software

Before any orthosis can be designed for a given segment model, it is necessary to check the surface and adjust the model to the ideal shape. In the first step, it is necessary to determine the number of triangles of the scan model. Each scan model in STL (Standard Triangle Language) format consists of a network of triangles that form the surface of the model. The number of triangles affects the surface accuracy of the model. The higher the number, the more detailed the model and the higher the file size. The reduction of the triangles is set to 95%. This significantly reduces the number of triangles, which also reduces the file size and makes working with the model faster and easier. The next step is to remove parts of the model that are irrelevant to the design of the device. When designing a thumb orthosis, the area proximal to the wrist is irrelevant and thus can be removed. Since the model is used as a basis for the design of the thumb orthosis, it is necessary to smooth the thumb area and its MCP (metacarpophalangeal) joint (Figure 2a). After a final check of the 3D positive and evaluation that the model is sufficient to design an orthotic device, one can proceed to the design of an individual thumb orthosis (Figure 2b).

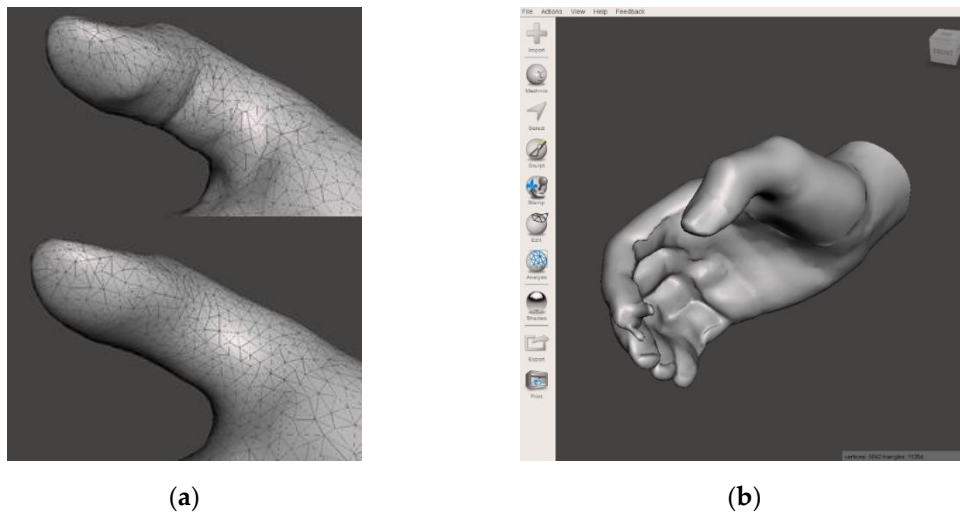


Figure 2. (a) Smoothing the thumb area; (b) Final positive for thumb orthosis design.

2.3. Thumb orthosis design in Meshmixer software

The design of an individual thumb orthosis consists of three parts:

- Sketch of the contact surface of the orthosis;
- Creation of an orthosis shell with offset to the positive surface;
- Orthosis shell thickness adjustment.

In the first step, it is necessary to sketch the contact area of the orthosis with its boundaries on the 3D positive. The orthosis should encircle the thumb with the area of its MCP joint, meaning that its boundaries are drawn transversely across the tip on the distal joint of the thumb and proximal around the carpal bone of the thumb (Figure 3a). After sketching the contact surface of the orthosis, it is necessary to create a gap/offset between the model and the positive, which should compensate for the inaccuracy of 3D printing and allow easier deployment of the device on the affected body segment. The distance of the contact surface of the orthosis from the 3D scan is set to 1 mm. This creates a shell with a constant distance from the surface of the 3D positive. The last step is to adjust the shell thickness. The thickness is set to 1.5 mm. After the final inspection of the 3D orthosis model (Figure 3b) and evaluation that the model is suitable to produce the current device, it is necessary to export the model in STL format and it can be imported into the 3D printer software.

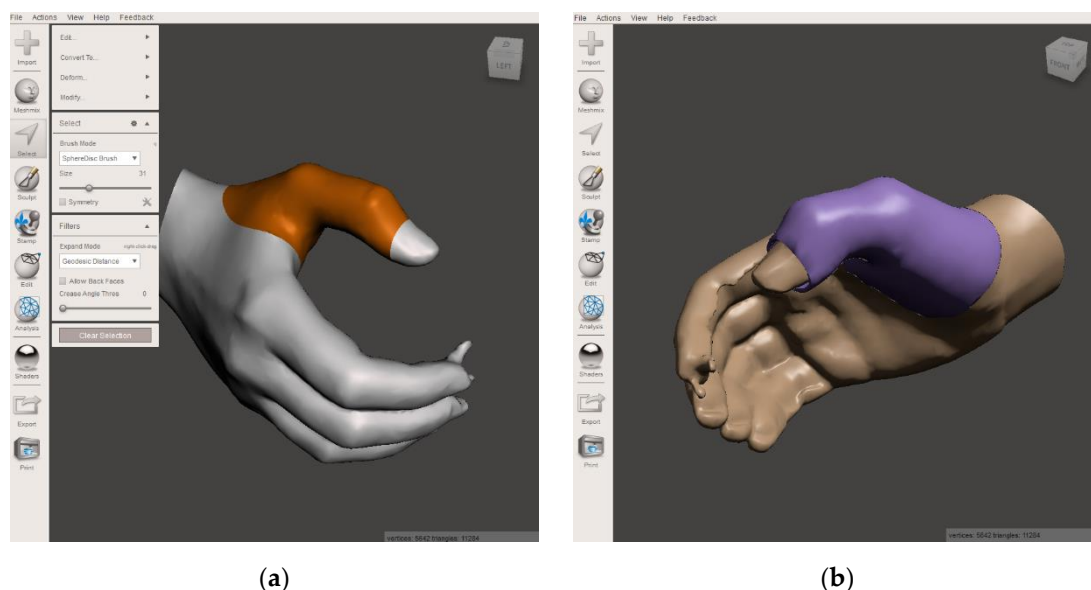


Figure 3. (a) Sketch of the contact surface of the thumb orthosis; (b) Final 3D model of a thumb orthosis.

3. Results

Preparation of CAD models for additive production consists in uploading the model to software designed to set individual parameters of 3D printing. The choice of software depends on the additive production technology used. Since prosthetic and orthotic aids are designed for production using FFF (Fused Filament Fabrication) technology, a suitable software for setting printing parameters is, for example, the freely downloadable PrusaSlicer (Prusa Research, Prague, Czech Republic).

In the first step, it is necessary to select the software mode, the type of printer used to produce the 3D model, the setting of the printing accuracy, the type of filament used to produce the object and the fill density of the produced object. After determining these basic parameters, it is necessary to import the 3D model into the software interface. After importing the model, you need to check and, if necessary, overwrite the print settings in the upper horizontal bar of the software. In the Print Settings column, it is possible to select preset print parameters of the model in System Presets, or to manually set individual print parameters (model layers, model fill, model edges, support structures, print speed, print settings, cooling, etc.).

After selecting the preset profiles and defining all the necessary parameters of printing, filament, and printer, it is advisable to correctly position the 3D model of the orthotic device. When positioning the thumb orthosis model, it is important to orient the model so that the thumb axis is vertical to the printer's working platform (Figure 4a). In this case, no support structures will be generated on the inner surface of the orthosis, and due to the orientation of the layering, the contact surface will be of better quality (Figure 4b).

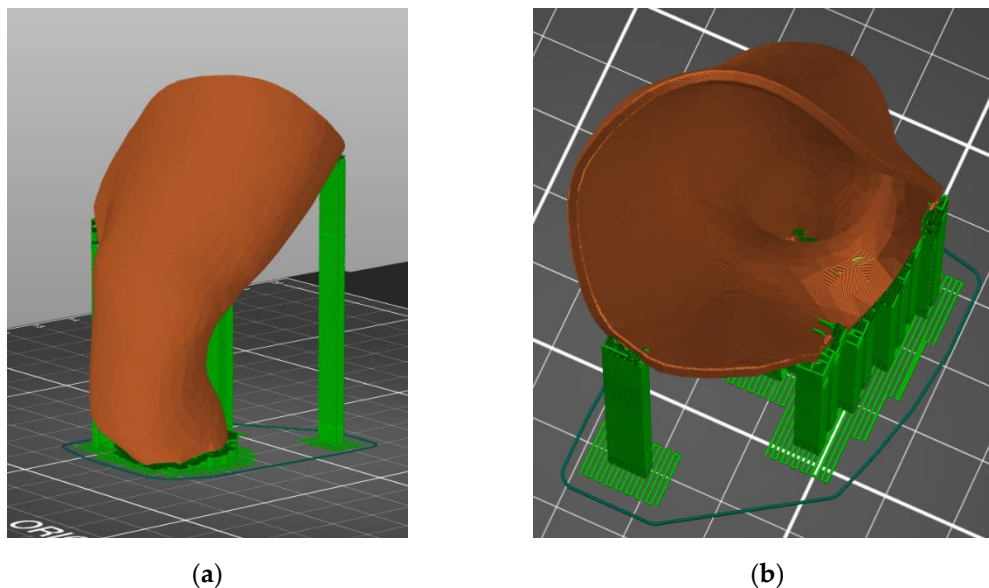


Figure 4. (a) Position of the 3D thumb orthosis model in the 3D printer software interface; (b) Absence of support structures on the contact surface of the thumb orthosis.

After setting important production parameters and thorough positioning of the model on the virtual platform, it is necessary to export this arrangement to a G-code file, which is a file that is supported by desktop 3D printers of the FFF type. It is loaded into the printer's memory and production is easily activated on it.

4. Discussion

Innovative methods in the hands of experts replace the unpleasant and time-consuming manual acquisition of the positive. The 3D scanning technique is used for data collection. The data obtained is processed by a computer program that creates a three-dimensional image of the model, where the orthopaedic technician can make corrections to create the final positive model. Software tools allow the professional to use a wide range of

adjustment tools, including rotation, rotation, scaling, levelling, and adding pressure or relief. The creation of digital models also brings other possibilities, such as the analysis of possible problems that may arise because of design, material selection and in connection with the production process. A general feature of the AM method is that the production is not carried out by removing the material as in milling, but by gradually adding material which is in the form of powder, granulate or filament in thin layers which are heat-bonded to each other. Thanks to AM, it is possible to produce complicated products that cannot be produced with everyday technologies, or, due to their complicated design, the financial costs of their production would be too high. Other advantages are production without the use of moulds and tools and the possibility of production from demanding, high-temperature materials. However, orthoses made using additive technologies require postprocessing, which usually consists of a surface treatment that varies depending on the technology used and the user's requirements.

Positioning models on the printer's virtual work platform is very important in terms of print efficiency and output quality. Depending on how the model is positioned, a support structure is generated, and the orientation of the layers is also determined. From this point of view, it is important to position the model so that no support structures are created on the contact surfaces of the orthosis. The support structures in these places can affect the quality of the surface, which can deform the shape of the contact surface and thus negatively affect the overall quality of the device. However, the orientation of the layering is important in terms of strength and surface quality of the model. Because the possibility of fracture between the individual layers must always be considered, it is important to position the devices so that cracks do not form on the device after random external forces (especially bending). Layering also affects the local surface quality of the models. Since the accuracy of the X and Y axes is higher in 3D printing, the surface of the model is more accurate on surfaces oriented vertically to the working platform. Therefore, it is necessary to position the thumb orthosis model as presented in the results.

5. Conclusions

The methodology of design and preparation of the thumb orthosis using modern approaches was presented. The modern approach to creating an orthotic device is to digitize the hand using 3D scanning technology to obtain the positive of the patient's body segment for the needs of 3D modeling of the orthotic device in freely downloadable CAD software and subsequently preparing it for additive production. The procedures given in the methodology can also be used in the production of other prosthetic and orthotic aids and devices, in the design of new, low-cost prostheses and orthoses, and for educational purposes in the field of prosthetics and orthotics.

Acknowledgements: This article was developed with support Slovak Research and Development Agency under the contract No. APVV-19-0290, project KEGA 041TUK-4/2019 Design of progress algorithms in additive technologies for the educational process in biomedical engineering, project KEGA 023TUK-4/2020 Increasing the synergy of methods of teaching biophysics using laboratory equipment and diagnostic devices aimed at measuring physical and technical quantities and the achieved results were created within the investigation of the project no. 2018/14432: 1-26C0, which is supported by the Ministry of Education, Science, Research and Sport of the Slovak Republic within the provided incentives for research and development from the state budget in accordance with Act No. 185/2009 Coll. on incentives for research and development.

Conflict of interests: Authors declare no conflict of interests.

References

1. Živčák J. et al. Individuálna ortotika horných končatín - 1. ed. Košice. 2016. p. 179 s. ISBN 978-80-553-3110-2.
2. Bowers D.M., Chui K.K. Neurological and Neuromuscular Disease Implications for Orthotic Use. In: Orthotics and Prosthetics in Rehabilitation. 4th ed. 2020. p. 259-293. DOI: 10.1016/B978-0-323-60913-5.00010-6.
3. Lunsford T.R., Contoyannis B. Materials Science. In: Atlas of Orthoses and Assistive Devices. 5th ed. Philadelphia. 2019. p. 7-41, DOI: 10.1016/B978-0-323-48323-0.00002-0.
4. Supan T.J. Principles of Fabrication. In: Atlas of Orthoses and Assistive Devices. 5th ed. Philadelphia. 2019. p. 42-48. DOI: 10.1016/B978-0-323-48323-0.00003-2.
5. Jorge M. Orthotics and Prosthetics in Rehabilitation: Multidisciplinary Approach. In: Orthotics and Prosthetics in Rehabilitation. 4th ed. 2020. p. 2-13. DOI: 10.1016/B978-0-323-60913-5.00001-5
6. International Organization for Standardization: Additive manufacturing [Interne]. Dostupné na: <https://www.iso.org/obp/ui/#iso:std:iso-astm:52900:ed-1:v1:en>.
7. Dechev N., Cleghorn W. L., Naumann S. Multiple fingers, passive adaptive grasp prosthetic hand. Mechanism and machine theory, 2001, 36.10: 1157-1173.
8. Zuniga J. et al. Cyborg beast: a low-cost 3d-printed prosthetic hand for children with upper-limb differences. BMC research notes, 2015, 8.1: 10.
9. Zuniga J. M., et al. An open-source 3D-printed transitional hand prosthesis for children. JPO: Journal of Prosthetics and Orthotics, 2016, 28.3: 103-108.
10. Palousek D. et al. Pilot study of the wrist orthosis design process. Rapid Prototyping Journal, 2014, 20.1: 27-32.
11. Mohammed M.I., Pearse F. Design and Additive Manufacturing of a Patient Specific Polymer Thumb Splint Concept. In: Solid Freeform Fabrication 2018: Proceedings of the 29th Annual International Solid Freeform Fabrication Symposium – An Additive Manufacturing Conference. November 2018.
12. Buonamici F. et al. A Practical Methodology for Computer-Aided Design of Custom 3D Printable Casts for Wrist Fractures. The Visual Computer, 36:375-390. DOI: <https://doi.org/10.1007/S00371-018-01624-Z>.
13. Barios-Muriel J.B. et al. Advances in Orthotic and Prosthetic Manufacturing: A Technology Review. Materials, 2020, 13:295. DOI: 10.3390/Ma13020295.
14. Fitzpatrick A. et al. Design Optimization of a Thermoplastic Splint. In: Solid Freeform Fabrication 2017: Proceedings of The 28th Annual International: Solid Freeform Fabrication Symposium – An Additive Manufacturing Conference. 2017.
15. Chen Y.J. et al. Application Of 3d-Printed and Patient-Specific Cast for The Treatment of Distal Radius Fractures: Initial Experience. 3d Printing in Medicine, 2017, 3:11:1-9. DOI: 10.1186/S41205-017-0019-Y.
16. Li J., Tanaka H. Rapid Customization System For 3D-Printed Splint Using Programmable Modeling Technique – A Practical Approach. 3d Printing in Medicine, 2018, 4:5:1-21. DOI: 10.1186/S41205-018-0027-6.
17. Fernandez-Vincent M., Chust A.E., Conejero, A. Low Cost Fabrication Approach For Thumb Orthoses. Rapid Prototyping Journal, October 2017, 23:6:1020-1031. DOI: [Doi.Org/10.1108/Rpj-12-2015-0187](https://doi.org/10.1108/Rpj-12-2015-0187).
18. Redaelli D.F. et al. 3D Printing Orthopedic Scoliosis Braces: A Test Comparing FDM with Thermoforming. The International Journal of Advanced Manufacturing Technology. 2020:111:1707–1720. DOI: 10.1007/S00170-020-06181-1.
19. Hale L., Linley E., Kalaskar, D.M. A Digital Workflow for Design and Fabrication of Bespoke Orthoses Using 3d Scanning And 3D Printing, A Patient-Based Case Study. Scientific Reports, 2020, 10:7028. DOI: 10.1038/S41598-020-63937-1.
20. Štefanovič B. et al. Arm and Forearm Scanning Methodology for The Development of An Orthotic Device for Tetraplegic Patients. In: Proceedings Of 3dbody.Tech 2020 - 11th International Conference and Expo On 3D Body Scanning and Processing Technologies. 17-18 November 2020. Online/Virtual.



Numerical simulation of clinching of HCT600X+Z steel sheets

Denis Cmorej¹, Ľuboš Kaščák¹

¹ Affiliation 1; Technical University of Košice, Department of Technology, Materials and Computer Aided Production; denis.cmorej@tuke.sk; lubos.kascak@tuke.sk

* Correspondence: denis.cmorej@tuke.sk; Tel.: +421 55 602 3519

Abstract: Nowadays, there are many reasons for using high-strength steel sheets in car body manufacturing. Car producers choose steel with good formability and the ability to absorb impact energy. DP (dual-phase) steels satisfy the above requirements. The application of DP steel sheets has led to the development of new materials joining techniques. Mechanical joining - clinching, is the innovative technique to join these progressive materials. In practice, simulation programs are used to optimize the joining processes before the joining process is implemented. One of the most used software for simulating the clinching process is Simufact Forming 16.0. Simufact Forming 16.0 software was used to simulate the joining of HCT600X+Z steel sheets. Due to the axisymmetric nature of the clinching process, the simulation was simplified to a 2D representation. The result of the simulation was compared with metallographic images after the clinching process.

Keywords: clinching, Simufact Forming, numerical simulation

1. Introduction

One of the most important problems in the automotive industry is the safe design, lightweight, and enhanced crash response of specific auto-body structures. These objectives lead to the increasing adoption of high-strength steel sheets for specific parts of auto-body members [1]. DP steels satisfy the above requirements. The dual-phase steels offer a combination of high strength and good formability because of their microstructure in which the hard martensitic or bainitic phase is dispersed in a ductile ferritic matrix. This type of steel is characterized by a good ability to redistribute stress and improve mechanical properties, including yield strength [2-4]. Clinching is an innovative technique to join also these progressive materials. The principle of clinching consists of interlocking the materials to be joined together using a special punch and a die. At the moment of contact of the material and the die, the material flows to the sides and creates a joint. The interlocking creation is necessary for the mechanical joints to carry the load. The active parts of the clinching tools are a punch, a die, and a sheet holder. By moving the specially shaped punch, the joined steel sheets are drawn into the cavity of the die. The die cavity is specially shaped so that interlocking occurs between the joined sheets [5-7]. In practice, simulation programs are used to optimize the joining processes before the joining process is implemented. One of the most used software for simulating the clinching process is Simufact Forming 16.0 [8,9]. The paper deals with the simulation of the process of mechanical joining - clinching of high-strength dual-phase steel sheets HCT600X+Z.

2. Materials and Methods

Used materials

In the experiment, one type of material was used – dual-phase steel HCT600X+Z. The thickness of the tested steel sheet was 1.5 mm. HCT600X+Z steel sheet was hot-dip galvanized on both sides. Table 1 shows the basic mechanical properties of the HCT600X+Z. The chemical composition of the steel sheets is shown in Table 2. The samples were cut to

a size of 40 x 90 mm, with an overlap length of 30 mm – see Figure 1. It was not necessary to clean the samples before the process of clinching. Figure 1 shows a test sample according to STN 05 1122.

Table 1. Basic mechanical properties of the observed materials

Material	Thickness [mm]	R _{p0,2} [MPa]	R _m [MPa]	A ₈₀ [%]
HCT600X+Z	1,5	373	606	24,8

Table 2. Chemical composition of the observed materials (% wt)

Material	Chemical composition				
HCT600X+Z	C	Mn	Si	P	Al
	0,08	1,78	0,01	0,014	0,045
	Nb	Ti	V	Mo	Cr
	0,002	0,001	0,002	0,179	0,211

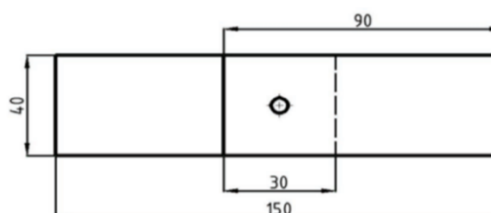


Figure 1. Sample dimensions according to STN 05 1122

Metallographic observation

In metallographic observation, the changes in the microstructure of HCT600X+Z material were observed. Interlocking, the thickness of the bottom of the joint, the thickness of the neck of the joint as well as the defects of the joints formed by the clinching were observed too. Microscopic observation was performed by light optical microscopes KEYENCE VHX- 5000 – see Figure 2.

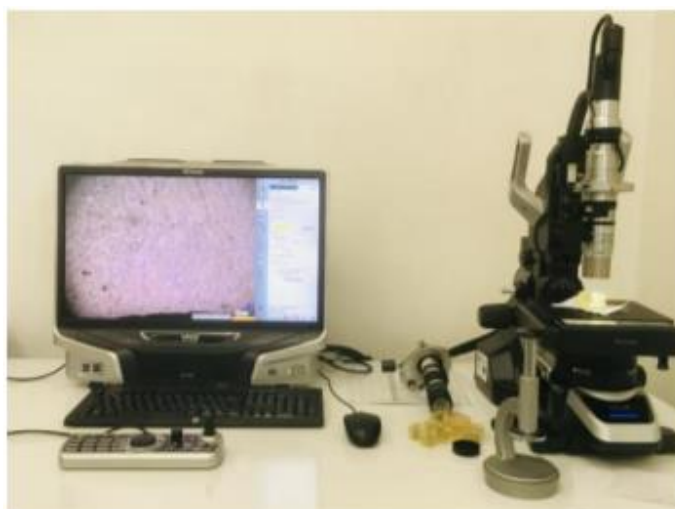


Figure 2. KEYENCE VHX- 5000

Clinching

Clinching is an innovative technique to join progressive materials. The principle of clinching consists of interlocking the materials to be joined together using a special punch and a die. At the moment of contact of the material and the die, the material flow to the sides and creates a joint. The active parts of the clinching tools are a punch, a die, and a sheet holder. By moving the specially shaped punch, the joined steel sheets are drawn into the cavity of the die. The die cavity is specially shaped so that interlocking occurs between the joined sheets. The process of clinching is demonstrated in Figure 3. The hydraulic press machine ZD 40 was used for clinching. A punch with a diameter of $\varnothing 5$ mm and a die with a diameter of $\varnothing 8$ mm were used. The parameters of clinching are described in Table 3.

Table 3. The parameters of clinching

Material	Number of joined sheets	Pressing force F [kN]	Punch diameter	Die diameter
HCT600X+Z (1,5mm)	2	70	$\varnothing 5$ mm	$\varnothing 8$ mm

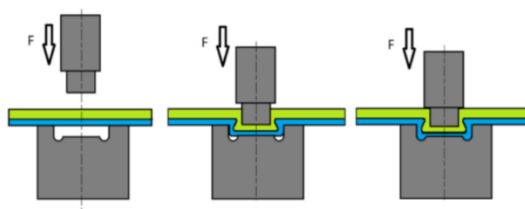


Figure 3. The process of clinching

Simufact Forming 16.0

Simufact Forming is a simulation software for users working with the technology of forming. Simufact Forming allows for both two-dimensional (axisymmetric and planar) and three-dimensional simulations on the same graphical user interface. Different types of materials common to forming technology can be simulated. In practice, simulation programs are used to optimize the joining processes before the joining process is implemented [8,9]. The working environment of the simulation program is shown in figure 4.

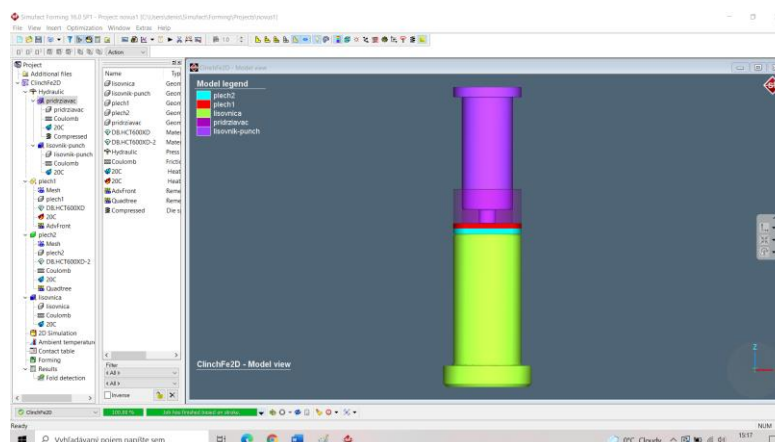


Figure 4. The working environment of the Simufact Forming 16.0

The Simufact Forming 16.0 software was used for the optimization of the joining process and mathematical representation of the problem of mechanical joining – clinching of two dual-phase steel sheets of HCT600X+Z. As part of the optimization of the joining process, different values of the punch stroke were compared within the simulations – see Figure 5. The optimal mechanical joint was obtained at the values of the punch stroke 4mm. The task was simplified on a 2D model because the tools and the joint itself are axially symmetrical. For this reason, the anisotropy of the joined materials will not be considered in the calculation. The basic parameters that had to be defined in the simulation include the friction coefficient, the holding force, and the distance of the punch stroke. In the process of the simulation, the punch can only be moved in the vertical position, with the punch making a vertical downward movement at a punch stroke of 3mm; 3,25mm; 3,5mm; 3,75mm and 4mm. When applying values above 4 mm, a defect occurs in the joint area. The contacts between the tools and joined materials as well as the contacts between the joined materials were modeled as frictional contacts. Between tool and sheet was defined special friction coefficient of 0.12 and between sheets was defined special friction coefficient of 0.2. The last boundary condition is a special sheet holder force of 100 N that acts on the body of the sheet holder to fix the joined materials during the simulation of the mechanical joining. At the moment the prescribed distance has been reached, the punch performs a backward movement to the starting position while at the same time the force of the sheet holder ceases to act. The punch, die and sheet holder were modeled as perfectly stiff, known as non-deformable bodies. The joined sheets were modeled as deformable bodies. It was subsequently defined the finite element mesh for joined materials (dual-phase steel sheets – HCT600X+Z) consisted of 100 elements.

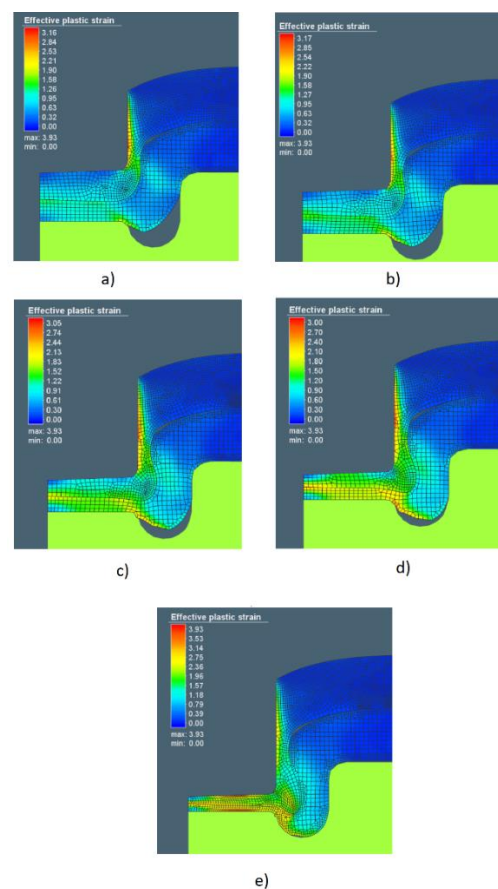


Figure 5. Influence of punch stroke height on joint formation a) punch stroke distance 3mm b) punch stroke distance 3,25mm c) punch stroke distance 3,5mm d) punch stroke distance 3,75mm e) punch stroke distance 4mm

3. Results

When applying 3mm; 3.25mm; 3.5mm and 3.75mm values of punch stroke height, there was no optimal joint of the sheets in the neck area of the joint (see Fig. 5). The optimal mechanical joint was obtained at the values of the punch stroke 4mm. When applying values above 4 mm, a defect occurs in the joint area.

Figure 6 shows the development of plastic deformation during the joining process of HCT600X+Z steel sheets in the 3 characteristic steps.

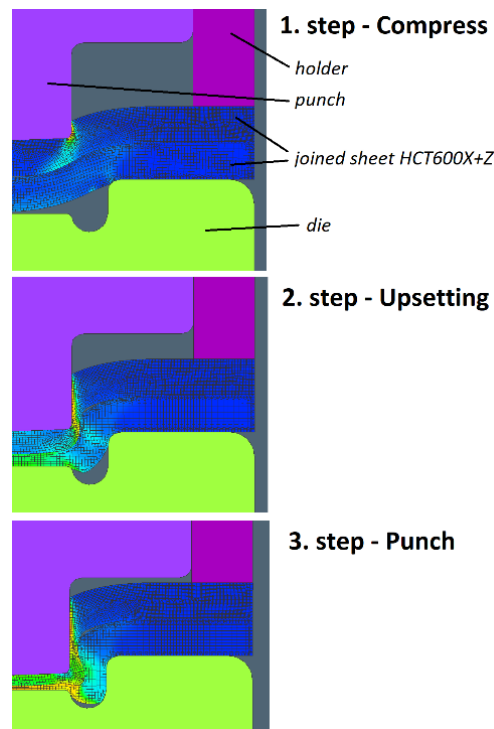


Figure 6. development of plastic deformation during the joining process

For better visibility of the presented results, the finite element mesh was used. The most critical area during clinching is the sheet metal on the punch side. The maximum plastic deformation during the process of clinching is located just in the upper sheet at the point where it is excessively thinned. This area is known as the area of the neck of the joint and is considered critical in terms of the process of clinching. It is possible to verify simulation to compare to results of a real joining process.

Figure 7 shows a comparison of the cross-sections between the real joint created by clinching (left side) and the joint resulting from the simulation (right side). Based on the results, real values of mechanical joining as clinching can be compared with values after simulation, such as the thickness of individual sheets or the interlocking between the joined sheets (called the "S" shape of the sheets) can be compared. Based on the visual comparison of the results, it is possible to state with certain tolerance that the simulation results correspond to the result of the actual joining process.

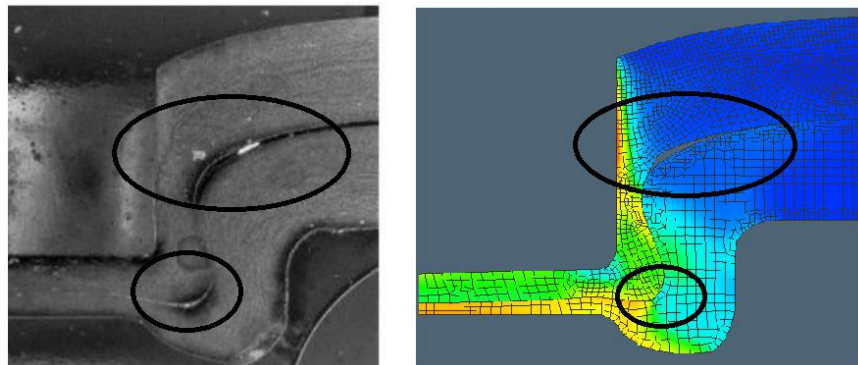


Figure 7. Comparison of the cross-sections between the real joint created by clinching (left side) and the joint resulting from the simulation (right side)

5. Conclusions

The paper presented the simulation of the clinching process. The simulation has been simplified into 2D conditions based on the axial symmetry of the entire joining process. The results of the simulation of the process of clinching in the form of the representation of the plastic deformation in the steel sheets during the individual mechanical joining stages were observed.

Based on the results of the performed experiments and based on the simulation, it can be stated:

- The joints created by clinching are classified as an environmentally friendly joining technology, they are less harmful to the environment, especially when joining hot-dip galvanized steel sheets.
- Based on the results, real values of mechanical joining as clinching can be compared with values after simulation, such as the thickness of individual sheets or the interlocking between the joined sheets (called the "S" shape of the sheets) can be compared.
- Based on the visual cross-section comparison of the results, it is possible to state with certain tolerance that the simulation results correspond to the result of the actual joining process.

Acknowledgments: The author is grateful for the support of experimental works by project **VEGA 1/0259/19** - Research of innovative forming and joining methods to improve the performance of thin-walled components.

References

1. L. Kaščák, et al.; Application of modern joining methods in car production. *Processes Examples Strength*. Rzeszów, pp.143.
2. K. Bzowski, et al.; Application of statistical representation of the microstructure to modeling of phase transformations in DP steels by solution of the diffusion equation. *Procedia Manufacturing*. 2018, vol. 15, pp. 1847-1855.
3. P. R. Spena; Hybrid laser arc welding of dissimilar TWIP and DP high strength steel weld. *Journal of Manufacturing Processes*. 2019, vol. 39, pp. 233-240.
4. S. Qin, et al.; Influence of phase and interface properties on the stress state dependent fracture initiation behavior in DP steels through computational modeling. *Materials Science and Engineering: A*. 2020, vol. 776, 138981.
5. F. Lambiase; Influence of process parameters in mechanical clinching with extensible dies. *The International Journal of Advanced Manufacturing Technology*. 2013, vol.66, pp. 2123-2131.
6. C. Shi, et al.; Forming mechanism of the repairing process on clinched joint. *Journal of Manufacturing Processes*. 2020, vol. 50, pp.329-335.
7. L. Kaščák, et al.; Finite element calculation of clinching with rigid die of three steel sheets. *Strength of Materials*. 2017; vol. 49, pp. 488-499.
8. L. Potgorschek, et. al.; Numerical simulation of hybrid joining processes: self-piercing riveting combined with adhesive bonding. *Procedia Manufacturing*. 2020, vol. 47, pp. 413-418.

9. P. Zbigniew, et.al.; Determination of the critical damage for 100Cr6 steel under hot forming conditions. Engineering Failure Analysis. 2021, vol. 128, 105588.



Design of an internal combustion engine using RCCI technology

Pavol Tarbajovský ^{1*}, Michal Puškár ²

¹ Faculty of Mechanical Engineering, TU Košice, Letná 9, 040 01 Košice, Slovak Republic; pavol.tarbajovsky@tuke.sk

² Faculty of Mechanical Engineering, TU Košice, Letná 9, 040 01 Košice, Slovak Republic; michal.puskar@tuke.sk

* Correspondence: e-mail@e-mail.com: pavol.tarbajovsky@tuke.sk; Tel.: +421 55 602 2355

Abstract: Dual-fuel mode internal combustion engines need perfect, special conditions to ignite mixture of air and fuel without usage of spark plug in the best possible moment which has high combustion efficiency. The homogenous conditions of the air-fuel mixture in the cylinder are even more demanding. During the lifetime of an internal combustion engines there were developed many ignition concepts, but the perfect mixing of fuel and air is essential for the most effective ignition, which is a real technical challenge. The solutions for dual-fuel engines contain the complexity of these problems which leads to the development of ignition systems used in internal combustion engines. The text shows basic working principle of this type combustion and construction idea how such an engine could be constructed for testing. However, the usage of dual-fuel system in the internal combustion engines needs much more research, testing and solutions necessary for its correct operation.

Keywords: Dual-fuel system; RCCI; homogenous air-fuel mixture

1. Introduction

The new type of ignition system, RCCI which stands for reactivity controlled compression ignition, has been found mainly to effectively increase burning of biofuels in diesel engines with reduced emissions of smoke and improved performance. With lower levels of smoke, decreased NO emissions can be reached simultaneously. The operation of RCCI is achieved by injecting two fuels with characteristics opposite to each other, which means, that one fuel has low reactivity and second fuel has high reactivity. Reactivity stratification is then created inside the combustion chamber by these two types of fuel. As low reactivity fuel injected into the combustion chamber can be considered alcohols because of their characteristics which are for example lower cetane number, lower viscosity, good vaporization characteristics and also higher self-ignition temperature. As high reactivity fuel can be considered this which have higher cetane number and lower self-ignition temperature, which is injected directly into the chamber near the end of combustion stroke, the fuel with low reactivity is pre-mixed with intake air, which can be achieved by fitting simple carburetor at the intake manifold and then sucked into the cylinder. Instead of carburetor, port or direct injection of alcohols can be implemented mainly to avoid problems which can occur during the use of carburetor.

High reactivity fuel initiates the combustion of low reactivity charge mixture. Oxygen enrichment combined with the RCCI engine is another option for further emission reduction and increasing performance. This type of combustion simultaneously reduces particulate matter and NO_x emission. RCCI mode increases Brake thermal efficiency (BTE) from 29.1% to 33.5% but with oxygen enrichment this efficiency value can raise to

36.2%. UHC and CO emissions are in the RCCI engine higher, but can be considerably reduced at all loads by using oxygen enrichment. In general, high BTE combined with very low emissions at all loads can be achieved by combining electric injection RCCI engine and oxygen enrichment.

RCCI mode increased BTE from 29.1% to 33.5% and incorporation of oxygen enrichment further enhanced BTE and efficiency of 36.2% can be achieved. In general, UHC and CO emissions are higher in RCCI engine, but oxygen enrichment can decrease these emissions considerably at all loads. It is possible to achieve high BTE and very low emissions at all loads by combining RCCI with electronic injection and oxygen enrichment [1-4].

2. RCCI technical principles

The change of combustion chamber and power supply system modifications are needed for an operation of the internal combustion engine in RCCI mode. Combustion chamber which can enable work of the single fuel, CI engine, will have problems with swirl ratio of low reactivity fuel and also hot spots on its surface can occur, which excludes the possibility of using low reactive fuel with octane number that does not secure resistance to spontaneous combustion at the hot surface of the combustion chamber. Additional cooling of some elements, which can be excessively heated up during the combustion process, is used in this case (e.g. injectors). In the Figure 1, the shape of combustion chambers of the RCCI engine are shown (with different compression ratio options) in compare to modern CI engines' combustion chamber.

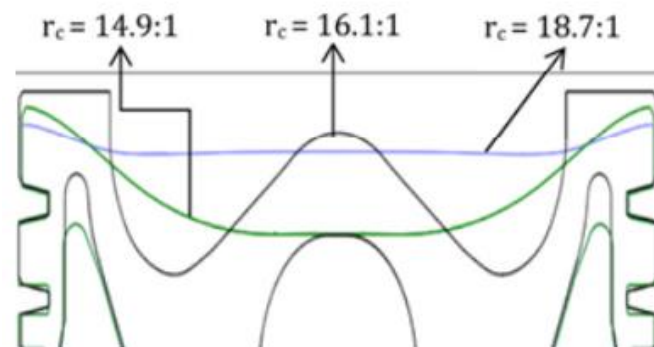


Figure 1. Comparison of classic CI piston and RCCI with the combustion chamber inside.

The RCCI engine combustion chamber differs from the classical CI diesel engine. The air-fuel mixture swirl ratio must be higher; combustion chamber surface can be much smaller and overall shape softer. Figure 2 shows cross section of the piston used in stock commonly used engine and piston which can be used in RCCI engine.

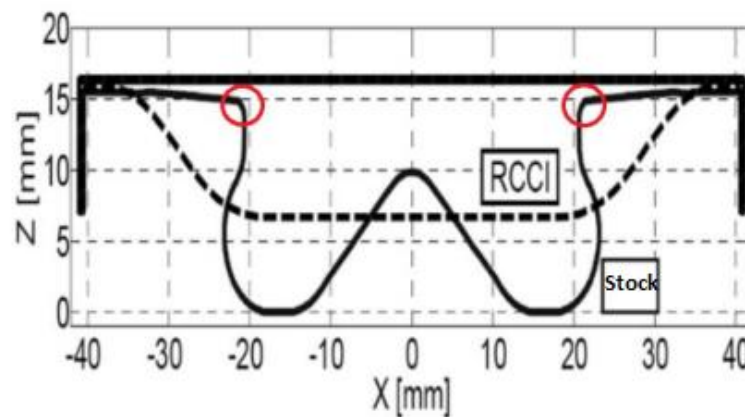


Figure 2. Cross-section drawing of modified piston used in RCCI engine (dotted line) and stock piston in commonly used engine.

Injection of high reactivity fuel in RCCI engine differs from classic diesel engine. High reactivity fuel injected directly in classic CI engine requires usage of combustion chamber which is located in the piston, but thus combustion chamber is designed only for one type of fuel. Dual-fuel mode needs different shape of combustion chamber. In the entire in-cylinder space over the piston there is low-reactive fuel which means that high reactivity fuel is delivered to an area which is already filled. This fact places an issue which cannot be solved only by changing injector design alone but the shape of stock piston must be custom made. Correct air-fuel mixture swirl ratio is very important to ensure right combustion of the charge. As shown in the Figure 2, red edges of the RCCI engines' combustion chamber represent serious barrier to the correct distribution of the injected highly reactive fuel inside the combustion chamber. According to researches, modified stock piston into the RCCI piston has proven an increase in the thermal efficiency of an engine. In the Figure 3 comparison of the stock and the RCCI piston is shown.

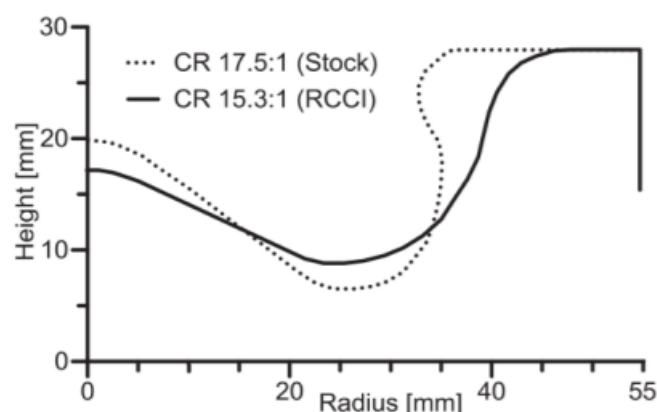


Figure 3. Piston bowl geometry differences in different compression ratios for the RCCI engine, and the conventional diesel engine.

RCCI engines' fuel supplying depends on the size of the engine and also on its' construction. In smaller commonly used engines in land vehicles like trucks and cars is space of cylinder head limited for usage of more than one injector. In such engines fuel supply is installed like shown in the Figure 4, where low reactive fuel is injected by Port Fuel Injection method while high reactive fuel can be directly injected into the combustion chamber (cylinder).

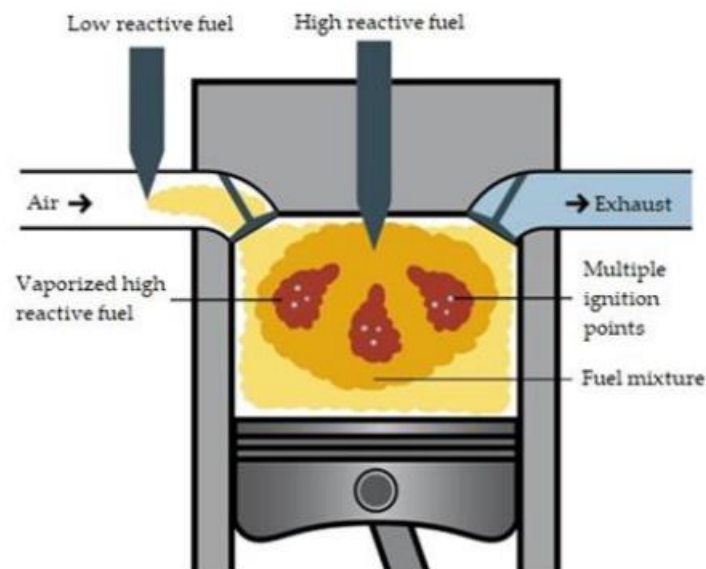


Figure 4. Ignition and combustion in the RCCI engine.

That fuel injection technology is commonly used in all engines capacity but the idea of the fuel is delivered may differ, but carburetor usage or the gaseous fuel inlet valve in the bigger engines are not basically different from each other with well-known technical construction [1-4].

3. Technical solution

With the suitable research done, construction solution of RCCI engine has been done. According to information about amount of injected fuel into the combustion chamber, custom piston has been designed. This custom piston used for RCCI mode of combustion engine can be seen in the Figure 5.



Figure 5. Custom design of piston for RCCI engine.

For technical/construction solution was chosen four cylinder, turbocharged internal combustion engine in which three cylinders will run in standard, SI (Spark Ignition), mode and one cylinder will run in RCCI (Reactivity Controlled Compression Ignition) mode. The cylinder in RCCI mode will be naturally aspirated what required modifications for exhaust manifold and also modifications for exhaust system. Modifications are shown in the Figure 6.

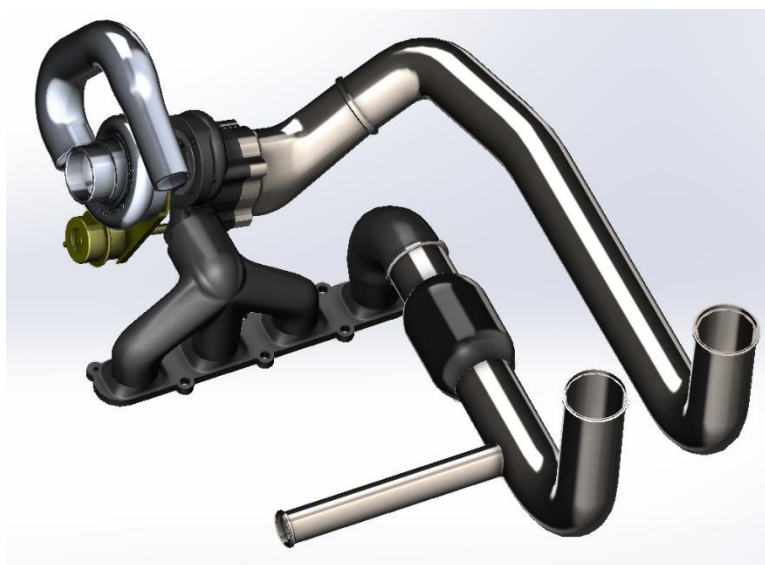


Figure 6. Exhaust system modifications.

This engine design includes solution which is used mainly in marine engines where intake fresh air is mixed with gases from the combustion chamber which are already burned (cooled down by catalytic convertor) and recirculate into the intake manifold, controlled by valve, and low reactivity fuel injected just before the entrance into the combustion chamber, shown in the Figure 7.



Figure 7. Technical solution of intake air and recirculation of already burned gases.

Since the one cylinder works in RCCI mode, implementation of second injector was needed. First fuel injector, which injects low reactivity fuel, is placed in the intake manifold right before combustion chamber while the second fuel injector is placed in the cylinder head and sprays high reactivity fuel directly into the combustion chamber equipped with custom designed RCCI piston. The fueling and custom shaped piston can be seen in the Figure 8.

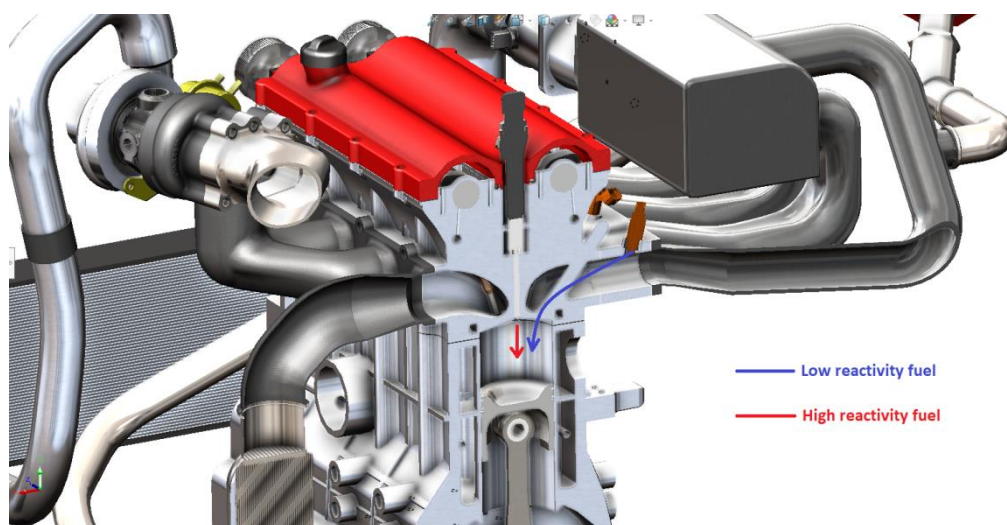


Figure 8. Injectors position.

Whole engine design, with used modification can be seen is in the Figure 9.

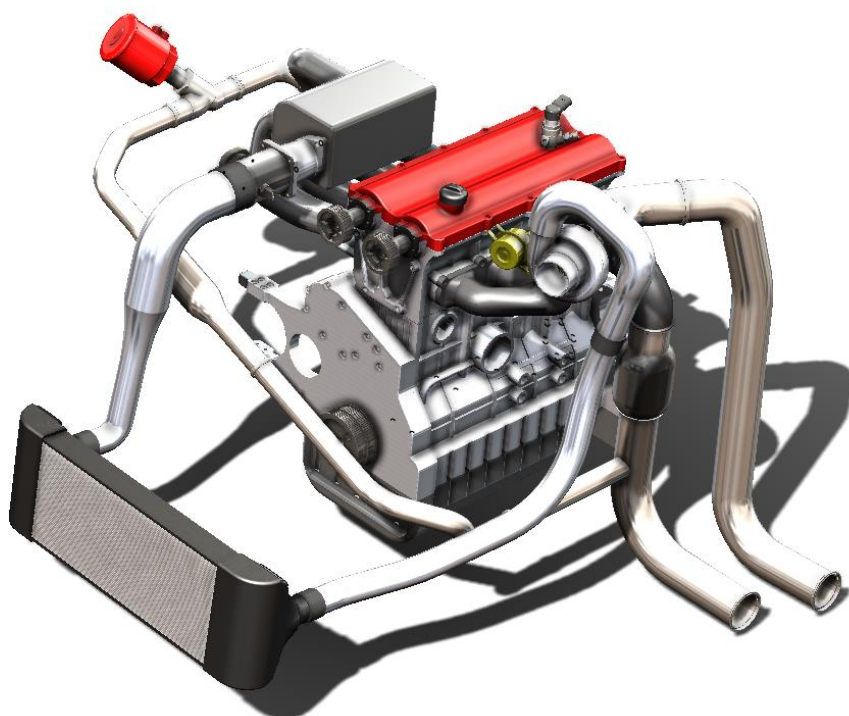


Figure 9. Design (construction solution) of the complete engine.

4. Conclusion

The RCCI engines can be the future for internal combustion engines because of their low emissions of NO, CO, UHC and PM. Technical solution of this type of engine has been done on the basis of previous researches and analysis done by many authors and can be tested in simulation programs which would show if modifications used in this work can be implemented into the real engine or further adjustments are needed.

Acknowledgments: This work was supported by the Slovak Research and Development Agency under the Contract no. APVV-19-0328. The article was written in the framework of Grant Projects: VEGA 1/0318/21 "Research and development of innovations for more efficient utilization of re-

newable energy sources and for reduction of the carbon footprint of vehicles” and KEGA 006TUKÉ-4/2020 “Implementation of Knowledge from Research Focused on Reduction of Motor Vehicle Emissions into the Educational Process.”

Conflicts of Interest: The authors declare no conflict of interest.

References

1. Kumar, N. (2019, July 11). *Study of oxygenated ecofuel applications in CI engine, gas turbine, and jet engine*. Advanced Biofuels. Retrieved December 14, 2021, from <https://www.sciencedirect.com/science/article/pii/B9780081027912000167>
2. Szamrej, G. A., Karczewski, M., & Chojnowski, J. (2021, September 25). *A review of technical solutions for RCCI engines*. Combustion Engines. Retrieved December 14, 2021, from <http://www.combustion-engines.eu/A-review-of-technical-solutions-for-RCCI-engines,142551,0,2.html>
3. Pachiannan, T., Zhong, W., Rajkumar, S., He, Z., Leng, X., & Wang, Q. (2019, June 7). *A literature review of fuel effects on performance and emission characteristics of low-temperature combustion strategies*. Applied Energy. Retrieved December 14, 2021, from <https://www.sciencedirect.com/science/article/pii/S0306261919310542>
4. Agarwal, A. K., Singh, A. P., & Maurya, R. K. (2017, April 2). *Evolution, challenges and path forward for low temperature combustion engines*. Progress in Energy and Combustion Science. Retrieved December 14, 2021, from <https://www.sciencedirect.com/science/article/pii/S0360128516300739>



Application of the calculated inverse kinematics of a robotic arm composed of URM modules to a defined trajectory

Ing. Štefan Ondočko*, prof. Ing. Jozef Svetlík PhD, Doc. Ing. Tomáš Stejskal PhD, Ing. Michal Šašala, Ing. Lukáš Hrivniak

Technical University of Košice, Faculty of Mechanical Engineering, Department of Manufacturing Machinery and Robotics (KVTaR); tomas.stejskal@tuke.sk, jozef.svetlik@tuke.sk, lukas.hrivniak@tuke.sk, michal.sasala@tuke.sk

* stefan.ondocko@tuke.sk; Tel.: +421 55 602 3238 (Letná 9, 042 00 Košice, Slovakia)

Abstract: The article describes the calculation of inverse kinematics of a robotics arm that is composed of URM modules. The calculation was realized for a concrete practical example of trajectories. It is based on an already existing solution algorithm, which was supplemented by calculation of positions important for the robot's operation. Instructions for possible corrections of trajectories in space have been added in order to avoid unsolvable and singular states. The accuracy of the calculation was quantified by the difference between the vector of the desired position, orientation, and the calculated vector of the desired position, orientation. The calculation and results were processed, visualized in the Matlab environment.

Keywords: inverse kinematics, Matlab, manufacturing technology, Jacobian, robotics

1. Introduction

The paper describes the inverse task of position kinematics in an open kinematic chain applied to a specific case of practical trajectories. It employs an algorithm designed and tested for solving the inverse function calculation [1] with an option of using a numerical method. Added has been the part describing the movement from the initial position based on a defined vector of joint variables, as well as the part representing the return back to the initial position. The robotic arm in question is a stationary one, composed of the so-called URM modules, the design of which is described in detail in [2, 3] and in terms of position kinematics, in, e.g., [4]. The solution is also applicable to other setups featuring this type of mechanism, that is, six rotating joints interconnected with rigid arms bent under various angles. A brief mention of important URM module properties are due, namely its unrestricted rotation around its own axis, availability of its own power source and modularity. Thanks to the last property mentioned, modules can be assembled into different types of configurations. These may be various setups, machines with several degrees of freedom. Addressing the inverse kinematics of a position means to look for such joint variables in a given kinematic chain that satisfy the desired position and the coordinate system orientation of the end effector. All this, naturally, presupposing knowledge of the mechanism's geometry, deeming its structural parts to be, in theory, absolutely rigid, or subject to minimal (negligible) strain. As long as the inverse function of dependence between the joint variables and the effector position in the Cartesian coordinate system can be solved analytically, it constitutes a great advantage because we arrive at the result through inserting the variables [5-7]. Unfortunately, in majority of cases, these equations cannot be solved analytically. Thus, different types of iterative numerical methods are applied, most frequently using the Jacobian [8-11] but also the heuristic approaches. What may happen in calculating the inverse function is demanding a position and orientation of the mechanism that is, under the given circumstances, out of question (ill-chosen trajectory), or for which more than one solution is available.

2. Constructing the trajectory

As mentioned in the introduction, through calculation, we are about to seek joint variables for the required position of the effector orientation of the robotic arm under development, with the path trajectory [12, 13] specified in space. In practice, a trajectory may represent a technological activity such as welding, milling, paint coating, and the like. First of all, it was necessary to choose as easily as possible a method of acquiring an evenly distributed set of points comprising the trajectory required. Even if not fast, a precise method for doing just that is a simple generation and assembly of individual parts into the required shape. To do this, it was necessary to write a custom program for such rendering and to extract an array of data further subjected to inverse calculation applied to our robotic arm. The program was expected to enable change in the trajectories' position in space, in their size and spacing. The aim of these requirements was to achieve better experimental opportunities. It goes without saying that this data array must have its sequence, since the trajectory has to be continuous in terms of the size of the sampling step in which the joint variables are modified. Thus, the rendering will consist of partial sections adjacent to each other in an exact sequence.

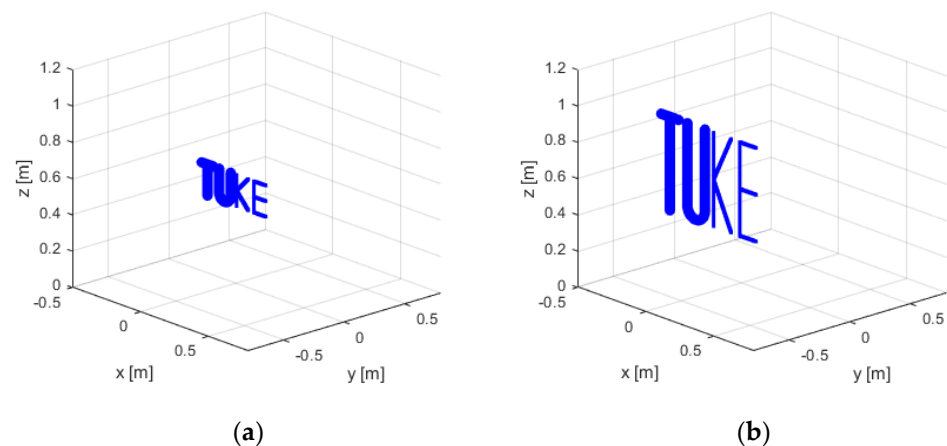


Figure 1. Output from the trajectory path generation program in the shape of „TUKE“ in MATLAB: (a) the size used; (b) illustration of how position in space, letter width constituting the trajectory, can be changed.

Naturally, such trajectory does not suit the inverse calculation of the mechanism's kinematic function. The following adjustments are, therefore, needed.

The trajectory must be continuous as to prevent sharp changes in joint velocities under the influence of immediate initial conditions in iteration calculation. Should that happen, the obtained state would be, of course, unsuitable due to various reasons. For example, under real conditions, interference with the work zone, where the trajectories are located, could occur as a result of different response of drives in time. In practice, this would mean damage to both the robot and the product, not to mention safety hazards. Thus, a suitable strategy for designing the sequence of individual trajectories is in order.

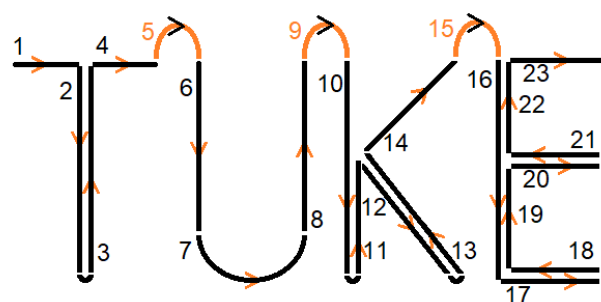


Figure 2. Sequence of individual trajectories in the 1 to 23 interval for inverse calculation

Individual generated points comprising the given trajectories from Figure 2 were saved in an Excel sheet as a data file with a prescribed attribute for choosing the proper variable, respecting the 1 to 23 sequence.

3. Calculation of joint variables and inverse kinematics

An algorithm was constructed to calculate inverse kinematics, tested for different iteration methods in [1]. The algorithm was supplemented with the calculation of joint variables between the initial „Home Position - HP“, with each joint rotated by 0° - see, e.g., [12], and the „Work Home Position - WHP“, in which the work organ is launched. I.e., if a work organ was on the effector, it would start working at the moment the work home position was achieved. Through calculating the joint variables between the given trajectory's final position and return to the HP, the „Endpoint - EP“ was added, too. This solution was chosen for its speed and reliability, without the need of falling back on calculating the inverse kinematics. It entails simultaneous moving of all joints of the mechanism (but this can also be sequenced) into the desired position established from the inverse function calculation for the position at hand. Thus, in such case it is crucial to know the above-mentioned HP, which constitutes the robot's initial position, and the WHP, where the trajectory is now calculated by means of inverse kinematics. This division is necessary because it is not possible to reliably address the inverse tasks in the entire work space for any trajectory. If the effector traverses the trajectory required, the calculation of the inverse task is completed and the immediate value of the joint variables vector for the EP is saved. The arm moves from the EP back to the HP. Therefore, the movement from the HP to the WHP takes place according to the following equation:

$$\mathbf{q} = \mathbf{t}(0;1) \cdot (\mathbf{q}_{\text{WHP}} - \mathbf{q}_{\text{HP}}) + \mathbf{q}_{\text{HP}} \quad (1)$$

Where $\mathbf{t}(0;1)$ is the increment (step) vector changing in the range between 0 and 1 for all joint variables and $t(0;1)$ will be the increment vector for one joint variable. \mathbf{I}_6 is the unit matrix the size of which is 6×6 .

$$\mathbf{t}(0;1) = t(0;1) \cdot \text{diag}(\mathbf{I}_6) \quad (2)$$

And the movement from the EP to the HP follows the equation below:

$$\mathbf{q} = \mathbf{t}(0;1) \cdot (\mathbf{q}_{\text{HP}} - \mathbf{q}_{\text{EP}}) + \mathbf{q}_{\text{EP}} \quad (3)$$

Calculated from the equations (1), (2) will be the individual vector values \mathbf{q} of joint variables. Joint variables vector for the HP is \mathbf{q}_{HP} , for the WHP, it is \mathbf{q}_{WHP} and for the EP, it is \mathbf{q}_{EP} .

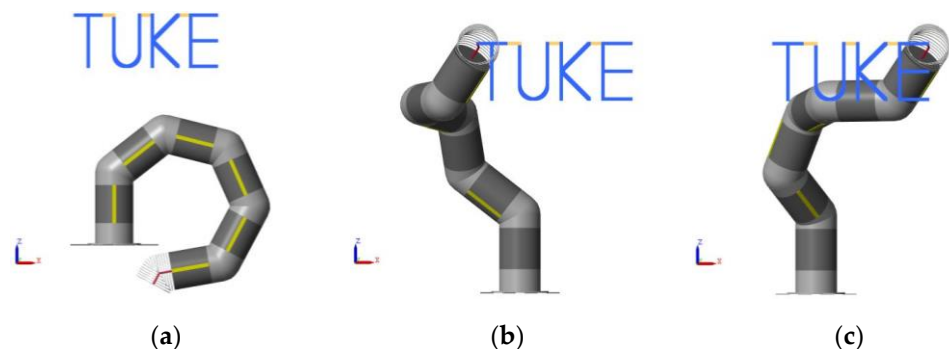


Figure 3. Individual initial positions for the „TUBE“ trajectory in MATLAB: (a) HP – home position; (b) WHP – work home position; (c) EP – end position

There are different iteration methods, but we chose the one applying the inverse Jacobian due to speed of calculation. Since the trajectory and the parameters were selected in a way to avoid singularity, other methods ceased to be necessary. Thus, the iteration method used satisfied the following equation:

$$\mathbf{q} = \mathbf{J}(\mathbf{q}_i)^{-1} \cdot (\mathbf{p}_d - \mathbf{p}(\mathbf{q}_i)_e) + \mathbf{q}_i \quad (4)$$

Where \mathbf{J} is the Jacobian matrix and it represents a change in the vector function of the position vector effector \mathbf{p}_e depending on the joint variables vector \mathbf{q}_i . The desired position and orientation of the effector vector is \mathbf{p}_d . The prior value of the joint variable from individual iterations is \mathbf{q}_i .

3.1. Precision of inverse calculation

Calculation precision was quantified by the Δ vector as a difference between the desired position vector \mathbf{p}_d and the calculated value vector $\mathbf{p}_e(\mathbf{q})$ in cartesian space according to the equation below

$$\Delta = \mathbf{p}_d - \mathbf{p}_e(\mathbf{q}) \quad (5)$$

In the full form then

$$\Delta = \begin{bmatrix} p_{dx} - p(q)_{ex} \\ p_{dy} - p(q)_{ey} \\ p_{dz} - p(q)_{ez} \\ \alpha_d - \alpha(q)_e \\ \beta_d - \beta(q)_e \\ \gamma_d - \gamma(q)_e \end{bmatrix} \quad (6)$$

Based on the equation (5) or (6), we can identify an error in the effector's position in cartesian space by using the equation to compute the Δ vector standard, i.e., we can write the following

$$\|\Delta\| = \sqrt{(p_{dx} - p(q)_{ex})^2 + (p_{dy} - p(q)_{ey})^2 + (p_{dz} - p(q)_{ez})^2} \quad (7)$$

Based on the equation (5) or (6), we can identify absolute errors in the effector's orientation in cartesian space defined by Euler angles as follows

$$\Delta_\alpha = |\alpha_d - \alpha(q)_e| \quad (8)$$

$$\Delta_\beta = |\beta_d - \beta(q)_e| \quad (9)$$

$$\Delta_\gamma = |\gamma_d - \gamma(q)_e| \quad (10)$$

3.2. Plotting the inverse calculation results

Equation (7) was used to calculate individual values of error in position with respect to the trajectory desired (Figure 2) and plotted on the chart in Figure 4. At the minimal admissible error of calculating the joint variables [1] $\delta=1 \times 10^{-6}$, the maximum error in the effector's position was $\|\Delta\|=5 \times 10^{-4}$ meters. This has to be taken in view of not small dimensions of the mechanism (maximum arm reach is slightly over 1.1 meter) see [4].

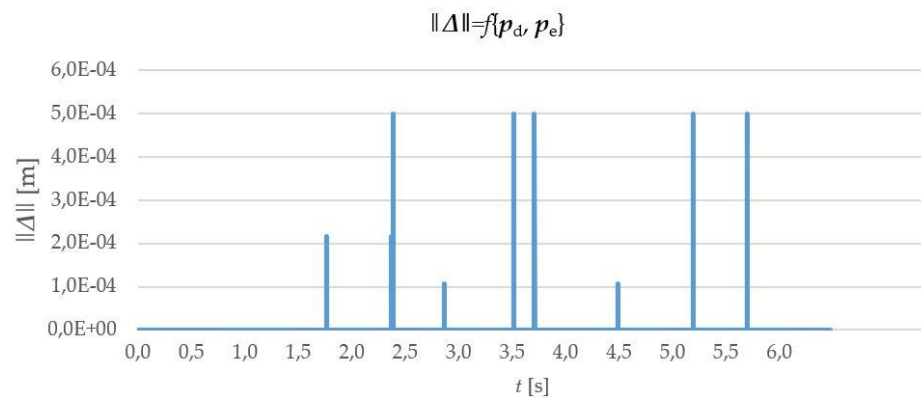


Figure 4. Position error values $\|\Delta\|$ for „TUKÉ“ trajectory in Figure 2.

According to equations (8), (9), (10), individual values of error in orientation defined by Euler angles gradually rotated by γ , β , α were calculated and plotted in the chart of Figure 5. At the minimal admissible error in calculating the joint variables [1] $\delta=1\times10^{-6}$ the maximum error in the Euler angle α of the effector was $\Delta\alpha=1.3878\times10^{-6}$ radian.

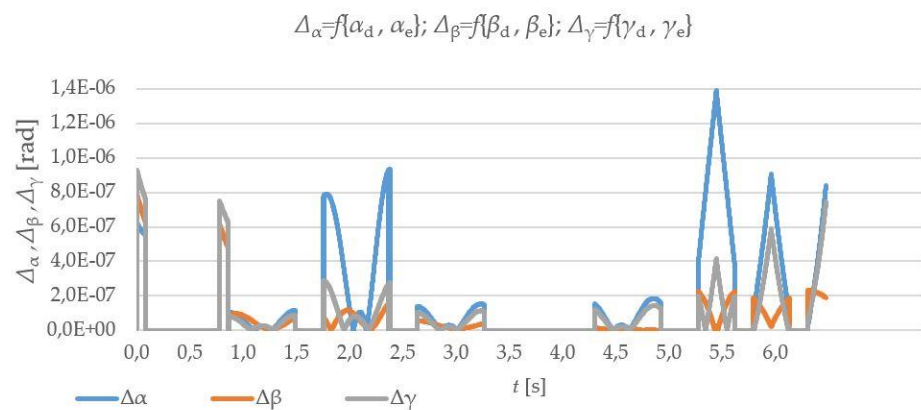


Figure 5. Orientation error values $\Delta\alpha, \Delta\beta, \Delta\gamma$ for the „TUKÉ“ trajectory from Figure 2.

The effector follows the trajectory composed of 6 477 points in the time horizon of 6.477 seconds with the error shown in Figure 4 and Figure 5. The entire rendering of trajectories takes up the area of about (0.5×0.2) square meters. The time needed for calculating the inverse function for this trajectory under the above-mentioned conditions ranged between about 30 to 40 seconds. The calculation can be made more precise by reducing the minimal admissible error in joint variables' calculation [1] δ . The calculated „TUKÉ“ trajectory and that of the virtual robotic arm's model was rendered in Matlab/Simscape/Multibody, see Figure 6.

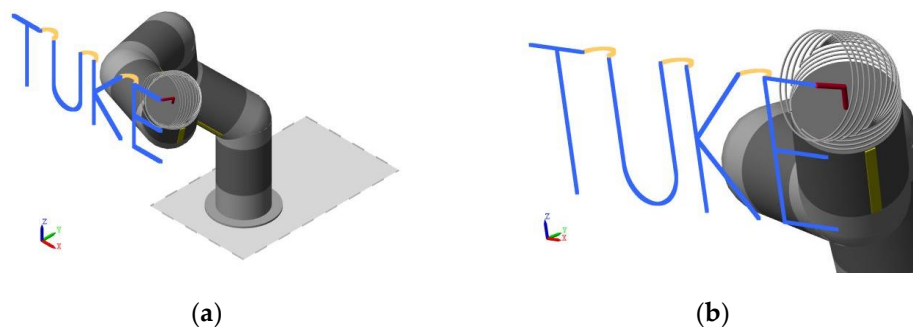


Figure 6. Matlab/Simscape/Multibody output: (a) Entire model with the trajectory; (b) Detail.

4. Discussion and Summary

Compared to version [1], the program for calculating the inverse task featured, among others, the part accounting for the movement from the HP to the WHP and from the EP to the HP, Figure 3. It is necessary to note here that the HP was configured for the state of least power consumption, since the system must conserve substantial energy when idle due to accumulative use of power. In addition, it was necessary to address the possibility of moving all trajectories in space to avoid the unsolvable states and also those of singularity. It was exactly due to this modification that enabled (experimental) discovery of such position in the work space under the initial condition of joint variables that avoided the undesirable states. Of course, this only holds under certain conditions. For example, a small change in the effector's orientation in space radically changes the situation. This is also the reason why we are considering an option to identify such imminent condition in the robot's work space and adjust the requirements accordingly. Last but not least, it should be noted that the effector here is represented by the end part of the mechanism, thus it is only logical it interferes with the trajectory. That is why the last bend is shown as a shell featuring a curved unmoving part described in more detail in, e.g., [2 - 4]. This part is planned to be fitted with a device, a tool, etc. In this way, the effector will constitute a „Tool Center Point – TCP“ [12, 13].

The task of this paper was to demonstrate the possibility of such concept to be applied to a practical requirement despite the assignment being anything but simple in terms of addressing it through inverse kinematics.

Acknowledgement: This work has been supported by the Research and Development Promotion Agency under the Contract no. APVV-18-0413 Modular architecture of production technology structural elements.

Conflict of interests: The authors rule out any conflict of interest. In designing the study, no role was played by any investors and the same holds true for the collection, analyses and interpretation of data, drafting the manuscript or decision making process on publishing the results.

References

1. Ondočko, Š.; Svetlík, J.; Stejskal, T.; Šašala, M.; Hrivniak, L. Comparison selected numerical methods for the calculation inverse kinematics of non-standard modular robotic arm consisting of unique rotational modules. *MM Science Journal*, 2021, 4468-4473.
2. Svetlík, J.; Štofa, M.; Pituk, M. Prototype development of a unique serial kinematic structure of modular configuration. *MM Science Journal*, 2016, 994-998.
3. Štofa, M. Experimentálny vývoj rotačných modulov pre stavbu sériových kinematických štruktúr vo výrobnéj technike. Ph.D. Tézys, Technická univerzita Košice, Slovensko, 30 Január 2020.
4. Ondočko, Š.; Svetlík, J.; Šašala, M.; Bobovský, Z.; Stejskal, T.; Dobranský, J.; Demeč, P.; Hrivniak, L. Inverse Kinematics Data Adaptation to Non-Standard Modular Robotiac Arm Consisting of Unique Rotational Modules. *Applied Sciences*, 2021, volume 11, issue 3, 0-15.
5. Murray, R. M.; Li, Z.; Sastry, S. S. *A mathematical introduction to robotic manipulation*. CRC press, 2017.
6. Grepl, R. *Kinematika a dynamika mechatronických systémů*. Akademické nakladatelství CERM, 2007.
7. Siciliano, B.; Khatib, O. *Springer handbook of robotics* (2nd Edition). Springer, 2016.
8. Paden, B.; Kinematics and Control Robot Manipulators. PhD thesis. Berkeley: University of California, Department of Electrical Engineering and Computer Sciences, 1986.
9. Peiper, D. L. *The kinematics of manipulators under computer control*. Stanford University CA, Department of Computer Science, 1968.
10. Otto, S.; Denier, J. P. *An introduction to programming and numerical methods in MATLAB*. Springer Science & Business Media. 2005.
11. Zhao, Y.; Huang, T.; Yang, Z. A successive approximation algorithm for the inverse position analysis of the general serial manipulators. *The International Journal of Advanced Manufacturing Technology*, 31(9-10), 1021-1027.
12. Robotics Glossary. Available online: <https://www.yaskawa.eu.com/products/robots/glossary> (accessed on 13 12 2021).
13. ISO 8373:2012(en) Robots and robotic devices – Vocabulary Available online: <https://www.iso.org/obp/ui/#iso:std:iso:8373:ed-2:v1:en> (accessed on 13 12 2021).



Methodology of the personalized implants manufacturing process by additive technology

Patrik Varga^{1*}, Radovan Hudák², Marek Schnitzer³, Jozef Živčák⁴

- 1 Technical University of Kosice, Faculty of Mechanical Engineering, Department of Biomedical Engineering and measurement, Slovakia; patrik.varga@tuke.sk
- 2 Technical University of Kosice, Faculty of Mechanical Engineering, Department of Biomedical Engineering and measurement, Slovakia; radovan.hudak@tuke.sk
- 3 Technical University of Kosice, Faculty of Mechanical Engineering, Department of Biomedical Engineering and measurement, Slovakia; marek.schnitzer@tuke.sk
- 4 Technical University of Kosice, Faculty of Mechanical Engineering, Department of Biomedical Engineering and measurement, Slovakia; jozef.zivcak@tuke.sk

* Correspondence: patrik.varga@tuke.sk; Tel.: 055 602 2378

Abstract: Advances in medicine and additive manufacturing have changed the way surgeons use patient data for personalized treatment. Polyetheretherketone (PEEK) is currently mentioned more and more as a suitable biomaterial in the field of cranioplasty. With the development of additive technologies, personalized implants in the field of medicine are appearing more and more often. As a result of examining the reliability of personalized implants using additive technology, it becomes a necessary effort. In this study, the process of production of cranial implants and their optimization was investigated. The results of the study revealed high dimensional accuracy and repeatability of the M220 3D printer using FFF technology and showed acceptable morphological similarity in terms of contour adaptation and continuity. In conclusion, personalized implants should be tested by simulating real situations where the implants are subjected to different external forces in different injuries.

Keywords: additive manufacturing 1; cranioplasty 2; patient specific implant 3; fused filament fabrication

1. Introduction

Cranioplasty is a surgical reconstruction procedure that restores the physiological functions of the cranium and restores the structure of cranial defects [1-2]. The goal of cranioplasty is also reconstruction from the point of view of aesthetics, which also improves the quality and mental well-being of the patient. Defects in the cranial part of the patient can occur with decompressive cranieotomies, which can lead to cranial infections, head injury, or head tumours [3-4]. Currently, great advances in the reconstruction of head defects have been recorded using various CAD / CAM software [5-7] and in parallel using various AM technologies. Using AM technologies and CAD / CAM software, it is relatively easy to design and manufacture personalized implants for a patient with a head defect, and this opens new possibilities for surgeons. There are already studies in this area dealing with the production of biomodels, surgical guides, prosthetic devices [8]. In the field of 3D printing, the most used technology is FFF / FDM technology, which is based on the extrusion of material usually in the form of a filament. Advances in these technologies enable the printing of high-temperature thermoplastics, e.g., PEEK, from which milling implants are commonly made, however, medical-grade PEEK have only recently been used [9-10]. As the use of 3D printing increases, questions are being raised about examining the reliability of the production of personalized implants from PEEK biomaterial [11-

12]. The aim of this study is to provide a methodology for the design and production process of personalized implants using 3D printing.

2. Methodology

This study describes the following processes: DICOM data processing in MIMICS software, implant production process using 3D printer M220.

2.1 DICOM data processing in MIMICS / 3-matic

M220 3D printers using FDM / FFF technology for PEEK material (Apium, Additive Technologies GmbH, Karlsruhe, Germany) were used to produce a personalized cranial implant. This 3D printer is designed to produce implants used in clean rooms with a constant temperature in the range of 10 - 30 ° C. The personalized implant was made of PEEK material with a filament diameter of 1.75 mm (PEEK 4000, Apium, Additive Technologies GmbH, Karlsruhe, Germany). To achieve the best 3D printing process, the support under the 3D implant model is designed automatically or manually to prevent the implant from deviating during 3D printing. The parameters of the 3D printing process can be found in Tab. 1 and in Tab. 2. After setting up the process in Simplify3D software (Cincinnati, OH, USA) it is necessary to generate a g-code from which the M220 3D printer software can read the parameters of the 3D printing process (Apium Print Control, Apium Additive Technologies GmbH, Karlsruhe, Germany) Fig. 1.

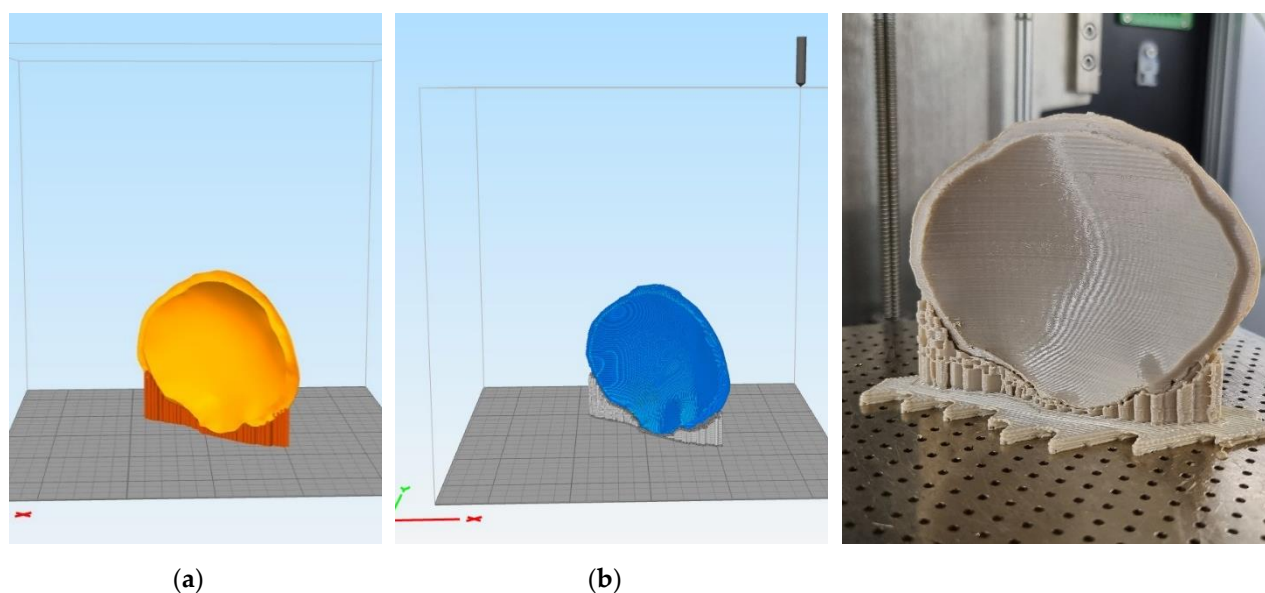


Figure 1. Personalized implant extrusion process: (a) Orientation of the implant in the slicing software; (b) Parameter setting and generating a g-code; (c) 3D printed cranial implant.

Tab. 1 Parameters for the Cranial implant printing process.

Extruder	Infill	Layer
Extruder diameter 0.4 (mm)	Internal Fill Pattern Rectilinear	Primary layer height 0.15 (mm)
	External Fill Pattern Rectilinear	Top solid layers 2
	Infill Percentage 100%	Bottom solid layers 2
	Angle 45°/-45°	Outline 2

Tab. 2 Parameters for the Cranial implant printing process.

Temperature	Support	Speed (mm/min)
Extruder temperature 485 (°C)	Support infill percentage 40 (%)	Printing speed 1900
Airflow temperature 130-280 (°C)	Support pillar resolution 3 (mm)	

The printing process before the final printing consists of the following quality control steps: (1) filament moisture control; (2) calibration of the plate by software and subsequently manually; (3) nozzle diameter calibration before separate implant printing.

To prevent deformation of the implant during printing, automatic raft generation has been activated and is integrated into the M220 3D printer software (Apium Print Control, Apium Additive Technologies GmbH, Karlsruhe, Germany). Subsequently, the printing process was started, and the production of the cranial implant was completed. To ensure repeatability, each implant must be placed in the middle of the building plate during printing to achieve an even heat distribution in the chamber. After extrusion, the implants and the implant support are separated from the raft using forceps and a chisel.

3. Discussion

Over the years, biomaterial PEEK has proven to be a good choice for the reconstruction of craniofacial defects [6,13-14], but at present little is known about implants made using additive technologies. With the advancement of additive technologies, prospects are emerging for personalized implants made of PEEK material manufactured using FDM technology [10-11,15]. The current literature on the geometric and morphological characteristics of personalized implants made from additive technologies is. Although few studies have evaluated the accuracy of cranial defect reconstruction using hospital-made implants, these studies are primarily focused on moulded acrylic prostheses [16-18]. One study focused on the quantitative evaluation of dimensional accuracy of personalized implants made using laser sintering technology in terms of print orientation [19]. In a study by Berrett et al. [19] stated that the transversely (horizontally) manufactured implants

showed the smallest deviation from the planned model. Therefore, due to the working principle of FDM technology, cranial implants were personalized in an axial orientation with minimal support structures. According to our results, our personalized implants have been printed to an acceptable extent in terms of dimensional accuracy for cranioplasty reconstruction procedures. In addition, the dimensional accuracy of the FDM technology indicates that the personalized cranial implants produced using the M220 3D printer had high repeatability with minimal deviations. Irregularities noted in the morphological adaptation of the implant to the contact area of the defect can lead to postoperative complications. The limitations of the study include simplifying the setup of printing processes. In the future, it would be appropriate to test personalized implants by simulating real situations where the implants are subjected to different external forces in different injuries. And analyse internal types of fills by non-destructive inspection, which would help accurately determine the accuracy of internal structures after printing processes.

5. Conclusions

In terms of geometric results, personalized cranial implants made using additive technology had high dimensional accuracy and repeatability. In addition, these cranial implants revealed clinically acceptable morphological adaptation and contour continuity. Accordingly, the results of this study are satisfactory with the expectations of the ceramic implant manufacturing process, but the specific attributes have room for further improvement. In the future, these personalized implants need to be tested biomechanically to see if they have sufficient strength for subsequent clinical use.

Acknowledgment: This article was developed on the basis of support obtained from the projects: ITMS2014 +: 313011V358, 01/2020 - 06/2023; ITMS2014 +: 313011W410, 05/2020 - 06/2023; ITMS2014 +: 313011V455, 11/2019 - 06/2023; STIMULES FOR RESEARCH AND DEVELOPMENT 1233/2018; KEGA 041TUKÉ-4/2019, 01/2019 - 12/2021; VEGA 1/0179/19, 01/2019 - 12/2021

Conflicts of Interest: The authors declare no conflict of interest.

References

1. Aydin S, Kucukyuruk B, Abuzayed B, Aydin S, Sanus GZ. Cranioplasty: Review of materials and techniques. *J Neurosci Rural Pract* 2011; 2:162-7.
2. Alkhaibary, A.; Alharbi, A.; Alnefaie, N.; Almubarak, A.O.; Aloraidi, A.; Khairy, S. Cranioplasty: A comprehensive review of the history, materials, surgical aspects, and complications. *World Neurosurg.* 2020, 139, 445–452.
3. Ali Alkhaibary, Ahoud Alharbi, Nada Alnefaie, Abdulaziz Oqalaa Almubarak, Ahmed Aloraidi, Sami Khairy, Cranioplasty: A Comprehensive Review of the History, Materials, Surgical Aspects, and Complications, *World Neurosurgery*, Volume 139, 2020, Pages 445-452.
4. Bonda, D.J.; Manjila, S.; Selman, W.R.; Dean, D. The Recent Revolution in the Design and Manufacture of Cranial Implants: Modern Advancements and Future Directions. *Neurosurgery* 2015, 77, 814–824.
5. Huys, S.E.; Van Gysel, A.; Mommaerts, M.Y.; Vander Sloten, J. Evaluation of Patient-Specific Cranial Implant Design Using Finite Element Analysis. *World Neurosurg.* 2021, 148, 198–204.
6. Scolozzi, P.; Martinez, A.; Jaques, B. Complex orbito-fronto-temporal reconstruction using computer-designed PEEK implant. *J. Craniofac. Surg.* 2007, 18, 224–228.
7. Eppley, B.L.; Kilgo, M.; Coleman, J.J., 3rd. Cranial reconstruction with computer-generated hard-tissue replacement patient-matched implants: Indications, surgical technique, and long-term follow-up. *Plast. Reconstr. Surg.* 2002, 109, 864–871.
8. Hoang, D.; Perrault, D.; Stevanovic, M.; Ghiassi, A. Surgical applications of three-dimensional printing: A review of the current literature & how to get started. *Ann. Transl. Med.* 2016, 4, 456.
9. Han, X.; Sharma, N.; Xu, Z.; Scheideler, L.; Geis-Gerstorfer, J.; Rupp, F.; Thieringer, F.M.; Spintzyk, S. An In Vitro Study of Osteoblast Response on Fused-Filament Fabrication 3D Printed PEEK for Dental and Cranio-Maxillofacial Implants. *J. Clin. Med.* 2019, 8, 771.
10. Dua R, Rashad Z, Spears J, Dunn G, Maxwell M. Applications of 3D-Printed PEEK via Fused Filament Fabrication: A Systematic Review. *Polymers (Basel)*. 2021 Nov 22;13(22):4046.
11. Honigsmann P, Sharma N, Okolo B, Popp U, Msallem B, Thieringer FM. Patient-Specific Surgical Implants Made of 3D Printed PEEK: Material, Technology, and Scope of Surgical Application. *Biomed Res Int.* 2018 Mar 19; 2018:4520636.

12. Sharma, N.; Aghlmandi, S.; Cao, S.; Kunz, C.; Honigsmann, P.; Thieringer, F.M. Quality characteristics and clinical relevance of in-house 3D-printed customized polyetheretherketone (PEEK) implants for craniofacial reconstruction. *J. Clin. Med.* 2020, 9, 2818.
13. Alasseri, N.; Alasraj, A. Patient-specific implants for maxillofacial defects: Challenges and solutions. *Maxillofac. Plast. Reconstr. Surg.* 2020, 42, 15.
14. Kurtz, S.M.; Devine, J.N. PEEK biomaterials in trauma, orthopedic, and spinal implants. *Biomaterials* 2007, 28, 4845–4869.
15. Nout, E.; Mommaerts, M.Y. Considerations in computer-aided design for inlay cranioplasty: Technical note. *Oral Maxillofac. Surg.* 2018, 22, 65–69.
16. Chamo, D.; Msallem, B.; Sharma, N.; Aghlmandi, S.; Kunz, C.; Thieringer, F.M. Accuracy Assessment of Molded, Patient-Specific Polymethylmethacrylate Craniofacial Implants Compared to Their 3D Printed Originals. *J. Clin. Med.* 2020, 9, 832.
17. Pijpker, P.A.J.; Wagemakers, M.; Kraeima, J.; Vergeer, R.A.; Kuijlen, J.M.A.; Groen, R.J.M. Three-dimensional printed polymethylmethacrylate Casting molds for Posterior Fossa reconstruction in the surgical Treatment of Chiari I Malformation: Technical note and Illustrative cases. *World Neurosurg.* 2019, 129, 148–156.
18. Stieglitz, L.H.; Gerber, N.; Schmid, T.; Mordasini, P.; Fichtner, J.; Fung, C.; Murek, M.; Weber, S.; Raabe, A.; Beck, J. Intraoperative fabrication of patient-specific moulded implants for skull reconstruction: Single-centre experience of 28 cases. *Acta Neurochir.* 2014, 156, 793–803.
19. Berretta, S.; Evans, K.; Ghita, O. Additive manufacture of PEEK cranial implants: Manufacturing considerations versus accuracy and mechanical performance. *Mater. Des.* 2018, 139, 141–152.

Research of sound absorption of recycled rubber in compact and loose form

Kristián Pástor ^{1*}, Miroslav Badida ²

¹ kristian.pastor@tuke.sk

² miroslav.badida@tuke.sk

* Correspondence: kristian.pastor@tuke.sk; Tel.: 055 602 2721

Abstract: The aim of this paper is to present the results of research into the acoustic properties of recycled rubber granules from old tires in two forms, in a compact and in a bulk form. The investigated acoustic parameter was the Sound Absorption Coefficient α . The measurements were performed in an impedance tube in the frequency band 100 - 2500 Hz. The aim of the research was to compare the acoustic properties of two forms of recycled material and to evaluate the differences or similarity of their properties.

Keywords: Loose fraction, Sound absorption coefficient α , Impedance tube, Recycled rubber,

1. Introduction

The acoustic properties of materials are playing an increasingly important role today. This is the reason why a number of new acoustically suitable materials with different sound-insulating properties appear and develop almost every day. Recycled components from automobiles over their lifetime are often used to develop such materials. These materials are used for passive sound control in the interior design of automobiles, factories, workshops, residential buildings, noise barriers, etc., to prevent unwanted noise. The determination of acoustic properties is therefore extremely important [1, 2, 3].

End-of-life vehicles represent a range of components (wastes) of different material composition that should be further recovered. Attention is focused mainly on problematic materials such as tires, car seats, carpets, upholstery, airbags, glass, etc., and on the development of technologies and techniques for waste recovery for acoustic, thermal insulation and other products [3].

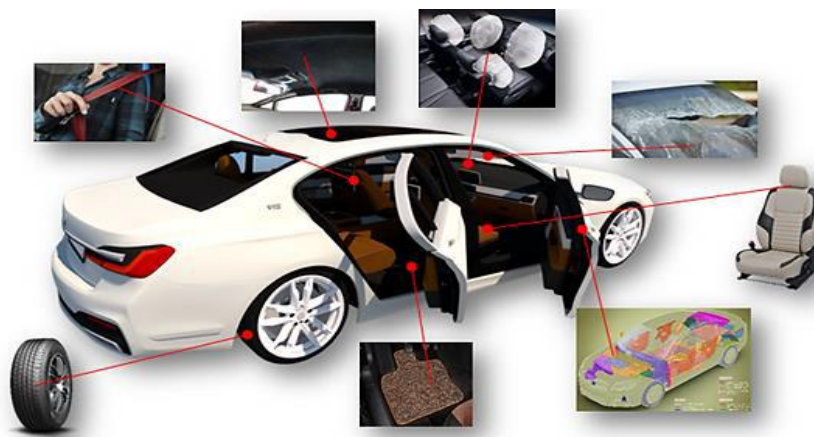


Figure 1. Materials suitable for recycling

Research in this area seeks to control and minimize the sounds that occur in machines, cars, homes and other places. There are a large number of studies and research experiments that seek to develop and discover new materials that can be used in various acoustic projects. For the analysis of these materials, sound absorption is one of the most important physical phenomena [4].

This paper deals with the analysis of acoustic properties, specifically the sound absorption coefficient α of recycled rubber from tires.

2. Sample preparation

The material studied in this research was recycled rubber from tires after their lifetime in two forms. The first form was a compact recycled rubber (Figure 2) and the second was loose recycled rubber (Figure 3).



Figure 2. Compact recycled rubber



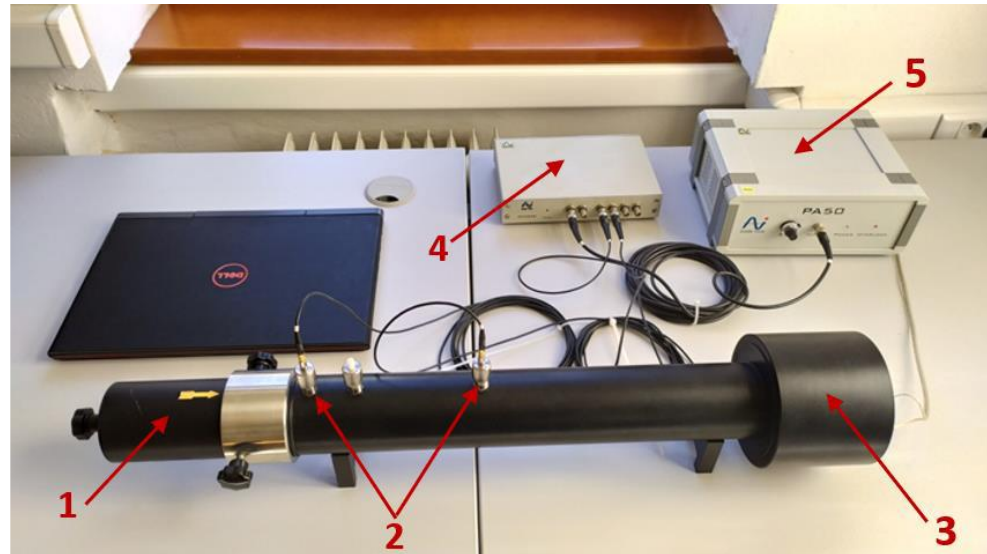
Figure 3. Loose fraction of recycled rubber

In order to be able to subject the loose fraction of recycled rubber to measurements in the impedance tube, this fraction was loosely poured without being pushed into a measuring capsule designed just to measure the acoustic properties of the loose materials in the impedance tube.

The dimensions of the samples were the same in both cases, namely a diameter of 60 mm and a thickness of 45 mm. The difference between the samples was their weight. The weight of the compact sample was 88.8 g.

3. Measurement procedure

The measurements were performed using an impedance tube in a two-microphone configuration using the transfer function method according to ISO 10534-2: 1998. The impedance tube has an advantage over other measuring methods due to its compactness, low cost and fast result. The impedance tube requires smaller samples of test material. A sound-generating loudspeaker is located on one side of the impedance tube and a sample holder is removable at the other end. Microphones are placed between the speaker and the sample. There are two, three or four microphone methods, depending on the number of microphones used in the measurement [1,2,5].



1 - Sample holder, 2 - Microphones, 3 - Built-in speaker, 4 - Four-channel analyzer, 5 - Power amplifier

Figure 4. Measuring apparatus for measuring the sound absorption coefficient α

The investigated parameter was the Sound Absorption Coefficient (α), which is a dimensionless number ranging from $<0.1>$. The closer the value of the coefficient is to the number 1, the better the sound absorption of the material. An impedance tube in a two-microphone configuration is used to measure the sound absorption factor of selected materials [6].

After calibration and connection of microphones according to the measured parameter and frequency band, we start the measurement, which is set to 40 seconds. After completing the measurement, we change the position of the microphones and repeat the measurement. We repeat this process 6 times. We will do this for the frequency band 100-800 Hz and then connect the microphones to the position for measuring the band 400-2500 Hz and repeat the procedure. The software processes the measured values and obtains their resulting values in the frequency band 100 - 2500 Hz. We consider this as one measurement and repeat it 5 times. The resulting values are then obtained by averaging these five measurements.

4. Analysis of results

The aim of this paper was to investigate the sound absorption of recycled rubber in compact and loose form in the frequency band 100 to 2500 Hz. The research results are expressed in the graphs in Figure 5 and Figure 6.

The results show that both forms of recycled rubber achieve the best sound absorption values at higher frequencies from about 800 Hz onwards. At lower frequencies, these values decrease.

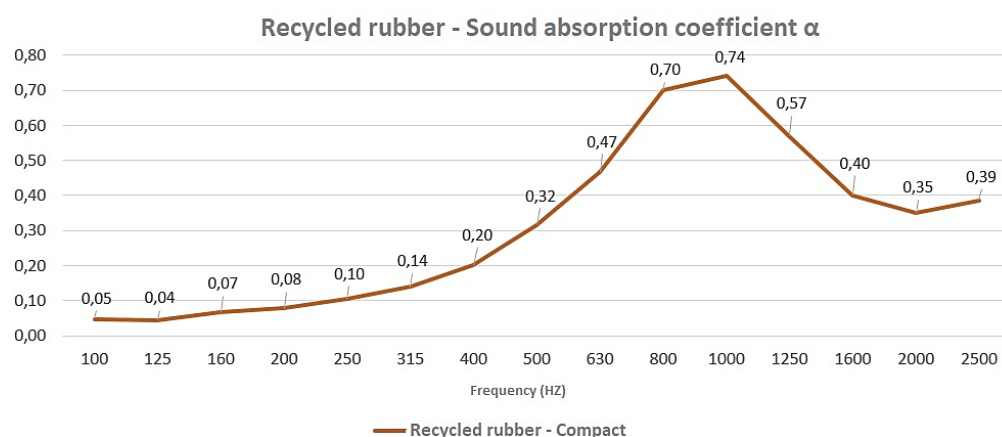


Figure 5. Results of measuring the sound absorption coefficient of compact recycled rubber

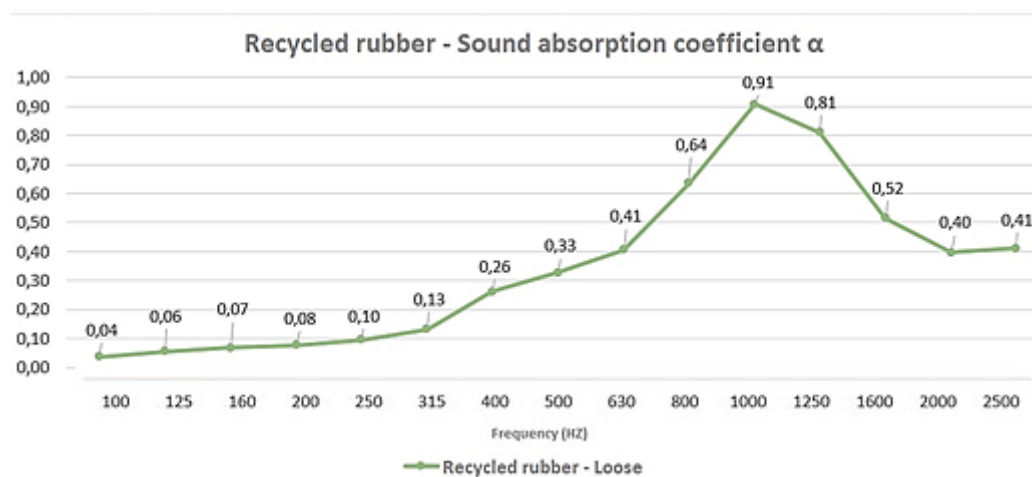


Figure 6. Results of measuring the sound absorption coefficient of the recycled rubber - loose fraction

A comparison of the results of the two forms of recycled rubber is also expressed in the graph in Figure 7.

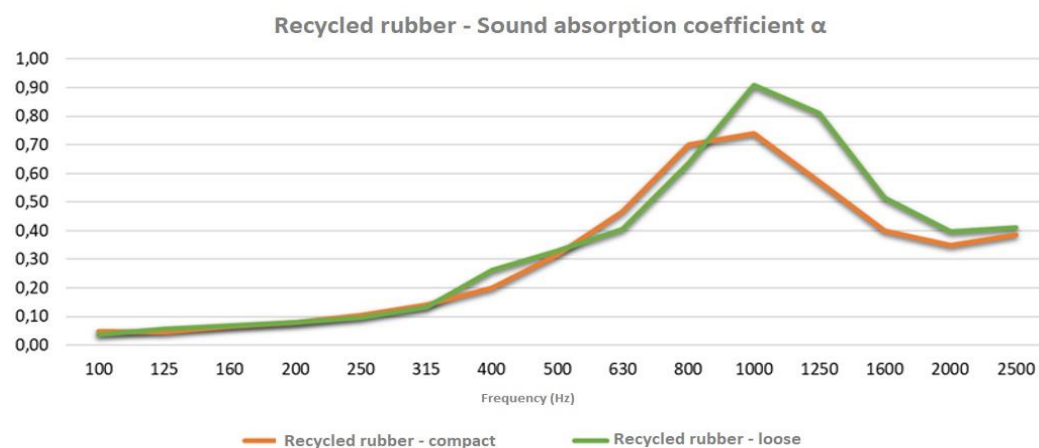


Figure 7. Comparison of the results of two forms of recycled rubber

Comparing the results of these two molds, we can see the loose form of recycled rubber having comparable sound-absorbing properties as the standard compact mold. In addition, it can be seen that at higher frequencies, the loose form has even outperformed the compact form with its values. The biggest difference can be seen at a frequency of 1000 Hz and higher. At this frequency (1000 Hz), the compact form reached a sound absorption coefficient of 0.74 and the loose form up to 0.91.

These good sound absorption properties can probably be attributed to the higher porosity of the loose sample as the porous materials are less reflective and thus better absorb sound.

5. Conclusion

Based on the results of this research, we can state that the loose form of recycled rubber has comparable sound-absorbing properties as the compact form and even achieves better values at higher frequencies. Since the frequency spectrum of traffic noise has its maximum in the range of 500 to 1500 Hz, the largest noise is caused by the frequency of 1000 Hz and just at the frequency of 1000 Hz and higher the loose form reaches a higher value than compact may be suitable for use in traffic noise control in noise walls. Another advantage of the loose mold is its lower weight due to the higher porosity and thus the need for less material for a comparable or better result.

Acknowledgment: The contribution was created on the basis of the solution of the project MŠVVaŠ SR KEGA no. 009 TUKE-4/2021 (50%) and the project MŠVVaŠ SR UNIVNET no. 021/0004/20 (50%).

References

1. Nireesh, J.; et al. Review of acoustic characteristics of materials using impedance tube. *ARPJ Journal of Engineering and Applied Sciences* **2015**, Vol. 10, No. 8, pp. 3319-3326. ISSN 1819-6608. Available online: http://www.arpnjournals.com/jeas/research_papers/rp_2015/jeas_0515_1928.pdf (Accessed on 07-09-2021)
2. Arunkumar, B.; Jeyanthi, S. Design and analysis of impedance tube for sound absorption measurement. *ARPJ Journal of Engineering and Applied Sciences* **2017**, Vol. 12, No. 5, pp. 1400-1405. ISSN 1819-6608. Available online: http://www.arpnjournals.org/jeas/research_papers/rp_2017/jeas_0317_5774.pdf (Accessed on 07-09-2021)
3. Badida, M.; et al. Progresívne technológie zhodnocovania odpadov v automobilovom priemysle, Spektrum STU Bratislava, 2021. ISBN 978-80-553-3867-5
4. Rosely, C.V.M.; Silva, R.H.A.; Linhares, T.M.; Rocha, C.M. The impedance tube construction and acoustic absorption study applied materials inside vehicles. *41st International Congress and Exposition on Noise Control Engineering* **2012**, Vol. 2, No.1, pp. 872-888, ISBN: 978-1-62748-560-9, Available online: https://www.researchgate.net/publication/289289454_The_impedance_tube_construction_and_acoustic_absorption_study_applied_materials_inside_vehicles (Accessed on 07-09-2021)
5. Labašová, E.; Ďuriš, R. Measurement of the acoustic absorption coefficient by impedance tube. *Research Papers Faculty of Materials Science and Technology Slovak University of Technology* **2019**, Vol. 27, No. 45, 2019, pp. 94-101, ISSN 1338-0532, Available online: https://www.researchgate.net/publication/338031592_Measurement_of_the_Acoustic_Absorption_Coefficient_by_Impedance_Tube (Accessed on 07-09-2021)
6. Měření zvukové pohltivosti materiálů, Laboratorní cvičení z Environmentální fyziky Fakulta technologická, UTB ve Zlíně, p. 8, Available online: http://ufmi.ft.utb.cz/texty/env_fyzika/EF_lab_02.pdf (Accessed

Kinematic analysis of redundant robot

Peter Ján Sinčák ^{1,*}, Ivan Virgala, ¹ Martin Varga ¹ and Michal Kelemen ¹

¹ Department of Industrial Automation and Mechatronics, Faculty of Mechanical Engineering, Technical University of Košice, 04200 Košice, Slovakia; peter.jan.sincak@tuke.sk (P.J.S.); ivan.virgala@tuke.sk (I.V.); martin.varga2@tuke.sk (M.V.); michal.kelemen@tuke.sk (M.K.)

* Correspondence: peter.jan.sincak@tuke.sk

Abstract: Redundant robots can be used for a wide spectrum of tasks such as inspections or minimally invasive surgeries. Focus will be on a subcategory of redundant robots called continuum robots. Many different mathematical models exist, however, main groups of models are the lumped and distributed parameter models. In this case, it was opted to use lumped parameter model subcategory called constant curvature assumption. The problem of modelling continuum robot can then turn into the mapping problem between the actuation coordinate system (tendon lengths), configuration coordinate system (arc parameters) and task coordinate system (coordinates of the end tip of the robot). The kinematic model is further implemented in MATLAB, to study the dependencies of the model parameters and their influence on the robot's movement. It is shown how basic actuation strategies are influencing the direction in which the robot travels and the robot's workspace is displayed based on the hardware limitation of the prototype. The future work will involve adding another segment so that the dexterity and versatility of the robot can be increased. It is also planned to use such model for training stages of control algorithm, based on the machine learning techniques to improve the dexterity of the robot in a challenging environment.

Keywords: redundant robots, kinematic modelling, simulation model, workspace

1. Introduction

Redundant robots are often described as robots with extra degrees of freedom that are necessary to accomplish a given task [1]. The extra degrees of freedom are allowing robots to have more options for achieving their task and therefore improving robots dexterity. One of the subcategories of redundant robots are so-called continuum robots. The main trait of such robots is high dexterity and manoeuvrability in various environments. These robots are used for various tasks such as industrial inspection tasks but also for minimally invasive surgeries (MIS). Many different approaches are focussing on modelling the movement of continuum robots, however, they are very much dependent on the concrete mechanical structure of the described robots. In [2], the approaches were characterized into two main groups, the distributed parameter models and lumped parameter models. The lumped parameter models are working with an assumption that each of the segments that are being actuated can be described by one circular arc. In the distributed parameter models, the infinite number of parameters describes the robots backbone as an arc in the task coordinate system, with continuous function along the length of the backbone, via state-space vectors. These models can therefore be geometrically exact and allow to obtain all possible shapes for the robot in the simulation and be used for the control strategies or designing stages [3]. This also means that the computation time can be higher than in the case of the lumped models. The lumped parameter models were extensively studied in [4-7]. These models are using assumptions to decrease the number of parameters that are used to define the arc, which can result in less accurate models but are easier to compute. One of the lumped models is the pseudo rigid body representation, which is dividing the backbone into a number of rigid links connected by springs. The length and

stiffness are then dependent on the forces that are acting on the robot and need to be set correctly. Such a model, independent of the load was introduced by [8]. Another approach used by the lumped models is the constant curvature assumption. Here the robots are assumed to be a series of mutually tangent sections, that can be viewed as arcs [9]. This approach is using three coordinate systems to map the movement of the robot to the lengths of the actuated tendons. Since this approach was used in our kinematic analysis, it is further described in section 2.

This paper focuses on the kinematic analysis of the continuum robot prototype, which is driven by three tendons, which are controlling one segment. The proposed mathematical model is implemented in MATLAB, hence the influence of the parameters of the model can be better studied there as well as their dependencies among each other. The paper is structured as follows: 1. Introduction, 2. Kinematic analysis of the continuum robot prototype, 3. Simulation of the kinematic model, 4. Conclusion.

2. Kinematic analysis of continuum robot prototype

The proposed prototype of the redundant robot can be seen in Figure 1. It consists of 11 sub-segments that are 10 [mm] high and sit on top of each other. In the centre of these sub-segments, a flexible backbone is located, which is keeping all the sub-segments aligned.

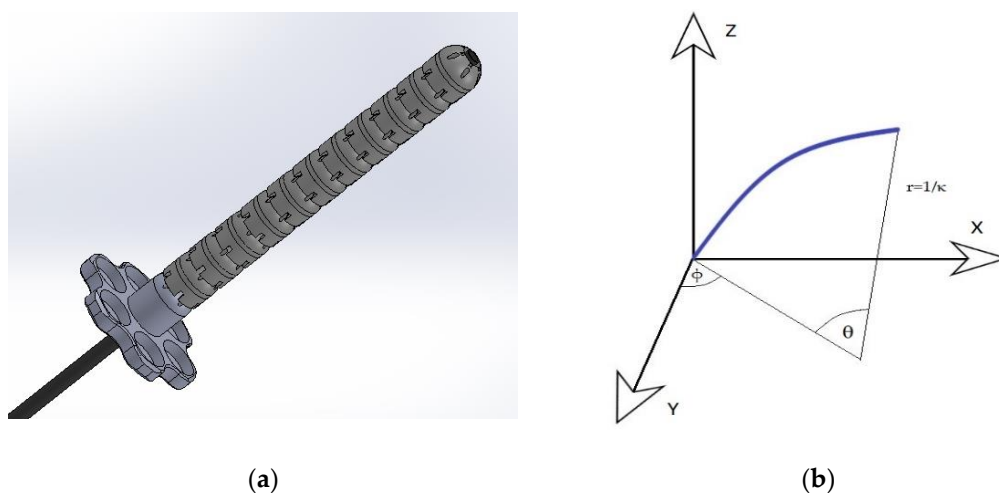


Figure 1. Prerequisites for the kinematic analysis: (a) Prototype used for kinematic analysis-11 sub-segments + base segment, central flexible backbone going through all segments; (b) Task coordinate system-blue line represents the central backbone of the robot. ϕ is the angle of rotation of the plane in which the robot bends, θ is the bending angle of the robot, r is the radius of the arc formed by the backbone ($r=1/\kappa$).

Each of these sub-segments has three holes that were evenly placed around the centre backbone. These holes act as guides for the tendons that are controlling the movement of the robot.

As mentioned in the introduction there are many possible ways to model such a redundant robot, however in this case it was opted to use the constant curvature approach, which is convenient due to its simplification. It describes the robot as several curves that are interconnected and form the shape of the robot. These curves can be described by the arc parameters, which are part of the configuration coordinate system. The problem of constant curvature now becomes a mapping problem among three different coordinate systems, this can be observed in Figure 2. The actuator coordinate system contains the cable lengths that are actuating the robot, the configuration coordinate system contains the arc parameters and the task coordinate system contains the Cartesian coordinates of the tip of the robot. As seen in Figure 2 the mapping can be done in two directions, one in

forward and one in the backward direction labelled with the index -1, meaning the forward or inverse kinematics.

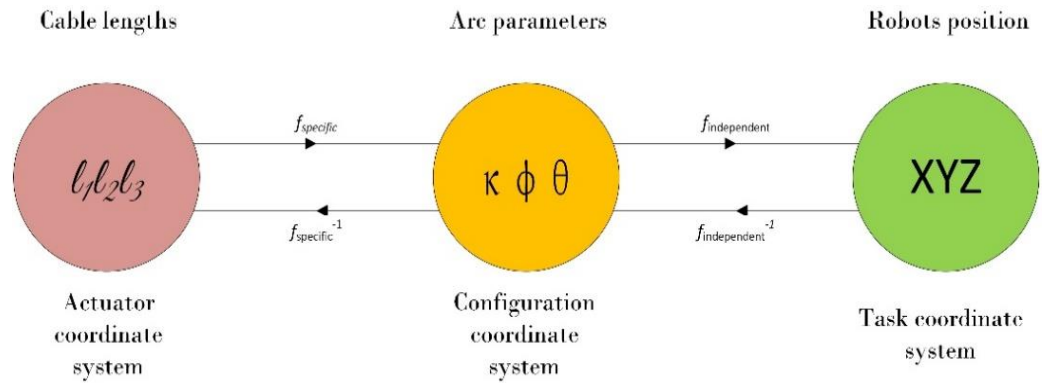


Figure 2. Mapping of the coordinate systems

The mapping from cable lengths to arc parameters is labelled as $f_{specific}$, since it is highly dependent on the specific design of the robot and its actuation system. The second mapping from arc parameters to robot position is labelled as $f_{independent}$, since this mapping is robot independent and can be applied to any robot that can be described by the constant curvature model.

The independent mapping of the robot is describing the robot pose in the Cartesian coordinate system in which the robot operates. The pose can be described by the point p , at the end of the tip of the robot which is an arc with the radius r , with the coordinates $\mathbf{p} = [r(1-\cos(\theta)) \ r \sin(\theta)]^T$ in the x-z plane and by the angle θ , which is the rotation about the y-axis. However, this is only in 2D space, to account for the movement in the 3D space the

$$\mathbf{T} = \begin{bmatrix} \mathbf{R}_z(\phi) & 0 \\ 0 & 1 \end{bmatrix} \begin{bmatrix} \mathbf{R}_y(\theta) & \mathbf{p} \\ 0 & 1 \end{bmatrix} \quad (1)$$

whole plane in which the robot bends has to rotate by the angle ϕ about the z-axis, which is shown in equation 1. This equation is called the transformation matrix and can be further developed in terms of arc parameters. The arc radius $r=1/\kappa$ and angle $\theta=\kappa s$, where s can be a point along the backbone anywhere from 0 to l . The developed transformation

$$\mathbf{T} = \begin{bmatrix} \cos \phi \cos \theta & -\sin \phi & \cos \phi \sin \theta & \frac{\cos \phi (1 - \cos \theta)}{\kappa} \\ \sin \phi \cos \theta & \cos \phi & \sin \phi \sin \theta & \frac{\sin \phi (1 - \cos \theta)}{\kappa} \\ -\sin \theta & 0 & \cos \theta & \frac{\sin \theta}{\kappa} \\ 0 & 0 & 0 & 1 \end{bmatrix} \quad (2)$$

matrix can be seen in equation 2. From this equation, the correlation between the X, Y, Z coordinates and arc parameters can be observed. Further, the $f_{specific}$ mapping has to be known so that the forward kinematics model can be used to model the movement of the robot based on the tendons length. To obtain the $f_{specific}$, three functions has to be known. The first function is the function of angle ϕ , which is the angle of rotation of the plane from the x-axis. This angle specifies the direction of the robot in the 3D space. If the angle ϕ is 0, the plane in which the robot bends is the x-z plane, however, if it is not 0 the robot moves out of this plane. The angle ϕ can be seen in equation 3. The second one is the arc curvature κ of the arc

$$\phi = \tan^{-1} \left(\frac{\sqrt{3}(l_2 + l_3 - 2l_1)}{3(l_2 - l_3)} \right) \quad (3)$$

$$\kappa = \left(\frac{2\sqrt{l_1^2 + l_2^2 + l_3^2 - l_1l_2 - l_1l_3 - l_2l_3}}{r(l_1 + l_2 + l_3)} \right) \quad (4)$$

$$\theta = \left(\frac{2\sqrt{l_1^2 + l_2^2 + l_3^2 - l_1l_2 - l_1l_3 - l_2l_3}}{3r} \right) \quad (5)$$

that is formed by the robots backbone with the arc radius r . This function can be seen in equation 4. The third function is the function of the angle θ , which is the bending angle of the robot in the plane, which is rotated by the previously described angle ϕ . This function can be seen in equation 5.

3. Simulation of the kinematic model

To test the proposed kinematic model, computer simulations were carried out. It was opted to use MATLAB as the simulation software. To implement the kinematic model of the robot into MATLAB, first, the inputs and outputs of the model had to be clarified. The inputs to the model in the MATLAB were the tendon lengths L_1 L_2 L_3 . These were used to calculate the arc parameters ϕ θ κ , which were further used to calculate the transformation matrix T . Output of the transformation matrix are the X Y Z coordinates of the end tip of the robot. Based on the variation in the tendon lengths, the robot's pose is changing and the robot's tip is moving. The strategy for the variation in tendon length can vary based on the position that is required from the robot to achieve. If only one tendon is being shortened and two are being lengthened, it is possible to move the robot in three directions, which are the direction of the shortening tendons. In Figure 3, it is the red, black and light blue coloured directions.

Another strategy is to shorten two tendons and lengthen one, which yields the same results, however the direction in which the robot moves is different, it is rotated by 60 degrees. In Figure 3, it is the green, dark blue and purple direction. In this figure, 6 differ-

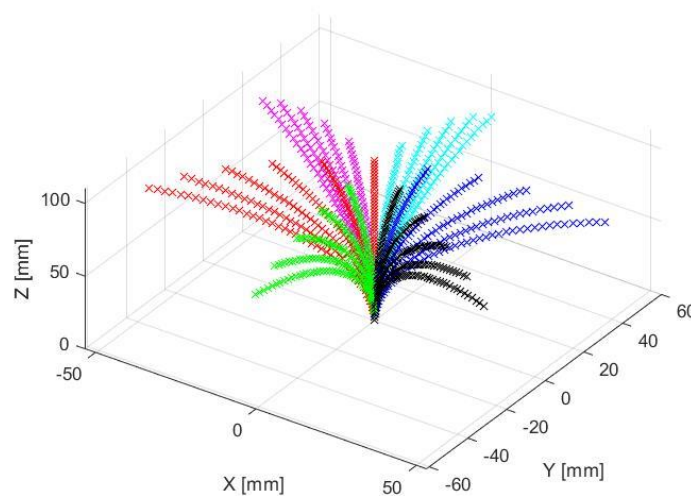


Figure 3. Robots pose in six directions

ent directions of the robot movements are shown. Each of these directions is rotated by 60

degrees from the previous one and in each one, there are multiple positions of the robot shown, where the previously mentioned strategies are employed. The dotted lines are symbolizing the shapes of the robots backbone, the last point being the end tip of the robot. To position the robot in between these directions two tendons have to be shortened, where one is more shortened than the other is. The more shortened tendon is then pulling the robot towards its direction, hence allowing it to achieve the positions in between these 6 initial directions.

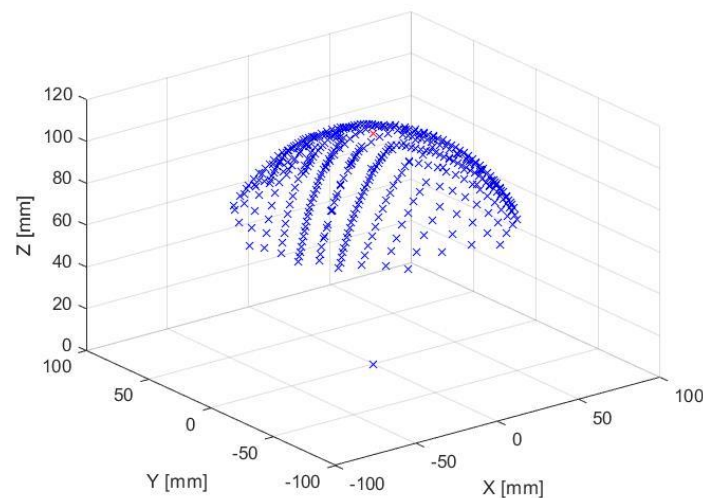


Figure 4. Workspace with the bending angle limited to 90 degrees due to hardware constraints

This can be very well seen in Figure 4. In this figure, the workspace of the robot can be seen. Each of the marks that are creating the workspace was generated, by employing the previously mentioned actuation strategies. The tendons were wound and unwound so that the whole workspace could be reached. The bending angle θ was also limited to ± 90 degrees due to the hardware limitation of the mechanical design. The resultant shape of the workspace is approximately 150 [mm] in diameter and it is showing the points that the robot can reach. Due to the hardware limitations, the workspace is not able to be the shape of a full sphere, however only cut from the top part of the sphere.

4. Conclusions

In this paper, kinematic analysis of a continuum robot prototype was presented, based on constant curvature assumption. It was shown, that the modelling of such robots can be a mapping problem between the actuator coordinate system and task coordinate system. The kinematic model was implemented in MATLAB, so that the relations between the actuation parameters, which are the tendons length, can be studied. This can be seen in Figures 3 and 4. Here different actuation strategies were observed as well as the workspace of the robot was defined. It was observed that in order to achieve all the coordinates multiple tendons have to be actuated. Two of the tendons have to be wound and one unwound. To achieve the position in between the 6 basic directions, the winding of the two tendons have to differ so that the shorter tendon is pulling the robot towards the desired point. The future work will involve adding another actuated section of the robot, which will increase the robot's versatility. In addition, the intention of creating a simulation model like this is to use it for the training of a control algorithm based on machine learning techniques in order to navigate in complicated environments.

Acknowledgments: The authors would like to thank to the Slovak Grant Agency VEGA 1/0201/21 and KEGA 030TUKE-4/2020. This work was also supported by internal project of Faculty of Mechanical Engineering IVG-21-01.

Conflicts of Interest: The authors declare no conflict of interest. The funders had no role in the design of the study; in the collection, analyses, or interpretation of data; in the writing of the manuscript; or in the decision to publish the results.

References

1. Chiaverini, S., Oriolo, G., & Maciejewski, A. A. (2016). Redundant Robots. In B. Siciliano, & O. Khatib (Eds.). Cham: Springer International Publishing. doi:10.1007/978-3-319-32552-1_10
2. Rone, W. S., & Ben-Tzvi, P. (2014). Continuum Robot Dynamics Utilizing the Principle of Virtual Power. *IEEE Transactions on Robotics*, 30, 275–287. doi:10.1109/TRO.2013.2281564
3. Renda, F., Cianchetti, M., Giorelli, M., Arienti, A., & Laschi, C. (2012). A 3D steady state model of a tendon-driven continuum soft manipulator inspired by octopus arm. *Bioinspiration & biomimetics*, 7, 025006. doi:10.1088/1748-3182/7/2/025006
4. Robert J. Webster, I. I., & Jones, B. A. (2010). Design and Kinematic Modeling of Constant Curvature Continuum Robots: A Review. *I. J. Robotic Res.*, 29, 1661–1683. doi:10.1177/0278364910368147
5. Chandramouli, S. R., & Rao, D. G. (2013, 2). Overview of Kinematics Design of Multi Section Planar Continuum Robot. *International Journal of Engineering Research & Technology*, 2. Retrieved from <https://www.ijert.org/research/overview-of-kinematics-design-of-multi-section-planar-continuum-robot-IJERTV2IS1198.pdf>, <https://www.ijert.org/overview-of-kinematics-design-of-multi-section-planar-continuum-robot>
6. Jones, B. A., & Walker, I. D. (2006). Kinematics for multisection continuum robots. *IEEE Transactions on Robotics*, 22, 43–55. doi:10.1109/TRO.2005.861458
7. Tian, Y., Yang, S., Geng, H., Wang, W., & Li, L. (2016). Kinematic modeling of the constant curvature continuum line drive robot. 2016 IEEE International Conference on Robotics and Biomimetics (ROBIO), (s. 289–294). doi:10.1109/ROBIO.2016.7866337
8. Su, H.-J. (2009). A Pseudorigid-Body 3R Model for Determining Large Deflection of Cantilever Beams Subject to Tip Loads. *Journal of Mechanisms and Robotics*, 1. doi:10.1115/1.3046148
9. Rao, P., Peyron, Q., Lilge, S., & Burgner-Kahrs, J. (2021). How to Model Tendon-Driven Continuum Robots and Benchmark Modelling Performance. *Frontiers in Robotics and AI*, 7, 223. doi:10.3389/frobt.2020.630245



EVALUATION OF CUTTING SURFACE QUALITY ON THE ELECTRICAL STEELS

Vladimír Rohal¹, Emil Spišák²

¹ Department of Technology, Materials and Computer Supported Production, Faculty of Mechanical Engineering, Technical University of Košice, Mäsiarska 74, 040 01 Košice, Slovakia; vladimir.rohal@tuke.sk (V.R.); emil.spisak@tuke.sk (E.S.)

* Correspondence: vladimir.rohal@tuke.sk; Tel.: +421556023519

Abstract: This work deals with the evaluation of cutting surface quality on the electrical steels. The theoretical part of this work contains knowledge related to electrical sheets manufactured by various manufacturers. One of the most important parameters of the cutting technology is the cutting gap that has got an essential impact on the formation of the cutting surface, on its shape, on the layout the strip of the cut and on the strengthening of material. The experimental part of this thesis is focused on the measuring of plastic shear zone, one of the main parameters for evaluating the quality of a cutting surface. It is characterized as the ratio of the thickness of the shear zone to the thickness of the fracture zone.

Keywords: cutting gap, cutting surface, shear zone, fracture zone, electrical steel

1. Introduction

Today, the emphasis is on efficiency and optimization in all directions, whether it is the cost of individual production operations or the optimization of individual aspects of production and technological processes, which ultimately determine the competitiveness of products in the market.

At present, steels with higher strength properties are coming to the market and used in the industry, so it is necessary to thoroughly investigate their behavior and use suitable tool steels for their processing, machining. Since cutting is one of the most frequently used surfaces forming operations, it is necessary to know its principles, regularities and correct setting of conditions during the cutting process.

At a time, when it is generally common trend to expand the use of electric cars on the market as much as possible, mainly due to declining stocks of non-renewable energy sources, as well as efforts to protect the environment more effectively, research and development in this area is extremely relevant. However, a significant part of the research in this area is devoted to sources of electricity, respectively development of batteries, which are subject to very high requirements. A significantly smaller part of the research is focused on improving the efficient use of stored energy, it means to reduce losses of electric motors. According to current knowledge, the quality of shear surfaces after cutting and assembling rotors and stators also influences the efficient use of stored energy.

The results of the shear cutting process are changes in the surface of the base material. These changes not only affect their geometric properties, but also change the physical, chemical and mechanical properties of the surface (microstructural changes, cracks and microcracks, microhardness, corrosion resistance, etc.). All these changes are part of the concept of surface integrity, which is one of the basic aspects in terms of quality requirements, especially in structural elements for stator and rotor cores in electric motors, where these requirements are very high due to functionality and reliability. [1-6]

2. Materials and Methods

For the needs of experimental verification of cutting conditions of electrical sheets, 3 types of electrical steels from different manufacturers were used. The individual sheet metal parameters are recorded in the Table 1.

Table 1. Sheet metal parameters

Samples	Embraco designation	Dimension [mm]	Sheet thickness [mm]	Presence of coating Y / N
A	T.K. 037 M660-50K S5H Tökölt	1070x1050	0,5	Y
B	V.A. 036 S1S-IS450- 50K HE	1380x1050	0,5	Y
C	A.M. 036 S1S M450-50K	1130x1150	0,5	Y

Electrical sheets were characterized (table 2) by a thickness of 0.5 mm, hardness at the level of 60 to 80 HRB, density at 7.75 to 7.85 g / cm³, the limit of permanent deformation is at the level of 353 to 520 N / mm², tensile strength 380 to 550 N / mm² and an elongation of 10 to 25%.

Table 2. Characteristics of materials

Material designation	Sheet thickness [mm]	Hardness HBR	Density [g / cm ³]	Rolling direction characteristics	
				Tensile strength [N / mm ²]	Elongation [%]
S1S	0,5	65-85	7,75	380-550	10-20
S5H	0,5	60-80	7,85	380-490	10-25

Characteristics of the product marked as T.K. 037 M660-50K S5H Tökölt:

Steel marked as M660-50K, 1.0361, non-alloy steel with a density of 7.85 g / cm³. Material definition based on EN 10341-2006: Cold rolled electrical sheets, non-alloy and alloy steels, without regular grain orientation, supplied in strips and coils in a semi-process state. The magnetic properties of this steel depend on the basic requirements of the customer, they are usually adjusted by annealing. [44]

Electric sheets with the designation M660- 50K, are delivered in semi-finished condition and the manufacturer for Embraco Spišská Nová Ves is the company ThyssenKrupp Bochum. [7, 8]

Characteristics of the product marked as V.A. 036 S1S- IS450- 50K HE:

Steel marked as IS M450-50 K HE is characterized by a shorter final annealing time, a homogeneous semi-finished product structure and stable processing at high efficiency. Steel is characterized by lower losses and higher magnetizability compared to standard steels. [9]

Electric sheets Isovac M450- 50 K HE are delivered in semi-finished condition and the manufacturer for Embraco Spišská Nová Ves is the company VoestAlpine Linz. VoestAlpine has a product protected by the ISOVAC® trademark.

Characteristics of the product marked as A.M. 036 S1S M450-50K:

Steel marked M450-50K, 1.0843, non-alloy steel with a density of 7.75 g / cm³. Material definition based on EN 10341-2006: Cold rolled electrical sheets, non-alloy and alloy steels, without regular grain orientation, supplied in strips and coils in a semi-process state. [10]

Electric sheets marked as M450-50K are delivered in semi-finished condition and the manufacturer for Embraco Spišská Nová Ves is the company Arcelor Mittal.

3. Results

3.1. Mechanical properties

The mechanical properties of electrical sheets were obtained experimentally and compared with the general characteristics of the manufacturers. The mechanical properties of the electrical sheets were verified by a tensile test on a TIRATES 2300 tearing device. The mechanical properties were measured in the rolling direction of the semi-finished product - 0 ° and in the direction perpendicular to the rolling direction - 90 °. The table 3 shows the measured values for M660-50K sheets manufactured by ThyssenKrupp Bochum.

Table 3. Mechanical properties of steel M660-50K ThyssenKrupp Bochum

Direction	Samples	R _{p0,2} [MPa]	R _m [MPa]	A ₈₀ [%]	Direction	Samples	R _{p0,2} [MPa]	R _m [MPa]	A ₈₀ [%]
0°	TA1-1	386	432	18,4	90°	TA2-1	397	440	16,8
0°	TA1-2	394	437	19,2	90°	TA2-2	397	437	11,9
0°	TA1-3	385	432	21,1	90°	TA2-3	392	437	16
0°	TA1-4	389	432	19,4	90°	TA2-4	392	435	14,9
0°	TA1-5	387	430	16,0	90°	TA2-5	386	436	13,6

Based on Embraco's internal designations, the M660-50 K semi-finished product belongs to the S5H semi-finished product group. This group is characterized by Rp0.2 values in the range of 353-470 MPa and Rm values in the range of 380-490 MPa.

The average value for the TA samples Rp0.2 was 390.5 MPa and Rm 434.8 MPa. It follows from the above that the guaranteed values of the manufacturers for the S5H group were also confirmed during the tensile test.

Based on Embraco's internal designations, the ISOVAC M450-50K semi-finished product belongs to the S1S group of semi-finished products. This group is characterized by Rp0.2 values in the range of 353-520 MPa and Rm values in the range of 380-550 MPa.

The average value for the TB sample (Table 4.) Rp0.2 was 407.7 MPa and Rm 478.3 MPa. It follows from the above that the guaranteed values of the manufacturers for the S1S group were also confirmed during the tensile test.

Table 4. Mechanical properties of steel ISOVAC M450- 50K VoestAlpine

Direction	Samples	R _{p0,2} [MPa]	R _m [MPa]	A ₈₀ [%]	Direction	Samples	R _{p0,2} [MPa]	R _m [MPa]	A ₈₀ [%]
0°	TB1-1	414	476	17,9	90°	TB2-1	405	481	15,3
0°	TB1-2	417	480	16,9	90°	TB2-2	400	476	16,6
0°	TB1-3	409	475	14,1	90°	TB2-3	399	477	19,1
0°	TB1-4	410	472	17,0	90°	TB2-4	405	482	17,9
0°	TB1-5	413	481	19,1	90°	TB2-5	405	483	18,4

Based on Embraco's internal designations, Arcelor Mittal's M450-50K semi-finished product belongs to the S1S group of semi-finished products. This group is characterized by Rp0.2 values in the range of 353-520 MPa and Rm values in the range of 380-550 MPa.

The average value for the TC samples (Table 5.) Rp0.2 was 358.6 MPa and the Rm 396.4 MPa. It follows from the above that the guaranteed values of the manufacturers for this steel from the S1S group were also confirmed during the tensile test.

Table 5. Mechanical properties of steel M450- 50K Arcelor Mittal

Direction	Samples	R _{p0,2} [MPa]	R _m [MPa]	A ₈₀ [%]	Direction	Samples	R _{p0,2} [MPa]	R _m [MPa]	A ₈₀ [%]
0°	TC1-1	358	394	26,2	90°	TC2-1	352	392	29,2
0°	TC1-2	360	398	26,0	90°	TC2-2	351	390	27,6
0°	TC1-3	356	392	21,6	90°	TC2-3	353	392	29,1
0°	TC1-4	354	389	24,4	90°	TC2-4	368	408	23,9
0°	TC1-5	367	403	22,1	90°	TC2-5	367	406	20,0

3.2. Experimental verification of the cutting surface by microscopic analysis

Experimental verification of the shear area by microscopic analysis was performed on a Keyence VHX-5000.

Figure 1 shows a microscopic analysis of samples (A1-A7, B1-B7 and C1-C7). The quality of the cutting surface can be seen on the samples depending on the cutting gap. The shear gaps for the purposes of the experiment were chosen at the level of 1,3,5,7% of the material thickness.

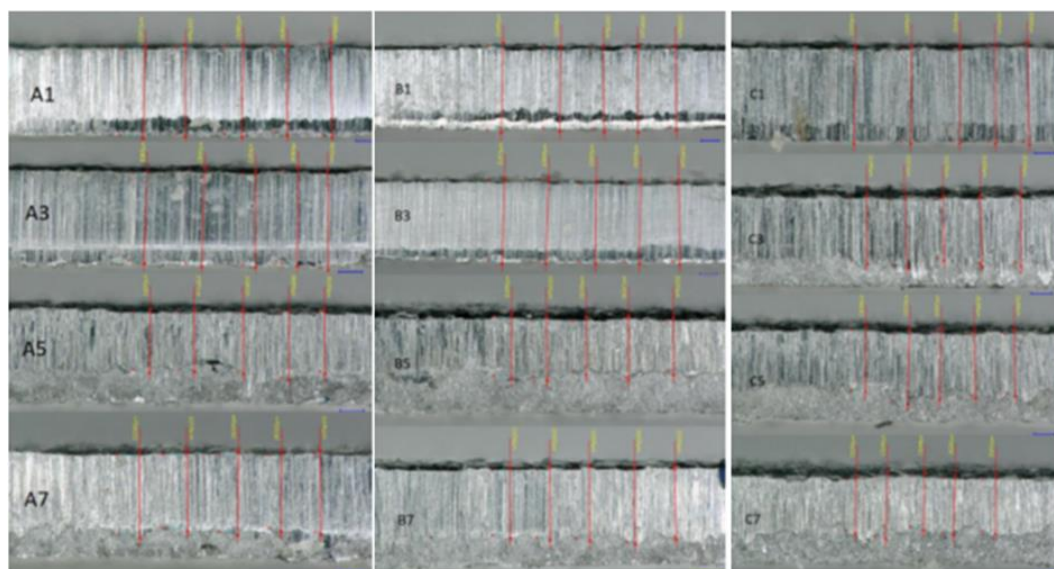


Figure 1. Microscopic analysis of samples A, B and C

One of the main parameters for evaluating the quality of a cutting surface is its "roughness". It is characterized as the ratio of the thickness of the shear zone to the thickness of the fracture zone (Table 6-8).

It is clear from the macroscopic analysis that the quality of the shear surface is directly proportional to the size of the shear gap. As the value of the shear gap increases, the percentage of the fracture zone also increases and, conversely, the shear zone decreases.

Table 6. Results of microscopic analysis of samples A

Samples	Thickness [mm]	Shear zone [mm]	Fracture zone [mm]	Shear zone [%]	Fracture zone [%]
A1	0,500	0,4756	0,0244	95,12	4,88
A3	0,500	0,4572	0,0428	91,44	8,56
A5	0,500	0,2836	0,2164	56,72	43,28
A7	0,500	0,3326	0,1674	66,52	33,48

The optimal cutting gap for cutting samples from M660-50K material is at the level of 1%. This fact also shows (Figure 2.) that the 1% gap is optimal for cutting these electrical sheets, as its content structure has the largest share of the shear zone, which in practice eliminates short circuits and undesirable processes in the proper operation of electric motors.

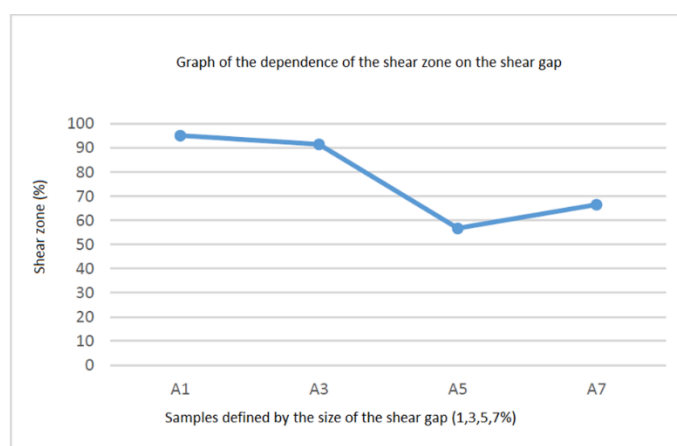


Figure 2. Graph of the dependence of the shear zone on shear gap for sample A

Table 7. Results of microscopic analysis of samples B

Samples	Thickness [mm]	Shear zone [mm]	Fracture zone [mm]	Shear zone [%]	Fracture zone [%]
B1	0,500	0,4788	0,0212	95,76	4,24
B3	0,500	0,4644	0,0356	92,88	7,12
B5	0,500	0,2496	0,2504	49,92	50,08
B7	0,500	0,305	0,195	61	39

The ISOVAC M450-50K HE samples (Figure 3.) with a 1% shear gap showed the best parameters for the quality of the cutting surface based on the measurement of the microscopic analysis. The shear zone had a thickness of 0.4788 mm and a fracture zone of 0.0212 mm, i.e. 95.76% and 4.24%, respectively.

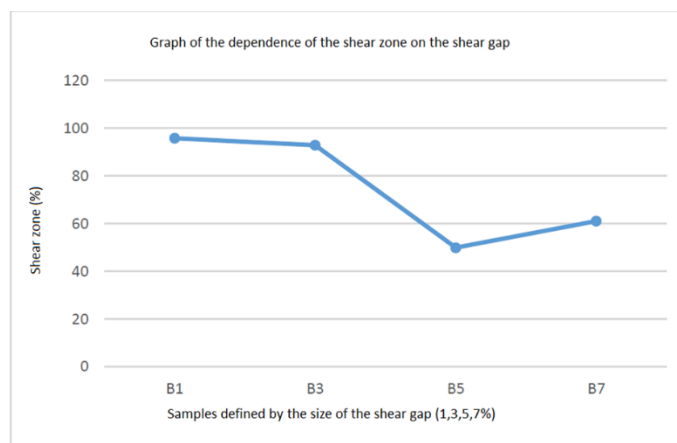


Figure 3. Graph of the dependence of the shear zone on shear gap for sample B

Table 8. Results of microscopic analysis of samples C

Samples	Thickness [mm]	Shear zone [mm]	Fracture zone [mm]	Shear zone [%]	Fracture zone [%]
C1	0,500	0,4446	0,0554	88,92	11,08
C3	0,500	0,3036	0,1964	60,72	39,28
C5	0,500	0,2994	0,2006	59,88	40,12
C7	0,500	0,2574	0,2426	51,48	48,52

As with all other observed samples, in the case of sample C-M450-50K (Figure 4.), the 1% shear gap showed the best parameters of the plastic shear zone and the fracture zone in the ratio 0.4446mm: 0.0554mm, 88.92%: 11.08%.

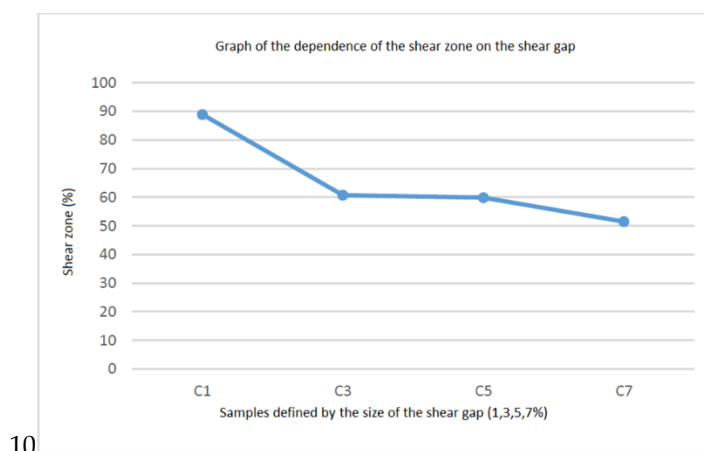


Figure 4. Graph of the dependence of the shear zone on shear gap for sample C

5. Conclusions

The ratio of the shear zone to the fracture zone depends on the size of the shear gap. Shear gaps for experimental purposes were chosen at 1%, 3%, 5% and 7% of the material thickness. Greater the shear zone is, then better quality of the cutting surface is created. These assumptions were confirmed during the experimental verification. The optimal (ideal) shear gap was evaluated as 1% shear gap for samples A and B. Sample A was manufactured by ThyssenKrupp Bochum and sample B by Voestalpine Linz. Sample A has a plastic shear thickness of 95.12%, sample B 92.88%.

The experiments showed that for samples A and B, it is possible to use a shear gap of 3%, provided that the quality of the cutting area is maintained. Sample A had a shear zone thickness of 91.44% and sample B 92.88%. The results of the other samples do not correspond to the sufficient quality of the cutting surface.

Acknowledgments: This paper was written with the financial support of the granting projects APVV-17-0381 and VEGA 1/0384/20.

References

1. Spišák E.; Kaščák L.; Majerníková J.; Džupon M. Analysis of cutting surface during cutting of electric sheets. *Strength of Materials*. Vol. 49, no. 4 (2017), p. 605-611. - ISSN 0039-2316
2. M'saoubi, R.; Outeiro, J.C.C.; Chandrasekaran, H.; Dillon, O.W.; Jawahir, I.S.S. A review of surface integrity in machining and its impact on functional performance and life of machined products. *Int. J. Sustain. Manuf.* 2008,1, 203.
3. Abrão, A.M.; Ribeiro, J.L.S.; Davim, J.P. Surface Integrity. In *Machining of Hard Materials*; Springer Science & Business Media: New York, NY, USA, 2011; pp. 115-141.
4. Vukota B. Sheet metal forming processes and die design. New York: New York Industrial Press, 2004. s. 215. ISBN 0-8311-3182-9.
5. Kellenbenz, R. *Handbuch der Umformtechnik*. Berlin: Springer Verlag, 2005. ISBN 978-3-662-07704-7.
6. Luo, S.Y. Effect of the geometry and the surface treatment of punching tools on the tool life and wear conditions in the piercing of thick steel plate. Elsevier, 1999, *Zv. Journal of Materials Processing Technology*. ISSN 0924-0136.
7. Krupp, Thyssen. Thyssen Krupp electrical steel India. [Online] 11. 12 2021. http://www.tkesindia.com/our_products.pdf.
8. Krupp, Thyssen. Thyssen Krupp. [Online] 11. 12 2021. <https://www.thyssenkrupp-steel.com/en/products/electrical-steel/electrical-steel-non-grain-oriented/powercore-k/content-page-68.html>.
9. Voestalpine. Voestalpine. [Online] 11. 12 2021. www.voestalpine.com/isovac.
10. Mittal, Arcelor. Arcelor Mittal. [Online] 11. 12 2021. <http://industry.arcelormittal.com/catalogue/D20/EN>.

Development of methods for drone noise assessment

Anna Yehorova^{1*}, Ervin Lumnitzer¹, Veronika Gumanová¹

¹ Technical University of Košice, Faculty of Mechanical Engineering, Department of Environmental Engineering

* Address for correspondence: anna.yehorova@tuke.sk

Abstract: Drones are developing rapidly recently in popularity in amateurly usage. Despite the great benefits drones have brought, their noise pollution is one of the concerns with their proliferation. Such a noise is completely new and it is characterized by a specific spectral composition and often subjectively felt a high degree of interference. The location of the noise source is also significant - tens, sometimes hundreds of meters above the ground, which characterizes aircraft noise. This, combined with the ever-increasing intensity, requires extensive research to be carried out in this area in order to avoid an increasing noise burden on the population. The presented publication proposes a methodology for assessing the impact of drones on humans and performed flight measurements at different speeds. As well sound exposure level values were evaluated and it was concluded that the SEL values are significant depending on the distance of the source from the measuring point.

Key words: drone, sound visualization, acoustic camera, noise load, frequency spectrum

1. Introduction

In nowadays, drones are increasingly used in various areas of our daily lives. Areas of drone use include art, agriculture and road management, energy and communications, mapping, terrain scanning, documentary, film and art, safety and environmental protection, etc. Many unmanned aircraft have become accessible to ordinary users in recent years, and their equipment is relatively complex and includes photo and video creation equipment, an autopilot system and various intelligent navigation systems that make controlling such aircraft quite simple. The use of drones in the near future will ensure great savings in materials, energy and human resources.

However, the use of drones also brings a number of noise problems. According to various surveys conducted mostly in the United States and Russia, the disturbing sound of drones is one of the most feared problems that drones can cause. In the presented work, after the analysis of available methodologies, attention is paid to achieving an improvement in the acoustic quality of the environment in which we live, work, and relax. The basic goal of the work was to test the methodologies for the assessment of acoustic descriptors, and to carry out initial measurements of drone noise in order to assess the negative effects of drones on humans.

2. Laws and regulations in drone area

The legal framework for the use of drones for private and commercial purposes is set out in EU Regulations 2019/947 and 2019/945 [1] [2] (EU Member States and EASA). They take into account the weight and technical parameters of the drone and the operation to be performed.

Implementing Regulation (EU) 2019/947 regulates the operating rules for drones, divides the operation of drones according to type and place of use, and also addresses their level of risk. Delegated Regulation (EU) 2019/945 describes the building regulations and characteristics of drones in different categories. For the first time, a standard EU

drone noise assessment is available in an annex to the delegated regulation in the Open Category.

The new rules ensure that drone operators - whether amateur or professional - clearly understand what is or is not allowed. They will cover all types of operations, from those not requiring prior authorization to those involving certified aircraft and operators, as well as minimum training requirements for long-haul pilots. It defines three categories "open", "specific" and "certified".

All these measures concern pilots, operators and the drones themselves. For now there is no detailed specification of the effects of drones on inhabited areas and human-inhabitants. As mentioned, Delegated Regulation (EU) 2019/945 only covers the standard assessment of drone noise. This is an indication of the guaranteed sound power level. This level should be determined according to STN EN ISO 3744: 2010 Acoustics. Determination of sound power levels and sound energy levels using sound pressure. Manufacturers are required to document the guaranteed sound power level under the CE marking. Therefore, further research is needed in this area.

3. Noise measurements from drone operation

The basic recommended measuring principles that can be used to assess the acoustic quality of drones and which we want to address in the further processing of the topic include:

- sound visualization by acoustic camera,
- the use of an acoustic compass for the analysis of the directional load of the population,
- sound level meter system,
- sound intensity measuring device,
- 3D visualization device.

To test the measurement principles, classical measurements were performed with a sound level meter system and sound visualization with an acoustic camera.

3.1. Measurements with an acoustic camera

The primary goal of any localization technique is to accurately analyze and visualize the source of the noise, most often directly on a photograph or video of the tested object. The sound source is usually represented as a color map, corresponding to the sound pressure distribution or also the place with the highest measured amplitude.

We measured the flight of one quadcopter with an acoustic camera at two speeds – high and low. The view of this quadcopter and its characteristics are shown in Figure 1 and Table 1.



Figure 1. The view of the quadcopter DJI Mavic Mini

Table 1. Characteristics of the quadcopter DJI Mavic Mini

Power supply:	2S Li-ion, 2400 mAh
Propellers:	4,7x2,6x2
Weight:	249 g
Shoulder length	107 mm

The following picture shows a view of a flying quadcopter and a visualization of the noise emitted from it.



Figure 2. Visualization of the noise emitted from quadcopter

Figure 3 shows the quadcopter low speed flight spectrogram. From the visualization results, we can determine the dominant frequencies that occur at a frequency of 8000 Hz.

A spectrogram is a visual representation of the frequency spectrum of an audio or other signal that changes with time or another variable. The spectrograms are used for a more detailed analysis of noise sources in which it is possible to analyze the amount of radiated noise depending on time, frequency and location.

A common format is a graph with two geometric dimensions: one axis represents time or RPM (Revolutions per minute), the other axis is frequency. The third dimension indicating the amplitude of a particular frequency at a particular time is represented by the intensity or color of each point in the image.

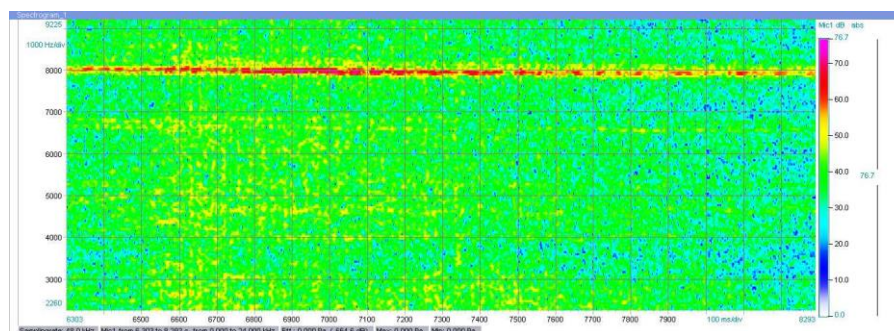


Figure 3. Spectrogram of a low speed flight of the quadcopter

Figure 4 shows the low speed flight spectrum of the quadcopter. The sound spectrum in acoustics is a combination of all the frequencies of which the evaluated sound is composed. It can be seen from this spectrum that the dominant frequency is 8000 Hz and that no other, resonant frequencies occur.

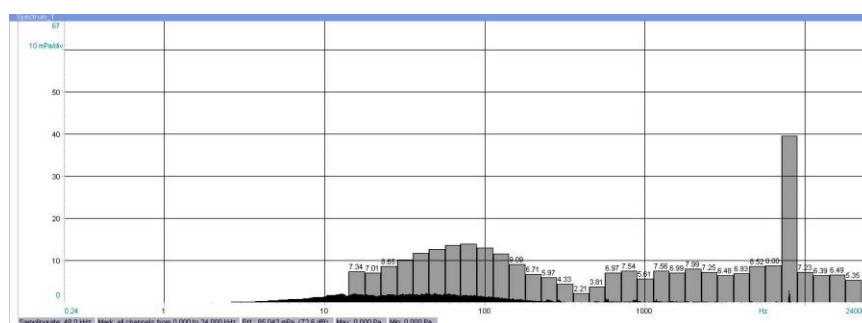


Figure 4. Spectrum of a low speed flight of the quadcopter

Figure 5 shows the quadcopter high speed flight spectrogram. From the results of the visualization we can also determine the dominant frequency at 8000 Hz and several other less significant frequencies - 6800 Hz and 4000 Hz. These less significant frequency components occurred at higher propeller speeds and higher engine loads.

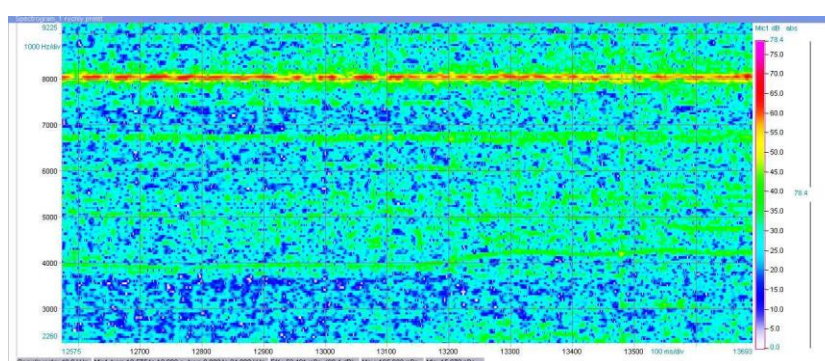


Figure 5. Spectrogram of a high speed flight of the quadcopter

Figure 6 shows the quadcopter high speed flight spectrum. From the above, it can be seen that the generated noise is more distributed throughout the spectrum.

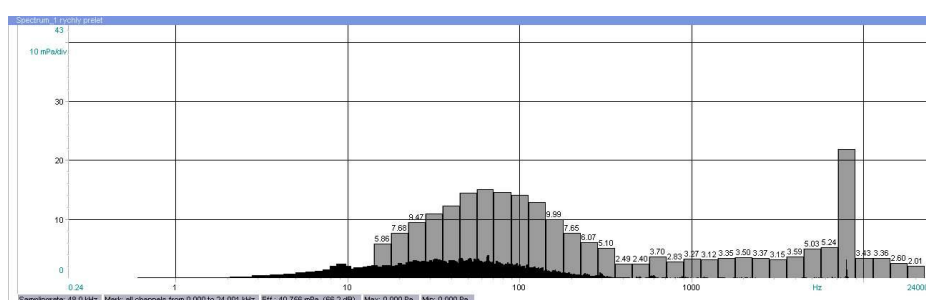


Figure 6. Spectrum of a high speed flight of the quadcopter

3.2. Measurements with a sound level meter system

Figure 7 shows a scene of the measuring points and the arrangement of the measuring devices in the experiment. The measuring microphones were arranged so that we could assess the effect of a flying drone on a person who is at ground level (1.5 m above ground level) and at several heights (the effect of drones on protected objects at level 2 to 3 above ground). The deployment and setup of the instruments had the task of analyzing acoustic events in terms of time domain.

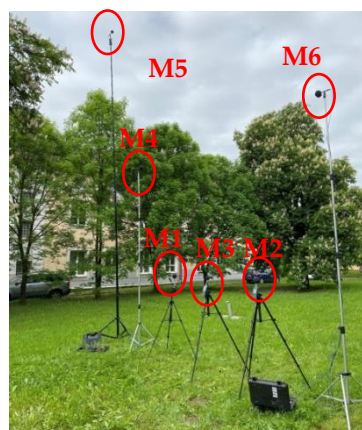


Figure 7. Scene of the measuring points

During the experiment, 2 sets of measurements were performed. The quadcopter flew back and forth at low and high speeds. Figure 8 shows the time record of all six measuring points and eight flights - four at low speed and four at high speed. From the mentioned time records, the variance of the measurement results at individual flights and the differences in the measured values at individual measuring points are obvious.

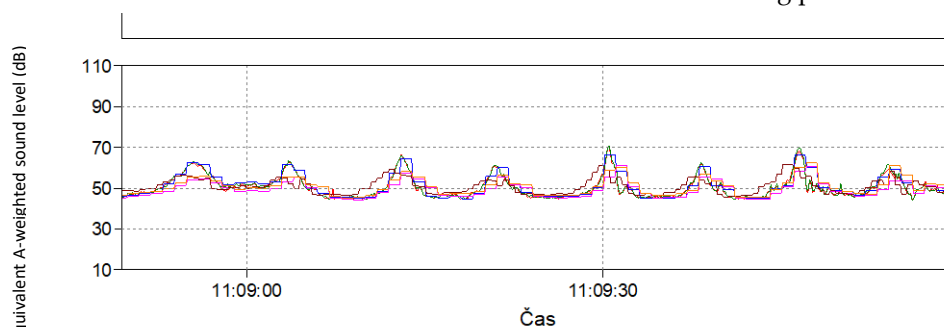


Figure 8. The time record from all measuring points for all quadcopter flights

Table 2 shows the sound exposure level (SEL) values that characterize the selected acoustic events, in our case one flight. In general, the sound exposure level expresses the total energy of an acoustic event and is referred to as L_{AE} . We use this quantity mainly in cases where the acoustic situation is created by individual separate acoustic events, such as vehicle and train crossings, aircraft flights, shooting, loading / unloading of goods and the like.

Table 2. Values of the equivalent sound pressure level of the investigated quadcopter at low and high speed flights

	Low speed, dB						High speed, dB					
Measuring point	1	2	3	4	5	6	1	2	3	4	5	6
L_{Aeq}	65,6	65,9	66,7	60,8	62,6	62,1	66,8	67,2	67,4	63,2	63,3	63,8

From the values above, the difference of the sound exposure level values for the individual measuring points can be clearly seen. Despite the relatively small distances of the measuring points from each other (in the order of 1.5 to 4 m), the differences between the values are relatively high (usually 2 or more dB). From this finding, it can be concluded that the SEL values are significant depending on the distance of the source from the measuring point.

5. Conclusions

The measurements that were performed and described in this paper were the first step in the design of a methodology for measuring drone noise and its effects on humans. In addition to the described measurements when flying through the vertical system of microphones, other measurements were performed through the horizontal system of microphones, which will be gradually incorporated into the new methodology.

When evaluating the measurement results with an acoustic camera from the spectrogram, significant differences were found. We have determined the dominant frequency at 8000 Hz in low and fast speed flights, but in a fast flight case we have noticed several other less significant frequencies - 6800Hz and 4000 Hz. These less significant frequency components occurred mainly because of higher engine loads, which means that this type of flight needs to be analyzed in more detail.

The conclusions resulting from the experiment include:

- drone noise can be characterized by a strong tonal component,
- amplitude is strongly dependent on flight speed - engine power,
- The difference between the emitted noise of different drones is significant.

This experiment is a basic input to the measurement and assessment of drone noise. After further elaboration of the issue, a comprehensive methodology will be created, which could serve in the process of product (drone) certification.

Acknowledgments: This paper was created within the project KEGA 011TUKE-4/2021.

Conflicts of Interest: The authors declare no conflict of interest

References

1. Vykonávacie nariadenie komisie (EÚ) 2019/947 z 24. mája 2019 o pravidlách a postupoch prevádzky bezpilotných lietadiel.
2. Delegované nariadenie komisie (EÚ) 2019/945 z 12. marca 2019 o bezpilotných leteckých systémoch a o prevádzkovateľoch bezpilotných leteckých systémov z tretích krajín.
3. LUMNITZER, E. et al.: Hodnotenie vplyvov fyzikálnych faktorov na zdravie človeka. TU, 2014.159 s.ISBN 978-80-553-1632-1.
4. YEHOVA, A. et al.: Methodology for increasing the quality of technical equipment / Anna Yehorova ... [et al.] In: Acta Technica Corviniensis : Bulletin of Engineering. Roč. 13, č. 4 (2020), s. 13-18 [online]. - ISSN 2067-3809 (online)
5. LUMNITZER, E., YEHOVA, A.: Akustické vlastnosti práčiek z pohľadu očakávania zákazníkov / Ervin Lumnitzer, Anna Yehorova In: Fyzikálne faktory prostredia = FFP : časopis o problematike fyzikálnych faktorov prostredia. - Košice (Slovensko) : IbSolve Roč. 10, č. 1 (2020), s. 16-21 [print]. - ISSN 1338-3922



Influence of spur gear bodies shapes on the weight of the transmission mechanisms

Samuel Sivák ¹, Silvia Maláková ²

¹ Faculty of Mechanical Engineering, Technical University of Košice, Letná 9, 042 00 Košice, Slovakia; Samuel.sivak@tuke.sk

² Faculty of Mechanical Engineering, Technical University of Košice, Letná 9, 042 00 Košice, Slovakia; silvia.malakova@tuke.sk

Abstract: Design effort in machine construction is put expenses on a possible minimum. This can be done by reducing the weight of the components used in machines. In regard of gearboxes, the bigger reduction of weight is possible on gear wheel. Therefore, it is essential to reduce mass from gear wheel bodies in any gearboxes, especially in large industrial ones. Reduction of weight and mass must be done in a way where mechanical characteristics of gear wheels do not change or change by a slight amount. Basic characteristics for gearing are meshing stiffness, stresses located in a structure of a gear body and overall lifespan of gearing. This research is aimed at weight reduction in gear wheels made by forging. Weight reduction is made possible by changing the structure of gear wheel bodies, while preferably retaining the mechanical characteristics. Five different shapes for gear wheel bodies are proposed and compared to solid body gear wheel and then compared between each other.

Keywords: spur gear; shapes of body; weight; optimisation

1. Introduction

Modern development of machines and means of production is driven by increase in performance and also in reduction of the overall mass of these machines and its components. Reduction of weight in gearboxes down to minimum can be cause of an increase in stress values, which can be a cause of various failures in machine parts [1-3]. Operation process of gears can cause malfunctions such as, pitting – formation and expansion, insufficient gearing stiffness, abrasion of gearing faces and more [4]. Different malfunctions group is gear failures, composed of insufficient quality gear material, technology by which the gear wheel was made, incorrect heat treatment of a gear, inadequate lubrication or improper lubricant, impurity particles in lubricant, badly mounted gears, insufficiently designed gear.

For the gear design, specially for large gear wheels, it is important take into account shape of the gear body from construction point of view. Basic principle in such case is to reduce the overall weight of the gear wheel body and yet meet the mechanical requirements such as stiffness and strength [5, 6]. Construction of lighter gear bodies depends on the shape, which finished gear wheel will have, and this shape is dependent on a manufacturing process to some degree. Gears can be manufactured as welded structures, by casting, by forging or by milling.

By removal of large quantities of mass, it is possible to increase vibrations of such gearbox. This is mainly caused by underdimensioned structure of gear body, where stresses are more concentrated and bigger. This makes the gear wheel to deform much more which conditions the vibrations to increase due to higher amplitudes. Unaddressed vibrations can cause a transmission error [7 - 9]. All this leads to higher noise emissions and have a detrimental effect on gearing service life.

2. Materials and Methods

There are various design types of gears. Gearing has normalized shape and therefore it is very important to retain this shape, but at the same time the body of the gear wheel is open to structural changes [10]. Change in the structure of the gear wheel is performed with the aim to reduce its overall weight. These changes should have no or minimal impact on physical characteristics of the whole gear wheel in a negative way [11]. The weight reduction is performed by removing the excess material from the gear wheel body. Removal of excess material yields not only the lighter gear wheel, but also cheaper manufacturing, easier maintenance, and better manipulation. Downsides which may occur with such changes can have a detrimental impact on correct meshing, stiffness of the gearing or noise [12].

This work is focused on a shape of gear wheel bodies, which have modified bodies. Such gears can be forged, cast, or welded. The shapes of the gear bodies are dependent on several factors. Factors may be the material used for the wheel, size of such wheel and use of the wheel

2.1 Body Shape of Forged Spur Gears

Forging in gear wheel production is mainly used to create semi-finished products. Later these semi-finished products are machined into a final shape. Methods for forged gear wheel manufacture involve open-die forging or impression-die drop forging. As stated above, the excess material is around the area where gearing profile will be at finished gear wheel.

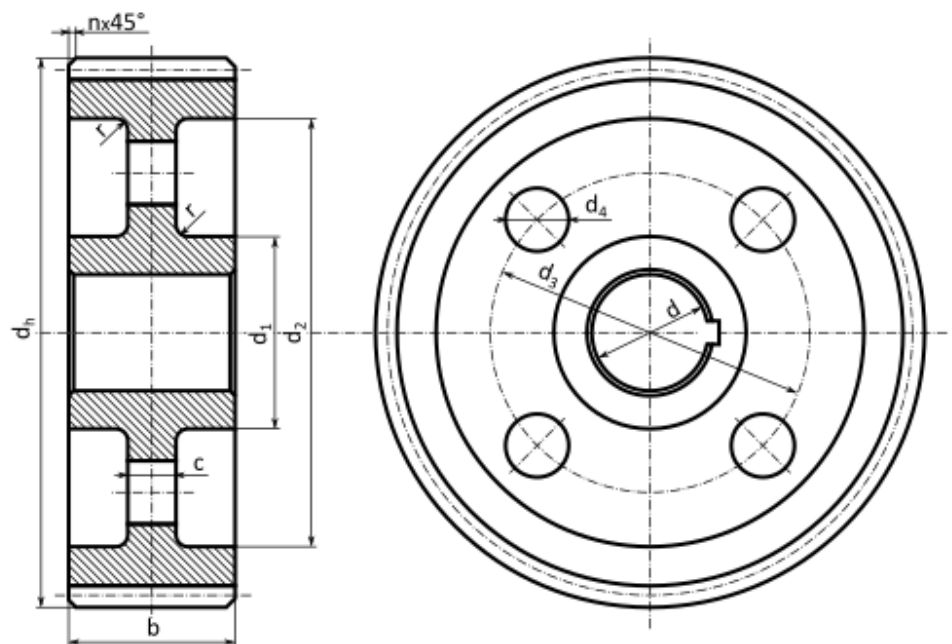


Figure 1. Scheme of a forged gear wheel body.

Equations given for the given forged wheel (Figure 1) are:

Shaft diameter

$$d = 0.32 \cdot a, \quad (1)$$

Hub diameter

$$d_1 = 1.6 \cdot d, \quad (2)$$

a is axis distance

Inner rim diameter

$$d_2 = d_h - 10 \cdot m, \quad (3)$$

m is modulus

Pitch diameter of relieve holes

$$d_3 = 0.5 \cdot (d_2 + d_1), \quad (4)$$

Holes diameter

$$d_4 = 0.25 \cdot (d_2 - d_1), \quad (5)$$

Plate width

$$c = 0.32 \cdot b, \quad (6)$$

Gearing chamfer

$$n = 0.5 \cdot m, \quad (7)$$

m is modulus

Radius


$$r = 5 - 10 \text{ mm}. \quad (8)$$



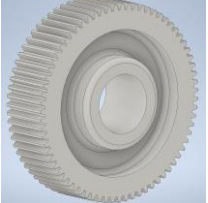
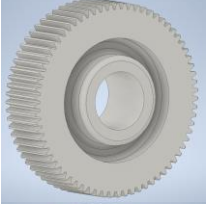

3. Results

The analyzed gear wheels have the same input parameters such as number of teeth, modulus, number of relieve holes (if any), shaft diameter and width of the gearing. All gear wheel body shapes are listed in Table 1 with short description of shape.

Gear wheel A is used as a reference wheel for the first analysis. This wheel has solid body without any structural changes, therefore it will be the heaviest one. All other shapes are then compared weightwise. Gear wheel B and C are made with relieve holes and a symmetrical relieve grooves. Number of relieve holes as well as the diameters are the same for both gear wheels. The rim thickness is the same as well, but the difference is in web thickness. Wheel C is thicker than wheel B so presumably it will be heavier, but it can yield better mechanical characteristics. Gear wheels D, E and F are made without relieve holes, only with a symmetrical relieve grooves. The web thickness is the same for all three wheels. Difference between these wheels is in a rim thickness, where wheel D has “normal” thickness, wheel E has its rim thickness drastically inflated and wheel F has its thickness drastically decreased.

Table 1. Table of gear wheel shapes with short description.

Title 1	Shape	Weight (kg)	Description
	A	8.986	Solid body gear wheel without any relieves

	B	5.132	Web thickness is 15 mm with 13 relieve holes, the rim thickness is 9 mm
	C	6.628	Rim thickness and number of relieve holes is same as for shape B, the web thickness is 35 mm
	D	6.647	Shape is without any relieve holes, web thickness is 15 mm, rim thickness is 18mm
	E	7.623	Web thickness is same as for shape D, rim thickness is 27 mm
	F	4.921	Web thickness is same as for shape D, rim thickness is 4.5 mm

The comparisons were made of each proposed shape to shape A. Data from Table 1 is processed in Table 2. Table 2 data is divided to 2 columns, where first column is weight difference of given shape to shape A in kilograms, the second column is this difference expressed as percentage.

Table 2. Weight comparison to A shape gear wheel.

Compared to	Weight difference (kg)	Difference (%)
B	3.854	42.89%
C	2.358	26.24%
D	2.339	26.03%
E	1.363	15.17%
F	4.065	45.24%

The graphical interpretation of Table 2 can be seen on Figure 2.

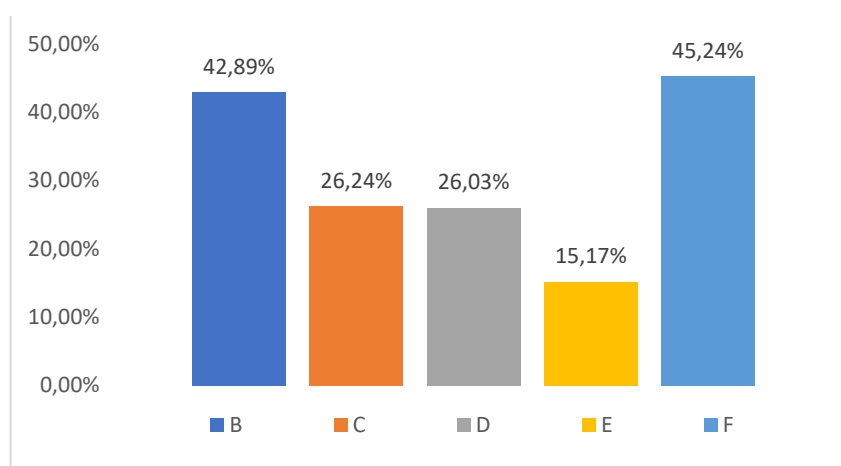


Figure 2. Graphical interpretation of weight reduction

Also, the comparison between shapes with relieve holes and shapes without them was made (Table 3). In Table 3 the A shape was no longer compared due to Table 2.

Table 3. Weight comparison to B and C shape gear wheel.

Shape	Difference compared to B (%)	Difference compared to C (%)
D	22.79%	0.29%
E	32.68%	13.05%
F	-4.29%	-34.69%

4. Discussion

From the Table 2 it is that the weight reduction was 42.89% for the shape B and 26.24% for the shape C. Shape C is obviously heavier given the thicker web dimension. The group without relieve holes had similar or even slightly better results. The Shape D had thicker rim but thinner web than shape C, yet the percentage difference for shape D to shape A was 26.03%, which almost on pair with shape C. Shape E had the lowest weight reduction from all shapes and it was 15.17%. This is a result of a much thicker rim dimension, the largest from all compared shapes. Shape F on other hand achieved the best result of 45.24%. Caused by the fact that this shape had the thinnest rim from all of the compared shapes. Also, the weight reduction for shape F and B are almost identical, the difference between these two is only 2.35%. It must be noted that the rim thickness for shape F was reduced beyond recommended value, which may lead to some unwanted mechanical changes i.e., bending of the rim, worsened meshing conditions or worse gearing stiffness.

Shapes were then compared in Table 3, where shapes with holes were compared to the shapes without relieve holes, which was done in a weight reduction way by percentage. Shape D and C have almost no difference weightwise, so the only difference in application of which shape should be used is on the manufacturing capabilities, given both should have good mechanical characteristics for meshing and stiffness of the gearing. Shape B had its weight reduced by almost $\frac{1}{4}$ compared to shape D and $\frac{1}{3}$ compared to shape E. This shape had second best overall reduction surpassed by shape F. Shape B is also 4.29% heavier than shape F, but as stated above, F variant can be prone to failures.

This research dealt only with weight reductions. The next aim will be to compare the weight loss to the stiffness of the gear wheel and gearing. How the shape influences the mechanical characteristics such as meshing stiffness. How and where it is appropriate to use these shapes.

Acknowledgments: This paper was developed within the project implementation KEGA 029TUKÉ-4/2021 "Implementation of modern educational approaches in the design of transmission mechanisms".

Conflicts of Interest: The authors declare no conflict of interest.

References

1. Dong, J.W.; Pei, W.C.; Long, H.Y.; Chu, J.; Ji, H.C. Solution of spur gear meshing stiffness and analysis of degradation characteristics. *Mechanika* **2020**, *26*, 153–160.
2. Czech, P.: Autonomous vehicles: basic issues. *Scientific Journal of Silesian University of Technology. Series Transport*. **2018**, *100*, pp. 15–22.
3. Flek, J.; Dub, M.; Kolar, J.; Lopot, F.; Petr, K. Determination of Mesh Stiffness of Gear – Analytical Approach vs. FEM Analysis. *Applied Sciences*. **2021**, *11*, 4960.
4. Kaššay, P.: Effect of torsional vibration on woodchip size distribution. *Scientific Journal of Silesian University of Technology*, **2018**, *99*, p. 99–105.
5. Jakubovičová, L.; Ftorek, B.; Baniari, V.; Sapietová, A.; Potoček, T.; Vaško, M. Engineering Design of a Test Device. *Procedia Engineering*, **2017**, *177*, pp. 520–525.
6. Monkova, K.; Monka, P.; Tkac, J.; Hricova, R.; Mandulak, D. Effect of the Weight reduction of a Gear Wheel on Modal Characteristics. *MATEC Web Conference*. **2019**, *299*, pp. 1–6.
7. Sapietková, A. Simplified computation methodology for contact forces on tapered rolling bearing with flexible parts. *Scientific Journal of Silesian University of Technology. Series Transport*. **2018**, *99*, pp. 177–182.
8. Kuľka, J.; Mantič, M.; Lummnitzer, J.: Analýza upevnenia čapu bubna separačnej linky. In: Medzinárodná vedecká konferencia katedier dopravných, manipulačných, stavebných a poľnohospodárskych strojov. Košice: TU, 2017, p. 111–120.
9. Figlus, T.; Koziol, M.; Kuczynski, L.: The Effect of Selected Operational Factors on the Vibroactivity of Upper Gearbox Housings Made of Composite Materials. *Sensors*, **2019**, *19/19*, 4240, p. 1–17.
10. Urbanský, M.: Comparison of piston and tangential pneumatic flexible shaft couplings in terms of high flexibility. *Scientific Journal of Silesian University of Technology: Series Transport*, **2018**, *99*, p. 193–203.
11. Wang, X.J.: Small Module Design of Ball Mill Main Drive Gear with $\Phi 2.4 \times 10$ m. *Advanced Materials Research*, **2013**, *787*, pp 490–494.
12. Zhao, N.; Sun, L.; Fu, B. Li.; Wang, Q.: Web Structural Optimization of the Big Aviation Herringbone Gear Based on APDL Language. *Applied Mechanics and Materials*, **2014**, *487*, pp 692–698.



Research on acoustic conditions around the wastewater treatment plant

Miroslava Badidová¹, Tibor Dzuro² and Lydia Sobotová³

¹ Technical University of Košice, Faculty of Mechanical Engineering, Department of Environmental Engineering; miroslava.badidova@gmail.com; Phone number.: +421 905 343 891

² Technical University of Košice, Faculty of Mechanical Engineering, Department of Environmental Engineering; tibor.dzuro@tuke.sk; Phone number.: +421 055 602 2673

³ Technical University of Košice, Faculty of Mechanical Engineering, Department of Environmental Engineering; lydia.sobotova@tuke.sk; tel.: +421 055 602 2793

Abstract: Industry and industrial areas are often found near human dwellings. One of the negative effects of the industry is the immission of noise emitted into the surrounding environment. As the concentration of the human population increases and industrial production increases, more and more people are exposed to the negative effects of noise. The contribution focuses on research into acoustic conditions around the wastewater treatment plant. The acoustic situation was mapped directly in the industrial plant and in the immediate vicinity, i.e. in adjacent villages. An important part of the research was the identification of dominant noise sources. An important step was the design of a technical solution to reduce the noise of the critical noise sources. Subsequently, a mathematical model was created – noise maps of the nearest surroundings of the wastewater treatment plant. Noise maps present acoustic conditions before and after the implementation of technical measures. Research has shown that the proposed measures were effective and highly effective.

Keywords: noise; emissions; immissions; environment;

1. Introduction

The WHO (World Health Organisation) [5] findings on environmental noise can be identified as a significant problem affecting negative health, but also the well-being of millions of the population in Europe. Environmental noise generated from transport, industrial production, etc. affects millions of people and has a significant impact on public health [3]. One in five people in Europe is exposed to environmental noise [5]. The fact that noise has serious negative impacts on human health and the fact that there is currently a large number of populations affected by environmental noise evokes considerable concern for many people. The authors of the paper focused their attention on the noise research generated by the technological equipment. Specifically, it is a wastewater treatment plant produced from pulp and paper production technology.

2. Characteristics of the waste water treatment plant

The wastewater treatment plant is part of a company that is oriented to the production of graphic and packaging paper. Production is carried out on 4 paper machines. Production is produced about 600,000 t/year of graphic and wrapping paper and production of about 300,000 t/year of recycled cardboard (corrugated) paper is starting. the wastewater treatment plant cleans up to 90% of the wastewater from the technological process of pulp and paper production. The treatment plant is also used for wastewater treatment from the urban agglomeration. The technological cleaning process itself consists of:

- mechanical degree of cleaning (edging, settling),

- biological degree of purification (biological oxidation, assimilation into biomass, active sludge),
- sludge management (thickening, drainage and sanitation of sludge).

Figure 1. shows the individual technological parts of the wastewater treatment plant.



Figure 1. Technological parts of the plant

The individual steps of the analysis of the current state of acoustic situation in the area of interest and the area itself are presented in Figure 2.

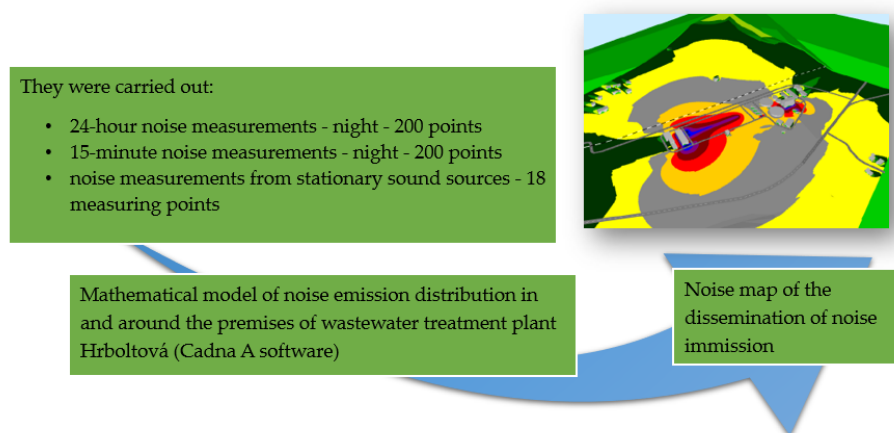


Figure 2. Procedure for the analysis carried out

3. Measurement of sound emissions from stationary sources

The aim of the measurements made was to determine the equivalent levels (EL) and the sound pressure of the stationary sound sources identified. These sound sources are presented in detail at work [3]. Measurements were carried out by soundprom meter NOR-140, microphones NOR-1225, calibrator NORSONIC NOR-1251 and measuring device TESTO 400 were used.

A pipe for air distribution to individual activation tanks has been designated as a critical sound source (Figure 3.).



Figure 3. Critical component of the plant

4. Technical solution for reducing noise emissions (immissories)

In the following section of the paper, the authors focused on a technical solution to reduce noise emissions of a designated critical sound source - the air distribution pipe. The basic technical parameters of the critical audio source are listed in the Table 1.

Table 1. Technical parameters

P.No.	Parameter	Value
1.	Pipe length	approx. 70 m
2.	Air pressure	60 to 63 kPa
3.	Airflow	62,000 to 64,000 m ³ /hour
4.	Air temperature before insulation	approx. 30 °C

The proposed technical solution for reducing the noise of a critical sound source is given in Figure 4.

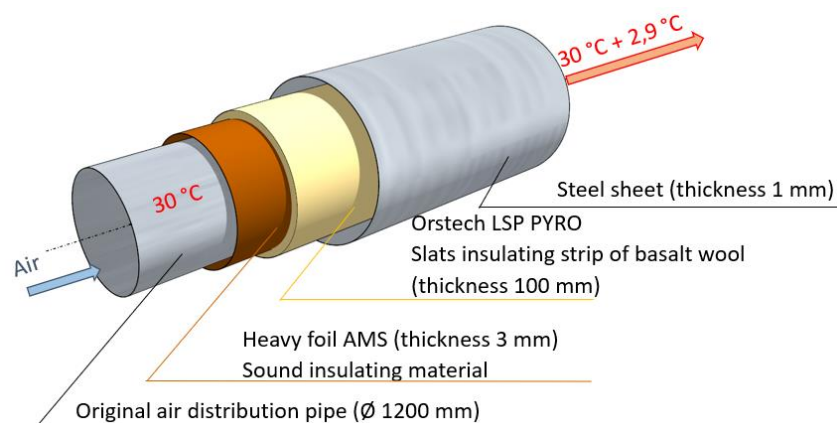


Figure 4. Technical solution to the problem

5. Verification of the effectiveness of the proposed technical solution

In order to verify the effectiveness (efficiency) of the proposed and subsequently implemented technical solution, measurements of sound (noise) have been carried out at identical locations in the dry cleaners' site and in its surroundings [3].

The resulting equivalent levels (EL) and sound pressure - stationary sources (before and after treatment) are given in Table 2.

Noise emission measurements in the immediate vicinity of the wastewater treatment plant were carried out at two measuring points – 24-hour measurements (the village of Hrboltová and Černová). The results of the measurements are presented in the work [3].

Table 2. Resulting equivalent values (EL) A and sound pressure (comparison)

Measuring point	Distance from source [m]	Location of the measuring point	L _{Aeq,T} [dB]	
			Before editing	After editing
M1	6	Compressor station north side	68,1	58,7
M2	3	Between the compressor station and the air distribution pipe	79,5	64,5
M3	9	Compressor station - south side	80,2	66,0
M4	6	Activation tanks – south side	68,7	60,1
M5	6	Activation tanks – south side	67,5	61,4
M6	6	Activation tanks – south side	63,5	60,2
M7	6	Activation tanks – south side	59,8	59,3
M8	25	Biofilter	62,4	58,4
M9	10	Entrance pumping station	63,6	63,4
M10	12	Sludge farm object	63,2	52,4
M11	6	Activation tanks – north side	61,8	54,4
M12	3	Air distribution pipes	72,3	65,4
M13	6	Activation tanks – north side	65,8	54,8
M14	3	Air distribution pipes	74,6	73,1
M15	3	Air distribution pipes	76,1	67,3
M16	6	Northwest boundary of the waste water treatment plant site	57,1	56,8
M17	4	Between the compressor station and the tram station	64,5	64,9
M18	8	Between the entrance pumping station and the sludge economy	66,4	59,1

6. Noise map - dissemination of noise immission

For the purpose of creating an idea of the spread of noise immissions in the immediate vicinity of the wastewater treatment plant, the following tables present EL A sound pressure values, namely in Table 3. (before adjustments) and Table 4. (after adjustments) at the points (calculation) to be established.

Table 3. Calculation of the L_{Aeq} value (calculation points of the territory in question (before adjustments))

Point	Description of the point	Height of point above ground [m]	Equivalent sound pressure A level –			Permissible values			Overrun		
			L _{Aeq} [dB]			L _{Aeq} [dB]			[dB]		
			state of play 2018								
			day	evening	night	day	evening	night	day	evening	night
V1	Hrboltová, land border House, Street. Priehrada No. 1	1,5	46,5	46,5	46,5	50	50	45	-	-	1,5
		3	49,2	49,2	49,2				-	-	4,2
V2	Hrboltová, in front of the facade kindergarten	1,5	47,5	47,5	47,5	50	50	45	-	-	2,5
		3	50,1	50,1	50,1				0,1	0,1	5,1
V3	Hrboltová, land border House, Street. Priehrada No. 2	1,5	48,6	48,6	48,6	50	50	45	-	-	3,6
		3	51,3	51,3	51,3				1,3	1,3	6,3
V4	Eastern boundary of Hrboltová	1,5	45,7	45,7	45,7	50	50	45	-	-	0,7
		3	48,7	48,7	48,7				-	-	3,7
V5	Černová, in front of the facade House, Street. Račkov No. 15	1,5	47,3	47,3	47,3	50	50	45	-	-	2,3
		3	51,2	51,2	51,2				1,2	1,2	6,2
V6	The northern boundary of the Wastewater treatment plants	1,5	64,5	64,5	64,5	70	70	70	-	-	-
		3	-	-	-				-	-	-
V7	Southern boundary of Wastewater treatment plants	1,5	57,5	57,5	57,5	70	70	70	-	-	-
		3	-	-	-				-	-	-

Figure 5. shows the calculation points. The output of mathematical modelling of noise conditions around the waste water treatment plant is the noise maps shown in Figure 6. and Figure 7.

Table 4. Calculation values of L_{Aeq} (calculation points of interest territory (after adjustments))

VP	Description of the point	Height of point above ground [m]	Equivalent sound pressure A level –			Permissible values			Overrun		
			L_{Aeq} [dB]			L_{Aeq} [dB]			[dB]		
			state of play 2018			day	evening	night	day	evening	night
			day	evening	night						
V1	Hrboltová, land border House, Street. Priehrada No. 1	1,5	39,4	39,4	39,4	50	50	45	-	-	-
		3	42,2	42,2	42,2						
V2	Hrboltová, in front of the facade kindergarten	1,5	40,1	40,1	40,1	50	50	45	-	-	-
		3	42,8	42,8	42,8						
V3	Hrboltová, land border House, Street. Priehrada No. 2	1,5	41,3	41,3	41,3	50	50	45	-	-	-
		3	44,3	44,3	44,3						
V4	Eastern boundary of Hrboltová	1,5	41,0	41,0	41,0	50	50	45	-	-	-
		3	43,0	43,0	43,0						
V5	Černová, in front of the facade House, Street. Račkov No. 15	1,5	43,0	43,0	43,0	50	50	45	-	-	-
		3	46,4	46,4	46,4						
V6	The northern boundary of the Wastewater treatment plants	1,5	54,4	54,4	54,4	70	70	70	-	-	-
		3	56,2	56,2	56,2						
V7	Southern boundary of Wastewater treatment plants	1,5	49,5	49,5	49,5	70	70	70	-	-	-
		3	53,0	53,0	53,0						

**Figure 5.** Calculation points**Figure 6.** Noise map (mathematical model) - surroundings of the treatment plant (before modification)

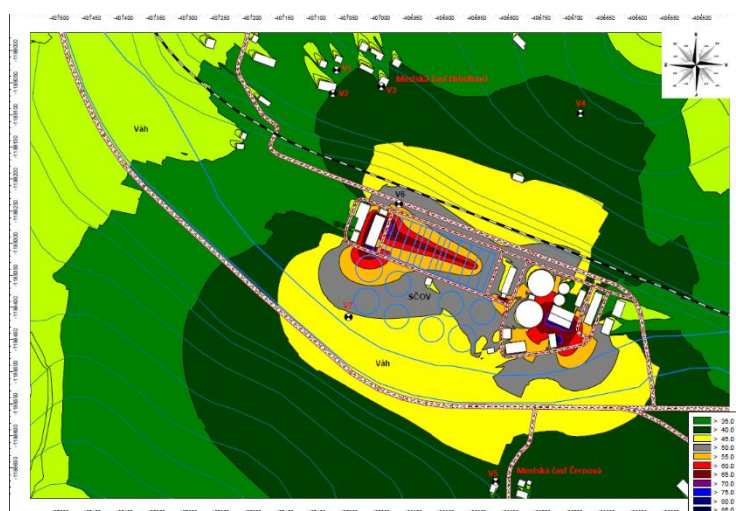


Figure 7. Noise map (mathematical model) - surroundings of the treatment plant (after modifications)

7. Conclusion

The authors of the paper focused on research into noise conditions around the wastewater treatment plant. They mapped the status quo, pinched the critical sources of the technology used, and devised a technical solution to reduce noise emissions at the sound source. The measurements carried out subsequently demonstrated the effectiveness (efficiency) of the proposed technical solution.

Acknowledgment

The contribution was based on the solution of the project Ministry of Education of the Slovak Republic KEGA No. 009 TUKE-4/2021 (50 %) and the project of the Ministry of Education of the Slovak Republic UNIVNET No. 021/0004/20 (50 %).

References

1. Badida, M.; Saturday, L.; Dzuro, T.: Engineering production and environment I. ELFA, s.r.o., Košice, 272 str., ISBN 978-80-553-3019-8.
2. Badida, M.; Saturday, L.; Dzuro, T.; Boďová, E.: Engineering production and environment II. ELFA, s.r.o., Košice, 354 str., ISBN 978-80-553-2674-0.
3. Badidová, M.: Proposal of options for reducing noise emission systems around the wastewater treatment plant. Thesis. SJF TU in Košice. 2021, 78 str.
4. Badid, M.; New, A.; Pástor, K.: Proposal for a trchnický solution to reduce noise emissions on air-dissecting pipes. Physical factors of the environment No. 02/2021, Vintage XI., 2021, ISSN 1338-39., with tr.5 – 9.
5. Environmental noise in Europa – 2020. EEA Report. No. 22/2019 European Agency, Copenhagen Denmark, 2020, ISBN: 1977-844, 100 p.
6. Moravec, M.; Badida, M.; Mikušová, N.; Saturday, L.; Swede, J.; Dzuro, T.: Proposed option for noise reduction from wastewater treatment plant: Case study. 2021. In.: Sustainability No. 4/2021, Vol. 4th, p. 1-22 online. – ISSN 3071-1050 (online).

Construction design of a heat transfer intensifier for low-pressure vessel for storing hydrogen

Filip Duda ¹, Natália Jasminská ², Tomáš Brestovič ³

¹ Department of Power Engineering, Faculty of Mechanical Engineering, Vysokoškolská 4, 042 00 Košice; filip.duda@tuke.sk

² Department of Power Engineering, Faculty of Mechanical Engineering, Vysokoškolská 4, 042 00 Košice; natalia.jasminska@tuke.sk

³ Department of Power Engineering, Faculty of Mechanical Engineering, Vysokoškolská 4, 042 00 Košice; tomas.brestovic@tuke.sk

Abstract: This article is about issue of hydrogen storage in the structure of metallic alloy based on elements La Ce Ni and addresses the design of a heat transfer intensifier in a low-pressure vessel, which is made from steel, and which is used for hydrogen storage.

Key words: Heat intensifier, heat transfer, hydrogen, hydrogen storage, metal hydride vessel

1. Introduction

Design and construction of low pressurised storage vessel must be based on standard STN EN 13322-2. The name of this In the face of global warming, efforts have intensified to discover, explore, and implement various new alternative sources of energy. Various states and their politic movements around the world are currently working to raise awareness about renewable sources of energy. In this context, hydrogen is considered as good candidate mainly because of its high thermal conductivity and prosperous effects on surrounding environment. Hydrogen however is not source of energy, but energy carrier. In this case suitable energy storage mechanism is required. There are multiple ways of storing hydrogen and those are: high pressurised storage, liquid cryogenic storage, and low pressurised storage in structure of metallic alloys. Low pressurised storage vessels for storing hydrogen are currently in development. The main disadvantage of low pressurised storage of hydrogen is the need of cooling the alloy while absorbing and heating the alloy while desorption of hydrogen. In this article low pressure vessel is considered.

2. Design of low pressurized storage vessel for hydrogen

Design and construction of low pressurised storage vessel must be based on standard STN EN 13322-2. The name of this standard is Pressure vessels for gas transport, design, and manufacture of refillable steel pressure cylinders. The vessel design consists of a primary vessel and a casing for coolant as shown on Figure 1.

TABLE 1. Mechanical properties of alloy 1.4306

0.2% Re (MPa)	Rm (MPa)	ρ (kg·m ⁻³)	μ	E (MPa)
200	500-700	8000	0.3	2.1·10 ⁵

Where: Re-yield strength, Rm-failure strength, ρ -density, μ -Poisson's number a E- Young modulus of elasticity.

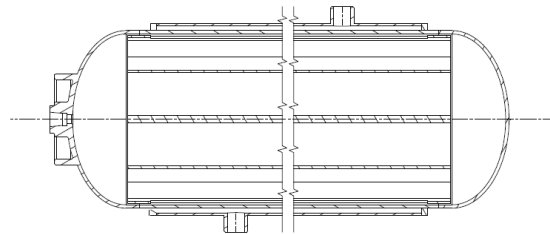


Figure 1 Design of low pressurised storage vessel

3. Design of internal heat intensifier for low pressurized vessel

The main task is to make a design of an internal heat intensifier for low pressurised storage vessel to improve heat transfer when filling a pressure vessel with hydrogen. The geometric design of internal transfer intensifier has five primary lamellas and ten secondary lamellas which are connected to primary lamellas. These lamellas altogether are connected in circular cross-section, which replicates diameter of low pressurised storage vessel. This geometrical element in storage vessel should increase the heat transfer area at the walls. The gap between the walls of primary vessel and internal heat intensifier is 1 mm. The internal heat transfer intensifier is shown on Figure 2.

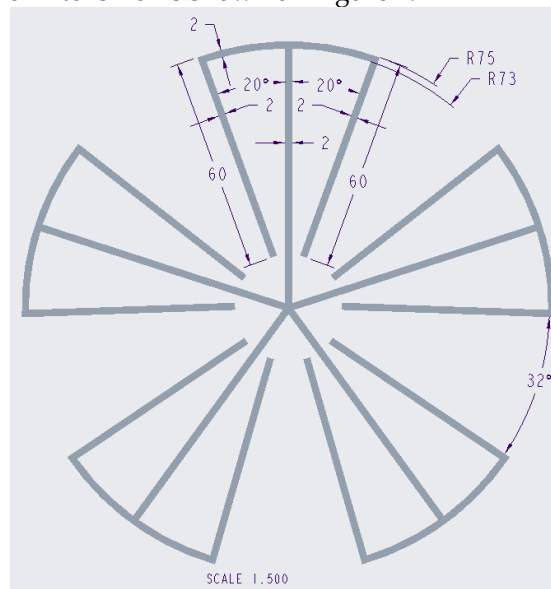


Figure 2. Design of internal heat intensifier

4. Simulation setting for internal heat intensifier

Internal heat intensifier with the main and ten secondary lamellas will be considered as shown on Figure 2. First thing to do in this simulation is to create simulation model in CAT program or within Ansys Workbench program. Simulation model consists of 4 parts which are: primary steel vessel, internal heat intensifier and metal hydride. After importing a model into Ansys CFX program it is necessary to create a mesh for each individual part as it is shown on Figure 3. Next part of simulation is to define all boundary conditions that will affect the simulation. One of the boundary conditions is that vessel is cooled by water on outer surface and the temperature of water is approximately 20°C. Flow of water is also considered as one of the boundary conditions and in this case the water flow is at speed of 0.3m·s⁻¹. Heat transfer coefficient between the pressure vessel and water was also calculated to simplify the simulation which is used as another boundary condition in simulation. Subsequently, a metal hydride alloy based on elements of La Ce Ni elements was defined and has these properties:

- Molar weight: $62,55 \text{ kg} \cdot \text{kmol}^{-1}$,
- density: $3250 \text{ kg} \cdot \text{m}^3$,
- Specific heat capacity: $430 \text{ J} \cdot \text{kg}^{-1} \cdot \text{K}^{-1}$,
- Thermal conductivity: $1 \text{ W} \cdot \text{m}^{-1} \cdot \text{K}^{-1}$.

In this simulation a filling time of 1200 s is considered.

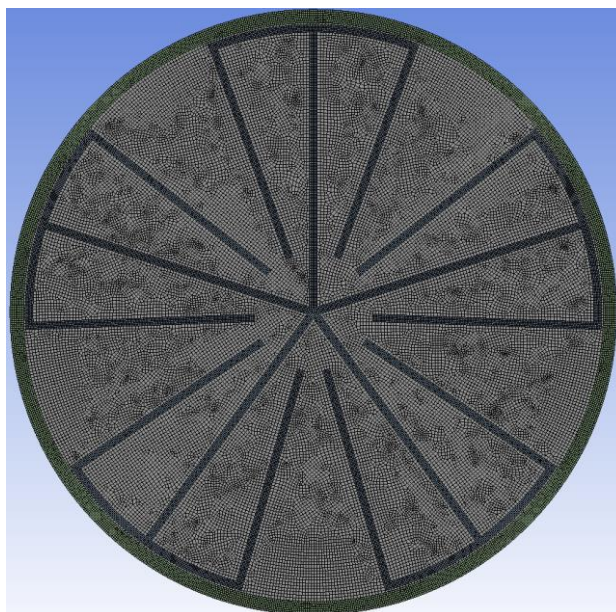


Figure 3. Mesh of the simulation model

TABLE 2. Simulation parameters

Metal hydride volume	$15\,698 \text{ mm}^3$
Mass of metal hydride	$51,0185 \cdot 10^{-3} \text{ kg}$
Mass of stored hydrogen	$7,295 \cdot 10^{-4} \text{ kg}$,
Volume of hydrogen	$8,117 \cdot 10^{-3} \text{ m}^3$
Generated heat	$8\,198,26 \text{ J}$
Internal generated heat	$6,8318 \text{ W}$
Intensity of internal heat source	$435,2 \text{ kW} \cdot \text{m}^{-3}$

Figure 4 shows all defined domains and boundary conditions in simulation program.

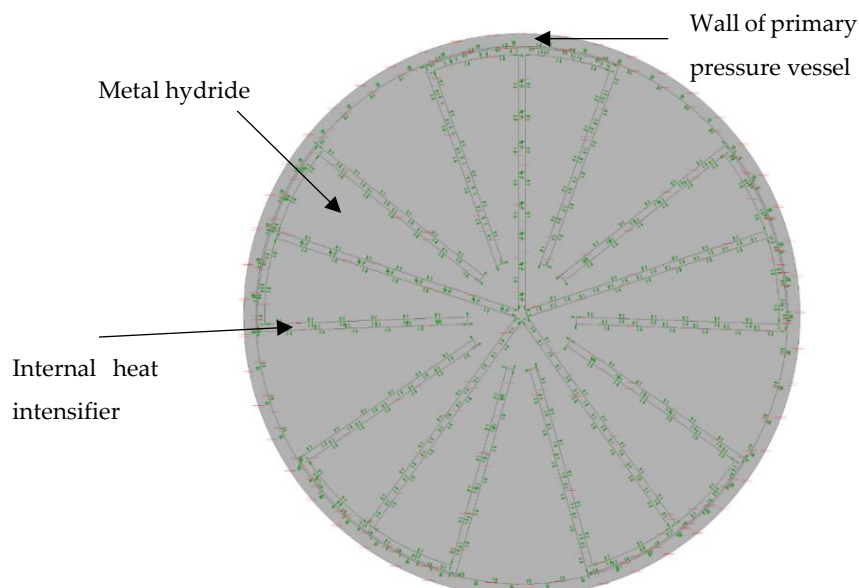


Figure 4. Boundary conditions of simulation model

5. Results of simulation

The generated temperature field in cross-section of the pressure vessel is visualised in Figure 5 where maximum temperatures after 1200 s is 89.53 °C. The warmest places are located exactly in the area between secondary lamellas as can be observed from Figure 5. Generated heat is very well removed from the centre of the vessel.

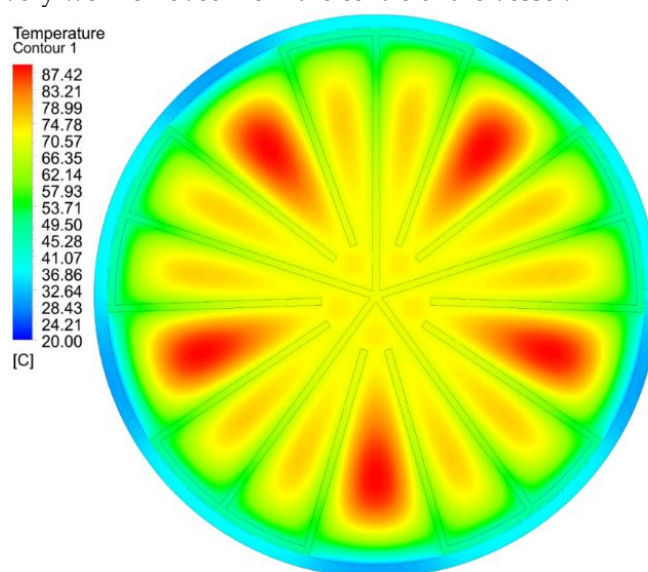


Figure 5. Generated temperature field in cross-section of pressure vessel

Figure 6 visualises minimum and maximum temperatures and temperature difference ΔT . In the last 200 seconds of simulation, maximum temperature curve is stabilised. Minimum temperature curve does not change from the middle of the simulation and remains on same value until the end.

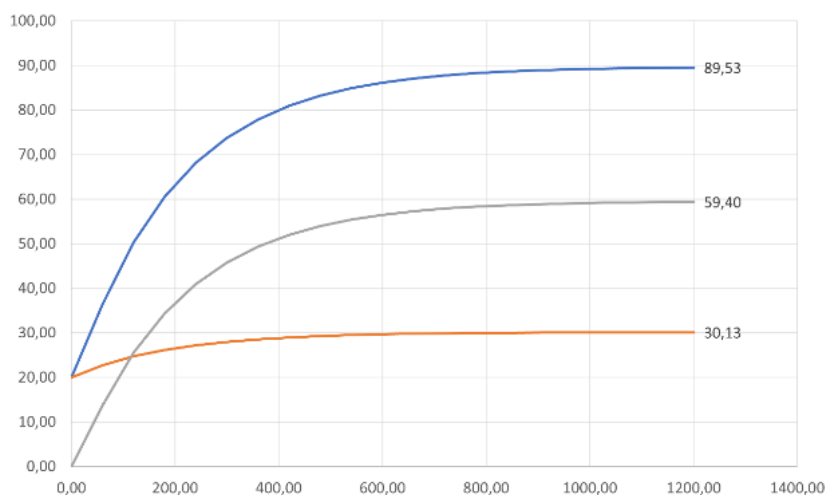


Figure 6. Coarse of minimum and maximum temperature curves and coarse of ΔT

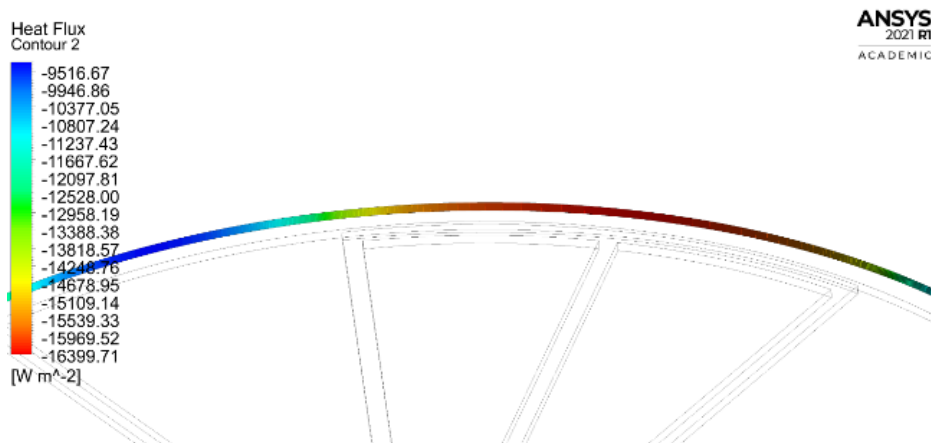


Figure 7. Heat dissipation by cooling

Figure 7 visualises heat dissipation from pressure vessel around the circumference of the steel shell. The highest values of heat dissipation are in places where either primary or secondary lamellas are located.

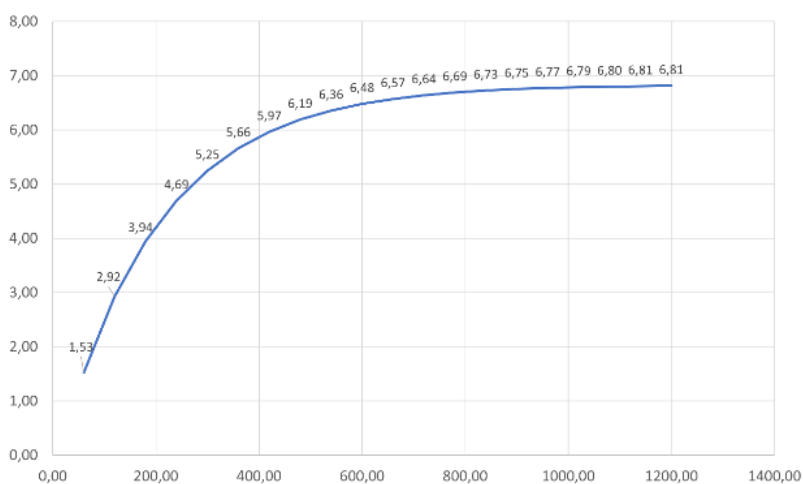


Figure 8. Cooling capacity over time

Figure 8 visualises the performance of pressure vessel when cooling during hydrogen filling. Maximum value reaches at 6.81W per 1mm model thickness. From Figure 8

can be observed, that the curve stabilizes from middle of simulation and does not have an increasing tendency

5. Conclusion

Hydrogen technologies represent a promising future in everyday use. Most promising future is in automotive industry and implementing hydrogen technologies in ordinary vehicles. Most common way to store hydrogen nowadays is by using high-pressure vessels mainly because of hydrogens low bulk density. Because of this disadvantage, storage in metal hydrides can be promising method for storing hydrogen. High pressures are not required while storing hydrogen in metallic alloys. The main disadvantages of storing in low pressure vessels are the low bulk density in the metal structure and very low value of thermal conductivity of used alloys. Main task of this article was to create an internal heat intensifier for efficient dissipation of heat from the core of primary vessel to outer shell, where the vessel is cooled by coolant which in case was water at 20 °C. The results of this simulation showed satisfactory results and values in all aspects of the study. Even better results can be achieved by optimizing geometric structure of internal heat intensifier by for example adding more lamellas or placing lamellas on different places in working environment.

Acknowledgments: This paper was written with financial support from the granting agency APVV within the Project Solution No. APVV-15-0202, from the granting agency VEGA within the Project Solution No. 1/0108/19 and No. 1/0626/20, and from the granting agency KEGA within the Project Solution No. 005TUKÉ-4/2019.

References

- [1]. Afzal, M. Mane, R. Sharma, P.: Heat transfer techniques in metal hydride hydrogen storage: A review. *International Journal of Hydrogen Energy* 42, 2017.
- [2]. Chibani, A. Bougriou, Ch. Merouani, S.: Simulation of hydrogen absorption/desorption on metal hydride $\text{LaNi}_5\text{-H}_2$: Mass and heat transfer. *Applied Thermal Engineering* 142, 2018.
- [3]. Valizadeh, M. Delavar, A. M. Farhadi, M.: Numerical simulation of heat and mass transfer during hydrogen desorption in metal hydride storage tank by Lattice Boltzmann method. *International Journal of Hydrogen Energy* 41, 2016.
- [4]. Jurczyk, Mieczysław.: *Handbook of Nanomaterials for Hydrogen Storage*. Singapore: Pan Stanford Publishing Pte. Ltd, 2018. ISBN 978-1-315-36444-5.
- [5]. Sankir, M a Sankir, D, N.: *Hydrogen Storage Technologies*. Scrivener Publishing LLC, 2018. ISBN 978-1-119-45988-0.
- [6]. Lipman, E, T a Weber, Z, A.: *Fuel Cells and Hydrogen Production*. New York: Springer Science+Business Media, 2018. ISBN 978-1-4939-7789-5.
- [7]. Züttel, A.: *MaterialsForHydrogenStorage*, Materials today, 2003.
- [8]. Klenovčanová, A., T. Brestovič a I. Imriš.: *VYUŽITIE FOTOVOLTAIKY NA VÝROBU VODÍKA ELEKTROLÝZOU VODY*, *Chem. Listy* 104, 122–129, 2010.
- [9]. Tóth, L., T. Brestovič a N. Jasminská.: *Absorption of Hydrogen in the HBond©9000 Metal Hydride Tank*, *International Journal for Innovation Education and Research*, 2018.
- [10]. Stolten, D.: *Hydrogen and Fuel Cells*, Weinheim: Wiley, 2010, 908 s. ISBN 978-3-527-32711-9.



Design of metal hydride tank with an internal heat intensifier

Šimon Hudák¹, Marián Lázár¹

¹ Faculty of Mechanical Engineering, TU Košice, Department of Power Engineering, Vysokoškolská 4, 042 00, Košice, Slovak Republic

This paper was written with financial support from the granting agency APVV within the Project Solution No. APVV-20-0205 and No. APVV-15-0202, from the granting agency VEGA within the Project Solution No. 1/0626/20.

Abstract: This article deals about the issue of improving the temperature management of a metal hydride tank, which being use for to reduce the energy consumption of hydrogen storage. The problem of absorption and adsorption of hydrogen gas in metals and cooling of metal hydride tanks in the process of hydrogen absorption is analyzed. The processed data are based on the current level of development of science and research in this area.

Keywords: metalhydride, hydrogen, tank, absorption, adsorption, desorption, alloys...

1. Introduction

On a global scale, means of transport are currently operated using mainly fossil fuels. Combustion thereof is accompanied with a release of certain substances to the surrounding environment, especially oxides of nitrogen and carbon, hydrocarbons, and solid particles. In an efforted air pollutants, relevant emission standards introduced in the EU are more and more stringent. A primary consequence thereof is reincreasing efficiency of combustion engines. The reduction of emissions cars down to zero was facilitated by introducing electric cars; however, it must be noted that their carbon footprint was just transferred to power plants that produce electricity. Also, environment-friendly production and disposal of used power batteries is currently very complicated. Replacing electric batteries with a hydrogen storage system comprising a fuel element facilitates the development of a car with a zero-carbon footprint. In this case, however, the problem of emissions is shifted again, just like in the case of electric cars, to areas where hydrogen is produced. As much as 96% of global hydrogen is produced from fossil fuels, primarily by partial oxidation of natural gas and steam reforming. Nevertheless, zero carbon footprint may be achieved by producing hydrogen from alternative energy sources using the electrolysis of water. We can say that the combustion of such hydrogen has a negligible environmental impact, from the fuel production stage up to the stage of fuel combustion in cars [2].

One way to store hydrogen is to compress it into pressure vessels as it is in a gaseous state at ambient temperature. When storing hydrogen in pressure vessels, it is necessary to increase the pressure enormously due to the low density of the gas, thus increasing the energy value of the stored hydrogen per unit volume. As a result of the increase in pressure in the vessel, it is possible to store more energy in the tank itself. However, the disadvantage is that increasing the pressure requires the use of thick-walled vessels, which, however, are very heavy and thus increase the total weight of the hydrogen storage device. Cylindrical or round shapes are used for safer distribution of compressive forces acting on the vessel walls. The spherical surface is generally the smallest of all geometrical units per unit volume, therefore heat exchange with the environment and loading are minimal, but on the other hand their production is very demanding, therefore cylindrical vessels are mostly used [1].

Another non-traditional way how to storage hydrogen at low pressure is using metal hydride alloys. During the hydrogen absorption into an intermetallic structure of an alloy, thermal energy is generated. As the temperature increases, the absorption process kinetics decreases, and the thermal field distribution becomes uneven due to the low thermal conductivity of powder materials. As a result, there are great temperature differences inside the powder alloy, and this is regarded as an undesired phenomenon. The heat transfer from and to the metal hydride alloy power may be increased by installing internal heat exchangers, thermal tubes etc.; which is the subject of this contribution as well.

2. Design of passive cooling modules to enable heat generated in the absorption process

During the adsorption of the hydrogen into the metal hydrides, a rapid pressure reduction can be observed compared to the compressed gas vessels at the same volume. The pressure drop is caused by the decomposition of the hydrogen molecule and the storage thus formed elemental hydrogen in the intermetallic structure of a metal alloy. The absorbed gas no longer contributes to the pressure in the tank until it is released from the alloy (desorption process).

This property is in terms of reducing the operating pressure in the metal hydride tank, so with a view to covering fuel consumption ensuring sufficient range is key and offers the possibility of implementing research activities mapping all the positives and negatives of these systems.

In this work, a cylindrical pressure vessel is designed, in accordance with the STN EN standard 13322, with a maximum operating pressure of 3 MPa (30 bar), serving on storage of hydrogen by absorption into the structure of a metal alloy. In the calculations, the characteristic properties of the metal hydride alloy were considered. This alloy contained elements such as Ti, Zr, Mn, V, Fe.

The designed metal hydride tank has a volume of 1.6 liters and its maximum operating pressure was set at 3 MPa (Fig.1). Its inner diameter is 50 mm with a wall thickness of 5 mm. The total length of the tank is 830 mm. This container can store 70 liters of hydrogen and is made of stainless steel 316 L.



Figure 1. 3D model of the metal hydride tank

Design of passive cooling modules

Since heat is generated in the process of absorbing hydrogen in the metal hydride, which takes place at a pressure of up to 3 MPa, it is necessary to design a cooling system that will dissipate excess heat. If no cooling occurs in this process, a so-called equilibrium state (pressure, temperature) is reached in a short time, at which the alloy is no longer able to absorb hydrogen. The variable parameter in the case of the designed tank, due to the limited maximum operating pressure in the tank, is the temperature.

In this proposal, I will focus on the design of a module that allows heat removal from the volume of the metal hydride alloy towards its edges to homogenize the temperature field of the metal hydride alloy. In addition to the homogenization of the temperature field in the metal hydride alloy, attention will also be paid to the design of a passive cooler, which dissipates the generated heat to the surrounding environment. In our case, we are

talking about an aluminum intensifier, which distributes the generated heat towards the shell of the tank, on which is placed a passive cooler, formed by circumferential ribs. The aluminum intensifier has a higher thermal conductivity than the thermal conductivity of the metal hydride alloy, which will increase the heat transfer from the volume of the metal hydride alloy towards the shell of the metal hydride (MH) tank [3].

The lamellae (ribs) placed circumferentially, have the shape of an annulus and are located on the shell of the MH tank along the main axis of the vessel (Fig. 2). The height of the lamella is 28 mm and the thickness is 2 mm with a observed spacing of 2 mm.

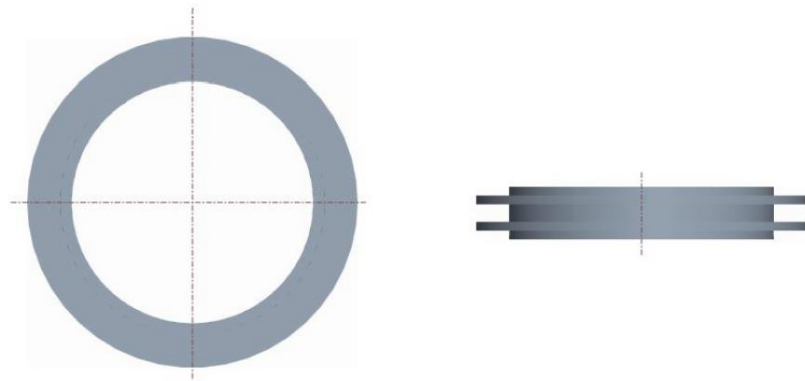


Figure 2. Geometry of lamellas located longitudinally in the main axis of the MH tank

Internal intensifier with cross lamellas, which gradually extend from the main axis (Fig.3). The first third of the main lamella, which is closest to the axis of the MH tank, is 1 mm thick. Above the first side (cross) lamella, the main lamella expands to 2 mm for more efficient heat dissipation and the thickness of the side lamellas is 1 mm everywhere. The intensifier consists of six main lamellas, which are arranged at an angle of 60° .

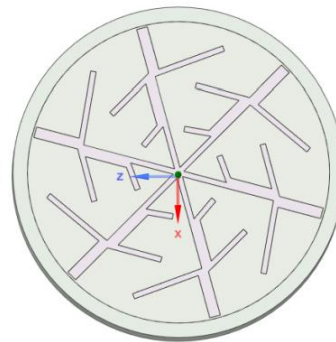


Figure 3. Inner intensifier with cross lamellas

The proposed heat intensifier was subsequently tested in the simulation tool ANSYS CFX. The first active cooling variant has the surface of the MH tank cooled by means of a shell heat exchanger in which the cooling medium flows. In the case of the second variant of the calculations, free convection was considered, where heat dissipation is ensured by means of a ribbed heat exchanger located on the shell of the MH tank (Fig.4). From the surface of the ribs, heat is transferred to the surrounding environment.

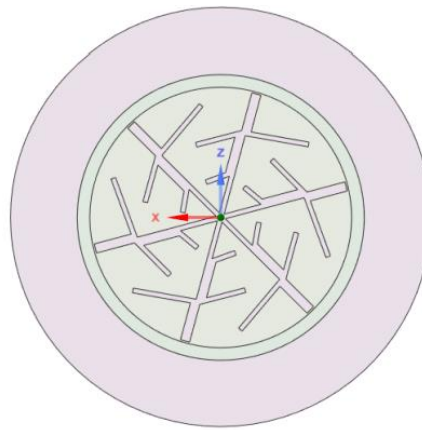


Figure 4. Ribbing with free convection on the shell of the MH tank

3. Water-cooled MH tank without and with heat intensifier

The temperature of the cooling water in both applications is at the inlet 10°C (Fig.5, Fig.6). The maximum temperature values have decreased significantly and have moved from the core of the container to the areas of the space between the lamellae, as can be seen in Fig. 6.

The installation of an internal heat intensifier also contributes to the homogenization of the temperature field in the volume of the metal hydride alloy, which contributes to improving the kinetics of the absorption process.

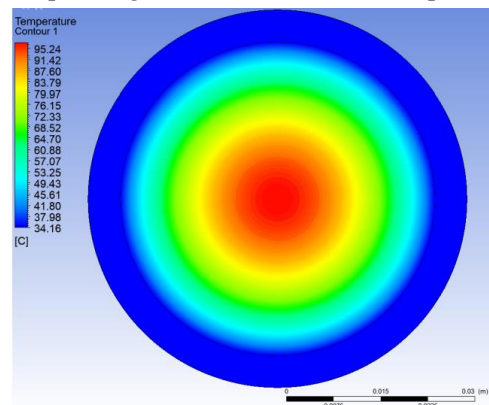


Fig. 5 MH tank with metal hydride without inner intensifier at cooling water temperature of 10°C – evaluation of the change of temperature in radial direction

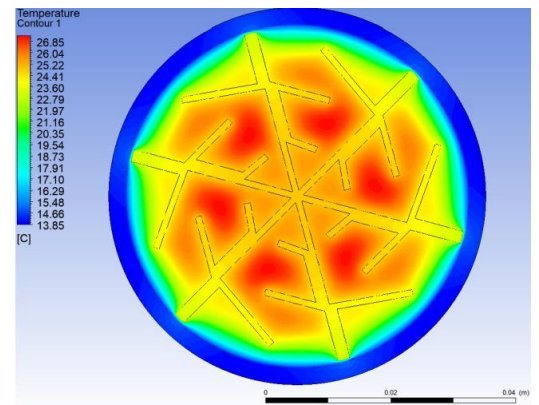


Fig. 6 MH tank with intensifier and his temperature field at cooling water temperature of 10°C

4. MH tank with external ribbing and heat intensifier

In this simulation, the external ribbing of the geometry around which the coolant (air) flows is used. For this reason, the heat transfer coefficient has changed compared to the previous simulation. The cooling air temperature was reset to 10°C . In contrast to the first case, where only an internal intensifier was used to stabilize the temperature field distribution, external heat exchangers were used in the following simulations to improve surface heat dissipation when using air as coolant instead of water. The use of air as a cooling medium reduces the overall requirements for the design of the tank due to simpler temperature management applications. Fig. 7 shows a temperature field without the use

of an intensifier and using external circumferential ribbing at a cooling air temperature of 10 °C. Fig. 8 shows the distribution of the temperature field in the hydrogen tank with considering the intensifier at cooling air temperature of 10 °C.

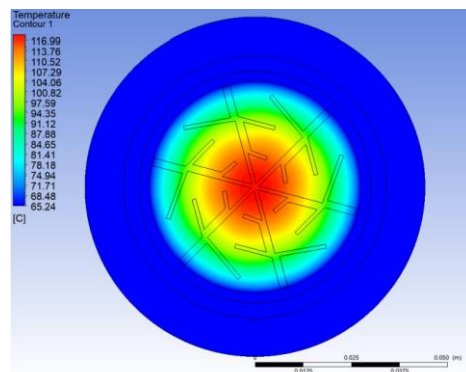


Fig. 7 Distribution of temperature field in the hydrogen tank without considering the inner intensifier at cooling air temperature of 10°C

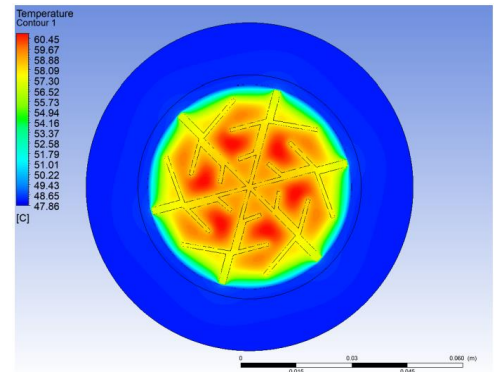


Fig. 8 Distribution of the temperature field in the hydrogen tank with considering the intensifiers at cooling air temperature of 10°C

5. Conclusions

From the simulations, it is clear that without the presence of an intensifier in the reservoir, the core overheats, while the heat flow from the core to the environment is impaired, due to the powder structure of the metal hydride alloy. With the use of the internal heat transfer intensifier, both in the case of the water-cooled tank and in the case of the air-cooled tank, the heat distribution within the entire cross-section of the tank was stabilized. In the case of a tank with an internal intensifier, which is cooled by water, the tank is kept at a lower temperature compared to the tank, which is cooled by free convection through a ribbed surface installed on the metal hydride tank. It can be stated that the intensifier significantly reduces the maximum temperature of the metal hydride alloy and contributes to a better homogeneity of the temperature field of the metalhydride alloy in the absorption-desorption cycle. Despite the qualitatively worse parameters of the heat dissipation achieved with the method of passive hydrogen tank cooling, the method is fit for broad spectrum use in the industrial applications, nevertheless. In stationary applications, where the lower kinetics of the absorption-desorption cycle is allowed, the method's use is highly justified in means of energy saving, which is necessary for the operation of active cooling systems.

References

1. BRESTOVIČ, T., JASMINSKÁ, N., LÁZÁR, M. Metal hydride tank cooling at hydrogen absorption into the La_{0.85}Ce_{0.15} Ni₅ alloy. 1st ed., EuroScientia, Belgium, 2017, p. 138.
2. BRESTOVIČ, T., PUŠKÁR, M., JASMINSKÁ, N., LÁZÁR, M. ROMANA, D., TÓTH, L., Analysis of the fast hydrogen release from the metal hydride container applied in automotive industry, Fire Safety Journal Volume 111, January 2020.
3. DANČOVÁ, M. Výskum možností zníženia energetickej náročnosti procesu chladenia metalhydridových zásobníkov, Diploma thesis, p. 58
4. HAHNE, E., KALLWEIT, J.: Thermal conductivity of metal hydride materials for storage of hydrogen: experimental investigation. Int. J. Hyd. Ener. 1998, p. 23,107-114.
5. KUMAR, A., RAJU, N. N., MUTHUKUMAR, P., SELVAN, V. P.: Experimental studies on industrial scale metal hydride based hydrogen storage system with embedded cooling tubes. Int. J. Hyd. Ener. 2019, p. 44. ISBN 13549-13560.
6. GARRISON, S. L., HARDY, B. J., GORBOUNOV, B. M., et. al.: Optimization of internal heat exchanges for hydrogen storage tanks utilizing metal hydrides. Int. J. Hyd. Ener. 2012, p.37, ISBN: 2850-2861.



Time dependence of the decrease in the odorant concentration in the natural gas mixture

Ivan Mihálik ¹, Tomáš Brestovič ²

¹ Department of Power Engineering, Faculty of Mechanical Engineering, Vysokoškolská 4, 042 00 Košice; ivan.mihalik@tuke.sk

² Department of Power Engineering, Faculty of Mechanical Engineering, Vysokoškolská 4, 042 00 Košice; tomas.brestovic@tuke.sk

Abstract: The article addresses the issue of changing the concentration of odorant added to natural gas and changing its properties in the pipeline depending on time. It describes various physical and chemical factors, such as absorption, adsorption, and oxidation, influencing the time dependence of the so-called odor fading, i.e. a decrease in the concentration of odorants in natural gas. The paper also evaluates experimentally obtained data on the change in odorant concentration in the pipeline as a function of time during the time when there is no flow in the pipeline.

Key words: Odorization, natural gas, odor fading

1. Introduction

Natural gas is one of the most important fossil fuels with significant applications in many areas of society. However, in addition to the many positives of its use, it is necessary to be aware of possible risks.

Natural gas is explosive at air concentrations in the range of approximately 4.4-17% [1]. The exact value of the interval depends on the actual composition of the natural gas and on the ambient temperature and the oxygen concentration in the air. Natural gas is non-toxic and does not cause a poisoning, but at higher concentrations it is unbreathable and suffocating for humans.

As natural gas is a colorless and odorless substance, the addition of odorants is necessary to guarantee safe operation and the possibility of immediate detection of a possible gas leak through the human olfactory.

2. Odorants

Odorants are particularly liquid substances with a characteristic odor which evaporate immediately under normal conditions in the pipeline. They are added to other odorless and usually dangerous substances to signal their presence without the need for any equipment.

They must have an unmistakable and unpleasant odor of sufficient intensity. Odorants must not leak out of intact pipes or disturb them themselves. On the other hand, they must have a good ability to pass through the soil layers so that they are recognizable by smell to people on the surface and thus determine the location of the gas leak from the pipe.

Odorants can be simply divided into two basic groups, specifically sulfur-based and sulfur-free odorants. However, mixtures of different types of odorants are currently used for the needs of industry. It allows to achieve optimal properties suitable for the specific application [2].

3. Odor fading

The odor fading can be defined as a gradual reduction in the odor intensity. This is caused by various chemical and physical processes that occur in the pipeline. These are processes such as absorption, adsorption and oxidation [3].

This unwanted process can be prevented by pickling the pipe. Pickling is the process of surface treatment of the inner walls of the pipe. During such a process various impurities are removed. At the same time, an increased amount of odorant is injected into the pipe. After some time in operation, in some cases it is necessary to repeat the pickling of the pipeline.

3.1. Absorption

Absorption is the process by which molecules of gaseous substances (absorbates) are dissolved and absorbed in solids (absorbents). Specifically, the odorant dissolves evenly throughout the volume of the pipe material. The odorant concentration gradually decreases until equilibrium is reached. After reaching this state, the absorbent is no longer able to absorb another amount of gaseous substance. This state is called the saturation state. The absorption process depends on the odorant concentration and also on the stoichiometry of the system [3].

However, desorption processes can also occur in distribution systems. In case of desorption, the odorant molecules are released from the pipeline into the natural gas. Similar phenomena were common especially in older pipelines, in which there was a naturally smelling gas transported in the past.

3.2. Adsorption

During the adsorption process, molecules of liquid or gaseous substances (adsorbates) are bound only to the surface of the solid or, in some cases, to liquid substances (adsorbent). Thus, unlike absorption, odorant molecules do not penetrate the entire volume of the piping material. The odorant molecules bind only to the inner wall of the gas line during adsorption.

Adsorption occurs due to surface energy. The walls of the pipe are not perfectly surrounded by atoms, so they can attach an odorant. Adsorption is divided into physical and chemical. Physical adsorption occurs under the influence of weak Van der Waals forces. Chemical adsorption is caused by covalent bonds.

In Figure 1. there is a graph of adsorption showing the relationship between adsorbate x and adsorbent m and pressure p at a constant temperature.

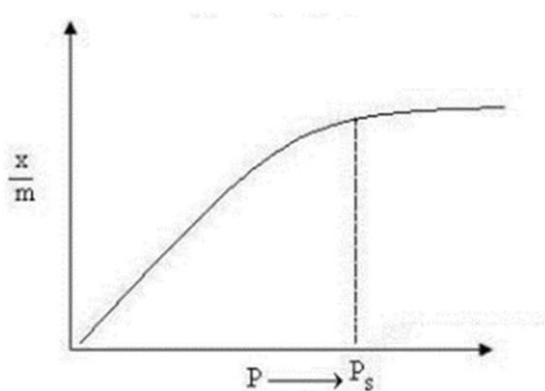


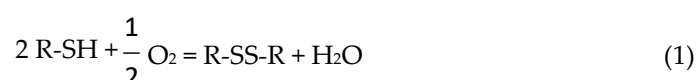
Figure 1. Adsorption isotherm

As the pressure increases, the adsorption also increases. After reaching the saturation pressure p_s , the adsorption no longer depends on the pressure [4].

3.3. Oxidation

During oxidation, a loss of electrons occurs, thus there is an increase in the oxidation number. This number indicates the sum of positive and negative atoms. Oxidation occurs during the reaction of iron oxide FeO, or other compounds, with the odorant. In this reaction, the chemical composition of the odorant changes.

Oxidation occurs most often in new steel pipes. Older or plastic pipes are less prone to oxidation. After the application of the new pipeline into the distribution network, the inner surface of the pipeline is porous and contains rust and scale. These metal oxides consist of iron oxide FeO, iron oxide Fe₂O₃ and iron oxide Fe₃O₄. They are highly reactive in contact with odorants. The oxidation of thiols to disulfides proceeds according to the following equation:



Adding FeO₂ to the equation would speed up the reaction even more. The disulfides thus formed then have a less pungent odor than the original thiols. This also changes the other properties of the odorant [3].

4. Decrease in odorant concentration as a function of time

To determine the time dependence of the odor fading in natural gas, or decrease of its concentration, an experimental measurement of the concentration of odorant TBM (tert-butyl mercaptan) in non-flowing natural gas in a closed pipe was performed within 97 days (Table 1). Electrochemical sensors were used to determine the concentration.

Table 1. Measured changes in odorant concentration in natural gas

Day	Odorant concentration in natural gas (mg·Nm ⁻³)
0	6.3
7	4.9
14	5.1
21	4.4
27	4.7
55	3.4
82	2.9
97	3.1

It is clear from the obtained data that, despite small deviations, the odorant concentration decreases in the long term. These slight short-term increase in concentration could be caused by the lack of sensitivity of the measuring devices. In addition, the possibility that various difficult-to-predict factors have caused the process of desorption of the odorant from the piping material back into the natural gas mixture should not be neglected.

The red trend curve in Figure 2, obtained by regression analysis provides an overall overview of the long-term decrease in the odorant concentration in natural gas. This curve is described by a polynomial equation of the 3rd degree:

$$y = -1.2318 \cdot 10^{-6} \cdot x^3 + 5.8341 \cdot 10^{-4} \cdot x^2 - 7.5129 \cdot 10^{-2} \cdot x + 5.9512 \quad (2)$$

where y represents the measured odorant concentration (mg · Nm⁻³) and x represents the day of measurement. The reliability of this curve is $R^2 = 0.9306$.

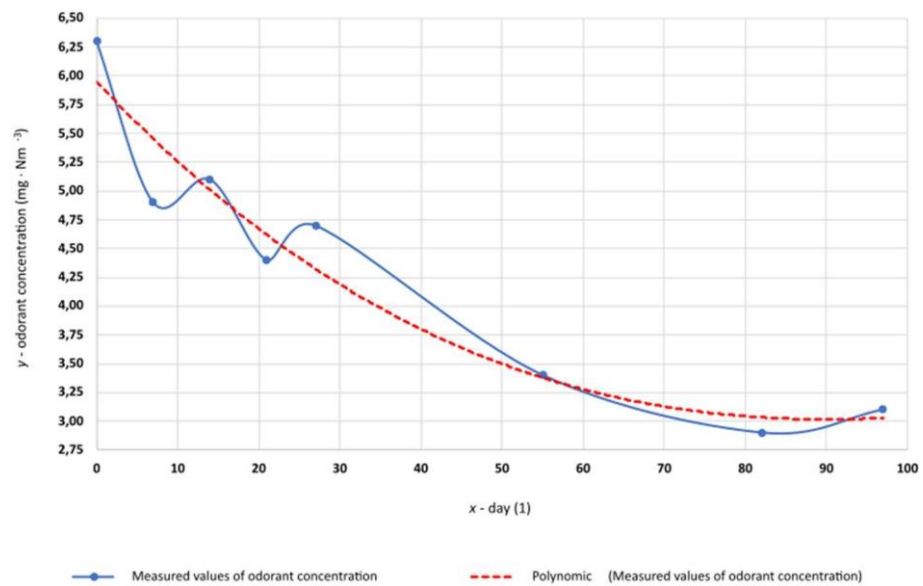


Figure 2. Time dependence of the decrease in the odorant concentration

5. Flow time and concentration decrease

When calculating the flow time, a pipe with a length of $l = 1500$ m and an inner diameter of $d = 0.1$ m was considered. Natural gas density $\rho = 26.58$ kg·m⁻³ at pressure $p = 3.075$ MPa. Average natural gas flow $Q_m = 1.8$ kg · h⁻¹ = 0.0005 kg·s⁻¹.

Then the following equation applies to speed v :

$$v = \frac{Q_m}{\rho \frac{\pi \cdot d^2}{4}} \quad (3)$$

$$v = \frac{0.0005}{26.58 \cdot \frac{\pi \cdot 0.1^2}{4}} = 0.0024 \quad (\text{ms}^{-1}) \quad (4)$$

At a velocity $v = 0.0024$ m·s⁻¹, the natural gas mixture passes through the entire pipeline in time t :

$$t = \frac{l}{v} \quad (5)$$

$$t = \frac{1500}{0.0024} = 625000 \quad (\text{s}) \quad (6)$$

$$t \cong 7.23 \quad (\text{days}) \quad (7)$$

After substituting the value $t = 7.23$ into equation (2) instead of x , an approximate concentration value $y = 5.44$ mg·Nm⁻³ was obtained after 7.23 days.

The minimum concentration that human olfactory can capture in a gas mixture is approximately 3.66 mg·Nm⁻³ [5]. After substituting this value into equation (2) instead of y and then expressing the value of x , it was found that to reach the minimum detectable

concentration, the gas in the pipeline would have to flow for approximately 44.33 days (Figure 3.).

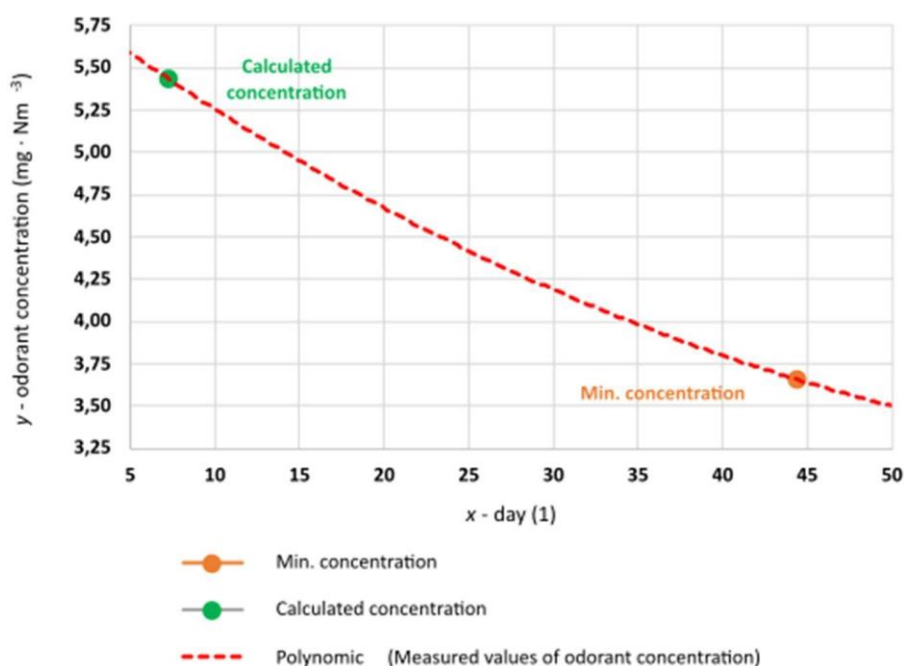


Figure 3. Comparison of calculated and minimum odorant concentration in natural gas mixture

6. Conclusions

The odorization of natural gas is a necessary process to ensure safe operation. To fulfill its warning function, the odorant must be present in a sufficient amount in the natural gas mixture. The data obtained and subsequent calculations show that, given the parameters of the pipeline and the given gas consumption, the flow rate is sufficient for the gas to reach the delivery point before the odorant concentration drops to a dangerous minimum. It would take approximately 6 times longer to reach a critical concentration.

Larger distances between delivery points and odorization stations, or a long-term decrease in natural gas flow, or a combination of these factors could be problematic. Therefore, it is necessary to ensure the optimal amount of odorant added to the pipeline, which is capable of covering the increased concentration losses.

Acknowledgments: This paper was written with financial support from the granting agency APVV within the Project Solution No. APVV-20-0205 and No. APVV-15-0202, from the granting agency VEGA within the Project Solution No. 1/0626/20.

References

1. innogy Slovensko s.r.o. [online]. Karta bezpečnostných údajov – Zemný plyn. [cit. 2021-11-03]. Available online: <<https://www.innogy.sk/sdoc/doc/plyn/ine/karta-bezpecnostnych-udajov.pdf>>
2. TENKRAT, Daniel – HLINČIK, Tomas – PROKES, Ondrej. 2010. Natural Gas Odorization [online], InTech. [cit. 2021-11-04]. Available online: <<https://www.intechopen.com/books/natural-gas/natural-gas-odorization>>
3. KILGALLON, R. 2015. Odourisation of CO₂ pipelines in the UK: Historical and current impacts of smell during gas transport. In: International Journal of Greenhouse Gas Control [online] 2015, Volume 37. Elsevier. [cit. 2021-11-04]. pp. 504-512. Available online: <<https://doi.org/10.1016/j.ijggc.2015.04.010>>
4. ARTIOLI, Y. 2008. Adsorption. In: Encyclopedia of Ecology [online]. Elsevier. [cit. 2021-11-05]. pp. 60-65. Available online: <<https://doi.org/10.1016/B978-008045405-4.00252-4>>
5. GREIM, Helmut. 2010. Part I: MAK Value Documentations. In: *The MAK-Collection for Occupational Health and Safety*. 2010, Volume 26. WILEY-VCH Verlag GmbH & Co. KGaA, Weinheim. 341 p. ISBN 978-3-527-32306-7



Processing of biogas from kitchen waste with a focus on hydrogen production

Lukáš Tóth ^{1,*} and Tomáš Brestovič ²

¹ Department of Power Engineering, Faculty of Mechanical Engineering, Technical University in Košice, Vysokoškolská 4, 042 00 Košice; lukas.toth@tuke.sk

² Department of Power Engineering, Faculty of Mechanical Engineering, Technical University in Košice, Vysokoškolská 4, 042 00 Košice; tomas.brestovic@tuke.sk

* Correspondence: lukas.toth@tuke.sk; Tel.: 055/ 602 4360

Abstract: The article deals with the possibilities of recovery of biodegradable kitchen waste. In addition to the most common methods of its current processing, it also solves the possibilities and procedures of biogas production, from which it would be possible to subsequently obtain e. g. hydrogen. In this case, it is possible to use biogas with a high concentration of methane to obtain hydrogen, which would then pass through the technology of WGS reactors, where methane and water vapor combine at an elevated temperature to form hydrogen and carbon dioxide.

Keywords: biogas; hydrogen; biodegradable waste; methane

1. Introduction

Due to the fact that since January 2021, according to Act 460/2019 Coll. to the obligation of municipalities and cities in Slovakia to introduce separate collection of biodegradable kitchen waste (BRO), it is necessary to consider their subsequent use. Due to possible exceptions to the law, it is necessary to realize that the law will apply to about 80% of local governments. As the sorting of biodegradable kitchen waste is currently unprofitable, it is necessary to find a way to obtain valuable products from the sorting of such waste, which would increase the attractiveness of this activity. Profits from the sale of products would reduce the costs of collecting and sorting this waste, which would more quickly meet the requirements and obligations to the European Union that result from the law.

2. Current state of the organic waste problem

Due to the fact that the annual production of biodegradable kitchen waste in Slovakia reaches the level of about 500 thousand tons, which is about 100 kg per person, this mass of energy usable waste has significant opportunities for the production of fuels that could be used as environmentally friendly fuel. Today, most of the biodegradable waste ends up in landfills, where microorganisms produce landfill gas, mainly methane, which has a significant impact on global warming, carbon dioxide, nitrogen oxides and hydrogen sulphide. The vast majority of these components have an adverse effect on the environment, whether in the form of gases that are released from the landfill and subsequently promote global warming, contribute to the formation of acid rain, or degrade air quality. Their negative impact can also contribute to soil and groundwater contamination, which in turn causes damage to the ecosystem in large areas.

According to the current decree, organic waste should be collected on an ongoing basis at least once every 14 days. According to observations from the surrounding countries of the European Union, which have already introduced this obligation, the collection of biodegradable kitchen waste is preferred every 7 days, or according to the needs of

filling collection containers primarily in summer, when faster decomposition of organic matter may occur. Decomposition of these substances already in the collection containers produces landfill gas in urban areas, which would significantly reduce the comfort of life of the inhabitants of such areas. It should be used for collection in municipalities with a predominance of family houses, especially the so-called bucket method, where households would be equipped with buckets of 7 - 25 liters, in which they should place decomposable waste. It is likely that after the introduction of this activity, in the case of agglomerations with family houses, smaller composting facilities will be created. Such facilities could be placed near every house or in the neighbourhood, which would result in the decrease of the amount and content of the biodegradable kitchen waste, which will need to be collected and processed. In the case of residential buildings, placing of brown collection containers with the volume of 120 - 660 liters is expected.

3. Current state of processing of biodegradable waste

The most common method currently used for the processing of biodegradable waste is their composting, or the use of fermentation equipment to accelerate the decomposition of waste and its sterilization due to elevated temperature. On the territory of Slovakia, composting stations are gradually being established in larger cities, where the natural decomposition of biodegradable waste occurs by means of microorganisms. The final product of these decomposition processes is humus and compost, which can be sold or used to fertilize urban greenery or gardens. EP and EC Regulation No 1774/2001 on animal by-products (replaced by EP and EC Regulation No 1069/2009) establishes a ban for the producers of kitchen and restaurant waste that is part of animal by-product, to feed terrestrial and farmed animals with this waste, with the exception of fur animals. In addition, the producer of such waste is obliged to ensure its processing. The operator of the facility is obliged to ensure the treatment of this waste in the following way: crush kitchen and restaurant waste into a fraction up to 12 mm in diameter and then subject it to thermal inactivation (hygienization) at 70 ° C for 1 hour. To address this obligation, local governments have the following technical options:

- composting plant with composting in open areas - is only a partial solution, it does not address the issue of kitchen waste according to European legislation, specifically the above-mentioned regulation on animal by-products,
- biogas plant - minimum capacity of 7000 t BRO per year, long transport distances BRO and thus increase the cost of BRO recovery,
- incineration plant - the problem is high investment costs and operating costs, a minimum capacity of 150,000 tons of BRO per year, long transport distances of BRO and thus an increase in the cost of recovering BRO,
- composting plant with BRO aerobic treatment technology (i.e. fermenter), including kitchen and restaurant waste, reaching the BRO recovery temperature required by the valid EC and EP Regulation No. 1069/2009. This is the most acceptable solution in terms of investment and capacity. The capacity of 1500-2000 t BRO covers the needs of local governments, which means short BRO transport distances and cost calculations given in the financial analyses of the prepared projects were the most economically acceptable in connection with the legal obligation to solve this problem.

At present, the production of biogas, which would be the most efficient method of processing biodegradable waste, is limited due to the inhomogeneity of the input raw material, when it is not possible to ensure an equal share of individual components in kitchen waste. Such a method of recovery of biodegradable waste comes into consideration in the case of waste recovery from places such as restaurants, canteens or supermarkets, where the type of waste and its suitability for subsequent biogas production can be precisely determined.

In an effort to use all types of biodegradable waste for high-gas methane production, which will be separated in the near future, it is necessary to carry out technological treatment such as particle reduction by grinding or chopping, followed by fermentation,

which disturbs larger organic chains, which improves and accelerates the subsequent process of conversion of organic compounds into biogas using methanogenic bacteria.

After fermentation, a residue remains - digestate, which is liquid or has a slurry consistency. It can be applied directly to agricultural land or, at lower water contents, it can be stabilized by composting.

Materials suitable for this technology are mainly agricultural waste, but also waste from the food industry, sludge from wastewater treatment and, in addition, kitchen and restaurant biological waste. Wastes with a humidity above 45% are especially suitable. The sanitation conditions set out in EC Regulation No. 1774/2001 EC apply to certain types of waste in a similar way to composting.

The process of converting organic matter into biogas takes place in several consecutive steps, each step involving a different type of bacteria and the final product of the cycle is subsequently converted by methanogenic bacteria into biogas, i.e. a gas with a high methane content, which is then possible to further energetically process.

4. Possibilities of using biogas methane

Biogas contains a large proportion of methane, which is one of the largest global warming factors and has a 25-times higher effect than carbon dioxide, which is considered the main greenhouse gas. The possibilities of using biogas are different. One of the most common is its direct combustion in cogeneration units during the production of electricity and heat.

One of the few technologies used is the WGS Reactor (water gas shift reactor). It is a plant in which water reacts in the form of steam with methane under the influence of the catalysts used. The presence of a catalyst is necessary for the reaction of the individual components to occur, according to equation (1). The most common catalyst is a layer of nickel oxide on an aluminium alloy, which is then pressed into porous pellets (Figure 1).



A reaction then occurs on the surface of these pellets. The main disadvantage of using this type of catalyst is its ability to clog with carbon release. Pellets need to be replaced after clogging. Thanks to the use of affordable materials without the presence of precious metals, their degradation and subsequent replacement is inexpensive.

The effective surface area of such pellets, depending on their type and method of production, is in the range of 3 - 30 m²·g⁻¹. Such area provides enough space for the reaction to take place. The most common substrate for nickel oxide is the CaAl₂O₄ alloy. For ZZC-11R and ZZC-12R alloys, the common inlet temperature is 430 - 650 °C and the outlet temperature ranges from 650 to 980 °C.



Figure 1. Different shapes of nickel-aluminum pellets.

It is possible to use a part of the collected biogas to heat the gas to the required temperature, which after combustion will ensure sufficient heating of the mixture, without the need for an external source of gas heating. The passage of methane through the WGS reactor results in a gas mixture in which the proportion of methane decreased

significantly, but at the same time the proportion of hydrogen increased which can be separated from the remaining biogas components and subsequently used as an energy source, either for direct combustion or in fuel cells.

Due to the controlled production and subsequent consumption of methane, there is no uncontrollable release into the atmosphere, as is the case with conventional municipal waste landfills. In contrast to conventional composting, in this case we obtain, in addition to fertilizers that can be applied to urban green areas or fields, also an energy-efficient product in the form of hydrogen. This method would make it possible to partially decentralize the methods of producing hydrogen as a fuel, while at the same time using biodegradable kitchen waste.

5. Conclusions

Due to the current state of development of technologies in the field of waste treatment, there is a possibility of obtaining biogas from biodegradable kitchen waste. Such a system would ensure not only the treatment of waste, but also the production of raw materials, which could become one of the critical resources for the development of the economy and transport in the near future. A system of hydrogen production from biodegradable kitchen waste could also significantly reduce the centralization of hydrogen production to smaller processing plants located near larger cities or agglomerations of smaller municipalities.

Acknowledgments: This paper was written with financial support from the granting agency APVV within the Project Solution No. APVV-20-0205 and No. APVV-15-0202, from the granting agency VEGA within the Project Solution No. 1/0626/20.

Conflicts of Interest: The funders had no role in the design of the study; in the collection, analyses, or interpretation of data; in the writing of the manuscript, or in the decision to publish the results.

References

1. STRAKA, F., kol.: Bioplyn. Praha, 2006, ISBN80 7328 09 6.
2. Aké budú novinky v zbere biologicky rozložiteľného kuchynského odpadu? Dostupné na: <<https://www.odpady-portal.sk/Dokument/105538/ake-budu-novinky-v-zbere-biologicky-rozlozitelneho-kuchynskeho-odpadu.aspx>>.
3. Zber a manipulácia biologicky rozložiteľného kuchynského odpadu zo zariadení spoločného stravovania Dostupné na: <https://www.uvzsr.sk/index.php?option=com_content&view=article&id=2767%3Azber-a-manipulacia-biologicky-rozloziteneho-o-kuchynskeho-odpadu-zo-zariadeni-spoloneho-stravovania&catid=93%3Abezpenos-potravin&Itemid=102>.
4. Spracovanie a zber Bioodpadu. Dostupné na: <<http://www.ekoray.sk/sk/BIO-odpad>>.
5. Zákon sa zmenil. Obce sa už triedeniu kuchynského bioodpadu nevyhnú Dostupné na: <<https://www.odpady-portal.sk/Dokument/105459/zakon-sa-zmenil-obce-sa-uz-triedeniu-kuchynskeho-bioodpadu-nevyhnu.aspx>>.
6. Mehariya S., Patel A.K., Obulisamy P.K., Punniyakotti E., Wong J.W.C.: Co-digestion of food waste and sewage sludge for methane production: Current status and perspective Bioresour. Technol., 265 (2018), pp. 519-531
7. Bruned Y. H.: Anaerobic co-digestion of algal sludge and waste paper to produce methane Bioresour. Technol., 98 (1) (2007), pp. 130-134.



Software support and additive technologies for veterinary applications

Gabriela Dancáková ^{1*}, Marek Schnitzer ¹, Alena Findrik Balogová ¹, Jozef Živčák ¹ a Radovan Hudák ¹

¹ Faculty of Mechanical Engineering, Department of Biomedical Engineering and Measurement, Technical University of Košice, Letná 9, 042 00 Košice, Slovakia; gabriela.dancakova.2@tuke.sk, marek.schnitzer@tuke.sk, alena.findrik.balogova@tuke.sk, jozef.zivcak@tuke.sk, radovan.hudak@tuke.sk

* Correspondence: gabriela.dancakova.2@tuke.sk; Tel.: +421 55 602 2655

Abstract: The purpose of this publication is to describe the process of implementing individual implants for veterinary applications. One of the main points is the description of individual software suitable for such use. The individual software are also compared in terms of their use in the individual implants modeled by them. Another part of the paper is focused on the use of 3D printing technology, also taking into account their use in individual implantology for veterinary applications.

Keywords: Individual implant; software; additive production; veterinary

1. Introduction

With the gradual introduction of additive technology and rapid prototyping in various industries such as engineering [1], electrical [2] or construction [3], additive manufacturing has also found application in the field of human medicine [4]. The production of individual implants, but also orthotic devices, is expansive and, due to this fact, additive production is gradually finding its place in veterinary applications [5].

An important part of the production of any product produced through additive production is its 3D modelling or 3D design. The production of individual proteinaceous devices using additive technology is a relatively complex process which, as in other industries, cannot be done without knowledge of the individual software and its operation [6] [7]. However, in the case of medical use, whether in human or veterinary applications, design, in addition to the software support itself, cannot be done without the support of appropriate diagnostic and imaging methods. One of the imaging methods used in the design of individual implants is computerized tomography or CT. Data in the form of DICOM are processed into stl. files using appropriate software. (Stereolithography), which can be further modified in these software to create individual 3D models [7] [8]. Another way to obtain this data, for example for the production of individual orthotic prostheses, is to use handheld 3D scanners such as Artec Eva [9]. The principle of data processing is similar to the previous case.

In addition to the production of implants, these software can also be used to plan surgery by printing 3D anatomical models. Surgical planning, especially for personalized hard tissue implants, is based mainly on conventional CT images or MRI images. Thus, for effective preoperative planning of a surgical procedure, its planning on 3D printed models based on CT information is possible. Another way is to simulate such surgery directly with software on a virtual model. However, this requires specific software functions to simulate surgical procedures and to calculate certain parameters such as volume distance and bone density. In the case of procedures requiring individual implants, the implants can be designed on a 3D model. An alternative to this approach is to work directly on a 3D model in a computer [10].

There are several types of software on the market used for 3D product modelling [11]. Some of them are their certifications directly intended for use in human medicine [12]. However, other non-certified software can also be used for this purpose - for example in the field of veterinary applications. This may be software that is freely available or software that requires a valid license to be purchased. In this publication, I will try to describe the software that was used in the design of implants for veterinary applications.

2. Overview of softwares

Whether it is the printing of 3D models for the planning of the operation or the design of the individual implant, both processes require the processing of CT or MRI images by specialized software for medical imaging. A powerful software interface is required to accept the inputs of all types or brands of scanners, to facilitate the selection of the anatomical structure made using imaging methods, and to link this information to 3D printing devices.

Surgical simulation on virtual models on a computer requires specific functions of the surgical simulation software and other software packages (CAD, FEA, CFD, etc.) [10]. Equally important is the "separation" of individual tissue types based on their bulk density. For these purposes, but also for design purposes, software such as Mimics or Vesalius 3D are used [25] [26] [27].

In addition to the software mentioned above, there are many other software that can be used to model and design 3D implants. However, not all of them are permitted for use in human medicine. As these are veterinary applications in this case, they can be considered in terms of availability.

2.1. Use of individual software in veterinary practice

In veterinary practice, certified software for human use from Materialize - Mimic is currently one of the most widely used software. This software has been used to a greater extent, especially in modeling implants with more complex geometry. Another advantage of this program was its use in the planning of surgery, which ultimately resulted in the total operating time required for implantation. This time was significantly shortened, which had a positive effect on the overall health and time required for the overall sedation of the animal. Other software used to create the implant included software such as Blender, MeshLab and Mesh-mixer (Autodesk). The first of these were used to model beaks for species such as toucan, goose or parrot. For simpler types of implants, software used in common practice such as SolidWorks and Pro Creo Parametric were used. In some cases, however, it was not quite possible to determine the type of software used to design the implants.

The table below (Tab. 1) provides an overview of the software used along with the type of tissue being replaced. The data from Table 1 were transferred to a graph (Fig. 1), where these software are clearly displayed with respect to their use on a number of cases.

Table 1. Summary overview of individual software and methods of 3D printing with regard to the replaced structure

	Replaced tissue	Software used	3D printing method
Birds	Toucan; parrot; house / Beak	MeshLab, Blender Chyba! Nenašiel sa žiaden zdroj odkazov. Chyba! Nenašiel sa žiaden zdroj odkazov. (3x toucan, parrot and goose)	not specified
	Eagle / Beak	SolidWorks Chyba! Nenašiel sa žiaden zdroj odkazov.	not specified
	Bird / Wing	Pro creo Parametric, Meshmixer [28]	PolyJet (Objet) [28]
Cats	Kolenný kĺb	Materialise Mimics Inovation Suite Chyba! Nenašiel sa žiaden zdroj odkazov.	DMLS Chyba! Nenašiel sa žiaden zdroj odkazov.
Turtle	Maxillofacial area (missing 60%)	Materialise Mimics Inovation Suite 3-Matic Chyba! Nenašiel sa žiaden zdroj odkazov.	EBM Chyba! Nenašiel sa žiaden zdroj odkazov.
Dogs	Limb reposition	not specified	EBM Q10plus Chyba! Nenašiel sa žiaden zdroj odkazov.
	Stabilization of the spine	not specified	EBM Q10plus Chyba! Nenašiel sa žiaden zdroj odkazov.
	Skull	3 cases - dogs; skull tumor Materialise Mimics, Materialise 3-matic (+Data processing) Chyba! Nenašiel sa žiaden zdroj odkazov. ADEPT software (+ the cranial plate was designed in) Chyba! Nenašiel sa žiaden zdroj odkazov.	SLM/DMLS Chyba! Nenašiel sa žiaden zdroj odkazov. AM400 (Renishaw) – The Renishaw AM 400 industrial 3D printer Chyba! Nenašiel sa žiaden zdroj odkazov.
	Foreleg - 5 dogs (osteosarcoma)	Catia V5 Chyba! Nenašiel sa žiaden zdroj odkazov.	DMLS - EOSINT M280 (+ Surgical guide; ABS – FDM) Chyba! Nenašiel sa žiaden zdroj odkazov.
	Knee joint	Mimics Materialise SLA-190, 3D Systems (+ full size replica) Chyba! Nenašiel sa žiaden zdroj odkazov.	Z 400 (3D printer) Chyba! Nenašiel sa žiaden zdroj odkazov. Powder – based Chyba! Nenašiel sa žiaden zdroj odkazov.
	Trachea (Two implants, 1 case study)	Meshmixer, Materialise Magics	PolyJet, Pneumatic Extrusion (Bioploter)

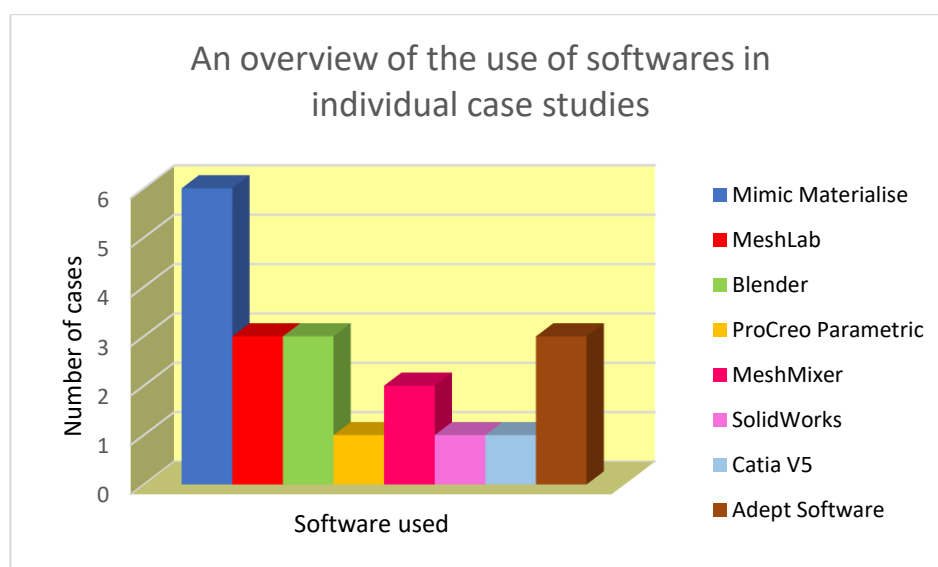


Figure 1. Graphical overview of the use of softwares in individual case studies

In addition to the use of individual software, Table 1 also shows the technologies used in 3D printing. In this case, however, it is not entirely possible to box the most used technology as in the case of software. The use of individual types of 3D printing technology depends mainly on the material used. In cases where materials paired with a group of metals were used as the material for the implant, the most used method was the DMLS method resp. SLM. The PolyJet method (Stratassys) was used the most for 3D printing from non-metallic materials, see. graph in Figure 2.

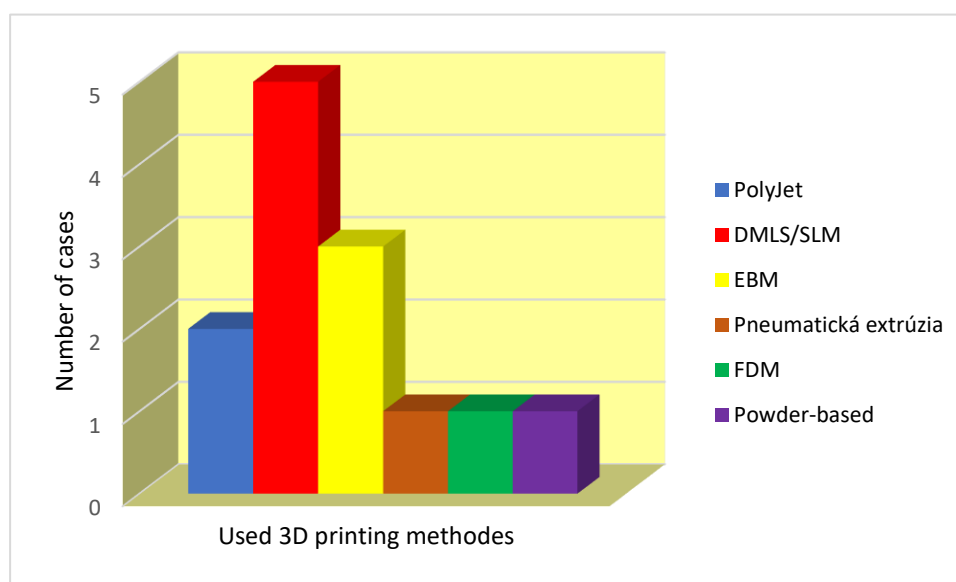


Figure 2. Graphic overview of individual 3D printing methods in individual case studies

4. Conclusions

From the above-mentioned graphs, it can be stated that in addition to certified software, it is also possible to use non-certified ones for veterinary practice. Although their percentages are different, they have ultimately served the purpose for which they were used. When using these software, it is important to be aware of the overall geometry and

complexity of the future implant before designing and designing, and to select the appropriate software based on that.

Acknowledgments: The achieved results were created within the investigation of the project no. 2018/14432: 1-26C0, which is supported by the Ministry of Education, Science, Research and Sport of the Slovak Republic within the provided incentives for research and development from the state budget in accordance with Act No. 185/2009 Coll. on incentives for research and development. This publication was created thanks to support under the Operational Program Integrated Infrastructure for the project: Center for Advanced Therapies of Chronic Inflammatory Diseases of the Locomotion System (CPT ZOPA), ITMS2014+: 313011W410, co-financed by the European Regional Development Fund. This research was supported by project KEGA 023TUKE-4/2020 Increasing the synergy of methods of teaching biophysics using laboratory equipment and diagnostic devices aimed at measuring physical and technical quantities.

Conflicts of Interest: "The authors declare no conflict of interest."

References

1. M. Greul, T. Pintat, M. Greulich. Rapid prototyping of functional metallic parts. *Computers in Industry*. 1995 Dec 28; 1: 23-28. [https://doi.org/10.1016/0166-3615\(95\)00028-5](https://doi.org/10.1016/0166-3615(95)00028-5)
2. T. Boratyński, M. Frankiewicz, P. Kaczmarek. Development, prototyping and evaluation of electric switching devices. *Prace Naukowe Instytutu Technologii Maszyn i Automatyzacji Politechniki Wrocławskiej. Konferencje*. 2004 85;42: 41-48. ISSN: 0867-7778
3. I. Gibson, T. Kvan, L. Wai Ming, L. Rapid prototyping for architectural models", *Rapid Prototyping Journal*. 2002 8;2: 91-95. <https://doi.org/10.1108/13552540210420961>
4. L. C. Hieu, N. Zlatov, J. Vander Sloten, E. Bohez L. Khanh, P. H. Binh, P. Oris, Y. Toshev. Medical rapid prototyping applications and methods. *Assembly Automation*. 2005 25;4:284-292. <https://doi.org/10.1108/01445150510626415>
5. O.L.A. Harrysson, D.J. Marcellin-Little, T.J. Horn. Applications of Metal Additive Manufacturing in Veterinary Orthopedic Surgery. *JOM*. 2015 Feb 67:647–654 DOI: 10.1007/s11837-015-1295-x
6. A. Wiberg, J. Persson, J. Ölvander. Design for additive manufacturing – a review of available design methods and software. *Rapid Prototyping Journal*. 2019 25;6:1080-1094. <https://doi.org/10.1108/RPJ-10-2018-0262>
7. R. Vaishya, A. Vaish. 3D Printing in Orthopedics. *General Principles of Orthopedics and Trauma*. Springer, Cham. 2019 May; 583-590. https://doi.org/10.1007/978-3-030-15089-1_26
8. D. Mitsouras, P. Liacouras, A. Imanzadeh, A. A. Giannopoulos, T. Cai, K. K. Kumamaru, E. George, N. Wake, E. J. Caterson, B. Pomahac, V. B. Ho, G. T. Grant, F. J. Rybicki. Medical 3D Printing for the Radiologist. *RadioGraphics*. 2015 Nov 35;7:1965-1988 <https://doi.org/10.1148/rg.2015140320>
9. V. Krajňáková, V. Rajčúková, R. Hudák, J. Živčák. Application of the Artec Eva scanner for orthotics in practice. *Lékař a Technika - Clinician and Technology*. 2019 49;3:92-96 <https://doi.org/10.14311/CTJ.2019.3.04>
10. *Advanced Manufacturing Technology for Medical Applications: Reverse Engineering, Software Conversion and Rapid Prototyping*. 2005 Dec; 79 – 92 ISBN: 978-0-470-01688-6
11. Computer-aided design. Wikipedia: the free encyclopedia [online]. San Francisco: Wikimedia Foundation, 2001, 2021 May. Dostupné z: https://en.wikipedia.org/wiki/Computer-aided_design#Software
12. Boost your career with the Mimics User Certificate. Materialise [online]. Dostupné z: <https://www.materialise.com/en/medical/mimics-innovation-suite/mimics-user-certificate>
13. 3D Desing. Bos Facility support [online]. Dostupné z: <https://www.bosfacilitysupport.nl/service/3d-design/http://arc-team-open-research.blogspot.com/2015/07/when-veterinary-medicine-and-3d.html>
14. Gabriela Dancáková. Individual animal implants/prosthetics. Message to: Paulo Miamoto. 11.05.2021
15. Eagle gets a new Beak created by 3D Printer. WordlessTech [online]. Sep 13, 2012. Dostupné z: <https://wordlesstech.com/eagle-gets-a-new-beak-created-with-a-3d-printer/>
16. 3D Printing Creates the World's First Replacement Knee Joint in a Cat. Materialise [online]. Dostupné z: <https://www.materialise.com/en/cases/3d-printing-creates-worlds-first-replacement-knee-joint-a-cat>
17. T. Wohlers, T. Gornet. History of additive manufacturing. Wohlers report. 2014. 118
18. Turkish specialists save life of Sea Turtle with a 3D printed jaw implant. Open Biomedical Initiative [online]. 2015 May Dostupné z: <http://www.openbiomedical.org/turkish-specialists-save-life-of-sea-turtle-with-a-3d-printed-jaw-implant/>
19. Gabriela Dancáková. Akut-3 turtle. Message to: Kuntay Aktas. 12.01.2019
20. Dogs & Bones: Help with bespoke titanium devices. GE Additive [online]. 2018 Nov. Dostupné z: <https://www.ge.com/additive/press-releases/dogs-bones-help-bespoke-titanium-devices>
21. Phillips, M. Parkes. (2020). Schedule feasibility and workflow for additive manufacturing of titanium plates for cranioplasty in canine skull tumors. *BMC Veterinary Research*. 2020 16;1:1-8. doi:10.1186/s12917-020-02343-1
22. AM 400 RENISHAW. Aniwa [online]. Dostupné z: <https://www.aniwaa.com/product/3d-printers/renishaw-am-400/>

23. A. Timercan, V. Brailovski, B. Lussier, Y. Petit, B. Seguin. 3D Printed Personalized Canine Prostheses. Substance: Scientific news and innovation from Éts. 2018 May. Dostupné z: <https://substance.etsmtl.ca/en/protheses-canines-personnalisees-imprimees-3d>
24. W. D. Liska, D. J. Marcellin-Little, E. V. Eskelinen, CH. G. Sidebotham, O. L. A. Harrysson, A. K. Hielm-Björkman. Custom Total Knee Replacement in a Dog with Femoral Condylar Bone Loss. Veterinary Surgery. 2007 Feb 36:293–301. doi:10.1111/j.1532-950X.2007.00270.x
25. How to segment bones in MIS & prepare them for 3D printing? Materialise [online]. Dostupné z: <https://www.materialise.com/en/academy-medical/mimics-innovation-suite/tutorials/bone-segmentation-for-3d-printing>
26. C. I. Robison, M. Rice, M. M. Makagon, D. M. Karcher. Duck gait: Relationship to hip angle, bone ash, bone density, and morphology. Poultry Science. 2015 May 94;5: 1060-1067. doi.org/10.3382/ps/pev050
27. T. Özel, P. J. Bártolo, E. Ceretti, J. De Ciurana Gay, C. A. Rodriguez, J. V. Lopes Da Silva. Biomedical Devices: Design, Prototyping, and Manufacturing, 2016 Sep. 71 (208). ISBN: 978-1-118-47892-9 Dostupné z: https://books.google.sk/books?id=0g3rDAAAQBAJ&pg=PA71&lpg=PA71&dq=vesalius+cad+software&source=bl&ots=1Tx8L0MEUR&sig=ACfU3U3i5Q8ybjk-vgsQimU_btkKacfdvg&hl=sk&sa=X&ved=2ahUKEwjrk0jq3Krx-AhUCKewKHcEDAxQQ6AEwEnoECAkQAw#v=onepage&q=vesalius%20cad%20software&f=false
28. Dancáková, G., Brouwer, N., Lancoš, S., Schnitzer, M., Rajtúková, V., Molnár, L., Kohan, M., Trebuňová, M., Živčák, J., Hudák, R.: Dizajn individuálneho implantátu na úpravu balansu pre sokola sťahovavého (falco peregrinus) po amputácii krídla, In: Novus Scientia 2021 : zborník príspevkov z 18. Medzinárodnej vedeckej konferencie doktorandov strojnícckých fakúlt technických univerzít a vysokých škôl. - Košice (Slovensko) : Technická univerzita v Košiciach s. 38-42 [online]. - ISBN 978-80-553-3798-2

Verification of the properties of tilt angle sensors

Ivana Koláriková ^{1,*}, Tatiana Kelemenová ¹ and Eduard Jakubkovič ¹

¹ Technical University of Košice, Faculty of Mechanical Engineering, Department of Biomedical Engineering and Measurement, Letná 9, 042 00 Košice, Slovak Republic

* ivana.kolarikova@tuke.sk, tatiana.kelemenova@tuke.sk, eduard.jakubkovic@tuke.sk

Abstract: Tilt sensors are designed to measure the angle of an object with respect to the force of gravity. These sensors determine the pitch and/or roll angle and output these values via the appropriate electrical interface. Tilt angle sensors play a very important role in many applications such as aviation instruments, portable computers, robotics devices, vehicles, etc. Therefore, it is significant that these sensors are accurate and have small measurement errors. In this work there were used three small tilt angle sensors mounted on a tilting platform. The sensors detected a change in the inclination of the platform. For each sensor there were created transformation and calibration functions from the obtained data. Furthermore, there were calculated regression equations, standard deviations and combined standard uncertainties. Based on the performed calculations, it was found that all three sensors have low values of standard deviations and standard uncertainties, so they are all convenient for measuring inclination. These results will be further processed so that their output units could be unified – changed all to angle degrees and thus comparable.

Keywords: measurement; tilt angle sensors; inclinometers; MEMS

1. Introduction

Tilt sensors are types of sensors that produce an electrical signal which is proportional to the degree of inclination with respect to one or more axes. These sensors are used to measure slope and tilt within a limited range of motion. Sometimes, the tilt sensors are referred to as inclinometers because the sensors just generate a signal, but inclinometers generate both readout and a signal.

These sensors are classified into different types and the classification of tilt sensors includes different devices and technologies to measure tilt, slope, elevation and inclination. There are three main types: force balance sensors, fluid filled sensors (capacitive or electrolytic) and solid state microelectromechanical systems (MEMS) sensors.

Force balance sensors are gravity referenced sensors and are anticipated for DC acceleration measurements. These sensors are frequently used in inclinometers and tilt meters. Force balance sensors are capable of measuring levels from 0.0001g to 200g, and the frequency range is from DC to 1000Hz. The advantages of these sensors include a change in broad measurement, insensitivity to temperature change and their high accuracy. The disadvantage of this sensor is its high cost.

The electrolytic sensors are used to measure an angle and the angle may be expressed in degrees, arc minutes, or arc seconds. Electrolytic sensors produce extremely accurate pitch measurements in many applications. These sensors easily maintain their high accuracy and small size. Capacitive sensors are designed to take non-contact measurements of inclination and tilt. These can operate both as switches and sensors. When the geometry of the capacitor is changed, the capacitor sensor relies on variation of capacitor. The main advantage of the capacitive sensor is its performance ratio and cost-effectiveness, whereas a limited response is the main disadvantage of this sensor.

Solid state MEMS are small sensors as they consist of movable proof mass plates that are attached to a reference frame through a mechanical suspension system. When the device tilts, this mass will move slightly, causing a change of capacitance between the mass and the supporting structure. The tilt angle is calculated from the measured capacitances. This is a technique of combining mechanical and electrical components together on a chip to generate a system of miniature dimensions. Small means that the dimensions are less than the thickness of human hair. These kinds of sensors have become mass market products with an excellent performance/cost ratio. MEMS sensors are key components in many medical, industrial, aerospace, consumer and automotive applications [1, 2, 3].

For purpose of this work three different tilt angle sensors were selected from the MEMS sensors category because these sensors are small and easy to attach to a small platform and all three of them should have great accuracy in measuring the angle. There are some differences between them, and the aim of this work is to verify their properties.

2. Measuring Chain and Measurement Methodology

In the measuring chain there were 3 tilt angle sensors: dual-axis thermal accelerometer MEMSIC 2125, three-axis accelerometer and gyroscope module with MPU6050 GY-25 and 1-dimensional capacitive inclinometer 8.IS40.14121 KÜBLER. MEMSIC 2125 was connected to oscilloscope GDS-1102-U GW INSTEK and power supply UNI-T UTP3313TFL-II. The same power supply was also used to power KÜBLER 8.IS40.14121, which was connected through a resistor to the digital multimeter Metrel MD9015. MPU6050 GY-25 was attached to microcontroller board Arduino Mega 2560 and then to computer with Arduino IDE. All three tilt angle sensors were connected to the tilting part of the aluminium construction. There was mounted digital protractor AG-82413B, which was used as our reference (working standard). A cross spirit level was fitted at the bottom of the structure so that we had the structure horizontally. Measuring chain can be seen in the Figure 1.

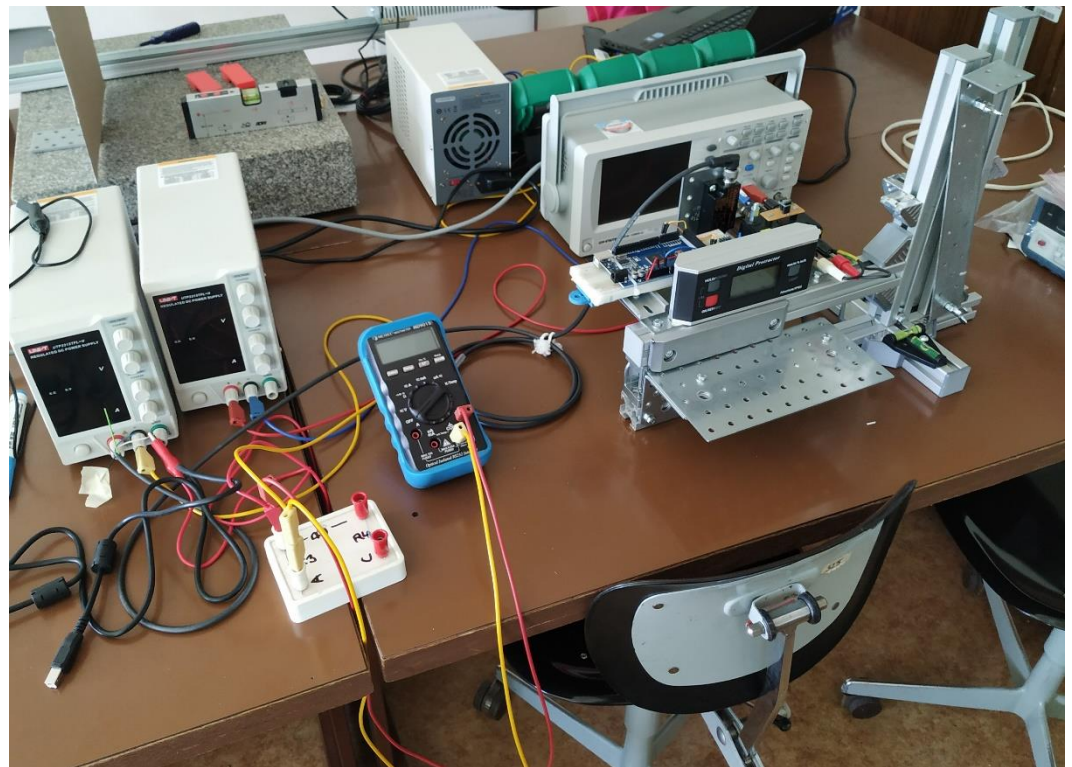


Figure 1. Measuring chain.

The aluminium construction had an articulation which made it possible to tilt the platform mounted with all three sensors including the standard from a horizontal position of 0 ° to an angle of inclination of 70 °, which was sufficient to verify the properties of the tilt angle sensors. The start of the measurement was at zero degrees and each time measurement took place the aluminum platform was moved by five degrees until 70 degrees was reached. Every 5 degrees, 10 values were measured on each sensor. An example from the measurement can be seen in the Figure 2.

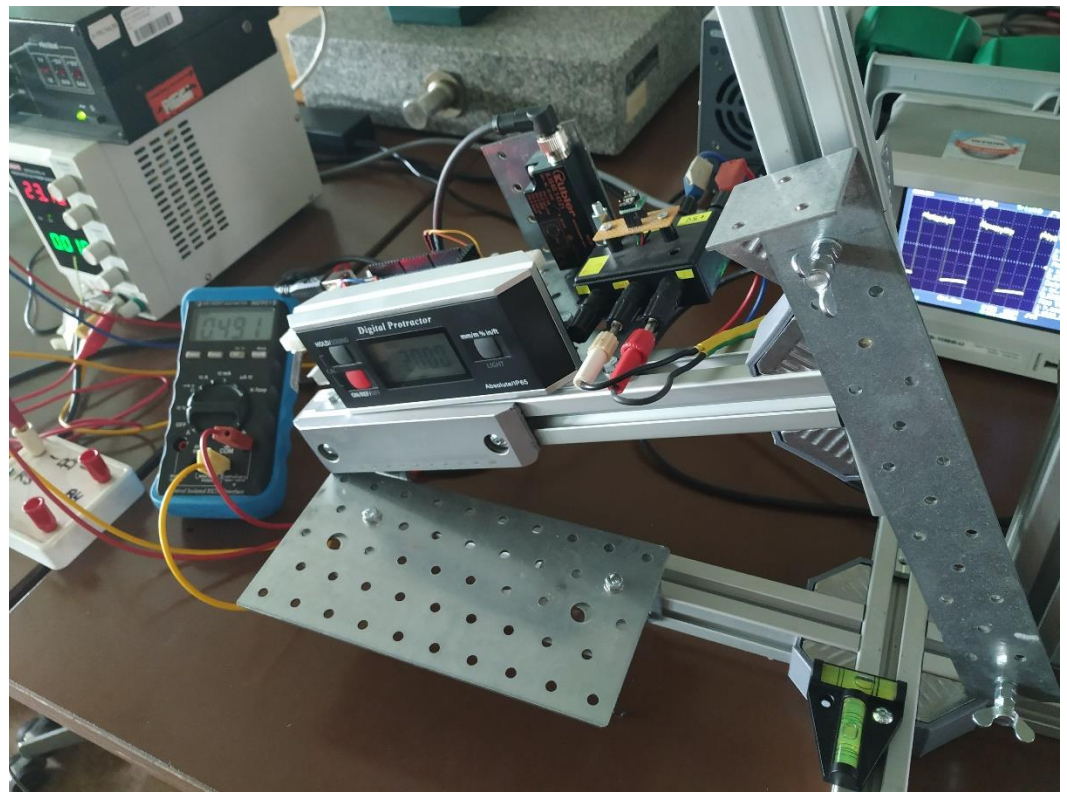


Figure 2. Measurement at twenty degrees.

3. Results

A total of 450 measurements were performed throughout the experiment, therefore there were made graphic representations of the collected data. The basic metrological characteristic - transformation function was evaluated for each measuring device. Transformation functions can be seen in the Figure 3, 4 and 5.

In the Figure 6, 7 and 8 can be found calibration function of each measuring device respectively and the regression curve was analyzed from which there were calculated regression equations and model.

Furthermore, there were calculated the standard deviations of the tilt angle sensors of which dependence on the tilt angle of reference can be seen in the Figure 9, 10 and 11.

Thereafter type A evaluation of standard uncertainty was calculated from standard deviations of used sensors. These uncertainties mentioned above were transferred to the graphs in the Figure 12, 13 and 14.

According to manufacturer of the multimeter Metrel MD9015 [4], maximum permissible error (MPE) of DC voltage for range from 250 mV to 2,5 V is:

$$MPE = 0,5\% * \bar{U} + 0,001 * 2 \quad (1)$$

Type B evaluation of standard uncertainty was calculated for the digital multimeter and it has the same units (Volts) as the results from Type A standard uncertainty. Thus, combined standard uncertainty could be calculated for the multimeter too. In the Figure

15 can be seen Type B evaluation of standard uncertainty and combined standard uncertainty.

For the accelerometer MPU6050 GY-25 [5] manufacturer says that resolution is $0,01^\circ$, then u_B was:

$$u_{B\text{ MPU}} = \frac{0,01^\circ}{\sqrt{3}} = 5,774 * 10^{-3}^\circ \quad (2)$$

The manufacturer of oscilloscope GDS-1102-U GW INSTEK [6] does not give MPE of the duty cycle, only maximum rise time of 3,4 ns was given, therefore u_B was calculated to be:

$$u_{B\text{ GDS 1102-U}} = \frac{3,4 * 10^{-9}}{\sqrt{3}} = 1,963 * 10^{-9} \text{ s} \quad (3)$$

For the accelerometer MEMSIC 2125 [7] manufacturer states that resolution is better than 1 mili(g), so this value will be considered as MPE and u_B was calculated to be:

$$u_{B\text{ MEMSIC}} = \frac{g * 10^{-3}}{\sqrt{3}} = \frac{9,81 * 10^{-3}}{\sqrt{3}} = 5,664 * 10^{-3} \text{ m/s}^2 \quad (4)$$

According to manufacturer of the inclinometer 8.IS40.14121 KÜBLER [8] repeat accuracy is $\leq 0.1\%$ of measuring range, therefore u_B was:

$$u_{B\text{ KÜBLER}} = \frac{0,1\% * 70^\circ}{\sqrt{3}} = 4,0415 * 10^{-3}^\circ \quad (5)$$

Type B evaluation of standard uncertainty for the microcontroller board Arduino Mega 2560 could not be calculated, because manufacturer does not provide any information on this issue.

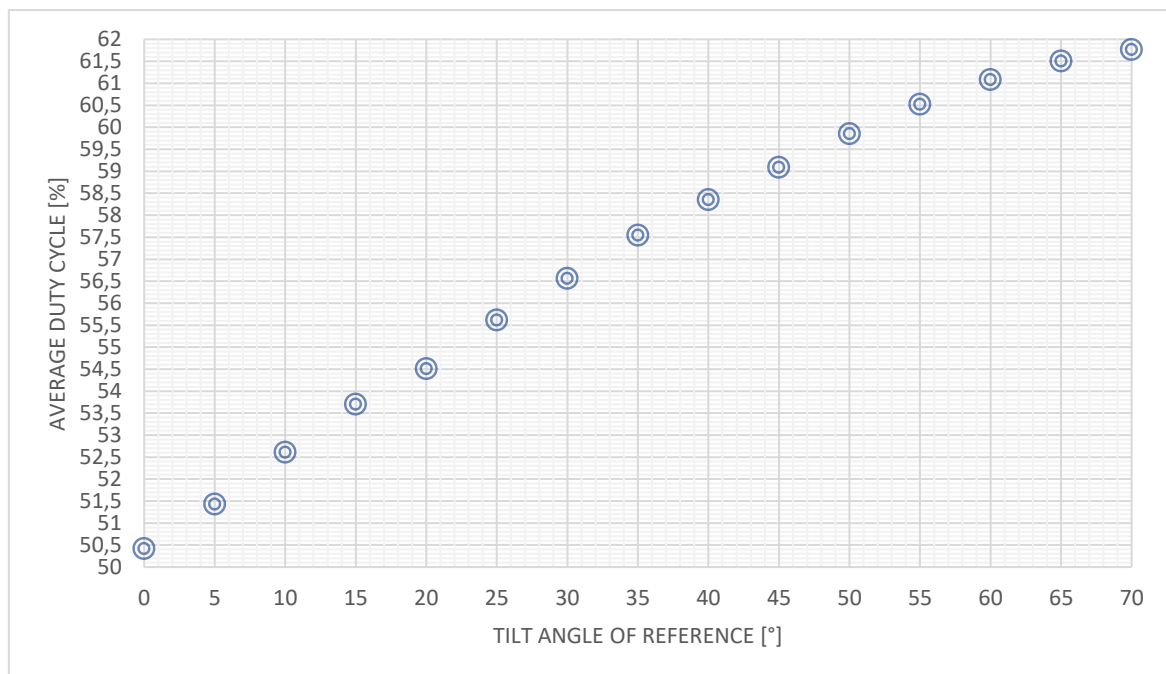


Figure 3. Dependence of the average duty cycle of MEMSIC 2125 on the tilt angle of reference.

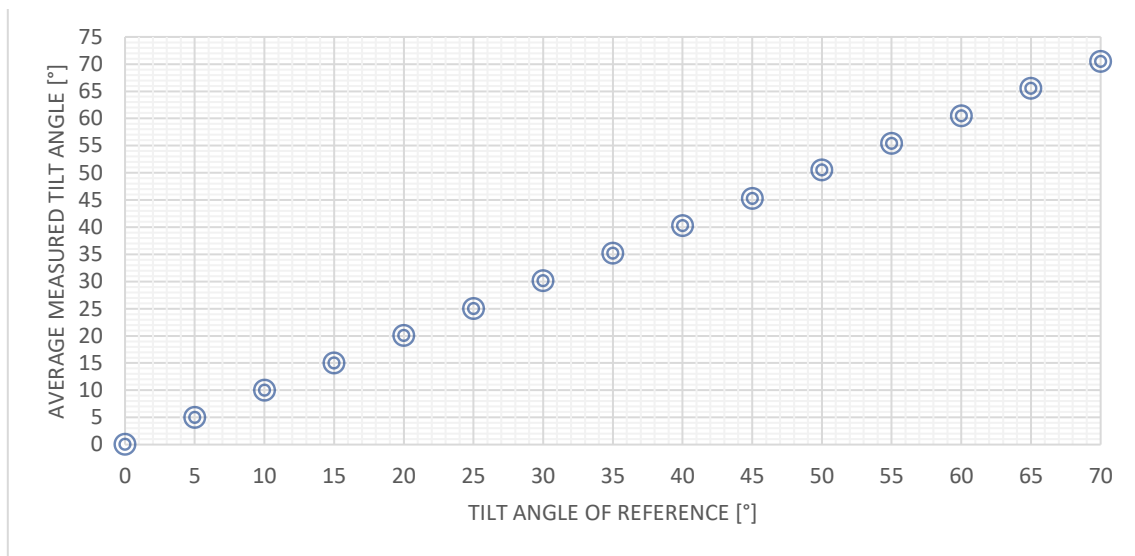


Figure 4. Dependence of the average measured tilt angle of MPU6050 GY-25 on the tilt angle of reference.

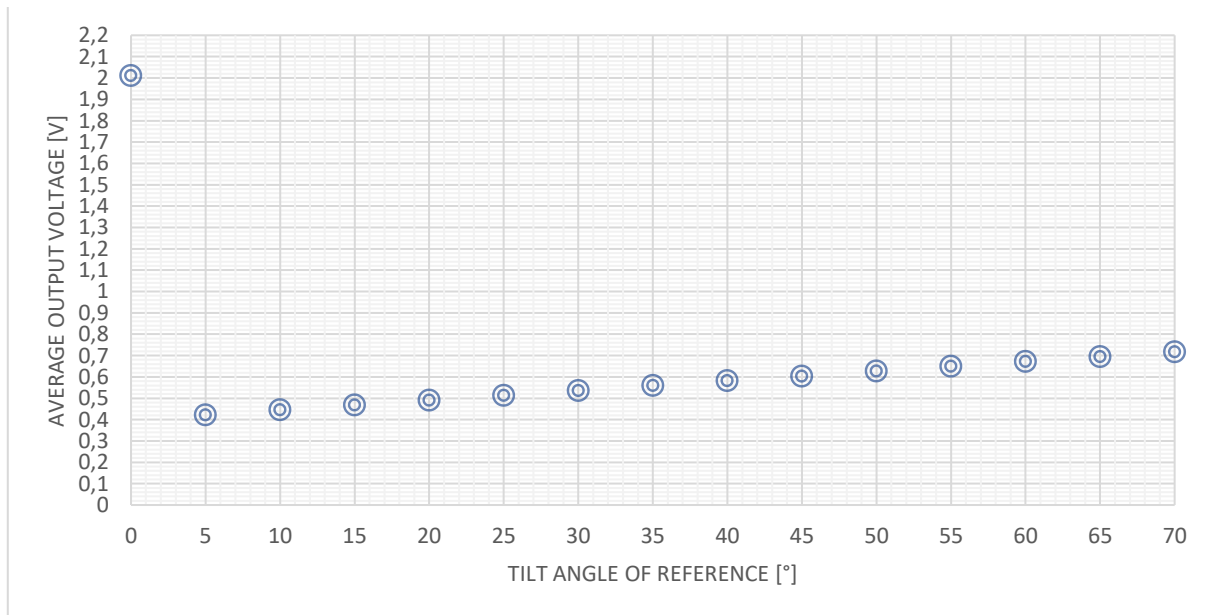


Figure 5. Dependence of the average output voltage of KÜBLER 8.IS40.14121 on the tilt angle of reference.

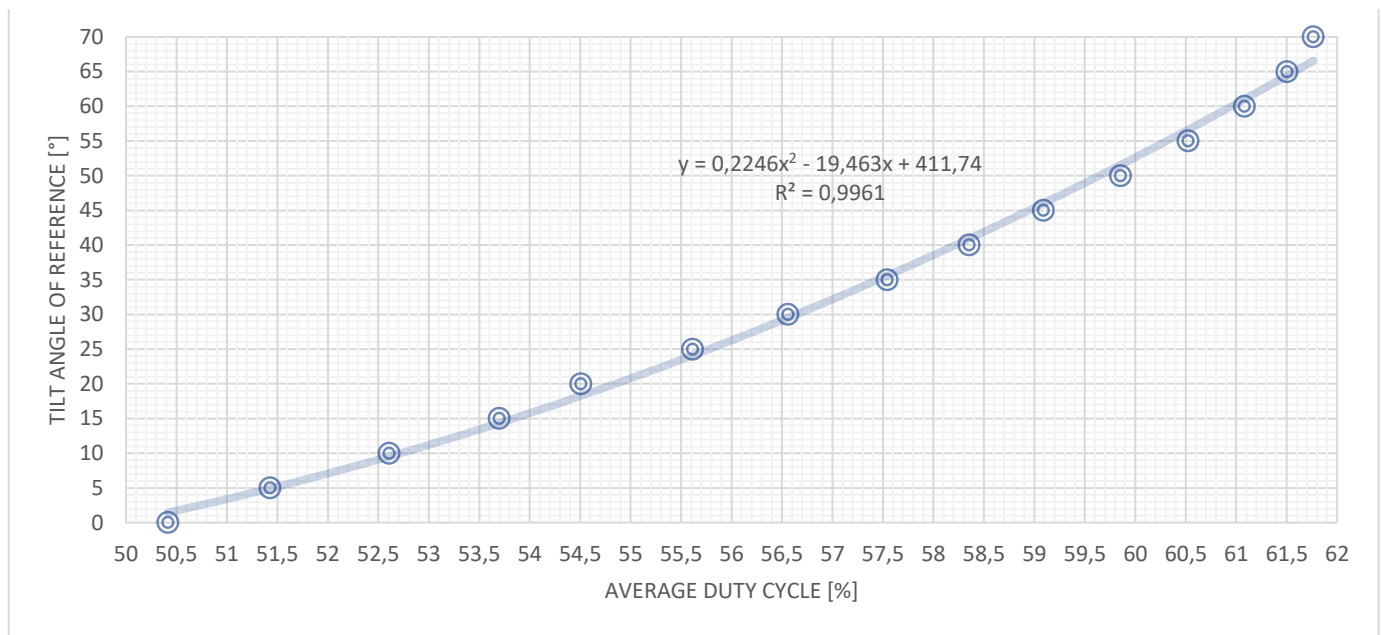


Figure 6. Dependence of the tilt angle of reference on the average duty cycle of MEMSIC 2125.

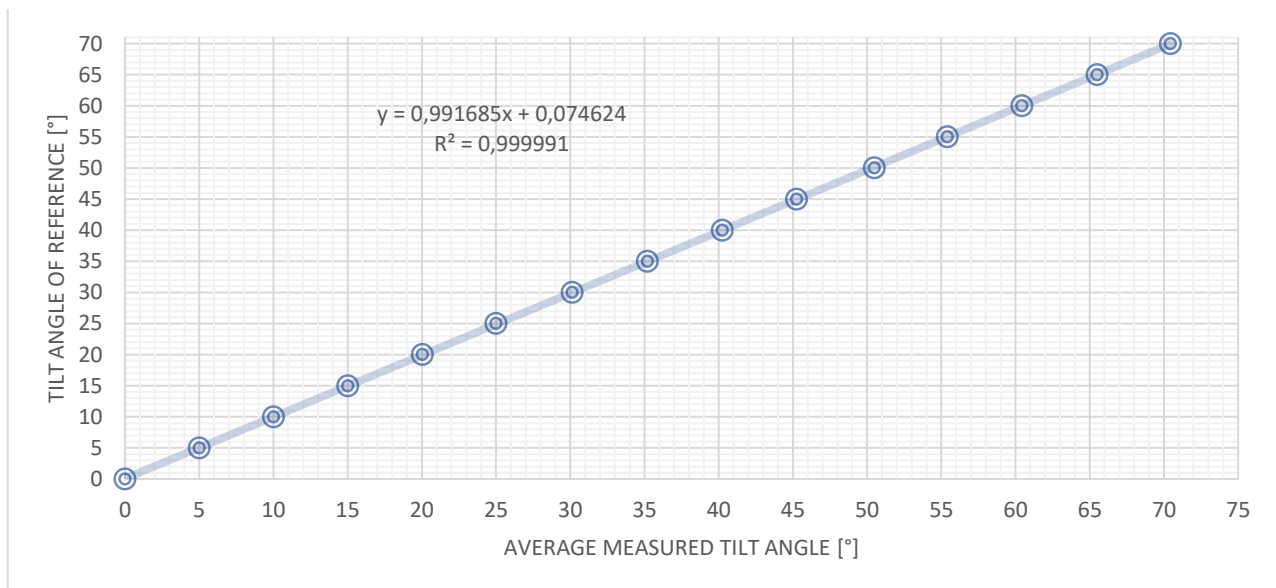


Figure 7. Dependence of the tilt angle of reference on the average measured tilt angle of MPU6050 GY-25.

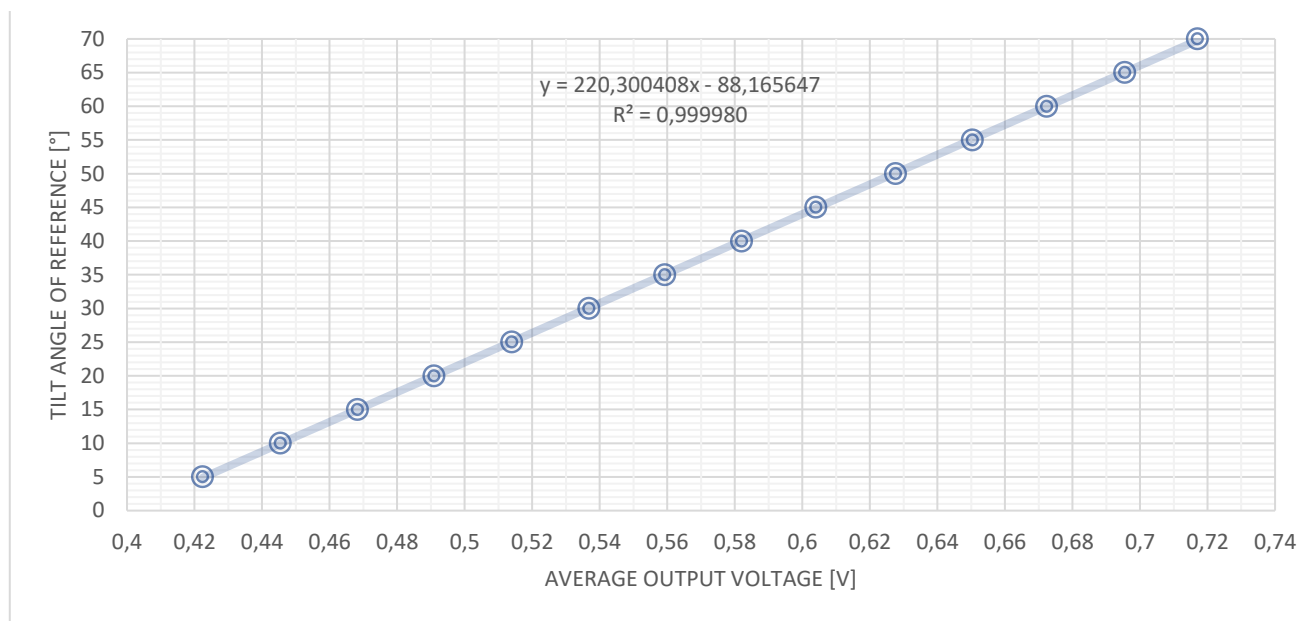


Figure 8. Dependence of the tilt angle of reference on the average output voltage of KÜBLER 8.IS40.14121.

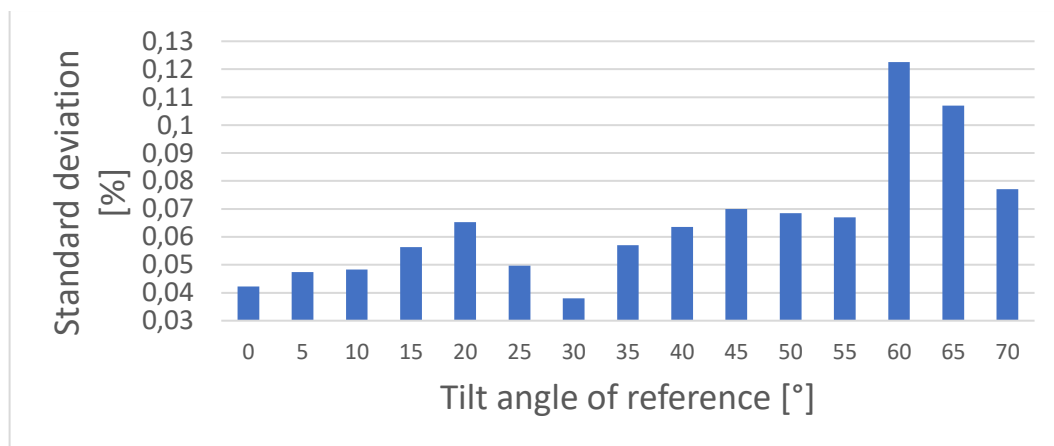


Figure 9. Dependence of the standard deviation of MEMSIC 2125 on the tilt angle of reference.

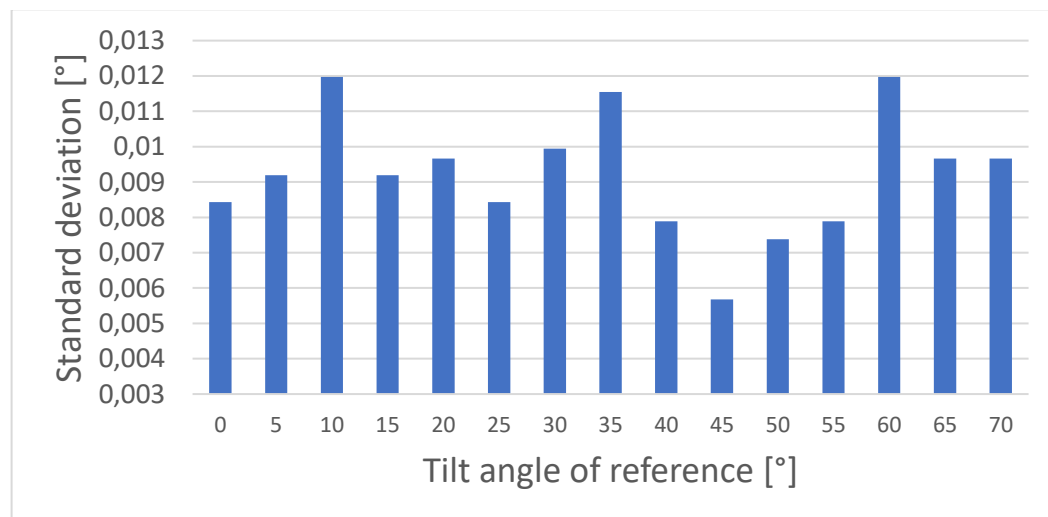


Figure 10. Dependence of the standard deviation of MPU6050 GY-25 on the tilt angle of reference.

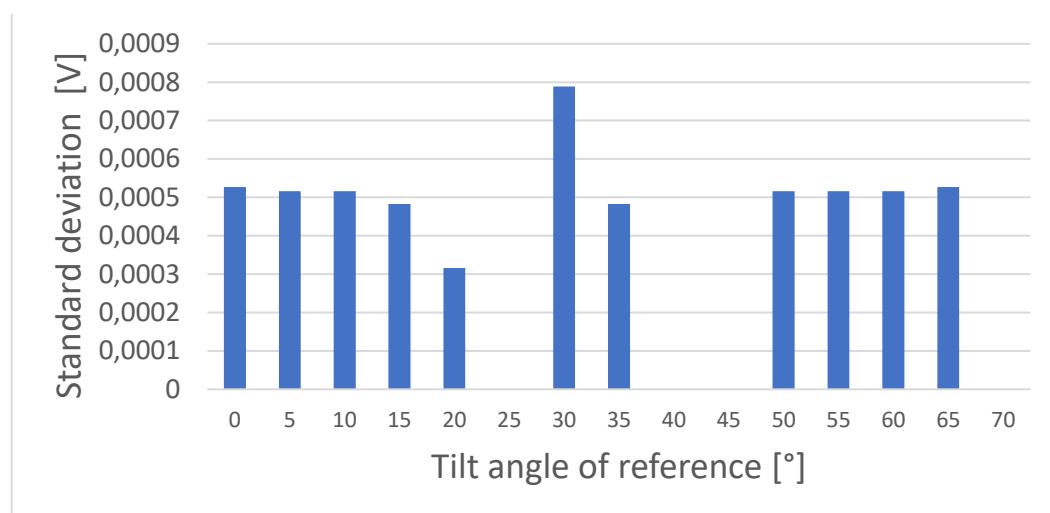


Figure 11. Dependence of the standard deviation of KÜBLER 8.IS40.14121 on the tilt angle of reference.

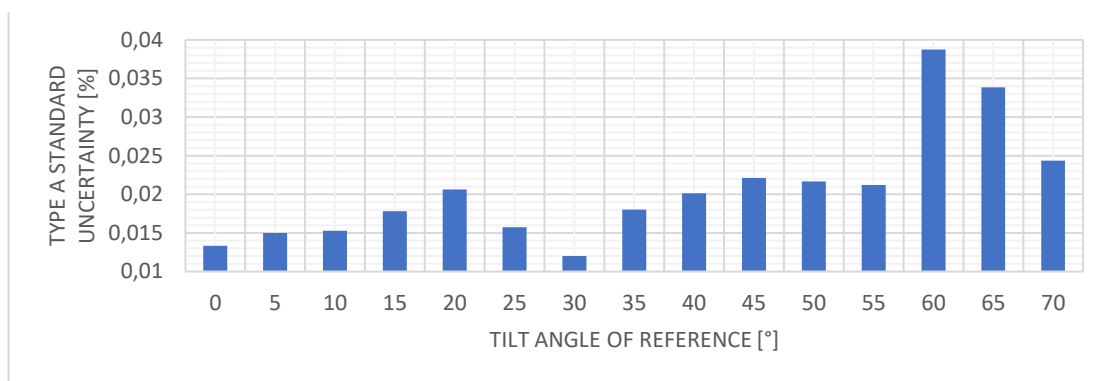


Figure 12. Dependence of the type A standard uncertainty of MEMSIC 2125 on the tilt angle of reference.

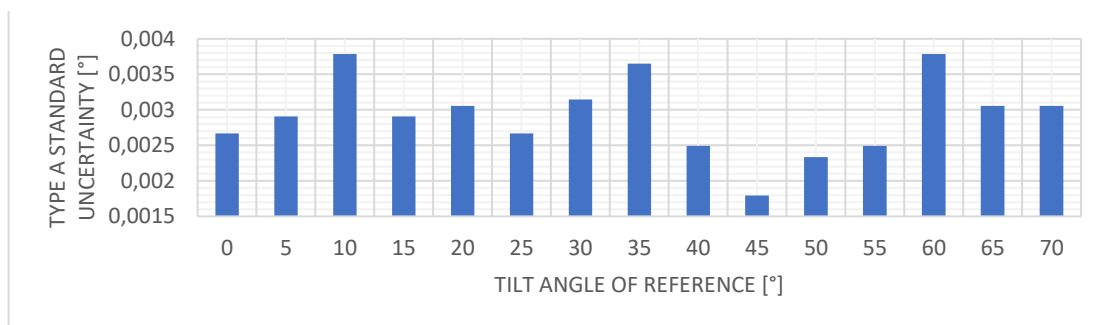


Figure 13. Dependence of the type A standard uncertainty of MPU6050 GY-25 on the tilt angle of reference.

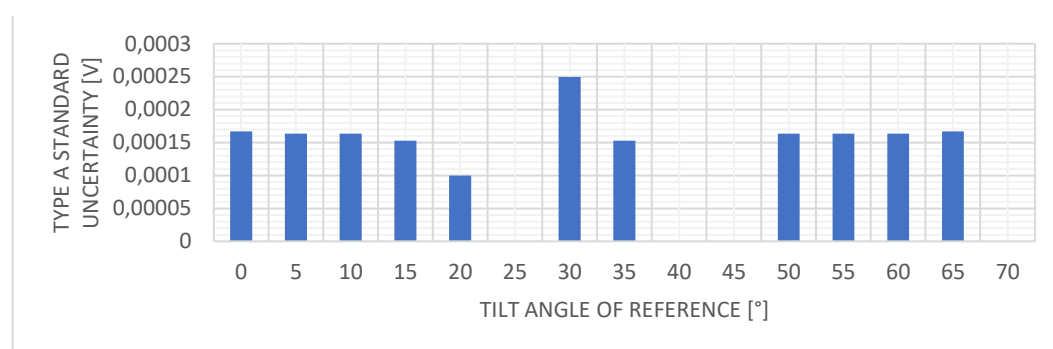


Figure 14. Dependence of the type A standard uncertainty of KÜBLER 8.IS40.14121 on the tilt angle of reference.

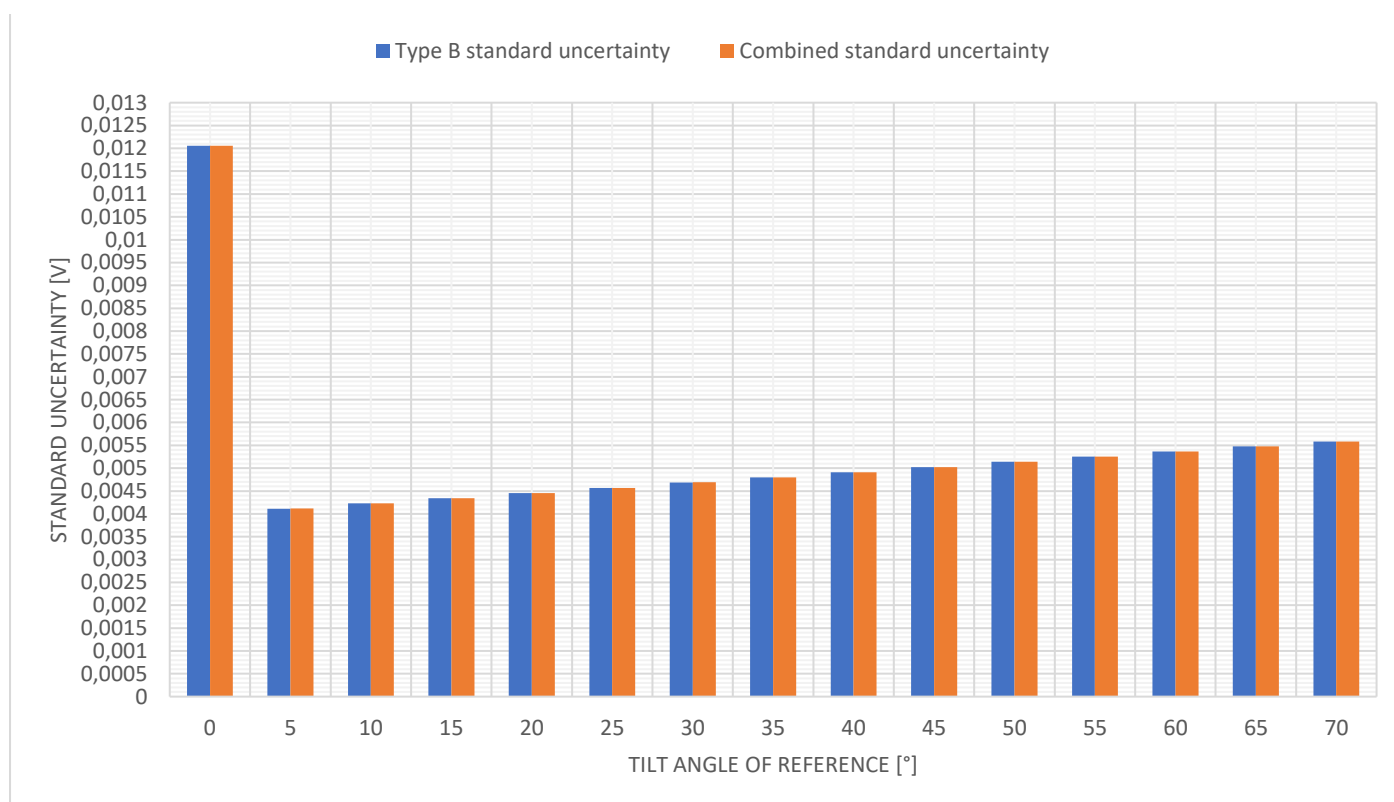


Figure 15. Dependence of the type B standard uncertainty of the multimeter Metrel MD9015 and combined standard uncertainty on the tilt angle of reference.

4. Discussion

During the experiment, a lot of data were evaluated and processed into individual graphs. The transformation functions in the Figure 3, 4 and 5 are dependences of the average measured output variable (of 10 measurements) on the tilt angle of reference.

Output of MEMSIC 2125 was measured in % of duty cycles and at 0°, the duty cycle started at around 50% and gradually raised up to 61,68% at 70° as can be seen in the Figure 3. Output of MPU6050 GY-25 was measured in degrees thus this tilt sensor was the best in the meaning of comparability to the reference. At 0°, average measured output was 0,016° and it raised in linear manner (Figure 4). The biggest difference in degrees was at 65° (reference) and measured average was at 65,506°. Output of KÜBLER 8.IS40.14121 was measured in Volts and at 0° was measured average 2,0115 V. In the Figure 5 it is visible, that this value is far away from following average values, therefore it is considered as dead band and true angle can not be measured. Later on output voltage raised in linear manner from 0,4224 V at 5° to 0,717 V at 70°.

Calibration function for this work could be described as dependence of tilt angle of reference on the output measured variable and in the graphs, there were analyzed regression curve was s from which there were calculated regression equations and model. In the Figure 6 (MEMSIC 2125) regression equation was second degree polynomial $y = 0.2246x^2 - 19.463x + 411.74$ and regression model was close to $R^2 = 1$: $R^2 = 0.9961$. In the Figure 7 (MPU6050 GY-25) regression equation was linear $y = 0.991685x + 0.074624$ and regression model was very close to one $R^2 = 0.999991$. In the Figure 8 (KÜBLER 8.IS40.14121) regression equation was linear $y = 220.300408x - 88.165647$ and regression model was the closest to one $R^2 = 0.999980$.

The standard deviations of the tilt angle sensors data were calculated and can be seen in the Figure 9, 10 and 11. In the Figure 9 (MEMSIC 2125) the standard deviations were between 0,038 % and 0,1226 %. In the Figure 10 (MPU6050 GY-25) the standard deviations were between 0,00568 ° and 0,01197 °, which was better than the MEMSIC 2125. In the Figure 11 (KÜBLER 8.IS40.14121) the standard deviations were between 0 V and 0,000249 V, which was the best result of all three sensors.

Dependence of the type A standard uncertainty of tilt angle sensors data on the tilt angle of reference can be seen in the Figure 12, 13 and 14. The lowest type A standard uncertainty can be seen in the Figure 14 (KÜBLER 8.IS40.14121), where the values were between 0 V and 0,000249 V. In the Figure 13 (MPU6050 GY-25) were the values between 0,0018 ° and 0,00379 ° and in the Figure 12 (MEMSIC 2125) were the values 0,012% and 0,0388 % so these values do not differ very much from the average value too.

In the Figure 15 (KÜBLER 8.IS40.14121) there were shown type B standard uncertainty of multimeter Metrel MD9015 and combined standard uncertainty. These values were very similar, because type A standard uncertainty for KÜBLER was very low. The values at 0 ° could be excluded because of dead band and then the values of combined standard uncertainty are between 0,004115 V and 0,005585 V.

5. Conclusion

These results of sensors will be in the next work processed further in depth so sensors could be compared in order to choose the best tilt angle sensor, which would be applied on an inclination tribometer, where it is necessary to determine the inclination when the body is set in motion.

Acknowledgments: This study was supported by projects VEGA 1/0168/21 1/0168/21 Research and development of testing and measuring methods in coordinate metrology and KEGA 016TUKÉ-4/2021 New educational technologies of metrologists for monitoring of production processes and post-processing of products.

Conflicts of Interest: The authors declare no conflict of interest. The funders had no role in the design of the study; in the collection, analyses, or interpretation of data; in the writing of the manuscript, or in the decision to publish the results.

References

1. Elprocus. Available online: <https://www.elprocus.com/tilt-sensor-types-working-principle-and-its-applications/> (accessed on 22. 11. 2021).
2. Spectron. Available online: <http://www.spectronsensors.com/primer-1.php> (accessed on 22. 11. 2021).
3. Posital. <https://www.posital.com/en/products/inclinometers/mems/MEMS-Technology.php> (accessed on 22. 11. 2021).
4. Conrad. Available online: <https://asset.conrad.com/media10/add/160267/c1/-/gl/000358509ML01/manual-358509-metrel-md-9015-handheld-multimeter-digital-cat-ii-1000-v-cat-iii-600-v-display-counts-2500.pdf> (accessed on 23. 11. 2021).
5. GME. Available online: <https://www.gme.sk/data/attachments/dsh.775-146.1.pdf> (accessed on 23. 11. 2021).
6. TME. Available online: <https://www.tme.eu/Document/a70afe3ad9a19849e9e0ee6b9fd43adf/GDS-1000-U.pdf> (accessed on 23. 11. 2021).
7. Mouser. Available online: <https://www.mouser.com/datasheet/2/321/28017-Memsic-MXD2125-Datasheet-461431.pdf> (accessed on 23. 11. 2021).
8. TME. Available online: <https://www.tme.eu/Document/0d0823c5602f2b548c177bdf31b1d16b/IS40-1-EN.pdf> (accessed on 23. 11. 2021).



Mechanical drive systems for ultra-light mobile devices

Miroslav Palko ¹, Maroš Palko¹, Viktória Krajňáková ² and Ján Král' ^{1,*}

¹ Ing. Maroš Palko 1; maros.palko@tuke.sk

¹ Ing. Miroslav Palko 2; miroslav.palko@tuke.sk

² Ing. Viktória Krajňáková, PhD.; viktoria.krajnakova@tuke.sk

¹ doc. Ing. Ján Král', PhD. 2; kral@tuke.sk

* Correspondence: viktoria.krajnakova@tuke.sk; Tel.: +421 55 602 2733

Abstract: In an effort to gain market leadership, vehicle manufacturers are striving to introduce vehicles that are timeless not only in terms of the materials used but also the technology used to produce them. These efforts are supported by various worldwide projects that give young people the opportunity to present their plans with the sole aim of attracting interest and demand. One such activity is the Shell Eco Marathon, an international competition that actively encourages young people to get involved in the development and production of experimental cars using new materials and alternative powertrains. The first race (1985-1999) was held at the Paul Richard circuit in France. In 2009, the race left this country for the first time and was held in Germany, then in 2015 in the Netherlands and since 2016 the competition has been held in England.

Keywords: automotive; internal commerce; internal combustion engine; propulsion system

Citation:

Received: date
Accepted: date
Published: date

1. Introduction

One of the important processes in the use and actual production of components for the automotive industry is the use of digitization, especially 3D scanners, which have found their wide application in the automotive environment. In this sphere, digitisation has become an essential part of the development and assembly process. Its introduction and operation significantly reduces the time required to construct or inspect components. This method of digitisation can also be referred to as development digitisation, as it is implemented in the design or development process of a vehicle or its components. Using 3D scanning, small components as well as large parts can be scanned. The choice of 3D scanner and scanning technology itself depends largely on what is being scanned. Of the wide range of these devices, some are ideal for scanning closer objects, i.e. short-range scanners, and vice versa for scanning more distant points, where medium- or long-range scanners are preferable. The choice of scanner is not the only key parameter, the method used and the purpose of scanning are also important elements.

2. Characteristics of the Shell Eco Marathon

The aim of the competition is to promote the ingenuity and design skills of the participants, to increase interest in technology, to introduce new technologies and materials in the field of vehicle and engine design and, last but not least, to deepen the overall knowledge of technology as well as to improve the language skills of the participants. The competition is open to both high school and university students from all over the world. [1] The vehicles are powered by thermal combustion engines or electric motors. Petrol, diesel, gas or alternative fuels H₂, solar systems, etc. are used as fuel. The fuel for the race is supplied by Shell. The competition vehicles are mainly tricycles of various designs and shapes. They are piloted by competitors aged 13 years and over, who pass the necessary tests, which are determined by the race organiser. [6] The race takes place on a usually standard circuit with a total length of 3636 m, which the competitors complete a total of 7 times. The total distance covered is 25.452 km, which must be covered within a time limit of 50 minutes and 34 seconds. After the distance has been covered, the fuel is added to the calibrated tank and the consumption in millimetres is determined, or the distance covered per 1 litre of fuel is calculated, or the consumption per 100 km. It is possible to make 4 attempts during the race, the best result of which will be included in the evaluation. [12] The engine can be switched off during the race, while the driving itself is always under the constant control of the judges. The SJF TUKE team participated in the race 16 times in total. The best performance so far was recorded by the team in 2019 with a total of 825 kilometres driven per litre of fuel (Fig. 1).

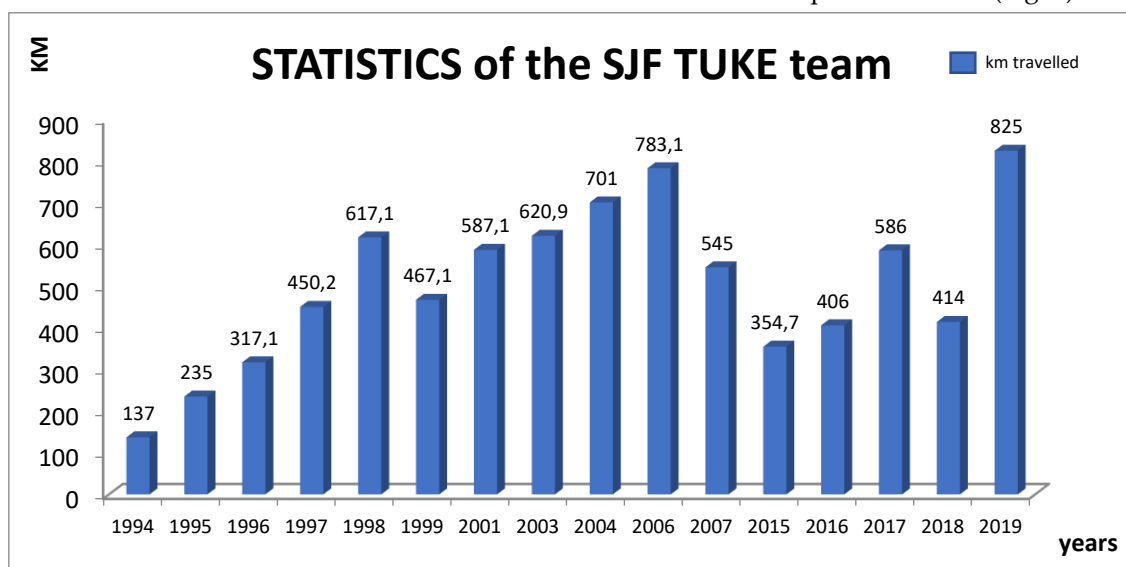


Fig. 1 STATISTICS of the SJF TUKE team [1]

3. Basic characteristics of the vehicles for the Shell Eco Marathon

One of the most important features of the Shell Eco Marathon race is the construction of a vehicle with the lowest possible weight, so special carbon materials are used for this purpose. The bodywork is self-supporting and made specifically for the pilot of the vehicle. A special manufacturing process has been used to ensure a small body thickness while maintaining the highest rigidity. All the components used in this experimental vehicle have been selected according to several criteria, the most important of which are quality and the lowest possible weight. [8] The positioning of the components was done in accordance with the idea of keeping the centre of gravity of the vehicle as low as possible to ensure sufficient stability of the vehicle. [13] As the race takes place on a multi-cornered circuit, it is very important to have the correct geometry of the spinning wheels, in addition to low weight and sufficient stiffness of the vehicle. When cornering,

each of the steered wheels moves in a different path because the inside and outside wheels go through the corner at a different turning radius. To achieve the best result in this competition, all possible passive drag and losses should be eliminated as much as possible. One of these losses may be due to poor steered wheel geometry, which can cause the steered wheels to brake the entire vehicle when cornering. [11] Despite the fact that the ultralight vehicle does not have shock absorbers, it was necessary to consider the stiffness of the axle so that it could support the wheel to some extent and return to its original position.

An important factor in the success of these races is not only building a low consumption engine, but also reducing wheel resistance, especially when cornering. Another integral part of the development of the experimental vehicle is the aerodynamic drag of the body, which has a great influence on its speed, stability, but especially on fuel consumption. [8] The external aerodynamic shape of the body must be designed to provide the best possible airflow, while at the same time providing the driver with enough space to ensure a safe view outside and to accommodate all necessary components.

Drive

The type and design of internal combustion engines are not restricted. However, they must only burn fuel provided by the organiser and must not burn engine oil (two-stroke engines are prohibited). [4] The most important points that must be observed are:

- Only an internal combustion engine may be used where 95 octane petrol supplied by Shell is used as fuel.
- The internal combustion engine must be a four-stroke
- The engine must not contain a carburettor, fuel injection must be electronically controlled
- Maximum fuel feed pressure is 5 Bar, no fuel filter is allowed
- Engine starting must be electric
- Turbocharging of the engine is prohibited
- Air filter is prohibited, intake manifold must be free of other components
- Intake air cooling is prohibited
- Gas recycling or engine venting must not be used for further combustion in the engine
- Only wheels that are not controlled by the driver may be driven
- The vehicle must not move spontaneously when started at idling speed[2]

External energy sources

For all fuel categories, stored pneumatic energy not replaced by the engine may only be used for the fuel injection system during competition. [15] Fuel pumps are allowed for all fuel categories provided they are mechanically driven. Electric fuel pumps are prohibited.

It is permitted to pressurize liquid fuel tanks to feed fuel to the engine only in the following cases:

- Compression shall be carried out using a transparent compressed air cylinder equipped with a relief valve set to a maximum pressure of 500 kPa
- The system shall incorporate a standard valve used for automobile tyres to allow verification/control of the setting pressure for the relief valve
- Said depressurisation shall be carried out in the starting area by means of an air pump
- The driver shall not change the pressure during the competition[2]

Auxiliary energy sources (chemical, latent energy from phase changes, etc.) are not allowed. The engine temperature can be regulated using pure pressurized water or a commercially available coolant. The pump for pressurizing the coolant can only be mechanically driven. External engine temperature control using external heating devices is limited to 100 °C[2].

External energy sources

The vehicle may only be equipped with one of the following approved fuel tanks supplied by the organisers:

- Prototype category: 30, 100 or 250 cc
- Urban-Concept category: 30, 100, 250 or 350 cc

Only tanks with a clearly visible mark demonstrating compliance with APAVE certification may be used for pressurised systems. APAVE tests fuel tanks and certifies their ability to withstand 500 kPa of pressure. [10] The fuel tank shall be mounted in an accessible and zero vertical position that allows for a burette height of approximately 1 metre in a filling situation. The fuel tank shall be mounted so that its top is a minimum of 50 mm below the protective cage and well clear of moving parts, batteries, heat sources and ignition. [16] The fuel tank shall be mounted so that its top is at least 50 mm below the roll cage and sufficiently far from moving parts, batteries, heat sources and ignition[2].

The fuel return line shall feed fuel into the fuel inlet below the fuel tank. For diesel engines, the return line may be fitted to the fuel filler cap only if the engine was originally equipped with a hand pump and the return line and pump have not been modified. Teams must equip their vehicle with a clean fuel line that is not susceptible to expansion under pressure (maximum internal diameter 8 mm). For all pressurised fuel systems, the hoses that connect the cylinder to the fuel tank cap must be flexible (need not be Rilsan/Nylon) to allow for easy connection[2].

The fuel system

Bidders shall provide a description and an accurate technical drawing of the fuel delivery system from the tank to the engine. This system shall be designed so that it can be completely drained and refilled before the competition. The fuel line between the tank and the engine must not contain any other components such as filters. [9] A second valve directly at the bottom of the fuel tank is tolerated. [18] For diesel engines, a fuel system solenoid shut-off valve is required in case of danger. Internal combustion engines with carburetors are prohibited (fuel injection is mandatory). The intake manifold must not contain any fuel (or accumulate any fuel) or exhaust gases when the vehicle is at the starting line prior to departure. [11] Air filters are not allowed in the intake system. Exhaust gases may not be recirculated during competition[2].

The fuel system must be easily accessible for inspection and measurement. It must be possible to adjust the fuel system to ambient pressure to accurately measure the fuel level in the tank. The pressurisation system shall be fitted with a pressure gauge and the operating pressure shall be clearly indicated on the gauge. The standard method of measuring fuel consumption for liquid fuels is by volumetric substitution of fuel consumed with a temperature-corrected fuel volume. The fuel consumption of all vehicles equipped with an internal combustion engine that have reached more than 1500 km/l shall be gravimetrically measured. Initially, a member of the technical team will fill the fuel system and then the entire fuel system (including tank, injectors and lines) will be weighed on a precision scale. All these components must be compact and easily separable for weighing purposes. Upon completion of a successful run, the entire fuel system shall be uninstalled and weighed again. This handling of the fuel system, including mounting and dismounting from the vehicle and transporting it to the weighing room, must be done by a competent team member with a valid access card. [10] The whole process of handling the fuel system will be supervised by a member of the technical team who will also carry out the weighing. Fuel is a volatile product. Therefore, it is not permitted to artificially raise the temperature of the fuel system which would result in vaporisation of the fuel. Cooling of the fuel system is also forbidden[2].

Vehicles using hybrid technology

The supercapacitor is the only permitted energy storage device for hybrid vehicles. Mechanical or hydraulic energy storage is not permitted. The use of any battery in a hybrid drive vehicle is prohibited. This capacitor shall be the sole source of stored energy for the electric motor driving the vehicle. [8] The two connectors must be installed safely outside the vehicle so that the voltage at the starting line can be measured. These connectors must be marked "Supercapacitor Voltage" The state of charge of the Supercapacitor will be checked before and after each run by measuring its voltage. The voltage measured after the competition run must be approximately the same as the voltage registered before it. [3] Otherwise, the supercapacitor must be recharged by starting the engine until its voltage is equal to the voltage recorded before the competition lap. The time taken to recharge the Supercapacitor by running the engine is then added to the recorded time of the respective competition round. The entire electrical circuit must be properly fused to prevent overloading of some of its parts. This fuse must be clearly marked on the technical drawings and must be easily visible and accessible[2].

Starter

An electric starter must be used during the competition. Hand starting is prohibited. It must be clearly stated that the starter must never be able to provide any propulsion to the car. Starter's light: A clearly visible red indicator light, equivalent in luminescence to a 21 W bulb, must be fitted to the rear of the car and must be clearly visible from both sides of the track to indicate any action by the starter. [7] If the track marshals report repeated or heavy use of the electric starter by a team, the organiser reserves the right to order an immediate inspection of the car. [4] If any non-compliance is observed, the team will be penalized accordingly. At the start, the starter and therefore the starter light must be extinguished by the time the rear wheel of the car crosses the start line. Failure to comply with this criterion will invalidate the round and will count as the maximum number of attempts[2].

Fuels

Fuels are provided exclusively by the competition organiser. Four types of fuel are provided for the internal combustion engines. Specifically, gasoline with the trade name Shell FuelSave 95, diesel fuel with the trade name Shell FuelSave Diesel, Ethanol E100 (denatured) and Shell Gas to Liquid (GTL)[2].

Benefits

- Helps reduce emissions - GTL produces more consistent and uniform molecules compared to conventional crude oil refining, resulting in better combustion characteristics for Shell GTL fuels in standard diesel engines. This helps reduce air pollutant emissions
- Can be used in existing diesel engines without the need for engine modifications, new infrastructure or vehicle investment - The properties of Shell GTL fuel allow it to be used as a direct replacement for conventional diesel fuels
- It is free of unwanted components such as sulphur, metals and aromatics - Natural gas is a much cleaner fossil fuel compared to petroleum, making it less harmful to the environment
- Readily biodegradable - Shell GTL fuel is more biodegradable than conventional diesel
- Better starting performance in cold conditions - due to higher cetane number
- Better safety, handling and storage - due to higher flash point [6]

4. Discussion

In an effort to gain market leadership, vehicle manufacturers are striving to introduce vehicles that are timeless not only in terms of the materials used but also the technology used to produce them. [7] These efforts are supported by various worldwide projects that give young people the opportunity to present their plans with the sole aim of attracting interest and demand.

This project serves as a motivation for the next steps of planning. The contest is divided into two main categories - urban concept and prototype. [9] The two categories are further divided according to the type of propulsion, whether it is an internal fuel engine, an electric motor or a hydrogen engine. [16] Our faculty is engaged in the Prototype category and the development of an internal combustion engine. Since the beginning of the

participation of the Faculty of Mechanical Engineering of the Technical University of Košice in these contests, it has been focusing on the development and construction of its own body and, last but not least, on the development and production of its own internal combustion engines that would achieve the best possible result in the competition.

References

1. SLOBODA, Aurel – BUGÁR, Tibor – SLOBODA, Oskar, KRÁL, Ján – KONEČNÝ, Branislav: 25 rokov experimentálnych vozidiel : Technická univerzita v Košiciach, Strojnícka fakulta, 2019, 141 s. ISBN 978-80-553-3328-1
2. SHELL ECO MARATHON 2020 OFFICIAL RULES [online]. : [cit. 10.05.2020]. Dostupné na internete: <<https://www.makethefuture.shell/en-gb/shell-eco-marathon/global-rules>>
3. GASOLINE [online]. : [cit. 17.05.2020]. Dostupné na internete: <<https://www.britannica.com/technology/gasoline-fuel>>
4. DIESEL FUEL [online]. : [cit. 17.05.2020]. Dostupné na internete: <<https://www.britannica.com/technology/diesel-fuel>>
5. ETHYL ALCOHOL [online]. : [cit. 17.05.2020]. Dostupné na internete: <<https://www.britannica.com/science/ethyl-alcohol>>
6. SHELL GTL FUEL [online]. : [cit. 17.05.2020]. Dostupné na internete: <<https://www.shell.com/business-customers/commercial-fuels/shell-gtl-fuel.html>>
7. SLOBODA, Aurel – BUGÁR, Tibor, - TOMKOVÁ, Marianna – SLOBODA ml., Aurel – PILA, Ján – TKÁČ, Zdenko: Konštrukcia automobilov I. : Technická univerzita v Košiciach, Strojnícka fakulta, 2006, 402 s. ISBN 80 -8073 – 718 - 5
8. TAJOMNÝ SVET ŠTVORTAKTOV [online]. : [cit. 28.05.2020]. Dostupné na internete: <<http://www.countrycross.sk/clanky/894-tajomny-svet-stvortaktov>>
9. WANKEL ROTARY ENGINE [online]. : [cit. 28.05.2020]. Dostupné na internete: <<http://www.citroenet.org.uk/miscellaneous/wankel/wankel2.html>>
10. MOTORY- JENOM PEKNY FOTKY [online]. : [cit. 02.06.2020]. Dostupné na internete: <<http://m-power.blog.auto.cz/2007-01/motory-jenom-peknay-fotky/>>
11. STRANKY PRE FANÚŠIKOV SUBARU [online]. : [cit. 02.06.2020]. Dostupné na internete: <<http://www.subaru-als.es-tranky.cz/>>
12. FERENC, Bohumil: Spalovací motory : Karburátory a vstříkování paliva. Praha: Computer Press, 2004, 388 s. ISBN 80-251-0207-10
13. SÚBOR: T CYCLE SEILIGER.PNG [online]. : [cit. 05.06.2020]. Dostupné na internete: <http://sk.wikipedia.org/wiki/S%C3%BAbor:T_cycle_Seiliger.png>
14. RAUSCHER, Jaroslav: Spalovací motory. Brno: studijní podklady, 2005, 235 s.
15. GRT GAZ ET LA JOLIVERIE, PARTENAIRES DE LA MOBILITÉ GAZ [online]. : [cit. 06.06.2020]. Dostupné na internete: <<http://www.grtgaz.com/fileadmin/medias/communiques/2015/fr/CP-GRTgaz-Joliveriemicrojoule-19032015.pdf>>
16. REMMI TEAM INFO [online]. : [cit. 06.06.2020]. Dostupné na internete: <<http://remmi-team.com/>>



The effect of Neurac movement therapy on the treatment of scoliosis

Bibiána Ondrejová ^{1*}, Lucia Bednarcíková ¹, Monika Michalíková ¹, Jaroslav Dulina ², Jozef Živčák ¹

¹ Technical University of Košice, Mechanical Engineering, Department of Biomedical Engineering and measurement, Letná 9, 04200, Košice, Slovakia;

bibiana.ondrejova@tuke.sk, lucia.bednarcikova@tuke.sk, monika.michalikova@tuke.sk, jozef.zivcak@tuke.sk

² Lucas Sports Centre s.r.o, Košice, Slovakia; dulinaj@gmail.com

* Correspondence: bibiana.ondrejova@tuke.sk

Abstract: Idiopathic scoliosis is a three-dimensional deformity of the spine, which most often affects children and adolescents. Untreated can cause severe movement restriction, progression of curvature and other complications associated with it. The cause is still unknown and is therefore considered a multifactorial disease. Current treatment options include, in addition to invasive surgical interventions, orthotherapy and movement therapy, which are the aim of this work. The work is focused on the effect of scoliosis using the RedCord system in a case study. It describes the principles and procedures of treatment with innovative and non-invasive movement therapy, which aims to restore functional movement patterns using a high level of neuromuscular stimulation. Part of the work is a case study of an adolescent patient with idiopathic scoliosis, who underwent treatment with Neurac RedCord therapy after the brace therapy. The anamnesis, kinesiological analysis of the patient, the therapy process and conclusions after treatment are presented.

Keywords: idiopathic scoliosis, movement therapy, Neurac

1. Introduction

Recently, due to a change in lifestyle, sedentary employment or school activities, where computer technology is used (incorrect sitting) as well as a persistent pandemic situation (absence of sports, clubs, physical activity) there is a development of diseases of the musculoskeletal system, in younger age categories it is mainly a diagnosis of scoliosis. Scoliosis is defined as "three-dimensional torsional deformity of the spine and torso" that causes abnormal lateral curvature in the frontal plane, axial rotation in the transverse plane, and abnormal curvature in the sagittal plane. It usually occurs among children and adolescents and often progresses untreated during growth. The consequences of deformity can sometimes be observed only in adulthood, when the patient primarily suffers from back pain, but secondary associated diseases of the musculoskeletal system, organs and cardiopulmonary system may also occur [1].

Although this is the most common spinal deformity among children and adolescents, a guaranteed effective treatment is still unknown. There are many approaches in the world to the treatment of this spinal disease, but they have all been developed primarily to achieve the same goal, namely to prevent the progression of the curve or to improve its condition and to prevent invasive surgery. In addition to correcting the curve during adolescence, the treatment of scoliosis also aims at the prevention or treatment of respiratory dysfunctions, the prevention or treatment of painful spinal syndromes and the improvement of the aesthetic aspect of deformity [1-3].

The most common parameter for the indication of scoliosis treatment are the degrees of Cobb angle (Figure 1).

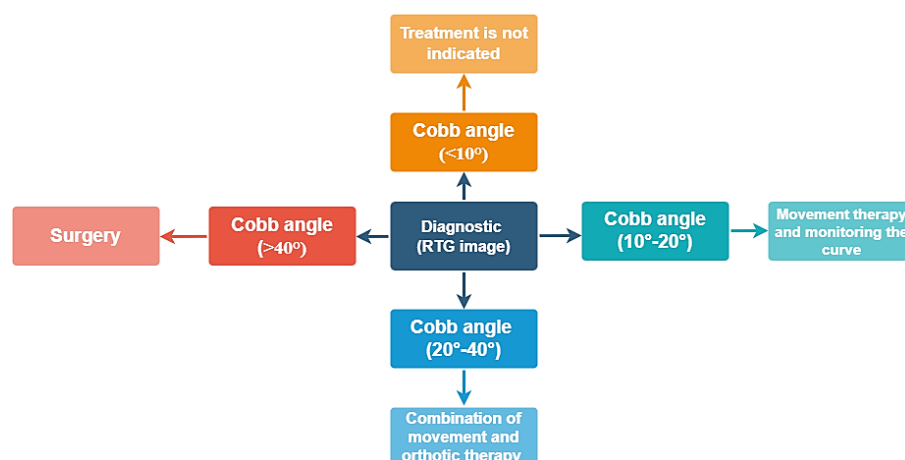


Figure 1. Scoliosis treatment indication according to Cobb angle.

As the most common causes of idiopathic scoliosis in adolescents include increased muscle tension and weakness of certain muscle groups, it is recommended to strengthen and exercise the muscular system using appropriate exercise plans designed by a physician, physiotherapist, or specialist in a given movement therapy. The criterion for selecting the right movement therapy is kinesiological analysis. The type of scoliosis, the size of the curve, the age and the ability to cooperate must be taken under consideration in the selection [4].

Non-invasive conservative treatment of congenital and acquired disorders of the musculoskeletal system is performed by the interaction of medical orthopedic devices (spinal prostheses). During the period of growth, there is a possibility of significant tissue remodeling, which can lead to effective correction of scoliotic curves using a corrective spinal orthosis. In adulthood, after the growth has stopped, deterioration and progression of the curve are no longer expected, leading to inadequate treatment for scoliosis, despite persistent problems. Reduction of these problems such as e.g. pain can be achieved through movement therapy [1-4].

Physiotherapeutic and orthotic treatment is based on long-term loading of the skeleton and connective tissues. As for the exercises that can be used in the treatment of scoliosis, they can be divided into conventional and new approaches. The possibilities of movement therapy for patients with IAS (idiopathic adolescent scoliosis) divided into conventional and new approaches are shown in the diagram (Figure 2) [4-5].

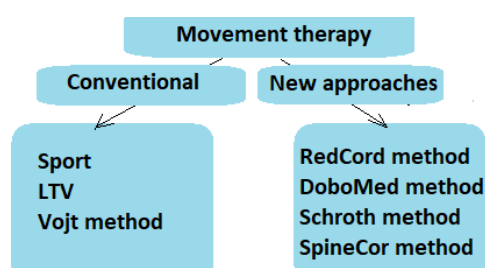


Figure 2. Conventional and new approaches in movement therapy.

The aim of this work is to present one of the new movement approaches to the possibility of affecting the scoliosis. For this purpose, Neurac RedCord therapy was chosen,

which is intended for the evaluation (recognition of weak links within the kinetic chain) and treatment of the neuromuscular system. The effectiveness of the method is based on scientific studies on the neurophysiology of pain and the musculoskeletal system and its positive effect is proven. The aim of the special exercises of the Neurac RedCord treatment method is to improve the interaction between the brain, locomotor receptors and muscles, which leads to reeducation, reactivation and ultimate restoration of normal function of inactive muscles. Neurac treatment has produced impressive results in many clinical cases, from patients suffering from chronic or acute pain to high-level athletes [6].

2. Materials and Methods

This case study was conducted at the Lucas Sports Center under the guidance of Bc. Jaroslav Dulina, who specializes in fitness training for athletes, physiotherapy and rehabilitation using the Redcord system.

The female subject was born in 2001 (consent to publication was provided by an adult patient) who was diagnosed with idiopathic scoliosis with an S-curve in 2016. The peak of the curve is Th9 and the Cobb angle was measured at 33°. Gybus present, scapular asymmetry, visible shoulder height difference and pelvic deviation present. Secondary deflection of the spine with an L2 vertex and a 20° Cobba angle. Primary curve is located in lumbar area of spine. The patient reports occasional pain in the right side of the cervical spine, scapula and tingling in the right upper limb. After X-ray examination (Figure 3), the patient was indicated with a spinal orthosis with a destructive effect on a 22-hour application with a combination of movement therapy SM system and LTV.

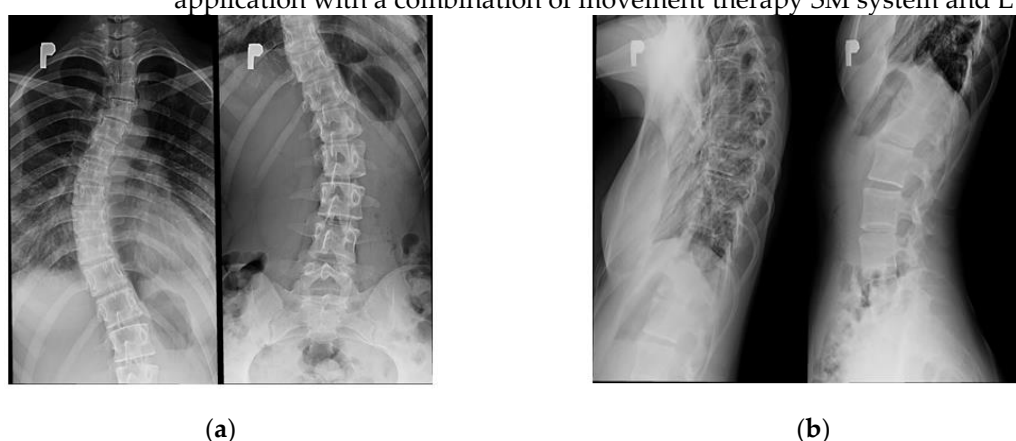


Figure 3. RTG images of the subject (a) image of Th spine (left), image of L-S spine (right) in frontal plane; (b) image Th spine (left), image L-S spine (right) in sagittal plane.

The patient's 22-hour daily application of the spinal orthosis (braces) lasted approximately 6 months, but due to associated back pain caused by pressure pads and worsening breathing during application of the orthosis, the number of daily application hours was reduced to 6-8 hours per day for another six months. Control examinations were completed in 2017 and 2018, when, however, there was no change in the initial finding. Due to persistent problems with back pain, in 2019 the patient began to undergo RedCord movement therapy.

The movement therapy itself was preceded by an examination to determine the current condition, which was performed by a physiotherapist in the form of posture aspects of the front, back, side and position on the 4 limbs.

When examining posture from the front, the subject had a slight shift of the pelvis to the right side, an asymmetry in the height of the collarbones and shoulders - the right side higher and the head inclined slightly to the right (Figure 4 (a)).

When examining posture from the side, the arch of the foot was visibly lowered. Shoulder protraction and a slightly weakened chest were also present. The head was advanced (Figure 4 (b)).

The position of the ankles and knees was normal during examination of posture from behind. The right posterior superior iliac spine was higher than the left. The thoracic region of the spine was inclined to the right with an overlap between the scapulas. The left scapula was placed higher than the right. Present asymmetry of the shoulder - left side above. The height of the upper limbs was also asymmetrical - the left side was higher than the right side (Figure 4 (c)).

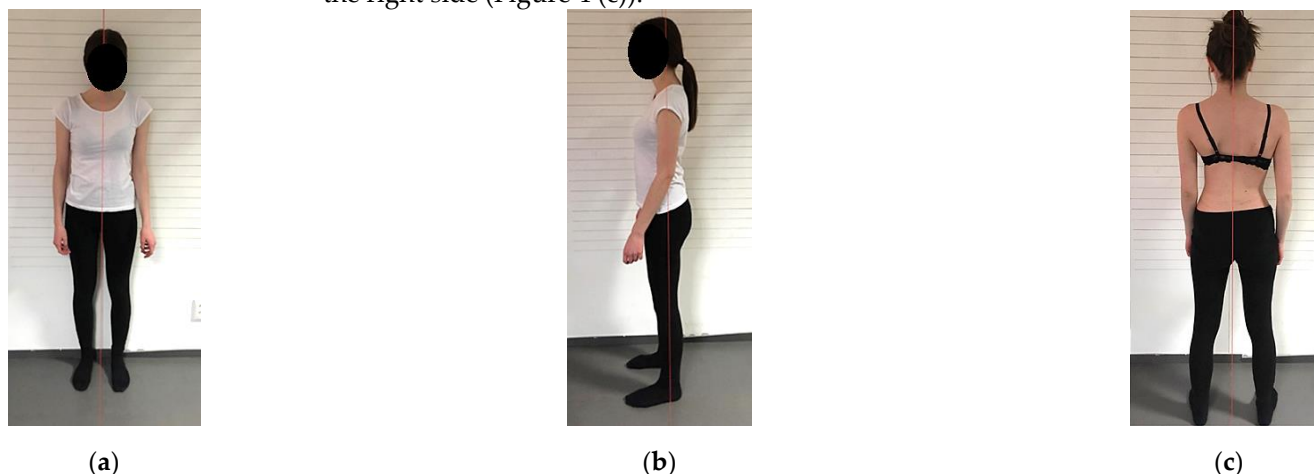


Figure 4. Examination of subject's posture: (a) front view; (b) side view; (c) rear view. (Dulina, J.)

Holding the body in position on the four highlighted the rotated pelvis - the right side higher than the left. The curvature of the spine in the thoracic part was inclined to the left. The thoracic region of the torso was also rotated - the left scapula placed higher than the right, also present overlap between the scapula inclined to the right (Figure 5).

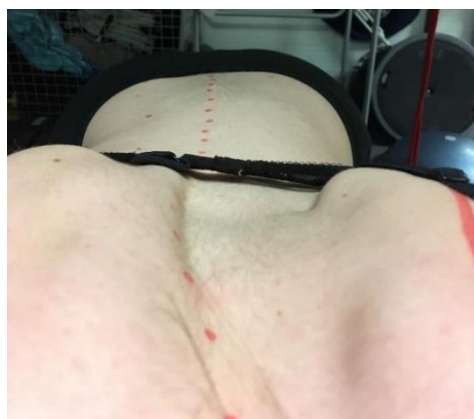


Figure 5. Visible deflection of the spine. (Dulina, J.)

According to the orthopedist's indication and from an initial examination by a physiotherapist, the subject was prepared for an intensive exercise program, which was planned for 3 weeks and consisted of 5 exercises in series. Therapy was focused on postural correction, functional stabilization, and pain reduction through the RedCord Neurac system.

The subject's exercise program consisted of the following 5 exercises:

Spine Scapular Retraction - retraction of the scapula in position lying on back;

- the purpose is neuromuscular control and functional stability of the scapula with stability of the torso with a focus on the dorsal myofascial chains, especially the interscapular muscles

Sitting Scapular Depression - depression of the scapula in sitting position;

- the purpose is neuromuscular control and functional stability of the scapulas and arms with a focus on the shoulder depressors

Supine Row - adduction;

- the purpose is neuromuscular control and functional stability of the scapula, shoulder and elbow with torso stabilization with a focus on the dorsal myofascial chain and elbow flexors

Supine Pelvic Lift - lifting the pelvis in position lying on back;

- the purpose is neuromuscular control and functional stabilization of the lumbar spine and pelvis, minimizing the involvement of hamstrings with a focus on the myofascial chain

Prone Bridging - plank;

- the purpose is neuromuscular control and functional stabilization of the stem and pelvis with a focus on the ventral myofascial chains

The patient completed 15 sessions under the supervision of a physiotherapist for 3 weeks. The length of one training was 45 minutes. The exercises were performed in 4 series of 10 repetitions, if the patient did not manage the quality of the exercise, the number of repetitions decreased. After the end of the first series, there was always an increase in the intensity of the exercise with the progression, the so-called with additional movement.

3. Results

After completing intensive training, the posture assessment of the subject was performed. It can be stated from the evaluation that the patient achieved a slight correction of the curve after only 3 weeks of intensive therapy and there was an improvement in the overall posture. This can be seen mainly in the thoracic spine, shoulder blades and shoulders. The inclination of the scapula and shoulder to the right has been elevated. There is a noticeable reduction in the height difference between the arms and scapulas - a reduced deviation in the height of the left and right side. The overlap between the scapulas has also been reduced - the scapulas are closer together. No correction in pelvic and lumbar area position is observable (Figure 6).



Figure 6. Examination of subject's posture: (a) Observation of the position of the scapulas and vertebrae after the first exercise – red: position before exercise, black –position after exercise.; (b) before therapy; (c) after therapy. (Dulina, J.)

Subjectively, the patient evaluates the therapy as effective. Indicates relief of cervical spine pain and right upper limb tingling. From an objective point of view, it is not possible to quantify the patient's condition after movement therapy, as no X-rays have been taken. One of the reasons is the termination of the growth of the subject and thus also the termination of the treatment of scoliosis. For these reasons, no significant progression of the curve is expected, which would lead to a negative affect on subject's health.

4. Discussion

The primary goal for improving the condition of patients with scoliosis is to strengthen weakened muscles and adjust muscle imbalances. Redcord therapy focuses on the treatment of the neuromuscular system and works on the principles of lability, relief and isolation of certain muscle groups. It achieves an ideal stabilization of the torso, activation of non-functional muscle groups and lightening achieves a suitable level of difficulty according to the ability of the individual. Therefore, the Redcord system can be considered as a suitable therapeutic movement therapy for patients diagnosed with scoliosis with an indication of movement therapy. However, orthotic therapy requires long-term application of the device, according to empirical experience, 10 hours or more, for torso braces, the application time is usually 23 hours per day, which is uncomfortable and discouraging for patients. With consistent patient monitoring and regular brace application, it is possible to stabilize the curve in 75% to 85% of cases, for improvement of the curve, the combination of orthotic and movement therapy is necessary. Regular exercise leads to strengthening of the body (prevention of muscle atrophy) with subsequent correction of the overall posture and muscle balance of the body. [2-6]

As this type of therapy is relatively new and the effect of the treatment of scoliosis is still being investigated, for the further research would be advisable to monitor the longer-term effect of this movement therapy on scoliosis with more subjects.

5. Conclusions

The work deals with the influence of scoliosis using the RedCord system. It is a relatively new suspension system, which includes Neurac exercises focused on the neuromuscular system. The paper presents a case study with the initial health status of the subject who was indicated for treatment with brace therapy in combination with rehabilitation. After a period of application of the brace, the patient began to experience back pain and breathing problems. Therefore, the subject underwent the indicated 3-week RedCord Neurac movement therapy under the guidance of physiotherapist Bc. Jaroslava Dulina. After evaluating the posture by aspect and subjective evaluation of the patient, it is possible to declare the therapy as effective and the primary goal of the therapy fulfilled.

Acknowledgments: This work was supported by the Slovak Research and Development Agency under the contract No. APVV-19-0290; project KEGA 041TUKE-4/2019 Design of progress algorithms in additive technologies for the educational process in biomedical engineering; project Open scientific community for modern interdisciplinary research in medicine (Acronym: OPENMED), ITMS2014+: 313011V455 supported by the Operational Programme Integrated Infrastructure funded by the European Regional Development Fund.

Conflicts of Interest: The authors declare no conflict of interest.

References

1. Fadzan, M.; Bettany-Saltiko, J.; Etiological Theories of Adolescent Idiopathic Scoliosis: Past and Present. *The Open Orthopaedics Journal*, vol. 11, 2017.
2. Grivas, T.B.; Mauroy, J.C.; et al. Brace Classification Study Group (BCSG): part one – definitions and atlas. *Scoliosis and Spinal Disorders*, 2016.
3. Berdishevsky, H., et al.; Physiotherapy scoliosis-specific exercises – a comprehensive review of seven major schools. *Scoliosis and Spinal Disorders*, (20) 2016
4. Kwang-Jun Ko; Seol-Jung Kang; Effects of 12-week core stabilization exercise on the Cobb angle and lumbar muscle strength of adolescents with idiopathic scoliosis. *Journal of Exercise Rehabilitation*, vol. 13 (2), 2017.
5. Karimi, M., ; Rabczuk, T.; Scoliosis conservative treatment: A review of literature. *Journal of Craniovertebral Junction and Spine*, 2018.
6. Neurac method, an active treatment approach. Available online: <https://redcord.com/medical-professionals/research/> (accessed on 10.12.2021).

Verification of Manufacturability and Material Selection for the Sheet Metal Part Using Numerical Simulation

Juliy Martyn Kulya^{1*} and Miroslav Tomáš²

¹ Department of Automotive Production, Faculty of Mechanical Engineering, Technical University of Kosice; juliy.martyn.kulya@tuke.sk

² Department of Automotive Production, Faculty of Mechanical Engineering, Technical University of Kosice; miroslav.tomas@tuke.sk

* Correspondence: juliy.martyn.kulya@tuke.sk; Tel.: +421 55 602 3528

Abstract: This article focuses on the prediction of manufacturability and material selection for the rubber forming part. The cover was used as a part model. Two materials were considered for production - drawing quality steel St14 and aluminium steel Al6016. Pam stamp software was used to create the simulation model. The constitutive material equations Hill 48 and Hollomon (Krupkowski) described the behaviour of the material during forming. Results were compared to the conventional deep drawing method by a rigid tool.

Keywords: rubber forming, conventional forming, steel sheet, aluminium sheet, numerical simulation

1. Introduction

Rubber forming is one of the unconventional forming technologies, as is hydroforming, electromagnetic forming, blast forming, and incremental forming [1-3]. Rubber forming is advantageous for the production of prototype stampings, where only the die is used and any blank holder is required, which simplifies the construction of the tool and the production of prototypes. We distinguish two basic methods of rubber forming. The Guerin method uses the principle of expansion of rubber enclosed in a steel case. The advantage is that the rubber leaves no marks on the surface. The disadvantage is the need for large forces, although large pressures have a positive effect on increasing plasticity [1,2]. The Marform method is also suitable for deep drawing of steel and non-ferrous sheets. The difference is in the layer of rubber, which is larger here. The height of the rubber must be at least three times the height of the molding in order to avoid rapid wear and loss of elasticity of the rubber [2,3].

In practice and research, several authors have compared rubber forming technology with other forming technologies. Peng et al. [4] investigated rubber forming for various molding materials, where they examined the hardness of the rubber to the result of the process. In the simulation, the authors used the hyper-elastic Mooney-Rivlin model to describe the properties of a rubber die. The results of the investigation were suitable rubber hardness and friction conditions to achieve a uniform molding without breaking. Afteni et al. [5], summarized rubber forming technologies, where they described the production of different types of moldings and different types of production methods: Guerin process, Maslennikov process, Marform process, Demarest process, Verson-Wheelon process, Verson hydroform process, and SAAB process. They also analyzed the results of numerical simulation of selected rubber forming technologies for selected types of moldings for the automotive and aerospace industries. Younis et al. [6] investigated the process of drawing a roll with rubber and used the experimental results to verify the numerical simulation of rubber forming. The rubber rod was made of polyurethane with different hardness and

thickness. Numerical simulation determined suitable process parameters for different shapes of the bottom of the cylindrical cups.

The article presents a case study of the manufacturability of a sheet metal component (cover) by the rubber forming method. The purpose of the study was to replace the production of a prototype cover stamping using a solid tool drawing method with a rubber drawing method and to evaluate the possibility of replacing the material in order to reduce the weight of the stamping.

2. Materials and Methods

In the simulations, a substantial part was to assess the possibility of changing the material for the cover molding in order to reduce the weight and at the same time to assess the possibility of rubber forming compared to the traditional method of production by forming with a rigid tool. The material suggested for the cover stamping was aluminum. The table defines the mechanical properties of aluminum Al6016, and steel St14, which were used in the simulation.

Table 1. Mechanical properties of steel St14 and aluminum Al6016

Material	E [MPa]	N [-]	ρ [kg.m-3]	r0 [-]	r45 [-]	r90 [-]	Re [MPa]	n [-]
St14	2.1.10 ⁵	0.3	7850	1.8	1.13	1.96	210	0.217
Al6016	7.10 ⁵	0.3	2700	0.38	0.48	0.66	116	0.26

2.1 Condition of plasticity

An Hill 48 anisotropic plasticity condition was used for both materials: [7,8]

$$\sigma_1^2 = \frac{r_0(1 + r_{90})}{r_{90}(1 + r_0)} \sigma_2^2 - \frac{2r_0}{1 + r_0} \sigma_1 \sigma_2 = (\sigma_1^y)^2 \quad (1)$$

2.2 Material hardening curves

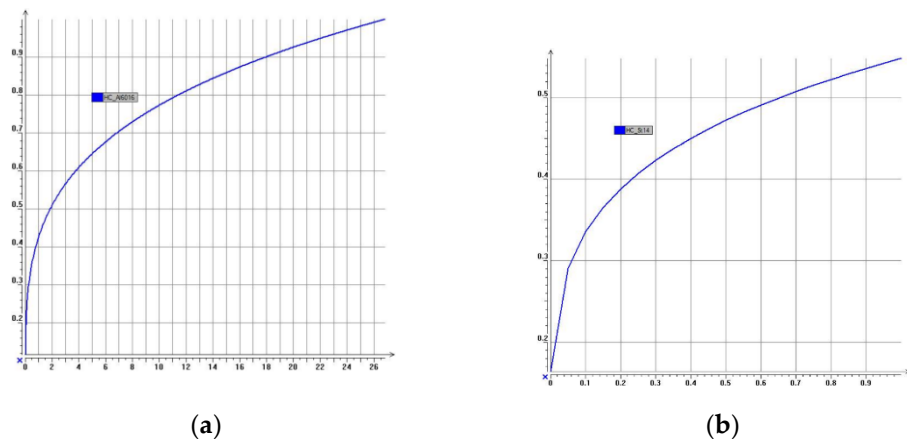


Figure 1. Material hardening curves: (a) Al6016; (b) St14

The Hollomon hardening model (Eq. 1) was used for the Al6016 material and the Krupkowski hardening model was used for the St14 material. (Eq. 2): [9,10]

$$\sigma = K \cdot \varphi^n, \quad (1)$$

$$\sigma = K \cdot (\varphi_0 + \varphi_{pl}), \quad (2)$$

where K is material constant, n is strain hardening exponent, φ_0 is offset strain. The values of constants for individual materials are in Tab. 2.

Table 2. Constants of material models

Material	K [MPa]	n [-]	φ_0 [-]
Al6016	425	0,26	-
St14	548	0,217	0,0038

2.3 Simulation settings

The Mooney-Rivlin hyperelastic material model was used to define the punch material. In Fig. 2 all the parameters of the punch material that were used for the simulation are shown.

Material type: Rubber
Material law: Mooney-Rivlin
Isotropic hardening

Parameters:
E: ν : ρ : 1.5E-6

ν for load: 0.499
☐ ν for unload: 0.499

A and B coefficients:
For load: A: 0.009 B: 0.005
For unload: A: B:

Nb of cycles for search between load/unload: 50
Nb of cycles for transition between load/unload: 300

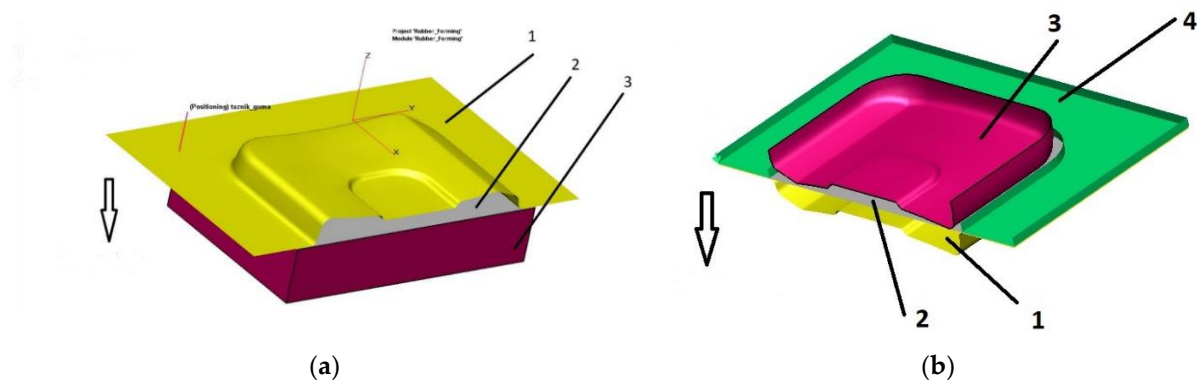
Figure 2. Parameters for the rubber punch material.

Mooney-Rivlin generalized model expresses density of deformation energy in the case of compressibility by the relation (Eq. 3): [4,11]

$$W = W(I_1, I_2, I_3) = A(I_1 - 3) + B(I_2 - 3) + W(I_3) \quad (3)$$

where : W is strain energy density, A and B are material parameters and $W(I_3)$ is a penalty function for incompressibility (using $\nu = 0,499$: Poisson's ratio), I_1 , I_2 and I_3 are the strain invariants. [11]

Different simulation models were modeled for different technologies, both simulation models ejected from the shape of the die (1), which was inserted into the PamStamp in the .igs format. Next, in PamStamp software, a rubber punch (3) for rubber forming and a rigid punch (3) for rigid tool forming technology, a blank (2) and a blankholder (4) for rigid tool forming technology were created. Finally, the shapes of the simulation model for individual technologies are given in the following figures.

**Figure 3.** Simulation models (a) Rubber Forming (b) Rigid tool

3. Results

The result of the simulation of deep drawing the cover from steel and aluminum sheet by Rubber Forming is shown in Figs. 4 to 5. The smallest thickness of the steel sheet was 0.869 mm in the corners of the stamping, which represents a thinning of the material by 27%. For aluminum sheet, the smallest sheet thickness in the same places was 0.784 mm (thinning 34%). The distribution of deformations and their comparison with the forming limit curve, determined according to the Keeler model, is shown in Fig. 5. For both materials, the strains are below the limit values, so that the stamping does not break when formed with rubber.

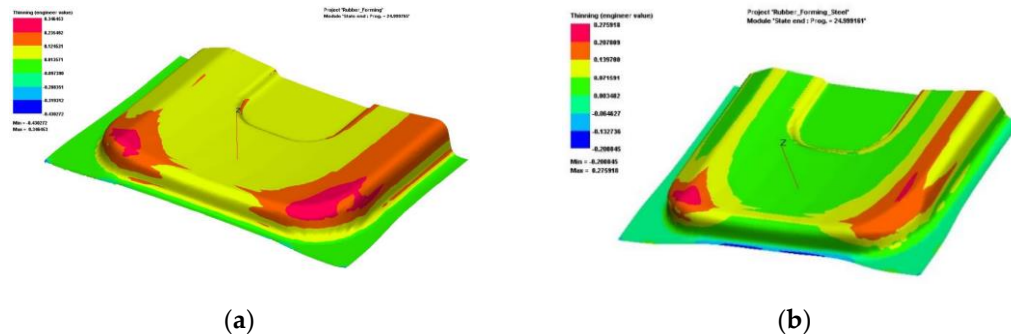


Figure 4. Thinning of metal sheets when formed by rubber : (a) aluminum sheet Al6016; (b) steel sheet St14.

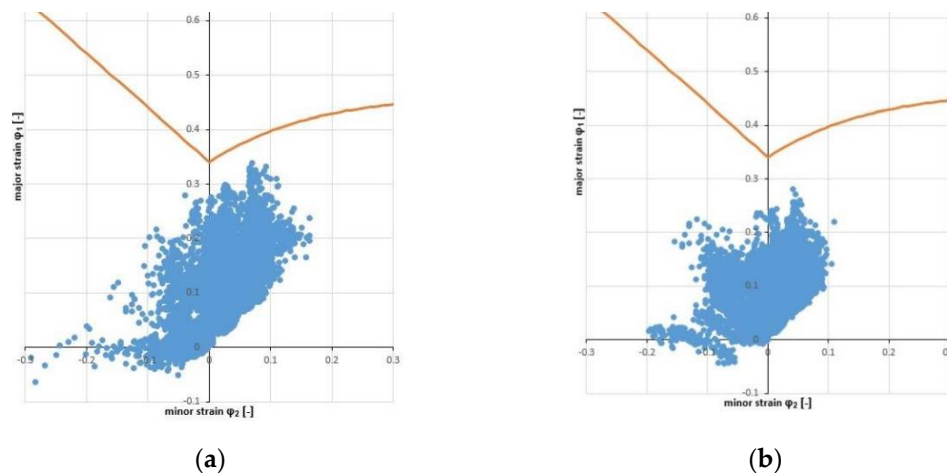


Figure 5. Analysis of fracture at rubber forming: (a) aluminum sheet Al6016; (b) steel sheet St14.

The result of the simulation of deep drawing of the cover from steel and aluminum sheet by rigid tool forming is shown in Figs. 6 to 7. The smallest thickness of the steel sheet was at the corners and at the point of the inner molding of the molding with a value of 1.06 mm, which represents a 11% thinning of the material. For the aluminum sheet, the smallest sheet thickness in the same places was 0.99 mm (thinning 17%). The distribution of deformations and their comparison with the forming limit curve, determined according to the Keeler model, is shown in Fig. 7. For both materials, the deformations are below the limit values, so there is no breakage of the forming when drawing with a rigid punch.

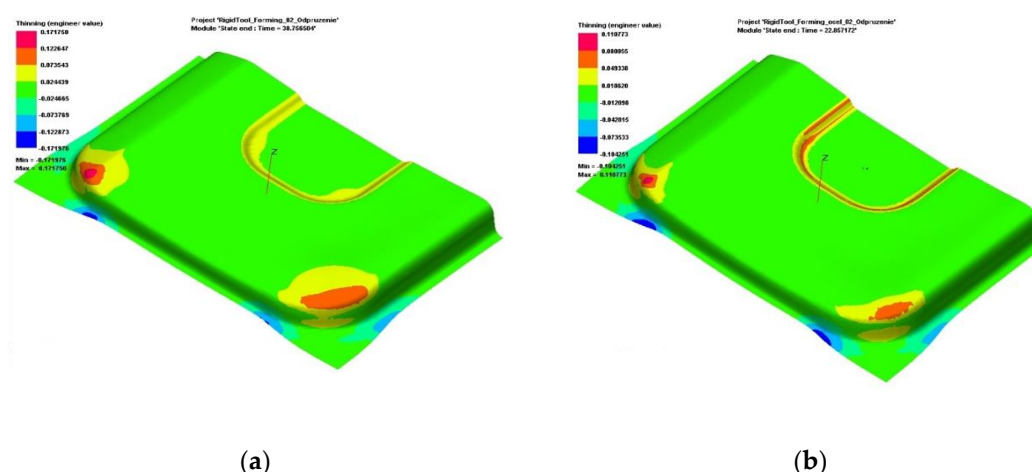


Figure 6 Thinning of metal sheets when formed by rigid tool: (a) aluminum sheet Al6016; (b) steel sheet St14.

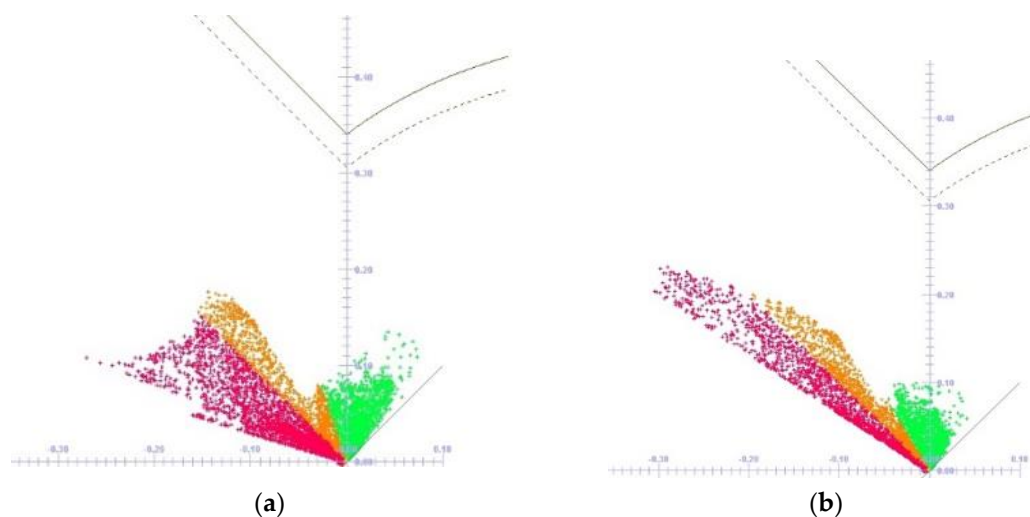


Figure 7. Analysis of fracture at rigid tool forming: (a) aluminum sheet Al6016; (b) steel sheet St14.

When comparing the results of the simulation of drawing with a rigid tool and rubber forming for the material Al6016, there is a greater change in thickness when rubber forming than when forming with a rigid tool (Table 3) - there is greater thinning of the material (twice as much as drawing with a rigid tool). The same trend was observed for the St14 steel sheet, where there was more than double thinning.

When comparing the strain distribution on the stamping, it is possible to state the development of strains in the area of tension-pressure ($\varphi_2 < 0$) for forming with a rigid tool. In contrast, in the case of rubber forming, there is a more pronounced development of strains in the area of uniform strains ($\varphi_2 = 0$) and in the area of tension-tension ($\varphi_2 > 0$). For both materials, a stamping fracture was not identified when rubber formed or when formed with a rigid tool.

Table 3. Comparison of selected values of numerical simulation.

		Thickness [mm]	Thinning [%]
Rubber Forming	steel	0.869	27
	aluminium	0.784	34
Rigid tool	steel	1.06	11
	aluminium	0.99	17

4. Conclusions

In this article, the results of a numerical simulation of a cover stamping are presented when two technologies – rubber forming and forming with a rigid tool – were considered for its production. Two materials for the blank, aluminum Al6016 and steel St14, were judged in simulations. For the punch in the case of simulation using rubber forming technology, the Mooney-Rivlin material model was set, while in the case of simulation using rigid tool forming we need to crate the punch and blank holder.

Based on of the simulation results, it can be stated that a higher quality part can be produced using rigid tool forming technology. With Rubber Forming technology, in the case of aluminum sheet metal, there is a large thinning of the sheet metal and a large springback. The main advantage of aluminum is its lower weight, and when forming with a rigid tool, it is possible to produce a product with sufficient quality from aluminum. The advantage of rubber forming technology is that there is no need for a punch and a blank-holder, which are replaced by the elastic rubber. Thus, rubber forming technology is suitable for the production of prototype stampings due to the shortening time for die production.

Acknowledgments: The work was carried out under the grant project VEGA 2-0080-19 “Prediction of weldability and formability for laser welded tailored blanks made of combined high strength steels with CAE support” and project APVV-0273-12 “Supporting innovations of autobody components from the steel sheet blanks oriented to the safety, the ecology and the car weight reduction”

References

1. Moravec, J. *Nekonvenčné metódy tvárnenia*, 1st ed.; Žilina : EDIS -University of Žilina, Slovakia, 2011; pp.187.
2. Lenfeld, P. *Tvárení II*, 3rd ed.; Liberec : Technical university of Liberec, Slovakia, 2016; pp. 110.
3. Tkačova, J. Selected conventional and unconventional mechanical technologies, 1st ed.; Kosice: Technical university of Kosice, Slovakia, 2017; pp. 183.
4. Peng, L.; Hu, P.; Lai, X.; Mei, D.; Ni, J.: Investigation of micro/meso sheet soft punch stamping process – simulation and experiments. *Materials & Design* **2009**, Vol. 30, p. 783-790.
5. Afteni, C.; Costin, G.; Iabob, I.; Paunoiu, V.; Virgil, T. A review on sheet metal rubber-pad forming. *The Annals of „Dunărea de Jos” University of Galați* **2018**, Fascicle VI, p. 1-6.
6. Younis, K. M.; Aljarjary, A. I.; Shukur, J. J. Numerical and experimental investigation of parameters affect the forming load during rubber pad sheet metal forming. *IOP Conference Series Materials Science and Engineering* **2019**, Vol. 518(3), p. 1-12.
7. Banabic, D. *Sheet metal forming processes – constitutive modelling and numerical simulation*; 1st ed.; Berlin Heidelberg : Springer-Verlag, Switzerland, 2010; pp. 301.
8. Šlota, J. *Numerical simulation of sheet metal forming*, 1st ed.; Kosice : Technical University, Slovakia, 2016; pp. 194.
9. Hrivnak, A.; Evin, E.; *Formability of metal sheets*, 1st ed.; Kosice : Technical University, Slovakia, 2004; pp. 223.
10. Tomáš, M.; Evin, E.; Kepič, J.; Hudák, J. Physical Modelling and Numerical Simulation of the Deep Drawing Process of a Box-Shaped Product Focused on Material Limits Determination, *Metals* **2019**, 9, art. num. 1058.
11. PamStamp users guide, ESI group 2020.

Production of filaments and optimization of the 3D printing process for PLA/PHB material with an admixture of a ceramic component

Samuel Lancoš^{1*}, Miroslav Kohan¹, Marek Schnitzer¹, Gabriela Dancáková¹, Tomáš Balint¹, Radovan Hudák¹

¹ Technical University of Košice, Faculty of Mechanical Engineering, Department of Biomedical Engineering and Measurement, Letná 9, 042 00 Košice

* Correspondence: samuel.lancos@tuke.sk

Abstract: The presented work describes the methodology of production and processing of composite filament as a promising material variant with the possibility of use in the biomedical industry. The primary part of the material consists of a polymer mixture containing the following materials: poly (lactic acid) (PLA): 85% by weight, polyhydroxy butyrate (PHB): 15% by weight, tris aminocyclopropenium (TAC): 5% proportion of the total weight of the mixture. The ceramic admixture consists of the following materials: hydroxyapatite (HA) and tricalcium phosphate (TCP), with a content of 10% by weight. Medically certified materials were used in the production. The production took place on the product line of devices and equipment (Filamentmaker, Dryer) from the company 3Devo, the Netherlands. The work includes a list of optimal conditions to produce filament intended for 3D printing, but also the necessary software modifications in the pre-processing phase. The result is a 3D print of an experimental sample using a Deltiq 2 device (Trilab, Czech Republic) designed for mechanical tensile testing.

Key words: extrusion; filament production; optimization; ceramics; composite material; 3D printing

1. Introduction

3D printing, also known as rapid prototyping or additive manufacturing, describes a process in which a computer-aided design (CAD) product is created by a layered application [1,2]. Unlike conventional manufacturing processes such as injection moulding, 3D printing ushered in an era of design freedom and enabled the rapid production of customized objects with complex geometries [3,4]. One of the main advantages of 3D printing is the ability to directly convert the concept into the final product in a convenient and cost-effective way. 3D printing has been used in industrial design since the 1980s. However, it has only adapted to medical use in the last decade [5,6]. Imaging data from routine computed tomography (CT) or magnetic resonance imaging (MRI) can be converted to a CAD file using a variety of 3D software programs.

While a range of 3D printing techniques have been developed for industrial applications, stereolithography (SLA), multi jet modeling (MJM), selective laser sintering (SLS) and fusion deposition modeling (FDM) are the main technological approaches that have also been explored in a clinical setting [7]. The FDM 3D bioprinting method is a common and simple method of using thermoplastic filaments as a bioprinting material [8]. The fibers are melted in the head of the 3D printer by heating and then used to create 3D structures.

Materials engineering is considered worldwide as a top priority for innovation and technological growth. Synthetic materials (such as PCL, PLA, PEG, PEEK) offer greater advantages over natural materials in that they can be adapted to specific physical properties and have greater uniformity than natural materials [9]. Mixing several materials and

adding additives (ceramics, carbon fiber, glass fiber) can significantly modify the mechanical and biological properties of the composite. When replacing bone tissue, the strength characteristics of a particular bone make it possible to adapt the mechanical properties of the implant by adding a certain percentage of the additive [10].

Both PLA and PHB are biodegradable polyesters and are used in consumer products by several industrial sectors due to their biocompatibility, biodegradability, and sustainability. They have comparable thermal and mechanical properties to conventional polymers, which has aroused great interest in investigating their physical properties for potential medical applications [11]. Attention has focused primarily on use in combination with ceramic additives.

In recent years, many favorable reports have been published on the use of bioactive materials such as HA and TCP as replacements for defective bones or teeth in dental, maxillofacial and orthopedic surgery. From a chemical point of view, they are known to be biocompatible, bioactive (i.e. have the ability to form a direct chemical bond with surrounding tissues), osteoconductive, non-toxic, non-inflammatory and non-immunogenic substances [12]. However, the use of HA-based systems was not entirely satisfactory due to the possible mobilization of free HA particles from the implant site with their possible migration outside the intended area [13]. To overcome these problems, common plastic materials, including poly glycolic and lactic acid (PLGA), PLLA and PCL, have been combined with HA and TCP (α -TCP, β -TCP) particles to form composite materials [14].

The aim of the work is to describe the methodology of filament production from PLA/PHB materials with ceramic admixture (HA, TCP) by extrusion. The resulting filament is then used for 3D printing of experimental samples. The task was to find the optimal parameters for the production and processing of 3D printing.

2. Methodology of printing fiber production

A mixture of PLA/PHB (85/15), TAC (5%) and ceramics was used to produce the target filament. The TAC additive contributes to the softening of the compound. The ceramic component consisted of two materials: TCP and HA (Captal®, UK). Both ceramic materials represented 10% by weight. The particle sizes of the ceramic powder were as follows: TCP (2-6 μ m), HA (<15 μ m). The pre-mixed material in the form of pellets was supplied in vacuum packs to prevent the absorption of moisture and impurities. Nevertheless, the pellets had to be dried before extrusion. The material was dried on an Airid Polymer Dryer (3devo, The Netherlands). The drying temperature was set at 45 °C for 4 hours after consultation with the equipment manufacturer. The drying process was performed to remove unwanted moisture during material transport, as the moisture of the material can affect the filament extrusion process itself [15].

2.1. Description of extrusion and optimal parameters in filament production

The process of transformation from pellets to fiber suitable for FDM 3D printing took place on a specialized equipment Filamentmaker - Composer series (3devo, The Netherlands), see Figure 1. Prior to extrusion, the equipment was placed in an air-conditioned room with a temperature of 18°C due to temperature adjustment. The device comprises 4 consecutive heating elements (material displacement direction: #4→#3→#2→#1), which gradually heat the material inside the horizontally positioned chamber. The Composer series has a rotating screw with a mixing element at its end. Using this screw, the material is transported from the hopper towards the nozzle of the device. Behind the nozzle is a filament diameter sensor and a traction system for moving the filament towards the spool. The mixing element also contributes to the perfect distribution of ceramics in the material.

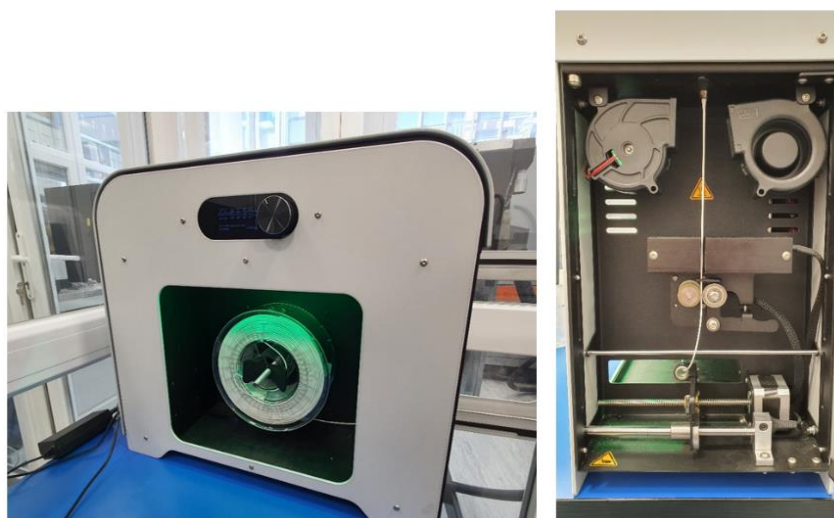


Figure 1. Extrusion process using the Filamentmaker - Composer series

Since there was a cleaning material - HDPE material - in the chamber of the device after the last extrusion process, it was necessary to heat the device to temperatures that would melt the material. The temperature of 180°C was set. This temperature was also a suitable starting point for the PLA/PHB/CER material. At these temperatures of heaters, after the pellets were loaded to the hopper, the outlet material appeared to be sufficiently viscous, as evidenced by compliance with the recommended value of the current drawn by the motor (approximately 2000mA). After the time when the HDPE material was completely replaced by the PLA/PHB/CER material, it was necessary to change the device settings based on a visual inspection of the output. Variables that have a significant effect on the extrusion result include ambient temperature, RPM (revolution per minute) and heater elements temperatures. The aim was to stabilize the flow through the nozzle and achieve a constant filament diameter - 1.75 mm. You can see the optimal combination of variables in Table 1.

Table 1. Optimal settings of the device in the production of PLA/PHB material with ceramic admixture

Heating element	#4	#3	#2	#1		Ambient temperature [°C]	18
Set temperature [°C]	154	175	178	176		Fan output	60
Real temperature [°C]	155	175	180	175		RPM [round/min]	3

3. Statistical evaluation of the produced filament

We consider the composite printing fiber to be the output of the production process using the determined optimal parameters of the device (see Figure 2, left). Due to the quantitative evaluation of the filament, the device itself has a built-in optical sensor with an accuracy of 43µm. Using an optical sensor, it was possible to observe the course of the filament diameter during the whole extrusion process with a sampling frequency of 1 second. Figure 2 shows the dependence of the measured filament diameter as a function of time.

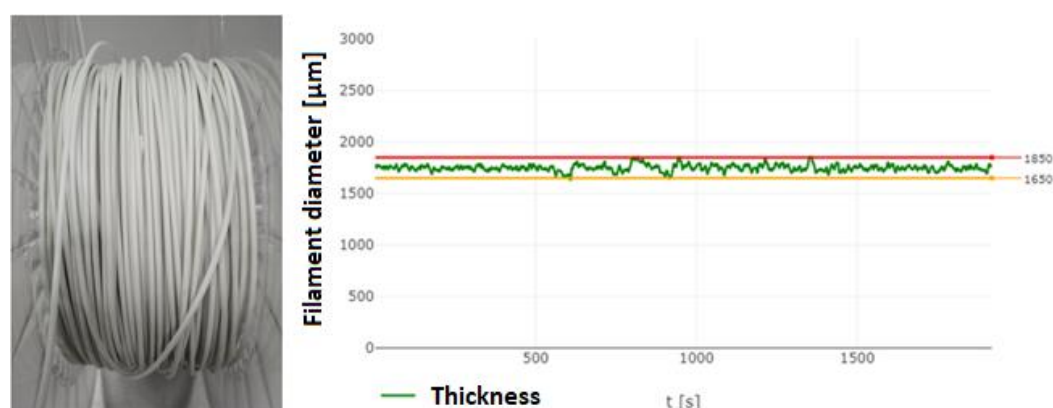


Figure 2. Time course of filament diameter, filament wound on a spool

From the graphical representation of the diameter, it is possible to record the apparent variation of the curve caused by the fluctuation of the material flow. This phenomenon can be attributed to several factors. The speed of the sliding screw tended to fluctuate (± 0.2 rpm) throughout the extrusion of the material. The addition in the form of a ceramic component significantly increased the viscosity of the material, making it more difficult for the propulsion system to maintain a constant RPM. Another factor was the deviations of the real temperatures from the values of the temperature of the radiators determined by us, as well as the room temperature. The diameter value was maintained between 1.862 and 1.638 mm. The results of the Filamentmaker, which is not intended for large-scale industrial production, must also be included in the results. For a quantitative description of the average, the record was evaluated using descriptive statistics (see Table 2).

Table 2. Basic characteristics of filament diameter variability

Maximum value [mm]	1.862		Standard deviation [mm]	0.032389
Minimum value [mm]	1.638		Variance [mm ²]	0.001049
Average [mm]	1.7493		Skewness of a distribution	0.135248
Variation range [mm]	0.224			

Based on the values proved above, it is proved that with the help of the determined device settings (heater temperatures, RPM, fan output, ...) it is possible to produce a filament with a total average diameter of 1.7493 mm. This data is the result of 1919 partial measurements of the optical sensor. The largest deviation from the required value of 1.75 mm was measured in a unique extreme case, i.e. + 0.112mm. Based on the positive skewness coefficient, we can say that the diameter of the produced filament had for the most part smaller values than the nominal value of 1.75 mm.

4. Optimization of 3D printing using PLA/PHB/CER filament

3D printing of experimental samples took place on a Deltiq 2 device from the manufacturer Trilab (Czech Republic). The mentioned printer works on the principles of FDM technology. Due to the planned mechanical tensile tests, the geometric shape of the computer model was identical to the test specimen given by the standard STN EN ISO 527-2, specifically type 5A (Figure 3). The last step before 3D printing of experimental samples was to find the appropriate software settings that the printer works with. Simplify3D software was used for this purpose. Main compound component, therefore the general configuration for this material was chosen. You can see the basic printing parameters in Table 3.

Table 3. Parameters used in the process of production of experimental samples

Default printing speed [mm/s]	20		Extrusion multiplier	1,4
Retraction speed [mm/s]	25		Coasting distance [mm]	0,2
Infill [%]	100		Top/Bottom solid layers	1
Infill extrusion width [mm]	0,6		Outline/Perimeter shells	1
Extrusion width [mm]	0,4		Internal infill angle offsets [°]	45/-45
Primary layer height [mm]	0,2		Fan output (%)	85

A major change from the general configuration for the PLA material was made in the material flow tuning (Extrusion Multiplier), where the value was changed from 1.0 to 1.4. This step significantly increased our flow, which affected the print quality. The best results were obtained at temperatures: nozzle 215°C, printing bed 70°C (see Figure 3-B). The print head feed speed was reduced to 20 mm/s due to the higher viscosity caused by the ceramic.

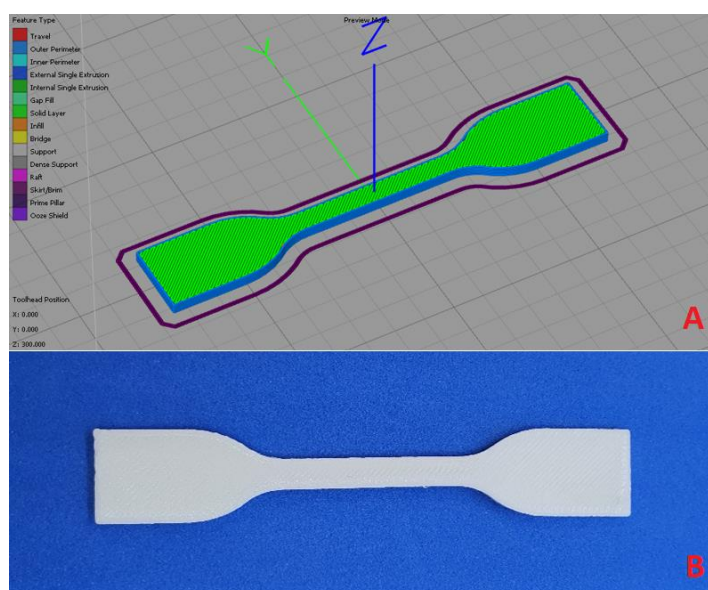


Figure 3. Experimental sample: A-in the Simplify3D software environment, B-after the 3D printing process

6. Conclusion

The result of the presented work is a brief description of the production and processing of filament from PLA/PHB/CER composite material. Based on the presented parameters of the extrusion equipment, it is possible to produce a filament with a diameter value of 1.7493 mm. Proof of the correctness of the set parameters is the long-term extrusion process without major diameter deviations. By configuring the 3D printing process in the Simplify3D software, it is possible to print the given experimental samples for mechanical testing, namely tensile tests of sufficient quality.

Acknowledgment: This research was supported by project VEGA 1/0179/19 Development and construction of low-cost modular prostheses of upper limbs manufactured by additive technologies; KEGA 040TUKE-4/2019 Use of digitization technologies for educational process support in the field of prosthetics and orthotics; KEGA 041TUKE-4/2019 Design of progress algorithms in additive technologies for the educational process in biomedical engineering; „Open scientific Integrated Infrastructure for the project: Center for Medical Bioadditive Research and Production (CEMBAM), code

ITMS2014 +: 313011V358, supported by the Operational Programme Integrated Infrastructure, funded by the ERDF“; Center for Advanced Therapies of Chronic Inflammatory Diseases of the Locomotion System (CPT ZOPA), ITMS2014+: 313011W410, co-financed by the European Regional Development Fund; Open scientific community for modern interdisciplinary research in medicine (OPENMED), ITMS2014+: 313011V455, , co-financed by the European Regional Development Fund.

References

1. GERSTLE, Theodore L., et al. A plastic surgery application in evolution: three-dimensional printing. *Plastic and reconstructive surgery*, 2014, 133.2: 446-451. Author 1, A.; Author 2, B. Title of the chapter. In *Book Title*, 2nd ed.; Editor 1, A., Editor 2, B., Eds.; Publisher: Publisher Location, Country, 2007; Volume 3, pp. 154–196.
2. HUNTER-SMITH, David James; CHAE, Michael Park; ROZEN, Warren. Image-Guided 3D-Printing and Haptic Modeling in Plastic Surgery. In: *Imaging in Plastic Surgery*. CRC Press, 2015. p. 811-822.
3. LEVY, Gideon N.; SCHINDEL, Ralf; KRUTH, Jean-Pierre. Rapid manufacturing and rapid tooling with layer manufacturing (LM) technologies, state of the art and future perspectives. *CIRP annals*, 2003, 52.2: 589-609.
4. SEALY, Winston. Additive manufacturing as a disruptive technology: how to avoid the pitfall. *American Journal of Engineering and Technology Research*, 2012, 11.10.
5. SRINIVASAN, Vivek; BASSAN, Jarrod. 3D printing and the future of manufacturing. In: *CSC leading edge forum*. 2012. p. 36.
6. AU, Anthony K., et al. 3D-printed microfluidics. *Angewandte Chemie International Edition*, 2016, 55.12: 3862-3881.
7. LI, Jipeng, et al. Recent advances in bioprinting techniques: approaches, applications and future prospects. *Journal of translational medicine*, 2016, 14.1: 1-15.
8. TURNER, Brian N.; STRONG, Robert; GOLD, Scott A. A review of melt extrusion additive manufacturing processes: I. Process design and modeling. *Rapid Prototyping Journal*, 2014.
9. WON, J. Y., et al. Evaluation of 3D printed PCL/PLGA/ β -TCP versus collagen membranes for guided bone regeneration in a beagle implant model. *Biomedical Materials*, 2016, 11.5: 055013.
10. ABDELWAHAB, Mohamed A., et al. Thermal, mechanical and morphological characterization of plasticized PLA-PHB blends. *Polymer degradation and stability*, 2012, 97.9: 1822-1828.
11. GERSTLE, Theodore L., et al. A plastic surgery application in evolution: three-dimensional printing. *Plastic and reconstructive surgery*, 2014, 133.2: 446-451.
12. EBRAHIMI, Mehdi; BOTELHO, Michael G.; DOROZHUKIN, Sergey V. Biphasic calcium phosphates bioceramics (HA/TCP): Concept, physicochemical properties and the impact of standardization of study protocols in biomaterials research. *Materials Science and Engineering: C*, 2017, 71: 1293-1312.
13. MIYAMOTO, Youji, et al. Basic properties of calcium phosphate cement containing atelocollagen in its liquid or powder phases. *Biomaterials*, 1998, 19.7-9: 707-715.
14. GUARINO, Vincenzo; CAUSA, Filippo; AMBROSIO, Luigi. Bioactive scaffolds for bone and ligament tissue. *Expert review of medical devices*, 2007, 4.3: 405-418.
15. WICHNIAREK, Radosław, et al. ABS filament moisture compensation possibilities in the FDM process. *CIRP Journal of Manufacturing Science and Technology*, 2021, 35: 550-559.

Research and development of a modular manipulator consisting of rotary modules with an unlimited degree rotation

Lukas Hrivniak ^{1*}, Jozef Svetlik ², Michal Sasala and Stefan Ondocko ⁴

¹²³⁴ Technical university of Kosice, Faculty of Mechanical Engineering, Department of production Systems and Robotics; lukas.hrivniak@tuke.sk, jozef.svetlik@tuke.sk, michal.sasala@tuke.sk, stefan.ondocko@tuke.sk

* Correspondence: lukas.hrivniak@tuke.sk

Abstract: The paper deals with the development of a unique rotation module with an unlimited degree of rotation. It is possible to build a modular manipulator from identical modules, which can be used in various applications not only in the field of mechanical engineering. The following article highlights the design of the URM module individually and at the same time the possibility to build a manipulator. Study of utilization of working space of assembled manipulator and wireless transmission of energy, which is used as a replacement of cabling in modules for manipulator supply.

Keywords: manipulator; modularity; rotation, URM.

1. Introduction

The Universal Rotary Module (URM) is a rotary module with an unlimited degree of rotation. It was developed and patented at the Technical University of Košice, Faculty of Mechanical Engineering, Department of Production Systems and Robotics. The author of the patent is prof. Ing. Jozef Svetlík, PhD. This solution is suitable for machines and equipment that need unlimited freedom of rotation in their operation. The modular principle is fully utilized in the design and construction of the module, that allows to assemble different machines and equipment using one type of module. In case the assembled machine is not suitable or it is necessary to assemble another one, thanks to the complete modularity it is possible to rebuild the initial solution and use the modules also in other applications. The proposed machines and devices can achieve different movement possibilities and degrees of freedom using the unlimited rotation of two adjacent modules, which are interconnected by movement linkage [1].

2. Rotary Module

The module is designed in a cylindrical shape. For this reason, all components are stored in the inner module body so as not to interfere with the module during unlimited rotation. Another reason for such storage of parts is permanent protection of components against environmental influences (Figure 1).

To ensure compatibility between servomotor, gearbox and encoder, each module has been equipped with a FAULHABER engine set. The encoder, servomotor and transmission are connected in series, individual components are firmly connected to prevent damage to the device during operation. The entire engine set is located in the center of the module and is mounted in the motor holder to protect it sufficiently from damage [2].

Due to the limited space in the URM, it was not possible to use commercially available boards, such as. Arduino or Raspberry Pi and the like. A tailor-made control board has been designed for the solution to meet all the requirements expected of it. Information is transmitted via Bluetooth. A series of tests have also shown the range of the bluetooth signal to a distance of approximately 30m, provided there are no major obstacles in the way. As a result, the safety clearance for the control of URM can be achieved even over

longer distances. The URM is controlled via a GUI that can run on any mobile device. The module's control board, together with the Bluetooth transmission interface and three batteries, are located inside the module body. The control board is directly supplied to the motor part of the module, which consists of the FAULHABER engine set [3].

The role of the accumulators in the URM is to cover the power supply of the motors during the whole operation of the module. They also serve as a temporary backup power source in the event of a power failure during operation. The accumulators will be continuously recharged using the proposed magnetic induction power module technology.

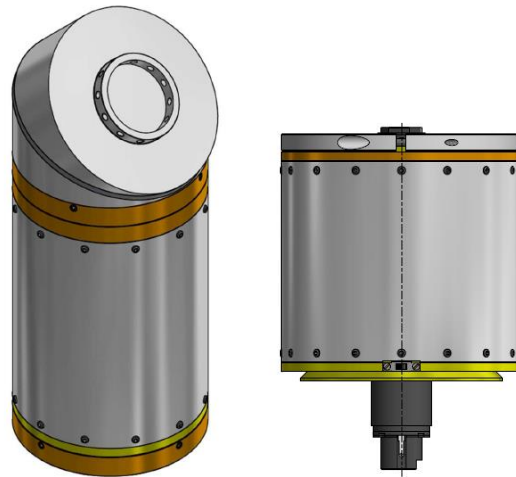


Figure 1. Rotary module with an unlimited degree of rotation

The URM was equipped with a new type of engine set, namely 1741U024CXR-IEH3-4096 + 20 / 1R-159: 1 [4]. The engine set includes:

1. DC - servomotor FAULHABER model 1741U024CXR:
 - End resistance $R - 26,9$
 - Nominal voltage $U_N - 24 \text{ V}$
 - Maximum speed $n_{\text{max}} - 9,000 \text{ rpm}$
 - Maximum efficiency $\eta_{\text{max}} - 75\%$
 - Torque $M_H - 26,2 \text{ mNm}$
2. Gearbox FAULHABER type 20 / 1R:
 - Number of gears 4
 - Gear ratio $159:1$
 - Maximum efficiency 60%
 - Torque 800 mNm
3. Encoder FAULHABER type IEH3-4096:
 - Frequency range $f - 875 \text{ kHz}$
 - Supply voltage $U_{DD} - 4,5 - 5,5 \text{ V}$
 - Phase shift between $A-B\Phi - 90 \pm 75^\circ$

The basic parameter of URM is the angle of curvature of the interconnecting passive members. This is a homogeneous structure so that the curvature of each manipulator module will be the same (Figure 2).

A homogeneous structure with 5° freedom of movement was subjected to a series of simulation tests with different angles of curvature of the passive members. The analysis of the workspace of the individual series structures with different angles of curvature of the couplers has revealed that the more the angle of curvature of the coupler increases, the more the work space of the individual series structures increases [5]. With a 30° and 45° curvature angle, the Z-axis working space is slightly smaller than the 60° and 90° curvature structures.

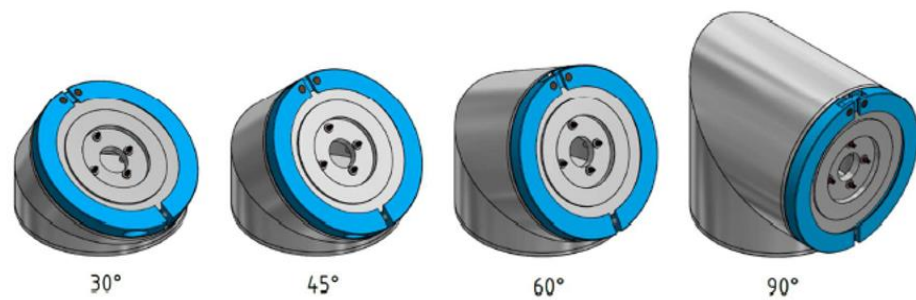


Figure 2. Possible passive members of URM

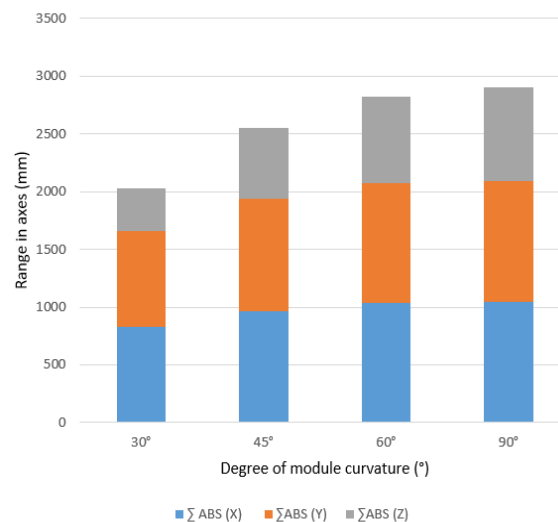


Figure 3. Comparison of the workspace sizes

Numerically generated general variables (rotation angles of the modules) in the matrices were inserted in the interval of $(0, 2\pi)$ and the tact of $1/2$ of the radian. For the best coverage of the simulation area of the degree of curvature of the passive module, 4 degrees of curvature angle were selected, particularly those of 30°, 45°, 60° and 90° (Figure. 2).

The 60° structure was chosen as the most suitable structure by curving the coupler. Using the partial transformation matrices and the overall transformation matrix, the points for the modular series structure workspace with 5 ° freedom of movement and 60 ° curvature of the coupler were calculated.

3. Wireless Transmission of Electricity

The key to the possibility of unrestricted rotation of the proposed motion module is the non-contact mode of energy and data transmission. The principle of wireless power transmission is based on an electromagnetic field (Figure 4) [13].

Individual variables express L1 - transmitter coil with diameter D, L2 - receiver coil with diameter D2, z - distance between coils, B - magnetic flux. The main factors affecting transmission efficiency are coil diameters D, D2 (mm), distance z (mm), coil offset d (mm). Obviously, the greater the distance between the coils, the angle of rotation between them, and also the mutual offset, the lower the power transfer capability.

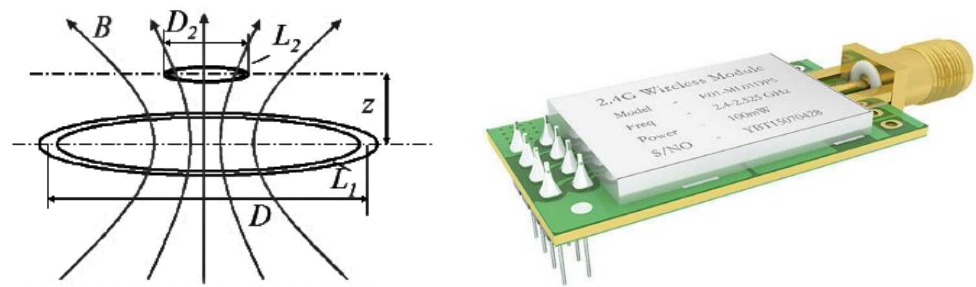


Figure 4. Basic principle of induction pair of loops for wireless power transmission (left), wireless module for data transmission NRF24L01 model E01-ML01DP5 (right)

This is due to the lower magnetic flux of the transmitter, because the magnetic field becomes thinner by distance. Therefore, it was important to place the coils in the module as close as possible [14].

Each device consists of two coils, one coil being a transmitter and the other coil a receiver. The transmitter coil creates a magnetic field around itself when connected to an electrical circuit. As soon as the receiving coil reaches the effect of this field created by the transmitter, the magnetic field changes to the electric current in the receiving coil. One of the disadvantages of the described solution is the loss, since neither of these transformations is 100% effective.

For URM module we used wireless data transmission via nRF module. nRF is a wireless module that enables communication between boards. In our case, it will be used for communication between URM modules that will be connected to the serial kinematic structure, as well as between the module and the control computer, which will send the necessary information to it.

4. Materials of Mechanical Parts

The originally considered design of the URM module provided for the use of metallic materials for all mechanical parts. However, the high weight of the metal parts caused the malfunction and unfavorable movement properties of the modules. Until now, all mechanical components of the modules were made of metallic materials, namely aluminum alloys EN AW 6060 AlMgSi0,5 (outer module cover), EN AW 6082 AlMgSi1 (motor holder), EN AW 7075 AlZnMgCu1,5 (other parts of the module). These alloys no longer allow for further significant weight reduction by design modifications and will therefore be replaced by components made of composite materials.

For the production of angular members and other mechanical parts for URM, 3D printing of the composite was chosen due to the simplicity, speed and accuracy of production.

The Markforged Mark Two 3D printer was used for production. The advantage of this 3D printer is the printing of continuous reinforcement of carbon fibers or HSHT fiberglass and thus obtain quality products with high strength (comparable mechanical properties with aluminum alloys) and low weight.

The printer prints the reinforcement inside the plastic matrix. Onyx Filament consists of two parts: nylon and small carbon fiber particles. Onyx is used as a thermoplastic matrix for composite parts. The table compares the mechanical properties of Onyx and ABS plastic (Table 1). Markforged offers a choice of several reinforcement materials such as carbon fiber, Kevlar, HSHT, fiberglass. In the table (Table 2) there is a comparison of the mechanical properties of the two most suitable materials for reinforcement. The comparison shows that carbon fiber was a suitable material for the production of parts for URM 02 as a reinforcement of the composite matrix [15, 16].

Table 1. Mechanical properties of selected thermoplastics [15]

	ABS	Onyx
Density (g/cm ³)	1,04	1,2
Modulus of elasticity (MPa)	2095	1401
Tensile strength (MPa)	29,5	36
Deformation at yield strength (%)	1,8	25
Breakdown stress (MPa)	22,9	30
Deformation at break (%)	16,3	58

Table 2. Mechanical properties of reinforced materials [15]

	Carbon fibers	HSHF fiberglass
Density (g/cm ³)	1,4	1,5
Tensile strength (MPa)	800	600
Tensile modulus (GPa)	60	21
Tensile stress at break (%)	1,5	3,9
Flexural strength (MPa)	540	420
Flexural modulus (GPa)	51	21
Flexural stress at break (%)	1,2	2,2

5. Modular Manipulator

Manipulators having at least 6 ° freedom of movement must be assembled to allow full handling. This is possible thanks to the URM, which allows us to assemble the manipulators from identical separate rotary modules (Figure 5). Modules are interconnected by hard link in serial system to kinematic structure of robotic arm. Thanks to the interconnection of different numbers of URM 01 modules it is possible to assemble a modular manipulator with a working space of different scope, movement and shape [8]. The workspace study was elaborated in chapter III.

In order to assemble modular kinematic structures with different degrees of freedom or different workspace sizes and shapes, passive couplers with different curvature angles have been developed for the URM [10]. Each passive member comprises at the bottom a transfer board and at the top a four contact needles. The transfer plate has the same contact surfaces as in the URM module and these surfaces are connected to the contact needles. This interconnection ensures the energy flow between the active URM modules (Figure. 5).

**Figure 5.** Kinematic chain composed of URMs for object manipulation (left) and passive member (right)

6. Conclusions

The rotary module with an unlimited degree rotation (URM) makes it possible to build a universal manipulator that can be used in various applications in and outside the

mechanical engineering field. The cylindrical design and the placement of all engine parts and electronics inside the module allow unrestricted rotation of adjacent modules. This is supported by the use of wireless transmission of electricity between modules. A study of the workspace shows that the best interface member is a passive coupler with an angle of 60° to move the manipulator efficiently within the workspace. The aluminum alloy was replaced with a continuous carbon fiber reinforced composite material for passive members. The production of parts was realized by additive technology. For all parts, the weight was reduced by more than 40%, which results in a reduction from the original combined weight of 2499.65g to 1402.64g, which represents a relief of 43.89%.

Acknowledgments: This work was supported by the Slovak Research and Development Agency under the Contract no. APVV-18-0413.

Conflicts of Interest: The authors declare no conflict of interest. The funders had no role in the design of the study; in the collection, analyses, or interpretation of data; in the writing of the manuscript, or in the decision to publish the results.

References

1. J. Svetlík, P. Demeč, "Rotational motion module designed for..." Patent 73-2010, ÚPV SR, 2011, 9p.
2. J. Svetlík, P. Demeč, J. Semjon, "Rotational kinetic module with unlimited angle of rotation," *Applied Mechanics and Materials*. 282 (2013) 175-181.
3. M. Štofa, J. Svetlík, M. Pituk, "Continue the development of universal rotary module," *Deterioration, Dependability, Diagnostics, Proceedings*. Brno: University of Defence, 2016 P. 39-46. - ISBN 978-80-7231-376-1
4. FAULHABER, "engine set" 1741 [online]. Dostupné na internete-<https://www.faulhaber.com/en/products/series/1741cxr/>.
5. P. Bozek, Y. Turgy, "Measurement of the Operating Parameters and Numerical Analysis of the Mechanical Subsystem," *MEASUREMENT SCIENCE REVIEW* 2014. Volume: 14, Issue: 4, Pages: 198-203.
6. J. Svetlík, P. Demeč, "Methods of Identifying the Workspace of Modular Serial Kinematic Structures," *Applied Mechanics and Materials*. 309 (2013) 75-79.
7. J. Dobránsky, P. Baron, M. Kočíško, M. Telišková, "Monitoring diagnostic indicators during operation of a print machine." 2015. In: *Advances in Science and Technology: Research Journal*. Vol. 9, no. 28 (2015), p. 34-39. - ISSN 2299-8624.
8. E. Kuznetsov, A. Panda, "Technology of industrial manipulator computer model development." *Transfer inovácií: internetový časopis o inováciách v priemysle*, online: <http://www.sjf.tuke.sk/transferinovacii/pages/archiv/transfer/37-2018/pdf/015-018.pdf>.
9. J. Svetlík ... [et al.], "Optimizing workspace for homogeneous assemblies of rotational motion modules," *SACI* 2018. - Timisoara : Politehnica University, 2018 P. 573-579. - ISBN 978-1-5386-4639-7.
10. M. Pollák, P. Baron, M. Kočíško, "Automation of Engineering Activities in Pre-Production Stages," *Lüdenschied : RAM-Verlag* - 2018. - 254 p.. - ISBN 978-3-942303-68-2.
11. A.A. Heidari, P. Pahlavani, "An efficient modified grey wolf optimizer with Levy flight for optimization tasks," *Applied Soft Computing*, vol. 60, pp. 115-134, November 2017.
12. R.-E. Precup, M.-C. Sabau, E.M. Petriu, "Nature-inspired optimal tuning of input membership functions of Takagi-Sugeno-Kang fuzzy models for Anti-lock Braking Systems," *Applied Soft Computing Journal*. 27 (2015) 575-589.
13. J.M. Fernandez, J.A. Borrás, "Contactless battery charger with wireless control link," US patent number 6,184,651, issued in February 2001.
14. N. Tesla, Apparatus for transmitting electrical energy, US patent number 1,119,732, issued in December 1914.
15. Markforged. 3D Printing Materials. 2020. Available online: <https://markforged.com/materials> (accessed 20.7.2021).

16. Markforged. 3D printing basics: “3D Printer Types & Technologies“. Available online: <https://markforged.com/resources/learn/3d-printing-basics> (accessed 20.7.2021).



Sound absorption analysis of materials using the Delany-Bazley prediction model

Veronika Gumanová ^{1*}, Lýdia Sobotová ², Kristián Pástor ³ and Anna Yehorová ⁴

¹ TUKE, SjF, Department of Environmental Engineering; veronika.gumanova@tuke.sk

² TUKE, SjF, Department of Environmental Engineering; lydia.sobotova@tuke.sk

³ TUKE, SjF, Department of Environmental Engineering; kristian.pastor@tuke.sk

⁴ TUKE, SjF, Department of Environmental Engineering; anna.yehorova@tuke.sk

* Correspondence: veronika.gumanova@tuke.sk; Tel.: 055/ 602 2643, Park Komenského 5, 042 00 Košice

Abstract: The aim of the paper is to compare the sound absorption of material samples obtained by the prediction method and measurement. The purpose is also to compare the acoustic performance of conventional and natural insulation material. The Delany-Bazley model, which uses airflow resistance as the sole property of the material, was used to predict the sound absorption coefficient α . The experimental measurement was performed on an impedance tube based on the method of transformation function and two microphones according to ISO 10534-2. Samples of two materials, mineral wool and hemp, were used for testing. The highest and lowest value for hemp was measured at a thickness of 40 mm. frequency 1000 Hz ($\alpha = \min. 0,09 - 100 \text{ Hz}$; $\max. 0.94 - 1000 \text{ Hz}$). The mineral wool sample achieved the highest absorption at 2500 Hz ($\alpha = 0.83$) and the lowest at 100 Hz ($\alpha = 0.13$). The prediction according to Delany and Bazley proved to be reliable with the exception of low frequencies.

Key words: sound absorption coefficient; impedance tube; Delany-Bazley model, mineral wool, hemp

1. Introduction

The deteriorating state of construction waste production and management is also stimulating research in the field of acoustics. At present, the development is aimed at improving the environmental footprint of existing acoustic or thermal insulation materials, but also at researching natural materials with better environmental impacts. Several studies have been devoted to the comparison of synthetic materials with natural alternatives from an acoustic and environmental point of view [1,2,3]. Available methods of testing materials for acoustic purposes are related to this issue.

The most used method of measuring the sound absorption of materials in the case of small samples is the impedance tube and the method of the transformation function using 2 microphones.

Several models have been developed to model the acoustic properties of porous materials, the most common of which are Delany-Bazley [4,5], Delany-Bazley-Miki [6] and Johnson-Champoux-Allard [7,8]. Some of them have been simplified by several authors [9] or adapted to the requirements of the material [10,11,12,13]. These models are based on taking into account various non-acoustic material parameters such as porosity, airflow resistance, tortuosity, thermal permeability and viscous and thermal characteristic length.

In the case of the Delany-Bazley model, it is necessary to know only one property of the material, which is the air flow resistance for a given thickness. This physical quantity can be obtained by measurement, calculation based on other material properties or specified by the material manufacturer. The model was compared with several other prediction models in [14,15,16,17].

The aim of this study was to determine the accuracy of the Delany-Bazley model prediction based on a comparison of the calculated values with the measured values. The benefit is also a comparison of the acoustic performance of mineral wool as a conventional material with the acoustic performance of hemp as its natural alternative.

2. Materials and methods

Testing materials were obtained from local suppliers of insulation materials from Slovakia. The samples were cut by water jet technology from smaller pieces of whole boards of mineral wool and hemp. The measurement in the impedance tube requires circular samples with a diameter of 60 mm. The samples were tested in thicknesses of 40, 60 and 80 mm (Fig. 1-2).



Figure 1. Mineral wool samples: thickness 60, 80, 100 mm



Figure 2. Hemp samples: thickness 60, 80, 100 mm

2.1. Determination of sound absorption coefficient (α) by prediction - Delany-Bazley model

Based on a large number of measurements of fibrous materials with a porosity approaching 1.00, Delany and Bazley proposed empirical expressions for the values of the complex wave number k_c and the characteristic impedance Z_c - quantities needed to calculate the surface impedance Z_s and the sound reflection factor r . The use of the model is conditioned by the boundary condition $0.01 < f / \sigma < 1.00$. The following relations apply to the calculation of the sound absorption coefficient α according to the Delany-Bazley model [18]:

$$Z_c = \rho_0 c_0 \left[1 + 0,0571 \left(\frac{\rho_0 f}{\sigma} \right)^{-0,754} - j 0,087 \left(\frac{\rho_0 f}{\sigma} \right)^{-0,732} \right] \quad (1)$$

$$k_c = \frac{\omega}{c_0} \left[1 + 0,0978 \left(\frac{\rho_0 f}{\sigma} \right)^{-0,7} - j 0,089 \left(\frac{\rho_0 f}{\sigma} \right)^{-0,595} \right] \quad (2)$$

$$\omega = 2\pi f \quad (3) \quad Z_s = -j Z_c \cot(k_c d) \quad (4)$$

$$R = \frac{Z_s - \rho_0 c_0}{Z_s + \rho_0 c_0} \quad (5) \quad \alpha = 1 - |R|^2 \quad (6)$$

where ρ_0 - air density [N.m⁻²],
 c_0 - speed of sound [m.s⁻¹],
 f - frequency [Hz],
 σ - air flow resistivity [N.s.m⁻⁴],

ω - angular frequency [s⁻¹],
 d - sample thickness [m],
 R - sound reflection factor [-].

2.1. Determination of sound absorption coefficient (α) by measurement in an impedance tube

An impedance tube from the manufacturer BSWA TECH - model SW466 and the transfer function method were used for the measurement. The measurement took place in two frequency bands (100 - 800 Hz and 400 - 2400 Hz), which were combined with the VA-LAB IMP software into the resulting frequency band of 100 - 2400 Hz. The figures 3-4 show the connection of the measuring chain for both frequency bands.

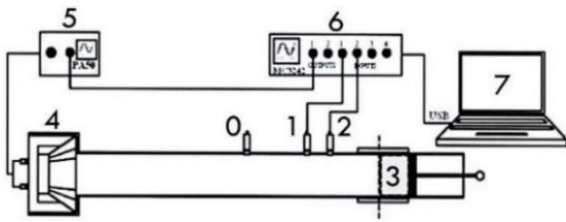


Figure 3. Measurement chain diagram for sound absorption coefficient in the frequency band 400 - 2500 Hz: 0 - microphone holder, 1, 2 - microphones, 3 - sample, 4 - sound source, 5 - amplifier, 6 - signal generator, 7 - frequency analysis system) [19]

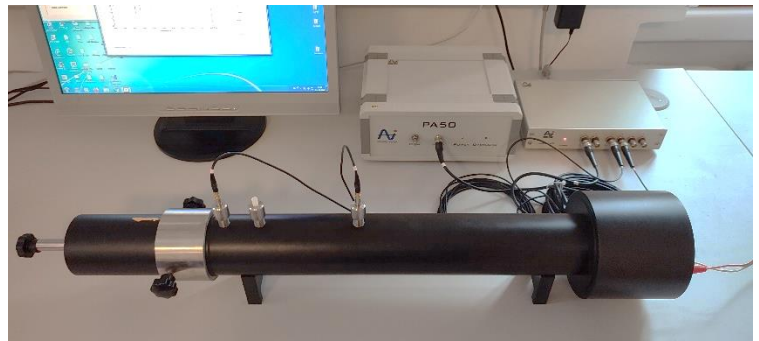


Figure 4. Measuring chain for the sound absorption coefficient in the frequency band 100 - 800 Hz in real conditions

2.1.1. Mathematical determination of sound absorption coefficient using the transfer function method (Two-microphone method)

In this method, plane waves in a tube are generated by a sound source and decomposition of the interference field is achieved by measuring the acoustic pressures at the two positions of the microphones located on the wall of the tube (Fig. 5). The sound absorption coefficient is determined from the transfer function H_{12} (equation (11)).

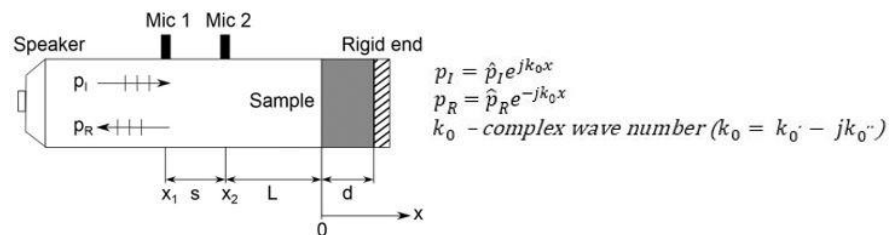


Figure 5. Schematic of two microphones method, x_1 - distance between sample and farther microphone, x_2 - distance between sample and closer microphone, s - distance between two microphones ($s = x_1 - x_2$), p_I - sound pressure of incident wave, p_R - sound pressure of reflected wave, d - sample thickness [20]

The following applies to the acoustic pressures p_1 and p_2 in the two microphone positions [21]:

$$p_1 = \hat{p}_I e^{jk_0 x_1} + \hat{p}_R e^{-jk_0 x_1} \quad (7) \quad p_2 = \hat{p}_I e^{jk_0 x_2} + \hat{p}_R e^{-jk_0 x_2} \quad (8)$$

The transfer function for the incident H_I wave and the reflected H_R wave has the form:

$$H_I = \frac{p_{2I}}{p_{1I}} e^{-jk_0(x_1 - x_2)} = e^{-jk_0 s} \quad (9) \quad H_R = \frac{p_{2R}}{p_{1R}} e^{jk_0(x_1 - x_2)} = e^{jk_0 s} \quad (10)$$

The transfer function for the total sound field H_{12} can be formulated using equations (7) and (8), and keeping $\hat{p}_R = r p_I$, as:

$$H_{12} = \frac{p_2}{p_1} = \frac{e^{jk_0 x_2} + r e^{-jk_0 x_2}}{e^{jk_0 x_1} + r e^{-jk_0 x_1}} \quad (11)$$

The sound reflection factor r in the reference plane ($x = 0$) can now be determined from the measured transmission functions, the distance between the sample and the farther microphone x_1 and from the complex wave number k_0 . By transposing equations (11), (9) and (10), the sound reflection factor r can be derived:

$$r = \frac{H_{12} - H_I}{H_R - H_{12}} e^{2jk_0x_1} \quad (14)$$

The following applies to the sound absorption coefficient α :

$$\alpha = 1 - |r|^2 \quad [-] \quad (15)$$

3. Results and discussion

The sound absorption coefficient is a dimensionless number and ranges from 0 (absolute echo) to 1 (absolute absorption). A comparison of the sound absorption coefficient of mineral wool and hemp obtained by measurement and calculation is shown in Figures 6-7 for the individual thicknesses.

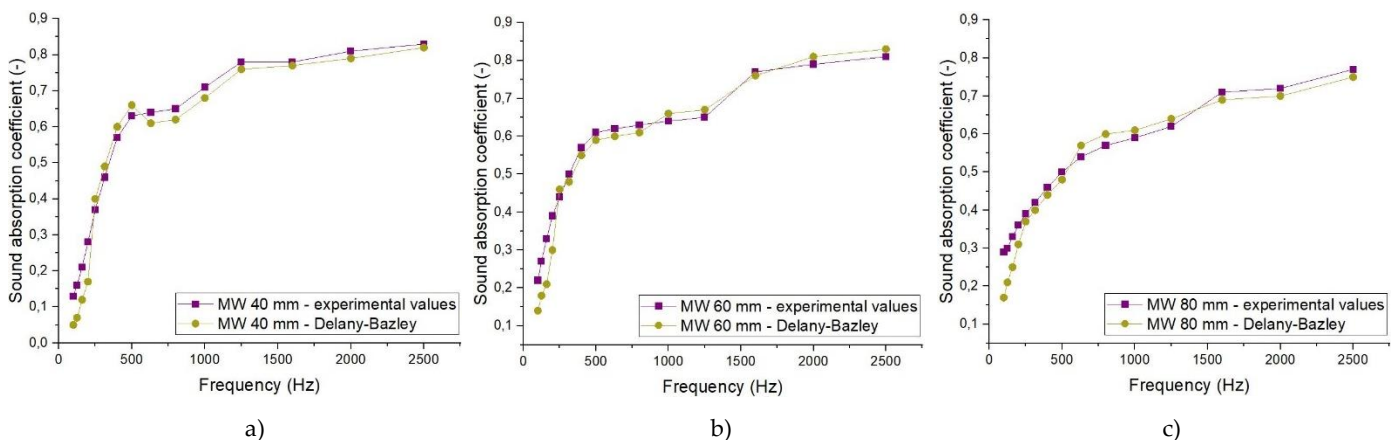


Figure 6. Comparison of mineral wool sound absorption coefficient values obtained by impedance tube measurement and calculation according to the Delany-Bazley model: a) 20 mm, b) 40 mm, c) 60 mm

At all thicknesses of 40, 60 and 80 mm, the measured sound absorption of the mineral wool gradually increased together with the frequency (40 mm: $\alpha = \min. 0,13$ (100 Hz) – $\max. 0,83$ (2500 Hz); 60 mm: $\alpha = \min. 0,22$ (100 Hz) – $\max. 0,81$ (2500 Hz); 80 mm: $\alpha = \min. 0,29$ (100 Hz) – $\max. 0,77$ (2500 Hz)). At a thickness of 60 mm, the values increased in the frequency band 100 - 400 Hz compared to a thickness of 40 mm. On the contrary, in the range of 500 - 2500 Hz, the values increased compared to those measured in 40 mm. At a thickness of 80 mm compared to 60 mm, higher absorption was measured only at a frequency of 100 and 125 Hz. At the frequency of 160 Hz, the same absorption was found in both thicknesses, and in the frequency band from 200 to 2500 Hz, the values gradually decreased compared to the 60 mm sample.

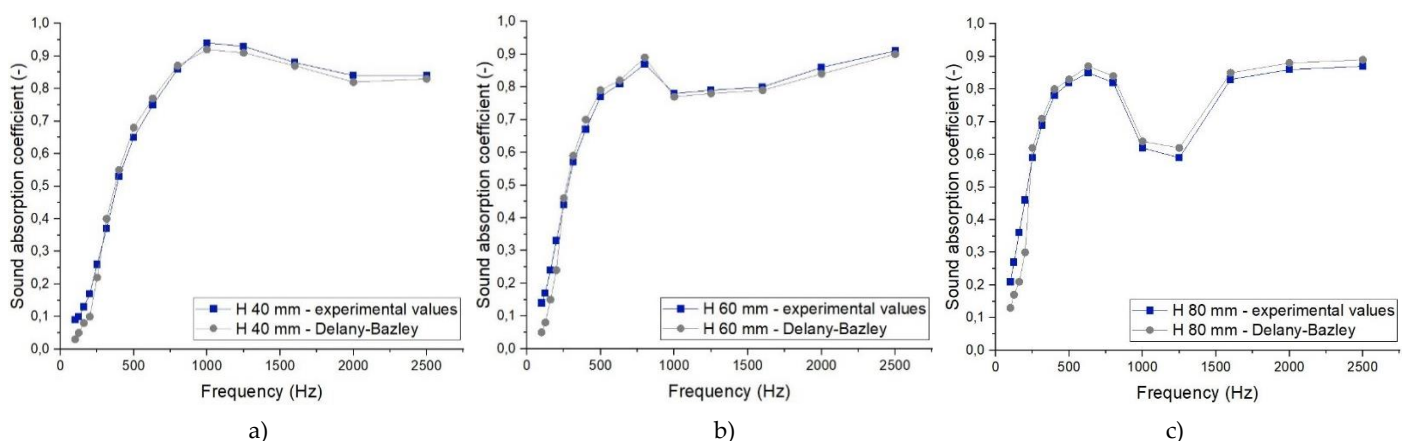


Figure 7. Comparison of the values of the sound absorption coefficient of the hemp sample obtained by measurement in the impedance tube and calculation according to the Delany-Bazley model: a) 20 mm, b) 40 mm, c) 60 mm

An R-F-R trend (rising-falling-rising) was observed in the curves of the measured values for hemp. At a thickness of 40 mm, the sound absorption capacity of the hemp sample increased up to the frequency of 1000 Hz, where the maximum was reached ($\alpha = \text{min. } 0,09 \text{ (100 Hz)} - \text{max. } 0,94 \text{ (1000 Hz)}$), then slowly decreased ($\alpha = 0,93 - 0,84 \text{ (1250 - 2500 Hz)}$). The values measured at the thickness of 60 mm increased up to a frequency of 800 Hz ($\alpha = \text{min. } 0,14 \text{ (100 Hz)} - 0,87 \text{ (800 Hz)}$), decreased slightly at a frequency of 1000 Hz ($\alpha = 0,78$), and from 1250 Hz ($\alpha = 0,79$) increased again with the highest value recorded at 2500 Hz ($\alpha = \text{max. } 0,91$). At a thickness of 80 mm, the sound absorption coefficient increased up to frequency of 630 Hz ($\alpha = \text{min. } 0,21 \text{ (100 Hz)} - 0,85 \text{ (630 Hz)}$). The rise trend was interrupted in the frequency range 800 - 1250 Hz ($\alpha = 0,82 - 0,59$) and resumed from 1600 to 2500 Hz ($\alpha = 0,83 - \text{max. } 0,87$). The data show that the higher the thickness of the material, the lower the frequency at which the decrease occurred (40 mm – 1000 Hz, 60 mm – 800 Hz, 80 mm – 630 Hz). The highest and lowest absorption was achieved at the thinnest thickness of 40 mm, but values very close to this maximum were also measured at a thickness of 60 mm.

As can be seen from the graphs for both materials, the Delany-Bazley model copied the measured curve with differences of several hundredths. The largest difference compared to the experimental values occurred in the frequency band 100 - 200 Hz (0.4 - 0.16). The closest differences were achieved from 1250 to 2500 Hz (0.01 - 0.03).

5. Conclusions

The Delany-Bazley model showed reliable results with the exception of the low frequency band from 100 to 200 Hz, in which the values tended to fall below the measured values by a difference greater than the middle and higher frequencies. The most accurate results were recorded at high frequencies from 1250 to 1500 Hz.

Hemp is one of the more sustainable materials, as the plant is able to reach a height of 4,5 m in 120 days and from one hectare it is possible to collect 12 tons of dry raw material, from which 8 tons of material is produced. In addition, it does not need any herbicides or insecticides and can be grown on the same soil for several years [22]. Mineral wool has excellent acoustic properties, but the most waste rock wool consists of three major components—silicon dioxide (SiO_2), calcium oxide (CaO), and aluminum oxide (Al_2O_3). These contaminants pose the biggest hurdle to recycling efforts, making it the most apparent reason behind million tons of waste rock wool piling up every year in landfills [23].

It follows from the findings that hemp can acoustically replace mineral wool, as it often achieves better or very similar values of the sound absorption coefficient. However, if hemp is to serve as an acoustic absorbent in combination with other purposes, the substitutability of other key properties must be the subject of further studies.

Acknowledgment: The paper was prepared within the project KEGA 009TUKÉ-4/2021: Implementation of the latest knowledge from recycling technologies for material recovery of product components at the end of their life cycle.

Conflict of interest: The authors declare no conflict of interest.

References

1. Arenas, J.P.; Sakagami, K. Sustainable Acoustic Materials. *Sustainability* **2020**, Vol. 12(16), 6540. <https://doi.org/10.3390/su12166540>
2. Santoni, A.; Bonfiglio, P.; Fausti, P.; Marescotti, C.; Mazzanti, V.; Mollica, F.; Pompoli, F. Improving the sound absorption performance of sustainable thermal insulation materials: Natural hemp fibres. *Applied Acoustics* **2019**, Vol. 150, 279-289. <https://doi.org/10.1016/j.apacoust.2019.02.022>
3. Bhingare, N.H.; Prakash, S.; Jatti, V. S. A review on natural and waste material composite as acoustic material. *Polymer Testing* **2019**, Vol. 80, 106-142. <https://doi.org/10.1016/j.polymertesting.2019.106142>
4. Yoon, G.H. Acoustic topology optimization of fibrous material with Delany-Bazley empirical material formulation. *Journal of Sound and Vibration* **2013**, Vol. 332, 1172-1187. <http://dx.doi.org/10.1016/j.jsv.2012.10.018>

5. Bhingare, N.H.; Prakash, S. An experimental and theoretical investigation of coconut coir material for sound absorption characteristics. *Materials Today: Proceedings* **2021**, Vol. 43, 1545. <https://doi.org/10.1016/j.matpr.2020.09.401>
6. Ayub, M.; Zulkifli, R.; Fouladi, M.H.; Amin, N.; Nor, M.J.M. A study on the acoustical absorption behavior of coir fiber using miki mode International Journal of Mechanical and Materials Engineering **2011**, Vol. 6, 343-349.
7. Abdi, D.D.; Monazzam, M.; Taban, E.; Putra, A.; Golbabaie, F.; Khadem, M. Sound absorption performance of natural fiber compsite from chrome shave and coffee silver skin. *Applied Acoustics* **2021**, Vo. 18, 108-264. <https://doi.org/10.1016/j.apacoust.2021.108264>
8. Levi, E.; Sgarbi, S.; Piana, E.A. Acoustic Characterization of Some Steel Industry Waste Materials. *Applied sciences* **2021**, 11(13), 5924. <https://doi.org/10.3390/app11135924>
9. Jones, P. W.; Kessissoglou, N.J. Simplification of the Delany-Bazley approach for modelling the acoustic properties of a poroelastic foam. *Applied Acoustics* **2015**, Vol. 88, 146-152. <https://doi.org/10.1016/j.apacoust.2014.08.013>
10. Caniato, M.; D'Amore, G.K.O.; Kaspar, J.; Gaspaella, A. Sound absorption performance of sustainable foam materials: Application of analytical and numerical tools for the optimization of forecasting models. *Applied Acoustics* **2020**, Vol. 161, 107-166. <https://doi.org/10.1016/j.apacoust.2019.107166>
11. Komatsu, T. Improvement of the Delany-Bazley and Miki models for fibrous sound-absorbing materials. *Acoustical Science and Technology* **2008**, Vol. 29, 121-129. <http://dx.doi.org/10.1250/ast.29.121>
12. Kino, N. Further investigations of empirical improvements to the Johnson–Champoux–Allard model. *Applied Acoustics* **2015**, Vol. 96, 153-170. <https://doi.org/10.1016/j.apacoust.2015.03.024>
13. Rubino, C.; Bonet Aracil, M.; Gisbert-Payá, J.; Liuzzi, S.; Stefanizzi, P.; Zamorano Cantó, M.; Martellotta, F. Composite Eco-Friendly Sound Absorbing Materials Made of Recycled Textile Waste and Biopolymers. *Materials* **2019**, 12(23), 4020. <https://doi.org/10.3390/ma12234020>
14. Kaihui, D.; Xiwen, W.; Jin, Y. Predicting Model of Sound Absorbing Properties of Cellulose-based Porous Materials Prepared by Foam Formin. *Journal of Natural Fibers* **2021**, 1-10. <https://doi.org/10.1080/15440478.2021.1990178>
15. Taban, E.; Khavanin, A.; Faridan, M.; Samaei, S. E.; Samimi, K.; Rashidi, R. Comparison of acoustic absorption characteristics of coir and date palm fibers: experimental and analytical study of green composites. *International Journal of Envirometal Science and Technology* **2020**, Vol. 17, 39-48. <http://dx.doi.org/10.1007/s13762-019-02304-8>
16. Taban, E.; Tajpoor, A.; Faridan, M.; Samaei, S. E.; Beheshti, M. Acoustic Absorption Characterization and Prediction of Natural Coir Fibers. *Acoustics Australia* **2019**, Vol. 47, 67-77. <http://dx.doi.org/10.1007/s40857-019-00151-8>
17. Soltani, P.; Taban, E.; Faridan, M.; Samaei, S. E.; Amininasab, S. Experimental and computational investigation of sound absorption performance of sustainable porous material: Yucca Gloriosa fiber. *Applied Acoustics* **2020**, Vol. 157, 106999. <https://doi.org/10.1016/j.apacoust.2019.106999>
18. Delany M.E.; Bazley, E.N. Acoustical properties of fibrous absorbent materials. *Applied Acoustics* **1970**, Vol. 3, 105-116.
19. Používateľský manuál k impedančným trubiciam BSWA TECH.
20. Wolkesson, M. Evaluation of impedance tube methods - A two microphone in-situ method for road surfaces and the three microphone transfer function method for porous materials. Dostupné online: <https://www.semanticscholar.org/paper/Evaluation-of-impedance-tube-methods-A-two-in-situ-Wolkesson/194651d41ea7b82c002356b68b559e644d8d0ba1> (prístup 19.11.2021).
21. ISO 10534-2. Acoustics — Determination of sound absorption coefficient and impedance in impedance tubes — Part 2: Transfer-function method
22. Chybík, J. Přírodní stavební materiály, 1st ed.; Grada Publishing: Prague, 2009; pp. 111-114.
23. Yap, Z.S.; Khalid, N.H.A.; Haron, Z.; Mohamed, A.; Tahir, M.M.; Hasyim, S.; Saggaff, A. Waste Mineral Wool and Its Opportunities—A Review. *Materials* **2021**, 14(19), 5777. <https://doi.org/10.3390/ma14195777>



Numerical analysis of mechanical properties of nanostructures

Ing. Sára Janigová¹

¹ Affiliation 1; sara.janigova@tuke.sk

Abstract: Graphene and its associated nanostructures (GANS) have been studied in detail over the last decades using both experimental and numerical methods. These structures are characterized by exceptional mechanical and other physical properties, which predisposes GANS to become the most important material technologies of the future in the aerospace, automotive, medical or military sector. The finite element method (FEM) is one of the most important numerical methods used for GANS analysis. FEM is a standard method of analysis and simulation of structural and mechanical elements, but its role in the field of numerical simulation GANS is still growing. This article documents the extensive use of FEM in nanostructures research. To this end, several research papers related to the analysis of mechanical properties of nanomaterials using the finite element method have been examined. This article will be used for future research in the field of graphene and nanotubes analysis, analyzing not only already applied research methods and their results, but also new research directions in the context of nanostructure simulations and input data for these simulations.

Keywords: nanomaterials; graphene; nanotubes; numerical analysis; Finite Element Method

1. Introduction

Graphene, which was discovered in 2004, began to be used in several branches of applied science and engineering due to its excellent properties. This paper focuses on the study of the mechanical properties of graphene and related nanostructures (GANS). Research in this area is based on two aspects:

1. methods designed/used to obtain as much information as possible on GANS,
2. results obtained by applying the proposed new methods.

In the first point, extensive experimental and numerical analyses were performed to study GANS, while they continue to focus primarily on numerical methods. The finite element method (FEM) is currently one of the most widely used numerical methods for GANS analysis, so this article also documents its widespread use and impact in the field of nanostructures. As for the second point, the results obtained include in particular electrical, mechanical, thermal, electronic, magnetic properties as well as medical, environmental, chemical and biological aspects. In this article, we will limit ourselves to the current state of affairs and results from the study of mechanical properties. The general knowledge of FEM and GANS is mentioned at the beginning. The following section lists the main numerical methods currently available for the study of GANS, as well as some of the most relevant works involving finite element modeling and prediction of GANS mechanical properties. Finally, the main recommendations for nanostructure research using FEM for the future are summarized [1].

2. General knowledge of finite element method and nanostructures

The finite element method has been evolving in the field of engineering since 1943 and is one of the most widespread numerical methods. The method is based on discretization of a large area to a finite number of elements and subsequent calculation and analysis of the behavior of individual elements [1].

Graphene is a planar group of carbon atoms that are joined by sp^2 C-C covalent bonds to form hexagonal cells. An illustration of these bonded carbon atoms can be seen in Figure 1. The arrangement of the carbon atoms can lead to both single-layer and multi-layer structures. Graphene is available on the market in the form of graphene oxide, reduced graphene oxide, graphene nanoplates or graphene flakes. The best-known forms of GANS include carbon nanotube (CNT), a rolled cylindrical version of graphene that can be synthesized by chemical vapor deposition or in an arc discharge process (Figure 1). We distinguish between single-walled or multi-walled nanotubes [2].

In particular, researchers are taking advantage of the structural benefits of CNTs by building networks of long CNTs. Other types of nanostructures are e.g. buckyball, spherical version of graphene that can be synthesized by the laser ablation process, graphene nanobands, flat versions of graphene with a high aspect ratio that can be synthesized by exfoliation and chemical vapor decomposition, carbon nanocoils, which are spiral forms of CNTs and can be synthesized by catalytic thermal decomposition and many others such as carbon nanocon, graphane, graphene nanofluoride, graphene nano-islands and intact graphene itself [2].

Scientists are also exploring the possibilities of interconnecting individual nanostructures and their properties. Researches present the possibilities of different configurations of carbon nanorings by connecting several multilayer nanotubes or a concept known as pillared graphene structure (PGS), which was created by combining several graphene sheets and nanotubes to create a 3D structure. The study also includes synthetic foams such as carbon graphitic foams, graphene-based fabrics, vertically arranged nanoareas, hybrid structures that combine two-layer graphene plates with double-walled nanotubes, or even graphene kirigami with a negative Poisson number [3].

3. FEM as a tool for analysis of graphene nanostructures

The first step in the implementation of FEM for the analysis of properties and behavior of structures of atomic and subatomic dimensions was the connection of FEM with molecular dynamics (MD) or molecular mechanics (MM). In this way, it was possible to link the behavior at the nano level with the behavior at the macro level. Several studies that have addressed this link have subsequently concluded a correlation between the two methodologies. When measuring the deformation of graphene sheets using both MD and FEM, the discrepancy in the results was only 5%. Another study examined torsions in nanotubes using both FEM and MM and found that both methods provided identical results for torsion angles and shear stress. The use of both MD and FEM in the analysis of bending and torsional stress energy in double-walled nanotubes also led to corresponding results. All these studies therefore led to the conclusion that the FEM serves as a reliable tool even at nano scales [1].

The number of publications focusing on the FEM analysis of nanostructures trying to predict their mechanical properties grows every year. However, modified FEM variants are also used as tools for designing nanomaterials. The spring-based FEM includes spring elements representing C-C covalent bonds, where the properties of the elements are being derived from the interatomic force constants of bending, tension and torsion [3].

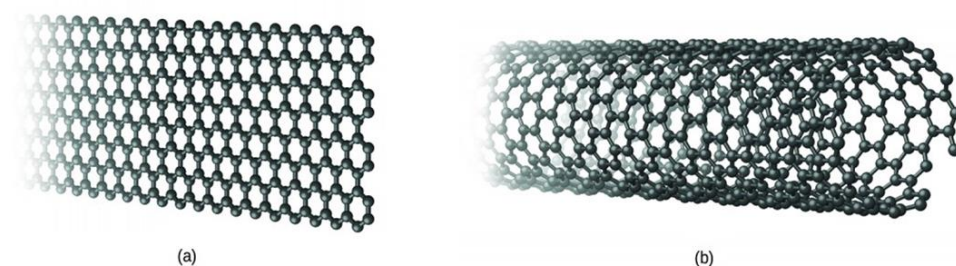


Figure 1. Basic types of carbon nanostructures, a) graphene, b) nanotube [4].

3.1. Models of carbon nanostructures

The most used method of representation of graphene sheet and nanotubes in FEM is the method of lattice spatial frame construction. Within FEM, each carbon atom is represented by a node, and the covalent bond is represented by a finite element. The Timoshenko beam, which represents the C-C bond and offers axial, off-plane and planar rotational degrees of freedom, is most frequently mentioned in the literature. The mechanical properties of this bond, such as E (Young's modulus of elasticity) and G (modulus of elasticity in shear), can be determined by the equations representing the equivalence between the deformation energy and the harmonic potential of a hypothetical beam of length L [3]:

$$\frac{k_r}{2}(\delta r)^2 = \frac{EA}{2L}(\delta r)^2, \quad (1)$$

$$\frac{k_\tau}{2}(\delta\varphi)^2 = \frac{GJ}{2L}(\delta\varphi)^2, \quad (2)$$

$$\frac{k_\theta}{2}(\delta\theta)^2 = \frac{EI}{2L} \frac{4+\Phi}{1+\Phi}(\delta\theta)^2, \quad (3)$$

where equation (1) describes the axial deformation, equation (2) the torsional deformation of the beams and equation (3) represents the shear deformation along the cross section. For circular cross-sections, the shear deformation constant can be expressed as [3]:

$$\Phi = \frac{12EIF_s}{GAL^2}, \quad (4)$$

where F_s represents the shear correction factor, which can be determined as:

$$F_s = \frac{6+12\nu+6\nu^2}{7+12\nu+4\nu^2}, \quad (5)$$

Combining equations (4) and (5) into equation (3) leads to a nonlinear relationship between the thickness d and the Poisson's constant ν of the equivalent beam [3]:

$$k_\theta = \frac{k_r d^2}{16} \frac{4A+B}{A+B}, \quad (6)$$

while values of constants are $k_r = 8,74 \times 10^{-7} \text{ Nmm}^{-1}$, $k_\theta = 9,00 \times 10^{-10} \text{ N nm rad}^{-2}$ a $k_\tau = 2,78 \times 10^{-10} \text{ N nm}^{-1} \text{ rad}^{-2}$. The equivalent mechanical properties of the C-C bond can be calculated by nonlinear optimization of equations (1) - (3). The C-C bond can then be modeled as a two-node beam, where the nodes represent atoms (Figure 2) [3].

3.2. Types of elements for nanostructure modeling

In addition to the use of beam-type elements for modeling C-C bonds (described in section 3.1), other types of elements can be applied in modeling these bonds and carbon nanostructures, e.g. springs, bars or frames that represent covalent bonds (C-C), or equivalent beams, bars, frames, planar elements, 3D elements, shells or axially symmetric elements representing the whole carbon nanostructure [2].

Most research articles have implemented models where C-C bonds have been represented by beam elements of predominantly Euler-Bernoulli and Timoshenko type. Their main advantage is the ability to model the tension, bending and torsion of C-C bonds, simplicity

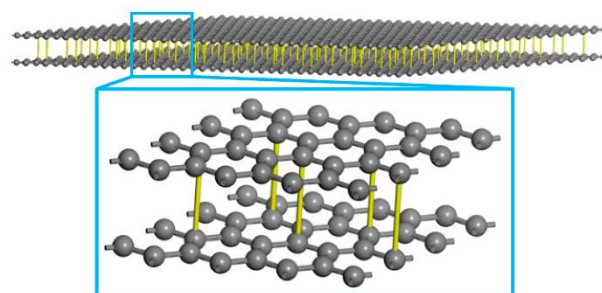


Figure 2. Two-layer graphene with C-C bond modeled as a two-node beam [5].

and calculation efficiency. The above disadvantages can be eliminated by using a spring element, which is also more suitable for analyzing nonlinear behavior. The beam and spring model of the hexene graphene cell is shown in Figure 3 [3].

3.3. Graphene thickness

The thickness of the element in the form of its diameter d can be calculated on the basis of the relations in above section, while the values k_r , k_θ and k_τ are available in the AMBER or MORSE format. The condition that must be met is that the cross section of the carbon bonding element is considered to be circular. Computational models of nanostructures with such thickness have been experimentally and analytically verified. However, if the carbon nanostructure is a continuum element, e.g. shell or plate, it is common to use a thickness of 0.34 nm. This 0.34 nm thickness is derived based on interatomic and interplanar distances between carbon atoms in multilayer graphene. Several measurement studies show that the thickness of single-layer graphene can vary from 0.4 to 1.8 nm, depending on the type of synthesis. The thicknesses of single-layer graphene and single-walled nanotubes determined in several publications range from 0.06 nm to 0.5 nm [6].

4. Mechanical properties of carbon nanostructures determined by FEM

Research on nanostructures is mainly devoted to the prediction of their mechanical properties, which have been mainly correlated with experimentally and analytically determined values. This section will deal with the values of Young's modulus (E), shear modulus (G), Poisson's ratio (μ), tensile strength (σ_T), buckling strength (σ_v) and vibration characteristics.

4.1. Young's modulus (E)

E values for graphene and nanotubes vary depending on their structure and the type of FEM analysis used. The highest value (2.9 TPa) was found for multilayer graphene using a space frame approach. The lowest E value for single-layer graphene is 0.35 TPa and comes from a combined model of molecular mechanics and FEM. Column graphene, a nanostructure formed by supporting graphene sheets with nanotubes which represent the function of columns, has values between 0.19 TPa and 0.73 TPa. The lowest value of E for single-walled nanotubes is 0.1 TPa, which was measured in a radial direction using the FEM space frame approach, while the highest value is 5.3 TPa for a single-walled nanotube system using a spatial FEM for wall representation and was found for a large zig-zag armchair structure [3].

4.2. Poisson's constant (μ)

The wide ranges of these values can be found in the articles for graphene and nanotubes. For better comparison, the lowest values within the range were selected to identify the stiffest possible nanostructure. The lowest predicted value (-0.001) is determined for single-layer graphene and this negative value indicates that graphene can behave as an auxetic material. The authors used a FEM space model with the introduction of a force of 1 nN/nm along the direction of the armchair structure at both edges, fixing the atoms in the center of the sheet. The highest value found is 1.4, when the authors constrained one end of the graphene armchair structure and loaded the other using shear and normal

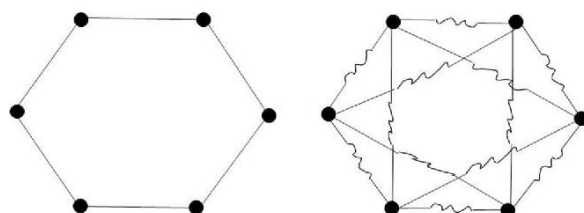


Figure 3. Beam (left) and spring (right) model of a hexagonal graphene cell [3].

force to predict E and G and then used Hooke's law to calculate μ . Such a high value was obtained due to the lower dimensions of the graphene (6.4 nm x 4.2 nm). In the area of nanotubes, values are available only for single-walled nanotubes, which range from 0.06, for the armchair structure with the constraint at one edge and the load at the other (the length of the nanotube was 24.6 nm). The highest value found for simple single-walled nanotubes is 0.96, for a model with an armchair structure and a 30 ° chirality angle which had a major influence on this value. The average value is around 0.5 [3].

4.3. Tensile stress (σ_T)

The highest value of tensile stress (σ_T) found is 425 GPa and was predicted for multilayer graphene, where shell elements were used and the armchair and zig-zag structure was compared, while the highest value was finally found for the zig-zag structure. The lowest value of σ_T is 0.62 GPa for bilayer graphene. The authors used mostly two approaches to derive the stress-strain diagram - a combination of molecular dynamics and FEM or space frame FEM. The σ_T values for nanotubes range from 3.5 GPa to 270 GPa, with the lowest value found for double-walled nanotubes using shell elements and the highest for single-walled nanotubes using spacial FEM [3].

4.4. Shear modulus G

The lowest values of shear modulus G (0.01 TPa) were found for bilayer graphene measuring 7.99 nm x 0.92 nm using spatial FEM. The reason for this low value may be the presence of weak van der Waals bonds between the two graphene sheets. The highest value of G 2.1 TPa was defined for single-layer graphene using spatial FEM. The average obtained value is around 0.63 TPa. Most publications that predict the shear modulus of nanotubes deal with the analysis of single-walled structures. The largest G value found for such a nanotube is 1.4 TPa, where the authors used continuous beam structures. Another large value of the modulus G is 1.25 TPa and it was obtained using a spatial model for twisted single-walled nanotubes with an arm-chair structure. The research confirms that twisted nanotubes offer higher shear stiffness compared to straight ones. The lowest value found is 0.32 TPa, when the authors used spring model characterized by lower directional stiffness compared to beams. The average value for CTNs is around 0.5 TPa [3].

4.5. Buckling strength

The buckling strength has been defined in the individual publications by means of various units, such as N/nm, nN or as a dimensionless quantity. In most cases, the authors used the spatial FEM to represent graphene and performed an eigenvalue analysis to calculate the buckling strength. The highest value (5.5 nN) was determined for a bilayer graphene measuring 10 nm x 10 nm, constrained at both ends. Even in buckling analysis, most publications focus on single-walled nanotubes subjected to axial compressive loading, transverse bending loading and temperature variations [3].

4.6. Vibrational characteristics

The highest natural frequency of 183 THz was found for fully fixed circular graphene, using the space frame FEM. The lowest predicted values were 5.1×10^{-5} THz for a single layer graphene used for a design of the resonator. A large number of publications in the field of vibration analysis are devoted to nanotubes, while their single-walled forms again predominate. The highest detected natural frequency of nanotubes is 30 THz, when the beam element method was used in the analysis and at the same time the lowest value (1×10^{-12} THz) was found using the same type of element [7].

5. Discussion

Most research in the field of graphene and its associated nanostructures currently focuses on the prediction of their mechanical properties using the finite element method.

This review suggests that some aspects of FEM modeling in nanostructures are already at a very good level. More detailed and confirmed aspects include:

1. FEM being accepted in the academic community as a tool for the analysis of carbon nanostructures.
2. The results obtained by FEM were verified against experimental, theoretical and other numerical methods.
3. At present, FEM is able to predict the mechanical properties of carbon nanostructures with reasonable accuracy. These properties include Young's modulus, Poisson's ratio, shear modulus, tensile strength, vibration characteristics and buckling strength.
4. FEM has proven to be an efficient and reliable tool for the analysis of carbon nanostructures with idealized geometries.

On the other hand, the overview also shows the need to pay more attention to aspects that are not currently described in more detail, such as:

1. Analysis of other variants of graphene, such as graphane and graphine, double- and multi-walled nanotubes, super-nanotubes or pillared graphene.
2. In addition to idealized geometries, it is necessary to analyze changes in mechanical properties in nanostructures with material defects that actually occur in them.
3. Most FEM analyzes have focused on describing the behavior of carbon nanostructures at the nanoscale, so there is the need to further extend FEM-based studies to also understand the macroscopic effects of these nanomaterials.
4. FEM modeling of carbon nanostructures needs to be transferred from academic area to practice. Multiscale FEM simulations must be extended to describe continuous physical behavior across whole material scale, from the molecular level to the final engineering components. Due to the excessive computational times and memory requirements for the devices, this task seems currently unfeasible, but such a challenge also needs to be addressed in order to solve the real problems in all industries, including automotive, biomedicine and aeronautics [3].

Acknowledgments: This paper was supported by the Ministry of Education of Slovakia Foundation under grant project VEGA No. 1/0500/20.

Conflicts of Interest: The authors declare no conflict of interest.

References

1. LU, Xiaoxing and Zhong HU. Mechanical property evaluation of single-walled carbon nanotubes by finite element modeling. *Composites Part B: Engineering* [online]. 2012, 43(4), 1902-1913 [quoted 2021-11-30]. ISSN 13598368. Available at: doi:10.1016/j.compositesb.2012.02.002
2. BAIMOVA, Julia A., Bo LIU, Sergey V. DMITRIEV, Narasimalu SRIKANTH and Kun ZHOU. Mechanical properties of bulk carbon nanostructures: effect of loading and temperature. *Physical Chemistry Chemical Physics* [online]. 2014, 16(36) [quoted 2021-11-30]. ISSN 1463-9076. Available at: doi:10.1039/C4CP01952K
3. ERTURK, Ahmet Semih, Yunus Onur YILDIZ and Mesut KIRCA. Mechanical behavior of a novel carbon-based nanostructured aluminum material. *Computational Materials Science* [online]. 2018, 144, 193-209 [quoted 2021-11-30]. ISSN 09270256. Available at: doi:10.1016/j.commatsci.2017.12.033
4. PAPAGEORGIOU, Dimitrios G., Zheling LI, Mufeng LIU, Ian A. KINLOCH and Robert J. YOUNG. Mechanisms of mechanical reinforcement by graphene and carbon nanotubes in polymer nanocomposites. *Nanoscale* [online]. 2020, 12(4), 2228-2267 [quoted 2021-12-10]. ISSN 2040-3364. Available at: doi:10.1039/C9NR06952F
5. CAO, Qiang, Xiao GENG, Huaipeng WANG, Pengjie WANG, Aaron LIU, Yucheng LAN and Qing PENG. A Review of Current Development of Graphene Mechanics. *Crystals* [online]. 2018, 8(9) [quoted 2021-12-10]. ISSN 2073-4352. Available at: doi:10.3390/cryst8090357.
6. BAO, Qiang, Zhenyu YANG, Zixing LU and Xiaofan HE. Effects of graphene thickness and length distribution on the mechanical properties of graphene networks: A coarse-grained molecular dynamics simulation. *Applied Surface Science* [online]. 2021, 570 [quoted 2021-12-10]. ISSN 01694332. Available at: doi:10.1016/j.apsusc.2021.151023
7. CHANDRA, Y., R. CHOWDHURY, F. SCARPA and S. ADHIKARICOR. Vibrational characteristics of bilayer graphene sheets. *Thin Solid Films* [online]. 2011, 519(18), 6026-6032 [quoted 2021-12-10]. ISSN 00406090. Available at: doi:10.1016/j.tsf.2011.04.012



Design modification of a high-speed turbine into a disassemblable and sterilizable assembly.

Ing. Tomas Breskovic ^{1*}, Ing. Samuel Lancos ², Dr. H. C. mult. prof. Ing. Jozef Zivcak PhD., MPH. ³ and prof. Ing. Radovan Hudak PhD. ⁴.

¹ Technical University of Kosice; tomas.breskovic@tuke.sk

² Technical University of Kosice; samuel.lancos@tuke.sk

³ Technical University of Kosice; jozef.zivcak@tuek.sk

⁴ Technical University of Kosice; radovan.hudak@tuke.sk

* Correspondence: Ing. Tomas Breskovic, Technical University of Kosice, Faculty of Mechanical Engineering, Department of Biomedical Engineering, Letna 9, 042 00 Kosice tomas.breskovic@gmail.com; Tel.: +421 910 221 425

Abstract: This article will be devoted to the transformation of the shape design of the top cover of a high-speed turbine into a detachable version. The original cover concept (design concept directly from the manufacturer) was determined to be non-removable. As the main requirement was a simple sterilization option, the top cover of the turbine must be redesigned so that it is easy to disassemble, sterilize and can be easily reattached. Ease of clamping is required mainly because the cover will be handled mainly by non-technical personnel. Based on the above-mentioned requirements, the cover clamping was chosen as a simple bayonet system. The cover was imported into Fusion360 modelling software using reverse engineering, where it was subsequently modified according to the specified requirements.

Keywords: high-speed turbine, blower, modelling

1. Introduction

The global COVID-19 pandemic has caused a shortage of critical medical resources. Above all, there was an acute shortage of fans. [3] Artificial lung ventilation is the only form of life support for the unconscious patient. It is divided into manual and controlled. In the case of manual, the supply of oxygen is ensured by the constant compression of the blowing bag, while in the case of controlled oxygen, the supply of oxygen is ensured by a turbine controlled by software. [1] Controlled ventilation also uses computational flow dynamics to help improve oxygen flow design. [2] In long-term operation, a mostly controlled form of ventilation is used because it is more suitable. The manual form of ventilation is physically demanding and requires the full attention of a doctor. [1]

Our main task was to convert the versatile, high-performance micronella turbine type U65HN-024KS-6 from Micronel (Pressure: 95 hPa, flow: 435 l / min, 24 V) (Fig. 1a, c) [4] into a detachable and sterilizable version to be able to use one device for multiple patients in a short time sequence. As the original turbine is not sterilizable, it must be replaced with a new one after each use, which is a disadvantage especially in a critical pandemic situation.

After disassembling the turbine, a 3D scan of the housing was created using a Metrotom from Carl Zeiss. The propeller was scanned using an EnvisionTech instrument primarily intended for scanning dental implants. (Fig. 1b)

Subsequently, it was agreed that the top cover will consist of two parts, the clamping (upper) and anchoring (lower). The lower part will be pressed on the flange using sealing rubber bands through which the original turbine cover was fixed.

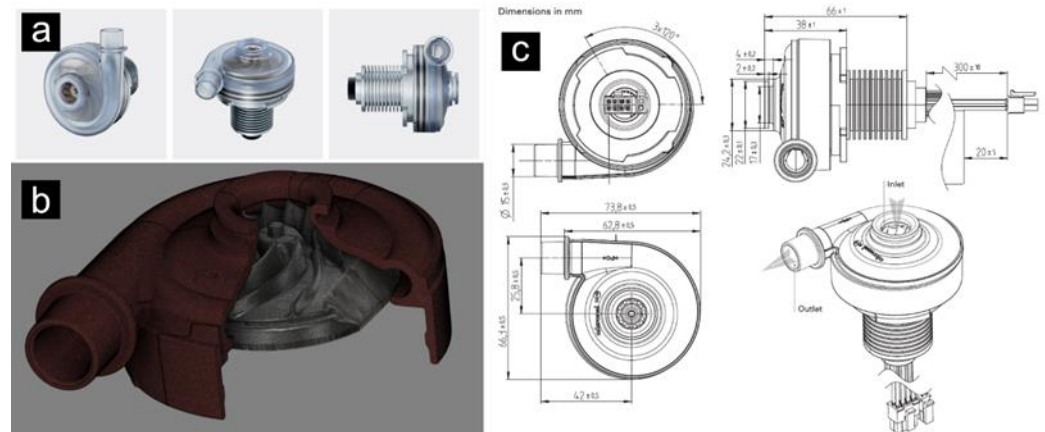


Figure 1 a-top, front and side view of the Micronel U65HN-024KS-6 turbine, b-3D scan of the turbine cover and propeller, c-basic parameters of the Micronel U65HN-024KS-6 turbine

2. Materials and Methods

First, it was necessary to divide the initial scan into four quarters. (Fig. 2a) The creation of cross-sections was necessary in order to be able to clearly define the shape of the turbine snail as well as the upper and lower cross-sections. Subsequently, sketches were created corresponding to the shape of the individual cross sections.

Since the central axis of the sketches for the individual cross-sections of the snail is not a uniform circle, it was necessary to create another sketch. This sketch gave us the axial position of the snail. Following the interconnection of individual cross-sectional sketches and the definition of the shape by means of a position sketch, the basic shape of a turbine snail was created. (Fig. 2b)

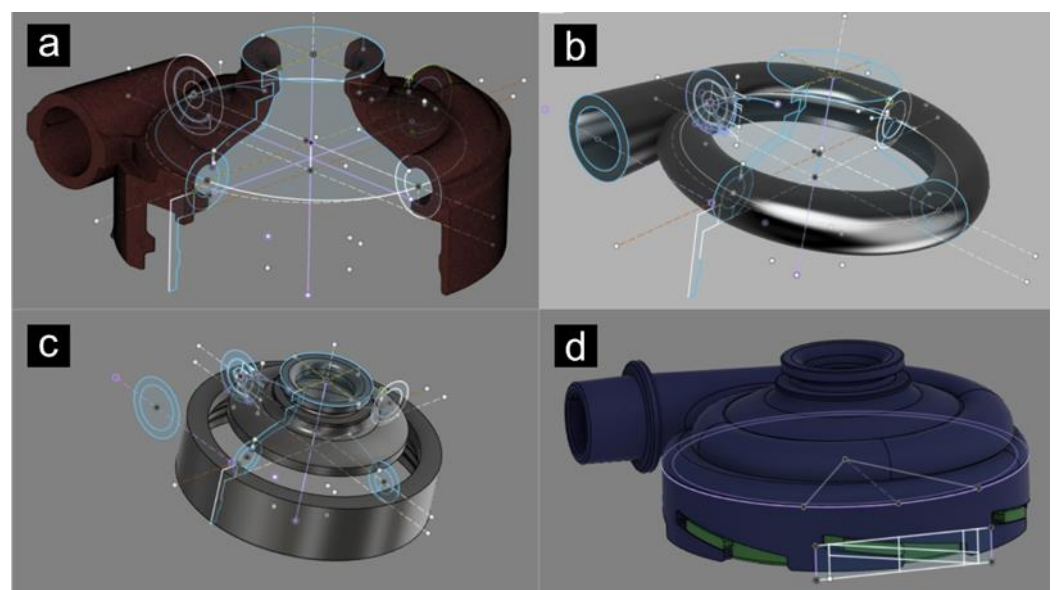


Figure 2 a-division of the 3D scan into four quarters, b-snail created by connecting four quarters by means of a guide curve, c-upper and lower shaped part of the turbine cover, d-bayonet clamping system

In order for the model to be complete, it was necessary to model the upper and lower shape of the turbine. These parts were created so that the individual cross-sections were shaped around the central axis of the object. (Fig. 2c)

To complete the basic model, it is still necessary to cut the upper and lower shaped part according to the shape of the snail. Subsequent connection of all three parts gave the basic, remodelled shape of the original turbine.

After modelling the front inlet and dividing the model into clamping (upper) and anchoring (lower) part, we only have to design the clamping of the turbine cover to the engine. The clamp was designed as a bayonet system. (Fig. 2d) This bayonet system was created using a diagonal sketch (Fig. 2d), the centric impression of which created a cutout in the clamping part and a fixing tooth in the anchoring part of the model.

The last part for the complete completion of the model is the fine-tuning of post-processing adjustments. Post-processing modifications mean rounding of edges, fine-tuning of shapes, re-modelling of additional cut-outs. (Fig. 3)

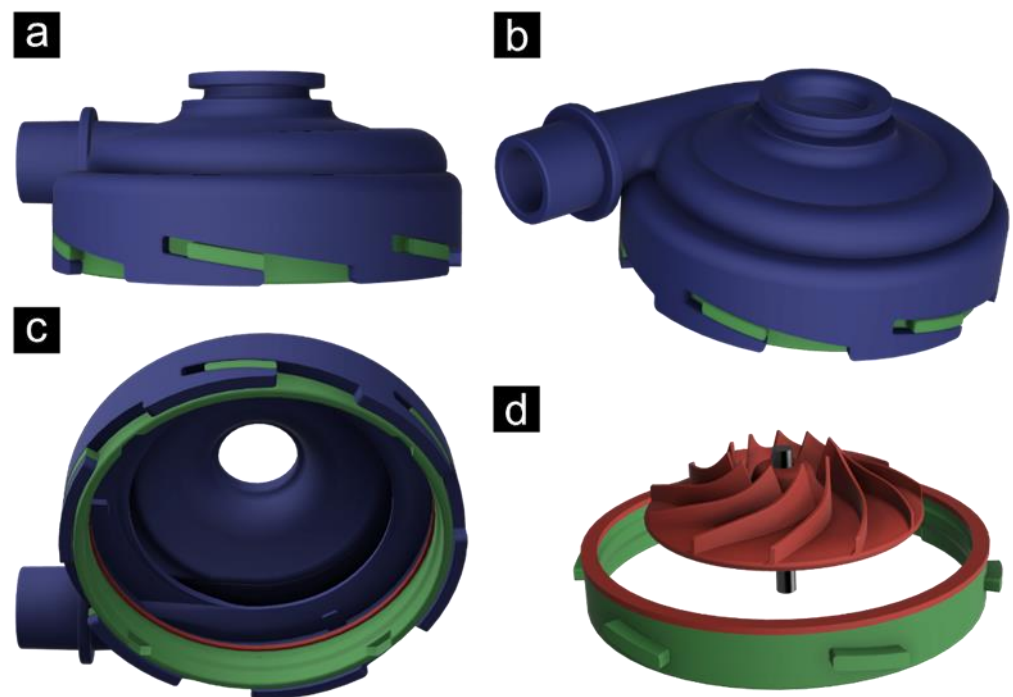


Figure 3 Finished model: a-side view, b-axonometric view, c-bottom view, d-clamping part together with the propeller

3. Discussion

The main task of the assignment was to model and modify not only the top cover but also the propeller of the high-speed turbine itself. Within the basic requirements, emphasis was placed on the fact that the cover and the propeller are easily removable and then sterilizable in Autoclave at a temperature of 134 ° C.

After modelling and extruding the cover, the initial visual assessments of the functionality of the model and the strength of the material took place. The results of the assessments were very good. This means that the cover is functionally and strength-wise functional.

Sterilization tests are still being performed. At the end of all tests, the cover will still be tested under load (with the turbine on) to completely eliminate any imperfections.

As for the propeller, there is an initial shape ready but after the printing and initial, visual assessment, several problems were discovered. The first problem is the plasticity of the material from which the propeller is extruded. The given material has very good strength properties, but it has one disadvantage, namely that it is too plastic (flexible) for thin cross-sections. This excessive plasticity causes a problem with propeller blades that are too flexible to properly serve their purpose. The given problem will be solved in the near future by adjusting the thickness and shape of the wing cross-section or by changing the material from which the propeller is extruded.

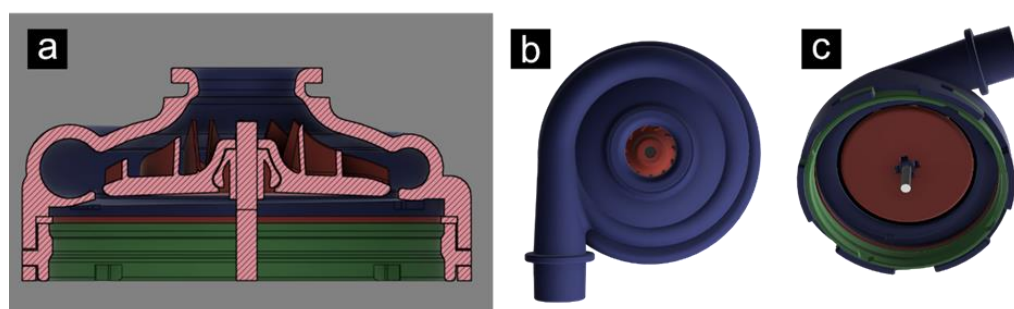


Figure 4 a-cross-section of the finished model, b-finished model together with the propeller from the top, c-finished model with the propeller from below

The second major problem with the propeller is its method of clamping to the rotor shaft. As an initial design, a simple impact system was created, which is not suitable for high-speed use of the propeller. The very problem with clamping the propeller is that it is not possible to combine the available metal and plastic material, because sterilization would result in different expansion, which could ultimately cause uneven balancing and thus stabilization problems at high speeds. We are working on solving defined problems. We believe that a suitable clamping method will be devised in the near future and that a suitable combination of materials will also be found that will not cause a problem with the sterilization and balancing of the propeller.

4. Conclusions

In conclusion, we can state that the process and progress of the development of the detachable cover of the high-speed turbine is going well. The prototype itself is ready and functional. After the end of the stress tests, the top cover will be ready for series production. However, the propeller itself remains a problem. To fully fulfil the task, it is necessary to eliminate the shortcomings associated with clamping and find the optimal material variants from which the propeller will be composed.

Acknowledgments:

This article is based on support received from projects: VEGA 1/0179/19, OPENMED, ESIF OPII/313011ATG9/

References

1. Fogarty, M., Orr, J., Westenskow, D., Brewer, L., & Sakata, D. (2013). Electric Blower Based Portable Emergency Ventilator.
2. Missal, S., Bhatekar, P., Itkar, P., Suryawanshi, V., & SD, P. ANALYSIS AND WEIGHT OPTIMIZATION OF CENTRIFUGAL BLOWER FOR CORROSION RESISTANCE MATERIAL.

3. Batteh, J., Li, L., Chiu, E., & Chaleff, E. (2021, September). Model-Based Development of the RespiraWorks Ventilator with Modelon Impact. In Modelica Conferences (pp. 471-483).
4. Micronel AG, Zürcherstrasse 51, 8317 Tagelswangen, Switzerland. Micronel Radial Blower U65HN-024KS-6 https://www.micronel.com/uploads/tx_micronel/Specification_U65HN-024KS-6_01.pdf



Production process simulations in Tecnomatix plant Simulation

Ján Kopec¹

¹ Park Komenského 9, 042 00, Košice, Department of industrial and digital engineering, Technical University of Košice, Letná 9, jan.kopec@tuke.sk

Abstract: Today, simulation is an integral part of the process of innovation and monitoring the performance of production processes. Animation is a natural improvement in the presentation of simulations, which are clearer thanks to animations and the customer can better evaluate the solution variants. The animation reflects the real movements of production equipment. In this article, we have chosen a simple production process, where the model of animation of 3D objects in simulation is addressed. The result is a significant increase in interest from the customer or co-solver.

Keywords: Tecnomatix plant Simulation, simulation, animation, methods

1. Introduction

This article presents the advantages of using simulations, their disadvantages, and their use. Cooperation with major Slovak companies is handled in our department. The importance of the animation itself lies in the fact that the simulation acquires significantly better properties for the inexperienced observer, and by using the digital twins of real machines and animating their movements, it is possible to better explore the most optimal machine layout. The main goal of this article is to point out the need and simplicity of creating animations in the program Tecnomatix plant Simulation, which will significantly improve cooperation with our companies.

2. Definition of the simulation process

The term simulation is an imitation of a real system and its dynamic processes in a simulation environment. The primary goal is to provide answers to the set goals, which need to be defined right at the beginning of the simulation solution. The result is the acquisition of knowledge for the real model, respectively. production. For a more detailed definition of the term simulation, the characteristic is used that simulation means the preparation, implementation, and evaluation of given experiments using a simulation model [1].

With the help of simulation, it is possible to transfer practically all processes, whether they are production or non-production processes.

2.1 Approach of Simulation

If we start from VDI guideline 3633, the simulation is strictly based on the following 8 points:

- problem definition,
- simulation proficiency testing,
- goal formulation,
- data collection and subsequent analysis,
- simulation environment modeling,
- execution of simulation actions,
- analysis of results and interpretation of results,
- documentation [2].

2.2 Advantages and disadvantages of using simulation for processes

A significant advantage of using simulation for processes is the fact that all the properties defined in the simulation solution can be designed without spending resources on implementation. As a result, the costs of eliminating the consequences of a wrong decision directly on the models are eliminated [1].

Another advantage is the ability to define the material flow rate. This makes it possible to thoroughly examine the accuracy of the simulation.

The simulation gives you the ability to make adjustments to the system, and it doesn't matter if it's a simple or complex system.

Working alone in a simulation environment can lead developers to possible improvements. And last but not least, the significant advantage of simulation is the possibility to use simulation models further in production.

The main disadvantages include the need for training in working in a given simulation environment, the information we have obtained through simulation is sometimes difficult to interpret and simulation modeling is very costly and time-consuming [2] [4].

3. Animation of 3D objects in the environment of Tecnomatix Plant Simulation

The Tecnomatix plant Simulation program is used as a simulation tool in our department. In cooperation with various companies that turned to us regarding the simulation model of their production environment, various simulations were processed in terms of complexity.

But a closer definition of machines is also needed for the customer, and the possibility of watching the animation of production movements would certainly be a welcome change.

Tecnomatix Plant simulation offers a database of material flow tools. The disadvantage is that the model does not always correspond to the machine in use. In fig. 1 is an illustration of a basic illustration of a simple manufacturing apparatus selected from a material flow toolbar

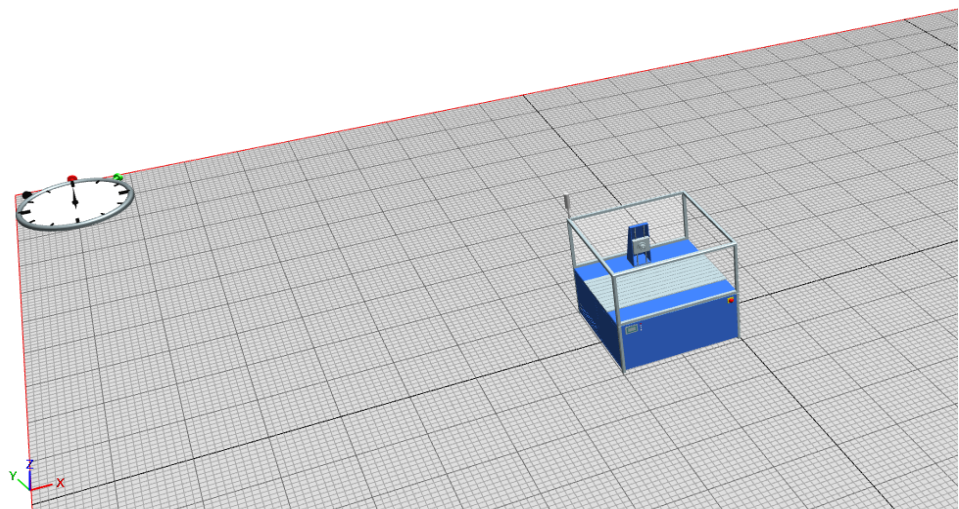


Figure 1. A simple tool for displaying production equipment

The first step to proper animation is to replace the basic simulation model. We can use the library directly in Tecnomatix plant Simulation or upload it to your digital plant model using a 3D modeling program such as Autodesk Inventor or SolidWorks.

When selecting the first option, select the 3D model and move the mouse cursor to the Edit section and select the Exchange Graphics option. Then the window with the machine library in s3d format will open. In fig. 2, the base model is replaced by a model that is a digital copy of the actual device.

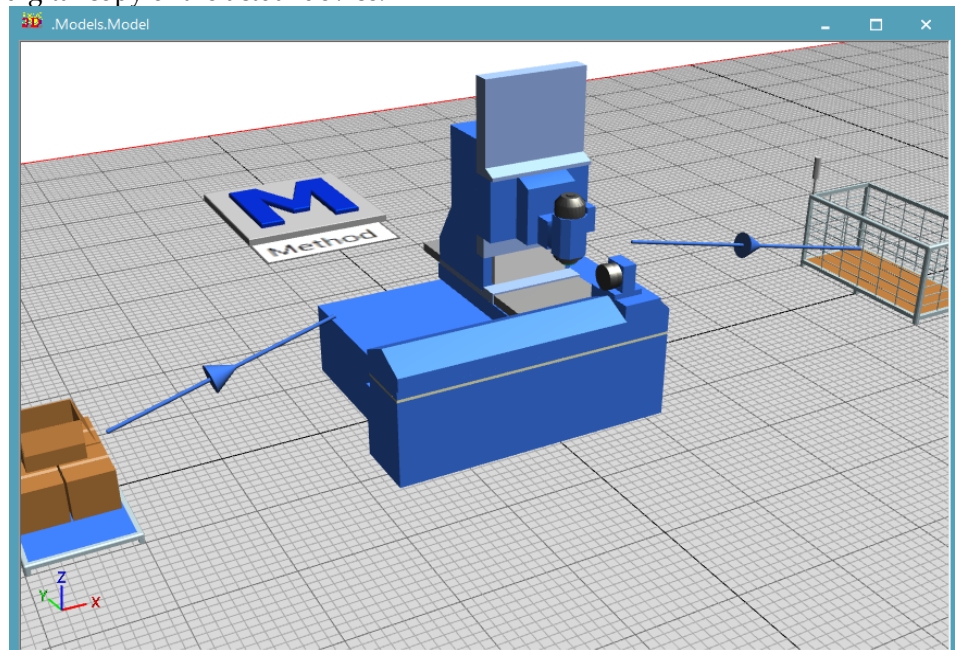


Figure 2. Replaced model. Specifically, it is a model of a vertical drilling machine

If the model is inserted into the program, it is necessary to right-click on the model and select the Show Graphic Structure option. This option displays the graphical structure of the 3D model.

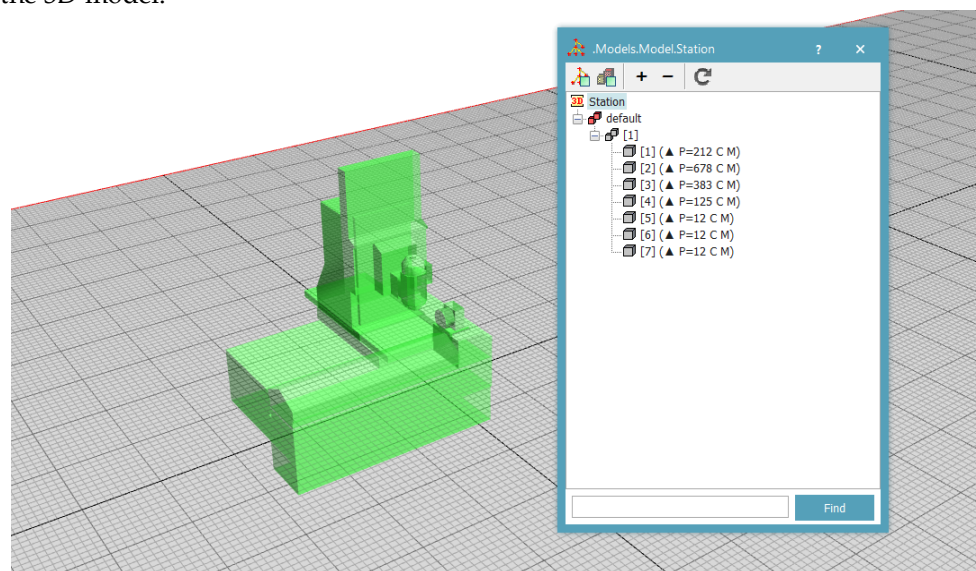


Figure 3. Graphics Structure tree

The replaced model is composed of several parts, just as each machine does not consist of one part. After opening the Show Graphic Structure, it is necessary to click on the "tree" (fig.3) and it is necessary to find the parts that represent the parts that are to be moved during the animation.

It is then necessary to find the parts of the machine that are to be moved in the tree. If we have this part behind us, it is necessary to mark the parts to be moved and select the Animatable Object option in the Edit section.

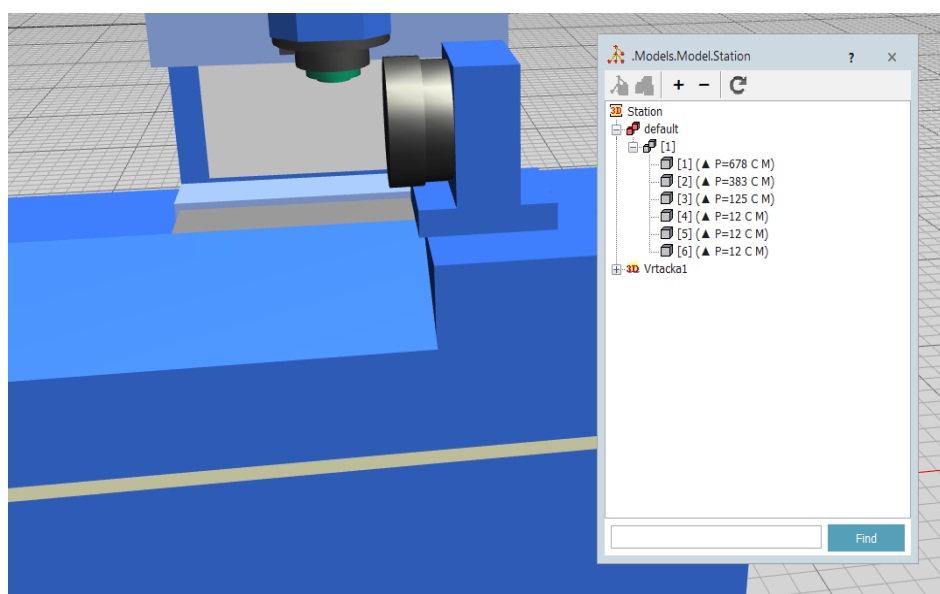


Figure 4. Creating a moving part

Right-click on the part in the tree that is to perform the movement, select it and select Edit 3D Properties from the options...

In the Self Animation bar, set the selected part's movement.

Click on the Add option to add a movement, define a name for it and define it (fig.5).

In this case, it is necessary to define the movement of the Z-axis as well as the movement of the Y-axis. In the Self Animation section, you must enter the name of the animation. In this case, it is the Pohyb1 and the Pohyb2 (fig.6). After saving the names, it is possible to define their movement along the axes. It is necessary to mark the given Animation paths and select the Edit option where it is possible to determine and simulate the movement along the given axis [3].

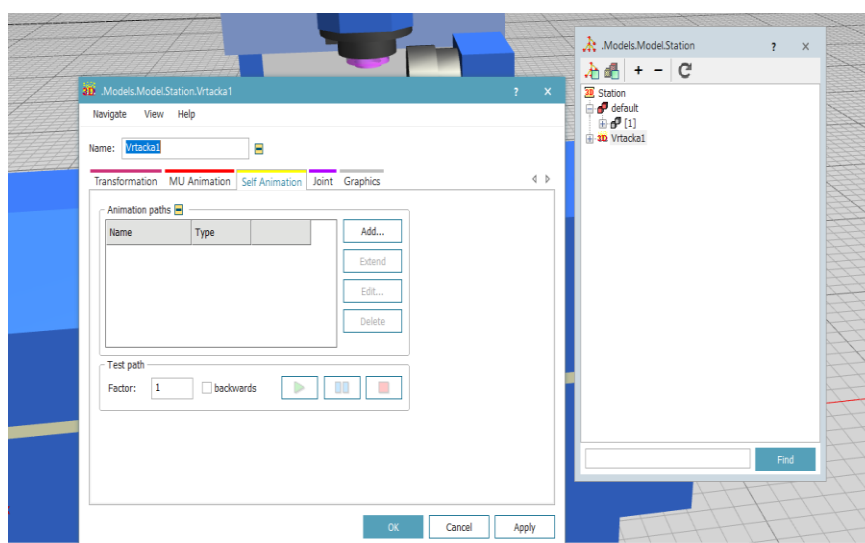


Figure 5. Add movement

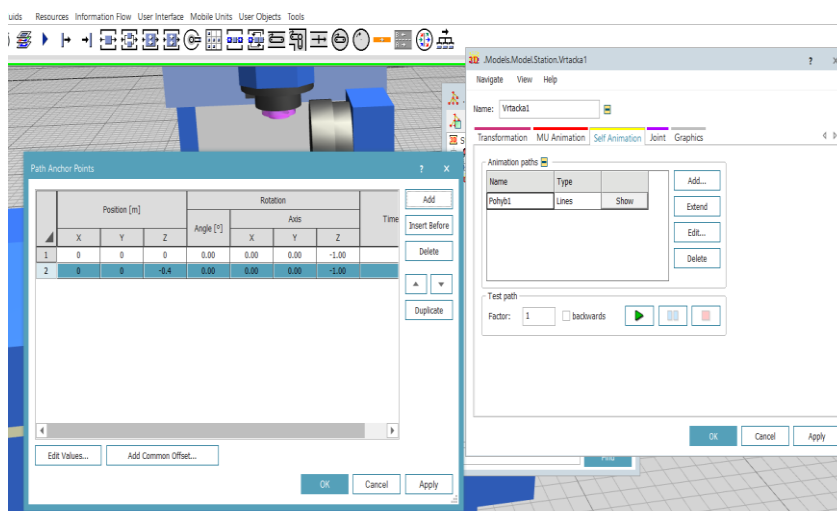


Figure 6. Edit movement in axis Y and Z

If we have completed all these steps, we need to create a method that will run the animation. In fig. 7 shows the whole method. In the first line, it is necessary to specify the name of the file, in our case it is Models. Model, followed by the name of the machine (Station). further progress is made in creating a method where it is necessary to define that the machine should move its parts. Since the machine performs 2 movements, it is necessary to define both movements. The following is a description of the description at the bottom of the method itself.

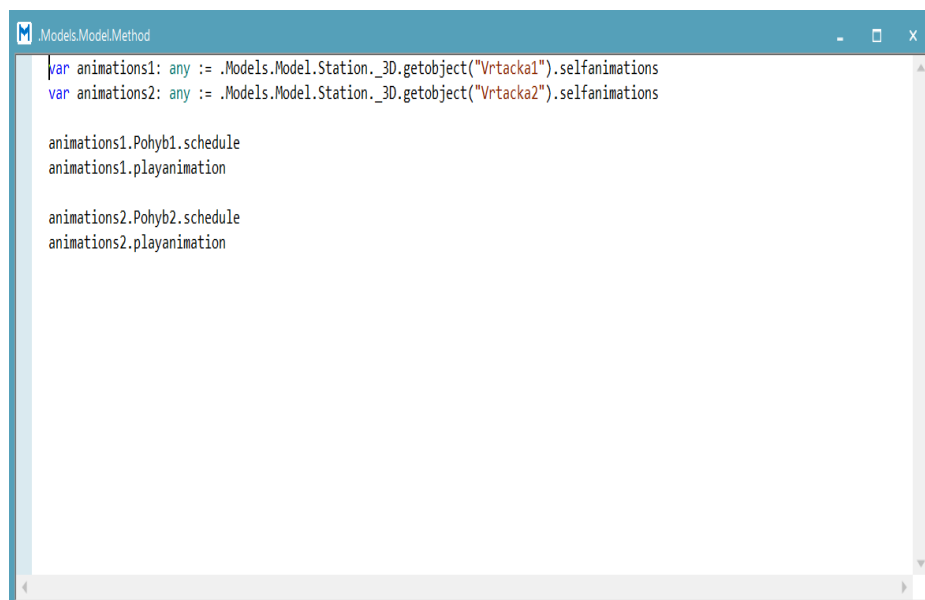


Figure 7. A look at a method designed to animate a machine

Fig. 8 shows a simple workplace for drilling into wood. For the program Tecnomatix plant Simulation it is necessary to create an input, the picture shows the left part and the output, which is shown in the right part. The inputs and outputs themselves would not matter; it is necessary to connect them with the production equipment. The method must also be inserted into the machine's graphical interface for the animation model itself to work.

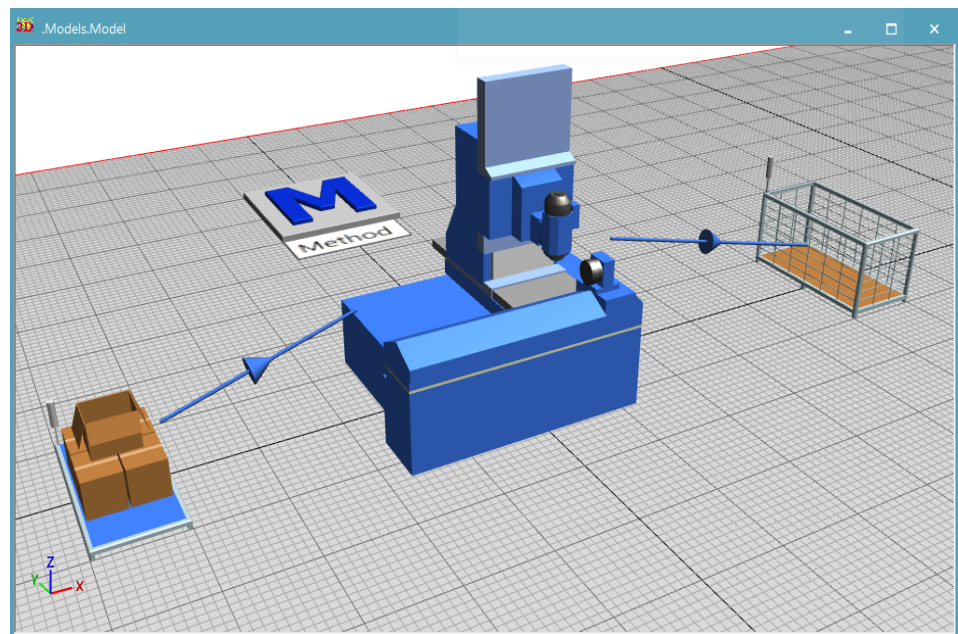


Figure 8. Interconnection of inputs and outputs in the Tecnomatix Plant Simulation program

The last slide shows a functional model that performs the functions shown by the method. The model is functional and can be tested by running a simulation.

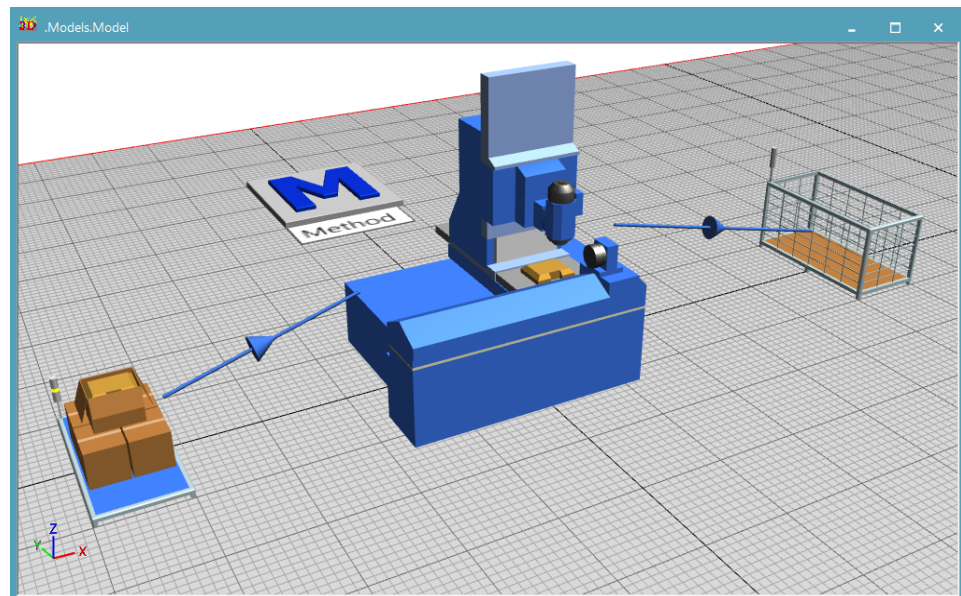


Figure 9. Simulation model running

5. Conclusions

At the end of my article, we would like to evaluate the results. The simulation complemented by the animation of 3D objects is significantly improved. The movement of the parts of the production equipment that are to perform the movement in the real environment using animation perform the appropriate movement. However, we ran into several problems creating this article and the simulation itself. When adding models, we used the library that the Tecnomatix Plant Simulation program contains. Models form tree groups, and some groups are interconnected so that if one part is to move, the other must move, even if the other part is not moving. After consulting with a SOVA employee, we stated that the division of tree groups is not possible. Another problem was adding models from

the program environment. If the simulation author has their machines, they need to be added in the correct format, specifically in .s3D or .jt format. The first format mentioned is a problem with this type of file, it is not commonly available. 3D modeling programs such as SolidWorks or Inventor Professional do not offer the option to select this type of format. The last shortcoming is the need to create a method where a problem may arise for insufficiently trained staff. Ultimately, the animation is a nice improvement to the simulation, but you need to have the proper knowledge of creating animations in Tecnomatix plant Simulation.

Acknowledgments: This article was created by the implementation of the grant project VEGA 1/0438/20, KEGA 001TUKÉ-4/2020, APVV-17-0258, and APVV-19-0418.

References

1. Trebuňa, P.; Aplikácia vybraných metód modelovania a simulácie v priemyselnom inžinierstve; Publisher: Strojnícka fakulta Technická univerzita v Košiciach; Edícia vedeckej a odbornej literatúry; Slovensko 2017; ISBN: 978-80-553-2835-5.
2. Bangsow, S.; Tecnomatix Plant Simulation, Modeling and Programming using Examples; Publisher: Springer; Switzerland, 2015; ISBN: 978-3-319-19502-5.
3. SOVA DIGITAL: Typy Tecnomatix/Výroba a logistika - Animácie 3D objektov v Plant Simulation, 2016 [Online]; Dostupné na internete: < https://www.youtube.com/watch?v=QV-52E4BAa4&list=LL&index=1&ab_channel=SOVADigitala.s.>
4. TREBUŇA, P., PEKARČÍKOVÁ, M., KLIMENT, M., TROJAN, J.: Metódy a systémy riadenia výroby v priemyselnom inžinierstve. Košice: TU v Košiciach, Strojnícka fakulta: Univerzitná knižnica, 2019. ISBN 978-80-553-3280-2.

Novus Scientia 2022

Zborník príspevkov z XVIII. Medzinárodnej vedeckej konferencie doktorandov
strojnícckých fakúlt technických univerzít a vysokých škôl

Názov: Novus Scientia 2022

Editor: © prof. Ing. Ján Slotá, PhD.

© Ing. Viktória Krajňáková, PhD.

© Ing. Jaroslav Melko

Vydavateľ: Technická univerzita v Košiciach,
Strojnícka fakulta, Letná 9, 042 00 Košice

Rok: 2022

Vydanie: prvé

Náklad: 70

Rozsah: 345

Miesto konania: Strojnícka fakulta, Technická univerzita v Košiciach

Dátum konania: 20.01.2022

ISBN 978-80-553-4085-2